Diss ETH No. 14421

STRUCTURAL AND GEOCHRONOLOGICAL STUDY OF THE LOWEST KOHISTAN COMPLEX, INDUS KOHISTAN REGION IN PAKISTAN, NW HIMALAYA

Gerold Zeilinger

Diss ETH No. 14421

STRUCTURAL AND GEOCHRONOLOGICAL STUDY OF THE LOWEST KOHISTAN COMPLEX, INDUS KOHISTAN REGION IN PAKISTAN, NW HIMALAYA

A dissertation submitted to the
SWISS FEDERAL INSTITUTE OF TECHNOLOGY ZURICH
for the degree of Doctor of Natural Sciences

Presented by Gerold Zeilinger
Diplom Geologe, Geologisches Institut der Universität Tübingen, Germany
Born November 21, 1968
Citizen of Germany

Accepted on the recommendation of

Prof. Jean-Pierre Burg	ETH Zürich	Referee
Prof. Lothar Ratschbacher	TU Bergakademie Freiberg	Co-referee
Prof. Urs Schaltegger	Université de Genève	Co-referee

Zürich, 2002

"Wenn ich nun aber eben diese Spalten und Risse als Buchstaben behandelte, sie zu entziffern hätte, sie zu Worten bildete und sie fertig zu lesen lernte, hättest du etwas dagegen?"

Johann Wolfgang von Goethe

(aus Wilhelm Meister)

Acknowledgements

Many colleagues and friends helped me during the time of my studies with their advice and collaboration. I especially would like to express gratitude to my supervisor Prof. Jean-Pierre Burg for his scientific advice. I am also very thankful to Laurent Arbaret, with whom I spent nearly half of my field-seasons, for all the helpful discussions, his scientific input and the permission to include our paper in this thesis. I am equally in debt to Urs Schaltegger for his experience in U/Pb dating, resulting in remarkable precise ages, the helpful discussions and also for allowing me to include our submitted paper in this thesis.

Especially, I would like to thank Robert Anczkiewicz for his help at the beginning of the project, for numberless discussions and sharing with me his experience on the ISZ during a field trip.

I wish to acknowledge our collaboration with Prof. Nawaz Chaudhry, University of the Punjab in Lahore, and Shahid Hussain and Hamid Dawood from Pakistan Museum of Natural History in Islamabad. Their assistance and support in dealing with the Pakistani authorities was crucial. I am also in debt to my driver Nadim for his experienced driving in the field.

I am in great debt to Jean-Louis Bodinier, University of Montpellier, for his scientific input and his help in the interpretation of the geochemical results. Peter Ulmer, Othmar Müntener and Jacques Martignole, University of Montreal, for help and advice in Petrology and Geochemistry.

I am thankful to Diane Seward and Vroni Gubler for Fission Track dating and Neil Mancktelow for helpful discussion, not only during a common field trip in Kohistan.

I would like to thank Bernard Célérier, University of Montpellier, for providing and introducing me to his paleostress analysis software, Martin Brändli for his GIS support, Edwin Gnos for the support during microprobe analyses at the University of Bern and Urs Gerber for perfect scans and photographs.

I wish to express my gratitude to Prof. Lothar Ratschbacher, University of Freiberg, and Prof. Wolfgang Frisch, University of Tübingen, for the support during my application for a doctoral position at ETH Zürich.

The project was financially supported by the Swiss National Found and ETH.

Last but not least I am very thankful to Alexandra Mauler, Giulio Viola, Paolo Garafolo, Auke Barnhoorn, Martin Schmocker, Luigi Burlini, Karsten Kunze, Misha Bystricky and office mate Laurent Desmurs for their friendship and all the other colleagues in the institute for providing a great atmosphere.

Ich möchte an dieser Stelle meinen Eltern und meinen beiden Brüdern ganz herzlich danken, die mich während meiner ganzen Studienzeit stets unterstützt haben.

CONTENTS

ABSTRACT

A northward dipping subduction active during Mid Cretaceous times began producing a volcanic arc prior to 100 Ma. This volcanic arc was installed on the oceanic crust somewhere in the Tethys around the equatorial zone: The Kohistan Arc Complex (KAC), now located between the Eurasian and Indian Plates, is bounded by two major suture zones, the Indus Suture Zone (ISZ) at its southern border and the “Northern Suture” at its northern border, and thus part of the NW Himalayan collisional system.

This research work aimed at elucidating two main questions: (1) Is there a fabric in the mid-crustal plutons that is related to the kinematics of the subduction system and (2) which deformation mechanisms were involved during the arc evolution. To constrain the geological setting, detailed mapping and structural traverses were carried out in the Indus region of NW Pakistan. Petrological and geochemical analyses were conducted on key lithologies to identify the magma origin and the metamorphic evolution. Geochronological measurements were carried out to provide time constraints on the magmatic (U/Pb on zircon) and exhumation (Fission Track on zircon and apatite) histories. Structural analysis of shear zones and paleostress analysis on faults document the deformation history of the southern (and former lower) part of the KAC.

The base of the arc is characterized by the mantle – crust transition between an ultramafic sequence at its bottom and a granulitic gabbro above. The overlying Metaplutonic Complex comprises sheared gabbros to diorites (e.g. Sarangar Gabbro in the Patan region) and a sequence composed of imbricate (meta-) gabbroic, dioritic, granitic and tonalitic rocks intruded in a crustal sequence. The Granulitic and Sarangar gabbros intruded the arc at its base at pressures of at least ca. 1.0 – 1.2 GPa under high temperature > 1000 °C. Strain localisation took place continuously from magmatic emplacement to solid state deformation during cooling of the plutons and formed 3 successive sets of shear zones. Set 1, composed of associated discrete Riedel and shear zones developed above solidus conditions during SW-ward thrusting. Continuous deformation from solidus (granulite facies conditions at ca. 800 °C and ~1.1 GPa) to amphibolite facies conditions of ~600 °C and ~0.8 GPa between 99 and 83 Ma formed the set 2 shear zones. The lower amphibolite facies set 3 shear zones (at ca. 550 °C and ~0.4 GPa) are differentiated by strain within thicker and retrograde mylonitic zones. The anastomosing pattern of shear zones described here probably represents arc-related deformation during subduction of the Tethys oceanic lithosphere below the KAC, because it is older than the collision between the arc and the Indian plate and most likely older than the collision of the arc with Eurasia along the “Northern Suture”.

The subduction related magmatism produced during 99-92 Ma the series of the above mentioned gabbros, diorites and granites with a calc-alkaline to tholeiitic character. The geochemical signature is similar to that of modern arc systems (e.g. Tonga, New Hebrides and Mariana). They were generated by partial melting of mantle with MORB-type Hf isotopic characteristics (εHf = +14). The formation of granites could be the result of partial melting at the base of the arc, a process which would efficiently remove and transport upward granitic components from the root of the arc. Extensional magmatism, 85 Ma ago (emplacement age of the Chilas Complex) tapped a more fertile mantle source (εHf = +10). Remelting of the deep base of the arc 82 Ma ago resulted in felsic peraluminous dykes, which again show MORB-type Hf isotopic compositions inherited from the initial rocks. A diorite intruded ca. 1865 Ma ago in the Indian Plate (at Duber Bazar) and represents a within plate pluton, unrelated to the arc history. The isotopic and geochemical results of analysed rocks indicate that the arc development is characterized by changes in melt source region and by processes of melt extraction and re-enrichment, leading to a maturation from a basic towards a more felsic composition of the arc crust.

After ca. 83 Ma further cooling and decompression (exhumation) took place. The zircon FT ages at the Indus valley are, in the footwall of today's ISZ geometry ~23 Ma and in the hanging wall ~42 Ma. This indicates, that the change from reverse to normal faulting at the ISZ was not later than 23 Ma. Normal faulting outlasted the termination of extension of ISZ segments elsewhere as is suggested by apatite FT ages (~3.7 Ma for the footwall and ~10 Ma for the hanging wall). This relatively young differential movement here across the ISZ is a local phenomenon caused by the growth of the "Besham Syntaxis", a possible small-scale equivalent to the Nanga Parbat "Syntaxis". This local phenomenon is most likely "decoupled" from the dynamic evolution during late, brittle deformation within the southern KAC. There, the dynamic evolution is characterized by a general N–S compression, disturbed by an E–W compression, tentatively related to the formation of the nearby Nanga Parbat "Syntaxis" and subsequent radial extension.

ZUSAMMENFASSUNG

Der Kohistan-Inselbogen-Komplex (KAC), ein ehemaliger vulkanischer Inselbogen, hat sich vor mehr als 100 Ma über einer in der Mittleren Kreidezeit initiierten Subduktionszone entwickelt. Dieser vulkanische Inselbogen bildete sich auf der ozeanischen Kruste der Tethys in äquatorialen Breiten. Der KAC befindet sich heute zwischen dem Eurasischen Kontinent und der Indischen Platte und ist durch zwei grosse Suturzonen begrenzt. Die Indus-Sutur-Zone (ISZ) bildet die südliche, die sogenannte Nördliche Sutur die nördliche Begrenzung des KAC. Der KAC ist ein in das NW Himalaja Kollisionssystem mit einbezogener ehemaliger vulkanischer Inselbogen.

Diese Studie beabsichtigt zwei wichtigen Fragen zu erörtern: (1) gibt es in den Plutonen des unteren bis mittleren Krustenstockwerks Strukturen, die im Zusammenhang mit der Kinematik einer Subduktion stehen und (2) welche Deformationsmechanismen wirken bei der Inselbogenentwicklung. Neben einer detaillierten geologischen Kartierung des Indus Gebiets im Nordwestens Pakistans wurden auch strukturgeologische Profile angefertigt, um den geologischen Aufbau festzulegen. Anhand petrologischer und geochemischer Analysen wird der Ursprung der Magmen und die metamorphe Geschichte dargestellt. Geochronologische Untersuchungen zeigen die magmatische Geschichte (U/Pb an Zirkon) und Exhumation (Spaltspurendatierung an Zirkon und Apatit) des südlichen KAC. Mit Hilfe von Strukturanalysen der Scherzonen und Paläospannungs-Analysen an Sprödbrüchen wurde die Deformationsgeschichte im südlichen (und ehemals unteren) Teil des KAC rekonstruiert.

Die Basis des Inselbogens ist charakterisiert durch einen Mantel – Kruste Übergang mit einer ultramafischen Sequenz im unteren und einem granulitischen Gabbro im oberen Bereich (Jijal Komplex). Der darüber folgende Metaplutonische Komplex besteht aus duktil verformten Gabbros und Dioriten (z.B. Sarangar Gabbro in dem Gebiet von Patan) und einer Abfolge imbrikierter (Meta-) gabbroischer, dioritischer, granitischer und tonalitischer Gesteine, die in eine Krustenabfolge intrudiert sind. Der granulitische und der Sarangar Gabbro sind unter Druckbedingungen von mindestens 1.0 – 1.2 GPa und Temperaturen >1000 °C an der Basis des Inselbogens intrudiert. Hier erfolgte eine kontinuierliche Lokalisierung der Verformung während der Abkühlung der Plutone. Von der magmatischen Inplatznahme bis hin zu Deformation im festen Zustand bildeten sich drei aufeinanderfolgende Scherzonen-Sets. Set 1, gebildet aus assoziierten diskreten Riedel- und Überschiebungs- Scherzonen, entwickelte sich oberhalb der Solidus-Bedingungen während einer SW gerichteten Überschiebung. Set 2 wurde durch eine kontinuierliche Verformung vom festen Zustand unter granulitfaziellen Bedingungen von ca. 800 °C und ~1.1 GPa hin zu amphibolitfaziellen Bedingungen von ca. 600 °C und ~0.8 GPa zwischen 99 und 83 Ma gebildet. Die Scherzonen der unteren Amphibolitfazies (ca. 550 °C und ~0.4 GPa), Set 3 sind durch eine Verformung innerhalb von mächtigen und retrograden Mylonitzonen gekennzeichnet. Das hier beschriebene anastomosierende Muster der Scherzonen ist älter als die Kollision zwischen dem KAC und der indischen Platte und höchstwahrscheinlich auch älter als die Kollision entlang der Nordlichen Sutur und spiegelt folglich die Subduktion ozeanischer Lithosphäre der Tethys unter dem KAC wider.

Der mit der Subduktion zusammenhängende Magmatismus produzierte zwischen 99 und 92 Ma die zuvor bereits genannte Serie von Gabbros, Dioriten und Graniten mit kalk-alkalischen bis tholeiitischen Charakter. Ihre geochemische Signatur ist vergleichbar der moderner Inselbogensystemen (z.B. Tonga, Neue Hebriden und Marianen). Die Gabbros, Diorite und Granite wurden durch teilweise Aufschmelzung des Mantels, der eine MORB typische Hf Isotopensignatur von εHf = +14 anzeigt, generiert. Die Bildung der Granite kann aber auch das Ergebnis einer teilweisen Aufschmelzung der Basis des Inselbogens sein, ein Prozess, der sehr effizient granitische Komponenten von der Basis des Inselbogens entfernt und sie im Inselbogen weiter nach oben transportiert. Extensionaler Magmatismus (Intrusion des Chilas Komplexes) hat eine fertilere Mantelquelle (εHf = +10) angezapft. Wiederaufschmelzung der Basis des Inselbogens vor ca. 82 Ma resultierte in felsischen, peraluminischen Gängen, die wieder eine vom initialen Magmatismus vererbten MORB typische Hf Isotopensignatur von εHf = +14 anzeigen. Erste geochemische Ergebnisse deuten darauf hin, dass die Inselbogenentwicklung durch Wechsel in den Ursprungsregionen der Schmelzen und durch Prozesse wie Schmelzextraktion und Wiederanreicherung charakterisiert ist. Die beiden letztgenannten Prozesse führten zu einer Reifung des urpsrünglich von basischen Gesteinen dominierten Inselbogenkruste hin zu einer vermehrten felsischen Zusammensetzung.

Ab ca. 83 Ma erfolgte eine weitere Abkühlung und Dekompression (Exhumation) des Metaplutonischen Komplexes. Die Spaltspurendatierung an Zirkonen ergab im Indus Tal im Liegenden der heutigen Geometrie der ISZ ~23 Ma und im Hangenden ~42 Ma. Das deutet darauf hin, dass die abschiebende Bewegung entlang der ISZ spätestens vor 23 Ma einsetzte. Die Abschiebung überdauerte hier in ihrer Aktivität die Extension entlang anderer Teilstücke der ISZ, wie aus der Spaltspurendatierung an Apatit (~3.7 Ma im Liegenden, ~10 Ma im Hangenden) hervorgeht. Diese junge differentielle Bewegung an der ISZ ist hier eine lokale Erscheinung, die mit dem Wachstum eines wahrscheinlich kleinräumigen Äquivalents der Nanga Parbat „Syntaxe“ einhergeht. Diese lokale Erscheinung ist wahrscheinlich von der dynamische Entwicklung während der späten, spröden Deformation innerhalb des südlichen KAC unabhängig. Die dynamische Entwicklung ist hier durch eine generelle N – S Einengung gekennzeichnet, die durch eine, wahrscheinlich auf die Bildung der Nanga Parbat „Syntaxe“ zurückzuführende E- W Kompression und darauffolgender radialer Extension gestört wurde.

Die vorliegende Studie zeigt, dass es Deformationsstrukturen an der Basis eines Inselbogens gibt, die im Zusammenhang mit der Kinematik einer Subduktion stehen. Die Lokalisierung der Verformung ist dabei verantwortlich für das anastomosierende Muster der Scherzonen.

1. INTRODUCTION

1.1 AIMS AND PROJECT BACKGROUND

This thesis is part of the research project # 20-49372.96 supported by the Swiss National Science Foundation. The project was a three-year interdisciplinary investigation to understand the deformation processes in volcanic arc systems during subduction. Two main questions were raised: 1) Is the mid-crustal fabric in deformed plutons related to the kinematics of the subduction system rather than collision and 2) which deformation mechanisms were involved during the arc evolution?

To answer these questions, the Kamila Shear Zone (Treloar *et al.*, 1990) was chosen as a case history. The aim of this thesis is to provide the regional setting and specify the geological history of the southern part of the Kamila shear zone in the Kohistan Arc Complex (KAC). Several methods were used, including detailed mapping, structural traverses, microstructural analysis, petrological analysis and geochronology.

1.2 GEOGRAPHIC OUTLINE OF THE STUDY AREA

The investigated area is located in NW Pakistan along the Indus, Kandiah and Natai valleys in the Kohistan area, N of Besham (Fig. 1.1). The central part covers a ca. 50 km long NE – SW area stretched from Duber Bazar (ca. 12 km N of Besham) in the SW to Dasu in the NE along the Karakorum Highway, which provides extraordinarily good and unweathered outcrops and a complete section through the crust of a former island arc (Tahirkheli *et al.*, 1979; Bard, 1983; Coward *et al.*, 1986). With extension of mapping into the smaller tributary valleys to the Indus River, the mapped area covers 2000 km^2. The morphology is characterised by steep slopes and gorges. Only few small plains, build up of quarternary river alluvium occur. Vegetation is generally sparse and localised on gentler slopes. Dense forests may be found in an altitude range of 2000 to 3500 m. In populated regions terrace cropping, mainly corn, is intensive.

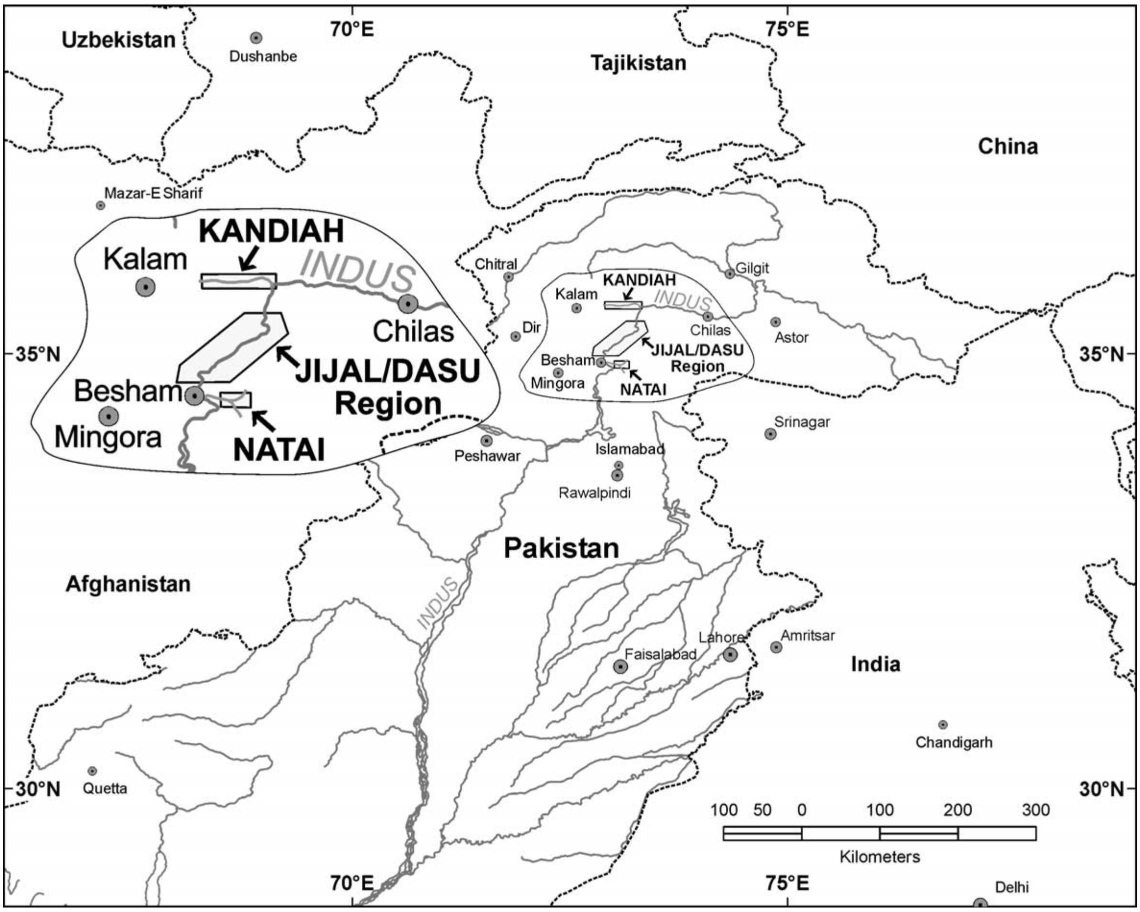

Fig. 1.1: Location of investigated areas (squared) in NW Pakistan. The main part extends along the Indus River north of Besham.

1.3 Tectonic Gross structure of the Himalaya and Geological Overview

1.3.1 Tectonic Evolution of the Himalaya

The break-up of Gondwana and subsequent opening of the Tethys was followed by subduction and northward drift of the Indian plate. The Indian subcontinent separated ca. 130 Ma ago from Gondwana (Johnson *et al.* 1976). The northward drift of the Indian plate can be divided into three different phases (Patriat & Achache, 1984): 1) relative drift velocity between Asia and the Indian plate of 15 – 20 cm/yr between 83 – 52 Ma; 2) relative drift velocity of less than 10 cm/yr between 52 – 36 Ma and 3) relative drift velocity of less than 5 cm/yr since 36 Ma. For the time span between 52 and 36 Ma the drift direction changed several times. The reduction of drift velocity around 52 Ma is attributed to the collision between the Indian plate and Asia. Precise timing of the collision is under discussion and ranges from 40 – 55 Ma based on paleomagnetic data

(Royer *et al.*, 1992; Klootwijk *et al.*, 1985) and goes up to ca. 65 Ma indicated by intercontinental migration of fauna (Jaeger *et al.*, 1989).

The paleogeographic position of the Kohistan Arc (Fig. 1.2), an intraoceanic island arc developed above the subduction zone, is conjectural. Nevertheless, existing data constrain the mid-Cretaceous position of the Kohistan Arc around the equatorial zone and close to the southern marginal terrane (Karakoram block) of the Eurasian continent (Yoshida *et al.*, 1996). At the same time, the Tajikistan and Tarim basins within Eurasia were located more than 2000 km to the north of the Kohistan Arc and Karakoram block (Yoshida *et al.*, 1996). Therefore a large convergence occurred between the terranes forming today the southern Eurasian continent (Molnar & Chen, 1978; Chen *et al.*, 1993). The Indian plate was, during this time, in the southern hemisphere (Klootwijk *et al.*, 1986a,b). In Middle Eocene times there is no significant difference in paleolatitudes between the Indian plate and the Kohistan Arc (Yoshida *et al.*, 1996) which points to complete suturing along the Indus Suture Zone.

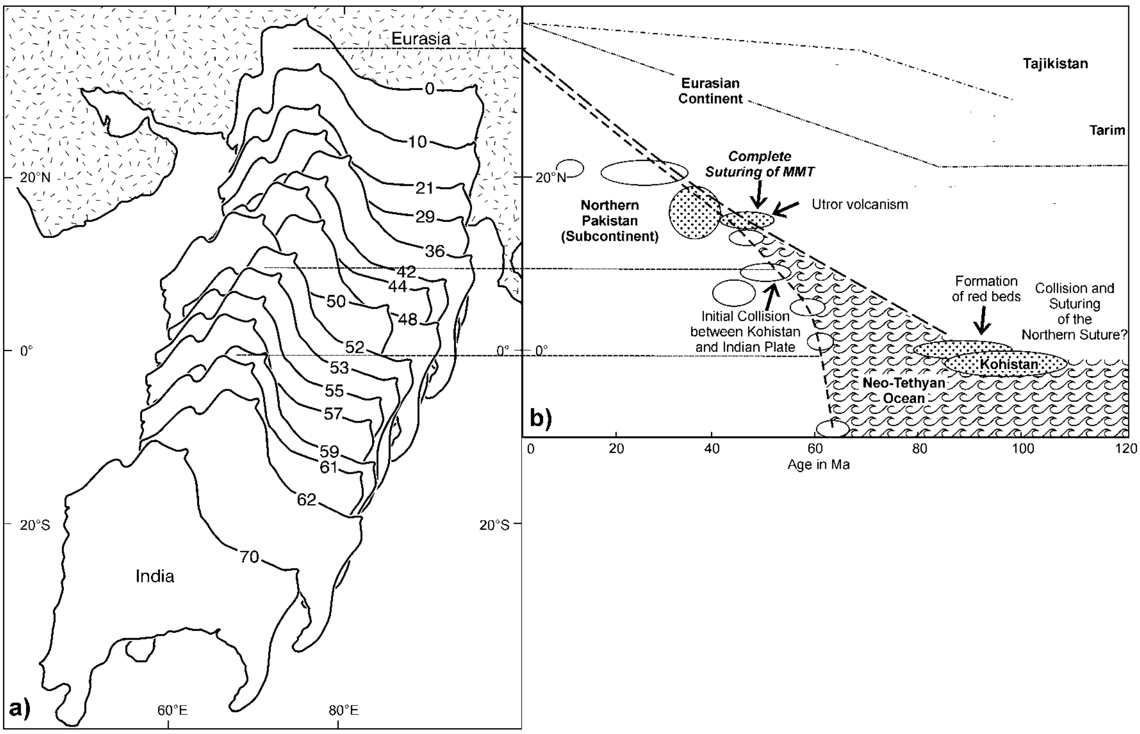

Fig. 1.2: a) Northward drift of India from 70 Ma (after Patriat & Achache, 1984) and b) paleo-latitudes of the Eurasian continent, Kohistan Arc Complex and India calculated and estimated by paleomagnetism (after Yoshida et al. 1996). The stippled lines represent the positions of (from S to N) northern Indian Plate, Kohistan Arc Complex, Tarim and Tajikistan (part of the Eurasian continent). The exact paleo-position of the Karakoram Block N of Kohistan is not known and not displayed. The Karakoram Block was separated from Kohistan by an ocean of unknown extent until 102±12 – 75 Ma (Petterson & Windley, 1985).

The structure of the resulting mountains has been summarised in several publications (e.g. Gansser 1964). From N to S the major tectonic contacts and units in between are:

▲ Indus-Yarlung Tsangpo Suture Zone (IYTSZ)

- The Tethyan Himalaya

▲ Southern Tibet detachment system (STDS)

- The High Himalaya

▲ Main Central Thrust (MCT)

- The Lesser or lower Himalaya

▲ Main Boundary Thrust (MBT)

- The sub-Himalaya

Since the Paleocene a significant amount of shortening, estimated to a maximum of 2000 km (Molnar & Tapponier, 1975; Molnar, 1984) took place between the Tethyan Himalaya and the Indian craton. Estimates based on balanced cross sections give significantly lower amounts of 500 – 700 km of shortening for northwestern Pakistan (Butler, 1986). Malinconico (1989) based his estimates on the remaining crustal volume in the orogen. His crustal model based on gravity profiles can account for a shortening of 570 to 1140 km. Whether the 2000 km of shortening are an overestimate or whether part of the shortening was accommodated by diffuse deformation and/or erosion is still under discussion. It is generally accepted, that a major part of the shortening was absorbed by large scale thrusts like the MCT, MBT and MFT which are parts of the fold-and-thrust wedge within the Indian Plate. The MBT forms, along with the MFT (Main Frontal Thrust) and the MCT a northward dipping decollement horizon which is traced to at least 225 km north of the Himalayan Mountain front at a depth of ca. 50 km beneath South Tibet (Seeber *et al*., 1981). In Pakistan the major tectonic units are slightly different and are, from N to S:

- Karakoram

▲ Northern Suture

- Kohistan Arc Complex (KAC)

▲ Indus Suture Zone (ISZ)

- Indian Plate.

1.3.2 Karakoram

The Karakoram range, of Gondwana affinity (Gaetani, 1997), forms the southern part of Eurasia. It was sutured along the Rushan-Pshart suture zone (Shvolman, 1978; Ruzhentsev & Shvolman, 1981) to the Pamir range during the Late Triassic. Three major subunits are distinguished: 1) The northern Sedimentary belt, 2) The Karakoram Batholith and 3) The southern metamorphic complex. The northern part is formed by unmetamorphosed Ordovician to Cretaceous sediments (Zanchi, 1993; Gaetani *et al.*, 1995). The central part is comprised of calc-alkaline plutons yielding Jurassic to Miocene ages (Searle, 1991). The mid Cretaceous plutons with ages of 95±5 (LeFort *et al.*, 1983) and 105.7±0.5 Ma (Fraser *et al.*, 1999) are related to northward subduction of the north Tethys lithosphere below the Karakoram (Debon *et al.*, 1987). The metamorphic rocks to the S of the Karakoram batholith record 3 phases of metamorphism: Jurassic (?) to lower Cretaceous (andalusite garnet grade), Barrovian type with a minimum age of 37 Ma (Searle, 1991) and contact metamorphism around the 21 Ma old Baltoro plutonic unit (Searle & Tirrul, 1991).

The closure of the Northern Suture (Tahirkheli *et al.*, 1979) is constrained to a minimum age of 75 Ma by the age of undeformed basic dikes which crosscut closure-related fabrics along the Northern Suture zone (Petterson & Windley, 1985).

1.3.3 Kohistan Arc Complex (KAC)

The Kohistan Arc Complex (Fig. 1.3) is sandwiched between the Karakoram terrane to the north and the Indian Plate to the south (Tahirkheli *et al.*, 1979; Bard, 1983; Coward *et al.*, 1986). The eastern limit is formed by the N-S trending Nanga Parbat syntaxis, which is a crustal antiform where the Indus Suture Zone (ISZ) is folded around a half-window of Indian crust (e.g. Treloar *et al.*, 1991a; Burg & Podladchikov, 2000). The syntaxis underwent rapid tectonic denudation and growth during the last 5 Ma (Zeitler *et al.*, 1989, 1993). To the east of the syntaxis, the Ladakh Arc is the eastern equivalent to the Kohistan Arc system. Both Arc Complexes may have represented a single island arc which collided with the southern margin of Eurasia before India collided with the system (Petterson & Windley, 1985; Coward *et al.*, 1986; Pudsey, 1986; Searle, 1991).

The Kohistan Arc Complex comprises Cretaceous and Tertiary igneous and subordinate sedimentary rocks which are divided into several distinct units and groups. They are, roughly from N to S: Yasin Group, Utor and Chalt Volcanics, Oceanic series, Kohistan Batholith, Chilas Complex, Metaplutonic Complex and Jijal Complex. This succession is interpreted as calc-alkaline plutons intrusive into an oceanic crust and overlain by the calc-alkaline lavas and associated sediments. Accordingly, the interpretation is an intra-oceanic arc that developed during the Cretaceous somewhere in the Tethys ocean (Tahirkheli *et al*., 1979; Bard 1983; Coward *et al*., 1986).

1.3.3.1 Yasin Group Sediments

Just to the south of the Northern Suture, the Yasin group consists of interlayered volcanoclastic sediments, volcanites and rather immature turbidites deposited in a deep-water environment (Tahirkheli, 1979, 1982; Pudsey, 1986). At the type locality, Pudsey *et al*. (1985) divided the group into an upper 2000 m thick sequence of shales with interbedded greenstones, probably tuffs, a middle 500 m thick unit with grey slates and distal turbidites and a lower part, consisting of volcano-lithic conglomerate and sandstones, tuffs, slates and rudist limestones with an Albian-Aptian fauna. The lithologies vary laterally. Sedimentation occurred most likely in an intra-arc and/or back arc basin (Pudsey, 1986; Khan *et al*., 1995).

1.3.3.2 Chalt Volcanics

The Chalt Volcanic Group comprises calc-alkaline andesites to rhyolites succeeding to andesitic lavas, tuffs and agglomerates of Early Cretaceous age (Petterson *et al*., 1991a). The Chalt volcanics are locally interbedded with the Yasin group. Low grade metamorphism is characteristic.

1.3.3.3 Oceanic series

To the southwest and within the Kohistan Complex, metasedimentary sequences of marine origin (Dir, Utror and Kalam Groups, Tahirkheli, 1979) yield Eocene fossils in upper-level limestones (Kakar *et al*., 1971; Khan, 1979; Sullivan *et al*., 1993). The Utror volcanics show low grade metamorphism and a variety of rocks similar to Chalt volcanics. Ar-Ar hornblende age for a basaltic flow within the Utror volcanics is 55±2 Ma (Treloar *et al*., 1989a).

1.3.3.4 Kohistan Batholith

The Kohistan Batholith is the principal unit of the Kohistan magmatic arc. It shows at least 3 formative stages (Petterson & Windley, 1991; Petterson *et al*., 1991b): an early suite of gabbro-diorites and trondhjemites formed within an island arc setting between 110 – 85 Ma; the main bulk was formed within an Andean type plate margin and comprises an older gabbro-diorite suite at 85 to 60 Ma and a younger granitic suite, emplaced at 60 – 40 Ma; and a postcollisional magmatism with leucogranitic sills and dikes between 40 and 26 Ma (Petterson & Windley, 1985). Stage 1 and early stage 2 plutons have isotopic signatures characteristic of a mantle derivation. The isotopic signatures of younger plutons show evidence for an increasing crust to mantle ratio, with the latest magmas being crustal derived. This evolution is interpreted as the result of arc thickening and lower arc melting following suturing to Asia (Petterson & Windley, 1991; Petterson *et al.*, 1993).

1.3.3.5 Chilas Complex

The Chilas Complex consists of a large, 8 km thick and 300 km long body of mafic - ultramafic rocks. The bulk rock type is noritic gabbro, locally layered with subordinate diorites. Several lenses of ultra-mafic-anorthosite associations (dunite, pyroxenite and peridotite) are interpreted as tops of mantle diapirs (Burg *et al.*, 1998). Timing for the emplacement of the Chilas Complex gabbronorites relative to the collision of the Kohistan Arc with the Karakoram plate is under discussion. The gabbronorites have intruded the Jaglot schist group to the north and the Metaplutonic Complex to the south. Treloar *et al.* (1996) suggest an emplacement of the Chilas Complex “after suturing” of the Kohistan Arc to the Karakoram Plate due to the low deformation of the Chilas Complex compared to the intruded older units. Granulite facies re-equilibration occurred short after emplacement of gabbronorites at 600 – 800 °C and 0.6 – 0.8 GPa (Jan & Howie, 1980; Bard, 1983). Amphibolite facies shears, related to the southwestward thrusting on a pile of imbricated calc-alkaline laccoliths, have taken place shortly after re-equilibration as indicated by cooling below 500 °C at around 80 Ma (Treloar *et al.*, 1989a) The Chilas complex may have provided the thermal energy for regional metamorphism within the Kohistan arc. Conventional zircon U-Pb age yields an age of ca. 84 Ma reported by Zeitler *et al.* (1981).

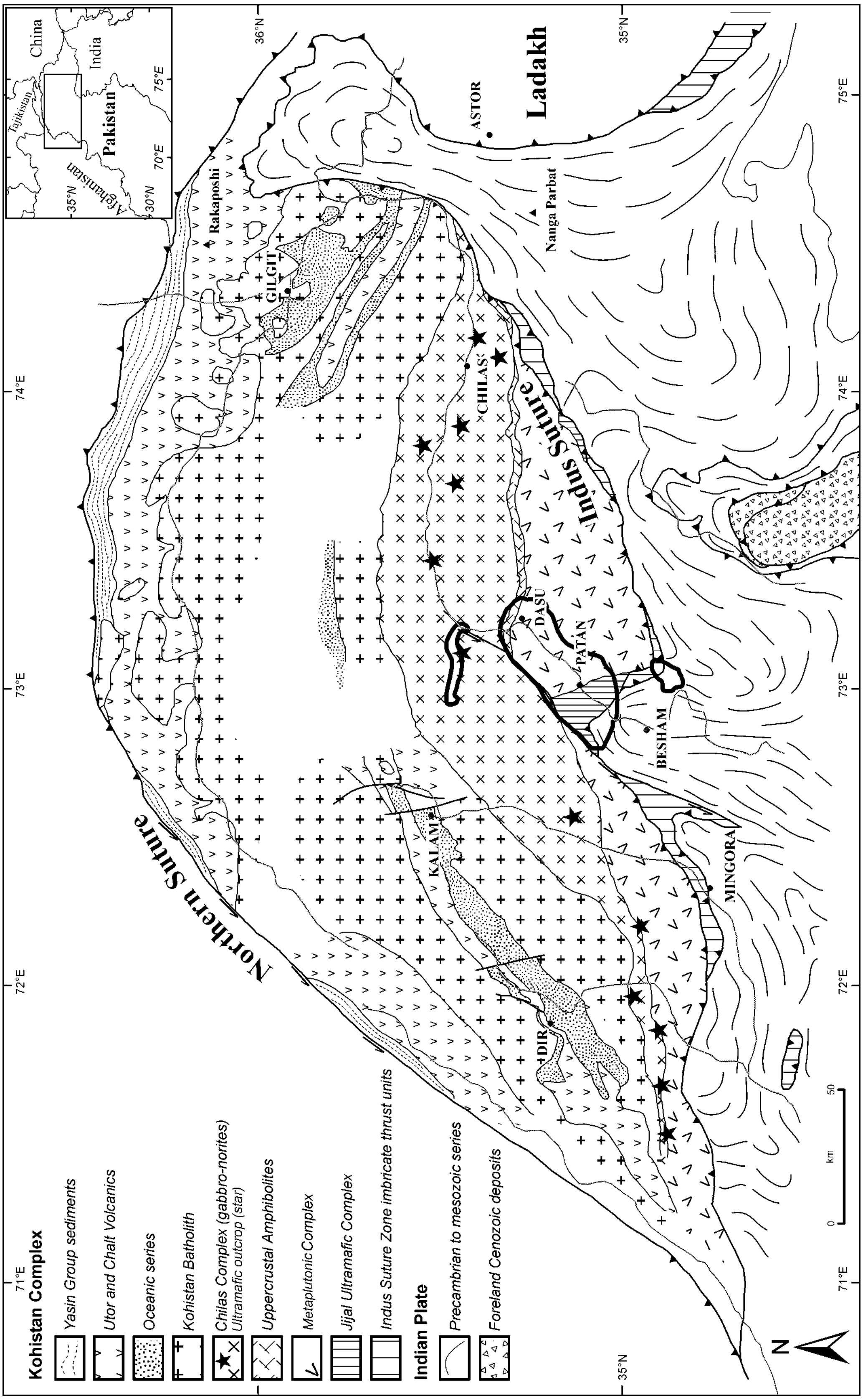

Fig. 1.3: Sketch map of the Kohistan Arc Complex (after Bard, 1983 and Burg et al., 1998). Mapped areas are circled.

1.3.3.6 Metaplutonic Complex

A thick pile of imbricated calc-alkaline laccoliths, metavolcanics and remnants of the Tethyan oceanic crust, variably sheared in amphibolite facies conditions forms the so-called Kamila amphibolite belt located between the Jijal and Chilas Complex (Tahirkheli *et al.*, 1979; Bard, 1983; Jan, 1988; Treloar *et al.*, 1990). The variety of lithologies summarized under the name Kamila amphibolite belt is not well represented by this term. In addition, the Kamila amphibolites s.s. (Treloar *et al.*, 1990), exposed in the region of Kamila, are only one part of the belt. In the Indus area metaplutonic rocks are dominant. The proposed name Metaplutonic Complex summarizes three subunits (Sheared gabbro-diorites, Kiru Sequence and Kamila Sequence) and emphasizes the essentially plutonic origin. Amphibolite facies conditions ended around 80 Ma (Ar-Ar cooling ages on hornblendes cluster, Treloar *et al.*, 1989a, Wartho *et al.*, 1996).

1.3.3.7 Jijal Complex

The Jijal Complex, is composed of more than 3 km thick ultramafic rocks overlain by garnet-plagioclase granulites. The sharp contact between the ultramafic rocks and the overlying granulites, with well preserved igneous structures, is the intrusive contact of lower crustal, calc-alkaline garnet-gabbros (the Granulitic Gabbro) within upper mantle rocks. The contact is also the lower boundary of the arc crust, i.e. the arc-Moho (Burg *et al.*, 1998). The Granulitic Gabbro underwent metamorphism at 750 to 1150 °C and 1.2 to 1.9 GPa (Ringuette *et al.*, 1999) and has later re-equilibrated at >700 °C and 1.5 ± 0.4 GPa (Jan & Howie, 1981), which are pressure conditions similar to those calculated from the underlying, unmetamorphosed ultramafic rocks. Sm-Nd age of the granulite facies assemblage is around 95 Ma (Anczkiewicz & Vance, 2000; Yamamoto & Nakamura, 2000).

1.3.4 Indian Plate

The contact between the Kohistan Arc Complex and the Indian Plate can be observed close to Jijal. In many parts the ISZ comprises a “mélange” with tectonic blocks of ophiolite, blueschists, greenschists, metavolcanics and metasediments (Jan, 1980; Kazmi *et al.*, 1984, Anczkiewicz *et al.*, 1998). The Indian Plate rocks comprise gneisses and Mid Proterozoic diorites belonging to the Besham Group (Tahirkheli, 1979). The Besham group forms a N-S trending antiform, a small-scale equivalent to the Nanga

Parbat Syntaxis (Coward, 1986; Treloar *et al.*, 1989c). Radiometric ages were obtained for an amphibolite sheet within a granite near Duber with Ar-Ar age on hornblende at 1920±24 Ma and for a granite near Duber with K-Ar age on biotite at 550±20 Ma (Treloar *et al.*, 1989a).

1.3.5 Study area: Indus Kohistan Region

The studied area provides a "section" through the lower units of the Kohistan Complex. It also includes part of the northernmost Indian plate. The main focus was given to the geology in the Indus valley and tributary valleys because of the good outcrop situation, accessibility and, the most important fact, the valley cuts the relevant units almost perpendicular to strike (Fig. 1.4).

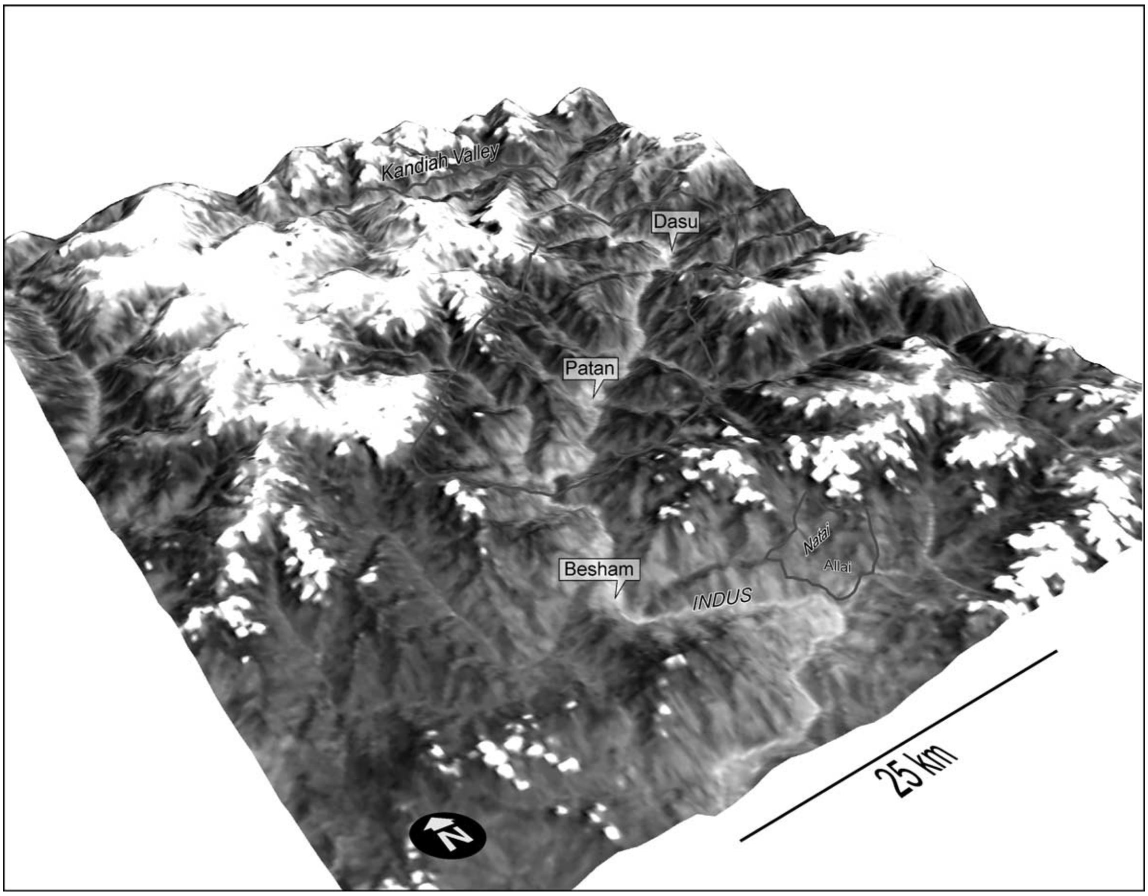

Fig. 1.4: Morphology of the Indus valley and mapped areas. 3D view of Landsat satellite image (Band 1, 2 and 3) was generated using interpolated Gtopo 30 elevation data (original ca. 1000 meter grid was interpolated to a ca. 333 meter grid with kriging method). Altitude is vertically exaggerated by 1.5.

Two more areas were investigated and partly mapped to provide additional information on the units bounding the area of interest: 1) to the N, the Kandiah valley, which screens a central part of the Chilas Complex and 2) to the S the Allai and Natai valleys for getting information on a part of the Indus Suture Zone, where a “mélange” is involved, in contrast to the ISZ at Jijal, where the contact is characterized by a narrow fault zone.

1.3.5.1 Kandiah Valley

The Kandiah is a ca. 30 km E-W striking valley within the Chilas Complex. At the E end the valley joins the Indus valley through a steep gorge, almost at the location where the Indus river bends from an E-W direction to a N-S direction. To the W the valley is terminated by a N-S trending up to 6257m high mountain chain that also builds the natural barrier to the Swat valley and Kalam.

The geology of the Kandiah valley is not mapped in detail. Only few publications and maps describe or provide data from this area. Yamamoto (1993) shows a retrograde metamorphic overprint for the Chilas gabbronorites. P-T estimates are 0.61 – 0.8 GPa and 607 – 720 °C (Yamamoto, 1993) for amphibolite facies assemblages which were later altered to greenschist facies assemblages. The metasediments intruded by gabbronorite in the central part of the Kandiah valley are interpreted as equivalent to the Gilgit metasediments (Searle & Khan, 1993).

1.3.5.2 Natai and Allai Valley

The Natai and Allai valleys are located to the ESE of Besham. The Allai valley forms a ca. 22 km long NW-SE valley northeast to the Indus valley with its NW part parallel to it. The confluence between the Indus valley and the Allai valley is ca. 4 km S of Besham. The ca. 3 km long Natai valley branches off perpendicular to the Allai valley (ca. 14 km upstream) towards the NE to the small village of Pastho. This valley provides a section through the eastern part of the Besham syntaxis.

Detailed studies of the mineralogy and geochemistry of the volcanic series involved in the Indus Suture Zone “mélange” in the Natai valley (Majid & Shah, 1985; Shah & Majid, 1985) describe a variety of lithologies ranging from ultramafic rocks, pillow lavas with associated meta-chert and limestone, greenschist and blueschist facies graywackes and lavas with a tholeiitic affinity. The ISZ is defined by the fault contact (named Shergarh fault by DiPietro *et al.*, 2000) between the “mélange” units and the

Indian Plate rocks and the fault contact between the "mélange" and the Kohistan Arc Complex, referred as Kohistan Fault. Treloar *et al.* (1989b) described the inverted metamorphic zoning in the footwall of the ISZ. The Map presented in chapter 2 is based on own observations completing an unpublished map from Lahmeyer International (Allai Khwar Feasability study, Lahmeyer International, 1998).

1.3.5.3 Jijal Dasu Region

The Jijal Dasu Region is described by several authors and a reasonable quantity of geochemical (e.g. Jan, 1988; Miller *et al.*, 1991; Jan & Windley, 1990) petrological (e.g. Yamamoto & Yoshino, 1998; Yoshino *et al.*, 1998; Ringuette *et al.*, 1999) and geochronological (Treloar *et al.*, 1990; Wartho *et al.*, 1996; Zeitler 1985; Yamamoto *et al.*, 2000; Anczkiewicz & Vance, 2000) data. Mapping is so far concentrated either on small areas like the Jijal Complex (e.g. Miller *et al.*, 1991) or limited to sections along the Karakoram Highway (e.g. Treloar *et al.*, 1990). The area is characterised by the steep Indus gorge and up to 4000 m high mountains. Several tributaries provide additional N-S sections in the Patan area and dominantly E-W stretching sections in the Dasu area.

The area covers two units of the Kohistan Arc Complex: 1) Jijal Complex and 2) "Kamila Amphibolite Belt" (Jan, 1988) or Metaplutonic Complex (defined and treated later for more details). A central feature, from the structural point of view, is the intense shear deformation in the Granulitic gabbro of the Jijal Complex and within the Metaplutonic Complex. The Kamila Shear Zone identified by Treloar *et al.* (1990) separates the Chilas Complex from the ultramafic rocks of the Jijal Complex. This up to 38 km wide zone is well exposed along the Karakorum Highway between Patan and Dasu.

1.3.6 Tectonometamorphic evolution of the Lower Kohistan Arc Complex

The early arc history is recorded in the Lower Kohistan Arc Complex. The following will give a brief summary about the main tectonometamorphic events.

Remnants of the Tethys crust are most likely preserved as fine grained amphibolites for which geochemical analyses suggest that the high Ti content has similarity to N- and E-type MORB (Kahn *et al.*, 1993; Treloar *et al.*, 1996). The subduction zone formed during Mid Cretaceous times and produced the volcanic arc. Dating of the granulite facies assemblage provided Sm-Nd ages of 95±2.7 (Anczkiewicz & Vance 2000), 118±12, 91.0±6.3 and 83±10 (Yamamoto & Nakamura 2000). These ages give the time of cooling below 700 – 800 °C. Anczkiewicz & Vance (2000) also show that parts of the Metaplutonic Complex underwent cooling below 700 – 800 °C at the same time (94.6±5.3 Ma, garnet amphibolite, Swat valley). Based on PT calculations (Yamamoto 1993; Ringuette *et al.* 1999) a major decompression affected the Granulitic gabbro as well as the Metaplutonic Complex (Anczkiewicz & Vance 2000). For the petrogenetic evolution of the Granulitic gabbro essentially two models are proposed: Burg *et al.* (1998) interpreted the Granulitic gabbro as intrusion within mantle rocks, now displayed as the Jijal ultramafics. Ringuette *et al.* (1999) give a similar interpretation, where cumulates emplaced at the base of the oceanic arc-type crust and underwent subsequently sub-solidus isobaric cooling. Yamamoto (1993) instead suggests heating and burial of two-pyroxene granulites during crustal thickening.

N of the Granulitic gabbro a sequence of metabasic rocks (so-called Kamila amphibolites) is representing the lower to mid crustal level of the arc. The origin of these sheared metabasic rocks is discussed. They represent either the oceanic crust on which the island arc was built (Bard, 1980), or they are a highly deformed, arc-type plutons and volcanite with possible ocean floor relics (Coward *et al.*, 1986). Jan (1988) also suggested that essentially metavolcanic amphibolites include rare sediments. Yamamoto (1993) proposed that the Kamila amphibolites are the hydrated equivalents of the Chilas Complex. Geochemical data indicate, that the Kamila amphibolites is comprised of subduction related intrusions, remnants of the oceanic crust and metasedimentary (-volcanic) portions (Khan *et al.*, 1993). The relative proportion of these different rocks varies strongly along strike. In the Indus area the Kamila amphibolites is built up mainly by metamorphosed plutonic rocks (Kazmi & Jan, 1997). Therefore the new term Metaplutonic Complex is suggested to emphasize the essentially plutonic origin. The Metaplutonic Complex includes the Patan sheared Gabbros and Diorites, the Kiru sequence and the Kamila sequence. Only the Kamila sequence is equivalent to the Kamila amphibolites s.s. (Treloar *et al.*, 1990). Metamorphic conditions were 550 – 650 °C and 0.9 to 1.0 GPa (Treloar *et al.*, 1990).

The Metaplutonic Complex was cooled below 500 °C at ca. 76±4 Ma based on Ar-Ar dating of hornblende (Wartho *et al*., 1996).

The metamorphosed plutonic rocks (hereafter called Metaplutonic Complex) and the Granulitic gabbro were intensely sheared, by an impressive anastomosing array of amphibolite facies mylonites within which fabric intensity varies. They were related to the southward propagation of shortening across the Kohistan Complex following suturing with Asia (Treloar *et al*., 1990). Deformation developed under different temperature conditions. High temperature deformation occurred probably in a range of 500 °C to 650 °C (Treloar *et al*., 1990; Yamamoto, 1993). The anastomosing shear pattern began probably to develop during granulite facies conditions short after the magmatic emplacement. A minimum age for the shearing is given by 83±1 Ma (Treloar *et al*., 1990), based on Ar-Ar dating on hornblende grains in a sheared gabbro of the southern Metaplutonic Complex. A K-Ar muscovite age of 66 Ma from a pegmatite that cuts the main shear fabric indicates that post shearing cooling had occurred by 60 Ma (Treloar *et al*., 1989a).

Later deformation below 450 °C shows cataclastic behaviour and greenschist facies rock assemblages. After the collision between the Kohistan Complex and subsequent thrusting onto the Indian Plate a major extensional phase took place. It is recognized from folds that indicate NE directed normal movement. These folds and normal faults are interpreted as collapse structures related to the backsliding of the Kohistan Arc (Burg *et al*., 1996; Vince & Treloar, 1996). The dynamic evolution during later, brittle deformation is represented by four stages chronologically ordered from field evidence as SSE–NNW compression, E–W compression, radial extension and SSW–NNE compression (see chapter 6 for details). The latter corresponds to the present-day stress field defined from seismic activity. The earlier faulting events were active during the Miocene, when convergence-related stresses were disturbed by the formation of the nearby Nanga Parbat and Besham syntaxes.

2. LITHOLOGIES AND STRUCTURES

2.1 TECHNIQUES

Mapping was carried out during 18 weeks of field work (summer 1997, spring 1998 and summer 1998) on Pakistan topographic sheets at a scale of 1:50.000. Landsat 7 ETM images, areal photographs and digital elevation model Gtopo 30 were additionally used for the recognition of lineaments. Outcrop and sample locations were defined with handheld GPS and additional field/map verification. All these data were combined for processing, analysis and map production in the Geographic Information System ArcInfo8/ArcView3.

2.2 MAPPED UNITS

The mapped units are described according to their structural position from the bottom to the top. The units refer to 1) Jijal Dasu region map (Fig. 2.1 and enclosed map), 2) the Allai and Natai valleys (Fig. 2.2), 3) sections for the Jijal Dasu map (Fig. 2.3, Fig. 2.4 and enclosed sections) and the Swat valley (Fig. 2.5). The reconnaissance geological map of the Kandiah valley is provided under subchapter 2.2.3.3 Chilas Complex (Fig. 2.12 and enclosed map).

2.2.1 Indian Plate

The Indian Plate lithologies were mapped along the Indus valley south of Jijal (Fig. 2.1) and in the Allai valley (Fig. 2.2). Immediately south of the northward dipping Indus Suture (see section A-A' in Fig. 2.3, section C-C' in Fig. 2.4 and Swat section, Fig. 2.5), the Indian plate is comprised of Proterozoic, strongly foliated and folded gneisses (IP-Gns). Folds in the mylonitic gneisses (Fig. 2.6a) are NNE trending, recumbent ESE vergent. Their axial plane is sub-parallel to the pervasive foliation and their axes (sub-) parallel to the SW trending stretching lineation. Kinematic determination from rotated feldspar clasts shows a dominant southwestward sense of shear. The gneisses belong to the Besham Group (Fletcher *et al.*, 1986), in a N-S trending open antiform oblique to the SW-ward directed older stretching lineation (Treloar *et al.*, 1989c). In places, the gneisses contain dark xenoliths of amphibolitic composition (Fig. 2.6b). Meta-(grano-) diorites (IP-Dr) are incorporated in these gneisses.

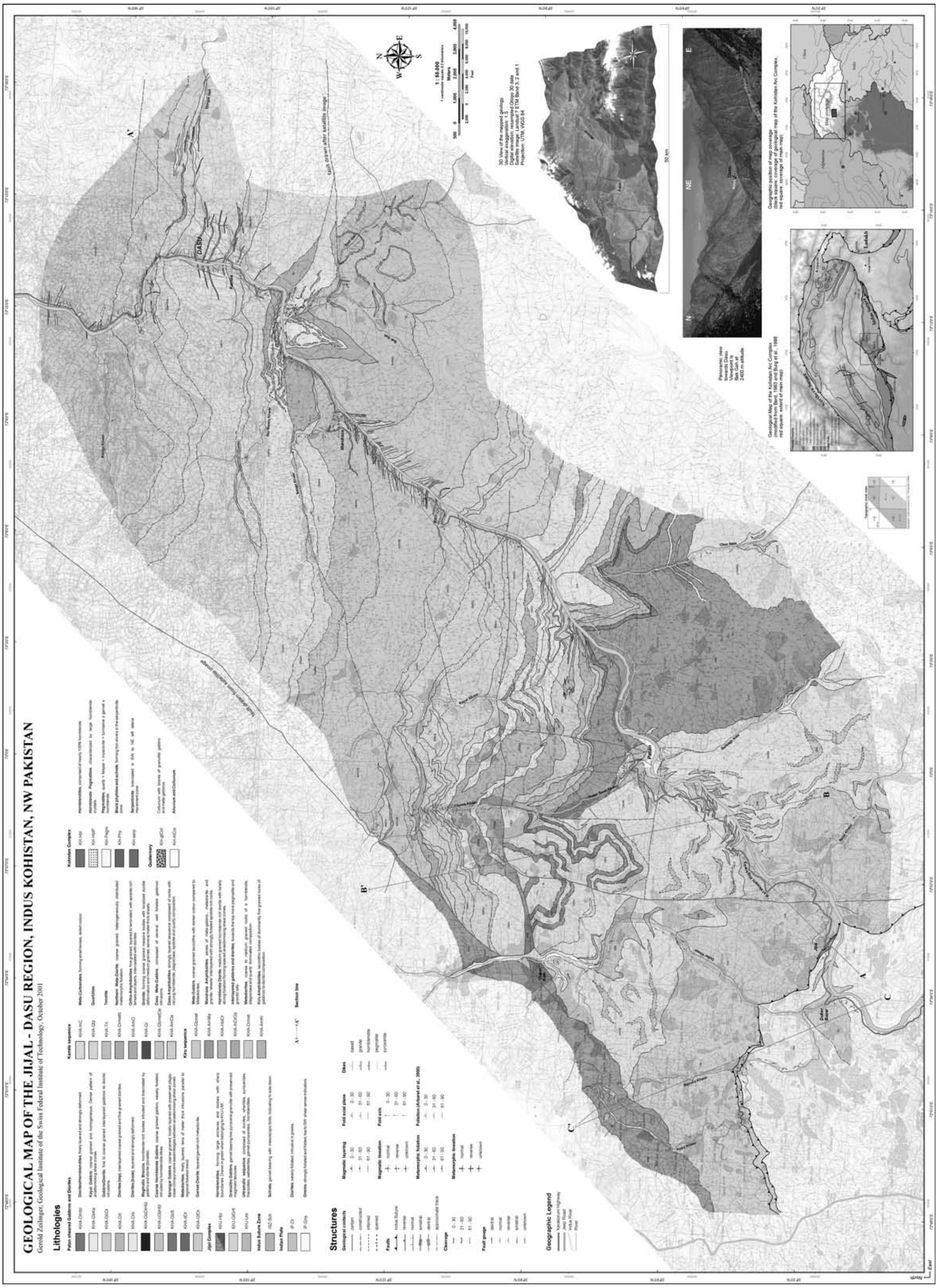

Fig. 2.1: Geological map of the Jijal Dasu region, reduced scale (original scale map is enclosed).

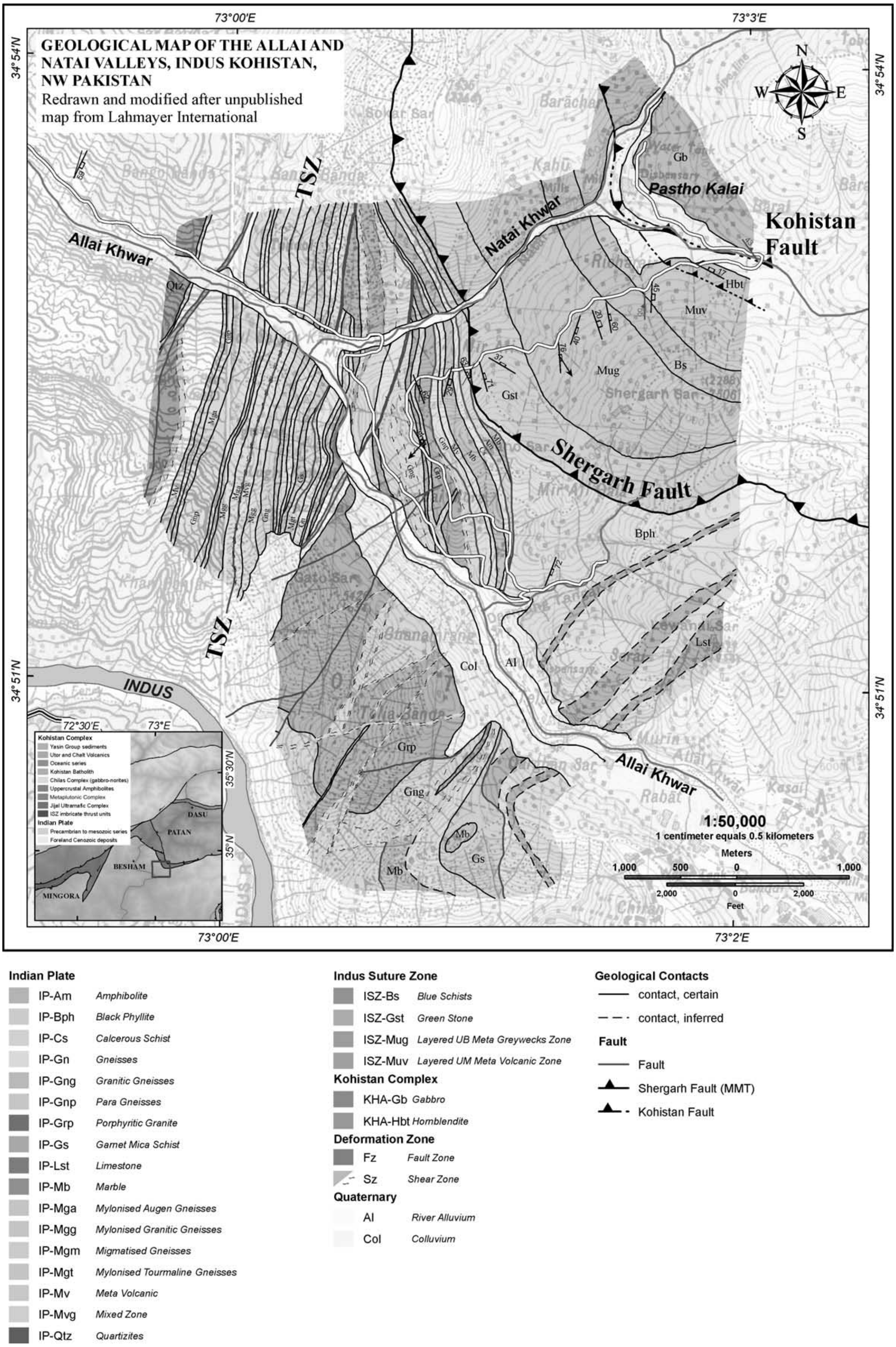

Fig. 2.2: Geological map of the Allai and Natai valleys.

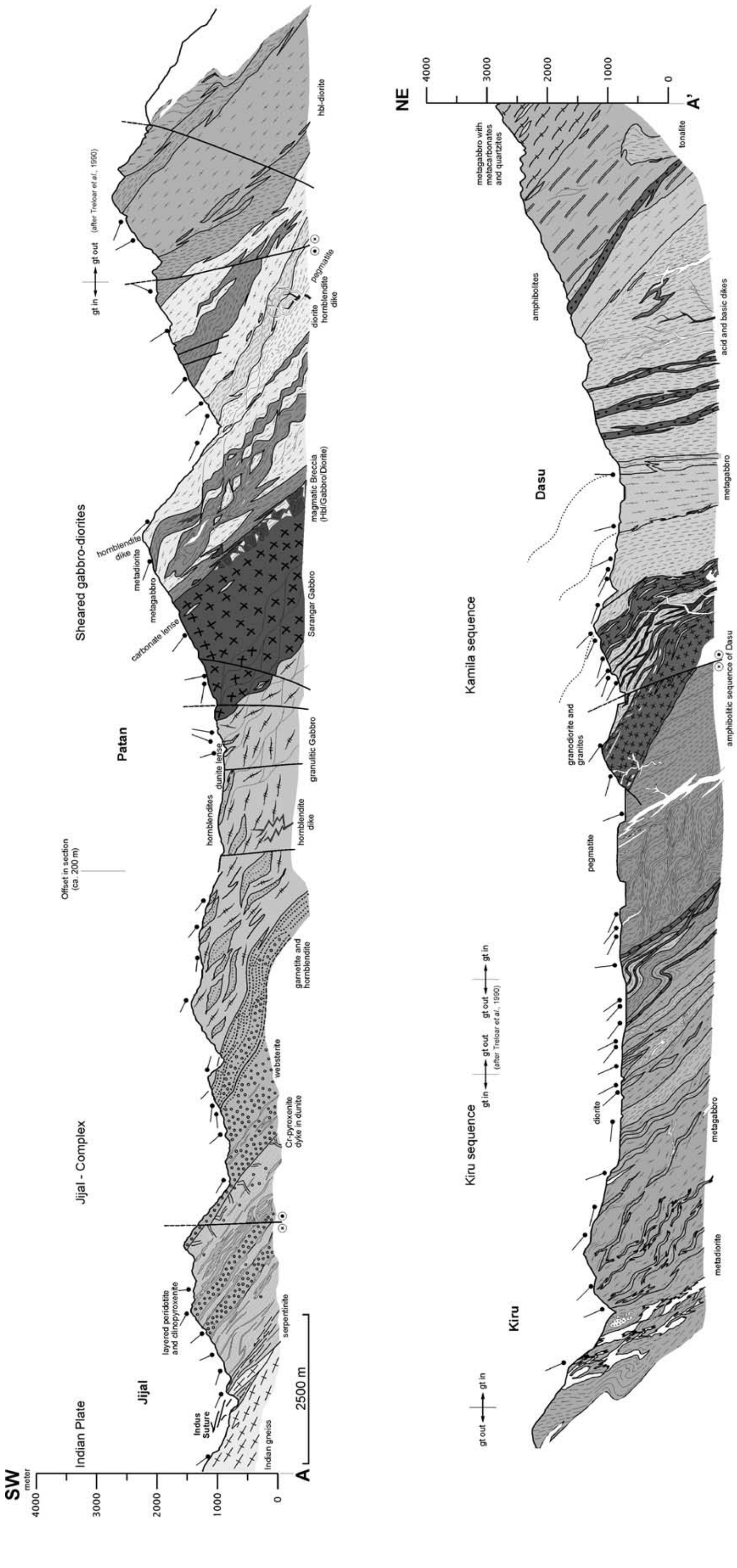

Fig. 2.3: Geological Section A-A' for the Jijal Dasu region, reduced scale (original scale section is enclosed).

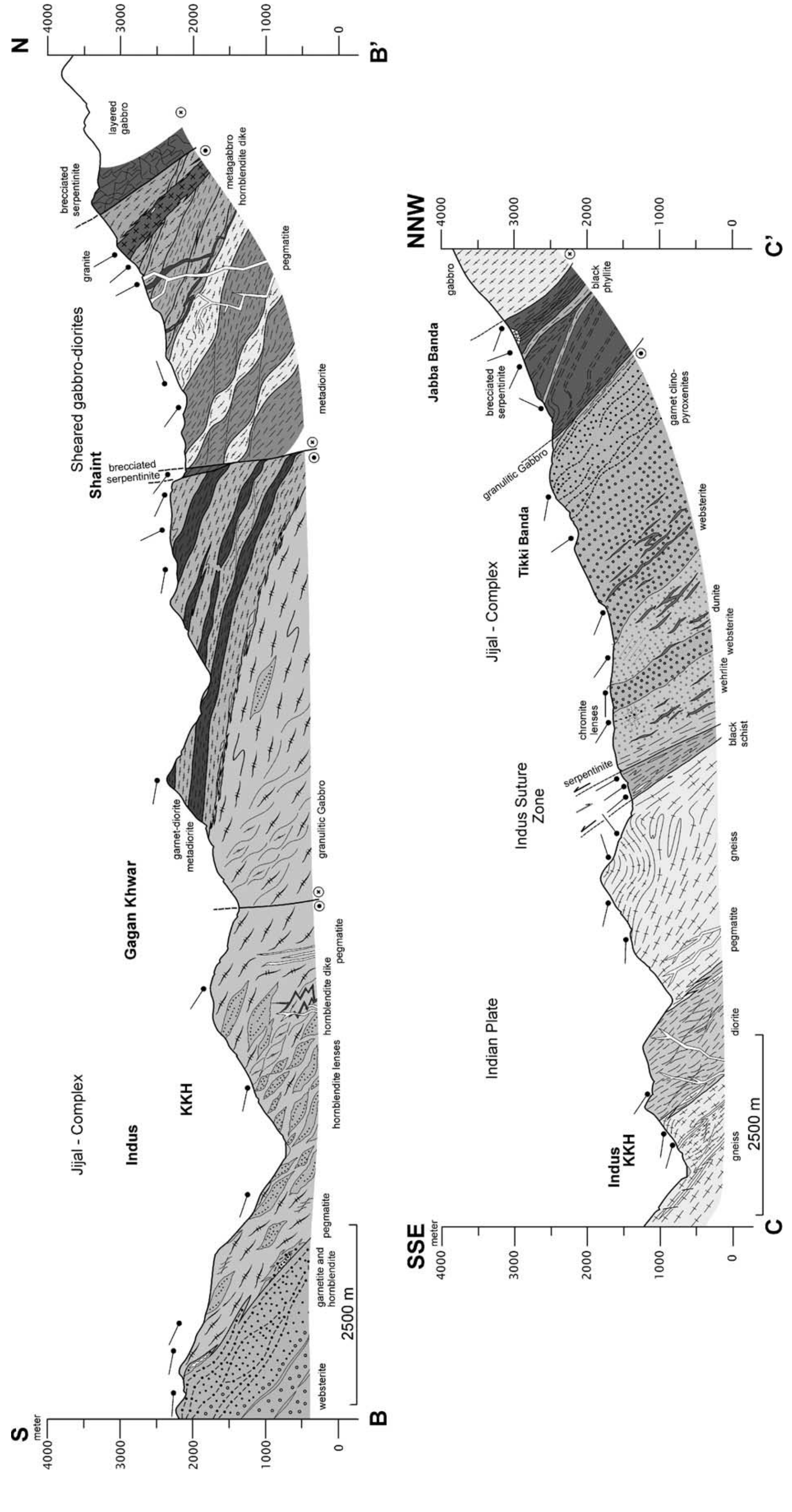

Fig. 2.4: Geological Sections B-B' and C-C' for the Jijal Dasu region, reduced scale (original scale sections are enclosed).

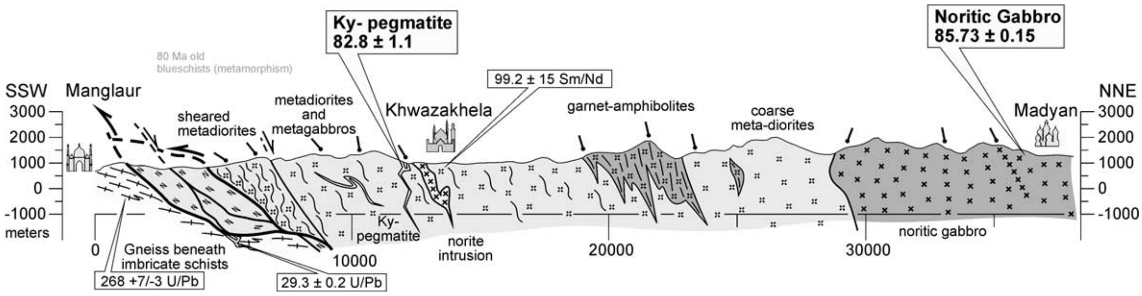

Fig. 2.5: Geological Section Swat valley (ages from Anczkiewicz, 1998; Anczkiewicz & Vance, 2000 and this study in bold).

The dioritic body (Fig. 2.6c) at Duber Bazar (so called Duber Diorite) is composed of:

K-feldspar + hornblende + plagioclase + quartz ± opaque oxides ± zircons ± epidotes.

The magmatic fabric is represented by a weak NE-ward dipping foliation defined by aligned hornblende and in part by a minor compositional layering. A stronger metamorphic fabric is concentrated at the borders of the up to 1000 m thick body. Internally the weak magmatic fabric is bend into occasional steep northeastward dipping reverse sense mylonitic shear zones. Ca. 30-80 cm thick pegmatites are generally undeformed and cut the magmatic foliation and the shear zones, across which they are occasionally slightly bent. Assuming that the shear zones developed during thrusting of the KAC over the Indian plate, intrusion of the pegmatites is late to post kinematic. The pegmatites were cut in places by steep, N-dipping normal faults, possibly related to the backsliding of the KAC along the ISZ (Anczkiewicz *et al.*, 2001).

In the Ranolia Khwar small scale recumbent folds of 1-2 m wavelength (northward plunging fold axis, eastward dipping axial planes) are frequent. Folding affects the gneisses beneath the Indus Suture.

The Allai and Natai Khwar provide a section from the core of the Besham antiform to its eastern limit. Descriptions for the regional geological units are given by several authors (e.g. Calkins *et al.*, 1975; Tahirkheli, 1979). The regional structure is described by e.g. Treloar *et al.* (1989c, 1991a) and DiPietro *et al.* (1999). The following description of units mapped in the Allai and Natai valley is based on own observations and Allai Khwar Feasability study (Lahmeyer International, 1998).

Marble beds are exposed in Natai Khwar directly below the lower ISZ fault contact and mark, together with the inter-layered amphibolites, the northern boundary of the Indian Plate. To the S of the lower ISZ fault contact black phyllites (IPH-Bph) intercalated with Limestone bands (IPH-Lst) are dipping ca. 70° ESE. They are members of the Banna group (Treloar *et al.*, 1989b). The amphibolites (IPH-Am) are strongly foliated (Fig. 2.6d) and strike NNW-SSE, dipping ca. 60° towards NE. The contacts between amphibolites and marbles (IPH-Mb) is locally sheared, and contains calcareous schist layers (IPH-Cs), probably retrograde, finely intercalated amphibolites and marbles. To the west, a series of gneisses, undifferentiated as IPH-Gn is underlying the amphibolites and marbles. The gneisses comprise paragneisses (IPH-Gnp) and orthogneisses (IPH-Gng). The paragneisses are mainly banded with distinct feldspar and biotite rich bands. They are well exposed along the Pashto road, where they dip ca. 65° E. The orthogneisses are variously strained. The mylonitic gneisses (IPH-Mga, IPH-Mgg and IPH-Mgt) are fine grained and contain amphibole, epidote and garnet. Migmatized gneisses (IPH-Mgm) are usually fine-grained and developed in thin bands at the contacts of porphyritic granites. The porphyritic granites (IPH-Grp) exhibit K-feldspars phenocrysts in medium to coarse grained groundmass of feldspar, quartz and biotite. The tourmaline granite is medium grained, equigranular and contains feldspar, quartz, muscovite, biotite and tourmaline with other accessory minerals. The granites are well foliated in shear zones. N-S trending bands of garnet mica schist (IPH-Gs) with a maximum thickness of about 50-60 m, highly sheared and fractured metavolcanics (IPH-Mvg) and metavolcanics mainly of basaltic composition (IPH-Mv) are interlayered with gneisses in the Allai Khwar. Towards Besham, a N-S trending, 60-70 m thick sequence of garnet bearing quartzites (IPH-Qtz) belongs to the metasedimentary portions of the Precambrian Besham gneisses.

2.2.2 Indus Suture Zone (ISZ)

Lithologies of the Indus Suture Zone were mapped along the Natai valley (E of Besham) and Ranolia valley (NE of Duber Bazar).

Along the Natai valley the ISZ is comprised of a ca. 2 km thick series of tectonically imbricated sheets, separated by a ca 40° E dipping lower fault contact from the Indian plate and by a ca. 70-80° NE dipping upper fault from the Kohistan Arc Complex.

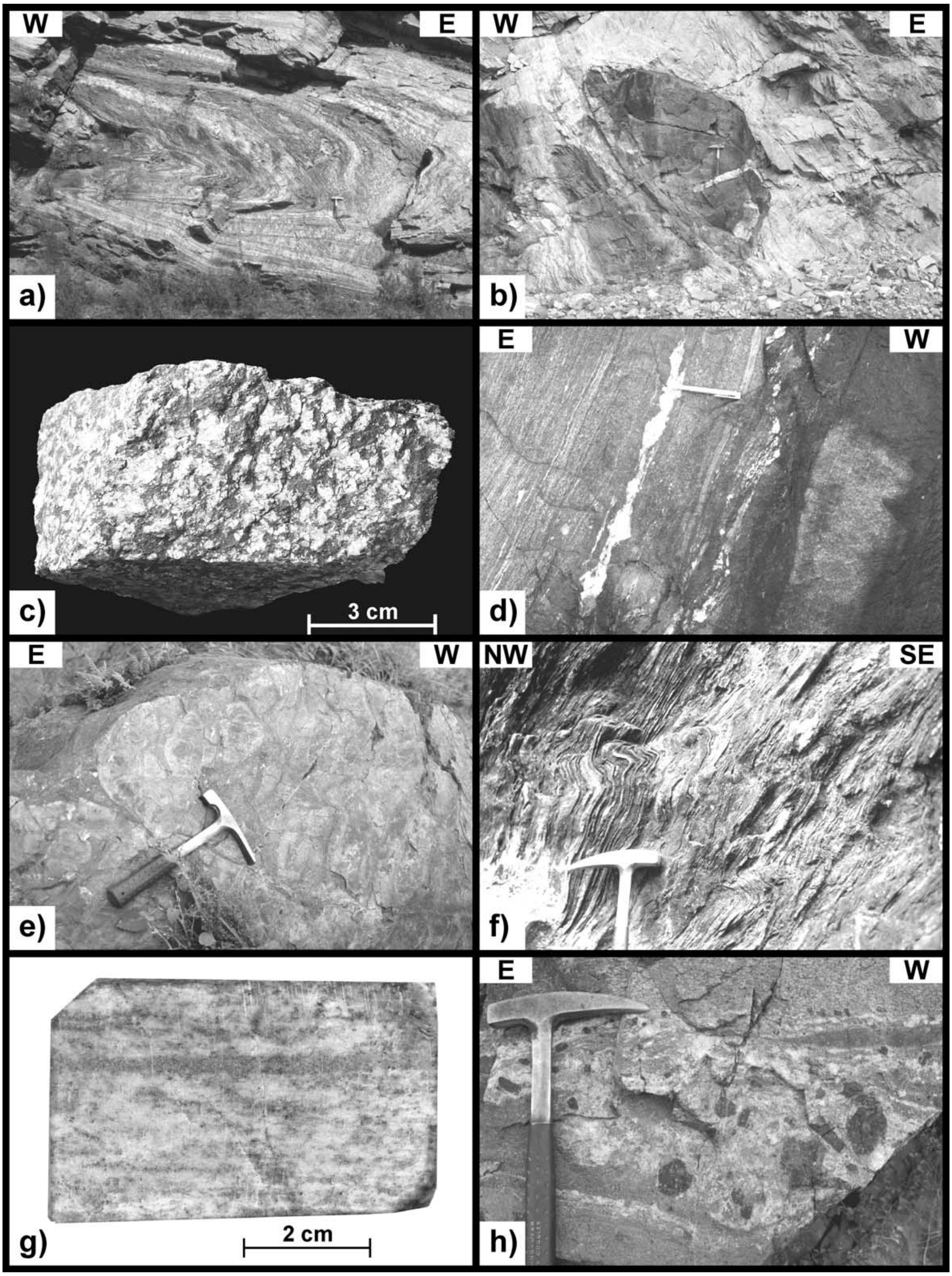

Fig. 2.6: a) E-verging folds beneath the Indus Suture, 300 m SW of Jijal at KKH; b) Amphibolitic pod in Indian Plate gneisses, 700 m E of Duber Bazar at KKH; c) Sample of Duber Diorite, a body intrusive in Indian Plate gneisses at Duber Bazar; d) Amphibolite with quartz band beneath lower ISZ-fault, Natai valley, along road, 2 km W of Pastho; e) Pillow lava in Natai valley, along road, 1 km S of Pastho; f) Phyllites of the ISZ "mélange" at Kopu Khwar with N-side down folds, ca. 5,5 km NW of Duber Bazar; g) Metadiorite of the Metaplutonic Complex at the hanging wall of the Kohistan Fault at Pastho Kalai; h) Garnet and hornblende bearing dike in gabbros 500 m S of Pastho Kalai, along road.

Upsection, the series comprises greenstone (ISZ-Gst), metagraywackes (ISZ-Mug), blueschists (ISZ-Bs) and meta-volcanics with pillow lavas (ISZ-Muv) (Fig. 2.6e). The greenstone consists of hornblende, epidote and chlorite rich layers interlayered with thin plagioclase bands. In the field they appear as well foliated, dark green rocks with occasionally stretched plagioclase and minor quartz bands. They are followed by a series of green to brownish metagraywackes. In the upper part the metagraywackes contain glaucophane (Shah & Majid, 1985). The metavolcanics have a dark-green to yellowish green colour on the fresh surface. They are mostly fine grained and contain plagioclase, hornblende, quartz, epidote and chlorite. Ellipsoidal pillows are a tens of centimetres to more than 1/2 meter in diameter and are enclosed in a yellowish green matrix. Chilling effects at the surface are glassy in appearance. The succession of lava flows and pillows is followed by low grade, fine grained and layered metavolcanics. They were originally tuffs, ashes and volcanic agglomerates. Their colour depends on the relative amounts of quartz, plagioclase, epidote, chlorite and hornblende. Ripple marks and graded bedding in metasediments prove that the sequence is not overturned.

In the Ranolia Khwar and Kopu Khwar (NW of Duber Bazar) the ISZ is comprised of an up to 100 m thick sequence of garnet bearing schists (ISZ-Sch), black at the lower part where they are dominated by micas, whereas in the upper part they are light green, epidote-rich with stretched feldspar clasts. They show a strong schistosity parallel to the northward dipping (40-70°) lower and upper fault contacts.

2.2.3 Kohistan Arc Complex

The rocks of the Kohistan sequence exposed close to Pastho Kalai are hornblendites (KHA-Hbt) and garnet-bearing gabbros and metadiorite sheets (KHA-Gb) (Fig. 2.6g), intruded by garnet - hornblende bearing dikes, similar to the rocks of the lower Metaplutonic Complex (Fig. 2.6h). They are variably foliated (ca. 45° towards E).

Within the lower part of the KAC, several lithologies were observed which are not limited to a specific group. They are: Small lenses of hornblendite (KH-Hbl). Hornblende pegmatites (KH-HblP) occur sporadically in the area N of Kiru, where they yield various degrees of deformation, close to Kiru, where they are boudinaged along shear zones (Fig. 2.7a) and N of Dasu, where only little to no ductile deformation affected them (Fig. 2.7b). Pegmatites (KH-Pegm) are frequent throughout the whole area and comprise:

quartz + feldspar + muscovite + tourmaline ± garnet ± hornblende ± biotite.

A high density of pegmatites is observed close to the granite sheets between Kiru and Dasu. Thickness ranges from centimeter to 20 m. A pegmatite cutting the main shear fabric south of Dasu yielded a K-Ar muscovite age of 66±3 Ma (Treloar *et al.*, 1989a). Ductile deformation within the pegmatites varies from nearly undeformed to intensely foliated (Fig. 2.7c,d).

In the SW to NE sinistral zone, bordering the mapped area to the NW, brecciated serpentinite (KH-Serp) occurs (Fig. 2.7e). Within this zone black phyllites and schists (KH-Phy) form "layers" up to 40 m thick, parallel to the deformation zone. They are observed in the northern part of Ranolia Khwar (Fig. 2.7f). The origin is not defined, but possible sources are the metasedimentary sequences of marine origin within the Kohistan Arc Complex, which were incorporated in the deformation zone.

2.2.3.1 Jijal Complex

The Jijal Complex is the lowest level of the Kohistan Arc Complex and is limited by the Indus Suture in the S and SW, by the serpentinitic zone in the NW and an intrusive contact to the Metaplutonic Complex in the NE (Fig. 2.1). It comprises essentially two units: an ultramafic dominated sequence and a mafic one. The ca. 3-4 km thick ultramafic sequence (KHJ-Um) is not differentiated on the map. The section has been described in details by Jan & Howie (1981), Bard (1983), Miller *et al.* (1991) and Burg *et al.* (1998).

The lowest part is a peridotite unit composed of dunites and wherlites interlayered with cm- to m-thick layers of fine-grained pyroxenites (Fig. 2.8a,b). Coarse grained websterites successively dominates up-section the peridotites. Hornblende is sparsely intergrown with websterite, but becomes abundant further up-section, where layers of coarse grained hornblendite occur. In the upper part of the ultramafic-mafic section garnet-hornblende pyroxenites are dominant (see section Fig. 2.3).

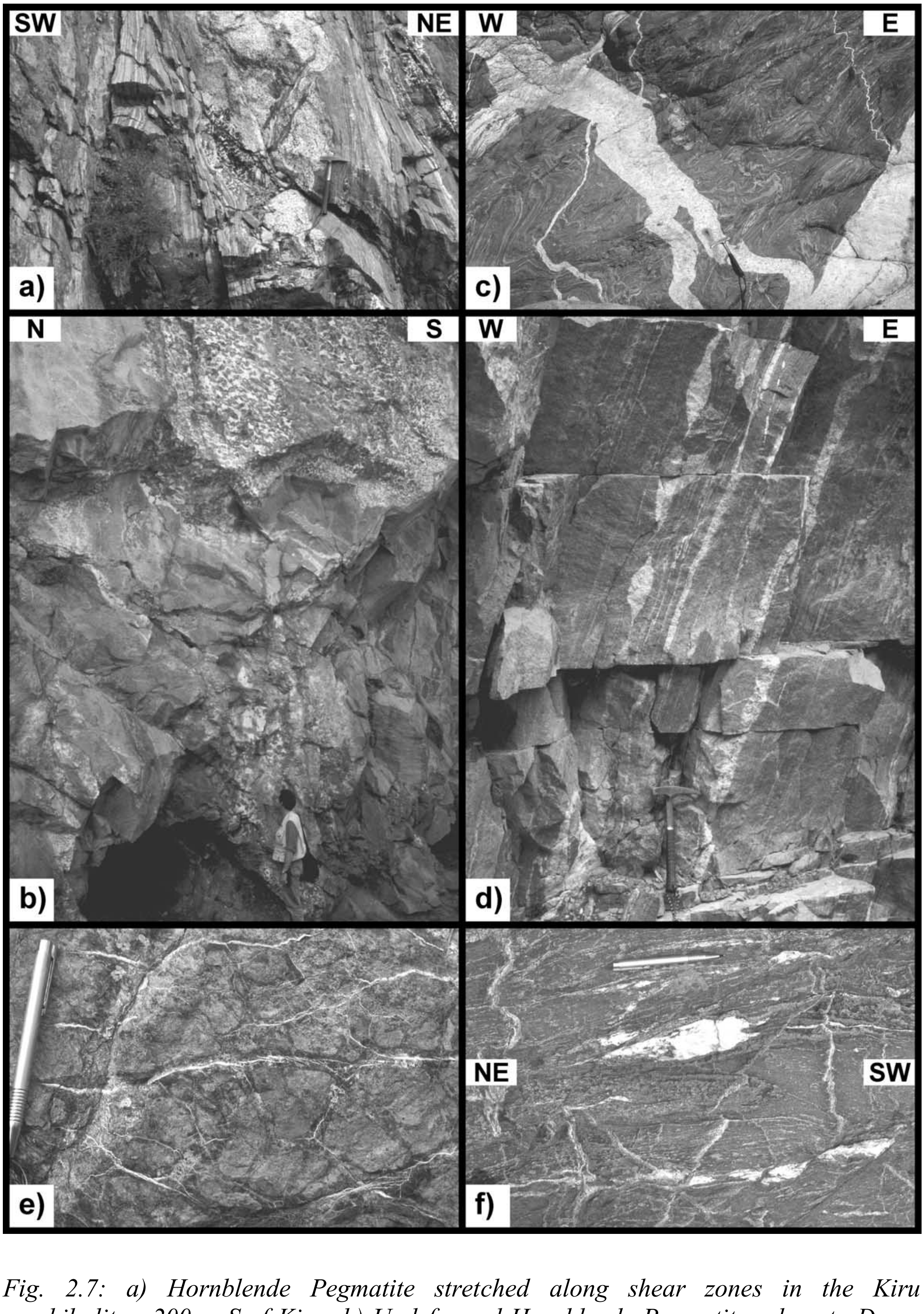

Fig. 2.7: a) Hornblende Pegmatite stretched along shear zones in the Kiru amphibolites, 200 m S of Kiru; b) Undeformed Hornblende Pegmatites close to Duga, 10 km N of Dasu; c) Pegmatites in fine banded and strongly folded amphibolites ca. 1,7 km NNW of Mandraza; d) Pegmatites in amphibolite with variable degree of boudinage, 2,5 km NNE of Dasu; e) Brecciated serpentinite in the sinistral fault zone, 2 km SW of Duber Kale; f) Phyllites within the sinistral fault zone, close to Kichar Banda, 10 km NW of Duber Bazar.

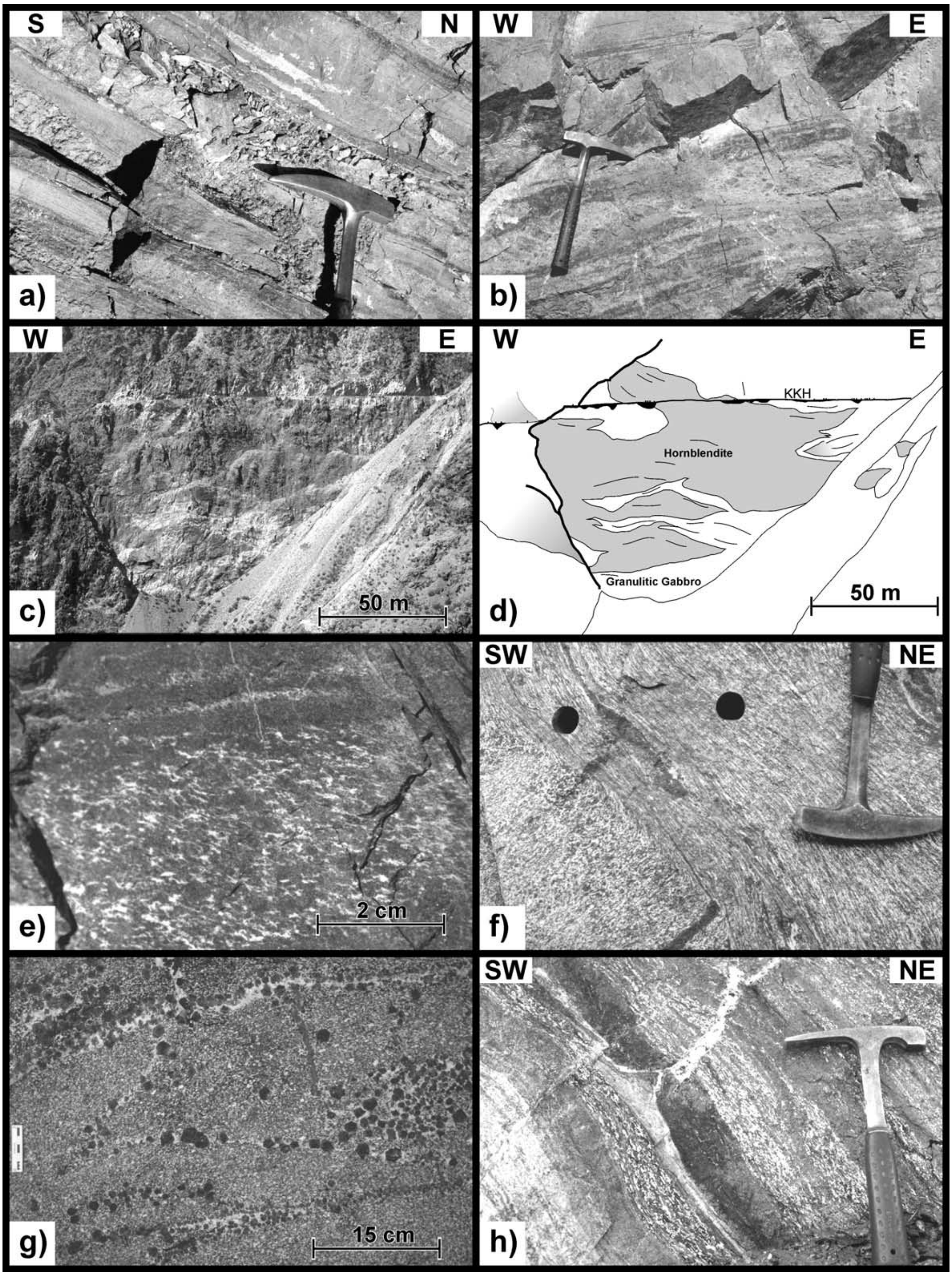

Fig. 2.8: a) Dunite layers intercalated with pyroxenites, ca. 1,5 km E of Jijal along KKH; b) Coarse grained pyroxene layers with dunite and chromite lenses, ca. 6 km N of Duber Bazar; c) Hornblendite lenses in Granulitic gabbro, view from the southern Indus River bed ca. 2.5 km SW of Patan towards NW; d) Interpretative sketch of c), see also hornblendite lenses in enclosed section A-A'; e) Layering of garnetite/Granulitic gabbro, ca. 1 km SW of Patan along KKH; f) Initial shear zone in Granulitic gabbro, 2 km SW of Patan; g) Feldspar segregation veins with aligned cm large garnets, ca. 500 m S of Patan along Indus; h) Melt extraction in Garnet-Diorite indicating "normal" layering, ca. 60km N of Patan in Chawa Khwar.

The gently northward dipping contact between garnet-hornblende pyroxenites and the overlying Granulitic gabbro (KHJ-GtGrlt) is interpreted as the exhumed petrological "Moho" (Burg *et al.*, 1998). The contact locally displays interdigitations and coincides with last occurrence of dunite flames in websterites and hornblendites. Hornblendite (KHJ-Hbl) and garnetite bodies are found within the Granulitic gabbro. Two intrusion relations are observed in the field: the Granulitic gabbro intruding Hornblendite lenses and Hornblendites intruding the Granulitic gabbro. The Hornblendites, forming large enclaves and bodies with sharp boundaries (Fig. 2.8c,d) are intrusions that may have stemmed from the underlying mantle (Burg *et al.*, 1998). Some hornblendite enclaves were intruded by the Granulitic gabbro and associated pegmatites, indicating that the Granulitic gabbro is intrusive into the hornblende-rich upper mantle.

The Granulitic gabbro, divided by Yamamoto & Yoshino (1998) into a two-pyroxene granulite and a garnet-clinopyroxene granulite is characterized by:

(orthopyroxene) + clinopyroxene + plagioclase + garnet +hornblende ± quartz ± ilmenite ± rutile.

Magmatic textures are locally preserved. Plagioclase is the dominant mineral in whiter layers (up to several tens of centimetres thick). The darker, mafic layers are pyroxene-rich (Fig. 2.8e).

The two-pyroxene granulite is locally replaced by coarse-grained garnet-clinopyroxene granulite (Yamamoto & Yoshino, 1998). Large garnets (up to a few cm in diameter) are concentrated along feldspar segregation veins (Fig. 2.8g). Foliation in the Granulitic gabbro dips generally towards NE (Fig. 2.8h). Ductile deformation within the Granulitic gabbro is expressed by anastomosing shear zones that show a dominantly top to the SW shear sense (Fig. 2.8f).

2.2.3.2 Metaplutonic Complex

The Metaplutonic Complex forms a thick pile of imbricated calc-alkaline laccoliths variably deformed in amphibolite facies conditions (Tahirkheli *et al.*, 1979; Bard, 1983; Treloar *et al.*, 1990). Remnants of the Tethyan oceanic crust are possibly preserved in enclaves. Field observations show that the definition of the Kamila amphibolite belt as a single unit (Jan, 1988) is inadequate. A new separation into 3 different zones is proposed, from S to N, i.e. bottom to top: a) Sheared gabbro-diorites (Patan region) comprising retrograde metagabbros with locally preserved igneous layering and showing a heterogeneously distributed deformation forming an anastomosing pattern of shear zones; b) Kiru sequence consisting of more than hundred meters thick imbricate intrusions of gabbroic to dioritic composition, intensely deformed along East-West trending shear zones and c) Kamila sequence, an amphibolitised sequence composed of gabbroic, dioritic, granitic and tonalitic rocks intruded in a crustal sequence, whose remnants are represented by fine layered amphibolites with epidote-rich lenses, enclaves of carbonates and quartzite bands.

2.2.3.2.1 Sheared gabbro-diorites (Patan region)

The Sheared gabbro-diorites, mapped in the north-eastern Patan area are directly lying on the Granulitic gabbro. The Garnet-Diorite (KHA-GtDr) (Fig. 2.4) is a layered, coarse grained garnet-rich meta-diorite well exposed on the W side of Chawa Khwar. The layering is constituted by garnet-rich, plagioclase-rich and hornblende-rich cm to m thick layers. Quartz and epidote complete the assemblages. The sharp contact to the Granulitic gabbro dips in the S with ca. 10° towards north and steepens to ca. 25° northward. The contact plane is irregular, forming bulges in a meter to tens of meter scale in the Granulitic gabbro. Up to a few meter sized, elongated enclaves of Granulitic gabbro occur above the contact indicating that the Garnet Diorite is intrusive into the Granulitic gabbro. Finely layered, tens of meter thick meta-diorite sills (KHA-dDr) are parallel to the north-dipping contact (Fig. 2.9a). The relation of the Garnet Diorite to the Sarangar gabbro (KHA-GbS) and the dioritic/gabbroic units to the N could not be determined, because the Garnet Diorite is cut by faults to the N and the E. The Sarangar gabbro, a coarse grained, locally layered gabbro (Fig. 2.9b,c) make up the outcrops E of Patan Banil Khwar and Gulbagh Khwar. The mineralogical composition within the main metamorphic fabric is dominantly:

hornblende + clinopyroxene + plagioclase ± quartz ± rutile ± garnet ± epidote.

Compositional layering is characterised by a varying amounts of plagioclase. The gabbro shows spectacular shear zones anastomosing around coarse grained, weakly deformed pods with well preserved plagioclase-clinopyroxene assemblages. The contact to the Granulitic gabbro partly sheared and bended by anastomosing shear zones, is observed at the S side of the Indus close to Patan.

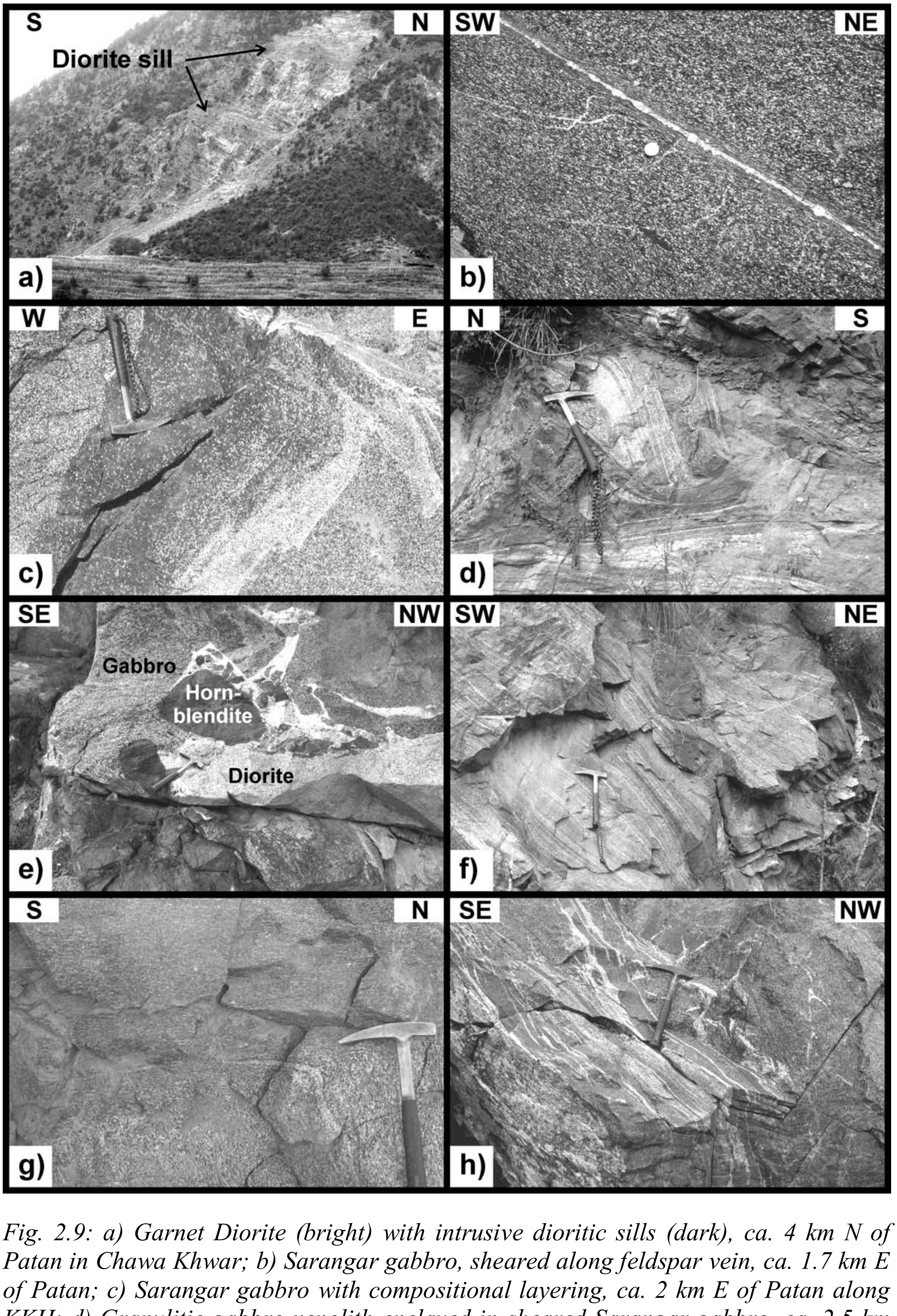

Fig. 2.9: a) Garnet Diorite (bright) with intrusive dioritic sills (dark), ca. 4 km N of Patan in Chawa Khwar; b) Sarangar gabbro, sheared along feldspar vein, ca. 1.7 km E of Patan; c) Sarangar gabbro with compositional layering, ca. 2 km E of Patan along KKH; d) Granulitic gabbro xenolith enclaved in sheared Sarangar gabbro, ca. 2,5 km N of Patan in Banil Khwar; e) Magmatic breccia with hornblendite (old), gabbro and diorite (young), 5 km ENE of Patan along KKH; f) At lower side sheared hornblende dike cutting diorites/hornblendites, ca. 300 m NE magmatic breccia, along KKH; g) Top to the S sheared Kayal Gabbro; h) Layered diorite (KHA-Drb), WSW of Kayal - Indus confluence at KKH.

The Sarangar gabbro is impregnating the Granulitic gabbro along a dense, but diffuse vein network, forming a 1-2 m wide transition zones. Above the contact small hornblende lenses (few m thick) occur. N of Patan a Granulitic gabbro pod is sheared within the Sarangar gabbro (Fig. 2.9d). The gabbro is intruded by hornblendite veins and garnet-bearing feldspar veins which are locally folded. A meta-carbonate enclave was incorporated in the gabbro (at the KKH ca. 500 m S of its northern contact), providing evidence that the gabbro was intrusive into metasediments under mid-crustal conditions of ca. 0.8-1.1 GPa (Yoshino *et al.*, 1998).

In the Chor Nala valley the Sarangar gabbro is underlain by a coarse grained, well foliated Hornblende Gabbro (KHA-cGbHbl) with sporadic cm large hornblende crystals. The assemblage contains also garnet and mica as retrograde metamorphic mineral. Thin, fine grained basic dikes cut the gabbro. The diffuse contact of this gabbro to the Granulitic gabbro dips gently N to NE and is characterised by an up to 3 m wide transition zone, where the gabbro impregnates the Granulitic gabbro along a network of small veins. In the Sarangar gabbro two ca. 50 m thick sill-like bodies of the same rock type are observed in the Chor Nala. The upper contact of the Sarangar gabbro is comprised in the eastern part (Indus valley) of a magmatic breccia (KHA-GbDrHbl) (Fig. 2.9e), where hornblende-rich rocks were intruded and brecciated by gabbros (Sarangar gabbro?) and diorites. N of Patan the Sarangar gabbro is bounded at its upper contact by finely layered and deformed diorites/hornblendites (KHA-DrHbl). Above the sharp contact up to ca. 1 m small enclaves of Sarangar gabbro were incorporated in the strongly SW-ward sheared diorites/hornblendites at its bottom parts. This could represent a sheared equivalent to the above mentioned magmatic breccia. To the top diorite layers are coarser grained, showing a plagioclase, hornblende, quartz, epidote and minor chlorite assemblage. They are folded and sheared along conjugated shear zones.

The diorites/hornblendites were intruded by hornblendite dikes and pegmatites. The hornblendite dikes are locally sheared but cut the foliation in the diorites in other places (Fig. 2.9f), suggesting a syn-shearing intrusion age. At the Indus section the Kayal Gabbro (KHA-GbKa) is intruded by several diorites/hornblendites sills. The Kayal Gabbro is coarse grained and similar to the Sarangar gabbro, but without layering. A dense pattern of anastomosing shear zones deforms the gabbro (Fig. 2.9g) and the contacts. Both sides of the lower Kayal valley along the KKH screen diorite bodies with a hornblende, plagioclase, quartz and accessorily minerals paragenesis. The basal diorites (KHA-Drb) are layered (Fig. 2.9h) and strongly sheared. Mylonitic anastomosing shear zones developed around lense shaped pods. The foliation is bent into the mylonite zones showing SW-ward shear. The bottom part of diorite was intruded by 1) the Kayal gabbro, as indicated by up to 10 m large gabbro enclaves in the diorite, by 2) garnet bearing veins and later 3) by hornblende - plagioclase – garnet pegmatites. They are distinguished from the upper diorite (KHA-Drt) comprised of an interlayered sequence of coarse grained and fine grained diorites intruded by hornblendite dikes. Some steeply northward dipping shear zones have normal sense (top to N) movement. The ca. 30° northward dipping upper contact is irregular and in places sheared in normal sense. Where un-sheared, small enclaves (a few tens of cm) of diorite are within the lowest meter of a coarse grained gabbro which is part of coarse grained interlayered gabbroic to dioritic intrusions (KHA-GbDr). The intrusions are interlayered in various thicknesses, ranging from a few m to hundred m and are distinguished by their colour contrast between dark and bright in the field, where the gabbros often have a higher amount of hornblende and therefore are darker than the diorites. This sequence is sporadically intruded by garnet bearing veins. At the top the gabbros interfinger with the Kiru sequence in a dike like manner forming an irregular contact.

2.2.3.2.2 Kiru sequence

Several steeply northward dipping mylonitic shear zones (with top to N movement) are observed at the lower contact to the sheared gabbro-diorites. The Kiru sequence consists of imbricate "amphibolites" intensely deformed along East-West trending shear zones. The lowest part is constituted by the Kiru Amphibolites (KHA-AmKi) comprised of up to hundred meters thick laccolithic bodies of dominantly fine grained rocks. The compositions range from gabbroic with hornblende, plagioclase, garnet, epidote and quartz to dioritic with hornblende, plagioclase, quartz, garnet and epidote. In places black, hornblende dominated layers of metaplutonic origin occur. Locally coarse grained rocks (Fig. 2.10a) are preserved. Lithologic boundaries are parallel to the main foliation and are generally dipping north. Steeply northward dipping to sub-horizontal mylonitic shear zones enclose blocks of variable size (<50 m).

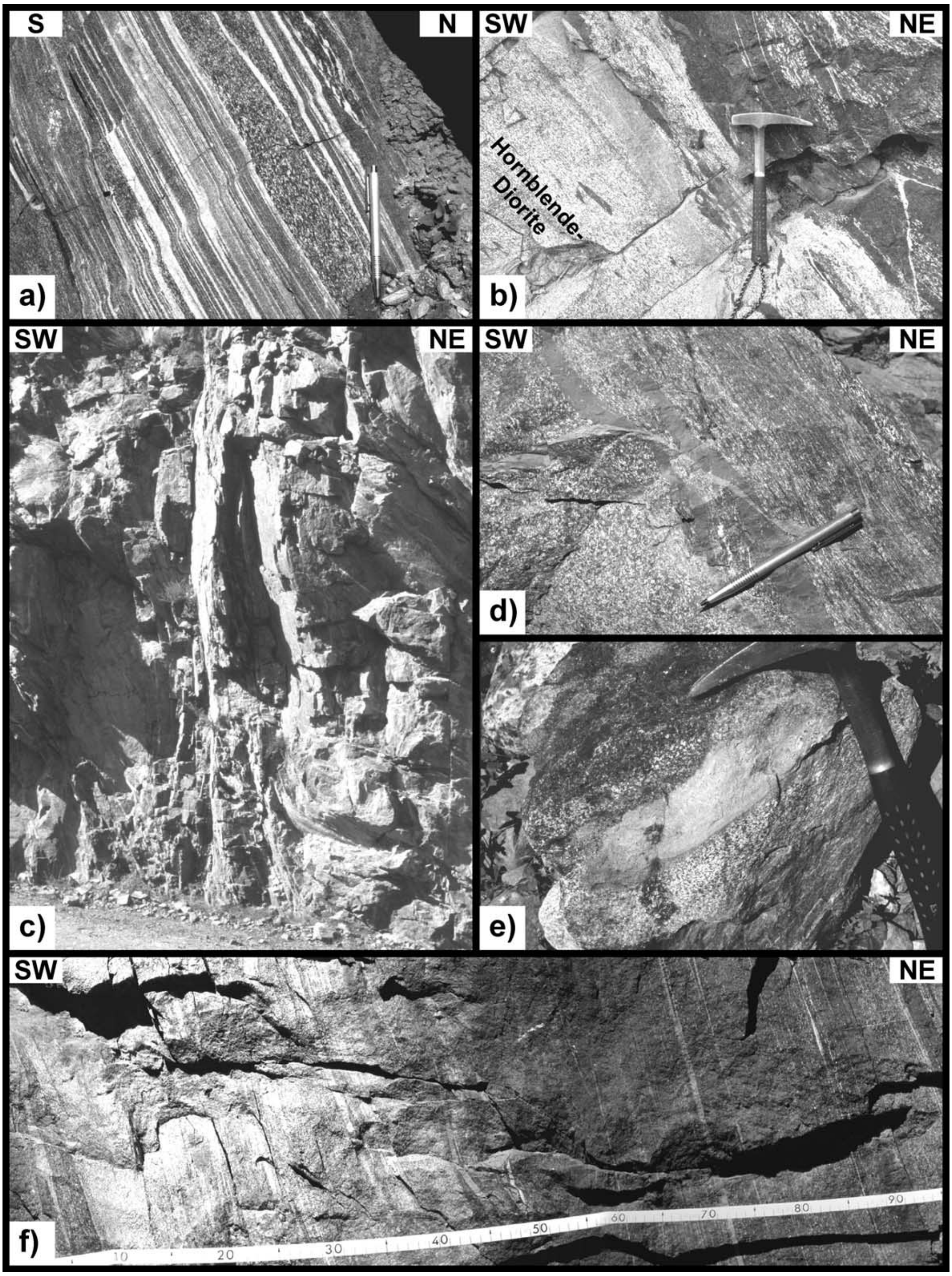

Fig. 2.10: a) Fine layered Kiru Amphibolite including a small dioritic sill (tip of pen), at Kiru; b) Hornblende Diorite intruding diorites/hornblendites of the Kiru Amphibolites, 2 km S of Kiru at KKH; c) Steep N-side down shear zone in Kiru Amphibolites, 4 km S of Kiru at KKH; d) Small hornblende lenses and basic dikes cutting a gabbro of the KHA-mDrGb unit, 1,5 km S of Kiru at KKH; e) Carbonate lense in gabbro (boulder) from the area 500 m S of Kando Banda; f) Interlayered diorites (bright) and gabbros (dark), 4,5 km N of Kiru.

A coarse to medium grained hornblende-rich diorite (KHA-HblDr) is in sharp contact and contains enclaves of Kiru amphibolites (Fig. 2.10b). It is composed of plagioclase, greenish hornblende, quartz and epidote, chlorite and titanite. The metamorphic fabric has overprinted the magmatic fabric and foliation is defined by the orientation of metamorphic hornblende. The contact at its base dips irregularly 40° northwards. Locally anastomosed shear zones are spaced by 50-100 m. The ca. 50° N dipping upper contact is more regular and parallel to main foliation. Just to the S of Kiru again, subvertical amphibolites with pegmatites (qtz + fsp + msc) and hornblende pegmatites appear. Partial remelting sporadically produced thin plagioclase veins within mylonitic zones. In the Kiru amphibolites top to the S shear zones are dominant. However, steep N-dipping, lower amphibolite facies (hornblende + plagioclase + epidote + quartz), shear zones show a top to N relative shear sense (Fig. 2.10c).

A series of (meta-) gabbro and (meta-) diorite bodies N of the Kiru amphibolites is summarized in a mixed unit (KHA-mDrGb). Hornblendite and basic veins intersect them sporadically (Fig. 2.10d). The good outcrop situation along the KKH permitted mapping several of these gabbros and diorites. Within the gabbros, lenses of meta-carbonates, which were not observed in the diorites, occur infrequently. The interlayered gabbros and diorites (Fig. 2.10f) were heterogeneously affected by amphibolitisation and deformation, some of them having preserved magmatic textures. Most of these imbricated bodies are hornblende-rich diorites and meta-diorites (KHA-Drmet). Towards the N the number of pegmatite and small granitic sheets increases.

The contact to the Mandraza amphibolites (KHA-AmMa) is set where dark, fine grained and strongly foliated amphibolites become dominant. They are cut by a swarm of SW-dipping, up to a few meters thick pegmatites. The Mandraza amphibolites are comprised of a series of coarse to medium grained meta-gabbros, hornblende-rich meta-diorites and granites of variable thickness not exceeding 100 m. They are interlayered with fine grained, hornblende dominated, strongly foliated dark hornblende-plagioclase-quartz-epidote rocks. Layering is due to alternating changes in hornblende and plagioclase contents. Occasionally, elongated (<20 cm) green to yellowish epidote lenses occur within the dark layers. Top to the SW shearing is expressed by flat to steep N dipping shear zones around 50-100 m wide lenses with asymmetrical shape (Fig. 2.11a,b). In the

Sangri Khwar, N of Mandraza, a unit of more massive, coarse grained gabbros and diorites appears. It probably is cut in its eastern part by the big granite body (the largest one on the map), as indicated by the bending of the ca. 60° N dipping foliation towards S. The uppermost metadiorite contains schlieren of fine grained, well layered, epidote-rich Dasu Amphibolites (Fig. 2.11c) within a meter thick zone below the contact.

2.2.3.2.3 Kamila sequence

The Kamila sequence is composed of amphibolitised gabbros, diorites, granodiorites granites and tonalites intruded in fine layered amphibolites with epidote-rich lenses, enclaves of carbonates and quartzite bands, interpreted to be remnants of a upper crustal sequence. The Kamila sequence is, compared to the Kiru sequence, characterized by the increased occurrence of granitic rocks. A nearly 1 km thick granite body (KHA-Gr) overlies the Mandraza amphibolites and bends at its base the steep N-dipping foliation of the amphibolites. These coarse grained granite is composed of:

quartz + plagioclase + muscovite + garnet ± epidote ± pyrite ± chlorite ± apatite ± zircon.

Below these mentioned granite body only metagranite sheets, up to 1 m thick, are intercalated with the Mandraza amphibolites. There the contact between amphibolite and granite is sharp and foliation/layering parallel. Within the bottom part of the big granite body amphibolite pods (fine grained dark meta-diorite) were stretched. Towards the upper part of the big granite body xenoliths of greenish, fine grained, epidote rich amphibolites of possibly metasedimentary origin are more frequent. Coarse grained, muscovite-rich pegmatites cut the generally ca. 40° N-dipping foliation. In places they are elongated and foliated parallel to the main foliation. The granite becomes strongly foliated near the contacts. N-dipping, less than 50 cm wide shear zones with a top to SW sense are spaced by ca. 20 to 60 m. A second ca. 500 m thick, E-W trending massive granite sheet occurs ca. 500 m more to the north. Between both sheets, interlayering of fine grained amphibolites (meta-gabbros and a greenish, fine layered variety of possible metavolcanic origin), granites and coarse grained pegmatites sheets make up to 50% of the outcrop (Fig. 2.11d). Bigger (>1 m in thickness) pegmatites cut the foliation of the amphibolites, but others are stretched, boudinaged and sheared, indicating syn- to post-deformation emplacement. Towards Kamila village the foliation steepens northward and the relative amount of granites and pegmatites decreases.

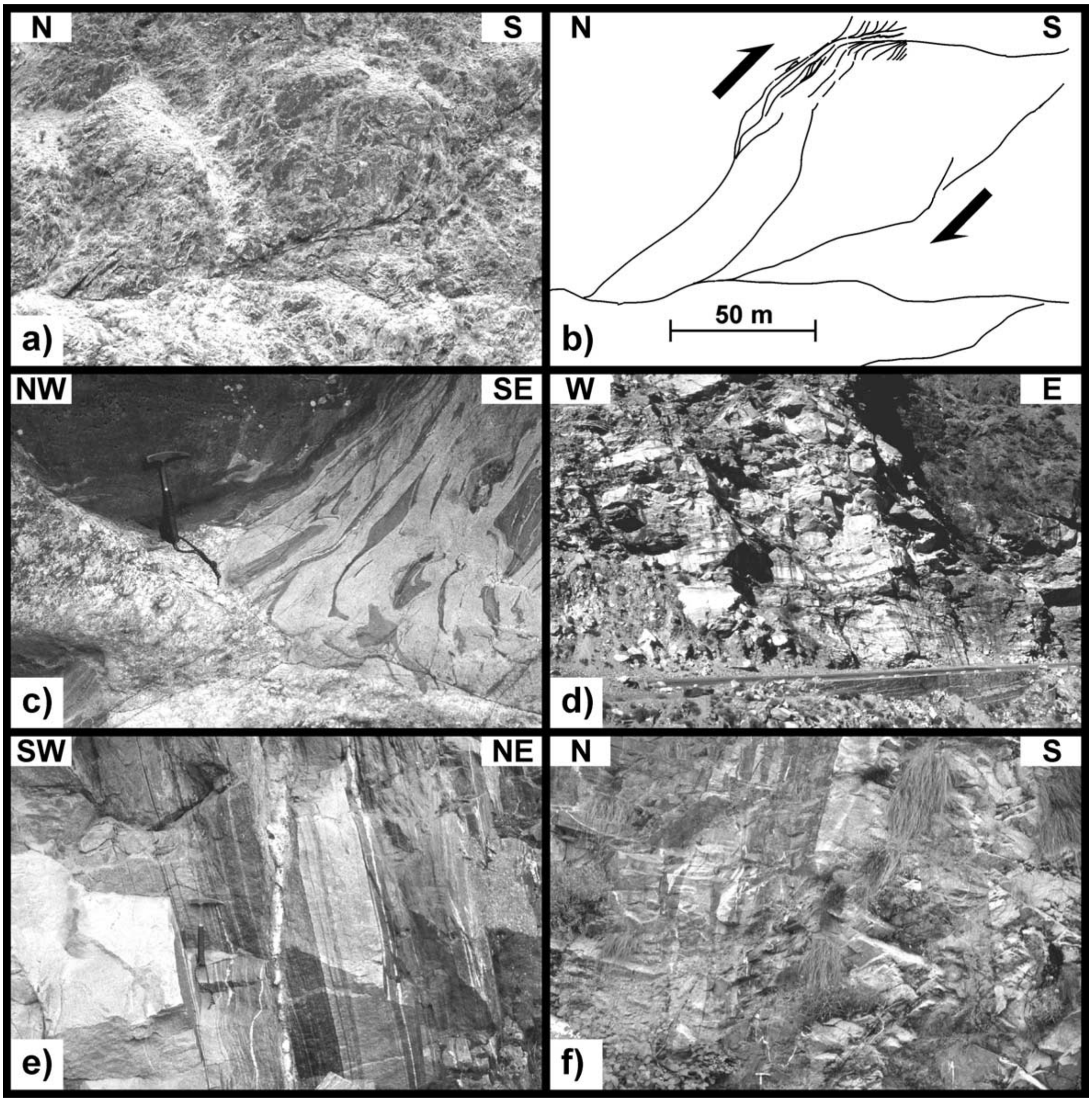

Fig. 2.11: a, b) Lense shaped block of gabbro enclosed in mylonitic shear zones, view to E side of Indus valley ca. 6 km N of Dasu; c) Contact between Dasu Amphibolites(dark) and metagabbro, cut by pegmatite, 2 km N of Mandraza; d) Granitic sheets in Dasu Amphibolites, location between the two granite bodies; e) Granite sills in a series of diorite and gabbro sheets, N of Kamila; f) Basic dikes cutting a diorite of the Dasu Amphibolites, 800 m N of Dasu.

Several thin (up to a few m) gabbro sheets getting more frequent, build up a nearly 1 km wide, E-W extended zone of gabbroic intrusions (KHA-GbmetDa) at Kamila.

The Dasu area is dominated by a strongly layered amphibolitic sequence (KHA-AmDa) composed of rocks with varying hornblende, plagioclase, epidote and quartz contents. Sheet-like gabbros and granites (Fig. 2.11e) contain smaller enclaves of dark, fine grained hornblende- and epidote-rich amphibolites. Basic and acidic dikes crosscut the amphibolitic sequence N of Dasu (Fig. 2.11f). The layer parallel foliation dips ca. 70° toward NNE in the vicinity of the northern metagabbro, which is cut by a more gently N-dipping granite on the northern flank of Dongai Gah. The metagabbro and the granite are intrusive into a series of dominantly fine grained, well layered to laminated amphibolites (KHA-AmO). They show green epidote-rich lenses and layers (Fig. 2.12a), most likely produced by a calcite rich (sedimentary?) source, sliced in dioritic magmas.

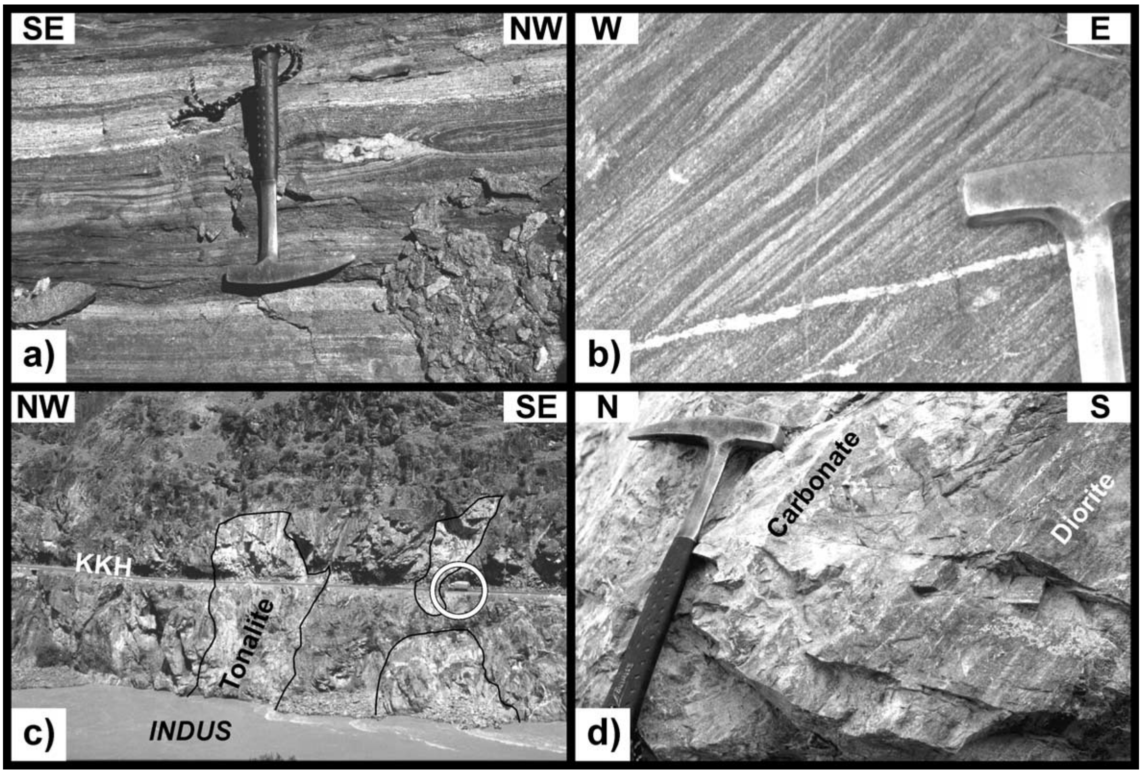

Fig. 2.12: a) Boudinaged epidote rich lenses of sedimentary origin in amphibolites (light grey left of hammer), 3 km N of Dasu; b) Laminated epidote- and hornblende-rich layers with weak graded bedding (younging towards top), ca. 3,1 km N of Dasu; c) Tonalite intrusion into amphibolites, 4 km N of Dasu, view towards NE; d) Carbonate lense in diorites along the KKH, 6 km N of Dasu.

Occasionally the few cm thick metasedimentary layers show graded bedding in originally volcano-detritic sediments (Fig. 2.12b). Several tonalite bodies (KHA-Tn) occur in the center parts of the sequence along the Indus valley (Fig. 2.12c). The contacts are generally sharp and sheared in places. The amphibolites are overlain by a massive, coarse grained diorite (KHA-DrmetN). Metamorphic foliation is heterogeneously distributed, steep northward dipping and sporadically bent by N-dipping, less than 1 m thick shear zones with a top to S sense. Meta-carbonates (KHA-mC) occur as m-sized enclaves in the diorite along the Indus valley (Fig. 2.12d). Vertical to steeply N-dipping sheet-like Quartzites bands (KHA-Qtz) of 10 to 20 m thickness occur ca. 6 km N of Dasu at the Indus valley, indicating a involvement of metasediments in the dominantly plutonic sequence of the Metaplutonic Complex.

2.2.3.3 Chilas Complex

The bulk rock type is noritic gabbro, locally layered with subordinate diorites. Gabbronorites and diorites (CH-Dr/Nr) and volcanodetritic metasediments (CH-VcS) were mapped along the Kandiah River (Fig. 2.13). The coarse to medium grained norites show a weak foliation. The gabbronorite is composed of:

clinopyroxene + orthopyroxene + amphibole + plagioclase ± quartz ± biotite ± oxides.

The magmatic fabric is preserved in parts. In places the gabbronorites are cut by undeformed feldspar dikes. In the western part of the Kandiah valley the gabbronorites unit contain also banded epidote-amphibolites. The size of the epidote-amphibolites bodies could not be determined, but most likely they are xenoliths of variable extend. A dioritic intrusions formed a magmatic breccia close to Zambil. Close to the eastern limit of the metasediments, peridotites outcrop along the road. Most likely they come from nearby lenses of ultra-mafic-anorthosite associations. The metasediments in the central part of the Kandiah valley have a northward dipping bedding. They are mm to cm thin muscovite rich layers (Fig. 2.14a) with quartz and calcite lenses folded in small scale around WNW-ESE trending fold axis.

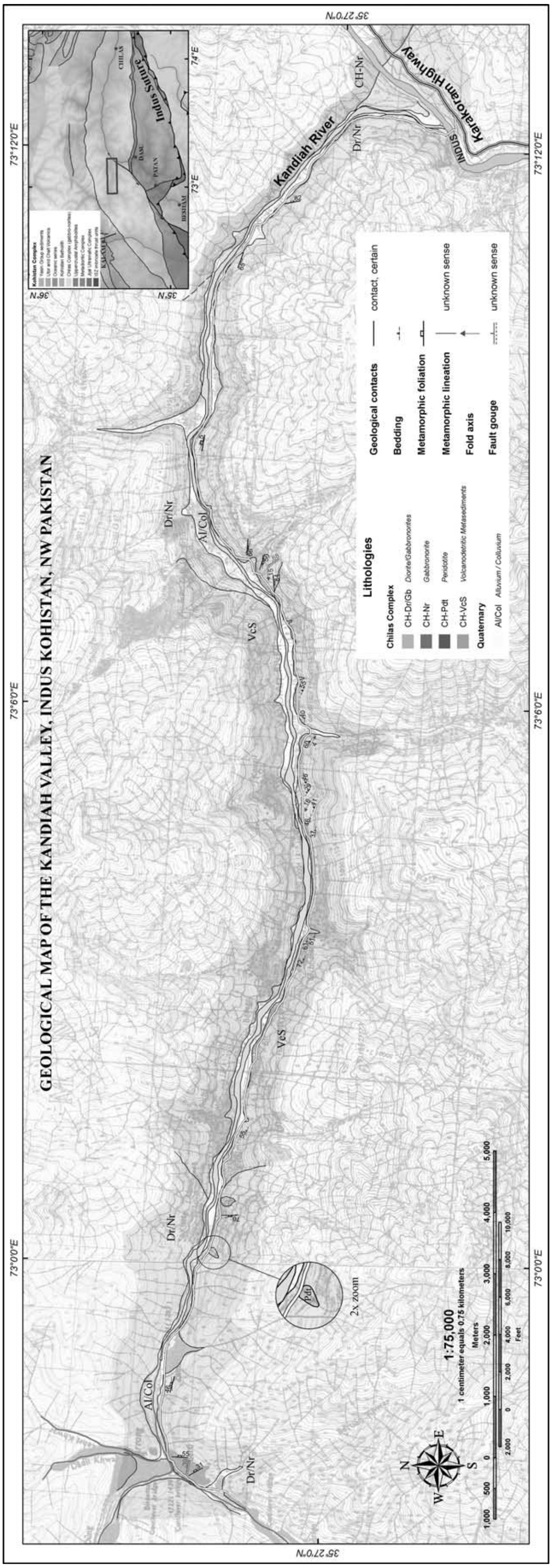

Fig. 2.13: Geological map of the Kandiah valley, reduced scale (original scale map is enclosed).

2.3 MAPPED FAULTS

Several distinct fault zones are recognized with different tectonic importance. The Indus Suture is the most important. It divides the crystalline shield rocks of the Indian Plate from the mafic and ultramafic rocks of the KAC. The Indus Suture close to Jijal is marked by a ca 35° northeastward dipping fault contact. Brittle deformation produced a serpentinite zone.

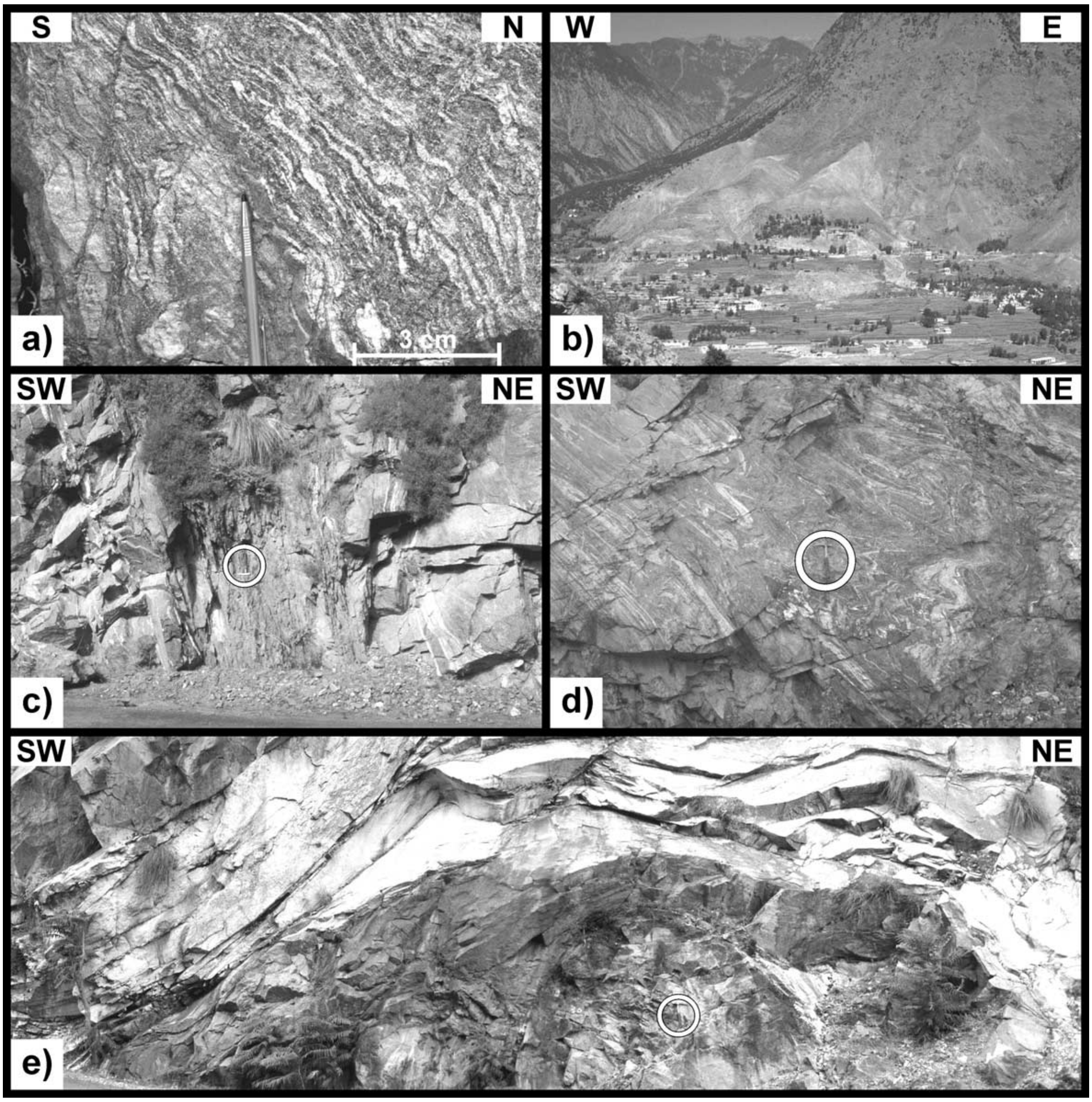

Fig. 2.14: a) Metasediments, mm to cm thin layered muscovite and quartz rich bands; b) Gentle slopes N of Patan made of fractured Granulitic gabbro and Sarangar gabbro indicating brittle activity; c) Steep dipping gouge zone, 3 km S of Kiru; d) Small scale, SW verging folding in gabbro; e) Folded granite sheet in Mandraza Amphibolites, ca. 1 km S of Mandraza.

Towards the W of Duber Khwar a ca. 100 m thick sequence of schists constitutes the ISZ with mesoscopic folds and kinkbands indicating a N-side down movement during ductile-brittle transition (Fig. 2.6f). The fault contacts between the Kohistan ultramafic rocks, the schists and the Indian Plate gneisses developed gouge zones with a N-side down movement indicated by striations. Immediately below the lower fault contact the Indian gneisses yield a northward plunging stretching lineation and a top to the S shear sense. Within the ISZ at Natai Khwar occasionally interlayered marble bands are sheared towards the SW. However, extensional structures like NE down facing folds and shear bands in schists in the metavolcanics and normal faults are dominant. The upper fault contact is dominantly brittle over a maximum 30 m wide zone. The associated small fault strands cut the metavolcanics and incorporate blocks of KAC rocks (DiPietro *et al.*, 2000).

A sinistral NE-SW trending fault also developed a serpentinite zone. It limits the mapped area to the NW and is traced on satellite images from the Indus River N of Dasu to N of Alpurai in the SW (Fig. 2.15). The relation to the Indus Suture remains open, but most likely the fault joins the Indus Suture N of Alpurai. The SW-ward continuation is a similar trending fault described by Anczkiewicz *et al.* (1998) in the Alpurai area, which acted first as a thrust and later as a sinistral strike slip fault. If this is the case, the NE-SW trending fault would cut into the ISZ and offset it.

Faulting in the Patan area is expressed by steep N-S and E-W trending faults. In the Patan Banil Khwar the contact between the Granulitic gabbro and the Sarangar gabbro is such a fault. In Patan and in the Gulbagh Khwar the contact between the Granulitic gabbro and the Sarangar gabbro is an intrusive one, excluding that the above mentioned fault is major tectonic contact between them. The widened Indus valley at Patan (Fig. 2.14b) shows fractured rocks and gouges indicative for active faulting.

Two major E-W striking faults are present between Patan and Dasu. The one ca. 3 km S of Kiru is a sinistral fault with a thrust component and developed a 2 m wide gouge zone (Fig. 2.14c). It joins the NE-SW trending fault zone at Duber, where a thin serpentinized zone was developed. The fault is steeply dipping north and offsets in its eastern part hornblende diorite against Kiru Amphibolites. In the western part it cuts into gabbros and diorites and is observed as a narrow brecciated zone in Chawa Khwar.

The fault 5 km S of Dasu is inferred from satellite images but could not be followed in outcrops (Fig. 2.15). Following mainly river beds, the actual fault contact is covered by quaternary sediments. Only at the SE corner, where the Indus turns towards W, a 1 to 2 m wide zone, of brecciated amphibolites is observed. The displacement and the sense of movement could not be determined. The fault limits to a certain extent the granite bodies to the N (southern granite) and to the S (northern granite).

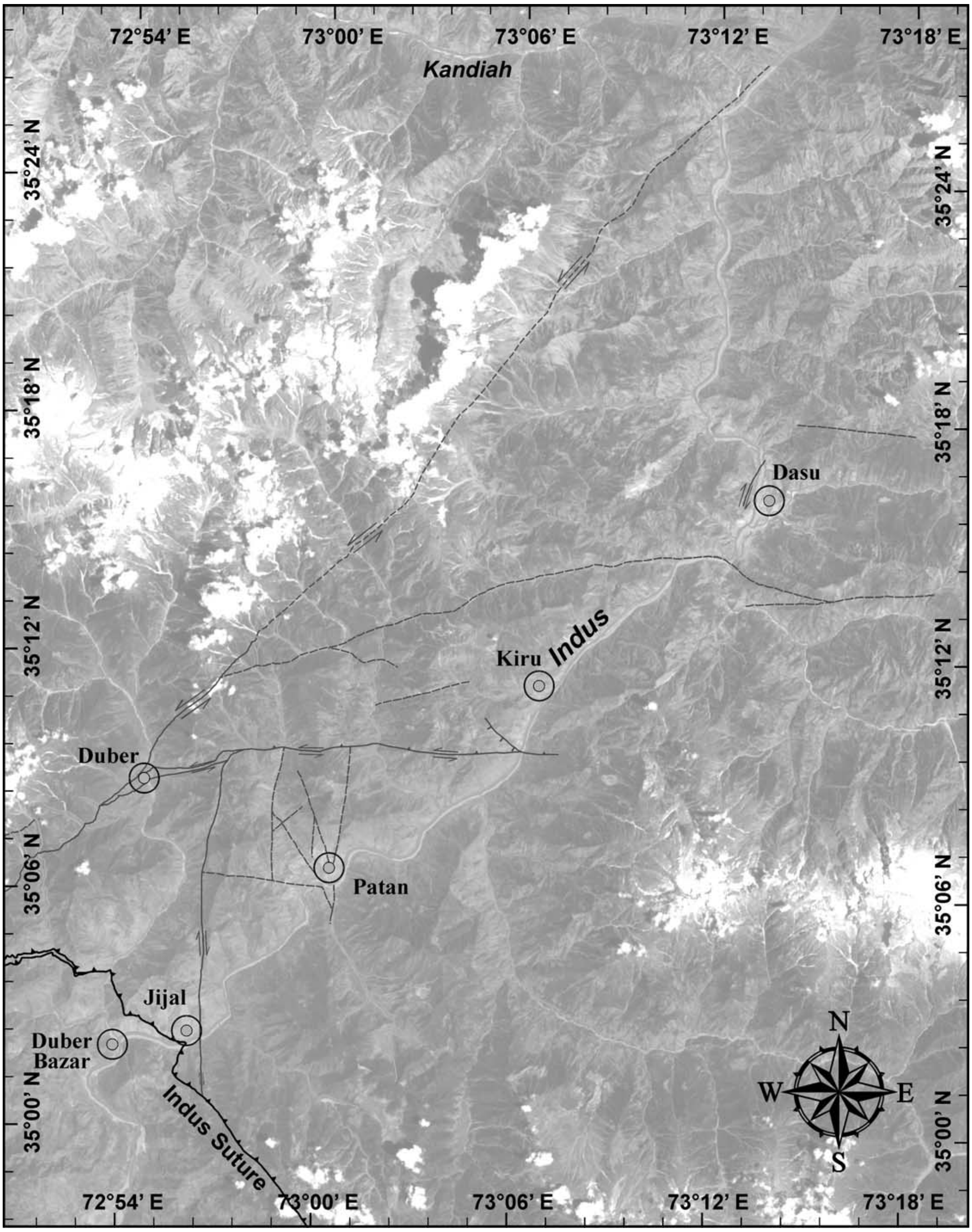

Large scale folding affected the Northern Indian Plate and produced the N-S trending Besham antiform. Folds observed within the KAC are generally small to mesoscale tight to isoclinal S to SW verging folds (Fig. 2.14d). Fold axis are dominantly E-W trending. The Kiru amphibolites show in places mesoscale S vergent, downward facing folds, indicating N-side down extensional movement. In strongly layered and foliated units, intrafolial folds have dominant SW- vergence. The granite and amphibolite sheets in the northern Kiru sequence are occasionally folded with a SW- vergence, like 3 km N of Kiru (Fig. 2.14e, Fig. 2.3).

3. PETROLOGICAL AND GEOCHEMICAL ASPECTS OF THE LOWER KOHISTAN COMPLEX

This chapter describes petrological and geochemical aspects and is intended to provide data and interpretations of selected lithologies. A more detailed investigation will require, despite a dense sampling grid covering the area, petrological/geochemical analyses of all various metaplutonics and metavolcanics. The following information is additional to findings previously published by several authors.

3.1 PETROLOGICAL CHARACTERISTIC OF SHEARED AND UNDEFORMED GABBROS, A COMPARISON

Investigations are concentrated on the petrological evolution in the anastomosing shear zones of the gabbros of the Patan region as well as on the pressure and temperature conditions of shearing. The area of interest is comprised of two different gabbros: 1) the Granulitic gabbro of the upper Jijal complex and 2) the Sarangar gabbro (NE of Patan). These samples are described in their successive assemblages and mineral compositions of each undeformed and mylonitic zones. One metadiorite of the Kiru amphibolites is then compared to the gabbros.

3.1.1 Methods

Mineral compositions were analysed using a Cameca SX-50 electron microprobe (University of Bern and ETH Zurich), equipped with five crystal spectrometers. Samples were coated with carbon. Operating parameters include an acceleration potential of 15 kV, a beam current of 20 nA and a beam size of ~1 µm. Probe analyses were recalculated using the program "Norm" by P. Ulmer (ETH-IMP). PT conditions were calculated using the program "Thermobarometry" (Spear & Kohn 1995).

3.1.2 Samples

Five samples were selected in order to represent a comparison between undeformed and mylonitic gabbros of the lower arc, which were affected by anastomosing shear zones and a metadiorite of mid crustal level: Two samples (13/01/01 and 94/04/01) from the Granulitic gabbro, two samples (16/01/01 and 90/02/01) from the Sarangar gabbro and one metadiorite sample (46/02/01) of the Kiru amphibolites (Fig. 3.1). The Granulitic and Sarangar gabbros show strong strain gradients from mylonitic to undeformed to weakly deformed rocks. Analyses were done for both deformation facies.

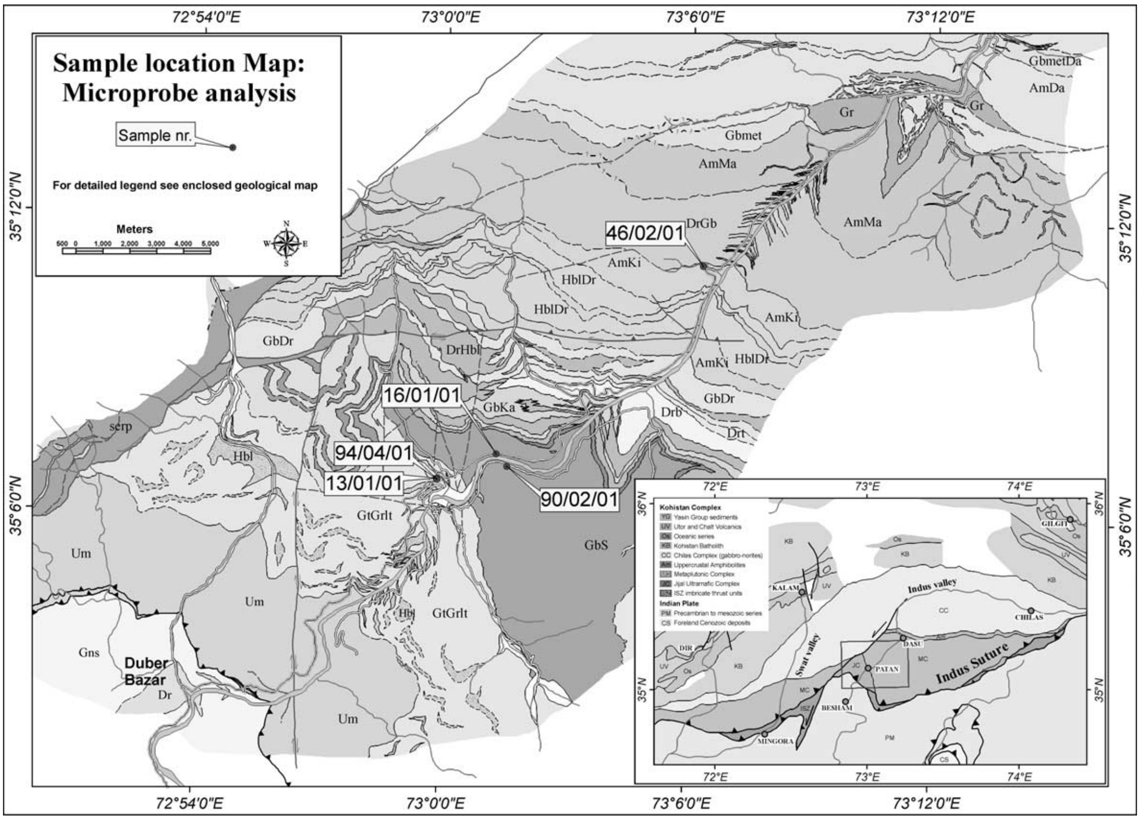

Fig. 3.1: Location map of samples used for electron microprobe analysis. Sample 13/01/01 and 94/04/01 are from the Granulitic gabbro collected along the KKH ca. 500 m SW of Patan. Sample 16/01/01 and 90/02/01 were collected in the Sarangar gabbro ca. 2 km E of Patan along the KKH and at the southern riverside. Sample 46/02/01 was collected ca. 300 m W of the metal bridge (KKH) at Kiru. GPS coordinates are given in appendix 3.1.

3.1.2.1 Granulitic Gabbro

The Granulitic gabbro is also labelled garnet granulite (e.g. Jan & Howie, 1981). The detailed petrography of the Granulitic gabbro has been presented by Jan & Howie (1981), Bard (1983), Miller *et al*. (1991), Yamamoto (1993), Yamamoto & Yoshino (1998) and Ringuette *et al*. (1999). It is divided into two rock types: a two-pyroxene granulite and a garnet-clinopyroxene granulite (Yamamoto & Yoshino, 1998). The analysed samples represent the garnet-clinopyroxene granulite.

The mineral content in the undeformed Granulitic gabbro is plagioclase (affected by saussuritization), clinopyroxene, garnet, amphibole, minor or accessory quartz, rutile, epidote, chlorite, opaque oxides and biotite. The mid to fine grained heteroblastic rock shows a granoblastic texture (Fig. 3.2). The original magmatic assemblage is partially preserved and was overprinted successively by granulite, amphibolite, epidote-amphibolite assemblages (Ringuette *et al.*, 1999).

The magmatic assemblage is represented by:

garnet + clinopyroxene + plagioclase + quartz ± ilmenite.

The existence of magmatic garnet is supported by the fact that inclusion poor garnet occurs in textural equilibrium with other cumulate phases such as clinopyroxene and plagioclase (Ringuette *et al.*, 1999). Most garnets and quartz grains in the analysed samples are possibly metamorphic phases. This is supported by the interstitial growth of garnet and quartz (Fig. 3.3a). The garnets have no pronounced zoning indicating a relatively fast growth under isochemical conditions. Crystallisation took place under granulite facies conditions. It is likely that, subsequently to crystallisation the enstatite component in clinopyroxene reacted with plagioclase to garnet and quartz. In this case the plagioclase composition would change to an albite richer composition, which is observed in the undeformed Granulitic gabbro with albite rich plagioclase (An_{25}).

In the mylonitic part of the Granulitic gabbro the magmatic assemblage is obscured.

The granulite facies assemblage is characterised by:

clinopyroxene + garnet + plagioclase + quartz ± rutile.

Clinopyroxene is hypidioblastic with lobate to symplectitic contacts to plagioclase. The sub- and anhedral garnets are poikiloblastic intergrown with quartz and are in equilibrium with plagioclase (Fig. 3.3a). Quartz is partly dynamically recrystallised (Fig. 3.3b). During amphibolite facies conditions clinopyroxene was overgrown by brown tschermakitic hornblende (Fig. 3.3c). The replacement of clinopyroxene by amphibole is domain-like in the undeformed parts.

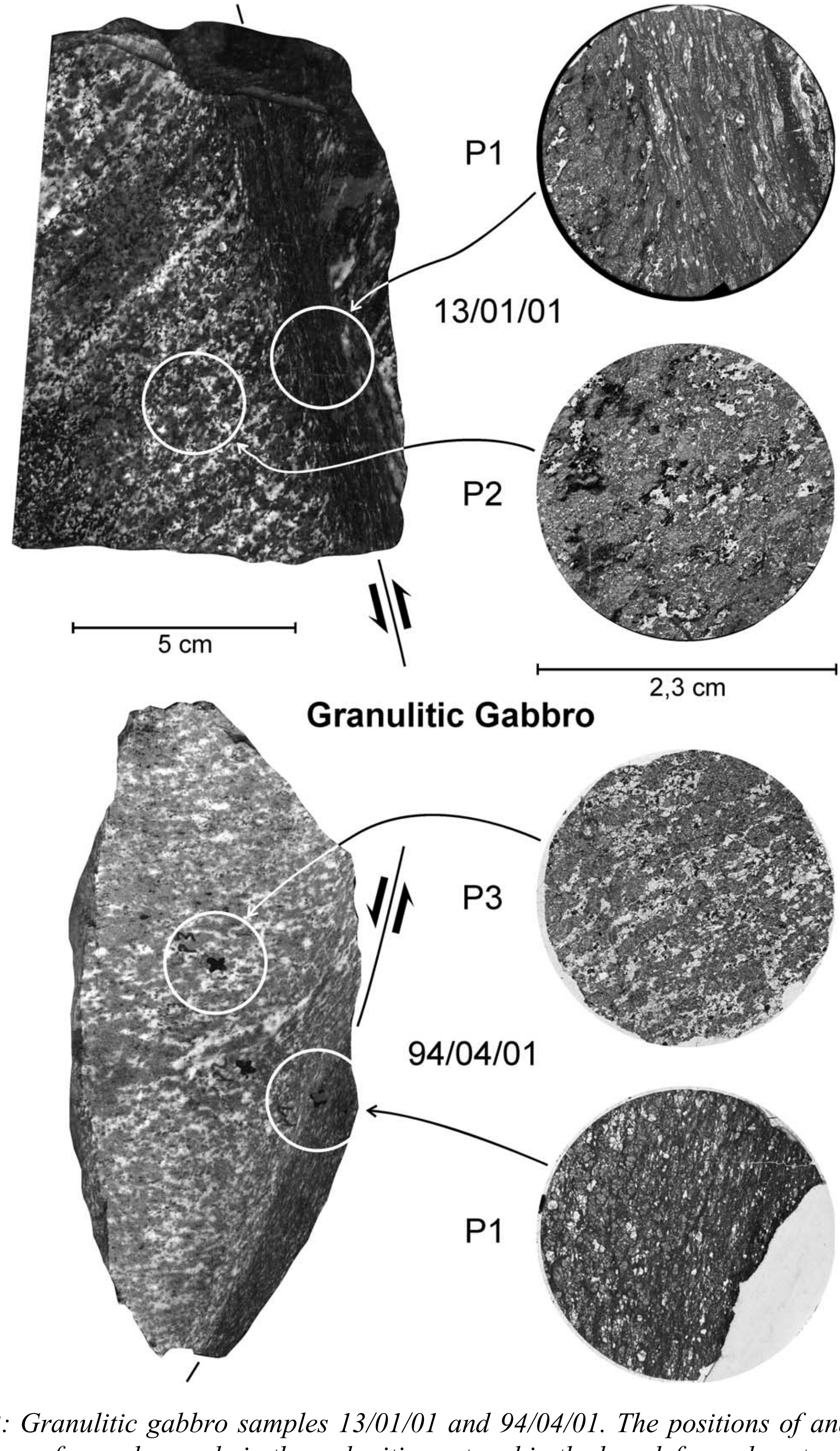

Fig. 3.2: Granulitic gabbro samples 13/01/01 and 94/04/01. The positions of analysed sections are for each sample in the mylonitic part and in the less deformed part.

The latest paragenesis, indicative for epidote-amphibolite facies conditions is:

greenish hornblende + epidote ± clinozoisite ± chlorite.

Beside a strong decrease in grain size, the decrease in amount of clinopyroxene and the increase of amphibole and quartz are the most striking phenomena when focusing on the mylonites. The garnet is porphyroclastic in the very fine grained matrix (~0.3 mm, mainly tschermakitic amphibole), partly rotated and fractured with new grown amphibole in fractures. Clinopyroxene fragments are incorporated in the matrix. Recrystallised quartz in the pressure shadows of garnets as well as the amphibole crystals oriented parallel to the foliation point to a high shear strain (Fig. 3.3d). Within the mylonites an amphibolite facies mineral assemblage overprints the granulite facies mineral assemblage. The foliation defined by hornblende crystals and few poikiloblastic garnets implies, that mylonites formed under granulite to amphibolite facies conditions.

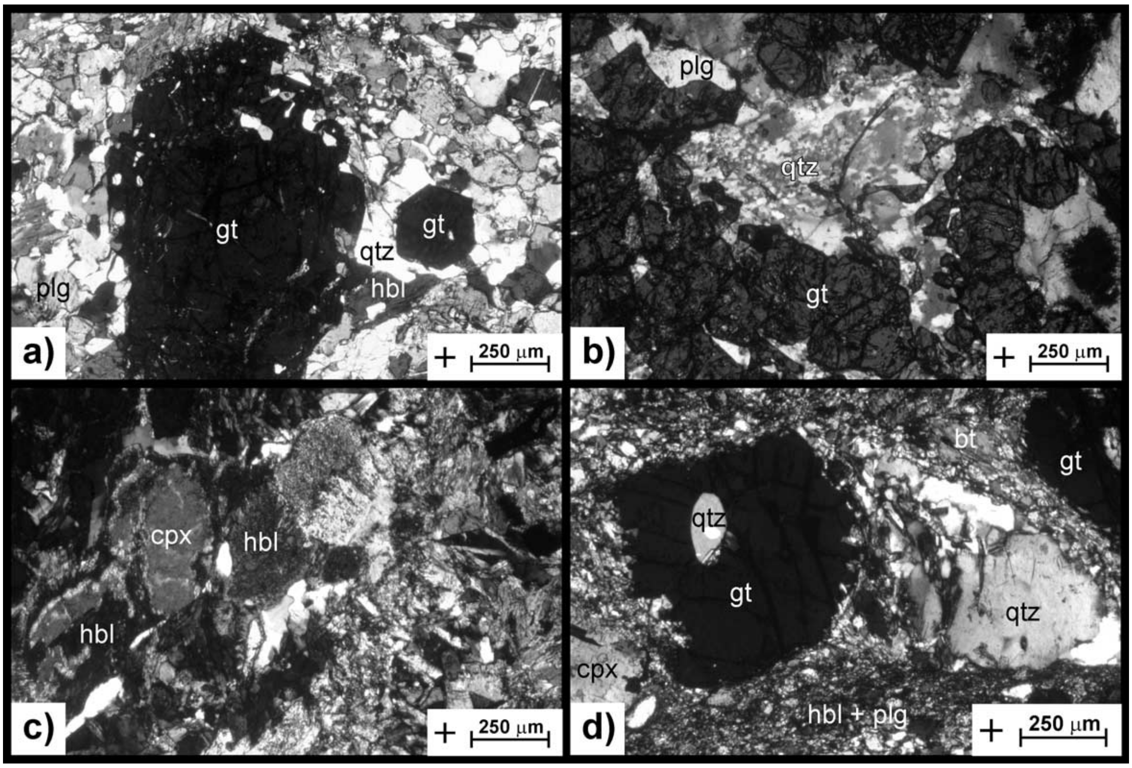

Fig. 3.3: Granulitic gabbro microphotographs: a) 94/04/01 P1, idiomorph garnet in contact to plagioclase and quartz; b) 94/04/01 P3, dynamically recrystallised quartz in less deformed part; c) 13/01/01 P2; overgrowth of pyroxene by hornblende; d) quartz in pressure shadow of garnet clast floating in a matrix of hornblende, pyroxene fragments and plagioclase. + crossed nicols.

3.1.2.2 Sarangar Gabbro

Previous petrological descriptions of the Sarangar gabbro agree that pods surrounded by anastomosing shear zones preserved pyroxene-bearing metagabbro (Treloar *et al.*, 1990) called pyroxene granulite by Yoshino *et al.* (1998). Both samples represent the transition of the relatively undeformed pods to the surrounding mylonites (Fig. 3.4). The dominant composition in the Sarangar gabbro is amphibole (mainly pargasite and tschermakite), pyroxene, plagioclase, rutile, ilmenite, epidote and quartz. In few cm long sections from undeformed spots to the centre of the shear zones the changes are significant in term of mineral assemblages, grain size and orientation of minerals.

The magmatic assemblage, crystallised under granulite facies conditions and only preserved in domains of the undeformed parts (Yamamoto, 1993), is:

pyroxene (opx + cpx) + plagioclase + epidote ± ilmenite ± quartz.

The hypidioblastic orthopyroxene is progressively replaced by clinopyroxene. The sporadic occurrence of poikiloblastic garnet may be due to the reaction mentioned by Yoshino *et al.* (1998):

orthopyroxene + plagioclase = garnet + quartz + clinopyroxene.

The reported granulite facies assemblage (Yoshino *et al.*, 1998) including garnet and rutile is overprinted by the amphibolite facies assemblage:

hornblende + plagioclase + quartz.

Interstitial brown to green hornblende, associated with quartz, occurs as rims between pyroxene and plagioclase (Fig. 3.5a). Yoshino *et al.* (1998) concluded that hornblende and quartz is probably produced by the reaction:

pyroxene + plagioclase + H_2O = hornblende + quartz.

Plagioclase and pyroxene are successively replaced by quartz and hornblende (Fig. 3.5b). Plagioclase shows an increase of symplectitic structures with pyroxene closer to the mylonite.

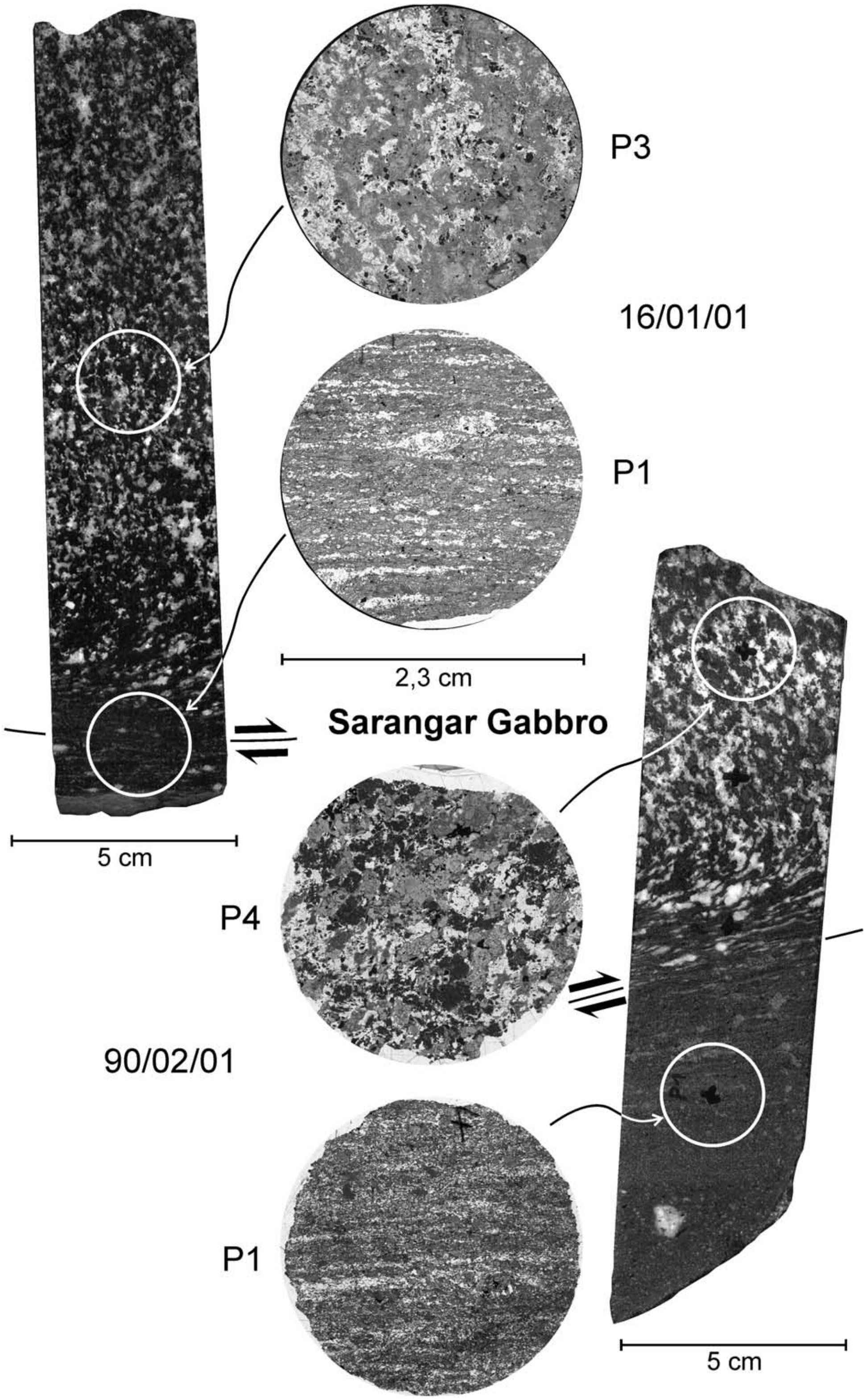

Fig. 3.4: Sarangar gabbro samples 16/01/01 and 90/02/01. The positions of analysed sections are for each sample in the mylonitic part and in the less deformed part.

Within the shear zone, no pyroxene was found. Garnet is abundant showing poikiloblastic growth (Fig. 3.5c) and is generally associated with rutile. Some garnets in the mylonites have helicitic rutile inclusions, suggesting a synkinematic growth of garnet (Fig. 3.5d). The amphiboles underline the fabric and are cut by small quartz veins. Amphibole composition (tschermakitic) is homogenous.

Ilmenite is sparsely preserved as inclusions in brownish hornblende. This points to the retrograde reaction (Bohlen & Liota, 1986):

ilmenite + plagioclase + quartz = rutile + garnet.

The macroscopic porphyroclasts (~2 mm) are plagioclase and quartz aggregates. The dominant, amphibolite facies assemblage is:

hornblende + plagioclase + garnet ± rutile ± quartz.

Chlorite and muscovite overgrow hornblende as late phases under greenschist facies conditions.

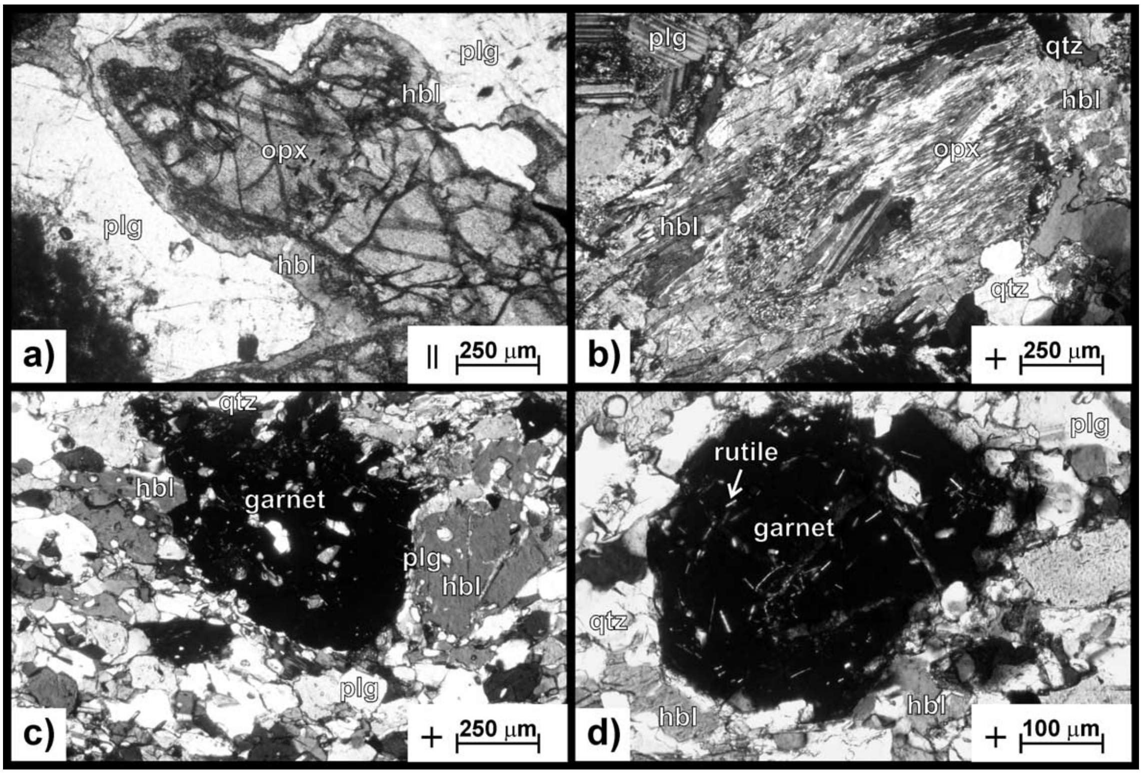

Fig. 3.5: Sarangar gabbro microphotographs: a) 90/02/01 P4, fractured orthopyroxene with hornblende rim indicates retrogression; b) 16/01/01 P3, orthopyroxene replaced successively by hornblende in the undeformed zone; c) 16/01/01 P1, typically poikiloblastic garnet in mylonitic zone with plagioclase, minor quartz and hornblende; d) 90/02/01 P1, new grown garnet in equilibrium to hornblende, plagioclase and quartz, with rutile inclusions in the garnet. + crossed nicols; || parallel nicols.

3.1.2.3 Kiru Amphibolite (Metadiorite)

The Kiru amphibolite sample is a fine grained metadiorite characterised by a well developed foliation defined by hornblende. The alternating plagioclase and hornblende rich layers on the millimetre scale form to the macroscopic foliation (Fig. 3.6a). The garnet free assemblage equilibrated under amphibolite facies conditions is:

hornblende + plagioclase + quartz ± biotite ± epidote ± titanite.

Titanite is rare (Fig. 3.6b). Biotite has corroded boundaries and zircons in its vicinity (Fig. 3.6c). The amphibolite facies assemblage was only little affected by retrogression as it is indicated by chlorite replacing sporadically hornblende (Fig. 3.6d).

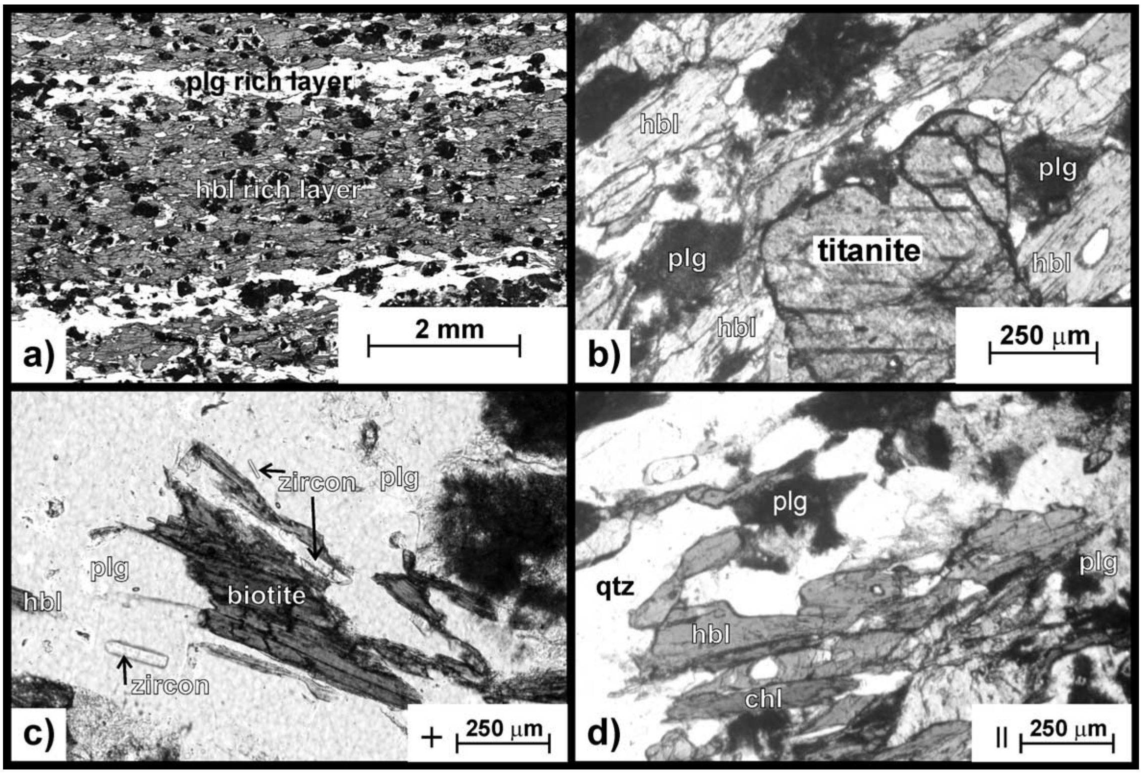

Fig. 3.6: Kiru amphibolite: a) alternating plagioclase (black when affected by saussuritization) and hornblende rich layers parallel to foliation which is defined by a preferred orientation of hornblende crystals; b) titanite as accessory phase; c) biotite affected by retrogression showing corroded boundaries; d) hornblende retrograde overgrown by chlorite. + crossed nicols; || parallel nicols.

3.1.3 Mineral composition

Mineral compositions show differences between the two gabbros and between the mylonitic and less deformed parts.

3.1.3.1 Plagioclase

The plagioclase composition in the undeformed Granulitic gabbro is An_{25-47}, clustered around a maximum of An_{40} for sample 13/01/01, and An_{43-55} for sample 94/04/01 (Fig. 3.7). Plagioclase grains are homogeneous. However, saussuritization may have changed the original composition. Plagioclase compositions in the mylonites are similar to those in the less deformed rock (Table 3.1).

Plagioclase composition in the less deformed Sarangar gabbro is An_{55-70}. Only few grains show a lower anorthite component, around An_{25}. Within the mylonite plagioclase of two different compositions is observed, one with An_{25-45} and one with An_{70-80} respectively. Sample 16/01/01 misses the latter, anorthite rich composition. The composition range between the less deformed parts and the mylonitic ones are not overlapping, pointing to a change of composition related to shearing and/or later alteration along the shear zones.

In the Kiru amphibolites plagioclase composition is in the range of An_{17-46}, similar to the plagioclase compositions measured in the Sarangar gabbro mylonite.

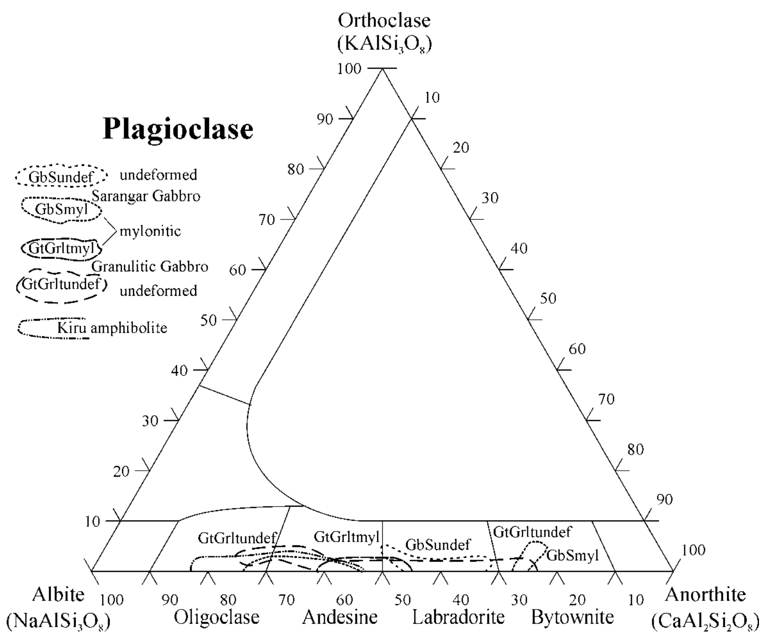

Fig. 3.7: Plagioclase compositions of granulitic gabbro, Sarangar gabbro and Kiru amphibolite.

Table 3.1: Representative (averaged, n = nr. of analyses) chemical composition of plagioclase. Single analyses are given in appendix 3.1.

Electron microprobe data

Mineral: plagioclase

	Granulitic Gabbro				Sarangar Gabbro				Kiru
	undeformed		*mylonitic*		*undeformed*		*mylonitic*		Amph.
Sample	13/01/01	94/04/01	13/01/01	94/04/01	16/01/01	90/02/01	16/01/01	90/02/01	46/02/01
Spot	P2	P3	P1	P1	P3	P4	P1	P1	P1
EMP-Nr.	MP2	MP6	MP1	MP4	MP13	MP10	MP11	MP7	MP19
SiO_2	58.78	57.11	58.55	57.06	53.71	53.50	59.38	59.12	59.16
TiO_2	0.01	0.01	0.01	0.01	0.01	0.01	0.01	0.05	0.01
Cr_2O_3	0.02	0.00	0.01	0.01	0.00	0.01	1.10	0.01	0.00
Al_2O_3	26.63	27.52	26.65	27.67	30.61	28.32	25.50	25.14	24.90
Fe_2O_3	0.03	0.01	0.04	0.00	0.02	0.07	0.02	0.09	0.25
FeO	0.04	0.05	0.04	0.07	0.06	0.05	0.03	0.15	0.00
MnO	0.02	0.00	0.02	0.00	0.02	0.01	0.01	0.03	0.02
MgO	0.00	0.00	0.00	0.00	0.00	0.01	0.00	0.01	0.03
NiO		0.02	0.00	0.01		0.02		0.02	0.01
CaO	7.80	9.92	8.07	9.70	12.39	11.62	7.59	7.09	7.07
Na_2O	6.93	5.77	7.01	5.86	4.50	4.87	7.35	6.39	7.98
K_2O	0.28	0.18	0.07	0.09	0.11	0.17	0.07	0.08	0.15
Total	100.53	100.60	100.47	100.47	101.42	98.65	101.08	98.18	99.58
Si	2.615	2.557	2.605	2.556	2.398	2.451	2.621	2.712	2.641
Ti	0.000	0.001	0.000	0.000	0.000	0.000	0.000	0.002	0.000
Cr	0.001	0.000	0.000	0.000	0.000	0.000	0.057	0.000	0.000
Al	1.396	1.452	1.398	1.461	1.611	1.530	1.327	1.358	1.310
Fe^3	0.001	0.000	0.001	0.000	0.001	0.003	0.001	0.003	0.009
Fe^2	0.001	0.002	0.001	0.002	0.002	0.002	0.001	0.006	0.000
Mn	0.001	0.000	0.001	0.000	0.001	0.001	0.001	0.001	0.001
Mg	0.000	0.000	0.000	0.000	0.000	0.000	0.000	0.001	0.002
Ni		0.001	0.000	0.000		0.001		0.001	0.001
Ca	0.372	0.476	0.385	0.466	0.593	0.571	0.359	0.348	0.338
Na	0.597	0.500	0.604	0.509	0.389	0.432	0.629	0.565	0.691
K	0.016	0.010	0.004	0.005	0.006	0.010	0.004	0.005	0.008
Σ Cations	5.000	5.000	5.000	5.000	5.000	5.000	5.000	5.000	5.000
Albite	0.606	0.504	0.608	0.522	0.394	0.427	0.634	0.611	0.667
Anorthite	0.377	0.485	0.388	0.473	0.600	0.563	0.362	0.384	0.325
Orthoclase	0.016	0.010	0.004	0.005	0.006	0.010	0.004	0.005	0.008
average of n	**25**	**26**	**15**	**25**	**6**	**35**	**25**	**59**	**24**

calculated with "Norm" program by P. Ulmer using: FELDSPAR Norm

Normalization on the basis of 5 CATIONS and 16 CHARGES

3.1.3.2 Garnet

Garnet compositions are in the less deformed Granulitic gabbro $Alm_{40-53}Prp_{23-42}Grs_{15-29}Adr_{01-03}$. In the mylonitic part the composition range is $Alm_{42-53}Prp_{28-42}Grs_{12-28}Adr_{02-04}$ (Fig. 3.8). Garnet composition does not change between the shear zones and the less deformed rock (Table 3.2).

In the Sarangar gabbro garnet occurs only sporadically in the less deformed parts. An analysis with $Alm_{48-51}Prp_{30}Grs_{18-21}$ (Yoshino *et al.*, 1998; Sample P5) is similar to the garnets in the Granulitic gabbro. Within the mylonitic zone garnet occurs as poikilolitic and euhedral neoblasts associated with rutile. Garnet is syn- to postkinematic as indicated by helicitic rutile inclusions and poikilolitic growth. The garnet composition range is $Alm_{55-69}Prp_{15-23}Grs_{11-25}Adr_{01-04}$ (Fig. 3.8) and therefore less pyrope pronounced as the analysis by Yoshino *et al.* (1998). Profiles across garnets are commonly flat. One garnet from the mylonite (13/01/01) has a grossularite richer rim, but weaker than in the profiles given from garnets in the Granulitic gabbro by Ringuette *et al.* (1999).

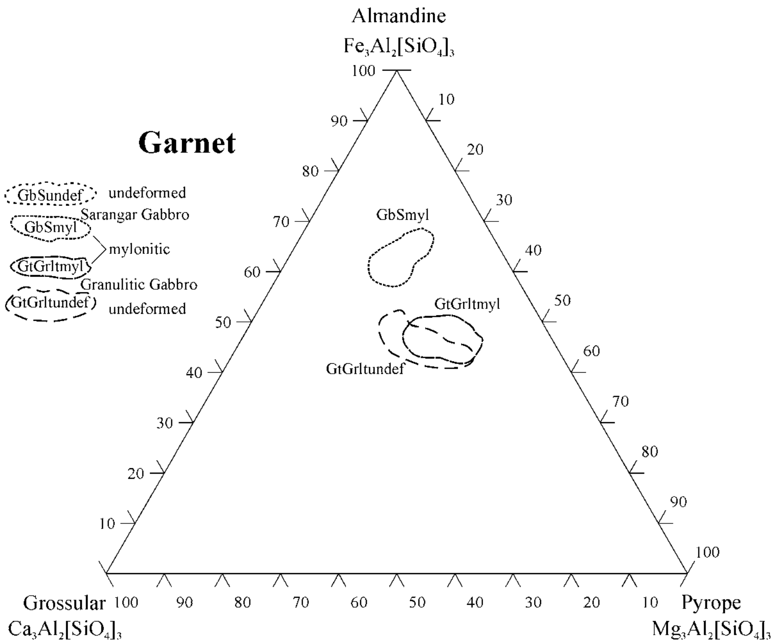

Fig. 3.8: Garnet compositions of Granulitic gabbro and Sarangar gabbro.

Electron microprobe data

Mineral: garnet

	Granulitic Gabbro				Sarangar Gabbro	
	undeformed		*mylonitic*		*mylonitic*	
Sample	13/01/01	94/04/01	13/01/01	94/04/01	16/01/01	90/02/01
Spot	P2	P3	P1	P1	P1	P1
EMP-Nr.	MP2	MP6	MP1	MP4	MP11	MP7
SiO_2	40.07	39.26	39.75	39.16	38.68	37.32
TiO_2	0.06	0.06	0.11	0.07	0.06	0.07
Cr_2O_3	0.03	0.01	0.02	0.00	0.01	0.02
Al_2O_3	22.45	21.63	22.19	21.65	21.77	21.30
Fe_2O_3	0.48	0.90	0.75	1.50	0.22	1.43
FeO	20.39	20.56	21.17	20.43	25.58	25.13
MnO	0.58	0.44	0.58	0.49	3.47	1.91
MgO	9.66	7.75	9.41	8.35	4.62	4.17
NiO		0.01		0.01		0.01
CaO	7.42	9.02	6.94	8.29	6.78	7.73
Na_2O	0.03	0.07	0.03	0.08	0.02	0.04
K_2O	0.02	0.01	0.01	0.02	0.01	0.01
Total	101.20	99.73	100.98	100.07	101.22	99.14
Si	2.997	3.007	2.991	2.987	3.002	2.962
Ti	0.004	0.004	0.006	0.004	0.004	0.004
Cr	0.002	0.000	0.001	0.000	0.001	0.001
Al	1.979	1.953	1.968	1.946	1.991	1.993
Fe^3	0.027	0.052	0.043	0.086	0.013	0.085
Fe^2	1.275	1.318	1.332	1.304	1.660	1.668
Mn	0.037	0.029	0.037	0.032	0.228	0.128
Mg	1.077	0.885	1.055	0.949	0.534	0.493
Ni		0.001		0.001		0.001
Ca	0.595	0.740	0.560	0.677	0.564	0.657
Na	0.005	0.011	0.005	0.011	0.004	0.006
K	0.002	0.002	0.001	0.003	0.001	0.001
Σ Cations	8.000	8.000	8.000	8.000	8.000	8.000
Grossular	0.182	0.219	0.162	0.182	0.179	0.176
Almandine	0.427	0.441	0.446	0.437	0.555	0.565
Pyrope	0.361	0.299	0.353	0.322	0.179	0.167
Spessartite	0.012	0.010	0.012	0.011	0.076	0.044
Andradite	0.014	0.028	0.021	0.045	0.007	0.044
average of n	**24**	**44**	**43**	**39**	**33**	**94**

calculated with "Norm" program by P. Ulmer using: GARNET Norm

Normalization on the basis of 7 CATIONS and 24 CHARGES

Table 3.2: Representative (averaged, n = nr. of analyses) chemical composition of garnet. Single analyses are given in appendix 3.2.

3.1.3.3 Pyroxene

Pyroxenes in the less deformed and mylonitic Granulitic gabbro have similar composition. They range from $En_{35-49}Fs_{10-21}Wo_{33-48}$ for the less deformed to $En_{35-45}Fs_{11-18}Wo_{42-48}$ for the mylonitic gabbro (Fig. 3.9 and Table 3.3). The composition is homogeneous at the grain scale. Analyses plot mainly in the diopside and augite fields.

The Sarangar gabbro has pyroxenes only in the less deformed parts. Clinopyroxenes ($En_{32-38}Fs_{19-26}Wo_{38-45}$) and orthopyroxenes ($En_{48-60}Fs_{35-52}Wo_{01-15}$) are coexisting (Fig. 3.9).

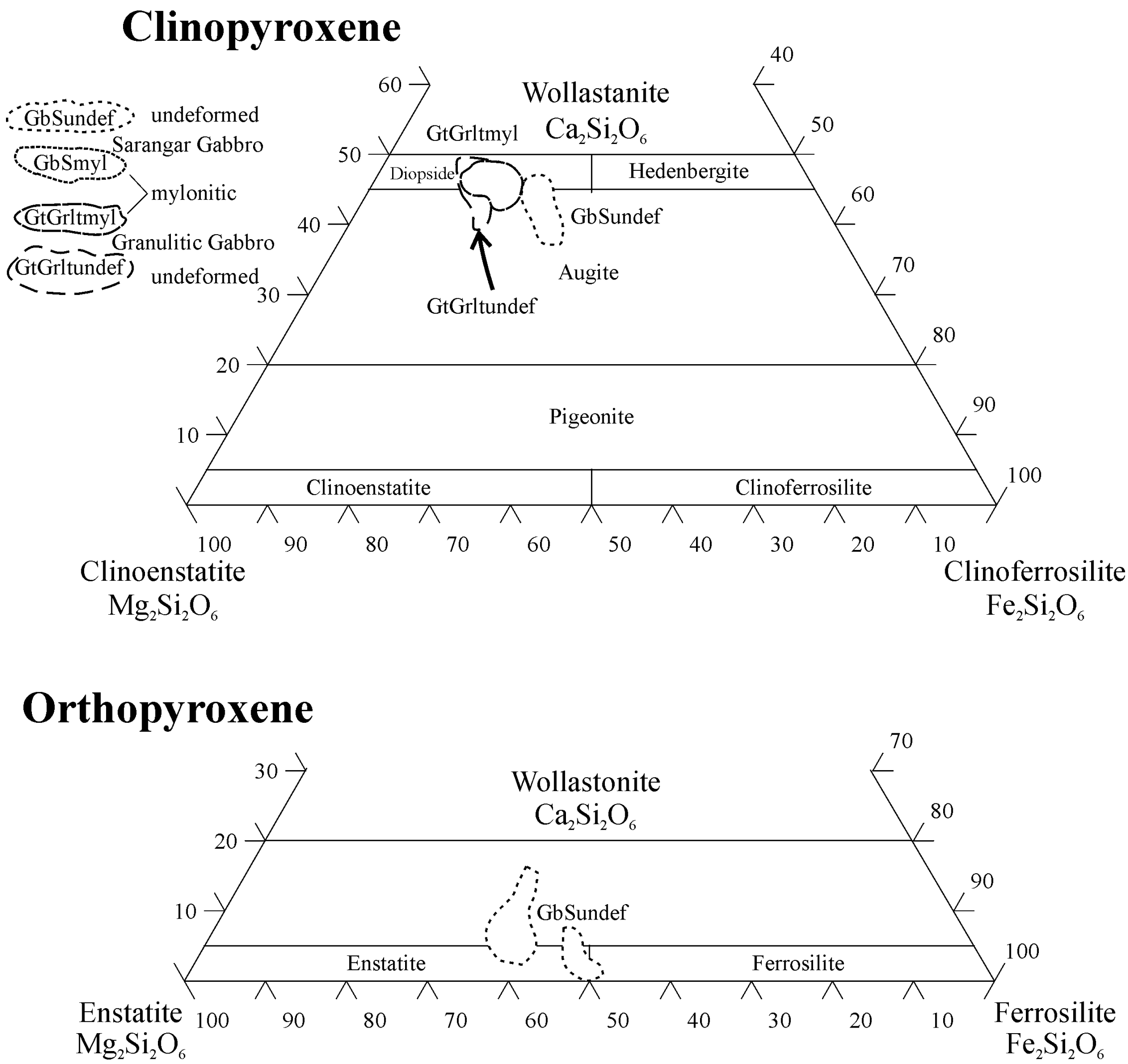

Fig. 3.9: Pyroxene compositions of Granulitic gabbro and Sarangar gabbro. Nomenclature after Morimoto (1988).

Electron microprobe data

	Mineral: clinopyroxene					*orthopyroxene*	
	Granulitic Gabbro				Sarangar Gb.	Sarangar Gabbro	
	undeformed		*mylonitic*		*undeformed*	*undeformed*	
Sample	13/01/01	94/04/01	13/01/01	94/04/01	90/02/01	16/01/01	90/02/01
Spot	P2	P3	P1	P1	P4	P3	P4
EMP-Nr.	MP2	MP6	MP1	MP4	MP10	MP13	MP10
						*	
SiO_2	51.48	50.50	50.86	50.84	49.79	53.60	48.87
TiO_2	0.59	0.55	0.55	0.54	0.35	0.07	0.08
Cr_2O_3	0.09	0.02	0.08	0.01	0.09	0.01	0.02
Al_2O_3	6.00	5.90	6.06	4.68	3.79	2.96	2.61
Fe_2O_3	0.00	0.00	0.00	0.00	0.00	0.00	0.79
FeO	7.57	7.66	6.91	8.52	11.97	20.71	27.61
MnO	0.07	0.04	0.06	0.07	0.33	0.80	0.74
MgO	12.33	11.77	12.06	12.05	10.81	17.14	16.07
NiO		0.02		0.01	0.02	0.00	0.02
CaO	20.65	21.90	21.13	21.80	20.85	2.73	0.80
Na_2O	1.28	1.18	1.28	1.19	0.66	0.34	0.06
K_2O	0.05	0.01	0.05	0.03	0.01	0.11	0.02
Total	100.10	99.55	99.03	99.75	98.67	98.47	97.69
Si	1.898	1.883	1.895	1.901	1.911	2.018	1.930
Ti	0.016	0.016	0.015	0.015	0.010	0.002	0.002
Cr	0.002	0.001	0.002	0.000	0.003	0.000	0.001
Al	0.261	0.259	0.266	0.207	0.171	0.131	0.121
Fe^3	0.000	0.000	0.000	0.000	0.000	0.000	0.023
Fe^2	0.233	0.239	0.215	0.267	0.384	0.652	0.912
Mn	0.002	0.001	0.002	0.002	0.011	0.026	0.025
Mg	0.678	0.654	0.669	0.671	0.619	0.962	0.946
Ni		0.001		0.000	0.001	0.000	0.001
Ca	0.816	0.875	0.844	0.873	0.857	0.110	0.034
Na	0.091	0.086	0.092	0.086	0.049	0.025	0.004
K	0.002	0.001	0.002	0.001	0.001	0.005	0.001
Σ Cations	4.001	4.014	4.003	4.024	4.017	3.930	4.000
xMg Fe(tot)	0.744	0.732	0.757	0.716	0.617	0.596	0.503
Wollastonite	0.365	0.388	0.377	0.397	0.391	0.055	0.017
Enstatite	0.339	0.323	0.334	0.328	0.304	0.478	0.456
Ferrosilite	0.117	0.118	0.107	0.130	0.189	0.324	0.439
average of n	**17**	**33**	**8**	**9**	**18**	**20**	**23**

cpx calculated with "Norm" program by P. Ulmer using: CPX Norm (Cawthorn & Collerson)
opx calculated with "Norm" program by P. Ulmer using: OPX Norm (Wood & Banno) *OPX Norm (Lindsley)
cpx normalization on the basis of 12 CHARGES and Fe^{3+} = Acmite
opx: CATIONS assuming stoichiometry and chargebalance

Table 3.3: Representative (averaged, n = nr. of analyses) chemical composition of pyroxene. Single analyses are given in appendix 3.3.

3.1.3.4 Amphiboles

In the less deformed parts of the Granulitic gabbro the amphiboles are ranging from magnesio-hornblende, actinolitic hornblende to actinolite in the Si – Mg/Mg+Fe^{2+} diagram (Fig. 3.10). In the mylonitic parts most of the analysed amphiboles plot in the tschermakitic hornblende and pargasite field, but also in the tschermakite field. Magnesio-hornblende is also observed in the matrix.

Amphiboles in the Sarangar gabbro are dominantly tschermakite and pargasite (Table 3.4). In the less deformed parts two distinct groups of compositions are present, one plotting in the fields of tschermakitic hornblende, tschermakite, ferro-tschermakite and ferroan pargasite and a less common one plotting in the field of actinolitic hornblende (Fig. 3.10). The actinolitic hornblende composition is typical for epidote-amphibole and greenschist facies conditions.

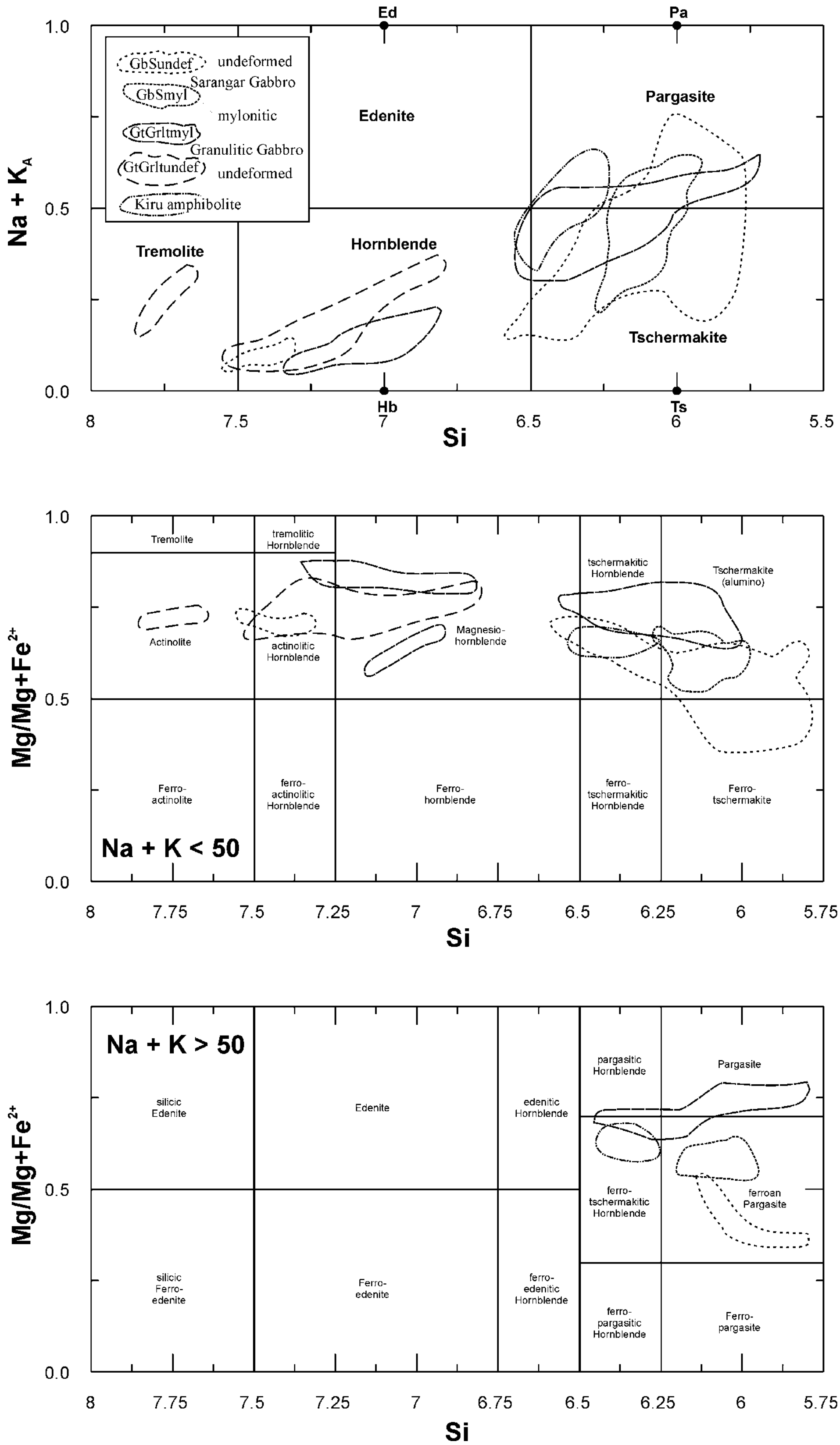

Fig. 3.10: Amphibole variation plots. The uppermost diagram shows the ranges of the measured amphiboles expressed as numbers of $Na+K_A$ and Si atoms per formula unit, whereas to two lower diagrams use the Si versus $Mg/Mg+Fe^{2+}$ plot. Nomenclature after Leake (1978).

Amphibole composition in the mylonitic part shows less variations and plot into small areas in the tschermakite field and ferroan pargasite field (Fig. 3.10). Few analyses are within the magnesio-hornblende and actinolitic hornblende fields (Fig. 3.10). Pargasite and tschermakite are the main phases of the mylonitic shear zones matrix. There is an overlap of composition for amphiboles from the less deformed and mylonitic part in the hornblende field.

Amphiboles in the Kiru amphibolites are homogenous tschermakitic hornblende and ferro-tschermakitic hornblendes (Fig. 3.10 and Table 3.4).

Electron microprobe data

Mineral: amphibole

	Granulitic Gabbro			Sarangar Gabbro					Kiru
	undeformed	*mylonitic*		*undeformed*			*mylonitic*		Amph.
Sample	13/01/01	13/01/01	94/04/01	16/01/01		90/02/01	16/01/01	90/02/01	46/02/01
Spot	P2	P1	P1	P3		P4	P1	P1	P1
EMP-Nr.	MP2	MP1	MP4	MP13		MP10	MP11	MP7	MP19
					*				
SiO_2	52.20	44.23	45.09	43.11	51.84	39.24	42.28	40.49	42.81
TiO_2	0.54	0.37	0.22	0.29	0.27	0.54	0.61	0.66	0.64
Cr_2O_3	0.07	0.03	0.01	0.03	0.03	0.02	0.04	0.03	0.03
Al_2O_3	6.93	15.47	13.69	16.01	5.78	16.76	17.01	16.14	13.59
Fe_2O_3	0.93	4.18	5.76	6.44	1.83	5.70	5.40	4.07	2.92
FeO	9.34	8.74	7.04	9.90	11.10	12.44	9.47	11.68	10.95
MnO	0.22	0.14	0.06	0.28	0.26	0.26	0.26	0.12	0.34
MgO	14.13	11.07	12.51	9.27	15.04	7.18	9.65	9.02	10.91
NiO	0.00	0.00	0.01	0.00	0.00	0.01	0.00	0.02	0.02
CaO	12.62	11.06	10.98	10.85	11.32	10.74	10.99	11.45	11.74
Na_2O	0.80	1.93	2.16	1.61	0.66	1.45	1.87	1.82	1.54
K_2O	0.24	0.51	0.51	0.58	0.18	1.29	0.57	0.63	1.00
Cl	0.00	0.00	0.00	0.00	0.00	0.00	0.00	0.00	0.00
H_2O	2.09	2.07	2.08	2.06	2.10	1.96	2.06	1.99	2.01
Total	100.09	99.81	100.13	100.44	100.41	97.58	100.22	98.10	98.49
Si	7.492	6.399	6.483	6.268	7.396	6.001	6.148	6.092	6.378
Ti	0.058	0.040	0.024	0.032	0.029	0.063	0.067	0.075	0.072
Cr	0.008	0.003	0.001	0.003	0.003	0.003	0.005	0.003	0.003
Al	1.172	2.640	2.331	2.746	0.973	3.017	2.915	2.861	2.387
Fe^3	0.100	0.456	0.623	0.703	0.196	0.648	0.590	0.460	0.327
Fe^2	1.121	1.058	0.850	1.206	1.324	1.599	1.152	1.470	1.365
Mn	0.026	0.017	0.007	0.035	0.032	0.033	0.032	0.015	0.043
Mg	3.022	2.388	2.679	2.006	3.197	1.635	2.090	2.022	2.422
Ni	0.000	0.000	0.001	0.000	0.000	0.002	0.000	0.003	0.002
Ca	1.947	1.716	1.694	1.691	1.730	1.761	1.713	1.845	1.873
Na	0.222	0.543	0.606	0.455	0.184	0.429	0.528	0.531	0.446
K	0.044	0.095	0.095	0.109	0.033	0.253	0.106	0.121	0.190
OH	2.000	2.000	2.000	2.000	2.000	2.000	2.000	2.000	2.000
Σ Cations	15.354	15.354	15.394	15.255	15.096	15.444	15.346	15.496	15.509
xMg Fe(tot)	0.612	0.612	0.642	0.510	0.678	0.420	0.545	0.512	0.589
Tschermak	1.531	1.531	1.429	1.785	0.627	1.794	1.792	1.566	1.239
Edenite	0.354	0.354	0.394	0.255	0.096	0.444	0.346	0.496	0.509
Plagioclase	0.284	0.284	0.306	0.309	0.120	0.239	0.287	0.155	0.127
average of n	**16**	**19**	**21**	**35**	**8**	**27**	**27**	**100**	**36**

calculated with "Norm" program by P. Ulmer using: Amphibole Norm NAMP *Amphibole Norm SK

CATIONS calculated on the bases of 23 oxygens and 13 cations + K + Na + Ca

*CATIONS calculated on the bases of 23 oxygens and averaged Fe3+

Table 3.4: Representative (averaged, n = nr. of analyses) chemical composition of amphiboles. Single analyses are given in appendix 3.4.

3.1.3.5 Biotite, Muscovite and Chlorite

Biotite and muscovite occur in the mylonites and sparsely in their vicinity. Biotite occurs frequently in contact to garnet in the Granulitic gabbro (Fig. 3.11a), whereas in the Sarangar gabbro biotite is a minor accessory mineral. In the Kiru amphibolite biotite is corroded at its boundaries.

White mica is concentrated to the plagioclase and quartz rich parts of the Sarangar gabbro mylonites, overgrowing amphibolite facies assemblages (Fig. 3.11b), thus indicating a greenschist facies overprint.

Chlorite, often filling the fractures in pyroxenes or replacing amphiboles, was formed during retrogression in the Granulitic and Sarangar gabbros and the Kiru amphibolite (Fig. 3.11c, analyses in Table 3.5). Chlorite is generally present in small amounts in the bulk rock, but in certain domains the concentration is noticeably higher. This indicates a localised greenschist facies overprint.

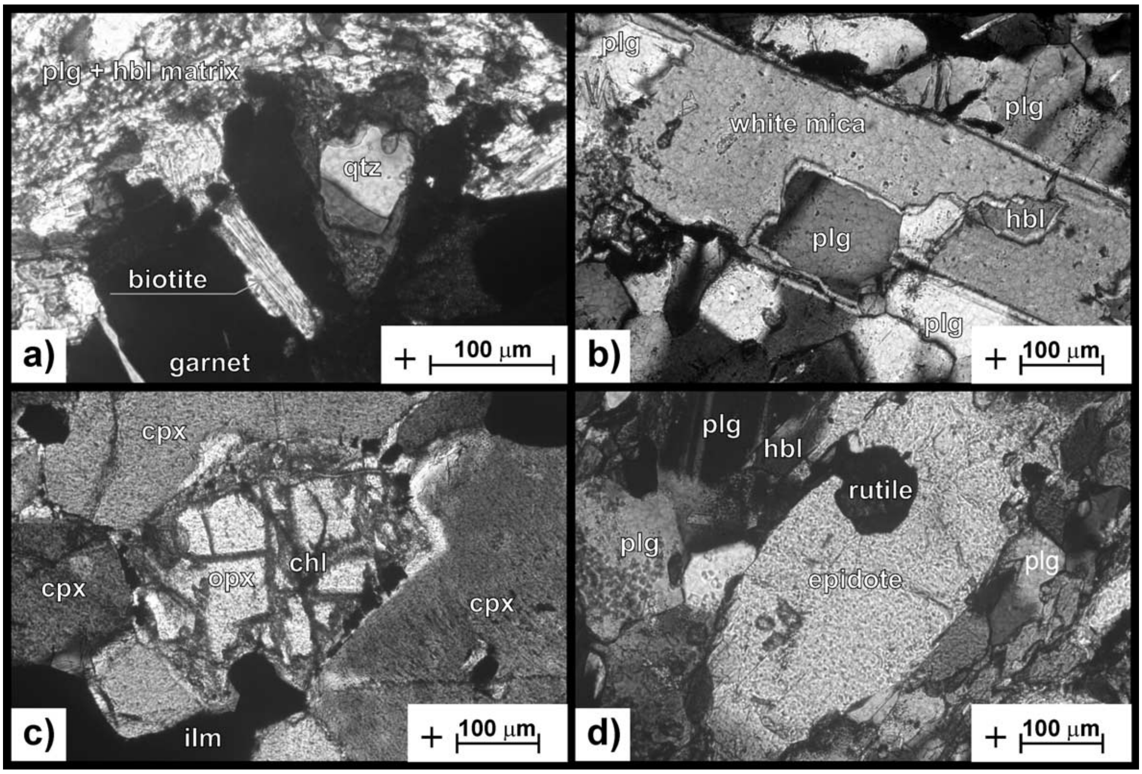

Figure 3.11: a) biotite as secondary phase grown in fractured garnet in a mylonitic granulitic gabbro (13/01/01); b) muscovite overgrows hornblende and plagioclase in a mylonitic Sarangar gabbro (16/01/01); c) chlorite as fracture fill of an orthopyroxene surrounded by clinopyroxene in an undeformed Sarangar gabbro (90/02/01); d) epidote with rutile inclusion in contact to hornblende and plagioclase in a mylonitic Sarangar gabbro (90/02/01). + crossed nicols.

Table 3.5: *Representative (averaged, n = nr. of analyses) chemical composition of biotite, muscovite and chlorite. Single analyses are given in appendix 3.5.*

Electron microprobe data

	biotite		muscovite	chlorite		
	Gr. Gabbro	Sarangar Gb.	Sarangar Gb.	Sarangar Gb.		Kiru
	mylonitic	*undeformed*	*mylonitic*	*undeformed*	*mylonitic*	Amph.
Sample	13/01/01	16/01/01	16/01/01	90/02/01	90/02/01	46/02/01
Spot	P1	P3	P1	P4	P1	P1
EMP-Nr.	MP1	MP13	MP11	MP10	MP7	MP19
SiO_2	33.71	31.77	45.97	29.81	24.28	33.55
TiO_2	1.72	2.39	0.06	0.10	0.06	2.02
Cr_2O_3	0.63	0.17	0.01	0.03	0.02	0.02
Al_2O_3	17.01	18.06	36.71	15.12	20.84	17.63
Fe_2O_3	1.03	15.44	2.02	0.00	0.00	0.00
FeO	15.61	6.89	0.00	26.20	25.84	14.85
MnO	0.04	0.16	0.02	0.19	0.25	0.18
MgO	12.46	13.56	0.81	14.31	14.66	14.81
NiO				0.02	0.01	0.03
CaO	0.16	0.89	0.02	0.31	0.10	0.78
Na_2O	0.21	0.12	1.18	0.03	0.05	0.12
K_2O	7.06	2.57	8.66	0.20	0.03	4.79
H_2O	3.77	3.97	4.60	2.30	2.28	2.47
Total	93.40	95.97	100.06	88.59	88.40	91.24
Si	2.683	2.400	2.997	3.889	3.191	4.066
Ti	0.103	0.136	0.003	0.009	0.006	0.186
Cr	0.039	0.010	0.000	0.003	0.002	0.002
Al	1.595	1.607	2.821	2.315	3.227	2.525
Fe^3	0.061	0.873	0.099	0.000	0.000	0.000
Fe^2	1.039	0.438	0.000	2.867	2.841	1.513
Mn	0.003	0.010	0.001	0.020	0.028	0.019
Mg	1.477	1.525	0.079	2.776	2.871	2.689
Ni				0.002	0.001	0.002
Ca	0.014	0.072	0.002	0.043	0.014	0.106
Na	0.033	0.018	0.150	0.007	0.013	0.027
K	0.717	0.247	0.720	0.032	0.004	0.725
OH				2.000	2.000	2.000
H	2.000	2.000	2.000			
Σ Cations	7.763	7.337	6.871	13.963	14.197	13.860
xMg Fe(tot)	0.573	0.538	0.432	0.494	0.503	0.640
average of n	**3**	**6**	**5**	**2**	**4**	**11**

biotite calculated with "Norm" program by P. Ulmer using: Mica Norm BIO (Standard)
CATIONS calculated on the bases of 11 oxygens 7 cations + Na + K + Ca
muscovite calculated with "Norm" program by P. Ulmer using: Mica Norm MUS (Standard)
CATIONS calculated on the bases of 11 oxygens and 6 cations + Na + K +
chlorite calculated with "Norm" program by P. Ulmer using: General OXIDE Norm all Fe(II+)
CATIONS calculated on the basis of 18. Oxygens

3.1.3.6 Epidote

Epidote occurs in all analysed samples (see Table 3.6). In the Sarangar gabbro epidote shows vermicular growth and rutile inclusions, indicative for fast crystallization at solidus condition (Fig. 3.11d). In the mylonites epidote concentration is higher in the garnet free domains and vice versa, suggesting that the Fe availability was decisive for the growth of epidote or garnet. In the other samples epidote is poikiloblastic or nematoblastic, pseudomorph after plagioclase and infrequently associated with muscovite.

Table 3.6: Representative (averaged, n = nr. of analyses) chemical composition of epidote. Single analyses are given in appendix 3.6.

Electron microprobe data

Mineral: epidote

	Granulitic Gb.	Sarangar Gabbro				Kiru
	mylonitic	*undeformed*		*mylonitic*		Amph.
Sample	94/04/01	16/01/01	90/02/01	16/01/01	90/02/01	46/02/01
Spot	P1	P3	P4	P1	P1	P1
EMP-Nr.	MP4	MP13	MP10	MP11	MP7	MP19
SiO_2	38.35	39.15	38.35	38.39	37.41	37.87
TiO_2	0.06	0.04	0.01	0.08	0.15	0.15
Cr_2O_3	0.01	0.01	0.01	0.01	0.03	0.01
Al_2O_3	27.24	28.36	27.41	27.46	26.78	27.48
Fe_2O_3	8.49	7.38	8.54	9.38	8.73	8.10
FeO	0.00	0.00	0.00	0.00	0.00	0.00
MnO						
Mn_2O_3	0.08	0.22	0.15	0.60	0.16	0.21
MgO	0.10	0.06	0.07	0.36	0.10	0.06
NiO	0.01	0.00	0.00	0.00	0.02	0.02
CaO	23.12	23.17	23.25	21.70	24.26	24.04
Na_2O	0.02	0.04	0.02	0.03	0.08	0.02
K_2O	0.02	0.03	0.01	0.03	0.01	0.01
H_2O	1.91	1.94	1.92	1.93	1.90	1.92
Total	99.40	100.39	99.72	99.91	99.60	99.87
Si	3.003	3.020	2.996	2.989	2.947	2.962
Ti	0.004	0.002	0.001	0.004	0.009	0.009
Cr	0.000	0.001	0.001	0.001	0.002	0.001
Al	2.515	2.578	2.523	2.519	2.485	2.533
Fe^3	0.501	0.429	0.502	0.551	0.518	0.477
Fe^2	0.000	0.000	0.000	0.000	0.000	0.000
Mn						
Mn^{3+}	0.005	0.013	0.009	0.036	0.010	0.012
Mg	0.012	0.007	0.008	0.042	0.012	0.007
Ni	0.001	0.000	0.000	0.000	0.001	0.001
Ca	1.940	1.915	1.946	1.808	2.047	2.014
Na	0.004	0.006	0.003	0.005	0.012	0.003
K	0.002	0.003	0.002	0.003	0.001	0.001
OH	1.000	1.000	1.000	1.000	1.000	1.000
Σ Cations	18.015	18.027	18.011	18.043	17.957	17.980
Zoisite	0.506	0.579	0.520	0.532	0.443	0.504
Epidote	0.484	0.419	0.481	0.498	0.517	0.477
average of n	**13**	**14**	**2**	**12**	**40**	**10**

calculated with "Norm" program by P. Ulmer using: Epidote Norm
CATIONS calculated on the bases of 12 oxygens and 1 OH-group
calculated with "Norm" program by P. Ulmer using: Sphene Norm
CATIONS calculated on the bases of 3 cations and 10 charges - Oh-group

3.1.4 PT calculations

Pressure and temperature conditions were calculated using the program "Thermobarometry" by F. Spear & M.J. Kohn (1995). This relatively easy to use program provides calculations of many published geothermometers and geobarometers and plots the results as lines of constant equilibrium (K_{eq}) on a PT diagram. K_{eq} lines were obtained for different reactions and calibrations. The intersections of K_{eq} lines of geobarometer- and geothermometer-reactions are marked with white circles, where compositions from the same minerals were used for calculations (Fig. 3.12).

Results for the undeformed Granulitic gabbro range between 625 – 905 °C and 0.65 – 1.29 GPa (Fig. 3.12, 13/01/01 P2 and 94/04/01 P3). The upper value was obtained with a garnet-plagioclase-clinopyroxene-quartz assemblage (measured in grain centre) and is in partial agreement with published conditions of 813 – 949 °C and 1.15 – 1.7 GPa (Yamamoto, 1993), 713 – 1134 °C and 1.53 – 2.19 GPa (Ringuette *et al.*, 1999) and 860 – 970 °C and 1.5 – 3.0 GPa (Anczkiewicz & Vance, 2000). The calculated pressure of 1.29 GPa is below the pressures presented by Anczkiewicz & Vance (2000) and Ringuette *et al.* (1999), possibly because our samples are close to a mylonitic zone. As described before the amphibolite facies assemblage is primarily developed in the mylonite. Therefore amphibolitisation is strong in the mylonite, declining towards the core of the undeformed pods. The sample, just a few centimetres away from the mylonitic zone, is probably more affected by some retrogression than those from the core of undeformed pods. The lower value used a garnet-plagioclase-hornblende-quartz assemblage (measured at grain rims). One garnet-plagioclase-clinopyroxene-quartz assemblage (measured at grain rims) yielded a pressure of 0.89 GPa at a temperature of 625 °C, showing a difference in pressure of 0.24 GPa to the one obtained with the garnet-plagioclase-hornblende-quartz assemblage at the same temperature. This discrepancy is due to applied reaction/calibration and gives an estimate of error. The results show clearly the retrograde character of the successive equilibration. The PT conditions for the mylonitic part (Fig. 3.12, 13/01/01 P1 and 94/04/01 P1) range from 600 – 900 °C and 0.54 – 1.19 GPa, with a pronounced pressure range of 0.75 – 1.0 GPa. Temperatures higher than 900 °C for shear zones are reported by Ringuette *et al.* (1999). The higher pressure and temperature values are obtained from porphyroclasts and their inclusions. A new grown garnet-hornblende assemblage yields a temperature of ca. 740 °C and pressure of 0.8 – 0.9 GPa. Small amphiboles in the matrix point to an equilibration temperature of 650 – 700 °C and amphiboles newly grown in fractures of garnet clasts yield temperatures of 680 – 770 °C.

PT conditions for the less deformed parts of the Sarangar gabbro range from 575 – 800 °C and 0.58 – 0.81 GPa (Fig. 3.12, 16/01/01 P3 and 90/02/01 P4). Garnet compositions were taken from the centre of garnet porphyroclasts in the mylonitic parts. Therefore the calculated pressures are most likely too low and should not be interpreted without confirmation by garnet independent geobarometers.

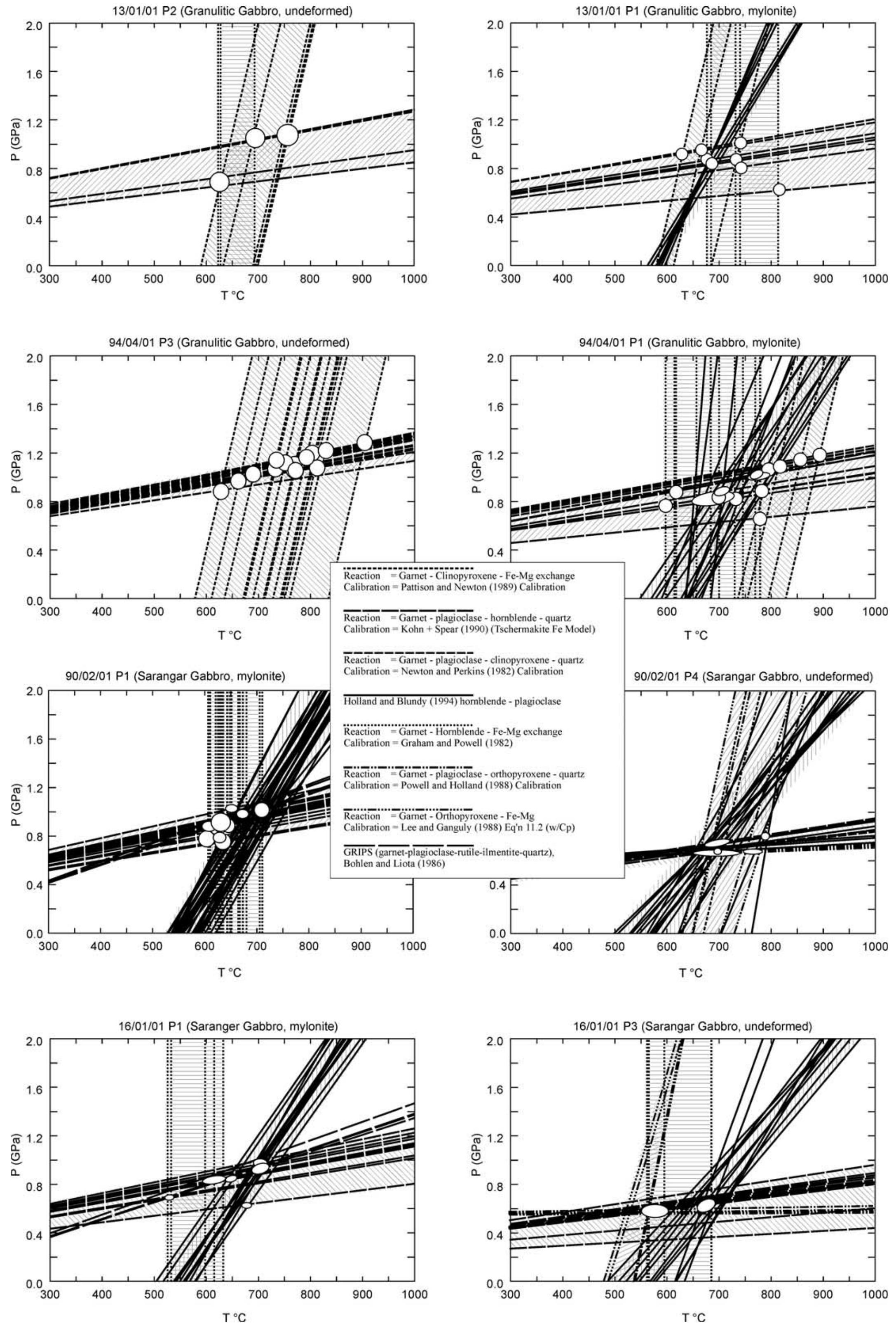

Fig. 3.12: PT conditions for Granulitic gabbro and Sarangar gabbro samples of the mylonitic zone and less deformed portions obtained by K_{eq} lines for specific reactions and calibrations. White circles mark crossings of K_{eq} lines calculated for same mineral compositions.

Peak conditions obtained with clinopyroxene-plagioclase-quartz assemblages are 760 – 870 °C and 0.82 – 1.1 GPa (Yoshino *et al.*, 1998). PT estimates from an amphibolite in the Swat valley is 690 – 860 °C and 0.7 – 0.9 GPa (Anczkiewicz & Vance, 2000), which is similar to the conditions of the Sarangar gabbro. In the mylonitic portion temperatures and pressure range from 525 – 710 °C and 0.58 – 1.0 GPa (Fig. 3.12, 16/01/01 P1 and 90/02/01 P1). New grown garnet-hornblende-plagioclase-quartz assemblage yielded conditions of 640 – 710 °C and 0.9 – 1.0 GPa. The lowest obtained temperature (525 °C) was calculated using the composition at the rims of the minerals (garnet-hornblende-plagioclase).

Metamorphic conditions for the "Kamila Amphibolite Belt" are estimated around 550 – 650 °C and 0.9 – 1.0 GPa (Treloar *et al.*, 1990) using a garnet-amphibole thermometry. Pressure temperature conditions were estimated for the Kiru amphibolite here with 0.7 – 1.0 GPa and 640 – 715 °C (Fig. 3.13). Temperatures were calculated using the hornblende-plagioclase geothermometer (Holland & Blundy, 1994). The temperature difference between the above mentioned estimates might be due to the different applied thermometers or differently equilibrated samples. Due to the lack of garnet in the analysed sample the pressure was estimated using the Al content in hornblende. This method is valid for a igneous assemblage (Schmidt, 1992) which is close (but not complete) to the assemblage in the Kiru amphibolites. Pressures are consequently only rough estimates.

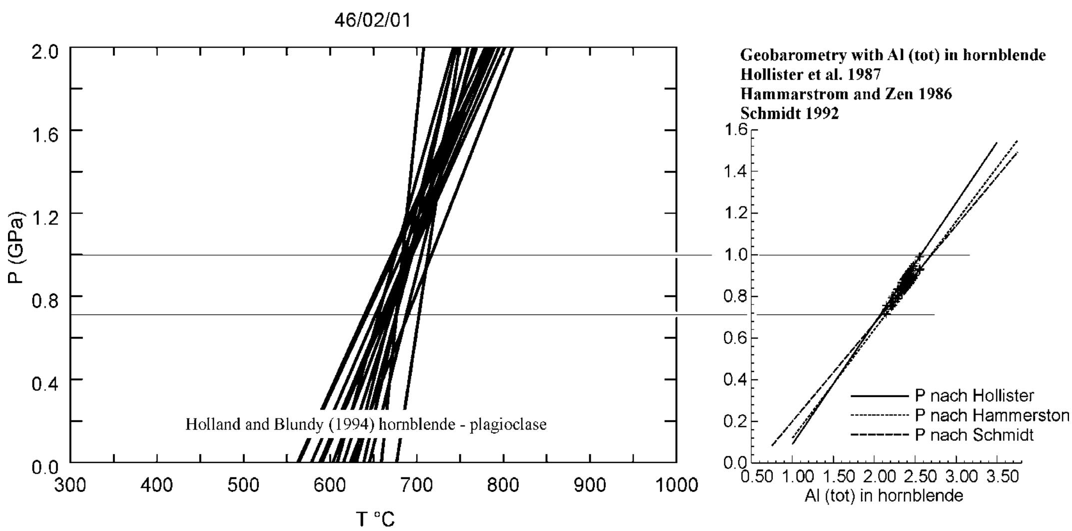

Fig. 3.13: PT condition for Kiru amphibolite. Temperature calculated after the hornblende-plagioclase geothermometer (Holland and Blundy, 1994). Pressure estimated by the total Aluminium content in hornblende.

Comparing the PT conditions inside and outside the mylonite of the Granulitic and Sarangar gabbros a pressure difference of ca. 0.2 GPa at the same temperature is noticed. The mylonitic zones of the Granulitic and Sarangar gabbros have similar pressure conditions, whereas the undeformed portions plot in higher pressure (Granulitic gabbro) and lower pressure (Sarangar gabbro) (Fig. 3.14). This effect is most likely the result of an underestimate of pressures in the undeformed Sarangar gabbro due to the applied geobarometers, which require garnet. The lack of applicable geobarometers, that fit the measured assemblage led to the use of an averaged garnet composition from the mylonite zone to complete the assemblages for the applied geobarometers. This does not represent a strict equilibrated (at least for garnet) assemblage. The calculated pressures for the undeformed Sarangar gabbro should therefore be considered only as imprecise minimum pressures.

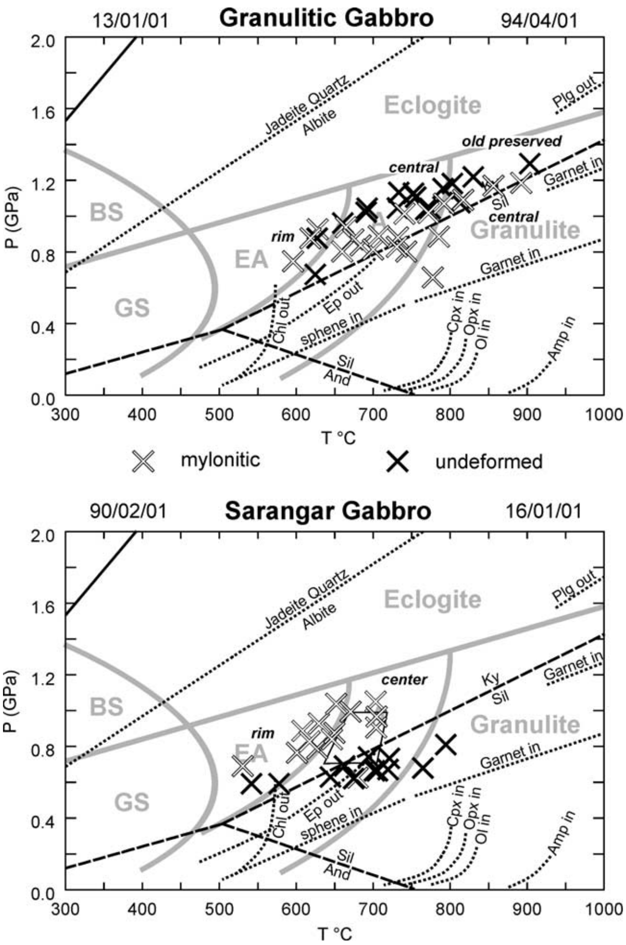

Fig. 3.14: Comparison between PT conditions of mylonitic and undeformed sample portions. The Granulitic gabbro yields ca. 0.2 GPa higher pressures in the undeformed parts than in the mylonitic zone, whereas the Sarangar gabbro yields higher pressures in the mylonitic zone. Black square in the lower diagram shows the obtained PT conditions of Kiru amphibolites.

3.1.5 Interpretation of petrological evolution and PT conditions

The PT conditions obtained in the mylonitic parts suggest that the development of the anastomosing shear zones started under granulite facies conditions at ca. 800 °C and ~1.0 GPa and continued under amphibolite facies to minimum ca. 550 °C and ~0.4 GPa. The integrated PT path (Fig. 3.15) can be split in three parts: 1) cooling to ca. 750 °C at ca. 1.0 GPa, 2) decompression between ca. 1.0 GPa to ca. 0.35 GPa at 550 °C and 3) cooling. The Kiru amphibolite equilibrated under amphibolite facies conditions at ca.0.7 – 1.0 GPa and 640 – 715 °C at the beginning of the decompression.

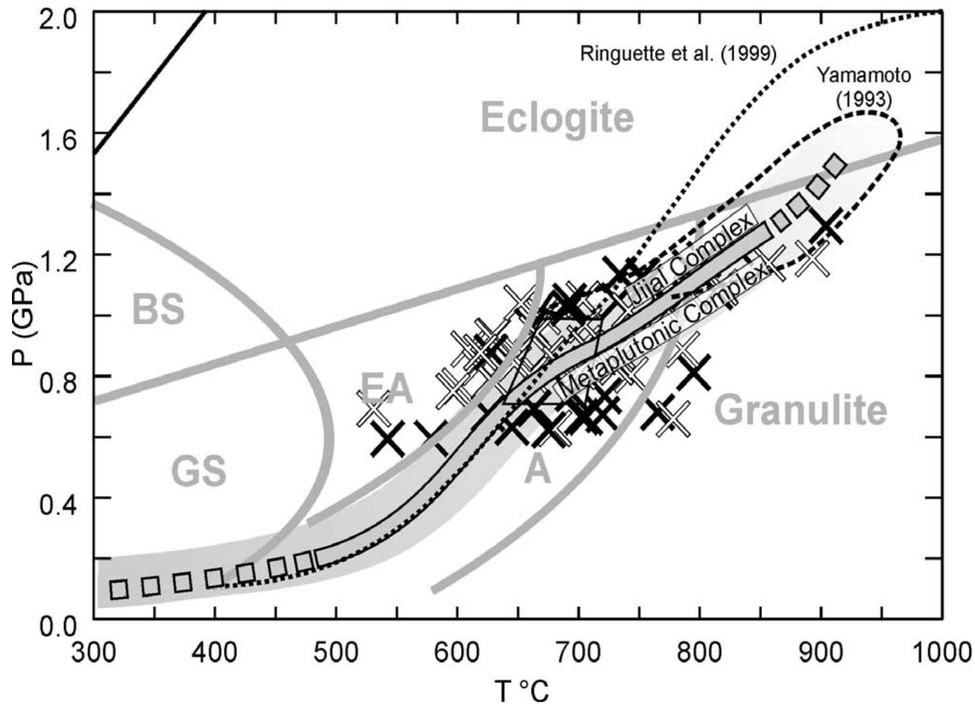

Fig. 3.15: Integrated PT path for the lowest Kohistan Arc Complex (Jijal and Metaplutonic Complex). Black square shows the obtained PT conditions of Kiru amphibolites. Stippled paths are representative for the Granulitic gabbro of the Jijal Complex (after Ringuette et al., 1999; Yamamoto, 1993). Metamorphic facies: GS = Greenschist, BS = Blueschist, EA = Epidote-Amphibolite, A = Amphibolite.

3.1.6 Discussion

Early magmatic crystallization of gabbroic magma in both the Granulitic gabbro and the Sarangar gabbro involved temperatures > 1000 °C (Yamamoto 1993; Yoshino *et al.*, 1998; Ringuette *et al.*, 1999). They agree about the amphibolite and greenschist facies retrograde path that followed this high-temperature stage. Some uncertainty exists over the high-temperature high-pressure evolution of the Granulitic gabbro, which resulted in different petrogenetic interpretations. Based on geothermobarometry of symplectites and inclusion-host assemblages of garnet, clinopyroxene and plagioclase, Yamamoto (1993) suggested that garnet growth occurred after magmatic crystallization during heating to temperatures of ca. 900 °C and burial to pressures < 1.5 GPa and before decompression began to amphibolite facies conditions at 700 °C and 1.0 GPa. He also argued that heating and burial are due to crustal thickening based on Al_2O_3 increase from core to rim in orthopyroxene combined with an increase in the grossular content of garnet. Crustal thickening would be caused by accretion of basaltic magma at mid- and upper crustal depths. Yoshino *et al.* (1998) suggest a similar process where heating and burial formed granulites in the Metaplutonic Complex, reaching conditions of ca. 800 °C and of 0.8 – 1.1 GPa for the maximum pressure. They estimated, based on the Al zoning of clinopyroxene and plagioclase a prograde path from ~0.8 GPa to ~1.1 GPa along with a slight temperature increase. Ringuette *et al.* (1999) favour a magmatic crystallization followed by a period of isobaric cooling, after which ca. 1.0 GPa of decompression occurred whilst the rocks remained above ca. 700 °C. They show that some garnet is in textural equilibrium with other cumulate phases such as clinopyroxene, plagioclase and amphibole, which attest for its magmatic origin. Core-rim pairs and compositional profiles across garnets and pyroxene indicate a quasi-isobaric cooling trend corresponding to the transition from the magmatic to the granulitic stage (Ringuette *et al.*, 1999). Garnet in the Granulitic gabbros then results from magmatic processes and sub-solidus isobaric cooling of cumulates emplaced at the base of the oceanic arc-type crust (Ringuette *et al.*, 1999). Burg *et al.* (1998) suggested a similar scenario with the Granulitic gabbros interpreted as gabbroic intrusions within mantle rocks. Anczkiewicz & Vance (2000) conclude that for garnet growth all above mentioned models require temperatures and pressures of over 850 °C at 1.5 – 2.0 GPa, followed by decompression of 0.5 – 1.0 GPa while the rocks were still above about 700 °C. PT data obtained by Anczkiewicz & Vance (2000) from the Granulitic gabbro and an amphibolite (Swat valley) of > 1.5 GPa and 900 °C and of 0.8 – 1.0 GPa and 800 °C respectively are consistent with both scenarios. PT conditions presented here most likely missed assemblages indicative for pressures > 1.5 GPa because the analysed samples are close to a mylonitic zone and are probably affected by retrogression. Pressures obtained for the Granulitic gabbro between temperatures of 800 – 900 °C plot in general ca. 0.3 – 0.4 GPa below the PT path proposed by Ringuette *et al.* (1999) and scatter between the prograde and retrograde path of Yamamoto (1993). For the Sarangar gabbro, the recorded maximum PT of 0.8 – 1.0 GPa and 800 °C is consistent with the maximum pressure conditions in the PT path of Yoshino *et al.* (1998). The data obtained here cannot exclude nor support a prograde phase in the PT history. The estimated PT conditions for the metadiorite from the Kiru amphibolites (0.7 – 1.0 GPa and 640 – 715 °C) are in partial agreement with the estimates for the "Kamila Amphibolite Belt" (550 – 680 °C and 0.45 – 0.65 GPa) by Jan (1988) and (550 – 650 °C and 0.9 – 1.0 GPa) by Treloar *et al.* (1990). The temperatures estimated for the metadiorite are ca. 100 °C higher than the previously published estimates. The relatively low pressure estimated by Jan (1988) could not be confirmed.

3.1.7 Conclusions

The PT evolution of the Granulitic and Sarangar gabbros is divided into 3 stages: 1) emplacement of gabbroic magmas under high temperature > 1000 °C (Yoshino *et al.*, 1998) and pressures above or around 1.5 GPa at ca. 100 Ma; 2) subsequent granulite facies metamorphism under intrusion conditions or with a prograde path of ΔP 0.3 GPa and ΔT 80 °C, as proposed by Yoshino *et al.* (1998) and 3) amphibolite facies overprint, that ended ca. 83 Ma ago. PT conditions suggested here for the development of anastomosing shear zones started in granulite facies conditions at ca. 800 °C and ~1.0 GPa and continued under amphibolite facies conditions to ca. 650 °C and ~0.7 GPa. Cooling of the Granulitic and Sarangar gabbros followed a similar path. Magmatic intrusion happened most likely at the base of an already thickened crust at depths of > 50 km (Ringuette *et al.*, 1999). The metadiorite from the Kiru amphibolite was equilibrated under amphibolite facies conditions at depths of approximately 30 km. This suggests, that the metadiorite was intrusive earlier or at the beginning of regional decompression in the crust of the arc at a level above the gabbros.

3.2 ARC MATURATION, INSIGHT FROM GEOCHEMICAL DATA

3.2.1 Sampling

Samples are representative of plutonic rocks in the Metaplutonic Complex. They were collected along the KKH, between Patan and Dasu (Fig. 3.16). Sample GPS coordinates are provided in appendix 3. Along a SW – NE profile the samples were collected in the following lithologies (Fig. 3.17): 1) metadiorite from the Indian Plate; 2) Sarangar Gabbro, sampling less deformed and mylonitic portions; 3) magmatic breccia with one darker and one brighter gabbro; 4) metadiorite with sheared and unsheared parts; 5) hornblende diorite, middle and upper part; 6) tonalite dike intrusive into Kiru amphibolites; 7) granites forming veins and massive laccoliths and 8) metagabbro intercalated with fine grained, greenish (metavolcanic?) amphibolites.

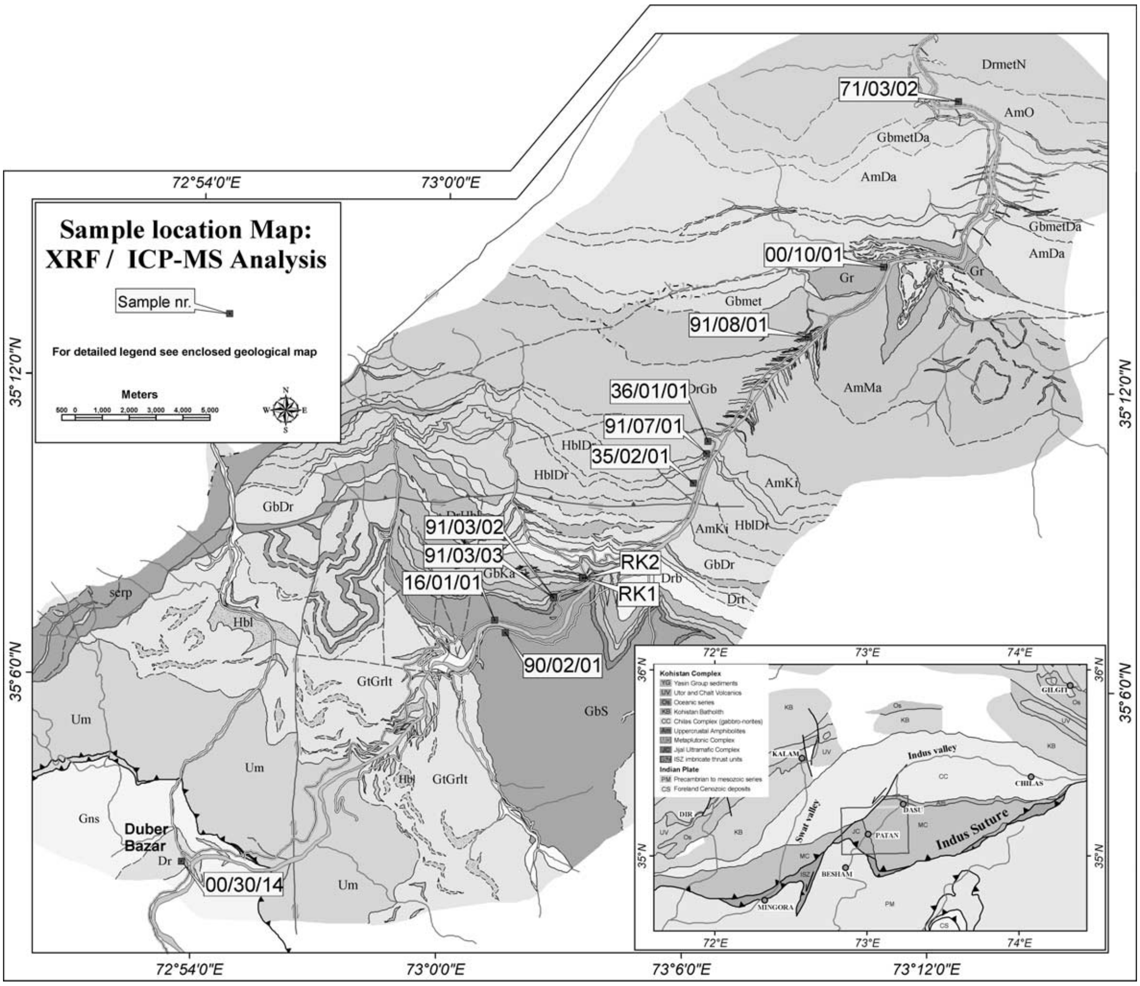

Fig. 3.16: Location map of samples used for whole rock and ICP-MS analysis. Sample 00/30/14 is from a metadiorite at Duber Bazar and is not in the arc related magmatism. All other samples were taken across the Metaplutonic Complex along the Indus River valley and represent major lithologies (gabbros, diorites, tonalites and granites).

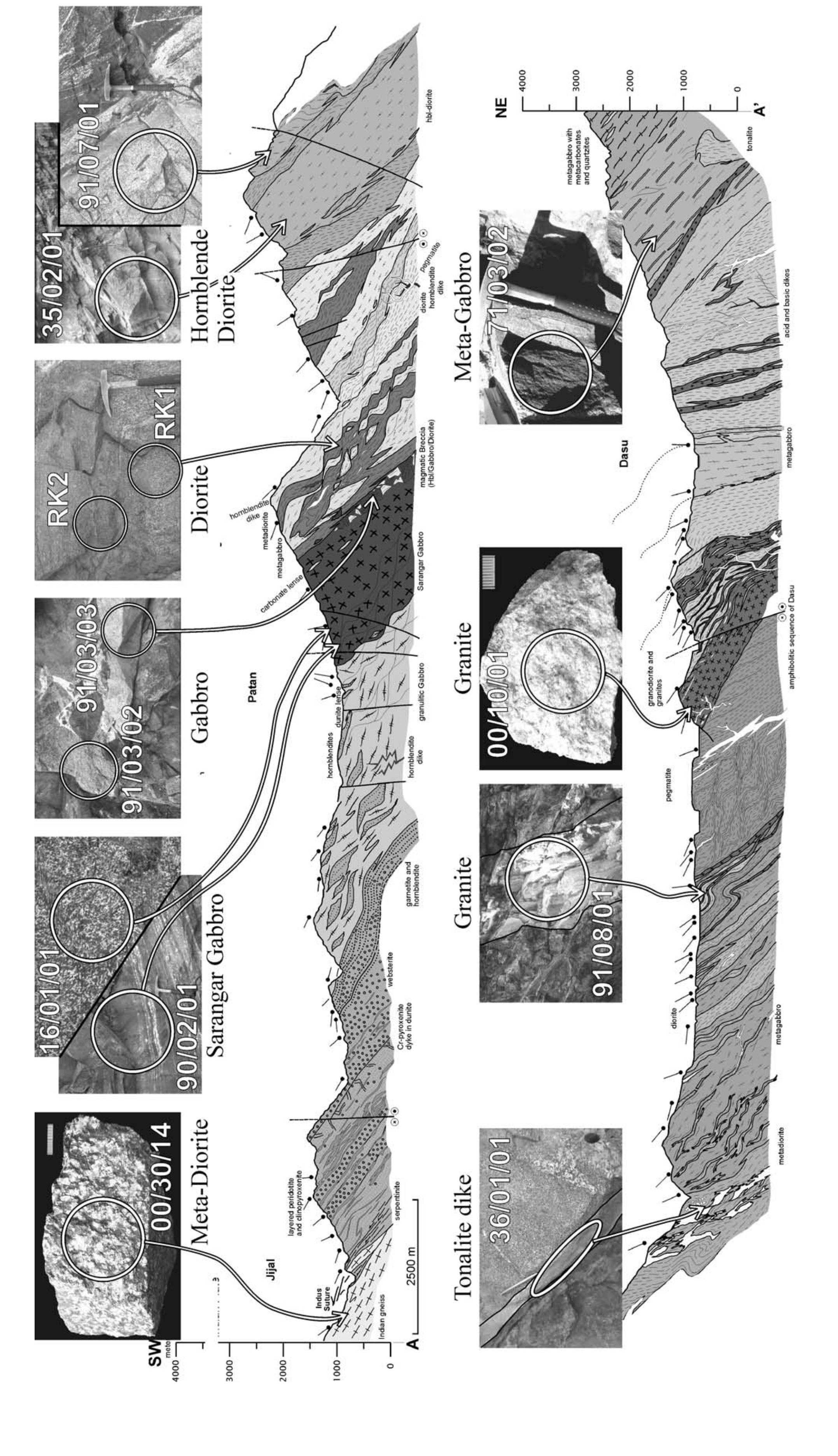

Fig. 3.17: Samples projected at the SW – NE profile along the Indus river. Photographs for details.

3.2.2 Analytical methods

Samples were ground in an agate mill. X-ray fluorescence (XRF) analyses were performed at ETH-IMP. Inductively coupled plasma mass spectrometry (ICP-MS) analyses were performed at ISTEEM, on a VG PQ2 quadrupole ICP-MS following the analytical procedure published by Ionov *et al.* (1992) for mantle rocks, with the refinements described by Godard *et al.* (2000 – EPSL Online Background Dataset).

3.2.3 Results

The results of XRF and ICP-Ms analysis are given in Table 3.7. The analysed samples range from 45.80 to 74.05 wt% SiO_2 and thus cover a wide range from basic to acid compositions. The major element variations show negative correlations for TiO_2, MgO, CaO and Fe_2O_3, positive correlation for $Na_2O + K_2O$ and no correlation for Al_2O_3, MnO and P_2O_5 when plotted against SiO_2 (Fig. 3.18). The decrease of TiO_2, CaO and Fe_2O_3 with differentiation is characteristic of calc-alkaline rocks (Miyashiro, 1975), confirming the role of plagioclase and magnetite as major fractionating phases in the evolution of the magmas (Wilson, 1989). The positive correlation of $Na_2O + K_2O$ is typical for calc-alkaline rocks. The magmas are aligned along a calc-alkaline trend close to the tholeiitic trend in an AFM diagram (Fig. 3.19). The calc-alkaline differentiation trend results in juvenile granites, crystallizing k-feldspar, plagioclase and quartz. The Chilas gabbronorite (data from Jan, 1988; Khan *et al.*, 1993 and Mikoshiba *et al.*, 1999) plots at lower Fe contents on a different calc-alkaline trend. The analysed rocks can be separated essentially in three groups: a) gabbros, samples 16/01/01, 90/02/01, 71/03/02, 91/03/02 and 91/03/03, b) diorites, samples RK2, RK1, 35/02/01, 91/07/01 and 00/30/14 and c) granites/tonalites: samples 36/01/01, 91/08/01 and 00/10/01. The calculated CIPW norm nomenclature of the rocks are qtz-gabbro for samples 16/01/01, 90/02/01 and RK2, gabbro for samples 71/03/02, 91/03/02 and 91/03/03, gabbronorite for sample RK1, qtz-diorite for samples 35/02/01 91/07/01 and 00/10/01, tonalite for sample 36/01/01 and granite for samples 91/08/01 and 00/30/14. This nomenclature is substituted in the following in the light of field and petrological descriptions. Samples RK2 and RK1 display geochemical features intermediate between the gabbros and diorites. They are more similar to diorites with regard to trace elements. Plotted in a TAS diagram (total alkalis versus silica) the Sarangar Gabbro is of more “evolved” character than the structurally higher gabbros (91/03/02 and 91/03/03) (Fig. 3.20). The tonalite (36/01/01) is clearly less “evolved” in term of major elements, than the granites. The tectonic setting under which the magmas were emplaced is an island arc or active continental margin setting as suggested by the comparison of modern volcanic rocks MgO-FeO-Al_2O_3 composition range with the analysed ones (SiO_2 range of 51 – 56 wt%) (Fig. 3.21).

XRF Analysis

facies	gabbro					diorite					tonalite/granite			volcanocl.
weight %	16/01/01	90/02/01	91/03/02	91/03/03	71/03/02	RK2	RK1	35/02/01	91/07/01	00/30/14	36/01/01	91/08/01	00/10/01	92/07/01
SiO_2	52.22	53.45	45.80	48.11	49.18	53.20	51.56	55.06	56.17	67.11	62.35	74.05	69.27	68.18
TiO_2	0.72	0.78	1.27	1.06	1.08	0.90	1.00	0.73	0.55	0.89	0.45	0.05	0.21	0.51
Al_2O_3	17.63	17.44	19.11	22.07	15.63	17.29	18.24	18.84	18.52	13.54	20.23	14.74	15.91	10.85
Fe_2O_3	9.62	9.28	11.84	8.17	9.24	10.18	10.86	6.21	6.31	6.57	2.67	0.85	3.10	3.56
FeO	0.00	0.00	0.00	0.00	0.00	0.00	0.00	0.00	0.00	0.00	0.00	0.00	0.00	0.00
MnO	0.17	0.15	0.14	0.08	0.16	0.18	0.18	0.11	0.14	0.06	0.02	0.15	0.05	0.05
MgO	5.28	4.62	5.13	3.14	7.82	4.48	4.70	2.89	2.66	0.62	1.07	0.17	0.91	1.58
CaO	9.69	9.45	10.49	10.45	11.21	9.35	9.74	8.17	7.93	2.91	7.16	2.01	4.38	5.06
Na_2O	2.52	2.87	3.32	4.32	2.63	2.79	2.90	4.58	4.27	2.98	4.52	3.64	3.73	2.36
K_2O	0.40	0.30	0.19	0.18	0.37	0.30	0.28	0.36	0.36	4.35	0.17	1.77	1.14	2.11
P_2O_5	0.12	0.11	0.34	0.26	0.13	0.16	0.19	0.30	0.22	0.26	0.14	0.06	0.10	0.09
LOI(1	0.90	0.92	1.53	1.65	2.04	0.55	0.21	1.87	1.78	0.71	0.43	1.19	1.03	4.93
Cr_2O_3	0.02	0.02	0.01	0.01	0.04	0.01	0.01	0.01	0.01		0.01	0.01		0.03
NiO	0.00	0.00	0.00	0.00	0.01	0.00	0.00	0.00	0.00		0.00	0.00		0.00
										(2			(2	
Total	99.29	99.39	99.17	99.50	99.54	99.39	99.87	99.13	98.92	100.00	99.22	98.69	99.83	99.31
ppm														
Zr	54	62	41	44	87	88	81	77	104	478	141	48	62.4	190
V	172	220	194	110	186	186	170	63	75	15.7	< 10	< 10	25	63
Cr	40	45	< 6	< 6	136	< 6	< 6	< 6	< 6	8.4	10	< 6	6.7	130
Ni	16	14	< 3	< 3	85	< 3	< 3	< 3	< 3	< 5	< 3	< 3	< 5	17
Cu	38	55	73	51	8	64	39	32	7	9.1	51	< 3	5.2	11
Zn	74	73	80	53	78	72	74	73	69	108	18	35	35.1	44
Ga	12	12	15	15	11	14	15	17	14	22.5	13	10	14.9	7
Sc	32	25	35	13	31	27	30	< 2	< 2		< 2	< 2		< 2
S	< 50	< 50	< 50	< 50	116	189	184	< 50	< 50		703	< 50		< 50

ICP-Ms Analysis

ppm	16/01/01	na	91/03/02	91/03/03	71/03/02	RK2	RK1	35/02/01	91/07/01	00/30/14	36/01/01	91/08/01	00/10/01	na
Cs	0.063		0.080	0.088	0.126	0.007	0.011	0.086	0.104	3.480	0.275	1.080	0.550	
Rb	2.951		0.852	0.948	4.726	0.688	0.593	1.873	2.690	154.000	7.420	50.777	41.600	
Ba	141.970		66.547	88.582	52.623	86.489	83.110	111.430	108.420	1508.000	129.040	1122.700	502.000	
Th	0.365		0.182	0.136	0.429	0.084	0.055	0.185	0.147	16.300	0.568	1.486	1.560	
U	0.118		0.067	0.046	0.128	0.028	0.023	0.055	0.039	3.380	0.119	0.418	0.380	
Nb	1.164		1.767	1.435	3.593	2.676	2.742	3.560	2.959	22.000	2.590	6.309	1.750	
Ta	0.066		0.073	0.058	0.220	0.114	0.114	0.142	0.123	1.830	0.183	0.520	0.110	
La	5.191		5.200	3.861	4.050	8.903	8.841	7.565	8.622	78.900	5.282	6.435	8.660	
Ce	11.951		14.808	10.247	11.324	22.041	22.478	19.543	21.519	144.000	11.313	13.360	15.300	
Pr	1.624		2.313	1.544	1.682	2.999	3.092	2.815	2.885	16.100	1.469	1.512	1.700	
Sr	249.800		352.590	480.700	203.990	274.440	287.830	582.420	427.920	212.000	518.190	194.930	327.000	
Nd	8.031		12.900	8.299	8.665	14.028	14.571	13.687	13.305	58.400	6.531	5.826	5.550	
Sm	2.281		3.717	2.405	2.516	3.556	3.614	3.275	2.950	10.400	1.341	1.228	0.804	
Eu	0.978		1.229	0.957	0.948	1.116	1.198	1.069	0.955	1.960	0.528	0.274	0.551	
Gd	2.737		4.322	2.861	3.106	3.762	3.894	3.190	2.866	8.250	1.106	1.288	0.665	
Tb	0.489		0.747	0.481	0.545	0.662	0.678	0.509	0.474	1.210	0.146	0.216	0.084	
Dy	3.139		4.586	2.974	3.529	4.113	4.231	3.000	2.890	7.450	0.756	1.386	0.479	
Y	21.516		27.998	18.279	24.275	29.156	29.980	20.625	19.826	38.800	4.933	11.366	2.490	
Ho	0.724		1.008	0.652	0.804	0.925	0.959	0.637	0.645	1.460	0.144	0.296	0.084	
Er	2.115		2.884	1.779	2.268	2.706	2.827	1.817	1.901	3.950	0.384	0.810	0.226	
Tm	0.316		0.406	0.248	0.333	0.412	0.426	0.265	0.291	0.599	0.054	0.125	0.031	
Yb	2.041		2.388	1.452	2.083	2.606	2.692	1.640	1.885	3.900	0.324	0.913	0.281	
Lu	0.336		0.380	0.220	0.335	0.418	0.433	0.246	0.304	0.558	0.050	0.148	0.044	
Pb	36.196		29.710	32.194	3.904	15.478	22.145	70.814	4.391	47.300	21.976	73.337	2.620	

(1 Loss of ingnition
(2 Emission ICP

Table 3.7: Chemical composition for samples from the Metaplutonic Complex (gabbro: 16/01/01, 90/02/01, 91/03/02, 91/03/03, 71/03/02; diorite: RK2, RK1; 35/02/01, 91/07/01; tonalite/granite: 36/01/01, 91/08/01, 00/10/01). Additional samples of volcanoclastic (92/07/01) and metadiorite from the Indian plate (00/30/14). na: not analysed.

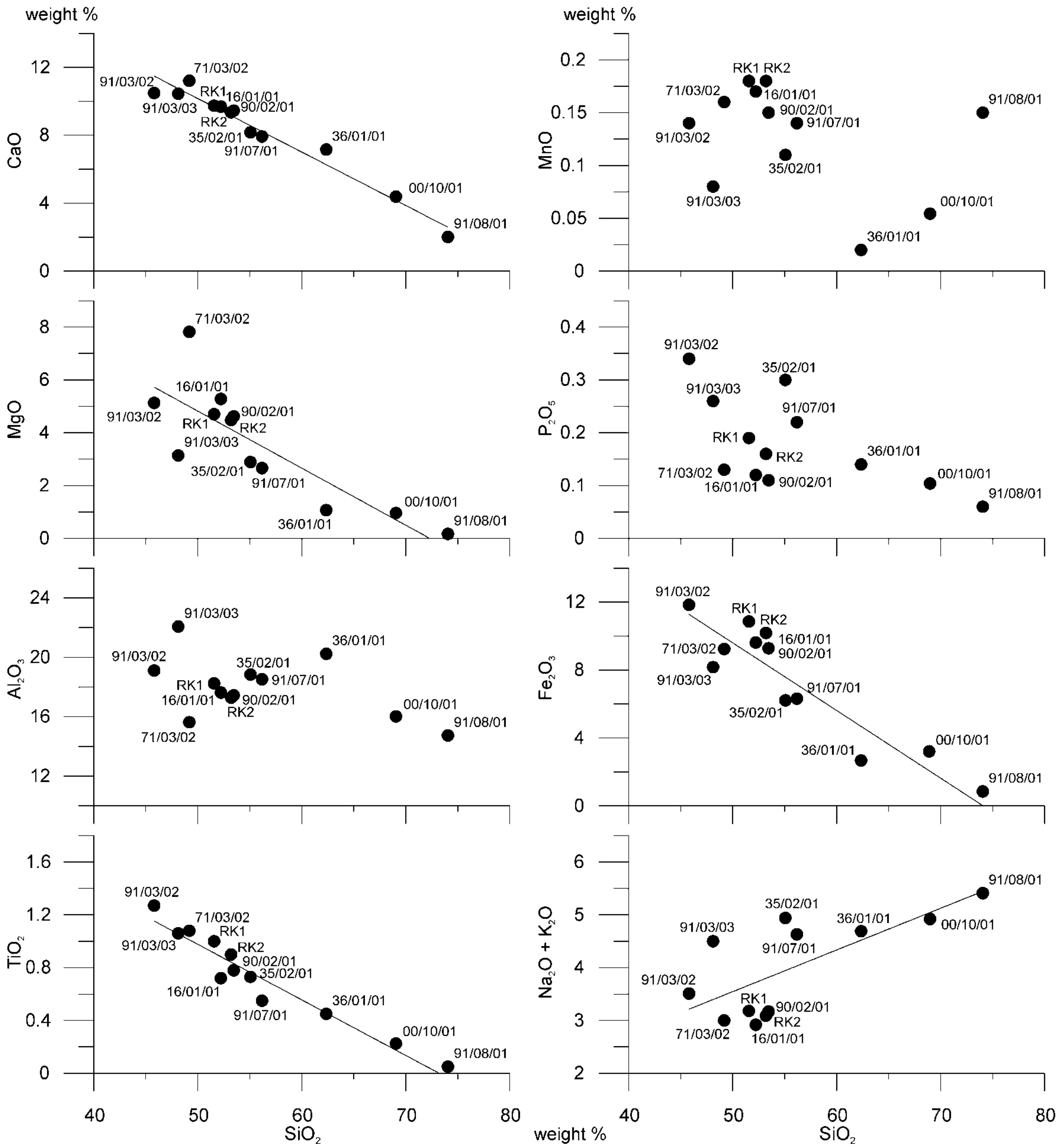

Fig. 3.18: Major element variation diagrams for the whole rock samples from the Metaplutonic Complex. The trends are typical for calc-alkaline magmas.

Samples 35/02/01 and 91/07/01 plot in the spreading centre island field. It must be noticed that the validity of the diagram is limited by the relative mobility of the major elements in basalts and that MgO and Al_2O_3 are mobile during greenschist facies metamorphism (Pearce, 1976). However, the gabbros of the Metaplutonic Complex plot around the same position. It is also noticed, that the analyses of Chilas gabbronorites (triangles in Fig. 3.21) cluster around a different position.

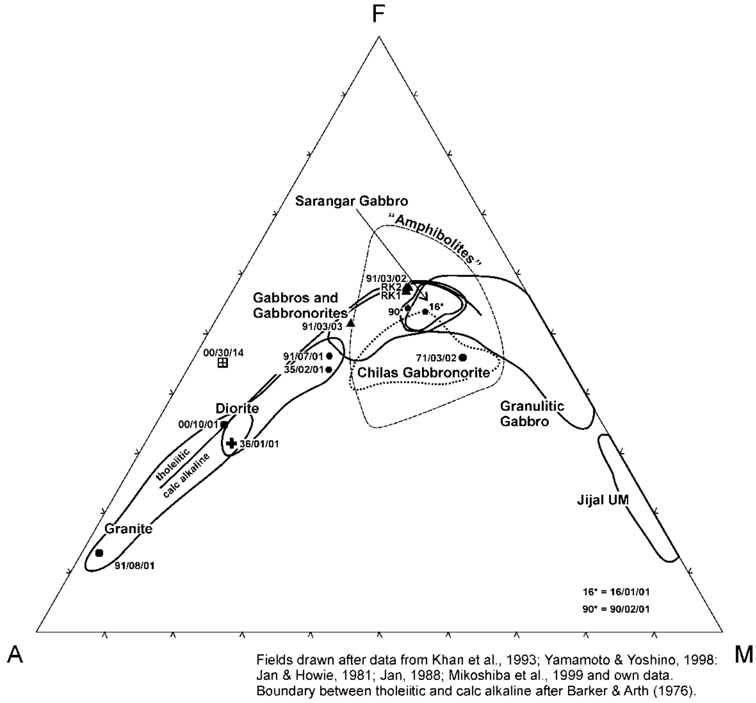

Fig. 3.19: AFM plot showing the calc alkaline/tholeiitic differentiation trend of the intrusives. The "Amphibolites" field includes amphibolites of plutonic and sedimentary parentage. The Chilas gabbronorites plot below the Metaplutonic Complex trend. Sample 00/30/14 is the Indian plate diorite and does not belong to the arc plutonics.

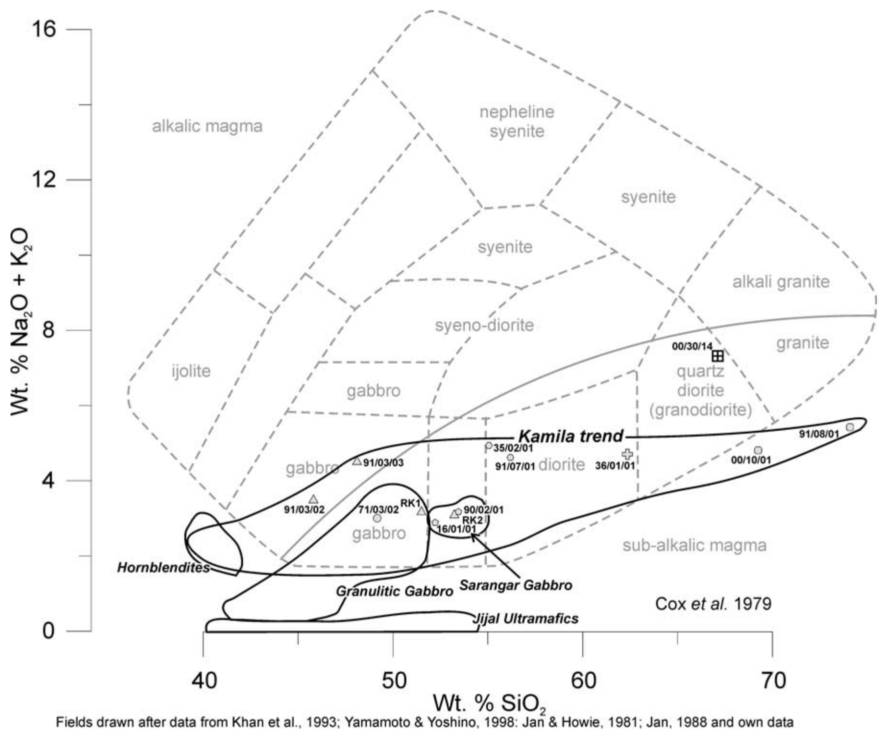

Fig. 3.20: Discrimination plot after Cox et al. (1979). The observed trend from gabbros to granites follows a relatively constant Na_2O + K_2O Wt.% value. TAS diagram (total alkalis vs. silica) adapted by Wilson (1989) for plutonic rocks. The Indian plate diorite (00/30/14) does not belong to the arc plutonics.

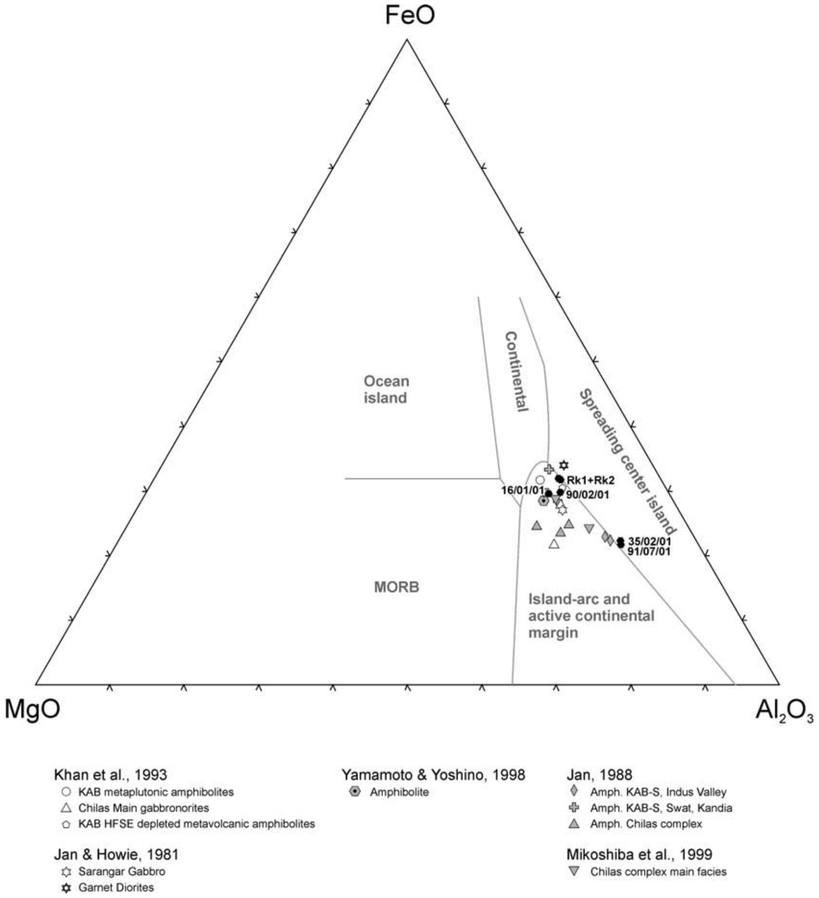

Fig. 3.21: Tectonic setting based upon the compositional range of recent volcanic rocks (after Pearce et al., 1977). Data points plot in the island-arc and active continental margin field. Labelled data: this study. (SiO_2 range: 51 – 56 wt%).

Insight to the genesis of the magmas represented by the analysed samples is provided by the trace element characteristics. The Zr and Hf values were taken from XRF analyses. Zr and Hf are strongly underestimated in the ICP-MS values because zircon is not dissolved during acid digestion procedure (which is especially adapted to mafic/ultramafic rocks). All ICP-MS analyses display anomalously low Zr values on chondrite- or primitive mantle-normalized diagram, compared with XRF analyses. This is evidence that Zr (and Hf) hosted by zircon was missed by ICP-MS. On the other hand, the XRF Zr values are about at the same level as MREE on normalized diagrams and display only subtle, positive or negative, anomalies. Therefore, ICP-MS Hf values were deleted from the data set and the Zr values were replaced by the XRF ones.

The trace element patterns of the analysed samples, normalized to primordial mantle abundance after Sun (1980) and McDonough *et al.* (1992) show similar patterns for the gabbros and diorites, whereas the tonalite/granites are depleted in Sm, Ti, Tb and Y and enriched in Rb, Ba, Th, U and K (Fig. 3.22a) The strong negative spike of Ti in sample 91/08/01 can be also caused by an effect of limit of detection (0.05 weight% TiO_2). The gabbros have some similarity with average MORB, except the strong Ba, Sr and P enrichment. The Chilas complex is more enriched in Rb, Ba, Th, U and K than the average Metaplutonic Complex plutonic (average of gabbros and diorites). For elements right of Nb the pattern is very similar for Metaplutonic Complex and Chilas plutonics with values of 5 to 10 times higher than primordial mantle values (Fig. 3.22b). The Kamila high-Ti and low-Ti amphibolites (Khan *et al.*, 1993) have higher Rb and Ba values than the average Metaplutonic Complex plutonics. The Kamila high-Ti amphibolites are interpreted as remnants of a pre-arc oceanic crust that formed within an intraoceanic setting (Treloar *et al.*, 1996). The Kamila low-Ti amphibolites have geochemical characteristics similar to subduction related origin and are interpreted as most primitive arc-related magmatic rocks within the KAC (Treloar *et al.*, 1996). They show a similar pattern as the average Metaplutonic Complex plutonics, except significant higher Th and K contents (Fig. 3.22b).

Trace element patterns occurring in the KAC are variable for volcanics and plutonics of different areas (Fig. 3.22c). The Jaglot Group volcanics demonstrate geographical and compositional provincialism within calc-alkaline to mildly alkaline compositions (Treloar *et al.*, 1996). The Hunza volcanics have komatiite-high-Mg basalt to high-Mg andesite compositions with typical subduction related trace element patterns (Petterson & Windley, 1991; Treloar *et al.*, 1996). The Utror and Mankial volcanics yield highly evolved calc-alkaline trace element compositions and show with andesites to rhyolites a wide compositional range typical for mature Andean type margins (Treloar *et al.*, 1996). The western arc volcanics (Petterson *et al.*, 1990) are less evolved than the Utror volcanics and may reflect lateral compositional variations (Treloar *et al.*, 1996). A direct genetic link, meaning that one the above mentioned volcanics reflect the upper crustal volcanic equivalent to the lower crustal plutonics of the Metaplutonic Complex is not evident.

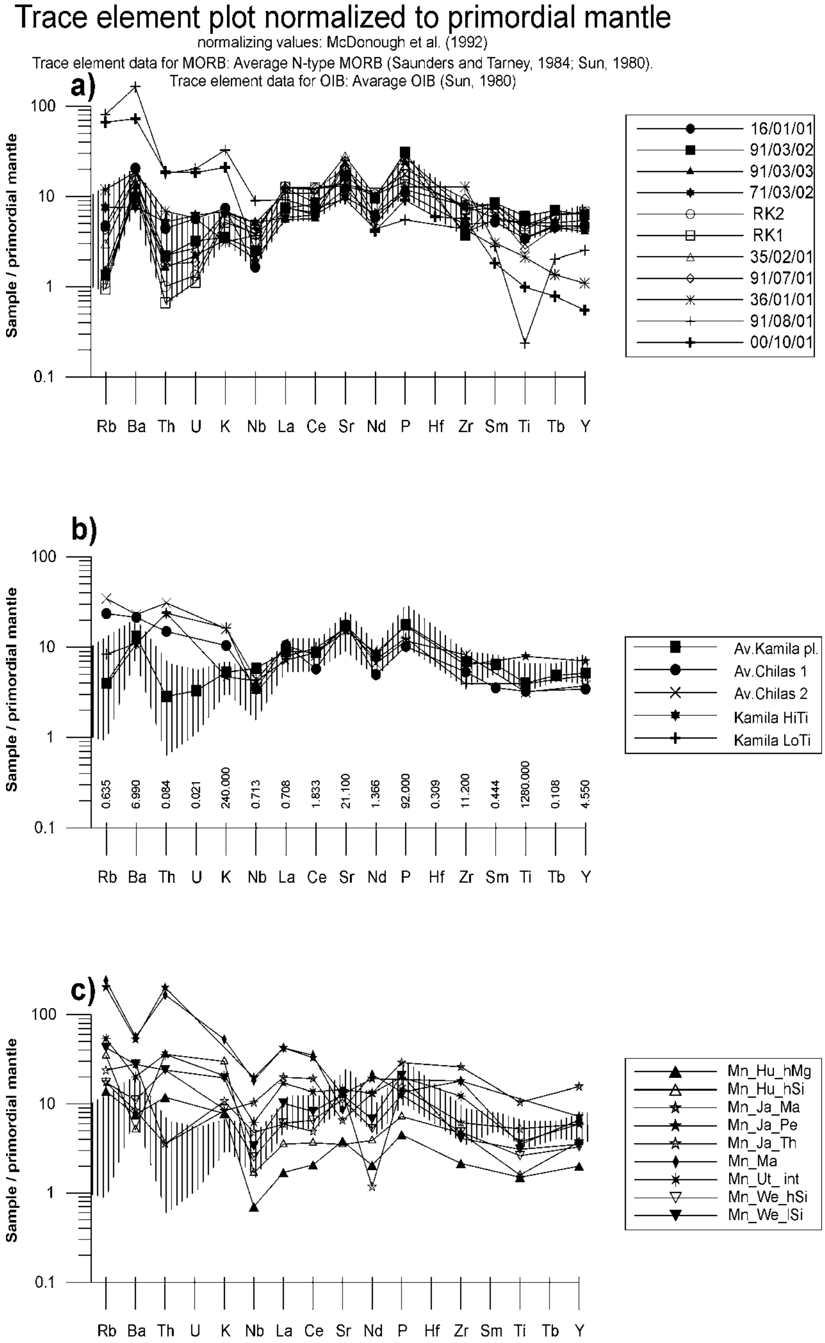

Fig. 3.22: Trace element plots normalized to primordial mantle after McDonough et al. (1992). a) Upper diagram: this study; b) centre diagram: average Metaplutonic Complex, Zeilinger, this work, n=8; average Chilas 1, Mikoshiba et al., 1999; Jan & Howie, 1981; Khan et al., 1993, n=21; average Chilas 2, Khan et al., 1989,1993, n=7; Kamila HiTi, Khan et al., 1993, n=7; Kamila LoTi, Khan et al., 1993, n=8; shaded field: gabbros and diorites, this work; c) bottom diagram: mean values of: Hu_hMg: Hunza valley high Mg (Petterson et al., 1991, n=6); Hu_hSi: Hunza valley high Si (Petterson et al., 1991, n=6); Ja_Ma: Jaglot Majne (Khan, 1994, n=5); Ja_Pe: Jaglot Peshmal (Sullivan et al., 1993, n=5); Ja_Th: Jaglot Thelichi (Khan, 1994, n=8); Ma: Mankial (Sullivan et al., 1993, n=5); Ut_int: Utror intermediate (Sullivan et al., 1993, n=5); We_hSi: western arc high Si (Petterson et al., 1991, n=13); We_lSi: western arc low Si (Petterson et al., 1991, n=5); shaded field: gabbros and diorites, this work.

The trace element and REE pattern of the gabbro-diorite sequence (Fig. 3.23a) can be subdivided in two segments: 1) to the right of La: REE, Sr, Zr, Ti and Y show relatively steady evolutions, with only subtle negative anomalies of the HFSE (high field strength elements) Zr and Ti, and positive anomalies of Sr (these anomalies may reflect plagioclase accumulation in some samples or/and they may represent the arc-type signature of parental melts); 2) to the left of La: most of the highly incompatible elements (HIE, notably Rb, Th, U, Nb and Ta) are strongly depleted relative to LREE. Exceptions are Ba (enriched) and Cs (enriched, but not for RK1 and RK2). The more LREE-enriched samples (RK2 and RK1) are the most depleted in Rb, Th and U. These elements are probably not direct correlated with LREE. The granites and tonalite are clearly distinguished from the gabbro-diorite sequence by gradual enrichment from moderately incompatible elements (HREE and Y) to the most incompatible elements (HIE, including Cs and Ba). Positive anomalies of Cs, Ba and Sr are yet distinguishable on this overall pattern, reminiscent of those observed in the gabbro-diorite sequence.

The REE patterns of the analysed samples, normalized to continental crust (Fig. 3.23b) and chondrite abundances (Fig. 3.23c) show similar patterns for the gabbros and diorites. The granite and tonalite patterns are relatively flat (except the Eu anomaly) when normalized to continental crust (Fig. 3.23b).

The gabbros and diorites yield a relatively high level of REE abundance (> 10 x chondrites). The lower gabbros are indistinguishable from the upper diorites with respect to HREE. However, they are less enriched in LREE, with more variable LREE segment. Sample 91/03/03 shows rather flat LREE segment (La-Sm), sample 91/03/02 is slightly depleted in LREE relative to MREE (La-Pr compared with Nd-Sm) and sample 16/01/01 is slightly enriched in La-Ce relative to Pr-Sm.

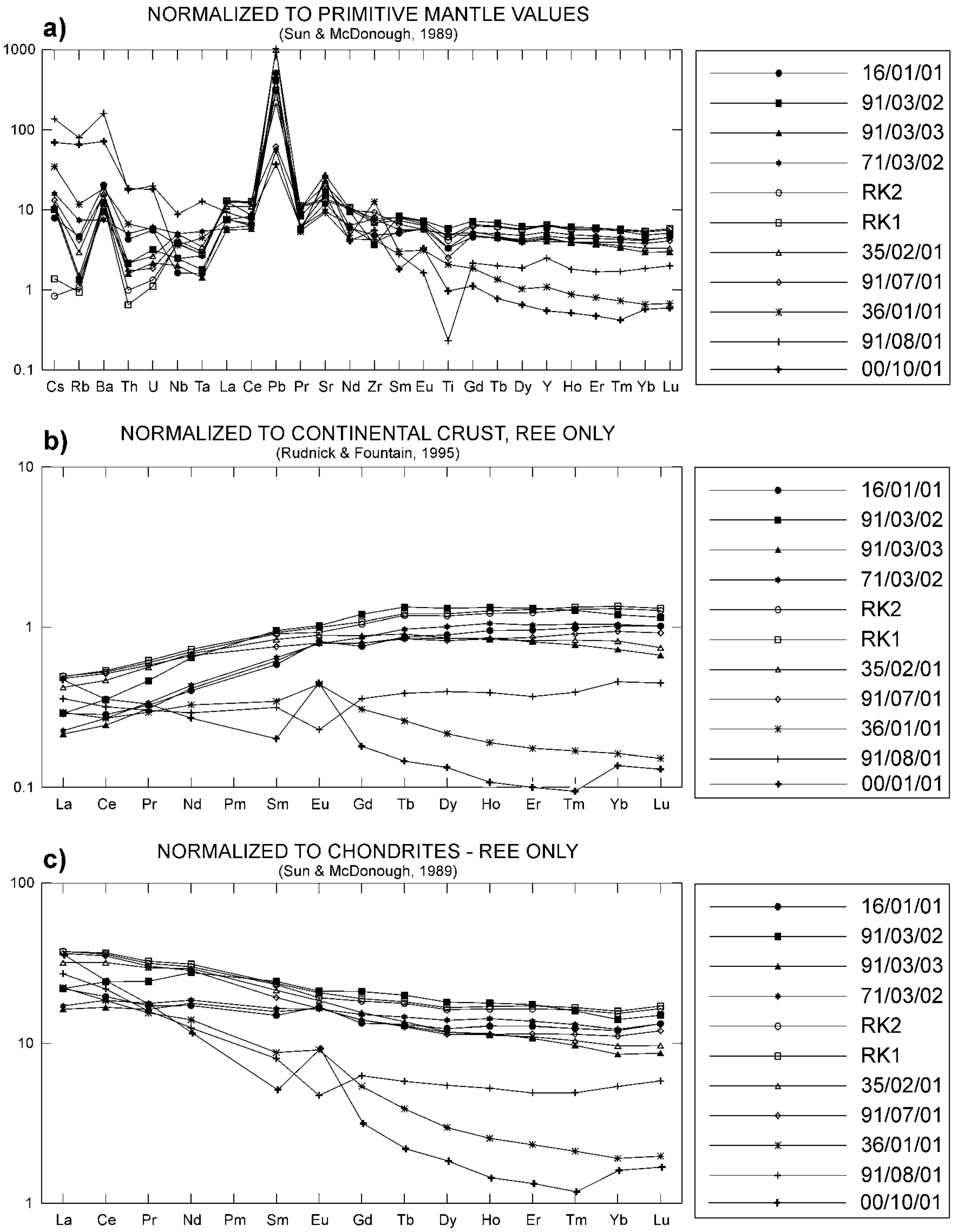

Fig. 3.23: Gabbros (filled symbols), diorites (open symbols) and tonalite/granite (cross symbols) presented in normalisation diagrams. a) upper diagram: trace and RE elements normalized to primitive mantle values; b) centre diagram: REE normalized to continental crust; c) bottom diagram: REE normalized to chondrites.

3.2.4 Interpretations

The lesser LREE enrichment in the lower gabbros, compared with the upper diorites, may partly result from a more "cumulitic" character. In particular, the flat or slightly depleted LREE segments of samples 91/03/02 and 91/03/03 may be explained by cumulitic amphibole. In addition, samples 16/01/01 and 91/03/03 show a small but significant positive Eu anomaly indicative of plagioclase accumulation (in sample 91/03/03, plagioclase accumulation is also attested by the anomalously high alumina content – 22.1%, not consistent with a "melt" composition). However, these cumulitic characters are relatively subtle and these gabbros cannot be considered as a proper "cumulate" sequence. The slight enrichment of La-Ce relative to Pr-Sm in sample 16/01/01 is significant, because the sample is the lowest in the sequence and it is clearly enriched in highly incompatible elements such as Rb, Ba, Th and U and more depleted in Nb and Ta compared with other samples (Fig. 3.23a). This indicates that this gabbro is less depleted than the other gabbros. The selective LREE enrichment in this sample probably results from pervasive infiltration of incipient melt fractions.

The diorites have relatively flat HREE segment (Dy-Lu) and are selectively enriched in LREE relative to HREE, with a narrow range of LREE contents (about 50 x chondrites for La) (Fig. 3.23c). They are devoid of positive Eu anomaly in spite of their relatively high plagioclase content. This indicates that the diorites are not cumulates. They have probably crystallized rapidly in nearly closed system and preserved a "parental" melt composition. The "parental" melt composition was LREE-enriched with a major element composition ranging from quartz-tholeiitic for samples RK2 and RK1 to andesitic for samples 35/02/01 and 91/07/01.

There is yet a clear differentiation trend from the lower gabbros to RK2-RK1 to the upper diorites, especially for major elements. If the sequence derives from a single parental melt, this would imply significant fractional crystallisation, which – in turn - would require that at least the less differentiated facies have a cumulitic character. Part of the differentiation by fractional crystallization probably occurred at deeper level in the Granulitic gabbros (J-L.Bodinier, pers. com.). Therefore the studied sequence has probably crystallized from heterogeneous, already differentiated "parental" melts.

The granites are characterized by fractionated REE patterns, with a marked enrichment of LREE relative to HREE. Compared with the gabbro-diorite sequence, the granites have comparable LREE content and mainly differ by a strong HREE depletion. In sample 36/01/01, which is rich in alumina (20.2%) and shows a positive Eu anomaly and a strong Sr spike (Fig. 3.23a), the HREE depletion might partly result from plagioclase accumulation. However, this hypothesis cannot be applied to sample 91/08/01 and 00/10/01. Therefore HREE depletion in granites is more likely the reflection of their equilibration with HREE enriched residual minerals such as garnet and/or amphibole. Together with field evidence, this suggests that the granites were generated by (hydrous) partial melting of rocks similar to the Granulitic gabbros or/and the hornblendite enclaves.

The trace element composition of the gabbro-diorite sequence normalized to the average oceanic arc volcanics composition (based on New Hebrides and Mariana data) displays an increasing depletion of the Kohistan gabbro-diorites of incompatible elements (Fig. 3.24a). The MREE and HREE (Sm to Lu), Nb and Ta are undepleted (Kohistan gabbro-diorites (KGD) / oceanic arc volcanics (OAV) = 1.06 ± 0.08). The LREE (La to Nd), Zr and Sr are slightly depleted, with increasing depletion degree from Nd to La (KGD / OAV = 0.9 to 0.6). Ba and Cs are a little depleted (KGD / OAV = 0.4 to 0.2) and Rb, Th and U are strongly depleted (KGD / OAV = 0.13 to 0.10). In contrast with lithophile trace elements, Pb is enriched in the Kohistan gabbro-diorites relative to the oceanic arc volcanics by a factor 5-6 (see Pb spike in figure Fig. 3.24b). The difference is probably the reflection of the siderophile character of this element. Pb is probably mainly hosted by a sulphide component. This can be explained by sulphide precipitation during crystallisation, due to melt saturation, or selective mobilization during a late partial melting event. Sulphide precipitation is unlikely as the lithophile elements indicate that there was very little amount of residual liquid segregated from the gabbro-diorite sequence. The hypothesis that the Kohistan parental melt was substantially different from New Hebrides and Mariana arc volcanics in term of Pb cannot be disregarded. The Tonga arc andesites and basalts are similar to the Kohistan gabbro-diorites (Fig. 3.26b) with patterns overlapping for Cs – Th and HREE segments (Gd to Lu). The elements from La to Ti are more enriched in the Kohistan gabbro-diorites than in the Tonga arc andesites and basalts, but follow a similar pattern. U and Nb values are different in the Tonga and Kohistan arc systems.

A comparison between estimated average continental crust composition (Rudnick & Fountain, 1995) and the Kohistan gabbro-diorite normalized to average island arc volcanics shows that for several elements the continental crust and the Kohistan gabbro-diorite sequence have almost symmetrical, opposite arc-normalized patterns (Fig. 3.24c). The element depletion in the gabbro-diorite sequence is mirrored by enrichment in continental crust (e.g., Rb, Ba, Th, U, La). HREE segments (Gd to Lu) are remarkably similar in arc volcanics, Kohistan and continental crust. However, some elements show a different behaviour: 1) the strong enrichment of Nb and Ta in arc-normalized continental crust is not coupled with a depletion of these elements in the Kohistan gabbro-diorites; 2) the strong enrichment of Pb in Kohistan (Fig. 3.23a) does not coincide with a negative anomaly in the continental crust and 3) the negative anomaly of Sr in the continental crust is not associated with a positive Sr anomaly in Kohistan. The particular behaviour of these four elements probably reflects the preferential partitioning in sulphides (Pb), Ti-oxides (Nb and Ta) and plagioclase (Sr). When these elements are disregarded, the symmetrical patterns suggest that the processes involved in continental crust maturation are somehow analogous to the differentiation mechanism responsible for incompatible element depletion in the Kohistan lower crust. However, the degree of crustal maturation which was achieved in the Kohistan island arc prior to accretion with India, is not known.

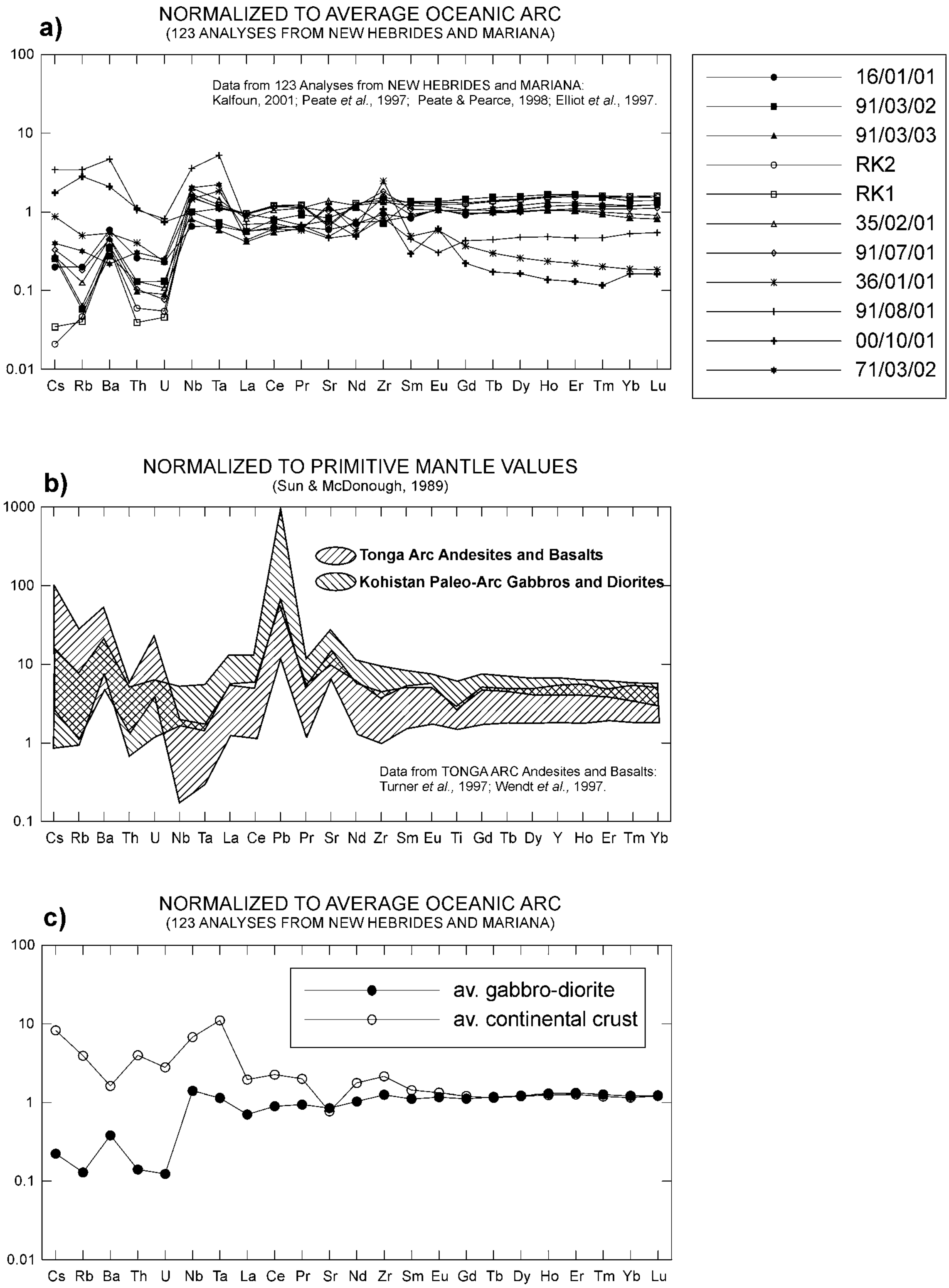

Fig. 3.24: Comparison between the lower KAC plutonics and recent island arc volcanics: a) normalized to average oceanic arc (New Hebrides and Mariana); b) Tonga arc and KAC gabbros and diorites and c) the lower KAC gabbros and diorites compared to average continental crust (Rudnick & Fountain, 1995) normalized to average oceanic arc (New Hebrides and Mariana).

Differences of the Kohistan gabbro-diorites to ophiolitic sequences can be demonstrated by comparing them to gabbros from Oman (values provided by Jean-Louis Bodinier, personal communication). When normalized to an olivine gabbro the strong relative enrichment for Cs to Zr, except for Sr, is notable (Fig. 3.25a).

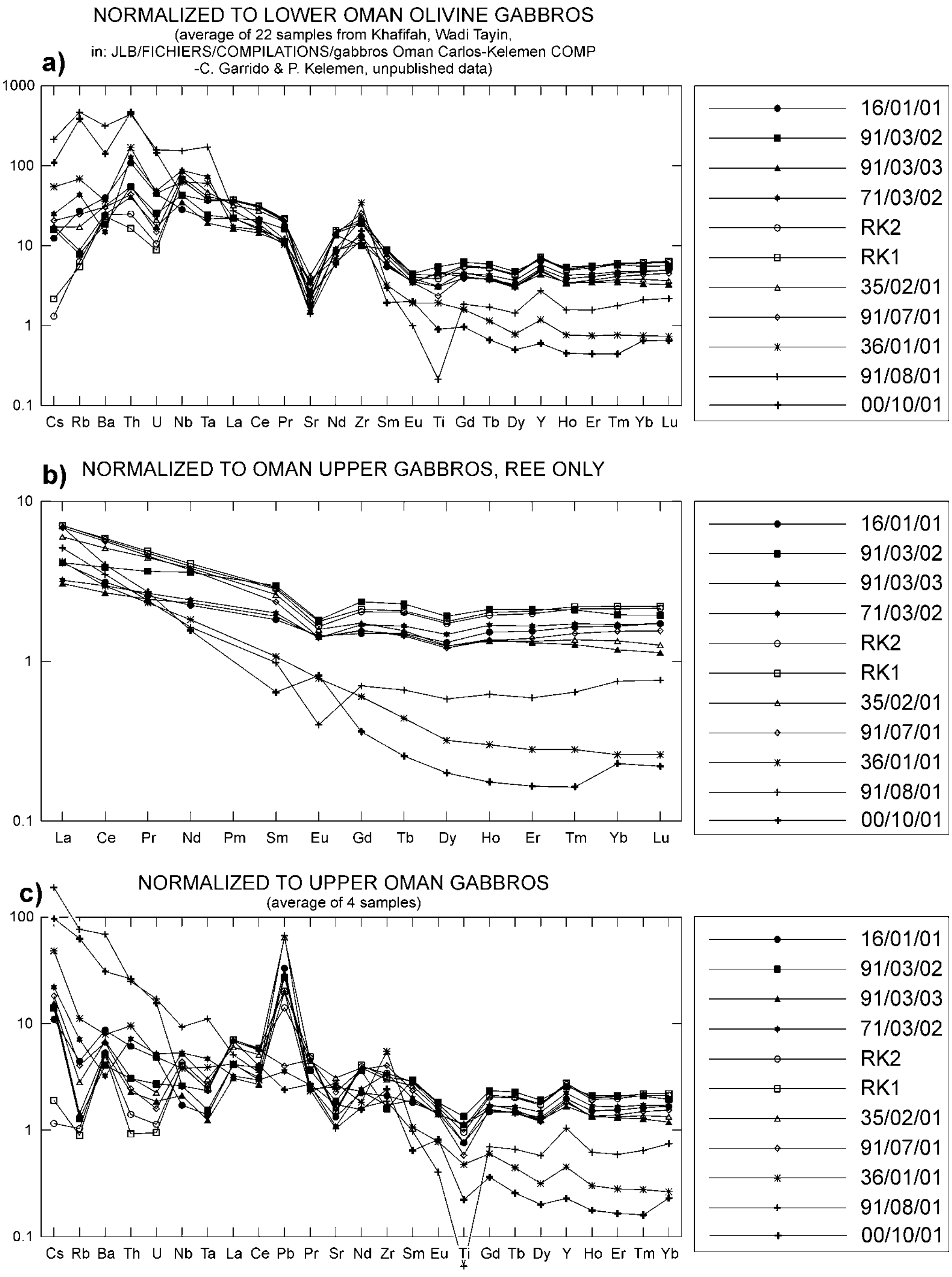

Fig. 3.25: Comparison between the lower KAC plutonics and Oman gabbros. a) upper diagram: normalized to olivine Gabbros; b) centre diagram: REE normalized to upper gabbros; c) bottom diagram: trace and RE elements normalized to upper gabbros. Normalization values provided by Jean-Louis Bodinier, personal communication.

The MREE and HREE are flat with values 3 to 8 times higher for the gabbro-diorites and around 1 (0.5 to 2) for the tonalite/granites. Comparing the Kohistan gabbro-diorites with upper gabbros from Oman the MREE and HREE are only slightly relative enriched by a factor of 2. The LREE instead show an increase with decreasing atomic number (Fig. 3.25b). The tonalite/granites are strongly enriched in incompatible elements and depleted in MREE and HREE. The gabbros have a strong Pb spike, the granites a strong Ti negative anomaly (Fig. 3.25c). The diorites RK1 and RK2 have Cs, Rb, Th, U values similar to the upper Oman gabbros. Despite of potential different "parental" melt sources the differences suggest also different processes during "maturation".

One additional sample (00/30/01) representing a diorite from the Indian plate was analysed. In contrast to the diorites of the Metaplutonic Complex the trace element pattern is similar to average upper crust (Weaver & Tarney, 1984) (Fig. 3.26a).

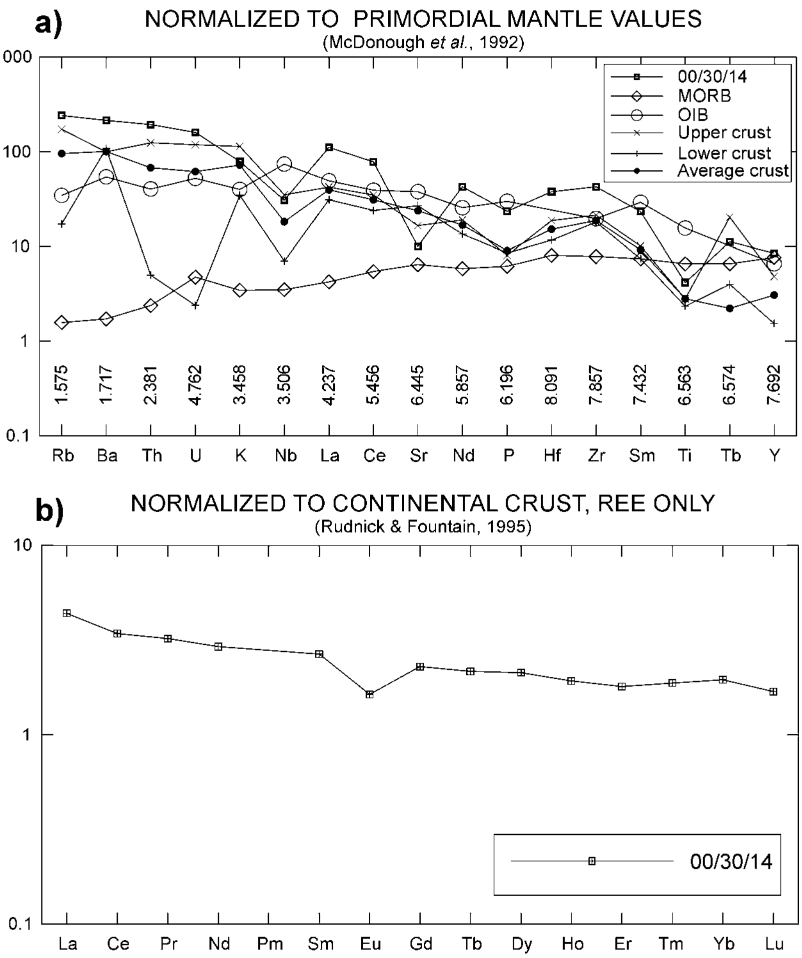

Fig. 3.26: a) trace element plot of the Indian plate metadiorite normalized to primordial mantle compared with MORB (Saunders & Tarney, 1984), OIB (Sun, 1980), upper crust (Taylor & McLennan, 1981), lower crust and average crust (Weaver & Tarney, 1984); b) REE values of the metadiorite normalized to continental crust.

The REE pattern normalized to continental crust (Fig. 3.26b) is relatively flat and enriched by a factor of 2 to 5, supporting the similarity to continental crust values.

Using the elements Nb, Y, Ta and Rb for tectonic discrimination after Pearce *et al.* (1984) the difference between the arc tonalite/granites, plotting in the volcanic arc granite field, and the Indian plate diorite, plotting in the within plate granite field, is emphasized (Fig. 3.27).

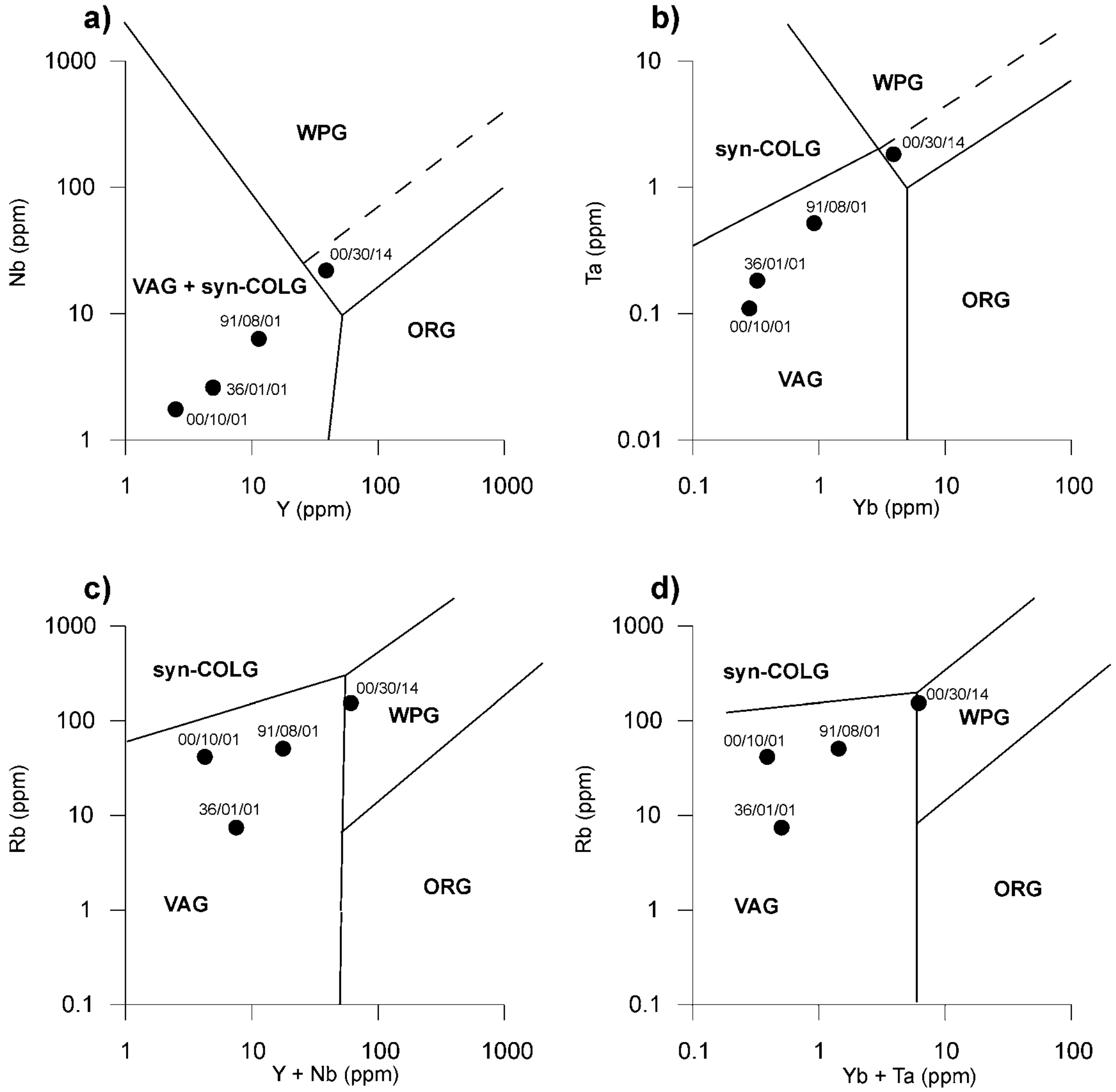

Fig. 3.27: Discrimination plots after Pearce et al. (1984) using a) Nb versus Y, b) Ta versus Yb, c) Rb versus Yb+Nb and d) Rb versus Yb+Ta. The granites/tonalites from the Metaplutonic Complex fall in the VAG (volcanic arc granite) fields. The metadiorite emplaced into the Indian plate instead belongs to the WPG (within plate granite) tectonic environment. (syn-COLG: syn-collisional granite; ORG: ocean ridge granite).

3.2.5 Discussion

The large ion lithophile elements (LILEs) Cs, Ba and Sr display nearly the same variations as the other highly incompatible elements (HIEs). The lowest Cs values and the smallest Sr anomalies are observed in samples RK2 and RK1 which are the most depleted in Rb, Th and U (Fig. 3.23a). The highest Ba concentration is observed in sample 16/01/01 (base of the Sarangar gabbro) which is the most enriched in Rb, Th and U (Fig. 3.23a). This is indicating that Cs, Ba and Sr were mobilized together with the other HIEs during incipient melting. Alternatively, similar to Pb, these elements systematically display positive anomalies relative to other HIEs and LREE on primitive mantle-normalized diagrams (with the only exception of Cs in samples RK2 and RK1, Fig. 3.23a). These anomalies are observed in the whole sequence from Jijal to Dasu, including the Granulitic gabbro and the granites (Fig. 3.29a,b). These anomalies represent most likely the primary, arc-type, geochemical signature of the mantle melt parental to the whole sequence.

The strong HIE depletion observed in most of the gabbro-diorite sequence may be considered as a cumulitic character, resulting from the segregation of residual liquid during fractional crystallization. However, this process hardly accounts for the strong depletion of Th, U, Nb and Ta relative to LREE in samples with typical “melt-type” REE patterns (e.g., RK2 and RK1). Conversely, the less differentiated samples (the lower gabbros, which have the lowest LREE contents) are less depleted in HIE than the other samples. Mineral accumulation during fractional crystallisation cannot explain the negative correlation between HIE and LREE. Based on the negative correlation (to samples RK1 and RK2) between HIE enrichment and distance from Patan (Fig. 3.28), a process involving incipient partial melting of rocks similar to the Granulitic gabbro and upward pervasive migration of HIE-rich small melt migrations through the Sarangar gabbro is likely.

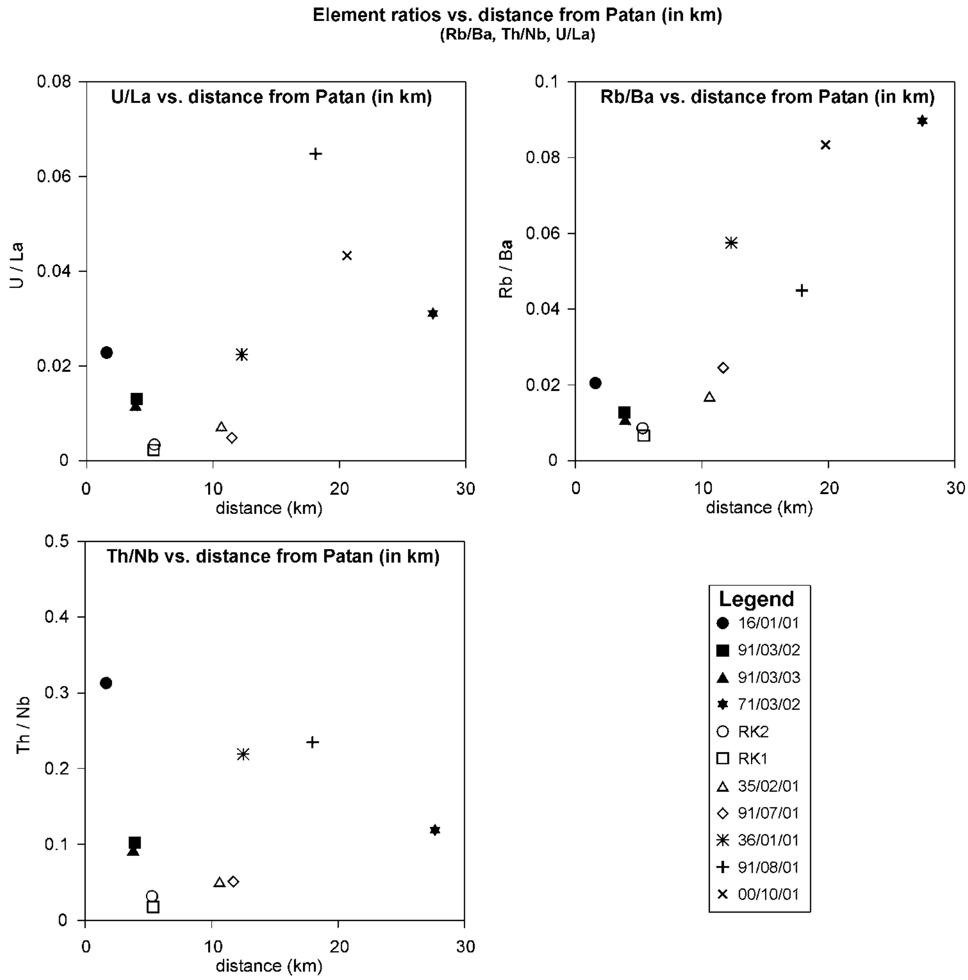

Fig. 3.28: U/La, Rb/Ba and Th/Nb ratios versus sample distance to Patan of the gabbros, diorites and granites in the Metaplutonic Complex (see Fig. 3.16 and 3.17 for locations.

The Granulitic gabbro (and the enclosed hornblendites) are strongly depleted in HIE, particularly Th (Fig. 3.29a). Strong depletion of Th and U (and other HIE) is a classic feature in granulitic terranes (Burton & O'Nions, 1988). HIE depletion in granulitic terranes has been ascribed to prograde granulitic metamorphism (Burton & O'Nions, 1988), due to dehydration associated with mica breakdown into garnet, as the latter cannot host much Th, U and "large ion lithophile elements" (LILEs). However, this process is unlikely, as there is no mica reported in the protolith of the Granulitic gabbro. Therefore, an explanation involving 1) incipient melting of Granulitic gabbros and hornblendites from the Jijal complex triggered/enhanced by dehydration of the hornblendites, and 2) the formation of silica- and water-rich small melt fractions migrating upwards is favoured. If the "lesser" HIE depletion recorded at the base of the

Sarangar gabbro is attributed to a re-enrichment process, it is then implied that the "most depleted" samples from the top of the Sarangar gabbro are more representative of the "protolith" (i.e., the original gabbro-diorite composition, before re-enrichment). This has to be proven by more analyses from the top of the Sarangar gabbro.

Both the Granulitic gabbro and the studied gabbro-diorite section have been strongly depleted in HIE (Fig. 3.29a) due to (hydrous) incipient melting, upward pervasive migration of small volume melts and local extraction of granites. In this scheme, the HIE/LREE ratio of a given sample will depend on a balance between HIE depletion by incipient melt extraction (earlier) and HIE re-enrichment by migrating melts (later). The Granulitic gabbro was more depleted than the gabbro-diorite sequence (Fig. 3.29a) and notably more than the granites/tonalites (Fig. 3.29b), and not significantly re-enriched. Conversely, the upper diorites were less depleted. The base of the lower gabbro sequence (Sarangar) was probably re-enriched by melts from Jijal complex, as attested by the selective enrichment of La-Ce relative to Pr-Sm in sample 16/01/01, which cannot be accounted for by a "lesser depletion degree". A direct comparison between the granites and the Granulitic gabbro, the hornblendites and the garnet pyroxenites was plotted (Fig. 3.29b,c) in order to see if the formation of granites could have taken place by partial melting of the Jijal complex. Partial melting would leave a HIE-depleted residue, which can be observed in the Jijal complex. The trace element signature of the granites is consistent with the partial melting hypothesis suggested for their HREE depletion.

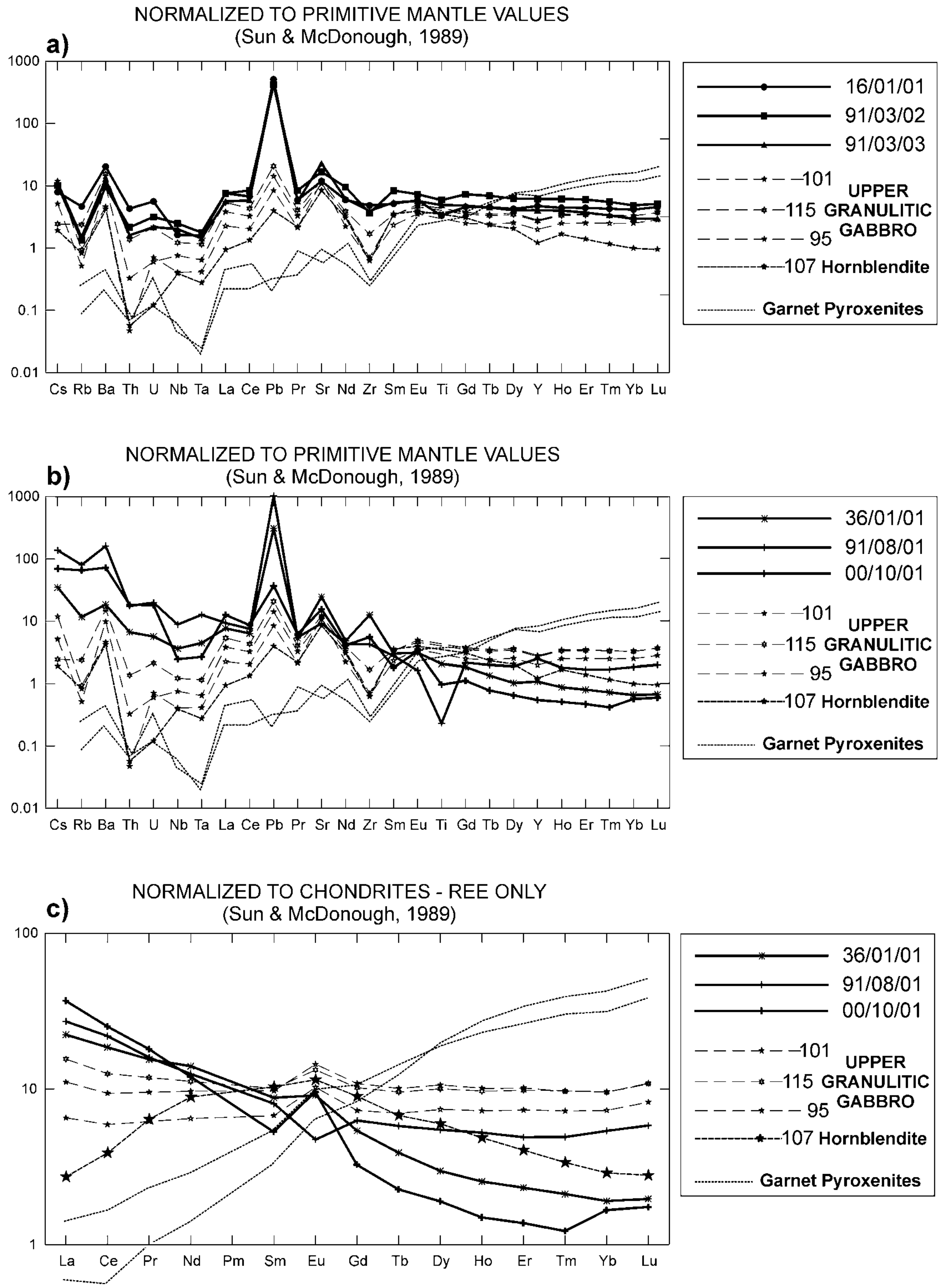

Fig. 3.29: Comparison between a) Sarangar gabbro, garnet pyroxenites, garnet hornblendites, and upper granulitic gabbro; b) granite/tonalite, garnet pyroxenites, upper granulitic gabbro; and hornblendites; c) granite/tonalite, garnet pyroxenites, upper granulitic gabbro and hornblendites; REE only. Data of garnet pyroxenites, upper granulitic gabbro and hornblendites provided by Jean-Louis Bodinier and C. Garrido, personal communication.

3.2.6 Conclusions

Samples from the Metaplutonic Complex cover calc-alkaline to tholeiitic differentiation trend gabbros, diorites, tonalites to granites, emplaced in a island (volcanic-) arc setting (Fig. 3.19, Fig. 3.21). Certain major element variations are aligned on correlations (when plotted against SiO_2) underlining the dominant calc-alkaline character of the magmas (Fig. 3.18). The Chilas complex is noticeably calc-alkaline (Khan *et al.*, 1993), indicating a less FeO rich calc-alkaline composition (Fig. 3.19). Trace element patterns of the Chilas complex and other volcanic and plutonic rocks from the Kohistan Arc complex (e.g. Hunza, Jaglot) are incoherent, reflecting the long lasting evolution of magmas, alteration processes and changes in tectonic settings (Fig. 3.22b,c).

The gabbros and diorites from the Metaplutonic Complex yield relatively similar trace element and REE patterns. Assuming they preserved a geochemical signature from the melts and/or melt-source, this indicates a common arc-type melt source. The relatively to the gabbros and diorites HIE enriched and HREE depleted granites and tonalite preserved positive anomalies in Cs, Ba, Sr and Pb, similar to the positive anomalies in the gabbros and diorites. Therefore, they are considered to be genetically related to the gabbros and diorites. The arc-type character of the analysed samples (only the Metaplutonic Complex ones) is evident by comparing them to recent oceanic arcs (Fig. 3.24). Despite small differences (especially for the HIE), the overall geochemical signature is similar to volcanics of the Tonga, New Hebrides and Mariana arc systems. The observed geochemical signature is different from 1) gabbros from the Oman ophiolite complex, excluding that the analysed rocks represent an ocean floor, and 2) from diorites from the Indian Plate (at Duber Bazar), excluding that the analysed rocks have been intruding a continental terrane during a rifting phase.

The Metaplutonic Complex gabbros and diorites, the island arc volcanics and the continental crust have almost identical concentrations of moderately incompatible elements, whereas the HIE depletion of the Metaplutonic Complex gabbros and diorites tends to “balance” the enrichment of the continental crust. The processes whereby a dominantly basaltic/transitional, juvenile arc crust evolves with time towards more acidic and HIE-enriched compositions akin to continental crust can be studied in the KAC. A superposition of primary magmatic, melt perculation and metasomatic processes are involved in the arc evolution. Based on the preliminary dataset, fractional crystallisation of the plutons/laccoliths seems to be a minor process in the Metaplutonic Complex, because none of the plutonic suites are cumulates with a primary compositional layering. This indicates that there was no common large magma chamber involved in the formation of the gabbros and diorites. Instead, a succession of melt batches with various differentiation degrees, preserving a common “source” signature, is more likely. A process that can partly explain the observed geochemical signatures is the incipient partial melting of lower arc section. Possibly triggered by dehydration of hornblendite facies a pervasive upward migration of small melt fraction would be the consequence. The effect on major elements would be very little and would show no effect on compatible trace elements at all. But a “draining” effect would transport Th, U and LILEs from the lower parts of the arc to shallower levels leading to their selective enrichment relative to slightly less incompatible elements such as LREE. Partial melting at the base of the arc is most likely the process responsible for the formation of granites. If partial melting was a process active continuously at the base of the arc crust or happened as distinct events has to be proofed by dating different granites. Partial melting, probably partly connected with the previous process, will efficiently remove granitic components from the base of the arc and transport them up to shallower levels.

The analysed rocks, even representing only a small part of the KAC, demonstrate a part of a set of spatial (lower section: gabbroic rocks → upper section: granitic rocks) and chronological trends (gabbros older than granites; see ages in chapter 4) in the overall geochemical evolution of the arc.

4. NEW GEOCHRONOLOGICAL CONSTRAINTS ON THE KOHISTAN ARC COMPLEX

Chapter 4.1 is "Changing mantle sources during island arc magmatism: U-Pb and Hf isotopic evidence from the Kohistan arc complex, Pakistan" by U. Schaltegger, G. Zeilinger, M. Frank & J.-P. Burg (submitted to Geology, 2001).

4.1 MULTIPLE MANTLE SOURCES DURING ISLAND ARC MAGMATISM: U-PB AND HF ISOTOPIC EVIDENCE FROM THE KOHISTAN ARC COMPLEX, PAKISTAN

4.1.1 Abstract

Supra-subduction volcanism in oceanic island arcs stems from the partial melting of the underlying mantle wedge and possibly from the subducting slab. The parental magmas undergo differentiation and eventually build up the juvenile arc crust. The fossil island arc sequence of the Kohistan Arc Complex (KAC) preserves a record of arc magmatism with a duration of over 20 million years. Thus, the KAC provides a unique opportunity to investigate potential changes in magma sources during arc evolution. Here we present high-precision U-Pb ages and initial Hf isotopic compositions of zircons from mafic to felsic rocks of the KAC. Hafnium isotopes in zircon have been shown to be a sensitive isotopic tracer of subtle changes in the source regions of magmatic rocks. Three magmatic pulses tapping geochemically different reservoirs are distinguished from initial to evolved stages of the KAC. Magmatism during initiation of the arc at 99-92 Ma was generated by partial melting of mantle with MORB-type isotopic characteristics. Extensional magmatism 85 Ma ago tapped a more fertile mantle source, most likely consisting of a >600 Ma-old metasomatically enriched mantle, or of mantle contaminated by an old sedimentary component. Remelting of the deep base of the arc 82 Ma ago resulted in felsic peraluminous dykes, which again show MORB-type isotopic compositions inherited from the initial stage. The isotopic results demonstrate that arc development, from initial to evolved stages, is characterized by several changes in melt source region. They show that there was subordinate continental influence and negligible importance of slab components for the Hf budget during the generation of the Kohistan Arc Complex.

4.1.2 Introduction

Island arc magmatism, as generated above a subducting oceanic plate, may either be derived from the slab or from the overlying mantle wedge. Evidence from active subduction systems suggests that slab melting is a rare process restricted to very hot and young slabs (Kay, 1978; Sigmarsson, 1998). Melts are commonly formed in the overlying mantle wedge, triggered by fluid release from the subducted slab. The mantle source of primary arc melts is considerably more depleted than typical mid-ocean ridge basalt (MORB)-type reservoirs (e.g. Davidson, 1996) and, therefore, requires unrealistically high temperatures to melt further. Continuous arc magmatism over millions of years implies either (re)fertilization of previously depleted mantle, or the tapping of new fertile reservoirs in the development of the arc. On the other hand we know of arcs with long lifetimes, e.g. 45 million years in the case of the Bonin arc, that apparently show a stable pattern of magma generation throughout their history (Arculus, 1994).

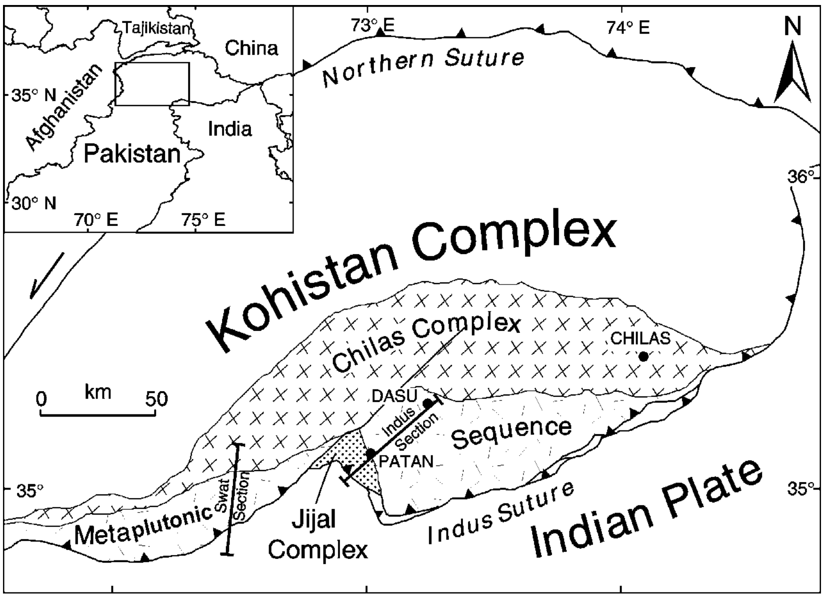

Fig. 4.1: Schematic geological map of the southern part of the Kohistan Arc Complex, after Burg et al. (1998). Analyzed material was sampled along the two cross sections of Indus and Swat valleys, respectively. Rocks of the central and northern Kohistan Complex - metasediments and associated volcanic sequences intruded by plutons of the Kohistan Batholith (Jan & Howie, 1981; Petterson et al., 1991b) were not investigated.

We investigated this paradox by studying time-resolved melt formation in a long-lived island arc system, using high-precision U-Pb dating and determination of initial Hf isotopes in zircon. The Kohistan Arc Complex (KAC) in northern Pakistan (Fig. 4.1) shows an undisturbed geological record from initial to more mature stages of arc formation; it was formed during Cretaceous north-dipping subduction in the Tethys Ocean between the Indian and Eurasian continental plates (Tahirkheli *et al.*, 1979; Coward *et al.*, 1986). The KAC formed during at least two major tectonic stages (Burg *et al.*, 1998): an initial arc-generating stage starting before 100 Ma and lasting to at least 90 Ma; and an extensional intra-arc rifting stage, during which huge volumes of noritic gabbros were emplaced between 85 and 80 Ma. Profiles in the Indus and Swat valleys provide a rare opportunity to investigate the source regions of melts emplaced during the first 20 million years lifetime of this island arc (Fig. 4.1).

4.1.3 Lithological units of the Kohistan Complex

Rocks of the Jijal Complex represent the sub-arc mantle-crust transition (Burg *et al.*, 1998); peridotites, pyroxenites and hornblendites are overlain by garnet- and 2-pyroxene metagabbroic granulites, representing the deepest exposed crustal rocks (Bard *et al.*, 1980).

The Metadioritic Sequence formed during early arc buildup and consists of a mid-crustal association of imbricate and variously metamorphosed gabbros, diorites and granodiorites with a geochemical trend between calc-alkaline and tholeiitic compositions (Treloar *et al.*, 1990; Khan *et al.*, 1993). Diorites and granites, the most evolved lithologies, form intrusive sheets within the metagabbros of the Metadioritic Sequence.

A large body of calc-alkaline noritic gabbros, the Chilas complex, intruded into volcanic and sedimentary rocks in the central part of the arc (Treloar *et al.*, 1996). Structural relationships suggest emplacement during the younger intra-arc rifting stage.

Subsequently, a number of kyanite-bearing pegmatoid dykes of peraluminous geochemical character intruded into the Metadioritic Sequence of the Swat valley (Jan & Karim, 1995).

4.1.4 U-Pb and Hf isotopic results

Sample locations and petrographic descriptions of studied samples are given in Appendix 4. The oldest rock dated by the U-Pb zircon technique is the Sarangar gabbro with an age of 98.9 ± 0.4 Ma (all $^{206}Pb/^{238}U$ ages; Tab. 4.1; Fig. 4.2a). It intruded into granulite-facies garnet-pyroxene gabbros of the Jijal complex, previously dated by the Sm-Nd pyroxene-garnet technique at 91.0 ± 6.3 Ma, 94.0 ± 4.7 Ma, 95.7 ± 2.7 Ma, and 94.6 ± 5.3 Ma (Anczkiewicz & Vance, 2000; Yamamoto & Nakamura, 1996, 2000). Dated intrusions within the Metadioritc Sequence include a granite sheet (97.1 ± 0.2 Ma; Fig. 4.2a) and a diorite stock (91.8 ± 1.4 Ma; Fig. 4.2b), both from the Indus valley. The Metadioritic Sequence is intruded by two different types of lithologies; a kyanite-bearing peraluminous dyke with very low-U zircons was dated at 82.8 ± 1.1 Ma (Fig. 4.2b) and the Chilas gabbronorite yielded a precise age of 85.73 ± 0.15 Ma (Fig. 4.2c).

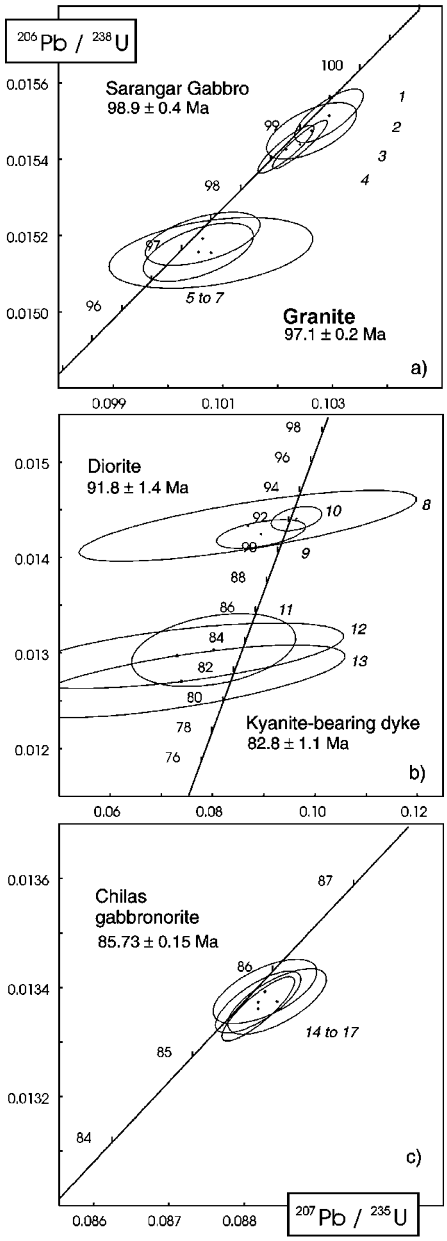

Fig. 4.2: U-Pb concordia diagrams with age determinations for the Sarangar gabbro and a granite (a) and for a diorite (b) from the Indus Valley; and a kyanite-bearing dyke (b) and the Chilas gabbronorite (c) from the Swat valley. Ellipses denote analytical uncertainty at the 2 sigma level of individual analyses.

The new age for the Chias gabbronorite lends support to the 84 Ma U-Pb zircon age obtained by Zeitler *et al.* (1980). The new ages of both felsic dykes and Chilas Complex coincide with Ar-Ar hornblende ages for the Metadioritic Sequence (85 to 80 Ma), which were inferred to date cooling of these rocks below temperatures of 550 °C (Treloar *et al.*, 1989a; Wartho *et al.*, 1996). These ages are older than obduction of the Kohistan Complex onto the Indian plate, which started about 60 Ma ago (Coward *et al.*, 1986).

The Hf isotopic compositions were determined from the same zircon microfractions used for U-Pb dating (see Table 4.1). Due to typically very low $^{176}Lu/^{177}Hf$ isotopic ratios of 0.005 in zircon, they represent initial Hf isotopic compositions at the time of melt crystallization. The εHf values of Sarangar gabbro (+14.1 ± 0.1), granite (+14.7 ± 1.6) and diorite (+14.0 ± 2.2) are analytically indistinguishable and are representative of a MORB-type mantle reservoir (Patchett & Tatsumoto, 1980; Nowell *et al.*, 1998). The Chilas gabbronorite yielded a significantly lower εHf value of +10.4 ± 0.05, pointing to a more fertile mantle source with time-integrated lower Lu/Hf, whereas the kyanite-bearing dyke shows a value at the level of MORB-type mantle (+13.9 ± 0.3).

Nr.	Concentrations				Atomic ratios						Age			
	U [ppm]	Pb rad. [ppm]	Pb non rad. [pg]	Th/U §	$^{206}Pb/^{238}U$ * †	Error ±2σ [%]	$^{207}Pb/^{235}U$ *	Error ±2σ [%]	$^{207}Pb/^{206}Pb$ * †	Error ±2σ [%]	$^{206}Pb/^{238}U$ * †	$^{176}Hf/^{177}Hf$	±2σ #	εHf (T) **
Sarangar Gabbro, Indus valley														
1	149	2.44	4.1	0.53	0.01553	0.37	0.1030	0.48	0.04808	0.31	99.3	0.283120	22	14.5
2	182	2.99	2.0	0.58	0.01544	0.33	0.1022	0.41	0.04803	0.19	98.8	0.283106	2	14.0
3	129	2.10	3.1	0.55	0.01545	0.33	0.1024	0.40	0.04806	0.17	98.9	0.283110	7	14.2
4	189	3.08	1.9	0.53	0.01549	0.39	0.1026	0.65	0.04805	0.52	99.1	0.283311	2	14.1
												Mean:		14.1±0.1
Granite, Indus valley														
5	358	5.82	1.7	0.60	0.01517	0.41	0.1006	0.81	0.04807	0.68	97.1	0.283096	28	13.7
6	507	8.98	8.5	0.55	0.01517	0.50	0.1005	1.68	0.04807	1.55	97.0	0.283114	16	14.3
7	1377	22.25	2.2	0.57	0.01512	0.37	0.1006	0.90	0.04797	0.78	97.3	0.283138	13	15.2
												Mean:		14.7±1.6
Diorite, Indus valley														
8	16.26	0.25	2.8	0.68	0.01435	2.12	0.0869	31.00	0.04392	29.50	91.8	0.283141	15	15.2
9	38.20	0.59	5.8	0.68	0.01426	0.86	0.0895	7.94	0.04550	7.54	91.3	0.283112	7	14.1
10	33.23	0.53	1.0	0.67	0.01442	0.71	0.0964	4.19	0.04848	3.97	92.3	0.283071	13	12.7
												Mean:		14.0±2.2
Kyanite-bearing dyke, Swat valley														
11	6.74	0.08	1.1	0.05	0.01304	2.40	0.0802	16.30	0.04459	15.70	83.5	0.283108	8	13.8
12	2.75	0.03	1.5	0.01	0.01299	2.16	0.0730	36.50	0.04077	35.20	83.2	0.283121	12	14.2
13	5.29	0.06	4.3	0.01	0.01272	2.44	0.0739	35.44	0.04214	33.80	81.5	0.283110	3	13.8
												Mean:		13.9±0.3
Chilas gabbronorite, Swat valley														
14	113	1.75	5.0	0.91	0.01337	0.36	0.0882	0.45	0.04783	0.24	85.6	0.283012	3	10.5
15	107	1.74	4.5	1.09	0.01337	0.35	0.0882	0.52	0.04778	0.36	85.7	0.283010	2	10.4
16	99	1.62	8.8	1.12	0.01337	0.37	0.0884	0.61	0.04792	0.45	85.7	0.283011	3	10.4
17	103	1.67	1.7	1.08	0.01340	0.36	0.0883	0.64	0.04776	0.51	85.8	N.D.		N.D.
												Mean:		10.4±0.05

*Corrected for fractionation, spike, blank and common lead
†Corrected for initial Th disequilibrium, using an estimated Th/U ratio of 4 for the melt
§Calculated on the basis of radiogenic $^{208}Pb/^{206}Pb$ ratios, assuming concordance
#Numbers refer to the last digits
**Epsilon Hf values were calculated with $(^{176}Hf/^{177}Hf)_{CHUR(0)}$ = 0.282772 (Blichert-Toft and Albarède, 1997)

Table 4.1: U-Pb and Hf isotopic data of zircons from the Kohistan Arc Complex.

4.1.5 Sources of arc magmatism

From previous age determinations it was assumed that the Kohistan Arc Complex was formed during a prolonged period starting before 100 Ma ago and ending with obduction onto the Indian plate 60 Ma ago or after. Samples of plutonic rocks, however, only span 20 million years from initial to evolved stages. The limited number of samples does not allow a final statement whether this duration is real or a bias of sampling statistics. In any case, the new time-resolved Hf isotopic values provide insights into the changing dynamics of melt sources and different mantle reservoirs within the 20 Myr life-time of this island arc.

The initial stage is characterized by the intrusion of gabbroic, granodioritic and dioritic lithologies. The oldest dated rock, the Sarangar gabbro, intruded into the garnet-pyroxene-granulites at temperatures and pressures in excess of 800 °C and 1.1 GPa (Yamamoto, 1993). The 96 to 91 Ma Sm-Nd mineral isochron ages of the granulites indicate system closure during cooling at around 650 to 750 °C (Mezger *et al.*, 1992; Anczkiewicz & Vance, 2000). This implies that the high-grade peak conditions recorded by these granulites (Ringuette *et al.*, 1999) were attained prior to 99 Ma.

The granite at 97 Ma is the first evolved melt that differentiated from mafic (ultramafic?) parental magmas. It is followed by the more mafic diorite intrusion 5 million years later. Thus, we speculate that the magmatic rocks were emplaced in several short pulses, each one possibly representing an individual magmatic differentiation cycle, but having the same MORB-type source as indicated by similar εHf values. Fluid metasomatism from the subducting oceanic crust leaves the Hf isotopic composition of the mantle wedge virtually unaffected, because slab fluids commonly have negative Hf anomalies (e.g. Pearce *et al.*, 1999). Hf isotopes are therefore believed to reflect the geochemical characteristics of the mantle wedge. We suggest that the mantle wedge is the principal source of the initial pulse of arc melts consisted of normal MORB-type mantle, in agreement with findings from modern arcs (White & Patchett, 1984).

The intra-arc rifting stage is dated by the 85.7 Ma age of the Chilas gabbronorite intrusion. The gabbronorites originated from the partial melting of a relatively shallow mantle source (Khan *et al.*, 1993) and emplaced at temperatures in excess of 800 °C and at pressures of approximately 0.8 – 0.9 GPa (Yoshino *et al.*, 1998) in an extensional tectonic setting. Renewed melting of previously depleted harzburgitic mantle would, however, require unrealistically high melting temperatures. Therefore, we suggest that either the original magma source was (re-)fertilized, or that the Chilas parental melts tapped a completely different source.

The Hf isotopic composition of the Chilas melts had an εHf value of +10.4 and is significantly lower than the older magmatic rocks of the Metaplutonic Complex, but well within the range of oceanic basalts (e.g. Nowell *et al.*, 1998). This suggests that an old mantle component with a lower time-integrated Lu/Hf ratio than MORB, or even sedimentary or continental crustal contaminants, were involved in the generation of the Chilas parental melts. Assuming melting of a metasomatised mantle with a $^{176}Lu/^{177}Hf$ ratio of 0.020, we arrive at a minimum age estimate of 600 Ma for this source. The same εHf value of + 10 may also be obtained by subordinate contamination of MORB-type mantle by Archean granitoid crust or detritus, or pelagic sediments.

The 82.8 Ma old kyanite-bearing felsic dyke relates to a third magmatic phase derived from a MORB-type reservoir again. The dykes have crystallised at 610 °C and 1.0 – 1.2 GPa (Jan & Karim, 1995). They probably originate from partial melting of granulitic, eclogitic or pyroxenitic lithologies from the deep base of the arc. Remelting of 20 Myr old mantle-derived materials is not expected to produce a discernible isotopic contrast in the Lu-Hf isotopic system. Therefore, we consider the eHf value of + 14 to be inherited from the initial stage of partial melting of a MORB-type mantle source. The data also indicate that the felsic rocks, including granodiorite intrusions in the Metadioritic Sequence as well as felsic dykes, are not derived from post-obduction melting of the overridden Indian plate but form part of the arc magmatic sequence.

4.1.6 Geodynamic implications for the Kohistan Arc

The U-Pb and Hf isotopic data from zircons of the Kohistan Arc Complex delineate a complex magmatic evolution from the initiation of an island arc to its mature stage. Since Lu-Hf is a very conservative isotopic system with respect to contamination by released slab fluids, changes in Hf isotopic characteristics probably reflect changes of source compositions within the mantle wedge. Therefore, these isotopic values indicate that mantle sources change in composition during the evolution of an island arc system.

Any tectonic models for the evolution of the arc system have to be consistent with these geochemical arguments.

The precise U-Pb age determinations of zircons clearly separate the inititation of the Kohistan Arc arc from pre-100 Ma to at least 90 Ma, when melts were derived from an asthenospheric MORB-type mantle, from intra-arc rifting starting at around 86 Ma when melts possessed a less radiogenic Hf signature.

We envisage four potential hypotheses for the origin of this lithospheric component in the Chilas intrusion (Fig. 4.3):

(1) Sediments or a sliver of continental Archean to Proterozoic crust within the oceanic lithosphere of the subducted slab; this would infer the existence of continental relics or detritus in the Tethyan oceanic domain.

(2) Subduction and melting of an old fertile mantle portion attached to a sliver of continental crust within the Tethys oceanic domain.

(3) Contamination by pelagic sediments from the oceanic basement of the arc edifice.

(4) Dragging of >600 Ma-old mantle with an intrinsic fertility into the hangingwall of the subduction zone - for instance a piece of Gondwana-derived lithosphere, from the back-arc area into the area of partial melting beyond the arc.

Trace and rare earth element compositions of the Chilas Complex are typical for arc-related rocks and point to generation of the melts in rather shallow levels of the mantle wedge (Khan *et al.*, 1993). The melts were contaminated by a "subduction component" containing large ion lithophile elements (K, Rb, Sr, Ba), light rare earth elements (Khan *et al.*, 1993) and increased Sr isotope ratios above mantle values (Mikoshiba *et al.*, 1999). Hafnium transfer from the slab into the mantle wedge (1, 2) would require partial melting of slab material and destabilization of Hf-bearing phases – zircon in the case of felsic crustal material, titanate phases (rutile and ilmenite) for more mafic lithologies. This conflicts with the depletion of Zr, Hf, and Ti in Chilas samples (Khan *et al.*, 1993), and is at odds with thermal models for subducting oceanic lithosphere. Contamination by pelagic sediments of the oceanic sub-arc crust (3, Fig. 3b) would probably produce lateral isotopic variations within the Chilas body, a hypothesis yet to be tested. Hypothesis (4) invokes dragging through mantle corner flow of a piece of old metasomatically enriched mantle from the the hangingwall of the subduction into the region of partial melting in the mantle wedge. This process would introduce a new fertile mantle component into the system, which could provide large volumes of evolved melts necessary to produce the huge Chilas intrusion. Neither of these hypotheses can, however, be substantiated with the present data at the present time.

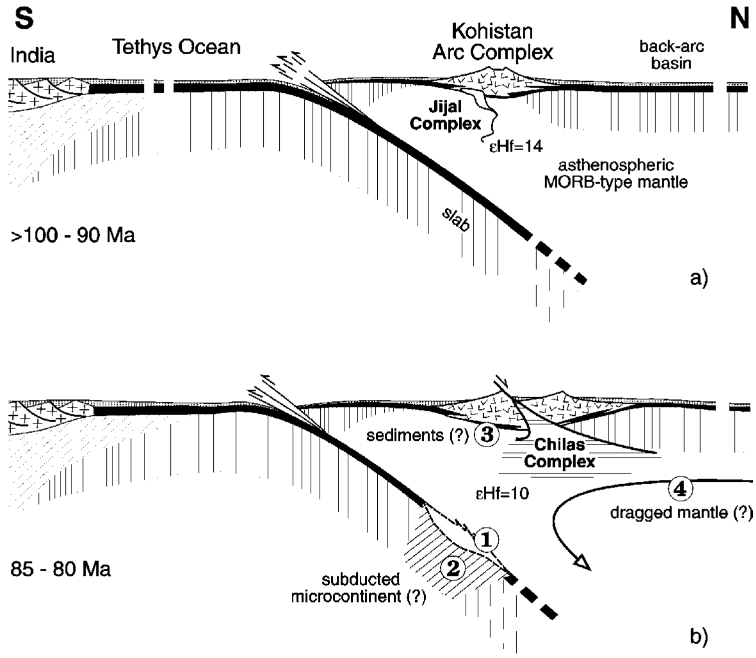

Fig. 4.3: Magmatic sources in a tectonic model for the initial arc buildup at >100-90 Ma (a) and for intra-arc rifting at 85-80 Ma (b). Hf isotopic values of the two phases of magmatism are indicated. Numbers 1 to 4 delineate hypothetical magma sources and are discussed in the text.

4.1.7 Conclusions

The Kohistan Arc Complex evolved within some 20 Myr from initial arc buildup (prior to 100 - 90 Ma) to a mature stage with back-arc spreading and magmatism (starting at 85 and lasting to at least 80 Ma ago). This mature stage is characterized by a shift in the Hf isotopic compositions of the magmatic liquids from MORB-type values (εHf = +14) to less radiogenic compositions (εHf = +10). The change of Hf isotopic composition of arc melts coincides with a drastic change in tectonic style, at the onset of intra-arc rifting and basin opening. The Hf isotope evidence demonstrates that the Kohistan Arc Complex is an intraoceanic island arc with minimal continental influence. Subducted components derived by melting of the slab itself were negligible for the generation of the melts.

Acknowledgements
We thank T. Bär, I. Ivanov and A. von Quadt for technical support and K. Kunze for cathodoluminescence images. The help of S. Hussain and H. Dawood with field logistics and sampling of the Chilas complex is kindly acknowledged. The study was supported by Swiss NF project grant Nr. 2000-49372.96. Discussions with J.-L. Bodinier, O. Müntener, P. Ulmer, U. Wiechert and H. Williams were very helpful and are highly appreciated.

4.2 PROTEROZOIC INTRUSION IN THE NORTHERN INDIAN PLATE

Immediately south of the northward dipping Indus Suture, the Indian plate is comprised of strongly foliated and folded metasediments, quartzo-feldspathic gneisses and sodic quartzo-feldspathic gneisses. The gneisses belong to the Besham Group (Fletcher *et al.*, 1986), which contains coarse grained metagranodiorites and metadiorites. The metadiorite body at Duber Bazar (Fig. 4.4) was dated by the U-Pb zircon technique with an age of 1858.8±7.2 Ma ($^{206}Pb/^{238}U$ age Tab. 4.2; Fig. 4.5, sample description in Appendix 4) and shows a similar age as the Shang granodiorite gneiss (ca. 17 km S of Duber Bazar.) with 1864±4 Ma (DiPietro *et al.*, 2001). The gneisses of the Besham Group formed 2120 to 2200 Ma ago and re-equilibrated during 1950 Ma metamorphism (Shah *et al.* 1992). Ar-Ar ages on hornblende determined by Baig (1991) and Baig *et al.* (1989) have been interpreted as one or more metamorphic episodes in the range of 2031±6 to 1865±3 Ma. Treloar *et al.* (1989a) obtained an Ar-Ar age on hornblende of 1920±24 Ma for an amphibolite sheet within a granite at Duber Bazar.

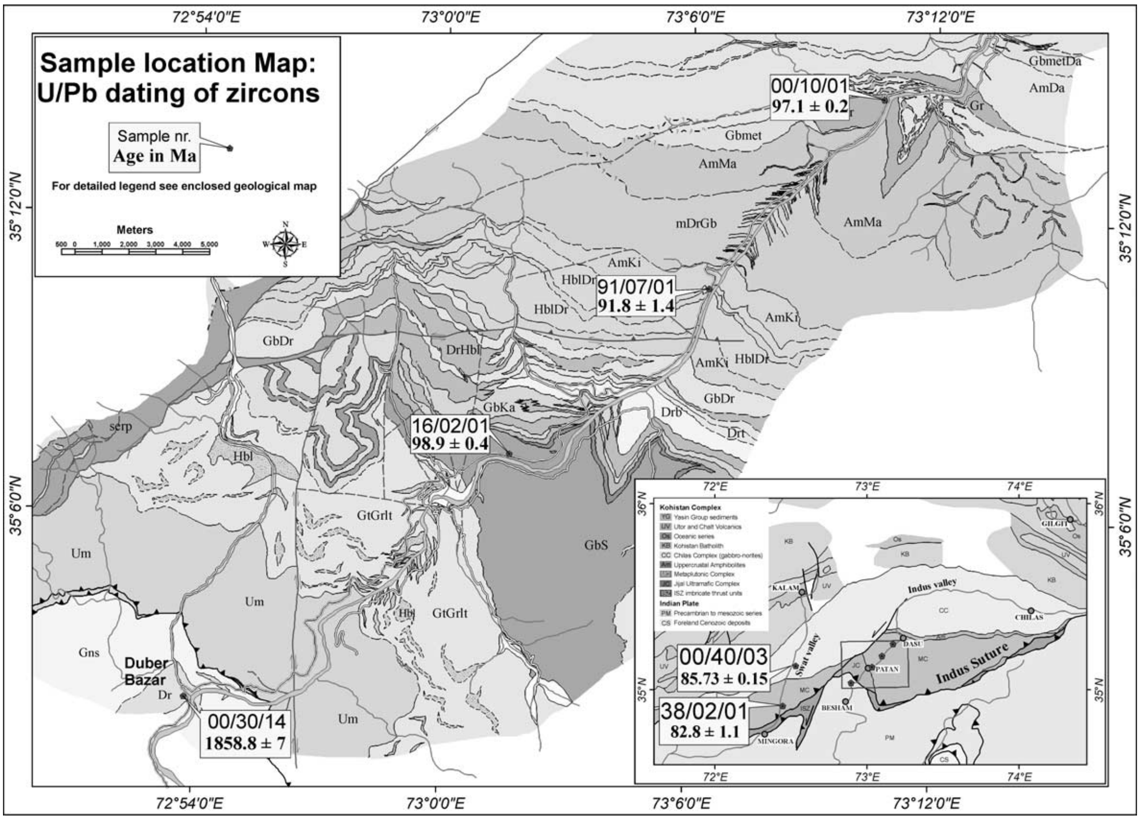

Fig. 4.4: Geological map of the southern part of the Kohistan Arc Complex with dated samples from the Metaplutonic Complex, Chilas Complex and the Indian plate diorite at Duber Bazar.

Nr.	Description	Weight	nr.	Concentrations				Atomic ratios							Apparent ages			Error
		[mg]	of grains	U	Pb rad. [ppm]	Pb nonrad. [pg]	Th/U b)	206/204 c)	206/238 d)	Error 2σ [%]	207/235 d)	Error 2σ [%]	207/206 d)	Error 2σ [%]	206/238	207/235	207/206	corr.
	a)																	
Diorite Indian plate, Swat Valley																		
18	prism tips	0.0316	4	376	131.45	2.4	0.43	104052	0.32727	0.33	5.1298	0.38	0.11368	0.10	1825.1	1841.1	1859.1	0.97
19	small spr	0.0156	6	232	78.47	2.9	0.45	24992	0.31502	0.34	4.9295	0.38	0.11349	0.11	1765.4	1807.3	1856.1	0.96
20	frags	0.0209	5	273	91.62	3.9	0.42	28915	0.31528	0.33	4.9383	0.38	0.11360	0.11	1766.6	1808.8	1857.8	0.96
21	spr	0.0329	5	210	67.80	15.2	0.41	8739	0.30394	0.33	4.7610	0.38	0.11361	0.11	1710.8	1778.0	1857.9	0.96

a) all zircon fractions abraded; prism = prismatic; spr = short-prismatic
b) Calculated on the basis of radiogenic Pb208/Pb206 ratios, assuming concordance
c) Corrected for fractionation and spike
d) Corrected for fractionation, spike, blank and common lead (Stacey & Kramers, 1975)

Table 4.2: U-Pb isotopic data of zircons from the Indian plate diorite.

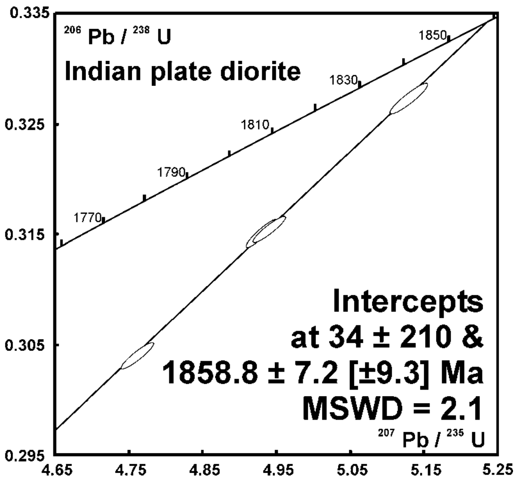

Fig. 4.5: U-Pb concordia diagram with age determination for the Indian plate metadiorite. Ellipses denote analytical uncertainty at the 2 σ level of individual analyses.

Ductile deformation is concentrated at the borders of the metadiorites. Thin (ca. 30-80 cm thick) pegmatites are generally undeformed and cut the weak, northeastward dipping foliation. This implies that the metadiorite, located ca. 300 m beneath the Indus Suture, was not or only little affected by the India-Kohistan collision. Furthermore, the Ar-Ar Hornblende age of ca. 1920 Ma (Treloar *et al.*, 1989a) was not reset during Himalayan collision, indicating that temperatures did not exceed the closure temperature of 530±50 °C (McDougall & Harrison, 1988). However, Himalayan metamorphism is recorded in the Swat area with Ar-Ar hornblende and muscovite ages ranging in their majority from 36 – 30 Ma (Anczkiewicz, 1998). The emplacement of the metadiorite is part of extensive intraplate plutonism around 1858 Ma in the Indian Plate as indicated by geochemical data (chapter 3.2).

4.3 EXHUMATION ACROSS THE ISZ, ANTIFORM GROWTH OR BACK SLIDING OF THE HANGING WALL?

4.3.1 Introduction

Studying the exhumation history of the Kohistan Arc Complex is a key for post-collisional tectonic interpretation. Zircon and apatite fission-track (FT) ages were used to constrain cooling through ca. 250 °C and 100 °C, respectively. Especially the comparison of these ages across faults gives insight in relative movements and also provide times, when the differential movement across the faults terminated. An extensive study was carried out by Zeitler (1985), providing fission track ages over the whole KAC (Fig. 4.6).

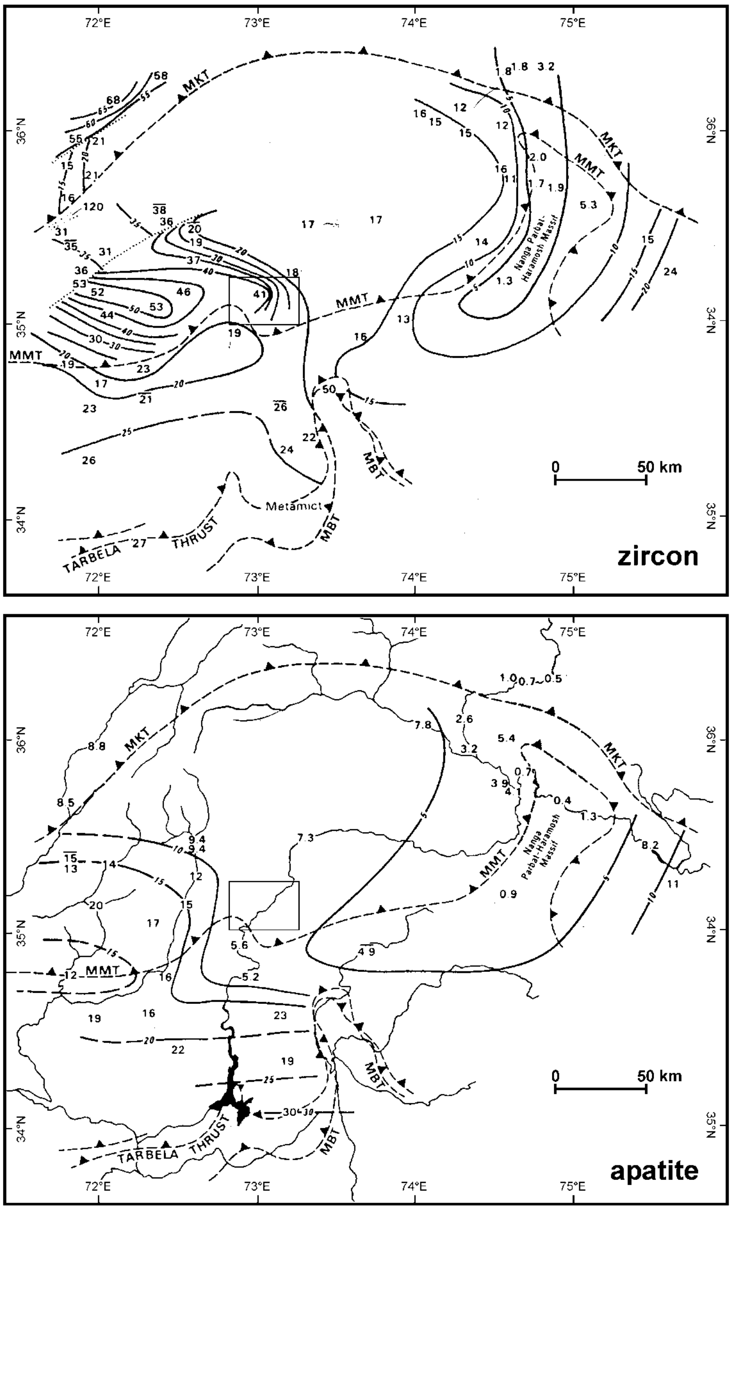

Fig. 4.6: Contoured zircon (upper map) and apatite (lower map) fission track ages of base-level samples (Zeitler, 1985). Area of this study is squared.

Prior to 15 Ma the cooling histories of both the KAC and the Indian Plate are different with the older ages in the hanging wall of the Indus Suture. Apatite ages are more similar on both sides of the Suture, leading to the interpretation that since 15 Ma no differential movement occurred across the Indus Suture (Zeitler, 1985). However, the contouring used by Zeitler (1985) smoothens the age pattern across major faults, which were not taken into account as discrete movement planes. Therefore, Zeitler's interpretation (Zeitler, 1985) is appropriate on a large scale but a more detailed study on distinct parts of the sutures is necessary. The following zircon and apatite fission-track ages were obtained in the Indus valley.

4.3.2 Results

Zircon and apatite fission-track ages were done on samples collected along the Karakoram Highway covering a ca. 35 km long section starting in the SW at Duber Bazar and ending in the NE 6 km SW of Dasu. Sample preparation followed the routine technique described by Seward (1989). Counting was carried out by Diane Seward at the ETH fission track lab. Etching of the apatite grains was done with 7% HNO_3 at 21 °C for 55 seconds. Zircon grains were etched in a eutectic mixture of KOH and NaOH at 220° C for between 20 and 50 hours. Irradiation was carried out at the ANSTO facility, Lucas Heights, Australia. Microscopic analysis was completed using an optical microscope with a computer driven stage ("Langstage" software from Dumitru (1995)). All ages were determined using the zeta approach (Hurford & Green, 1983) with a zeta value of 355 ± 5 for CN5 and 120 ± 5 for CN1. They are reported as central ages (Galbraith & Laslett, 1993) with a 2σ error (Table 4.3). Where possible, 20 crystals of each sample were counted for age determination. The magnification used was x1250 for apatite and x1600 (oil) for zircon. Horizontal confined track lengths were measured at x1250.

Several samples from the Jijal Complex and southern Metaplutonic Complex failed FT dating due to the lack of zircon and/or apatite or due to an extremely low U content in apatite. This prevented some ages being determined on several apatite samples in particular because the density of spontaneous tracks was so very low. Any determination would yield ages with such large errors that they would have not been useful in comparing them with neighbouring samples. In the Indian Plate a deformed metadiorite from ca. 100 m beneath the ISZ close to Jijal (sample 00/30/12), representing the footwall of the ISZ was dated and yields zircon and apatite FT ages of 22.6±2.6 (2σ) Ma and 3.7±1 Ma respectively (Fig. 4.7 for sample location, table 4.3 and appendix 4 for details). In the southern Metaplutonic Complex, representing the hanging wall of the ISZ four samples could be dated. The oldest dated zircon FT age is yielded by a coarse grained pegmatite cutting the dioritic host rocks ca. 5 km NE of Patan with 41.8±8.8 Ma (sample 56/02/01). A coarse-grained hornblende diorite from ca. 1 km S of Kiru yields a zircon FT age of 27.9±5.2 Ma (sample 91/07/01). The northernmost dated sample was collected ca. 200 m S of the bridge where the Karakoram Highway and the Indus River bend sharply towards the E. This coarse grained granite yields a zircon FT age of 23.6±5.6 Ma (sample 00/10/01). Only one apatite FT age was obtained in the Metaplutonic Complex. The sample was taken ca. 3 km E of Patan in an undeformed part of the Sarangar gabbro and yields an apatite FT age of 10.6±2.4 Ma (sample 16/02/01).

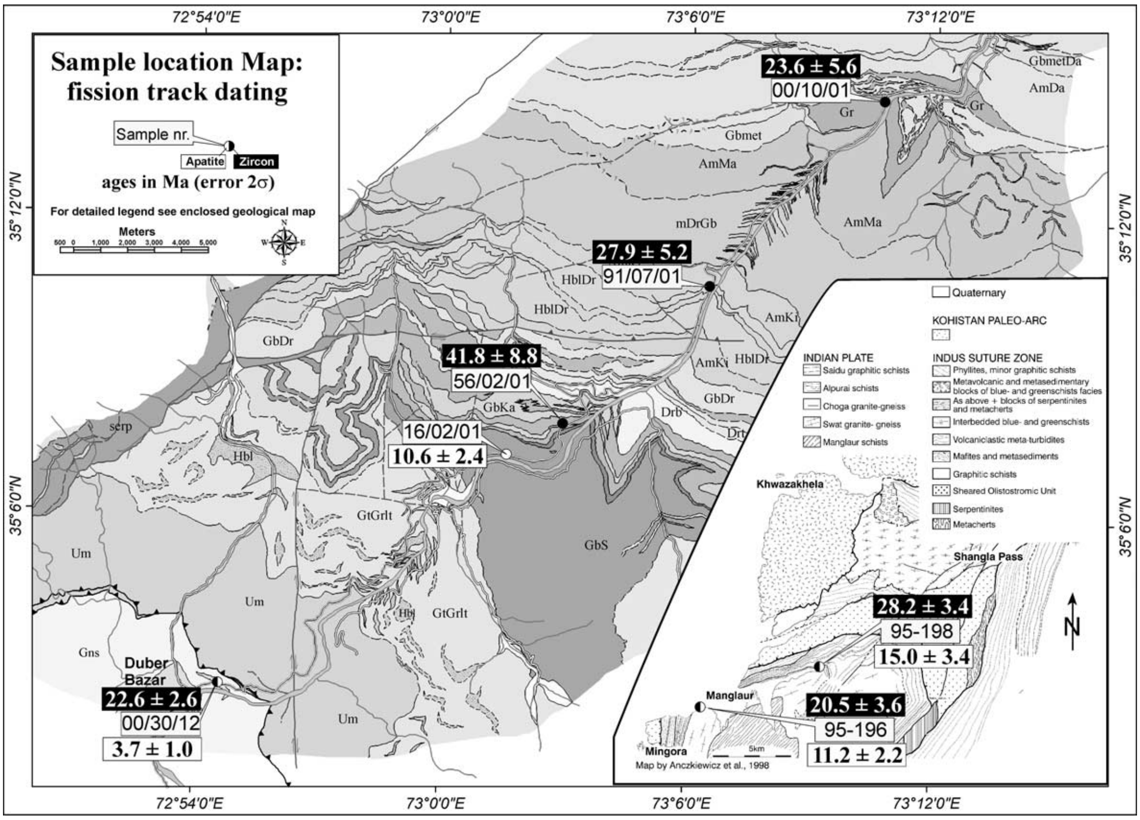

Fig. 4.7: Zircon fission track samples from the Metaplutonic Complex and the Indian plate diorite. Inset: Map of lower Swat region with two ages on the Indian Plate (Anczkiewicz, 1998 and D. Seward, unpubl.).

Sample number	Mineral	Number of grains	Standard track density x 10^4 cm^{-2} (counted)	ρ_s x 10^4 cm^{-2} (counted)	ρ_i x 10^4 cm^{-2} (counted)	U conc. ppm	$P(\chi^2)$ (Variation %)	Central Age ± 2σ (Ma)
95-196	A	16	110 (2439)	12.9 (111)	225 (1929)	26	97 (0)	11.2 ± 2.2
95-198	A	20	122 (2439)	10.8 (82)	156 (1185)	16	83 (0.3)	15.0 ± 3.4
16/02/01	A	20	121 (2808)	0.73 (126)	14.5 (2509)	2	12 (25)	10.6 ± 2.4
00/30/12	A	20	130 (2978)	3.64 (60)	24.3 (4007)	23	8 (25)	3.7 ± 1.0
95-196	Z	12	49.1 (2376)	287 (378)	414 (546)	338	8 (18)	20.5 ± 3.6
95-198	Z	8	56.2 (2376)	473 (885)	563 (1054)	400	11 (9)	28.2 ± 3.4
56/02/01	Z	20	73.3 (2543)	14.6 (180)	15.3 (189)	8	100 (0)	41.8 ± 8.8
00/10/01	Z	4	64.8 (2543)	223 (151)	372 (252)	230	22 (9)	23.6 ± 5.6
91/07/01	Z	20	71.6 (2543)	39.2 (217)	60.7 (336)	33.9	66 (10)	27.9 ± 5.2
00/30/12	Z	20	69.3 (2543)	532 (1726)	1002 (3253)	578	0 (19)	22.6 ± 2.6

Table 4.3: Zircon fission track results from the Metaplutonic Complex, the Indian plate diorite and two ages of lower Swat region (Anczkiewicz, D. Seward, unpubl.). A = apatite, Z = zircon. ρs and ρi represent sample spontaneous and induced track densities; $P(\chi^2)$ is the probability of X^2 for v degrees of freedom where v = no. of crystals – 1. λ_D = 1.55125 x 10^{-10}. Zeta = 355 ± 5 for apatite and CN5, 120 ± 5 for zircon and CN1. Samples were irradiated at the ANSTO facility, Australia. Ages are reported as central ages (Galbraith, 1981). Detailed table with sample coordinates is provided in Table Appendix 4.2.

4.3.3 Tectonic Interpretation

The FT ages yield low temperature tectonothermal information. There is clearly a younging across the Indus Suture from north to south. Within the Metaplutonic Complex ages show an opposite younging direction. The difference in zircon cooling ages could represent tilting effects, or discrete events across faults. If the latter is the case across the ISZ then there is evidence for a relative back sliding of the hanging wall (KAC) along the ISZ. The jump across the ISZ is significant for both, zircon and apatite FT data. The difference between the zircon FT ages representing footwall and hanging wall of today's ISZ geometry of ca. 20 Ma points to an onset of normal faulting during this time span. The apatite FT ages point to a maximum exhumation rate of ca. 0.8 mm/a in the footwall over the last 3.7 Ma and of ca. 0.3 mm/a for the last 11 Ma in the hanging wall. The young apatite FT ages in the Indian Plate (3 to 5 Ma) may reflect a still growing Besham antiform (Coward, 1986; Treloar *et al*., 1989c). To the W, in the Swat valley, apatite FT ages in the Indian Plate are older. Two samples collected by R. Anczkiewicz ca. 4 km NE of Mingora (sample 95-196) and ca. 5 km ENE of Manglaur (sample 95-198) yield ages of 11.2±2.2 Ma and 15.0±3.4 Ma respectively (D. Seward, unpubl.; Fig. 4.7, inset), indicating a faster and/or younger exhumation in the Indus area. As a preliminary interpretation the zircon and apatite FT data indicate normal faulting along this specific part of the Indus Suture from 23 Ma to at least 3 Ma. This contradicts the termination of differential movement at around 16 Ma on the Indus Suture (Zeitler, 1985; Vince & Treloar, 1996). The northward younging direction of ages within the KAC may be interpreted with rotations and the subsequent relative faster exhumations of the northern part against the southern part of the KAC (Fig. 4.8).

The difference of ca. 14 Ma between the 41.8 Ma zircon FT age 6 km NE of Patan and the 27.9 Ma zircon FT age 1 km S of Kiru is significant. An E-W trending, ca. 70-80° northward dipping reverse fault is the prominent fault between the sampled rocks. Rollover geometries are the result of half grabens formed during crustal extension that is accommodated by listric shaped normal faults, causing collapse of the hanging wall (Hamblin, 1965). Rollovers have been observed in rift basins worldwide (e.g. Bally, 1983; Nunns, 1991) and geometric and physical models of hanging wall collapse are described (e.g., Gibbs, 1983; Rowan & Kligfield, 1989; Groshong, 1990; White & Yielding, 1991). In the investigated area no basin developed in a rollover setting during extension is recorded. This implies the following possibilities: 1) the subsidence in the southern edge (hanging wall located north of footwall) of the hanging wall was not large enough to create a sediment filled basin along the Indus Suture, 2) the theoretic rollover surface was always above sedimentation level and 3) the whole geometry was exhumed faster relative to subsidence in the hanging wall and sediment filled basins trapped north of the Indian Plate were eroded subsequently. The development of rollover geometry is characterised by a rotation of the southern part of the hanging wall. As shown in the tectonic sketch presented in Figure 4.8 the rotation brings the early antithetic normal fault into the position of an apparent reverse fault.

Backsliding of the hanging wall is reported on several places of the ISZ: the Naran region (Burg *et al.*, 1996), the Indus region (Vince & Treloar, 1996) and the Swat valley (Anczkiewicz, 1998). The earliest onset of extension is estimated by Burg *et al.* (1996) at 47 Ma, based on dated peak metamorphism of 47±3 Ma from SHRIMP U-Pb analysis of zircon rims (Smith *et al.*, 1994). Extension was completed at ca. 20 Ma (Burg *et al.*, 1996; Vince & Treloar, 1996) based on ages from Zeitler (1985). A comparison of the cooling ages from the northern, middle, southern Metaplutonic Complex and the Indian Plate along the same SW-NE section as in Figure 4.8 shows that the relative normal movement along the Indus Suture outlasted the 20 Ma (Fig. 4.9).

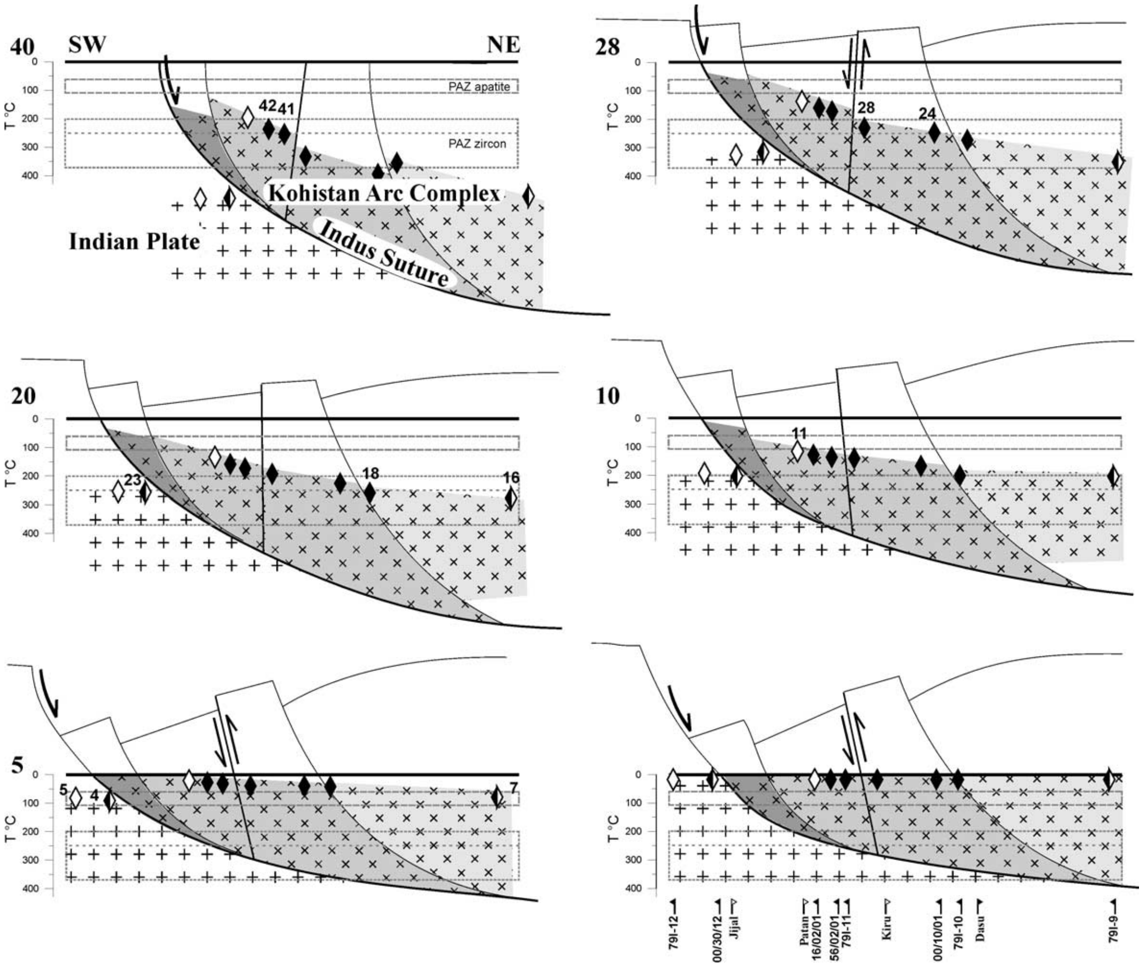

Fig. 4.8: Tectonic sketch integrating available FT-ages on a SW-NE profile along the Indus River. A rollover effect in the hanging wall rotates an early antithetic normal fault to an apparent reverse fault. Ages in Ma are given for samples when passing the 250° and 100 °C isograde. The time steps of 40, 28, 20, 10, 5 Ma and recent reflect midpoints of certain time ranges. Samples: ◊: apatite, ♦: zircon, ◊♦: both; PAZ: partial annealing zone; 79I-samples from Zeitler, (1985). Simple depth temperature correlation is used and does not reflect real conditions.

The zircon FT ages of 41.8 Ma for the southern Metaplutonic Complex and the apatite FT age of 3.7 Ma for the Indian Plate are in agreement with the FT ages obtained by Zeitler (1985) (41.4±2.6 Ma and 5.6±2.3 Ma). Two explanations for the young differential movement across the ISZ in the Indus region are left: 1) The KAC was backsliding along the ISZ as a block until ca. 3 Ma or 2) the recent growth of the Besham antiform is decoupled from the overlying KAC (here mainly the Jijal Complex) and the ISZ is accommodating the differential "growth" with normal faulting (Fig. 4.10).

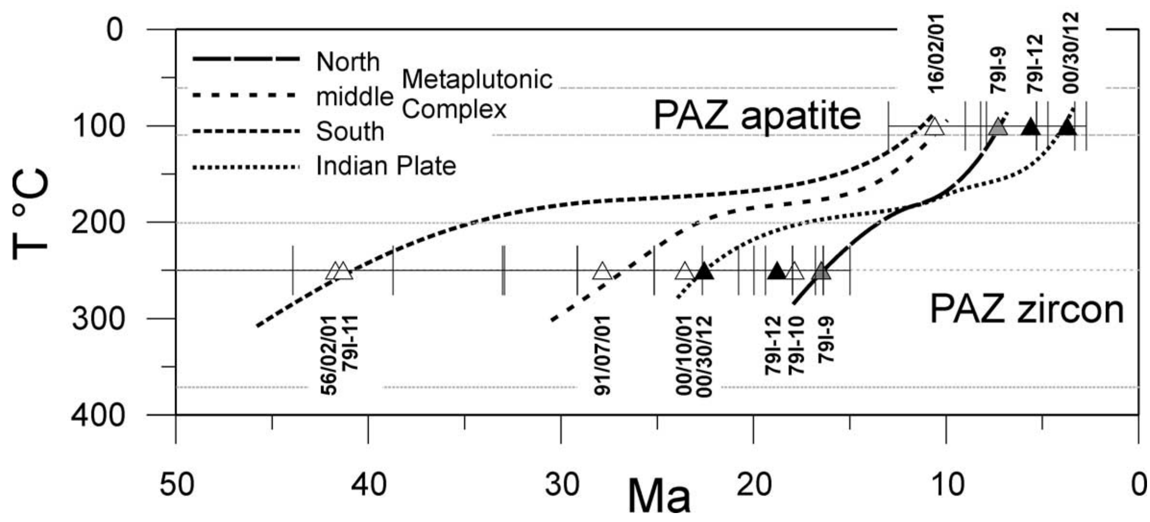

Fig. 4.9: Temperature – time plot showing the cooling history of four different blocks as shown in Fig. 4.8. They are from S to N: Indian Plate, southern, middle and northern Metaplutonic Complex. Cooling paths are rough estimations and not modelled. PAZ: partial annealing zone; 79I-samples from Zeitler, (1985).

The first explanation is unlikely because apatite FT ages younger than 5 Ma are not observed within the Indian Plate along the whole length south of the contact to the KAC. Instead in the Swat valley apatite FT ages on both sites of the Indus Suture are comparable with ca. 11-15 Ma in the south and 15-17 Ma (Zeitler, 1985) in the north, indicating no or little relative movement across the Indus Suture later than 15 Ma ago. The second explanation is consistent with the young apatite FT ages in the Indus area S of the ISZ and older ages E and W of the Besham antiform (Fig. 4.7). Therefore, following conclusion is drawn: the young differential movement across the ISZ in the Indus area is a local phenomena caused by the growth of the Besham antiform and the ISZ is accommodating the differential “growth” with normal faulting.

The duration and the onset of the Besham antiform growth are not directly dated. Assuming the Besham antiform represents a small-scale equivalent to the Nanga Parbat Syntaxis (Coward, 1986; Treloar *et al.*, 1989c) with close generic relation to the Nanga Parbat Syntaxis, located ca. 100 km E of the Besham antiform, the timing can be estimated. The rapid denudation during growth of the Nanga Parbat lasted some 4 Ma (Burg & Podladchikov, 2000). It started not earlier than ca. 5 Ma ago (Zeitler *et al.* 1989, 1993). This implies for the Besham antiform an onset of denudation during growth younger than 5 Ma with a probably faster exhumation at the beginning of the buckling which may be represented by the 3-4 Ma apatite FT age. A recent growth is noticeable in topographic features. The Indus River excavated a steep gorge S of Thakot (ca. 16 km S of Besham). However, earthquakes or seismicity does not report recent normal faulting along the Indus Suture. Therefore it is not known, if normal faulting along the Indus Suture N of Besham is still an active process.

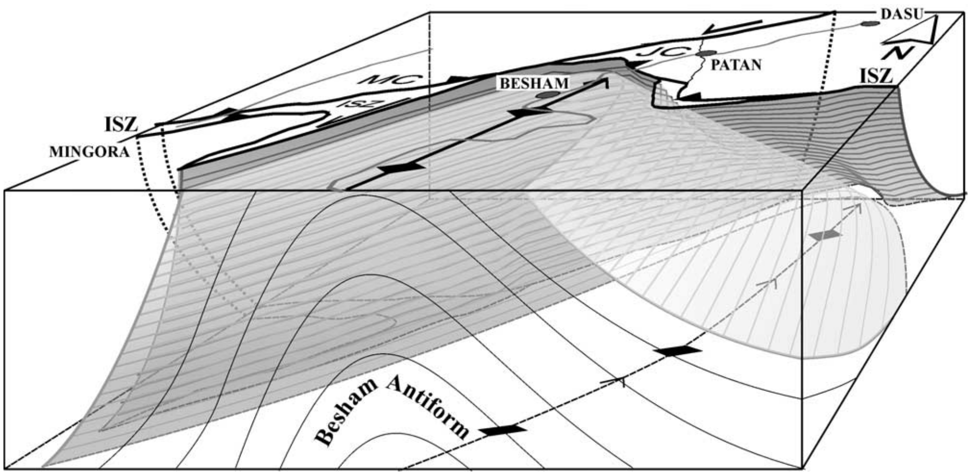

Fig. 4.10: Simplified block diagram showing the Besham antiform descending towards north beneath the Kohistan Arc Complex along the ISZ (MC: Metaplutonic Complex, JC: Jijal Complex).

5. ANASTOMOSING SHEAR ZONES IN THE LOWER KOHISTAN COMPLEX

Chapter 5.1 is "Pre-collisional anastomosing shear zones in the Kohistan arc, NW Pakistan" by L. Arbaret, J.P. Burg, G. Zeilinger, N. Chaudhry, S. Hussain and H. Dawood (Arbaret *et al.*, 2000).

5.1 PRE-COLLISIONAL ANASTOMOSING SHEAR ZONES IN THE KOHISTAN ARC, NW PAKISTAN

Abstract

Ductile strain localisation commonly forms a pattern of shear zones anastomosing around lenses of less deformed rock. Initiation and development history of anastomosing shear zones, which are little documented, are studied through the description of the structures and the deformation history of plutonic rocks that form the lower crust of the Kohistan Complex. Structures and textures developed in these rocks result from primary magmatic to solid state regional strain overprinted by anastomosing shear zones. The primary strain was mainly acquired during magmatic emplacement at 100-90 Ma. Strain localisation took place continuously from magmatic emplacement to solid state deformation during cooling of the plutons and formed 3 successive sets of shear zones. Set 1 is composed of associated discrete Riedel and thrust shear zones developed above solidus conditions during SW-ward thrusting. Continuous deformation from solidus to amphibolite facies conditions between 100 and 83 Ma formed the second set of shear zones. The lower amphibolite facies set 3 shear zones are differentiated by larger strain recorded in the thicker mylonitic zones and enlargement of the spacing between shear zones during cooling. The anastomosing pattern of shear zones described here probably represents arc-related deformation during subduction of the Tethys oceanic lithosphere below the Kohistan Arc Complex.

5.1.1 Introduction

Ductile strain is commonly concentrated into narrow shear zones, anastomosing around lenses of lower strain, the symmetry of the anastomosing pattern reflecting the symmetry of the bulk deformation history (Gapais *et al.*, 1987). Anastomosing patterns are commonly reported (e.g. Mitra, 1978; Ramsay, 1980; Harris & Cobbold, 1984;

Gapais *et al.*, 1987; Lafrance *et al.*, 1998), but with limited information on their geometric detail and growth history. Therefore, the way such anastomosing patterns form and evolve remains an open question. In particular, the relationships between regionally distributed strain and strain localisation in shear zones is not clear.

We aim to provide preliminary answers in describing the structures and deformation history of the plutonic rocks of the lower Kohistan Complex. Some of these plutonic rocks display an early fabric that defines the regional pattern, but an important part of the deformation resulted in strain localisation into shear zones anastomosing around lenses of less, or undeformed rock (Treloar *et al.*, 1990). We argue that the regional background strain is composite and was mainly acquired during magmatic emplacement of the various plutons. The later anastomosing shear zones result from the nucleation and growth of three successive sets of shear zones sharing similar directions. Our petrologic information does not improve previous P-T estimates, which will be referred to in the following paragraphs. Therefore we will not duplicate here the geothermobarometry of these rocks. Correlation between structures and the P-T-time history provides a detailed tectonic evolution of the lower part of the Kohistan Complex.

5.1.2 Geological setting

The Kohistan Complex was an island arc within the Tethys ocean during the Late Mesozoic (Tahirkheli *et al.*, 1979; Bard, 1983; Coward *et al.*, 1986). The tectonic history involves the 102 to 75 Ma old accretion to the Asian plate, to the north (Petterson & Windley, 1985; Treloar *et al.*, 1989a) and closure of the Tethys ocean, to the south, at *c.* 55 Ma, followed by obduction of the Kohistan Complex onto India (Coward *et al.*, 1986). Our structural analysis was focused on the southern, i.e. lower, part of the arc sequence (Fig. 5.1). The study area is comprised of meta-gabbros, hornblende-gabbros and diorites intruded by, and intruding, hornblendites (the southern part of the Kamila Amphibolite Belt, Treloar *et al.*, 1990; Khan *et al.*, 1993). The southernmost gabbro is granulitic (it is the upper part of the Jijal Complex, Jan & Howie, 1981; Bard, 1983; Yamamoto & Yoshino, 1998). The structurally upper gabbro, named in this study Sarangar gabbro, forms the lower part of the Patan Complex of Miller *et al.* (1991). The detailed petrography of these rocks has been presented by Jan

& Howie (1981), Treloar *et al*. (1990), Miller *et al*. (1991), Yamamoto (1993), Yoshino *et al*. (1998) and Ringuette *et al*. (1999). All agree that they represent calc-alkaline magmas emplaced during the arc activity (Khan *et al*., 1993). Ductile deformation related to the Kohistan / India fault contact (the so-called Indus Suture or Main Mantle Thrust, Tahirkheli *et al*., 1979) is limited to a few hundred meters above this major fault (Burg *et al*., 1998). It was therefore important to know why ductile deformation in shear zones (Treloar *et al*., 1990) was appearing several thousand meters higher in the Kohistan sequence, and to understand the kinematics involved in this deformation event. We will argue that it is an arc related shear deformation synthetic to the subduction zone above which the arc has grown.

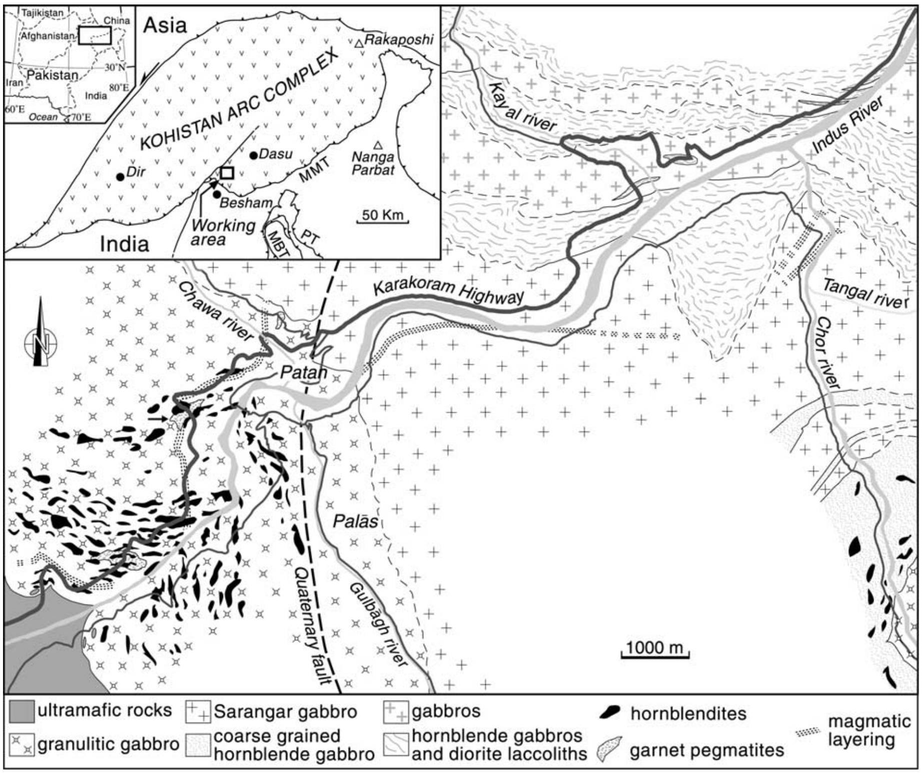

Fig. 5.1: Simplified geological map of the working area. Inset: localisation in the Kohistan Complex (modified from Bard, 1983 and Burg et al.*, 1998).*

5.1.3 Regional strain

The regional strain is defined by heterogeneously distributed foliations with associated mineral lineations. Two-dimensional mineral shape anisotropy has been measured in sections parallel to the lineation and perpendicular to the foliation (XZ planes of rocks) to estimate the orientation intensity of the mineral fabric (Fig. 5.2). We applied the intercept method (Rink, 1976; Launeau *et al.*, 1990; Launeau & Robin, 1996) to feldspars because they are both the most common and the weakest mineral phase in all the studied rocks. Measurements close to the shear zones were not taken into consideration in order to avoid later strain effects.

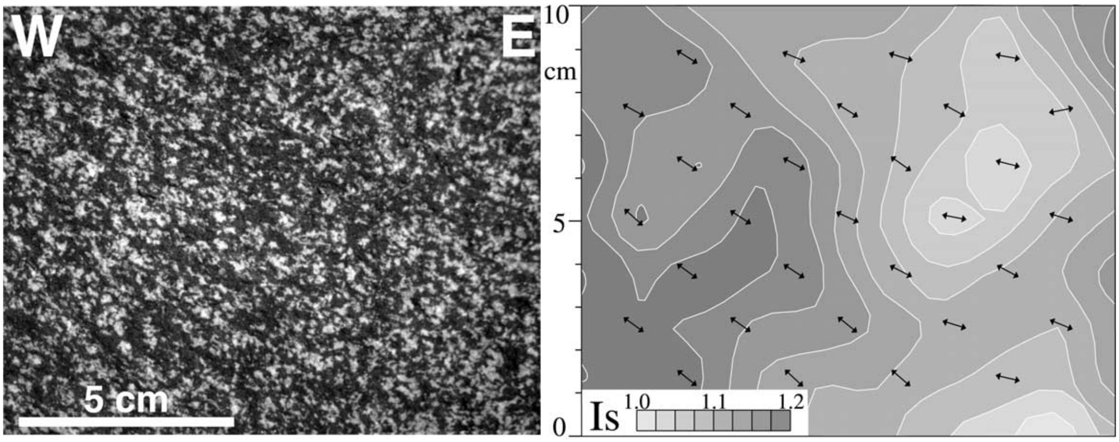

Fig. 5.2: Example of image analysis performed in an XZ section of the magmatic assemblage (left) showing the centimetre-scale variation of the fabric intensity Is of plagioclase between 1.05 and 1.2 (right). Note that the foliation trace (black double arrows) remains constant all over the image, independently of the fabric intensity (Sarangar gabbro, location in Fig. 5.14).

Two intensity fabrics were recognised. The weak one (1.05 to 1.2, Fig. 5.2) is recorded in the core of the two structurally lower gabbros (Fig. 5.3). The weak intensity fabric corresponds to the shape preferred orientation of the magmatic assemblages characterised by cumulate textures. The cumulate assemblage of the lowermost granulitic gabbro is composed of hypidiomorphic pyroxene, garnet, plagioclase and amphibole in textural equilibrium (Ringuette *et al.*, 1999). Fabrics of this assemblage describe the *c.* 40° NW-dipping foliation and the *c.* 35° NW-plunging lineation (Fig. 5.3 and 5.4). In the coarse grained Sarangar gabbro that lies to the north of, and above the granulitic gabbro (Fig. 5.1), weak intensity fabrics correspond to the coarse grained magmatic cumulate, garnet-free assemblage of pyroxene and plagioclase (Fig. 5.5a). These intensity fabrics describe E-W trending vertical foliations bearing a W-plunging lineation (Fig. 5.3 and 5.4).

The highest intensity fabrics (1.2 to >1.6) were measured in three main locations. First, in the granulitic gabbro, the high intensity fabrics progressively replace the magmatic, low intensity fabrics, in particular toward the basal contact with ultramafic rocks (Fig.

5.3). Higher intensity fabrics mark a transition from magmatic to solid state deformation by plastic deformation of plagioclase and rigid rotation of pyroxene and other mineral phases towards the pluton boundaries. Local S-C structures and the angular relationship between the mineral fabric and magmatic layering indicate a bulk SW-ward shear (Fig. 5.5b).

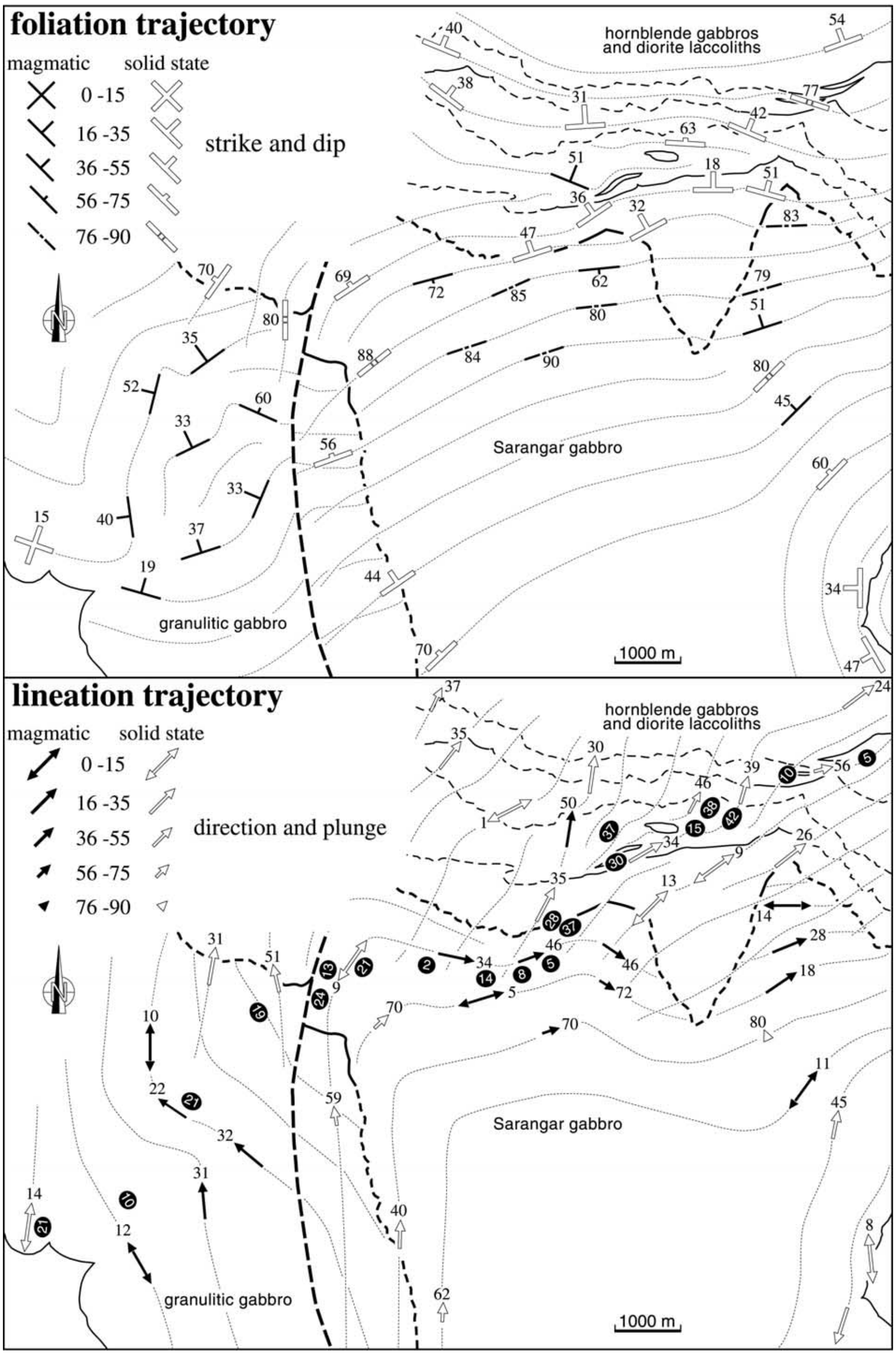

Fig. 5.3: Trajectories of magmatic and solid state foliations and lineations. Black ellipses indicate direction and intensity (percentage of anisotropy) of fabric measured in XZ planes.

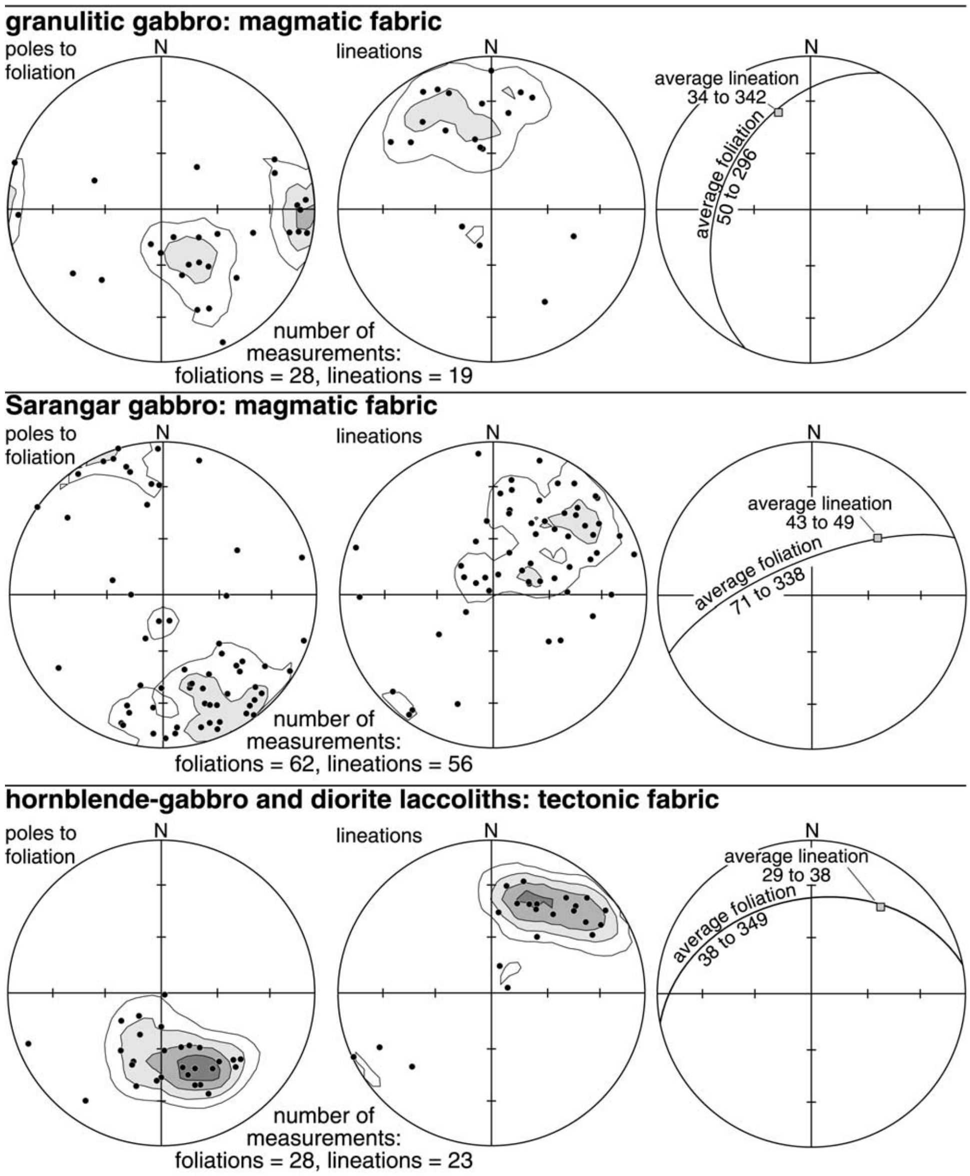

Fig. 5.4: Lower hemisphere equal area projections of poles to foliations and lineations. Starkey density contours: 2, 4, 6 and 8%.

The second location of high intensity fabrics is the contact between the Granulitic and the Sarangar gabbros. The extension of this fabric on both sides of the contact has a maximum width of about 2000 m. In the Sarangar gabbro, this high intensity fabric of oriented pyroxene and deformed plagioclase decreases and progressively gives way to a magmatic fabric towards the core of the pluton. Consistent foliation, lineation and kinematic directions and this geographic distribution suggest that the periplutonic high-intensity fabric was solid state, ductile deformation at the boundary with the granulitic gabbro, during the Sarangar gabbro emplacement. In the granulitic gabbro, the high intensity fabric has overprinted the magmatic fabric (Fig. 5.3). These structural relationships indicate that the Sarangar gabbro is younger and has intruded the cooler than solidus granulitic gabbro.

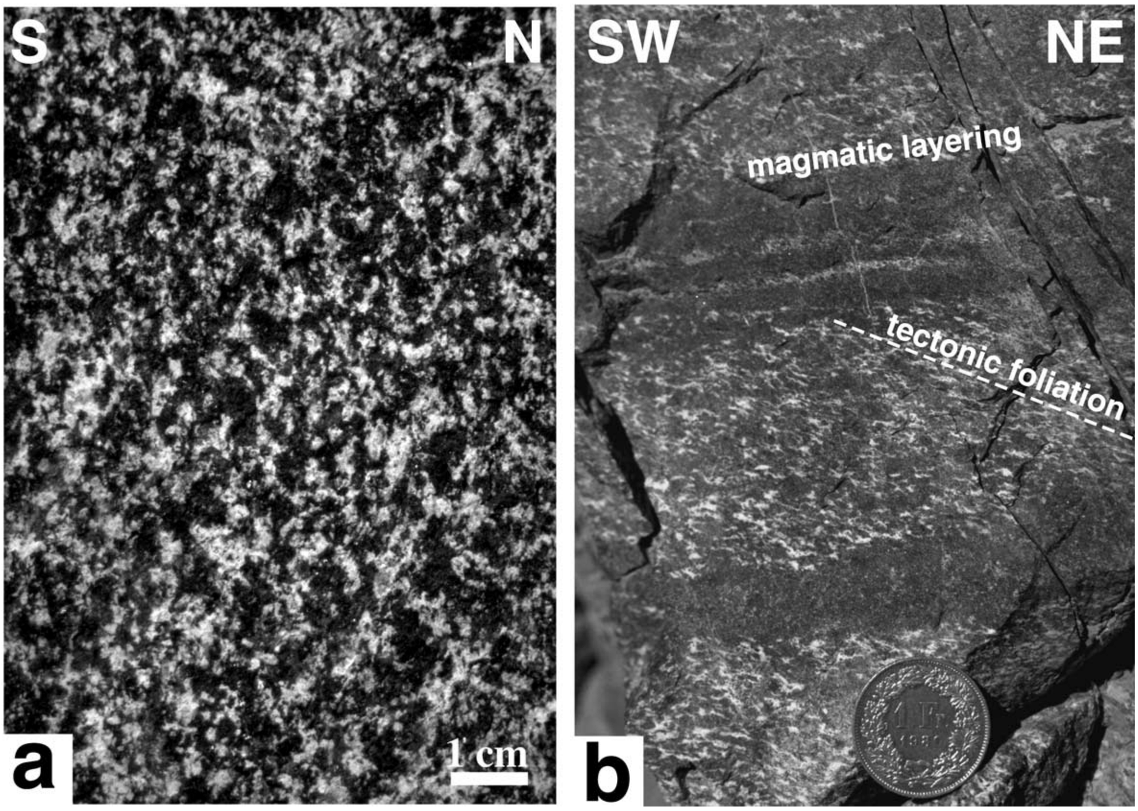

Fig. 5.5: (a) Magmatic texture in the Sarangar gabbro in an XZ section, trace of the foliation is vertical. (b) Crosscutting relationships between the magmatic layering and the trace of the tectonic foliation indicating SW-ward shear in the granulitic gabbro. Coin size = 23 mm. Locations in Fig. 5.14.

Finally, strong and homogeneous orientation intensity fabrics occur throughout the hornblende-gabbro and diorite laccoliths that have intruded the Sarangar gabbro to the north (Fig. 5.3). Attitudes have an average 38° N-dip foliation with a NE-striking lineation (Fig. 5.3 and 5.4). There is no preserved magmatic fabric in these rocks whose deformation is fundamentally solid state with rotated porphyroclasts indicating SW-ward sense of shear, as recognised also in the northern parts of the Kamila belt (Treloar *et al*., 1990).

The metamorphic history of the granulitic gabbro includes sub-solidus isobaric cooling of the magmatic paragenesis within granulite facies conditions (T~750 °C and P~1.8 GPa, Ringuette *et al*., 1999). A Sm-Nd cooling age of 91 Ma (Yamamoto & Nakamura,

1996) is slightly younger than Sm-Nd and Rb-Sr ages of 96 and 101 Ma, respectively, measured by Anczkiewicz & Vance (2000). Preserved plagioclase-clinopyroxene assemblages indicate crystallisation at 800 °C and 0.8 – 1.1 GPa in the Sarangar gabbro (Yoshino *et al*., 1998), whose age is not available. However, it should be bracketed by the 100-90 Ma old granulitic gabbro and the regional hydration phase at about 83 Ma (Ar-Ar age of amphibole, Treloar *et al.,* 1990).

Therefore, the regional fabric fundamentally reflects magmatic emplacement of mafic, calc-alkaline magmas during the pre-collisional arc formation.

5.1.4 Shear strain localisation

Shear strain localisation is responsible for the anastomosing pattern of shear zones in the Kamila Shear Zone (Treloar *et al*., 1990) from which we have separated three successive sets.

5.1.4.1 Set 1

Set 1 is composed of shear zones less than 1 m long and a few centimetres wide (Fig. 5.6 and 5.7). They bend the earlier magmatic foliation and layering, where present, without noticeable change in grain size and mineral assemblage. These shear zones apparently formed at conditions above the solidus because the magmatic paragenesis remained stable in their most deformed centres. Set 1 shear zones were found along structural and compositional discontinuities and within the bulk rock mass where they may be cut by millimetre-thick feldspar-rich magmatic joints (Fig. 5.7). Structural discontinuities are discrete, feldspar-rich magmatic joints, hornblendite boundaries and few millimetres thick veins of quartz, feldspar and amphibole (Fig. 5.8), which supports the interpretation of set 1 shear zones being above solidus features.

Most of set 1 shear zones have a normal sense in the field and are organised in two orientation populations (Fig. 5.9). The dominant one corresponds to shallowly S-dipping to horizontal shear zones with a SE- to SW-vergence. The second, apparently conjugate population, is formed of homogeneously NE-verging, N-dipping shear zones. These conjugate populations could indicate some sub-vertical flattening. However, field observation shows that many of the NE-verging shear zones are localised along upper and lower borders of hornblendite bodies that have rotated consistently with the bulk SE- to SW-ward shear (Fig. 5.6). Reverse set 1 shear zones developed along more homogeneously NE-dipping planes with the same lineation direction as the normal shear zones. Thus, reverse and normal set 1 shear zones are kinematically consistent. Differences in orientation fit Riedel orientations known in movement zones (Riedel, 1929). The most common population of normal SW-ward shear zones would represent Riedel shears R (Fig. 5.6). The reverse N-ward shear zones have an attitude consistent with R' Riedel shears (Fig. 5.6). We contend that the NE-dipping reverse shear zones were the closest to the main shear plane (primary shear bands D or, rather, thrust shears P, Tchalenko, 1968). Indeed, they are nearly parallel to the regional lithological boundaries of intensely sheared rocks (the regional reference plane), which were nearly horizontal before tilting of the Kohistan Complex subsequent to its obduction over India (Tahirkheli *et al.*, 1979; Coward *et al.*, 1986).

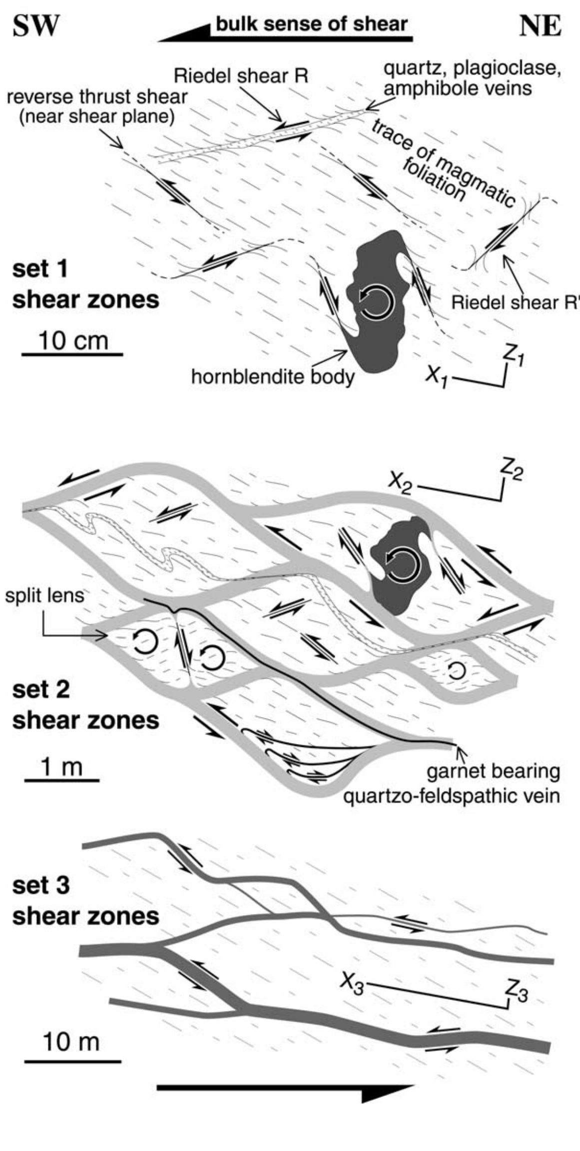

Fig. 5.6: Synthetic sketch of the three successive sets of shear zones. Set 1, centimetre-scale shear zones are developed along Riedel orientations consistent with a general, nearly horizontal SW-ward shear during the late magmatic emplacement of the gabbros. Upper amphibolite facies set 2 shear zones developed later along the same orientations as set 1 shear zones. Lengthwise propagation of set 1 shear zones formed a metre-scale, anastomosing pattern in which partial melting yielded garnet bearing quartzo-feldspathic veins. NE-ward normal set 2 shear zones developed essentially in response to rotation of hornblendite bodies and split lenses. The third set of shear zones, characterised by a larger spacing, developed in lower amphibolite facies conditions along and within similarly oriented set 2 shear zones.

All Set 1 shear zones are therefore attributed to a general SW-ward shear. Set 1 shear zones have the same orientation in both the granulitic and the Sarangar gabbros, independent of the magmatic fabrics. We conclude that set 1 shear zones are responses to regional stresses. Limited grain size reduction in their centres and measurements of the passively curved foliation indicate shear strains $\gamma < 5$ (March 1932; Ramsay, 1980). The geographical distribution of these shear zones is undetermined because solid state deformation in the other plutons and Set 2 shear zones may have overprinted them.

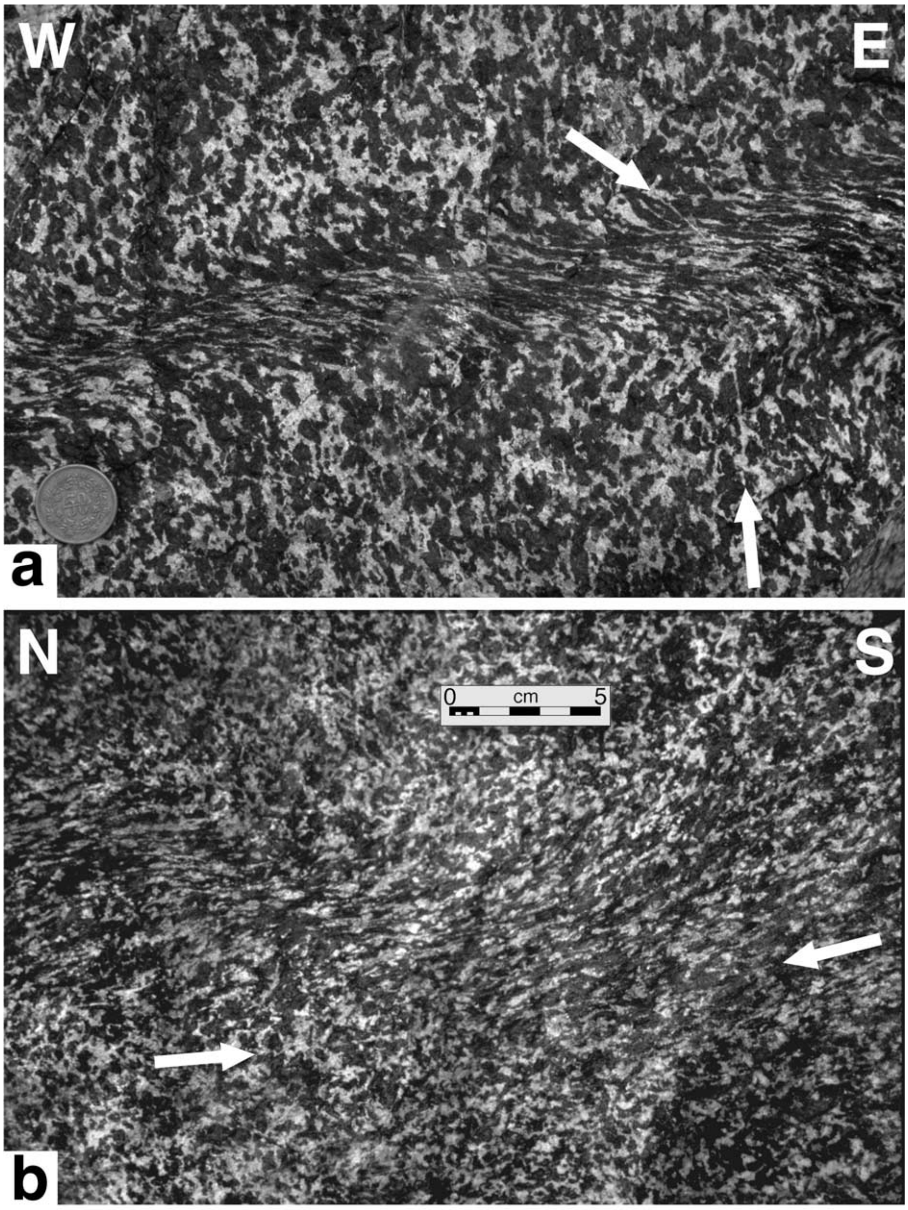

Fig. 5.7: Set 1 shear zones (location in Fig. 5.14). (a) Normal W-ward Riedel shear zone crosscut by a plagioclase-rich magmatic joint (arrows). (b) Lengthwise terminating set 1 shear zone. Arrow as in (a).

5.1.4.2 Set 2

Set 2 is the most spectacular anastomosing pattern of mylonitic shear zones that wrap around lenses of less deformed rock with their long axis plunging to the north-east (Fig. 5.6 and 5.10). Bordering continuous strain gradients include progressively curved rock-foliations whose fabric intensities increase to 1.9. The replacement of diopside and hypersthene by ferroan pargasitic to tschermakitic hornblendes (Treloar *et al.*, 1990) is correlated with the increasing intensity of the fabric in the strain gradients. However, pyroxene porphyroclasts exist in the mylonite, which suggests that metamorphic conditions were dry enough to prevent full retrogression.

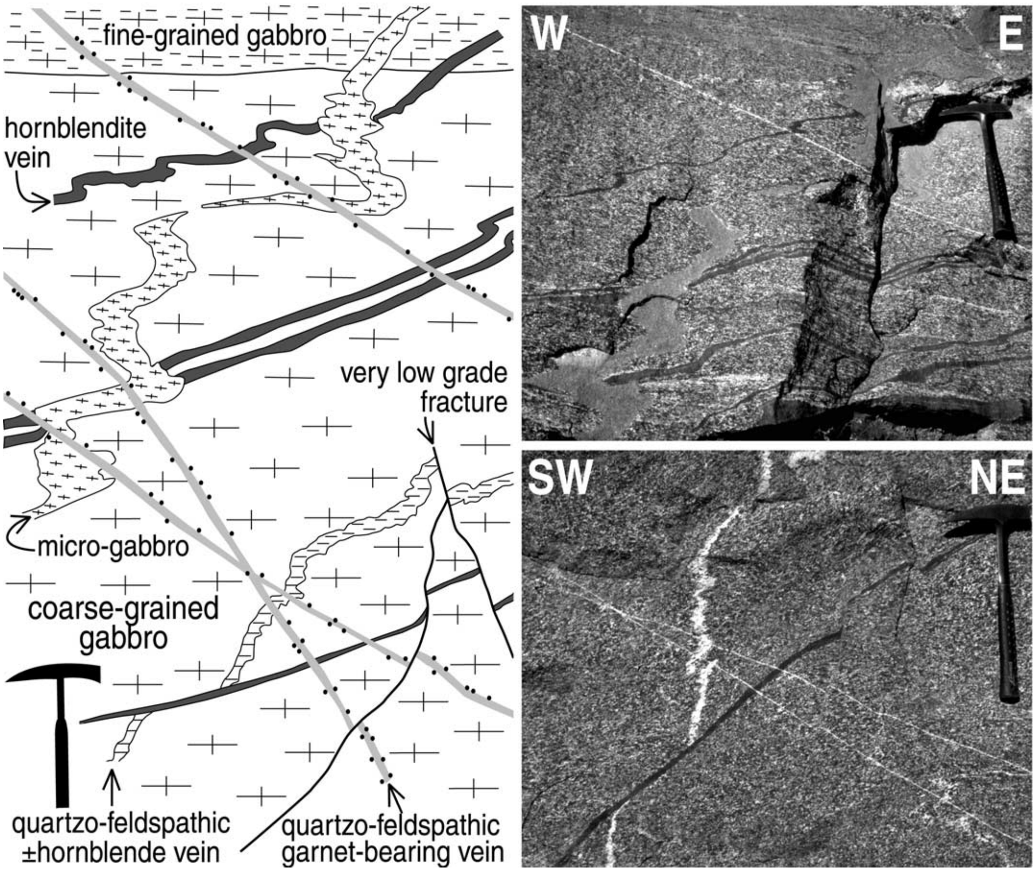

Fig. 5.8: Synthetic sketch of crosscutting relationships between structural features in the Sarangar gabbro based on two successive outcrops (rigth).

66 % of set 2 shear zones are N-dipping to flat-lying, SW-verging reverse shear zones bearing a *c.* 30° NE-plunging lineation (Fig. 5.11). They branch into horizontal to W-dipping, SW-verging normal shear zones bearing a *c.* 14° SW-plunging lineation. The change in attitude accommodates the shape of the preserved rock lenses. 11% of set 2 shear zones are NE-verging normal shear zones that developed, as some of the set 1

zones, around the tips of rotated hornblendite bodies (Fig. 5.6). The other set 2 shear zones correspond to reactivated, similarly oriented SE-verging set 1 shear zones. The thickness of the mylonitic centre of set 2 shear zones, defined by mylonitic foliations parallel to the shear zone borders, varies along a single shear zone from less than 5 cm to more than 4 m (Fig. 5.12). Centimetre-wide splay shears may occur within lenses in response to rapid direction changes of set 2 shear zones or between rotating parts of split lenses (Fig. 5.6 and 5.10b).

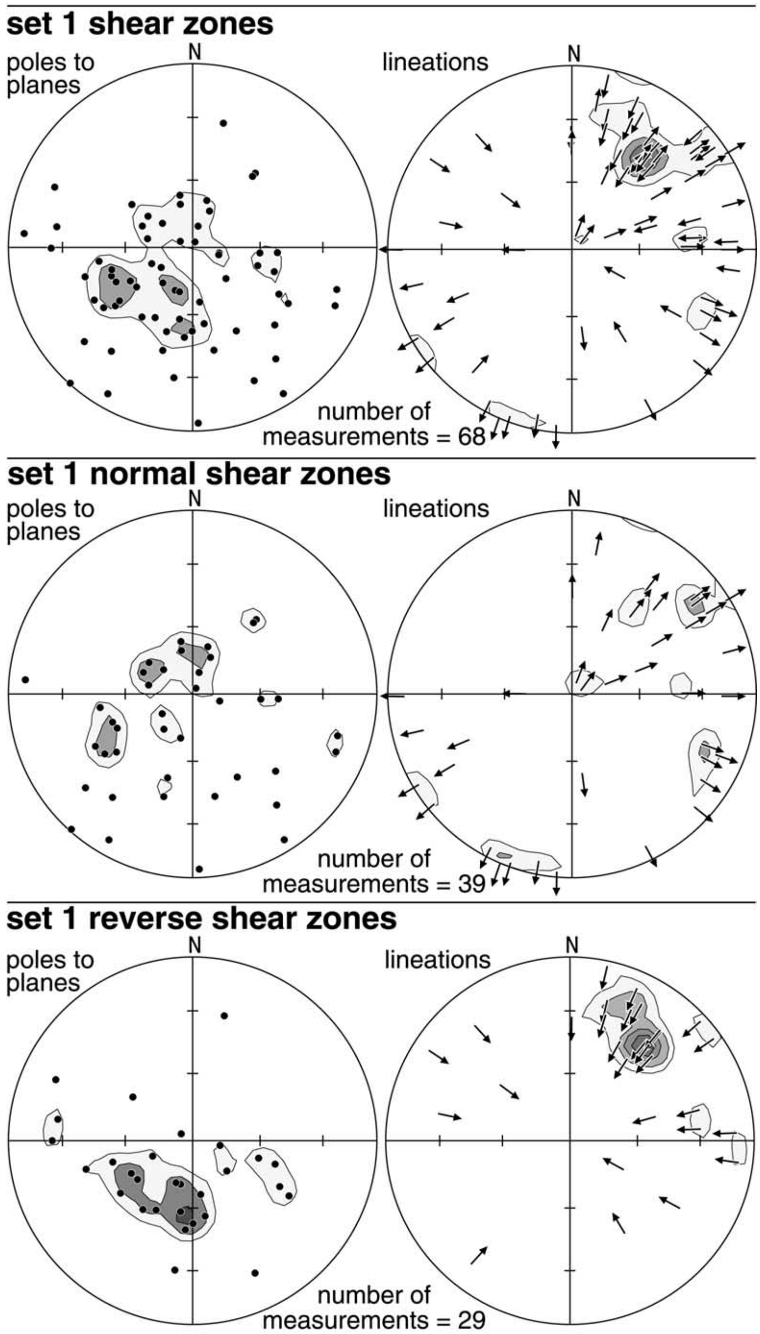

Fig. 5.9: Lower hemisphere equal area projections of poles to planes and stretching lineations of set 1 shear zones, arrows pointing to the shear direction. Starkey density contours: 2, 4, 6 and 8%..

Long axes, **a,** and perpendicular short axes, **c,** of rock lenses were measured on 60 regularly shaped lenses of less-deformed gabbro observed in XZ outcrops with respect to the stretching lineation and foliation of the bounding set 2 shear zones. Measurements were limited for sake of reliability to less than 5 m long lenses. Axis **a** versus axis **c** define a linear relation at any scale (Fig. 5.13). Similar asymmetric lens shapes at all scales and strongly dominant SW-vergence indicate that set 2 shear zones developed during distributed non coaxial deformation (Gapais *et al.*, 1987).

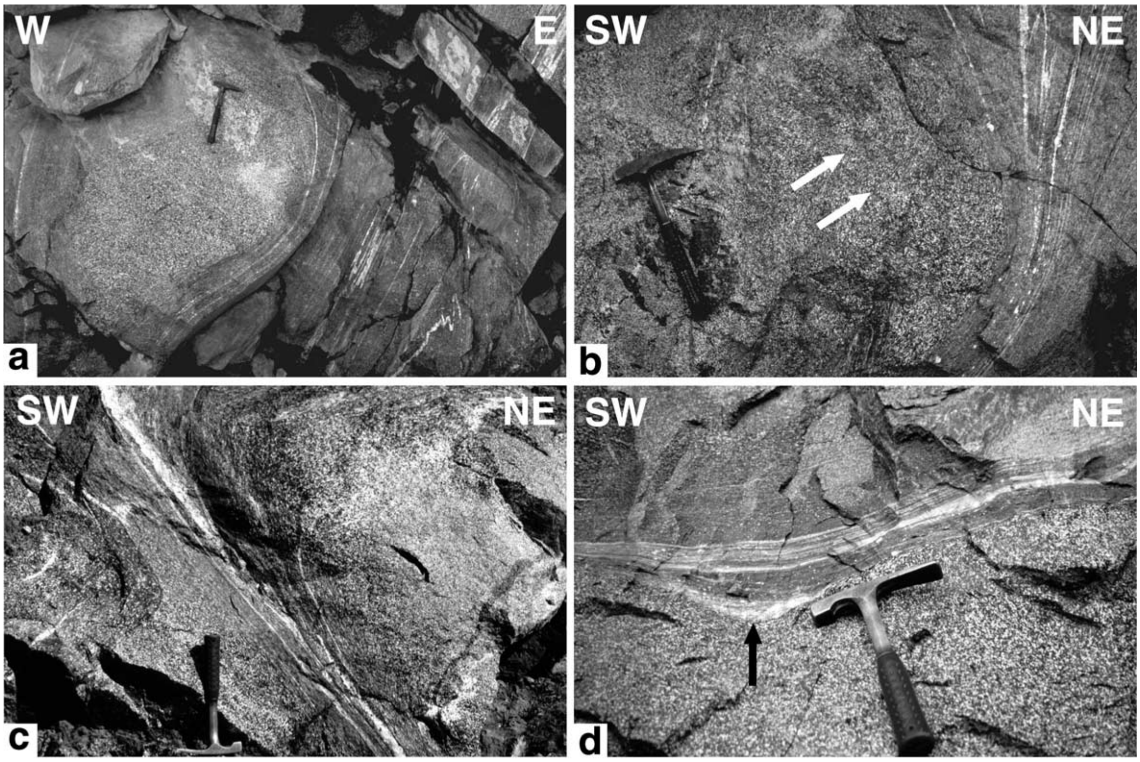

Fig. 5.10: Set 2 shear zones pattern (location in Fig. 5.14). (a) Shear zone wrapping around a lens of undeformed gabbro. (b) Rapid change in orientation of a shear zone inducing nucleation of centimetre-wide splay shears in the lens (parallel to the white arrows). (c) and (d) Syn-mylonitic quartz-felspar garnet-bearing veins in set 2 shear zones with (black arrow in d) undeformed segment of vein in a transtensional zone in a neck region of a lens of the Sarangar gabbro.

Set 2 shear zones occur over the whole area (Fig. 5.14). In the Sarangar gabbro, they form a pervasive pattern with an average spacing of 8-10 m between shear zones. This regular spacing indicates periodicity in their distribution. The anastomosing pattern becomes dense, forming metric lenses of less deformed rock along the contact with the underlying granulitic gabbro in which the set 2 pattern has a metric distribution above the hornblendite-rich area. In the lower part of the granulitic gabbro, the spacing between set 2 shear zones increases in the hornblendite rich area. No shear zone was found in the lowest 1000 m. In the hornblende-gabbros and diorite laccoliths, to the north, i.e. above the Sarangar gabbro, spacing between set 2 shear zones is about 50 m.

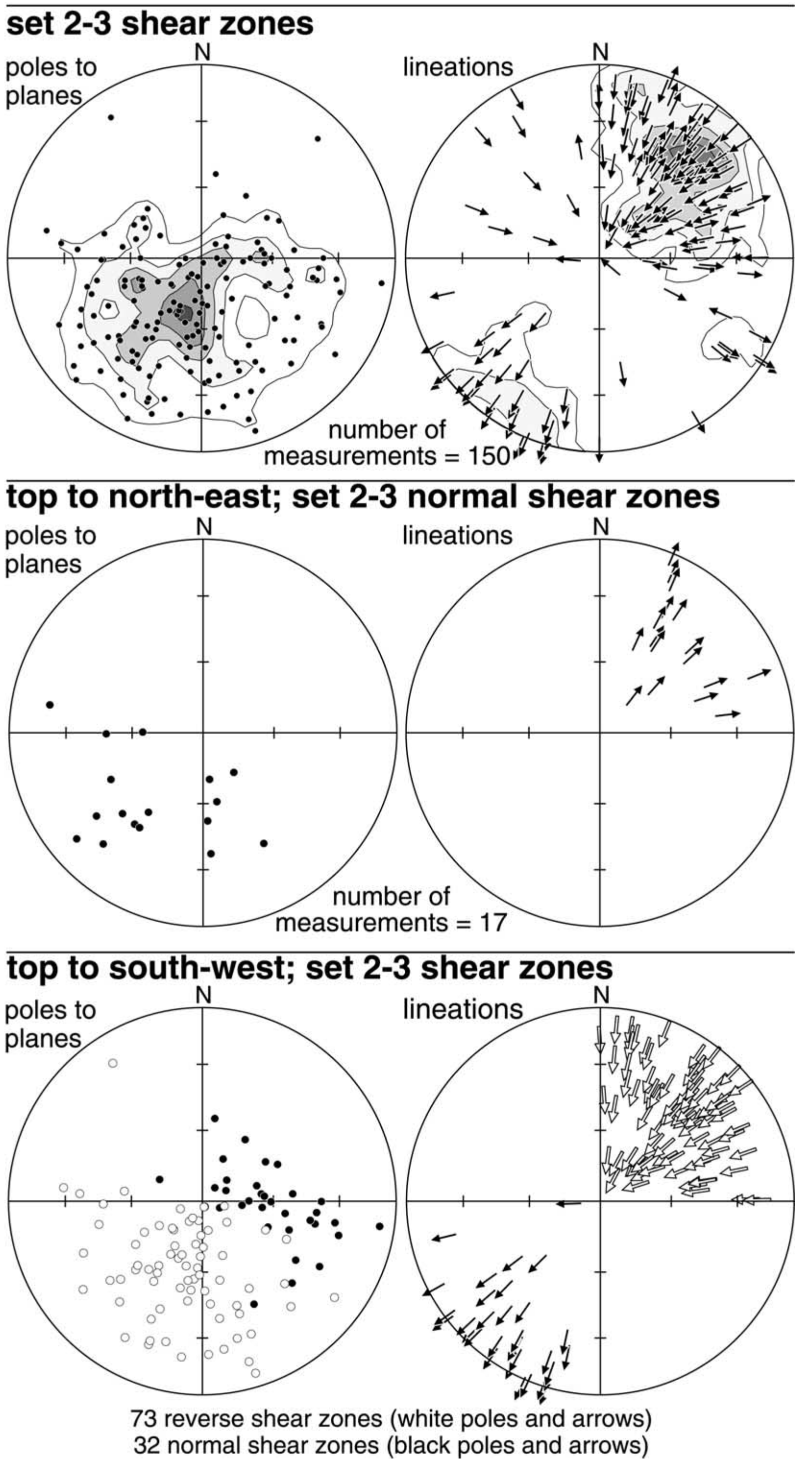

Fig. 5.11: Lower hemisphere equal area projections of poles to planes and stretching lineations of set 2-3 shear zones, arrows pointing to the shear direction. Sense of shear determination is based on the curvature direction of foliations and the geometry of feldspar and garnet porphyroclasts in mylonites. Starkey density contours: 2, 4, 6, 8 and 10%.

Metamorphic conditions associated with set 2 shear zones were estimated at 550-650° C under pressures of 0.9-1.0 GPa (Bard, 1983; Treloar *et al.*, 1990). Partial melting in set 2 mylonites generated quartz-plagioclase-garnet bearing segregation veins, some of which having been deformed by subsequent shearing (Fig. 5.10c) while others remained almost undeformed in transtensional zones between lenses (Fig. 5.10d). Partial melting points to temperatures exceeding 650 °C under pressures of > 0.8 GPa (Burnham, 1979) for the initiation of set 2 shear zones, which is consistent with the upper amphibolite facies crystal plasticity described by Treloar *et al.* (1990).

The minimum age for set 2 shear zones is inferred from the 87 Ma amphibole-epidote-paragonite assemblage that has partially overprinted the granulitic assemblage in the granulitic gabbro (Anczkiewicz, 1998).

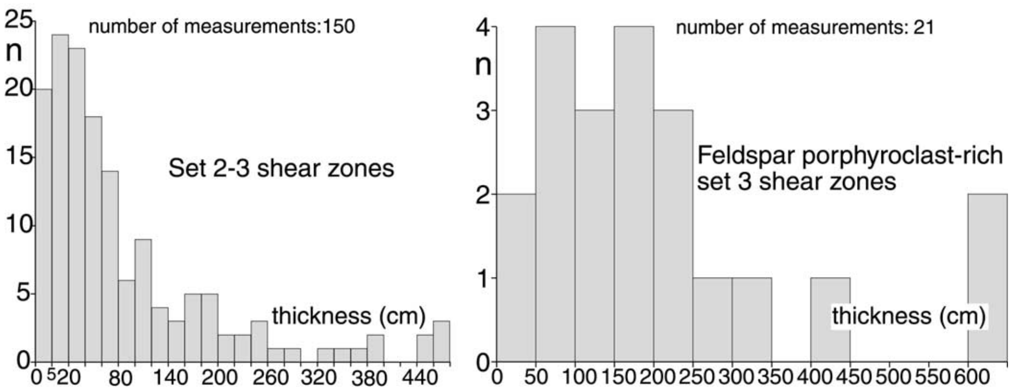

Fig. 5.12: Thickness distribution of mylonitic central zones of set 2-3 shear zones (average thickness = 1.27 m; median value = 50 cm) and feldspar porphyroclast-rich set 3 shear zones (average thickness = 2.8 m and median value = 1.9 m).

5.1.4.3 Set 3

Set 3 corresponds to several, tens metres long, shallow S-dipping to 30° NE-dipping shear zones with a wavelength of over 50 m (Fig. 5.6 and 5.15). Thickness distribution of the set 3 ductile mylonite zones presents a unimodal distribution (Fig. 5.12). Mylonitic zones display strongly foliated and fine-grained matrix containing plagioclase with brittle deformation and relicts of amphiboles. Grain size reduction and rotated porphyroclasts of garnet and plagioclase derived from stretched pegmatite veins indicate shear strain $\gamma > 10$. Curvature of the foliation along with the hornblendite and felsic veins within the shear zone boundaries indicate SW-ward shearing in set 3 shear zones (Fig. 5.15b). Set 3 shear zones, which contain metric lenses of undeformed rock, developed along and within, similarly oriented set 2 shear zones. The mylonitic assemblage is composed of quartz, plagioclase, amphibole and porphyroclastic garnet. This assemblage points to lower amphibolite facies conditions, which are not dated but are probably around the 83 Ma Ar-Ar age proposed for the end of the regional amphibolite facies metamorphism (Treloar *et al.*, 1989a; Wartho *et al.*, 1996). Set 3 shear zones distribution is limited to the Sarangar gabbro and the hornblende-gabbro and diorite laccoliths with an average spacing of over 50 m (Fig. 5.14).

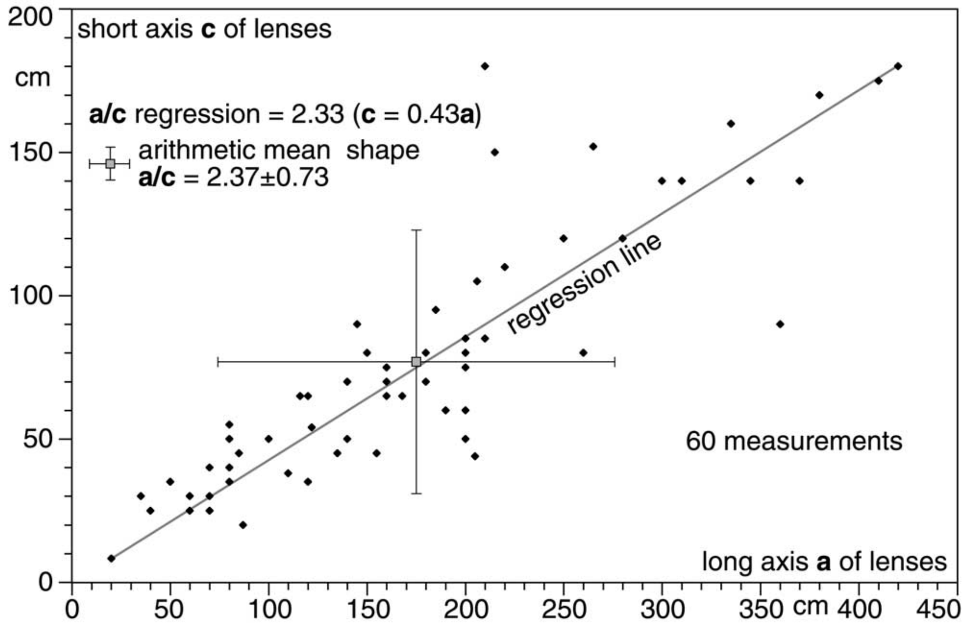

Fig. 5.13: Major axis a versus short axis c calculated from lenses of less-deformed gabbro observed in outcrop sections perpendicular to the foliation plane and parallel to the stretching lineation of the surrounding shear zones. Long axes of lenses vary between 35 cm to 420 cm and perpendicular short axes range from 8 to 180 cm.

5.1.5 Discussion

The geometry of the anastomosing pattern and kinematic analysis of strain localisation from regionally distributed fabrics provide a preliminary answer to the deformation history of the plutonic rocks forming the lower part of the Kohistan arc.

The composite regional fabric, developed above solidus conditions, fundamentally reflects magmatic emplacement of mafic, calc-alkaline plutons around 100 – 90 Ma. The onset of shear strain localisation is marked by the occurrence of set 1 shear zones whose Riedel-type attitudes were controlled by regional stresses. The continuous evolution from magmatic fabrics to solid state deformation indicates that strain localisation began above or at solidus conditions of the mafic magmas. Similarity of attitudes suggests that the asymmetric anastomosing pattern of set 2 and set 3 shear zones formed by the lengthwise propagation of the set 1 shear zones. This cooling evolution is marked by a progressive increase in spacing of the array of shear zones.

Treloar *et al.* (1990) regarded shearing in the Kamila Amphibolite Belt at temperatures greater than 500 °C until 80±5 Ma as the major expression of arc thickening produced by collision with Asia, to the north, between 102 and 75 Ma. Treloar *et al.* (1996) revisited this scenario and suggested that heating metamorphism and melting of the lower arc were rather related to magmatic underplating and intra arc-rifting (Khan *et al.*, 1989, 1993).

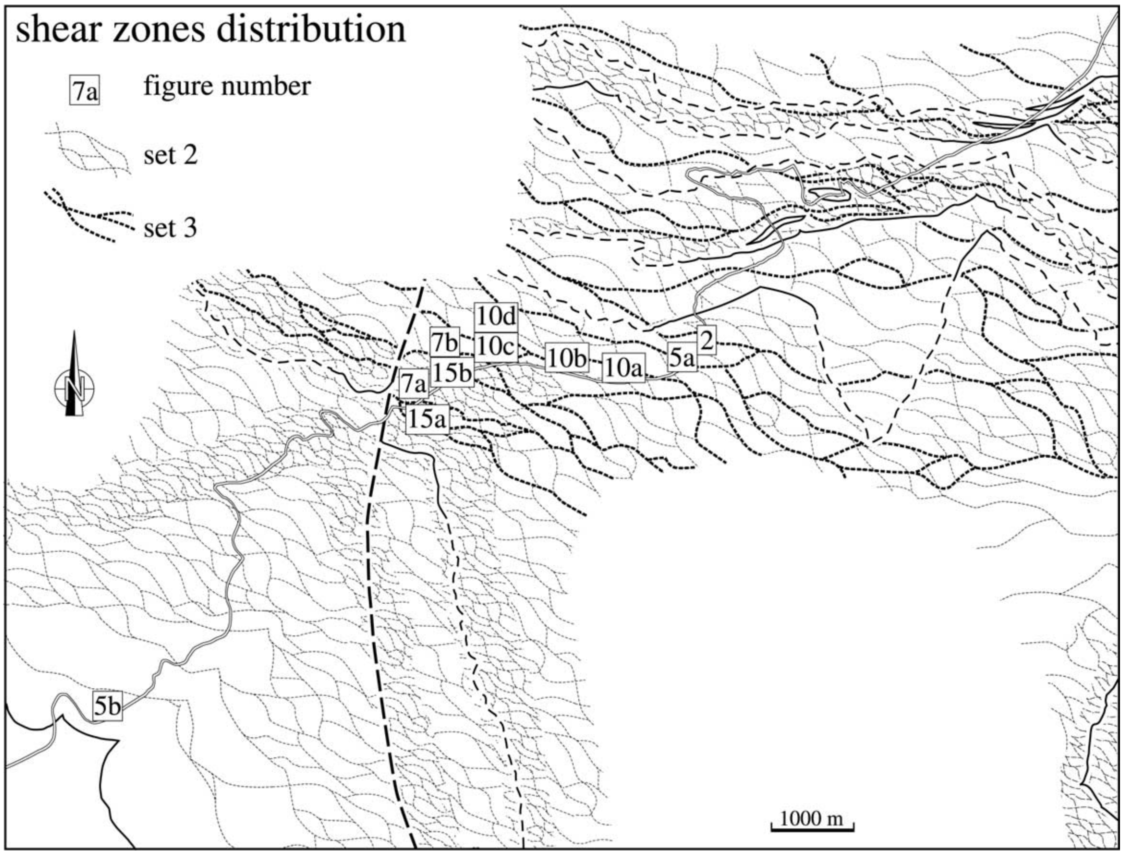

Fig. 5.14: Distribution and density of the set 2 and 3 shear zone patterns. Squared numbers give location of photographic plates.

Age constraints indicate that SW-ward thrusting responsible for the three successive sets of anastomosing shear zones was active between 100 and 80 Ma at the latest. This supports the interpretation in terms of progressive development of the anastomosing pattern during magmatic, quasi isobaric cooling and subsequent retrogression through the hornblende blocking temperature of the calc-alkaline plutons.

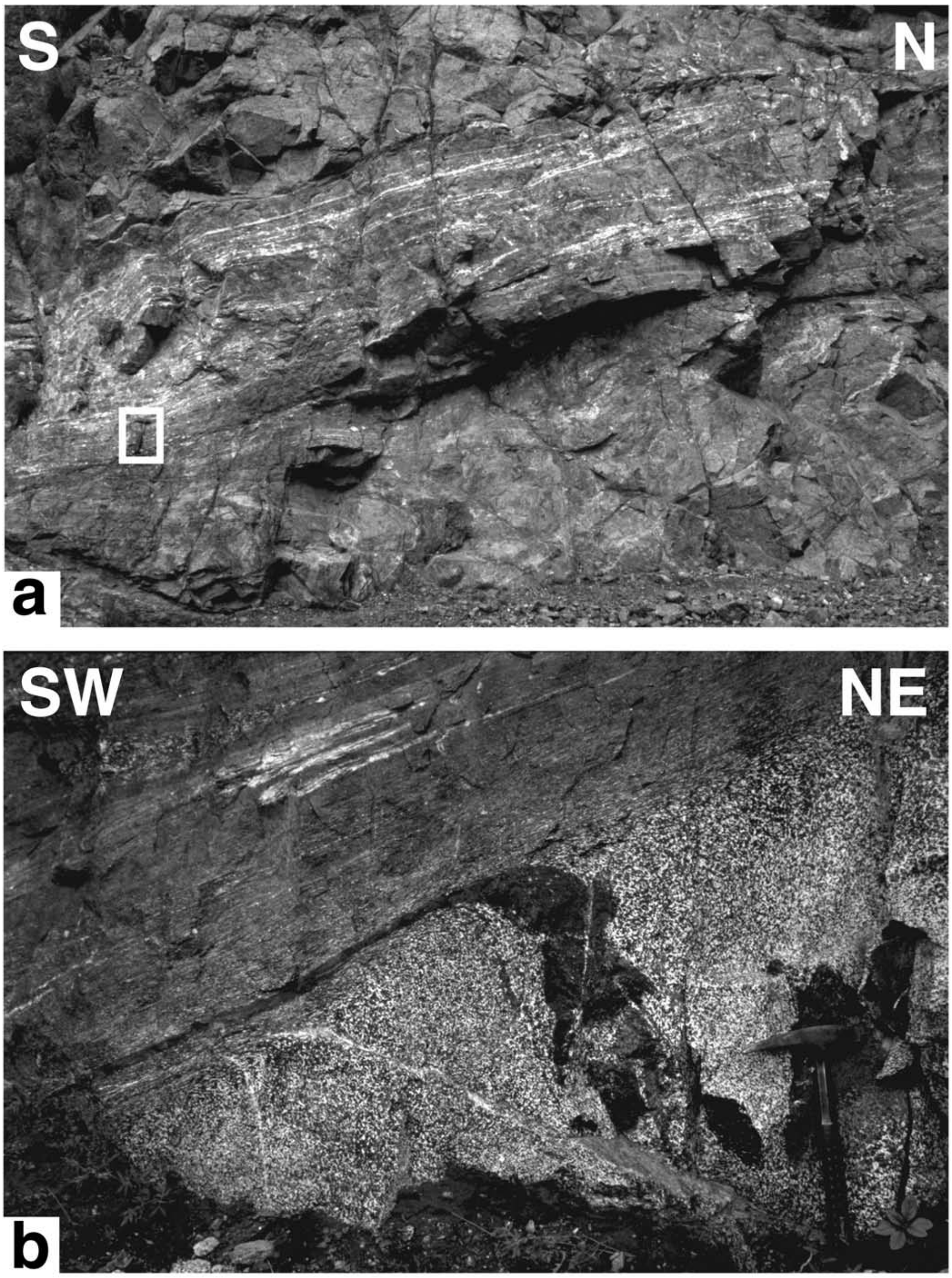

Fig. 5.15: Set 3 shear zones (locations in Fig. 5.14). (a) Feldspar-rich normal shear zone (scale hammer is squared). (b) Hornblendite and felsic veins curved within the lower boundary of a SW-ward normal shear zone.

This time span range includes shearing in the Kamila Amphibolitic Belt between 100 and 83 Ma (Treloar *et al.*, 1990) but also the extensional emplacement of the Chilas Complex (Burg *et al.*, 1998) at *c.* 84 Ma (U-Pb age, Zeitler *et al.*, 1981). Because of apparent age discrepancy and the structural presence of an extensional zone between the southern Kohistan and the Northern Suture, with Asia, we do not follow Treloar *et al.* (1996) in their collisional interpretation of the studied shear zones and shear fabrics. Instead, we attribute the shear zones anastomosed in the lower part of the Kohistan, to arc-related deformation during northward subduction of the Tethys lithosphere below the Kohistan Complex. The sense of subduction has imparted the bulk, syn-magmatic sense of shear.

5.1.6 Conclusion

The calc-alkaline plutons forming the lower part of the Kohistan Complex have recorded the dynamics during their emplacement and subsequent solid state deformation. Regionally distributed magmatic-related fabrics and set 1 shear zones developed under solidus conditions. Set 2 and 3 anastomosing shear zones were superposed onto set 1 shear zones, with increasingly localised deformation along Riedel shear directions. The anastomosing pattern has grown through lengthwise propagation of initially discrete set 1 shear zones while thickening of the propagating shear zones remained minor. These events occurred successively between 100 and 83 Ma during the continuous SW-ward shearing, probably initiated by subduction accretion of the Tethys lithosphere below the Kohistan arc.

Acknowledgements

Supported by the Swiss National Science Foundation (grant 20-49372.96). We thank D. Seward for her patient correction of the preliminary version of this text and P. J. Treloar and J. Grocott for detailed reviews of the manuscript. N. Chaudhry, S. Hussain and H. Dawood acknowledge support of their institutions.

5.2 Spatial shear zone distribution

Chapter 5.2 provides additional supportive data for chapter 5.1 and extends the investigated area to the north.

5.2.1 Approach of data analysis

Close to 450 ductile shear zones were measured in the mapped area. A statistical approach groups these data and shows mean values. Before calculating mean values, a grouping of the data was done according to geological aspects. Geological criteria were: a) lithologies, b) structural similarity and c) direction of tectonic transport. Six lithologies (respectively areas) were chosen based on the results of detailed mapping and structural appearance: 1) Indian Plate, 2) Granulitic gabbro and Sarangar gabbro (Patan area), 3) Northern sheared Gabbros and Diorites, 4) Kiru Amphibolites, 5) Kamila Sequence and 6) Northern Kamila Sequence. The Indian Plate rocks are structurally decoupled from the Kohistan Arc Complex along the Indus Suture and therefore treated as a distinct area. The Granulitic gabbro and Sarangar gabbro are two large intrusive bodies with similar ductile deformation structures without a decoupling horizon in between. In the Northern sheared Gabbros and Diorites lithologies alternate in laccolitic intrusions from gabbros, hornblendite gabbros, diorites, norites and tonalites. A dense pattern of anastomosing shear zones is observed in some of the coarse grained gabbros which alternate with interlayered coarse grained and fine grained diorites. This difference to the appearance of the Sarangar gabbro in the south and to the Kiru Amphibolites in the north suggested grouping the Northern sheared Gabbros and Diorites as a single area. In the Kiru Amphibolites shear plane orientations are dominantly E-W striking and the pronounced anastomosing pattern observed towards the south disappeared. The area comprises sills of dominantly fine grained rocks of gabbroic to dioritic composition, interlayered gabbros and diorites with more pegmatite and granitic sills towards the north and a medium grained hornblende-rich diorite with locally strong foliation forming spaced anastomosing shear zones. The Kamila Sequence is build of several lithologies like fine banded amphibolites, granite, metagabbros and hornblendites. The sheet wise granitic intrusions are characteristic. Ductile shearing is concentrated in the finer grained amphibolites and gabbros, whereas the bulkier granite sheets are internally less affected. The Northern Kamila Sequence comprises in its southern part coarse grained amphibolites alternating with fine grained amphibolites and tonalitic intrusions and in its northern part a coarse grained metagabbro with quartzite sheets and xenoliths of meta-carbonates. Ductile shearing is weaker than in the Kamila Sequence and more heterogeneous distributed in its northern part. This above briefly described lithologies/areas and their distribution and appearance of the ductile shear zones led to the applied separation.

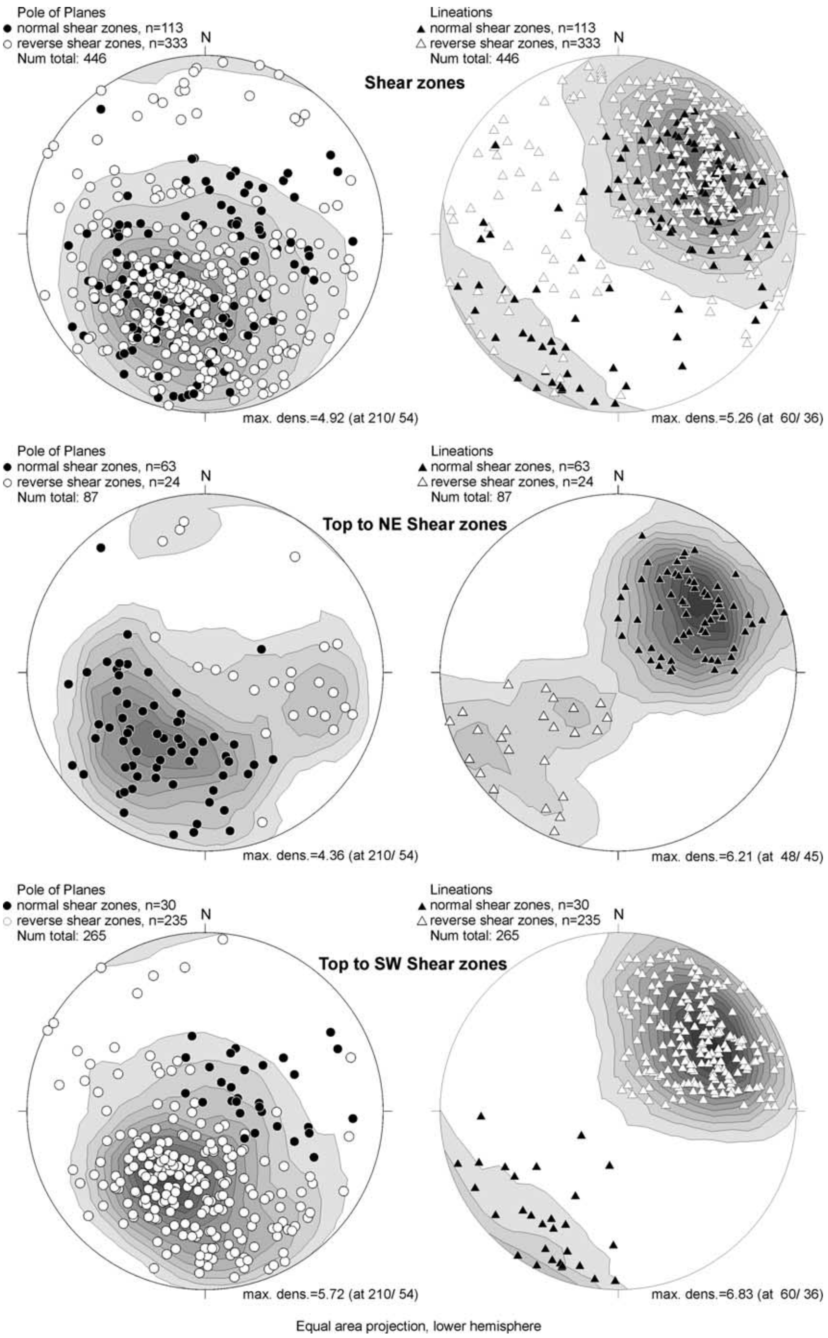

Fig. 5.16: Equal area projection, lower hemisphere, of 446 measured shear zones within the investigated area. Plots on the left side show pole of planes, plots on the right side show lineations. Contouring is done with small circle count and contour interval 0.5. The overall NE-SW trend is clearly visible with contours.

Beside a regional separation data were grouped according to their orientation of stretching lineation and sense of shear. This was done with following reasons: 1) a main tectonic transport towards the SW occurred in the Lower Kohistan Arc Complex as recognised in the study of Treloar *et al.* (1990) and in the results shown in chapter 5.1, 2) top to the NE shear zone account for ca. 20% of the data, therefore they have statistical importance and possibly reflect a tectonic event different to the top to the SW shearing and 3) shear zones not representative for top to SW or top to NE shearing were treated separately to identify other regional preferred orientations. Separated segments are: 1) for transport to SW (Lineation 0-90° and 180-270°), 2) transport to NE (Lineation 0-90° and 180-270°) and 3) SE-NW transport (Lineations in SE and NW quadrants).

Mean foliations and lineations were calculated using a grid (spacing ca. 800 meter) and calculating the mean direction for each grid cell. The actual number of data for one cell can range from 2 to ca. 28 with an average of ca. 10 measurements for a counted grid cell (cells with 1 measurement were rejected). The mean direction (foliation or lineation) for each grid cell containing more than two measurements is plotted with one symbol. For each of the six lithologies/areas, a lower hemisphere equal area projection provides the measurements (see also appendix for data).

5.2.2 Results

The shear zone data presented here (Fig. 5.16) show a similar pattern in the lower hemisphere projection as set 2 and set 3 shear zones defined in chapter 5.1 (Fig. 5.11). However, a direct analogous to set 2 and set 3 shear zones cannot be done, especially for the northern parts, where shear zones are of less anastomosed character. The statistical maximum of the shear plane poles plunges ca. 45 towards SW. The lineations plunge with ca. 35° towards NE. A separated analysis of shear plane poles for top to NE shear zones and top to SW shear zones provided the same maximum contouring orientation of ca. 210/55. Lineations belonging to top to NE shear zones generally dip towards NE and are similar to the orientation of the top to SW shear zone lineation, but with opposite sense of shearing.

The regional distribution of shear plane poles is shown in Fig. 5.17. In the Patan area the poles scatter due to the geometry of anastomosed shear zones, but still define a maximum at ca. 230/60. Towards the N, in the northern sheared gabbros and diorites the poles are more concentrated in the SW quadrant. Most striking is the pronounced E-W strike of shear zone planes within the Kiru amphibolites with an average dip of 50° towards N. This reflects a transitional (?) change in the shear zone appearance from an anastomosing pattern in the Sarangar gabbro to a more parallel pattern in the Kamila Amphibolites.

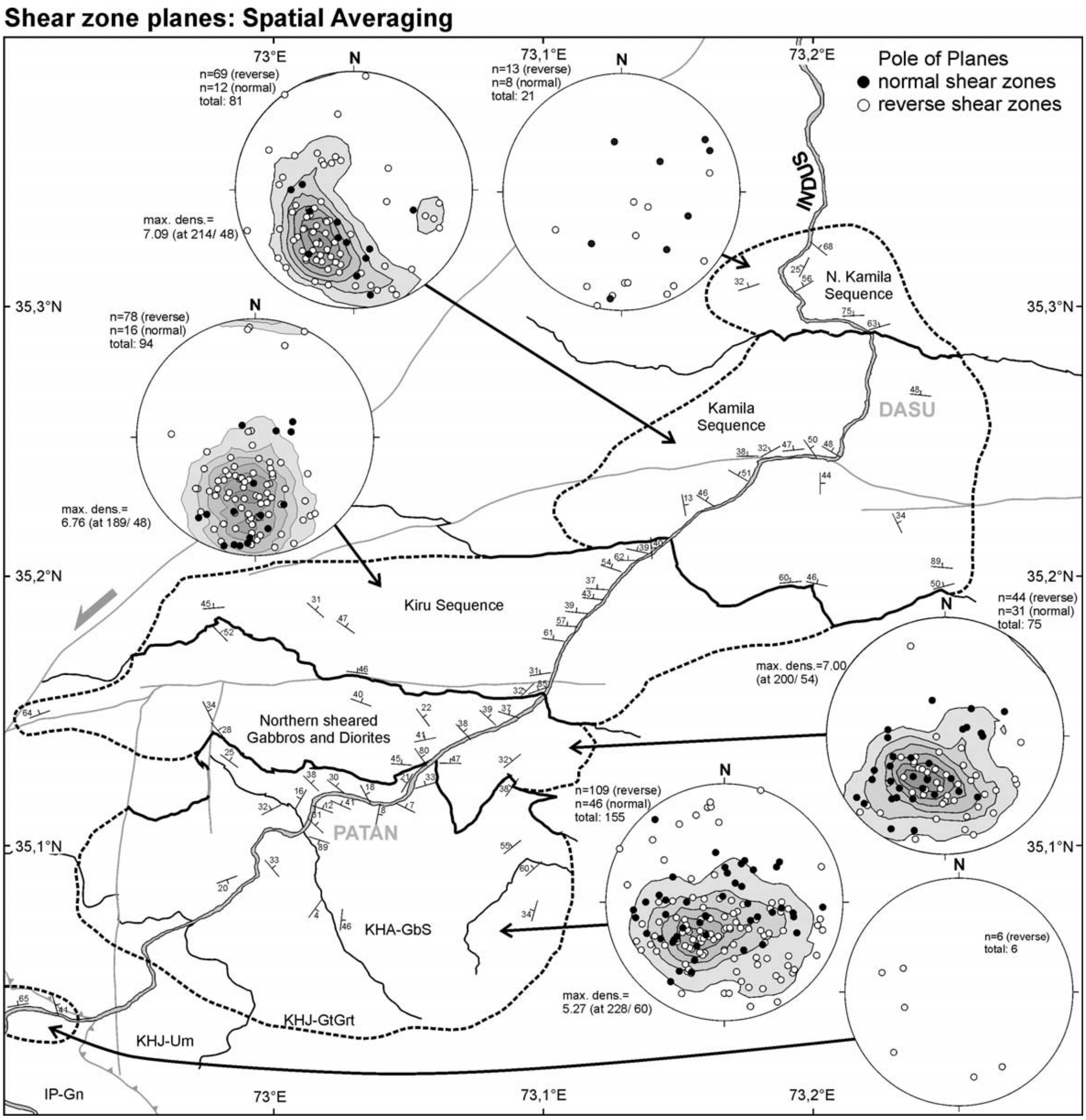

Fig. 5.17: Spatial Distribution of shear zone planes and lower hemisphere equal area projections of pole to planes. Foliations shown on the map were calculated using a grid (spacing ca. 800 meter) and calculating the mean direction for each grid cell. Therefore the actual number of data for one cell can range from 2 to ca. 28 with an average of ca. 10 measurements for a counted grid cell (cells with 1 measurement were rejected). Lower hemisphere equal area projections of pole to planes account for each of the six areas and provide the measurements. Contouring is done with small circle count and contour interval 1.

Shear zone planes within the Kamila sequence are more scattered, defining a maximum of ca. 215/50 for the poles. The mean orientations are similar for normal and reverse sense shear zones.

Top to SW Shear zone lineation: Spatial Averaging

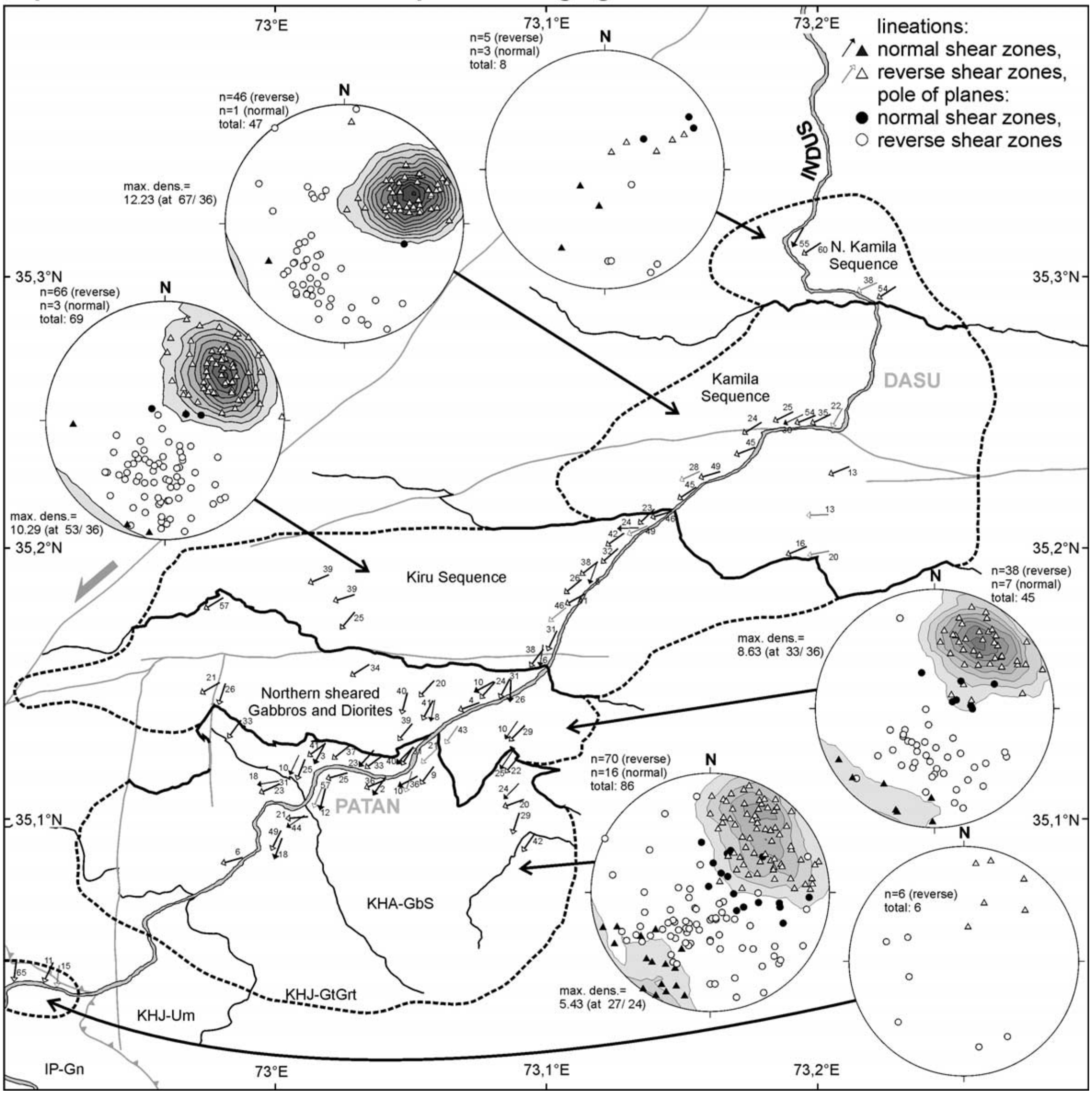

Fig. 5.18: Spatial Distribution of lineations representing top to SW shear zones and lower hemisphere equal area projections of lineations of set 2-3 shear zones. Lineations shown on the map were calculated using similar procedure and settings as described in Fig. 5.17 except for top to SW normal shear zones, where cells with 1 measurement were not rejected. Lower hemisphere equal area projections of lineations and pole of planes belonging to them provide the measurements. Contouring is done only for lineations.

Looking at the orientations of lineations related to southwest-ward transport direction, a difference between the southern and northern parts can be observed (Fig. 5.18). In the Patan area the orientations of the lineation varies within the NE quadrant and a significant number plots also in the SW quadrant. Also the lineations plotted on the map show that the SW plunging lineations (normal sense) and NE plunging lineations (reverse sense) are not concentrated in specific locations. At outcrop scale they are coexisting, which is explained with the bending of the shear zones around the undeformed pods (see Fig. 5.6), with the vast majority being reverse sense shear zones. In the northern sheared gabbros and diorites the orientation of the lineations is similar to that of the Patan area. Within the Kiru amphibolites the lineations show a consistency in orientation, slightly oblique to the dip direction of the shear zone planes. Only in the more western part lineations are a more westward directed than along the Indus valley, but they still keep their relative orientation to the shear plane consistent. The regional metamorphic foliation is bended there as well, suggesting that the orientation of shear zones follow the direction predefined by regional foliation, which is almost parallel to the lithological boundaries. The Kamila sequence displays a very homogenous orientation for the lineations at ca. 70/35. Lineations are oblique to the shear planes, suggesting a sinistral strike slip component during shearing. The lineations measured within Precambrian gneisses directly in the footwall of the ISZ show SSW thrusting, the direction in which the Kohistan Arc Complex was thrust over the Indian Plate.

The top to NE shear zones are frequent in the Patan area and the northern sheared gabbros and diorites (Fig. 5.19) and are northeast-directed normal set 2 shear zones (for definition refer to chapter 5.1.4) developed essentially in response to rotation of hornblendite bodies and split lenses. The lineations show a preferred orientation of ca. 60/40 and 40/35. In the Kiru amphibolites the normal shear zones are concentrated in the northern part. The lineations cluster around a mean value of 50/60 which is almost 20° steeper than the lineations in the southern ares. The shear planes are also generally steep dipping towards N. Within the Kamila sequence the top to NE shear zones play a less significant role.

Shear zones not fitting the top to the NE or top to SW relative transport criteria are summarized in Fig. 5.20. The variation in lineation orientation in the Patan area is strong and is most likely due to the anastomosing geometry of the shear zones. To accommodate deformation around lens-shaped undeformed pods, especially at the tips of the lens, shear direction varies from the dominant NE-SW direction. In the Kamila sequence the SE-NW directed lineations are noticeable. Their orientation relative to the shear planes point to sinistral strike slip component.

Top to NE Shear zone lineation: Spatial Averaging

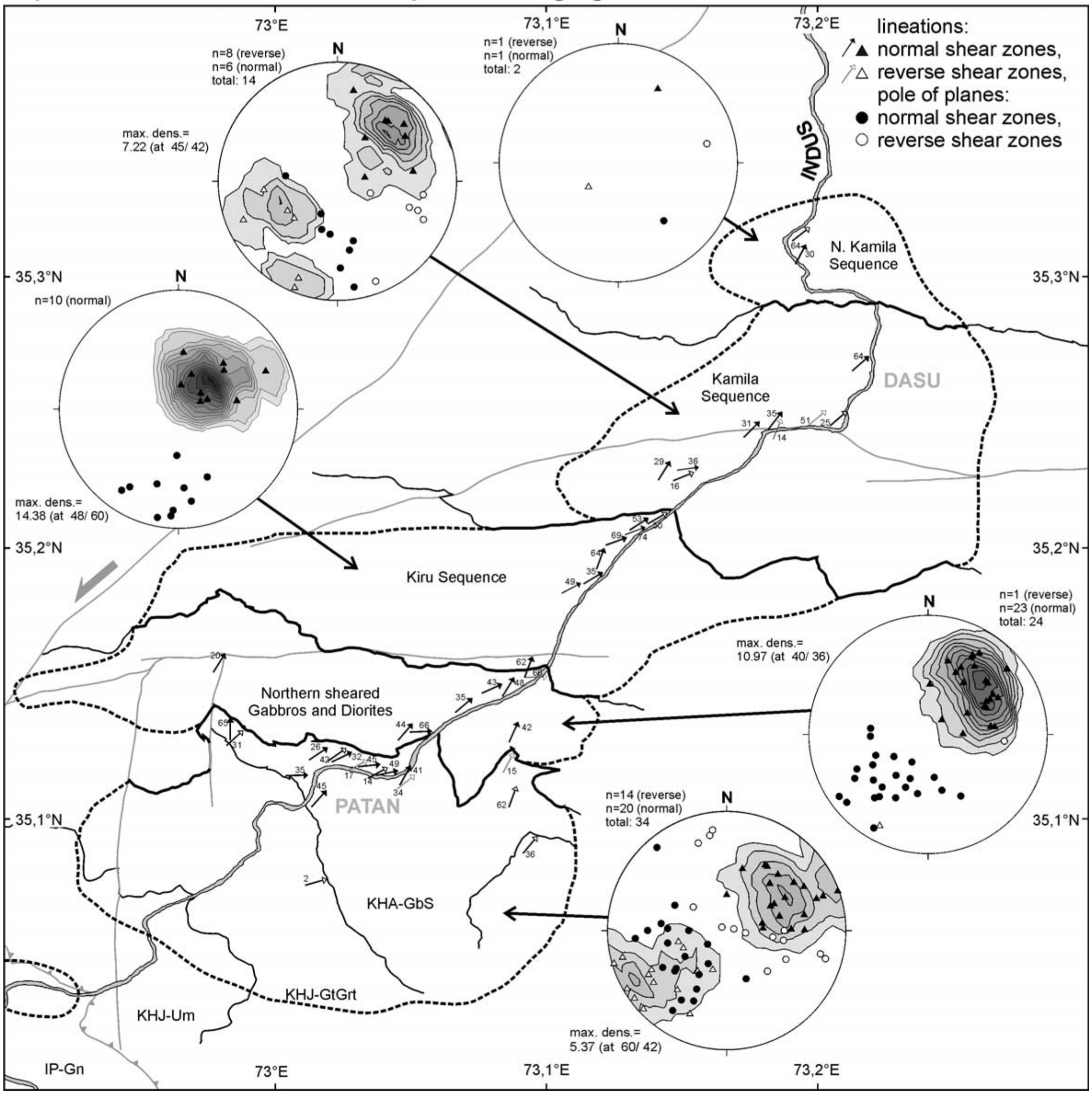

Fig. 5.19: Spatial Distribution of lineations representing top to NE shear zones and lower hemisphere equal area projections of lineations of set 2-3 shear zones. Lineations shown on the map were calculated using similar procedure and settings as described in Fig. 5.17. Lower hemisphere equal area projections of lineations and pole of planes belonging to them provide the measurements. Contouring is done only for lineations.

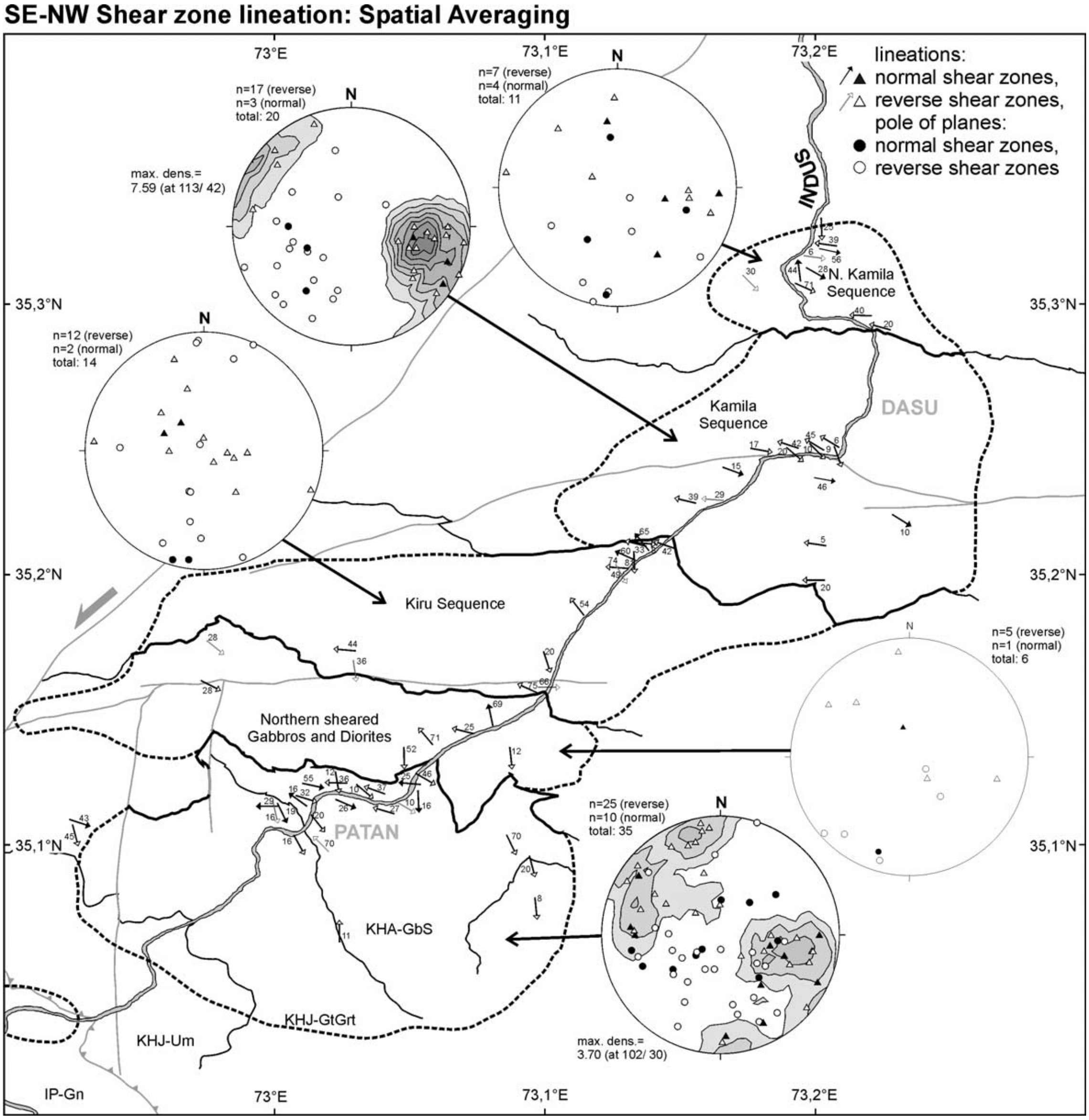

Fig. 5.20: Spatial Distribution of lineations representing shear zones with NW and SE directed lineations and lower hemisphere equal area projections of these lineations. Lineations shown on the map were calculated using similar procedure and settings as described in Fig. 5.17. Lower hemisphere equal area projections of lineations and pole of planes belonging to them provide the measurements. Contouring is done only for lineations.

5.2.3 Interpretation and Discussion

The orientations of shear planes, lineations and a bulk sense of shear towards SW for amphibolite facies shear zones in the Patan area and for the northern sheared gabbros and diorites is similar to the shear zones described in chapter 5.1. Most of the data presented here were obtained on the same shear zones used for defining set 2 and set 3 shear zones (chapter 5.1). They are explained by the development of anastomosing shear zones as described in chapter 5.1.

Shear zones in the Kiru amphibolites are heterogeneously distributed. In the coarse grained diorites and gabbros shear zones can be observed as discrete zones, dominantly mylonitic developed with a thickness of centimeter to half a meter and an average spacing of 50 to 100m. The fine grained amphibolites are distinguished in banded and unbanded (Treloar *et al.*, 1990). The banded amphibolites are characterised by alternating hornblende-rich and plagioclase rich layers commonly a few cm wide. Most of these fine grained, banded amphibolites are intensely sheared plutonics and meta-volcanics and/or meta-sediments (Treloar *et al.*, 1990). The mylonitic assemblage is composed of quartz, plagioclase, amphibole and porphyroclastic garnet. This assemblage points to amphibolite facies conditions, which are not dated but lasted probably until the 83 Ma Ar-Ar age proposed for the end of the regional amphibolite facies metamorphism (Treloar *et al.*, 1989a; Wartho *et al.*, 1996). The steep to north dipping shear planes are parallel to regional foliation and are well exposed along the contacts between coarse grained and banded amphibolites (Fig. 5.21b). Within the banded amphibolites spacing is variable. The shear zones in the Kiru amphibolites are more parallel without a pronounced anastomosing pattern. Pods enclosed by anastomosed shear zones are larger than tens of meter, leading to a more parallel pattern in the outcrop scale. The more gently dipping shear planes crosscut the regional foliation (Fig. 5.21a) and are interpreted as being a later shearing event in the continuous SW-ward shearing. Spacing between the flat shear zones is around 50 to 100m. In the northern part of the Kiru amphibolites several N-side down shear zones are observed in a zone, where lithology alternates sheet-wise between coarse grained diorites, gabbros, fine grained banded and unbanded amphibolites within tens to hundreds of meter. The mylonitic assemblage is composed of quartz, plagioclase, amphibole, epidote and porphyroclastic garnet which points to epidote-amphibolite facies conditions. These shear zones may reflect an extensional phase. The timing of the N-side down shear event remains unclear but should be prior to the end of the regional amphibolite facies metamorphism. A suitable linkage for the extensional phase is an intra arc-rifting event proposed by Khan *et al.* (1989, 1993) with the extensional emplacement of the Chilas Complex (Burg *et al.*, 1998) at about 85 Ma. Possible mechanism for the extension are: 1) Retreating subduction zone as proposed by Treloar *et al*. (1996), based on a scenario described by Royden (1993) and 2) gravity collapse of an abnormal thickened crust.

Shear zones in the Kamila sequence are observed within fine to coarse grained meta-gabbros and meta-diorites. Two large granite sheets are not pervasively sheared, probably reacting in a more rigid manner. Between the two granite sheets pegmatite-swarm are stretched and sheared (Fig. 5.21c). Within this zone the top to SW shear zones comprises a sinistral dip-slip component within the frame of dominantly SW directed relative transport, indicated by a top to the W-WSW shearing direction oblique to the roughly NE dipping shear planes.

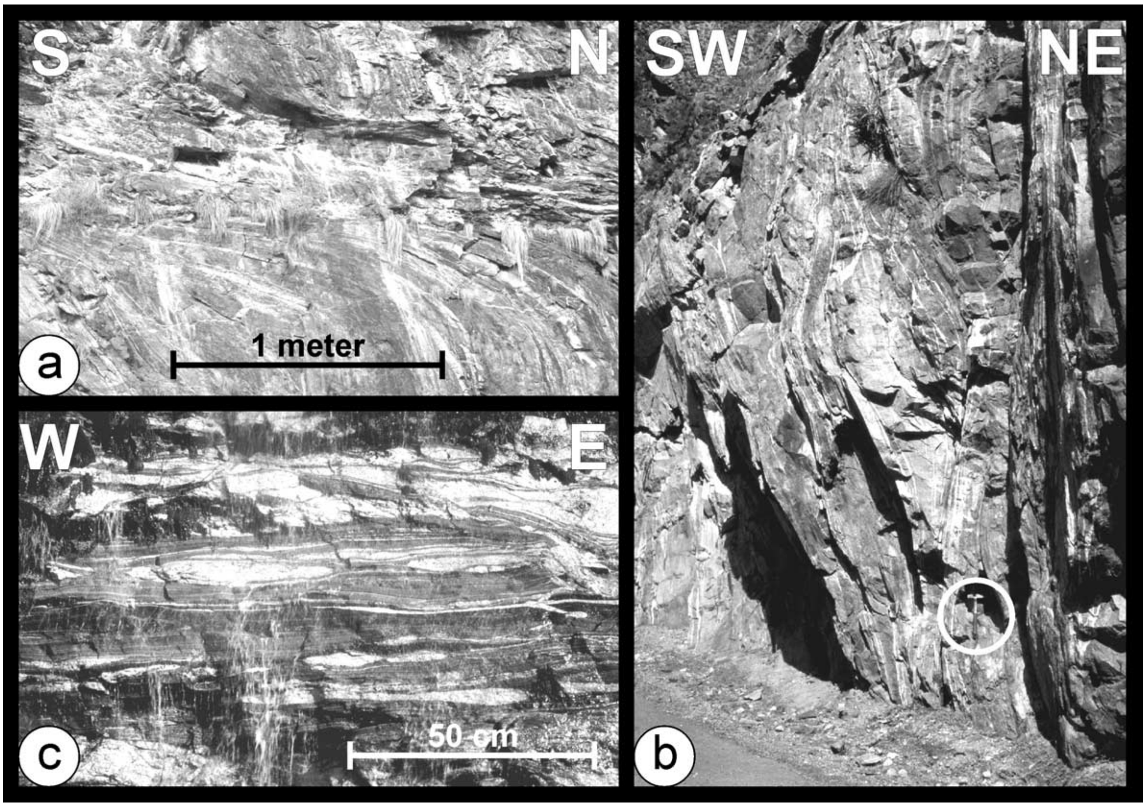

Fig. 5.21: Different shear zone pattern in the central Metaplutonic Complex: a) flat dipping top to SW shear zone close to Kiru; b) steep to N dipping top to SW shear zone within metadiorites close to Kiru; c) gently northward dipping shear zone in amphibolites with sheared pegmatite lenses between the two big granite bodies.

5.2.4 Conclusions

The presented shear zones in the Patan area and in the northern sheared gabbros and diorites reflecting with their varying orientations the shape of the anastomosing shear zone pattern are interpreted as set 2 and set 3 shear zones (as defined in chapter 5.1). Towards the N shear zones are getting more parallel, especially where lithology alternates between coarse grained meta-plutonics, fine grained amphibolites and banded amphibolites, reflecting a strong layer parallel strain localisation. The anastomosing pattern is less developed and expressed dominantly by flat lying to gently N dipping shear zones, cutting the layer parallel shear zones (Fig. 5.21a). In the Kamila sequence shearing is dominantly SW directed.

The time span range for shearing in the Kamila Amphibolitic Belt between 100 and 83 Ma (Treloar *et al.*, 1990). The continuous SW-ward shearing, probably initiated by subduction accretion of the Tethys lithosphere below the Kohistan arc, produced the anastomosed shear zones in the lower part of the Kohistan arc. However, there is evidence for an extensional phase expressed by lower amphibolite facies N-side down shear zones in the northern Kiru amphibolites. They are probably related to an intra arc-rifting event (Khan *et al.*, 1989, 1993) contemporaneous to the extensional emplacement of the Chilas Complex (Burg *et al.*, 1998) at about 85 Ma.

6. FAULT SYSTEMS AND PALEO-STRESS TENSORS IN THE INDUS SUTURE ZONE

Chapter 6 is "Fault systems and Paleo-stress tensors in the Indus Suture Zone" by G. Zeilinger, J.P. Burg, N. Chaudhry, H. Dawood and S. Hussain (Zeilinger *et al.*, 2000).

ABSTRACT

Analysis of fault-striations measured in the Kohistan part of the Indus Suture Zone (NW Himalaya, Pakistan) has been carried out to document dynamic evolution during the brittle stage of the collision of India and Asia. Processing of the data with a direct inversion method identified four stress fields which were chronologically ordered from field evidence as SSE–NNW compression, E–W compression, radial extension and SSW–NNE compression. The last corresponds to the present-day stress field defined from seismic activity. The earlier stress fields are related to times during the Miocene, when convergence-related stresses were disturbed by the formation of the nearby Nanga Parbat and Indus syntaxes.

6.1. INTRODUCTION

In NW Pakistan, the Kohistan Complex developed as an island arc above the northward subducted Tethyan lithosphere during the Mesozoic (Bard, 1983; Coward *et al.*, 1986). The southern boundary of the Kohistan Complex is the Indus Suture (the Main Mantle Thrust = MMT of Tahirkheli *et al.*, 1979), which is a crustal-scale, 35 - 50° northward dipping fault contact (Malinconico, 1989), along which the Kohistan Complex has been thrust over India (Fig. 6.1). Collision between India and Kohistan began at about 65 Ma (Beck *et al.*, 1996), and continued with subsequent obduction onto India (Coward *et al.*, 1987).

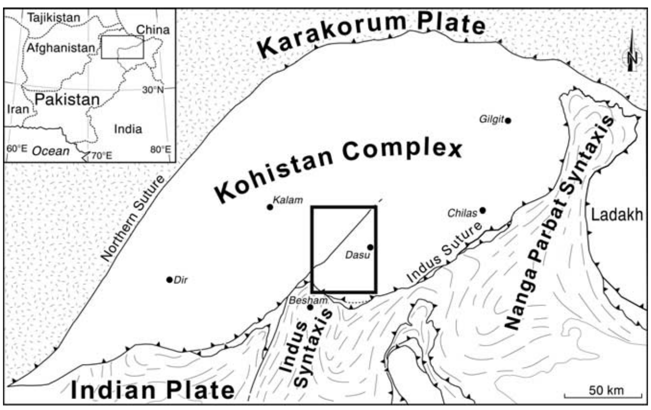

Fig. 6.1: Studied area (squared) located in the structural framework of Northern Pakistan, with the Kohistan Complex, main sutures and syntaxes.

The syn- and late-collisional history of the Indus Suture includes southward directed thrusting and extension (Treloar *et al*., 1991a; Burg *et al*., 1996). Fission track ages (Zeitler *et al*., 1982) record the termination of significant differential movement across the Indus Suture at 15 Ma.

Ductile structures have been investigated by several authors (e.g. Coward & Butler, 1985; Coward *et al*., 1986, 1987; Treloar *et al*., 1990; Arbaret *et al*., 2000) in order to understand early collisional processes. However, faulting is an important part of the long-lived deformation history that has produced the present day structure of the suture zone (Fig. 6.2a). Some areas are seismically active (Seeber & Armbruster, 1979) and it is evident in the field that, despite the lack of surface rupturing during particular earthquakes (e.g. Pennington, 1979), rocks have been fractured. This study concentrates on the analysis of fault-striations (Fig. 6.2b and 6.2c) in order to document the dynamics of this part of the Indus Suture Zone during hypercollision.

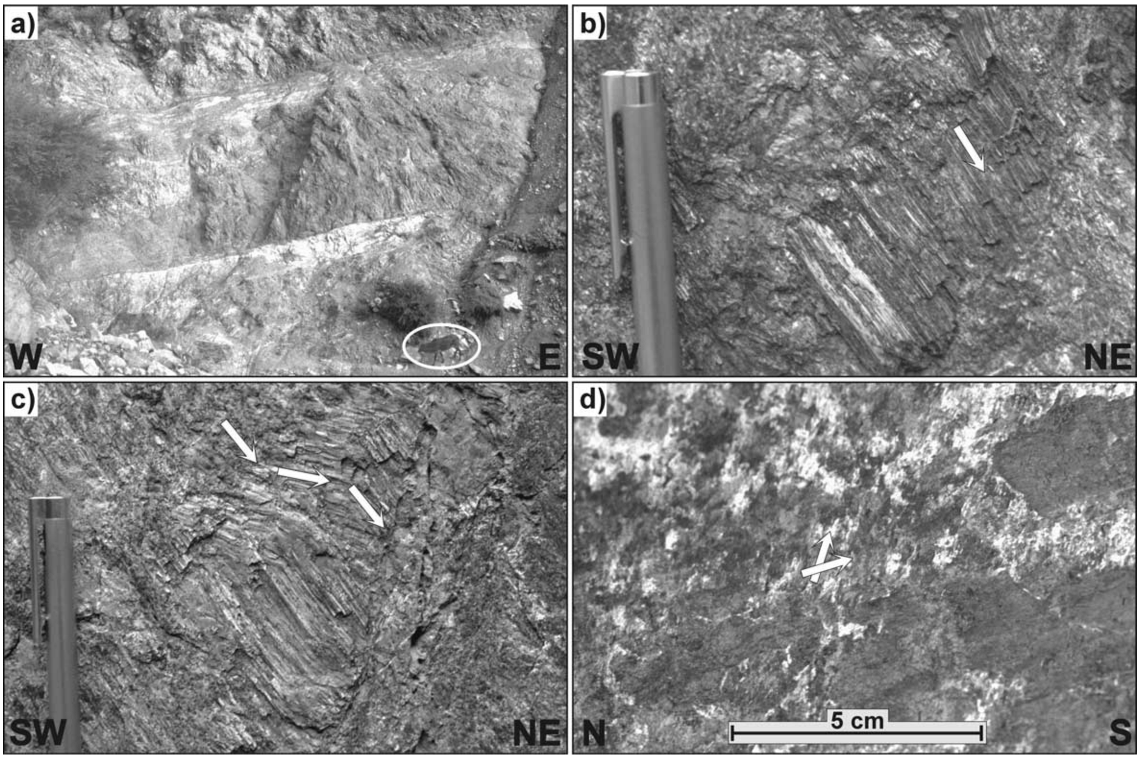

Fig. 6.2: a) fault zone in meta-gabbro, 4 km NE of Duber Kale (locality in Fig. 6.4) (circled cow as scale). Slip plane: 305/36. This fault shows sinistral movement and is attributed to population 4. b) normal fault (slip plane 129/88) with serpentine fibres (046/58) indicating the downward relative movement of the hangingwall block (4 km N of Duber Bazaar located in Fig. 6.4). c) same fault plane as 1b with several fibre orientations: 046/58 and 050/21; fibre continuity indicates a relatively short change in movement direction. For fault population distinction only the principal fibre direction was used, fitting population 3. d) superposed striations on one fault plane (slip plane 290/18), the older one (lower arrow, 274/17, population 2) is cut by the younger one (upper arrow, 011/03, population 4).

The investigated area straddles the Indus Suture and comprises three main units that are from S to N, i.e. from the structurally lowest (Kazmi & Jan, 1997; Treloar *et al.*, 1996):

- The Indian unit that includes granodiorite and intensely foliated and folded gneisses with a marked SW trending stretching lineation (Coward *et al.*, 1988; Treloar *et al.*, 1989b).

- The lower Kohistan unit comprising ultramafic and mafic rocks at the bottom, and mainly gabbros, hornblende-gabbros, diorites, norites, amphibolites and small bodies of hornblendite (the Kamila Amphibolite Belt of Jan, 1988) towards the top.

- The Chilas Complex which is composed of gabbro-norite and subordinate diorites (Jan *et al.*, 1984).

6.2. Method

Ca. 650 measurements of fault/striation pairs from 30 sites form our data set. Outcrops defined as sites are sections not longer than 100-200 m. The size of faults, quality of criteria for sense of movement and faulting style (for example discrete plane versus gouge zone) were also noted in order to characterize homogeneous fault populations. In particular, we distinguished faults with new crystallization (chlorite, apatite etc.) from "dry" faults with striated slip planes and without new crystallization, indicating that "dry" faults were formed at lower temperature, closer to the surface, and therefore later than the crystal coated planes. Conjugate fault sets were used in the field for a first estimate of the bulk shortening (compression) direction giving evidence of separate faulting events. Superposed striations on single fault planes further supported the chronological classification (Fig. 6.2d). These field observations, which yielded homogeneous data sets, were the key for computer aided fault distinction and stress tensor calculations. A first computer analysis of single-site data consistently required more than one stress tensor to explain the field measurements. Consequently, fault striation data have been separated for every site to determine successive stress tensors (Fig. 6.3). Data processing was carried out with Software FSA written by B. Célérier, which is based on a direct inversion algorithm (Bott, 1959; Compton, 1966; Etchecopar *et al.*, 1981). Assumptions of the method are: 1) Direction of the resolved shear stress on the fault is parallel to the measured striation and records the slip direction on the fault; 2) Slip on each fault is independent from other new or reactivated faults and 3) the stress directions are homogenous on the scale of a site.

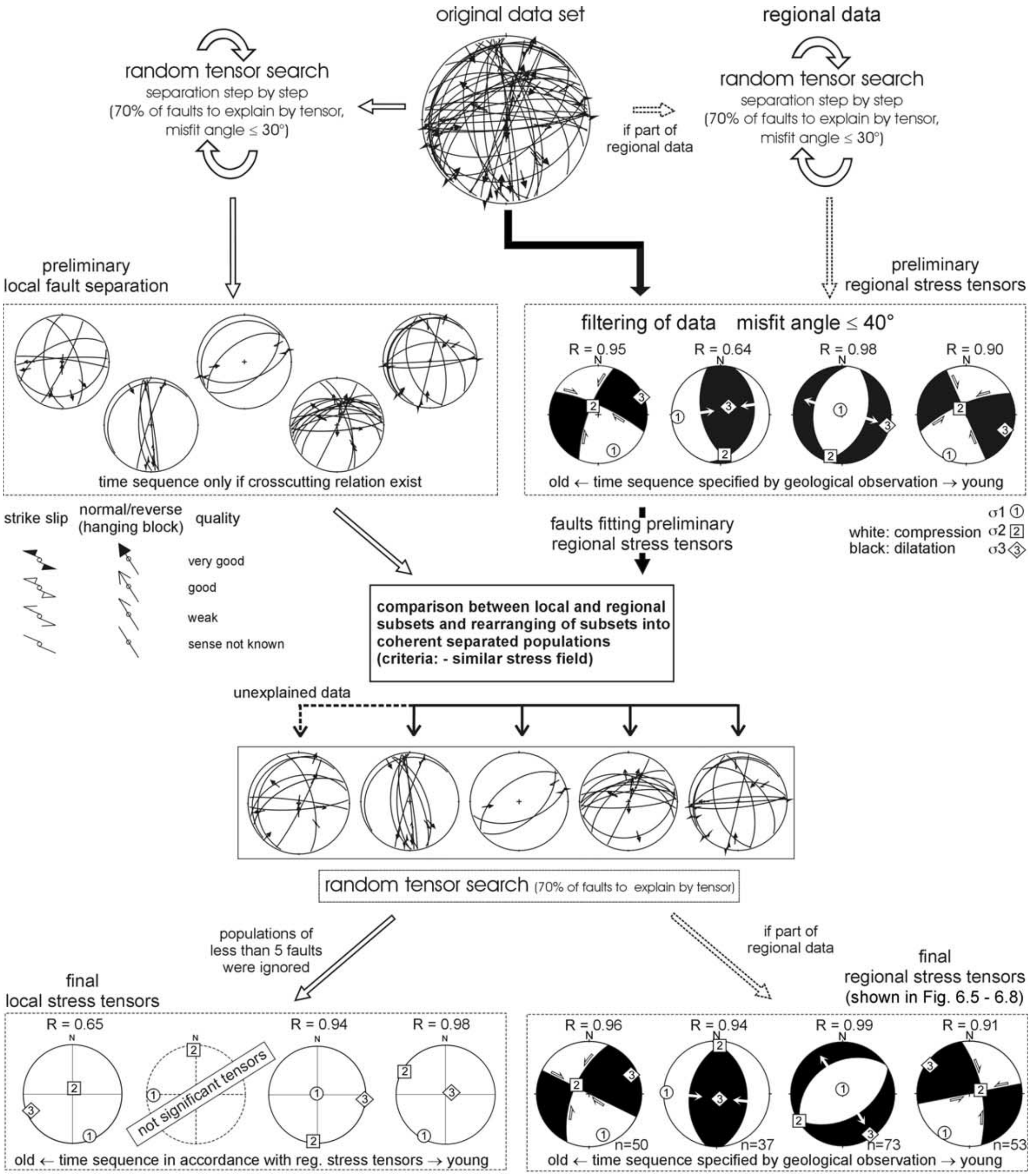

Fig. 6.3: Data processing illustrated with data set 29/08 (6 km NE of Patan along the Karakorum Highway, length of section 150 m). This site is part of the "regional data set", a combined set of measurements belonging to an area where faulting can be assumed to be homogeneous. Once the successive, preliminary regional tensors have been calculated from the "regional data set", each site was filtered through these stress tensors (misfit angle ≤ 40°). In addition, data sets from each site were separated without employing the regional stress tensors. Both resulting subsets were compared and rearranged to populations with coherent σ1 directions. These separated faults were processed again with a random tensor search to obtain local deviations in terms of shape and orientation of the local stress tensor. Populations of less than 5 faults and unexplained data were considered to be not significant. Therefore they are not shown in Fig. 6.5 to 6.8.

To ascertain regional stress fields, 248 measurements within a single rock unit, a metagabbro of Lower Kohistan, near Patan, were processed as one data set (Fig. 6.4). The aim was to eliminate small, local deviations and to integrate over a large area the bulk brittle tectonics. In the first processing step, tensors of maximum ($\sigma 1$), intermediate ($\sigma 2$) and minimum ($\sigma 3$) principal stresses (positive in compression) best fitting 30% of the measurements were randomly calculated. This random tensor search is a Monte Carlo approach to search a stress tensor that best explain the slip directions. This mainly follows the method proposed in Etchecopar *et al.* (1981) and Etchecopar (1984). In a first step of the random tensor search, the stress tensor data are generated by using a random variable, so that the orientations are uniformly distributed in space. In a second step, for each tensor, the angular misfit between the predicted and observed slip direction for each fault slip data is computed. In a third step, for each tensor, an average angular misfit, is computed. An adjustable percentage of the fault slip data must be explained. The angular misfit is the average of the angular misfit for the chosen percentage of the data that have the lowest angular misfit. In a fourth step the tensors are ranked by increasing value of the angular misfit and only the first tensors are retained. These stress tensors are the most compatible with the fault data set.

The best fitting tensor integrated the highest number of misfit angles < 30° and as close as possible to 0° between the optimal tensor for each fault/striation pair and the calculated ones. After extracting the corresponding fault data and checking their consistency as a population compared with field determination, computation was performed on the extracted population with a stepwise increase of the best fit for 40, 50, 60 and finally 70% of the measurements. The stepwise increase is justified by the fact that every extraction decreases the number of possible faults in the extracted data set. This procedure yielded 4 bulk stress tensors that explain 70 % of four separate populations embracing most of the 248 measurements. These 4 tensors were taken as the preliminary regional, yet smoothed, reference because they approximately fit compression/extension directions estimated from conjugate sets in the field. About 10% of the measured faults were not consistent with any of the four reference tensors.

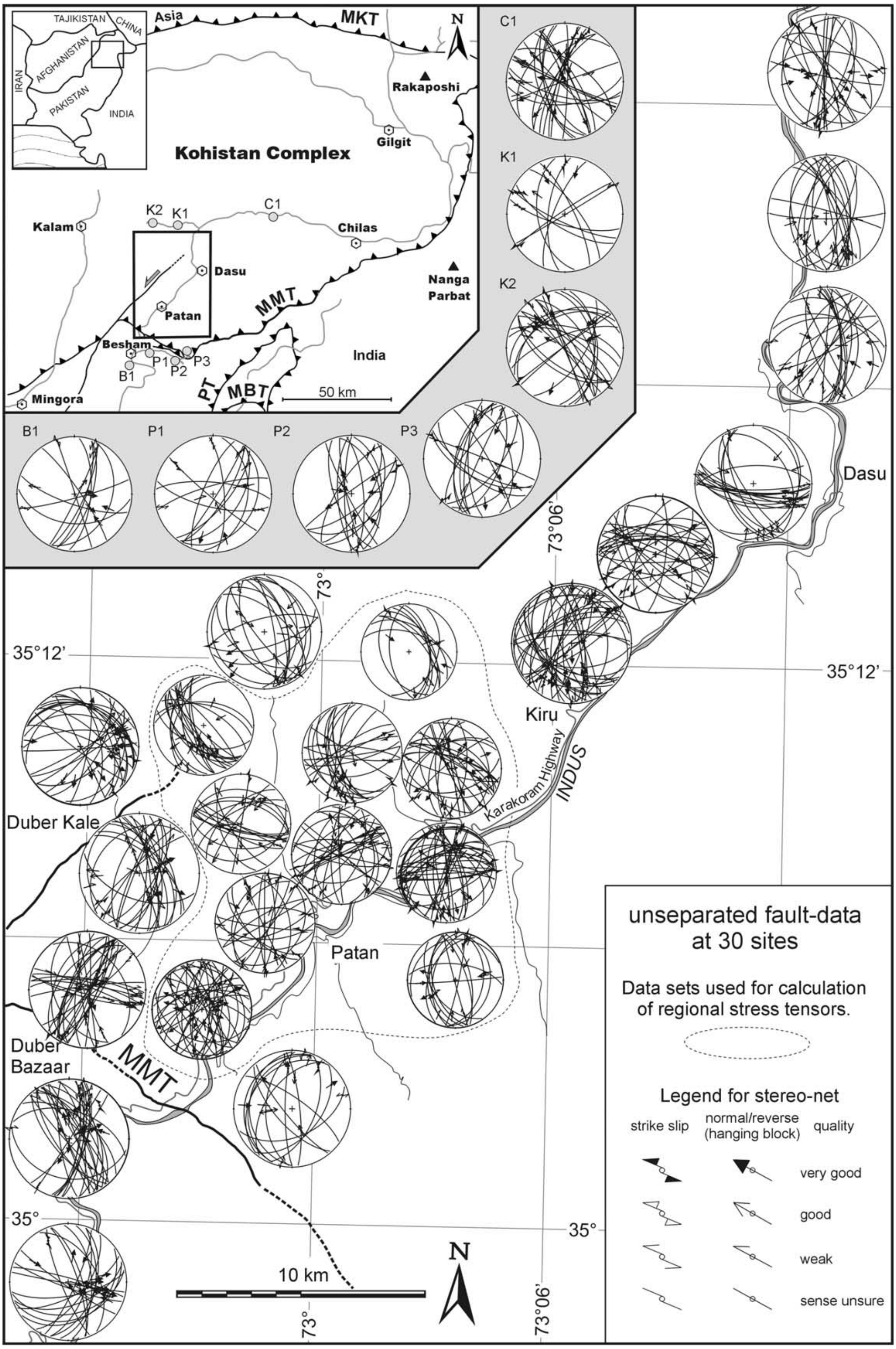
TAJIKISTAN
CHINA
AFGHANISTAN
IRAN
PAKISTAN
INDIA
Asia
MKT
N
Rakaposhi
Gilgit
Kohistan Complex
K2
K1
C1
Kalam
Chilas
Dasu
Nanga Parbat
Patan
MMT
Besham
P1
P2
P3
B1
PT
MBT
India
50 km
Mingora
C1
K1
K2
B1
P1
P2
P3
73°06'
Dasu
73°
35°12'
35°12'
Kiru
Karakoram Highway
INDUS
Duber Kale
Patan
Duber Bazaar
MMT
35°
35°
10 km
N
73°
73°06'
unseparated fault-data at 30 sites
Data sets used for calculation of regional stress tensors.
Legend for stereo-net
strike slip
normal/reverse (hanging block)
quality
very good
good
weak
sense unsure

The unexplained fault planes may be due to local accommodation between adjacent, rotating blocks, thus recording local deformation unrelated to the regional deformation. Treated together the un-explained faults did not yield any acceptable stress tensor.

Data from every site were then separated by successively imposing the 4 regional stress tensors and calculating the misfit angle of each fault/striation pair. Pre-existing anisotropy in the rocks caused by foliation and earlier fault planes justified allowing a misfit of 40° as the separation criterion for fault data fitting each tensor.

The obtained data subsets were compared to populations identified from geological observation. Results overlapped by more than 75%. We rearranged the subsets by comparing faults best fitting the tensors obtained through single site separation with the fault population obtained by imposing the regional tensors. The main criterion for rearranging the subsets was the similarity of the mean stress direction independently from the misfit angle.

In order to obtain the local orientation of the stress tensors, each subset underwent a further random tensor search accounting for 70% of the subset. Each local stress tensor has specific orientation and R-ratio, which is defined as $R=(\sigma1-\sigma2)/(\sigma1-\sigma3)$ and describes the shape of the stress ellipsoid (Célérier, 1988; Célérier, 1995). An R-value close to 1 indicates small differences between $\sigma2$ and $\sigma3$. R close to 0 indicates that $\sigma1$ and $\sigma2$ are almost equal.

The four regional tensors were not obtained at every site. Some tensors may have escaped calculation either because the relevant fault population was locally too small, or because the site area did not deform during the particular brittle event. A few fault data could be attributed to one or other of two different stress tensors. Omission of these data did not affect either calculation. Regional correlation from site to site relies on both the orientation and the shape of stress tensors and the chronological sequence based on field relationships between identified fault and striation sets.

Fig. 6.4 (left page): Unseparated data from 30 sites. Sites used for calculation of the regional stress tensors are not separated by major faults and they are clustered in one, reasonably small geographic area (marked by dashed line) in a single rock unit (a massive metagabbro). Fault/striation plotted in stereo-net, lower hemisphere (fault plane: great circle, striation: arrow, pointing towards movement direction of the hanging block).

A question is whether the direct inversion method is a valid tool for separating multiphase data sets. We might get only mixed stress tensors which are geologically meaningless (Nemcok & Lisle, 1995; Lisle & Vandycke, 1996). The latter assertion is correct when calculating stress tensors on inhomogeneous data sets without taking geological observations such as fault style and conjugate faults into account. The computed results presented here were verified by information independent of our computation to avoid mixed stress tensors. Although our attempt is not free from uncertainties inherent to areas of complex-deformation, the results give a plausible overview of the development and the succession of stress fields in this particular area of the Himalayas.

6.3. RESULTS

The distribution of the calculated stress tensors depicts 4 regional stress fields.

6.3.1. Population 1: SSE – NNW directed σ1 + ENE – WSW σ3

Population 1 faults are dominantly steep N–S (sinistral) and (dextral) WNW–ESE strike-slip faults (Fig. 6.5). They are sharp planes with chlorite crystallization and/or a few centimetres to half a meter thick gouge zones. The R-values vary from site to site from 0.31 to 0.99 pointing to a nearly uniaxial SSE–NNW compression at some places. Site deviation from the regional stress field is mainly expressed by swapping σ2 and σ3, which is consistent with R ≅ 1. Ca. 20° plunges of some σ1 axes are attributed to block rotations due to later faulting and/or to local variations in stress field orientation.

6.3.2. Population 2: E – W directed σ1 + subvertical σ3

Population 2 faults are dominated by 30° to 55° dipping thrust faults and secondary, steep strike-slip faults well defined N of Dasu and N of Duber Kale (Fig. 6.6) where sinistral reverse movement is notable in a broad serpentinized zone, which is the northern continuation of the Alpurai fault (Anczkiewicz *et al.* 1998). Fault thickness ranges from one centimeter to few decameter. Faults often display gouge zones and/or tectonic breccias. Local plunges (< 15°) of σ1 are attributed to late block tilting and/or to local variations in stress field orientation.

Fig. 6.5 (right page): Population 1, dominantly strike-slip faults fitting SSE–NNW directed σ1. R-values and direction of stress axes are plotted for each site (lower hemisphere, 1: σ1, 2: σ2, 3: σ3). Orientation of regional stress axes plotted as "beach-ball" (white: compression, black: dilatation, arrows: expected movement on intersection between compressional and dilatative quadrants). Distribution of misfit angle is given in a histogram (n: number of faults, x-axis: misfit angle) and the stress tensor aspect ratio R is represented in a Mohr circle diagram (τ: shear stress, σn: normal stress).

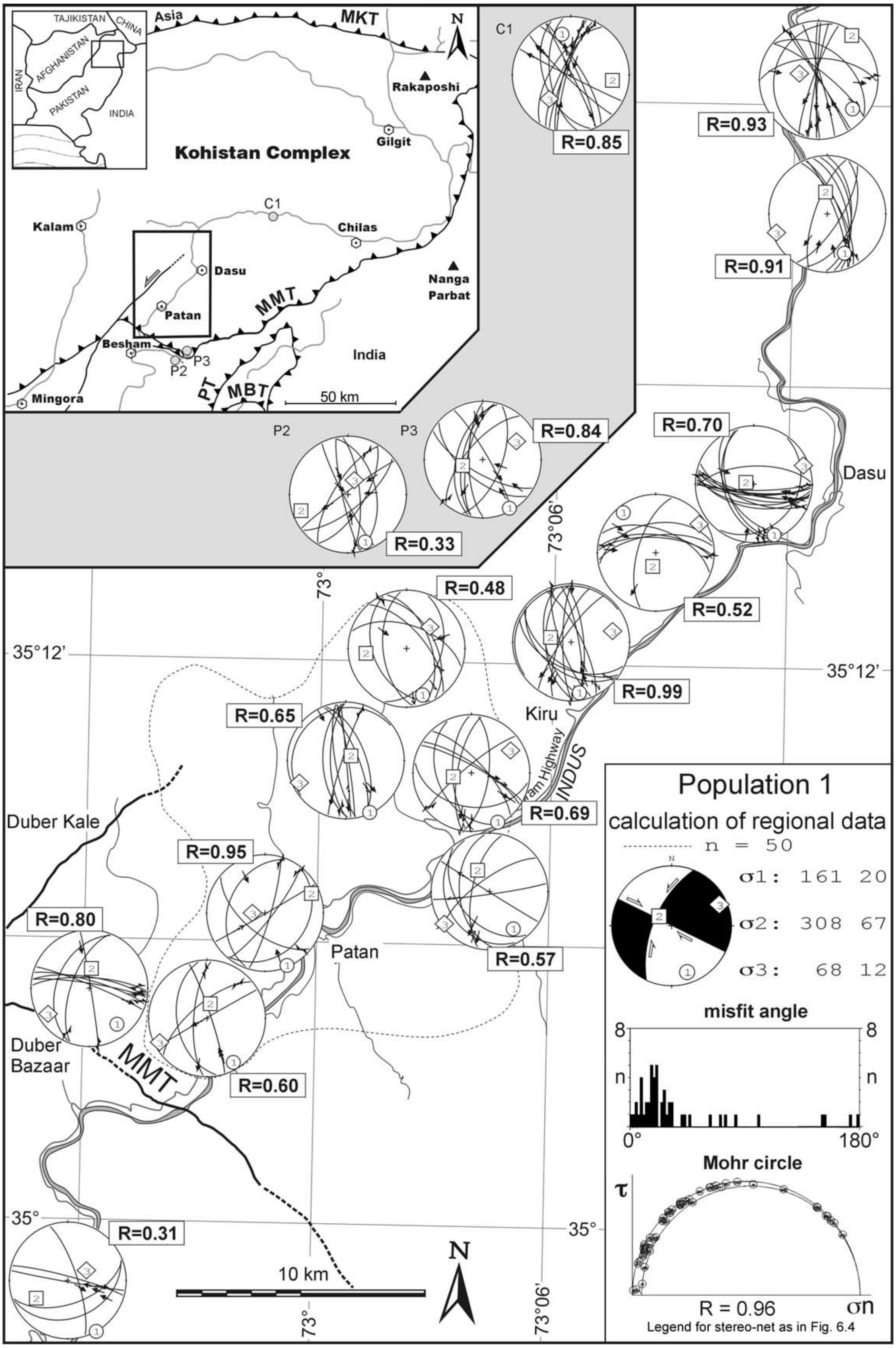

TAJIKISTAN
CHINA
AFGHANISTAN
IRAN
PAKISTAN
INDIA
Asia
MKT
N
Rakaposhi
Gilgit
Kohistan Complex
C1
Kalam
Chilas
Dasu
Nanga Parbat
Patan
MMT
Besham
P2
P3
India
Mingora
PT
MBT
50 km
R=0.85
R=0.93
R=0.91
R=0.84
R=0.33
R=0.70
Dasu
73°06'
R=0.52
R=0.48
73°
35°12'
35°12'
R=0.99
Kiru
R=0.65
Karakoram Highway
INDUS
R=0.69
Duber Kale
R=0.95
R=0.57
Patan
R=0.80
R=0.60
Duber Bazaar
MMT
35°
35°
R=0.31
10 km
N
73°
73°06'
Population 1
calculation of regional data
n = 50
σ1: 161 20
σ2: 308 67
σ3: 68 12
misfit angle
8
n
0°
180°
Mohr circle
τ
R = 0.96
σn
Legend for stereo-net as in Fig. 6.4

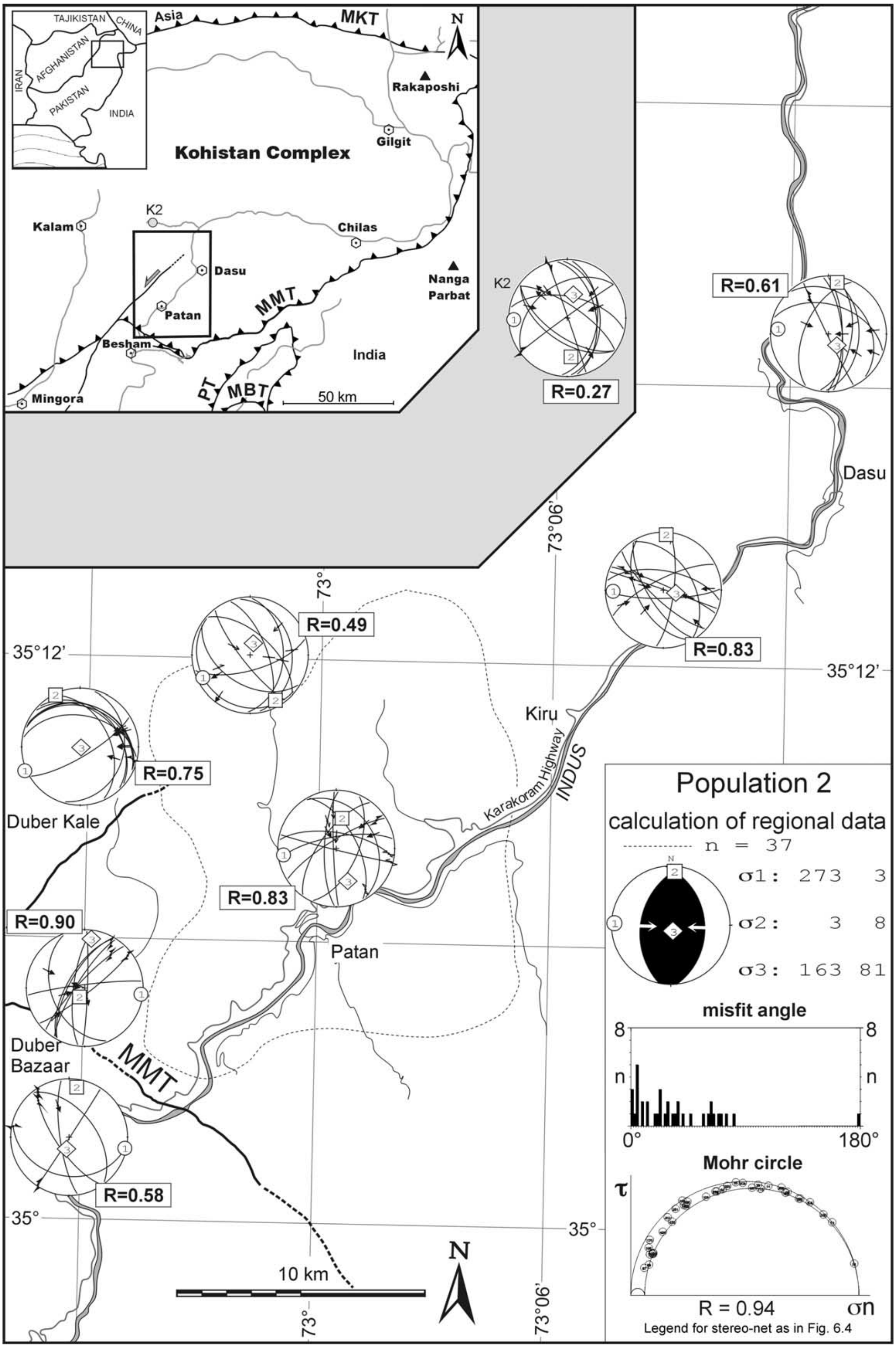

Fig. 6.6: Population 2, strike-slip and thrust faults that were activated by E–W compression. Legend as Fig. 6.5.

Highest R-values (0.75-0.90) are within the Kohistan Complex. Smaller R-values to the S of the Indus suture and towards the N of Patan imply a different shape of the stress ellipsoid in the footwall ($\sigma2 > \sigma3$, $\sigma3$ subvertical) and immediate hanging-wall ($\sigma2 \approx \sigma3$, $\sigma2$ subvertical) of the Suture. This suggests a direct influence of the Indus Suture on the stress distribution.

6.3.3. Population 3: WNW – ESE extension (subvertical $\sigma1$)

Normal faults, occurring as slicken-sided fault planes and as wider gouge zones can be observed in many places. The calculated stress tensors are characterised by N–S and E–W extensional directions (Fig. 6.7). R-values dominantly close to 1 indicate little difference between $\sigma2$ and $\sigma3$, i.e. radial extension. Sites with $R < 0.6$ have preferred E–W directed $\sigma3$. N of Dasu and in the Kandiah valley (K1 and K2, Fig. 4), normal faults do not play a significant role whereas closer to Chilas (C1, Fig. 6.7) normal faulting is better expressed. This seems to indicate that brittle extension was more localised than earlier brittle deformation.

6.3.4. Population 4: SSW – NNE directed $\sigma1$ + WNW – ESE $\sigma3$

Population 4 is defined by a set of dry N–S dextral and conjugate SW–NE sinistral strike-slip and subordinate thrust faults (Fig. 6.8). Fault planes are neat fractures without crystallization on their surfaces. Movement indicators are Riedel shears and striae on weakly polished planes. This fault population is dense around Patan but little represented within India, which suggests some brittle “decoupling” between the Indian footwall and the allochthonous Kohistan Complex. R ranges from 0.25 to 0.98 with a majority of ratios ≥ 0.8. The interchangeable orientation of $\sigma2$ and $\sigma3$ points to faulting under close to surface conditions (small burial loads). Single sites with low R-ratio have either $\sigma2$ or $\sigma3$ subvertical which means that this difference reflects very local effects and depends whether thrust faults ($\sigma3$ steep) are more abundant than strike-slip faults ($\sigma2$ steep).

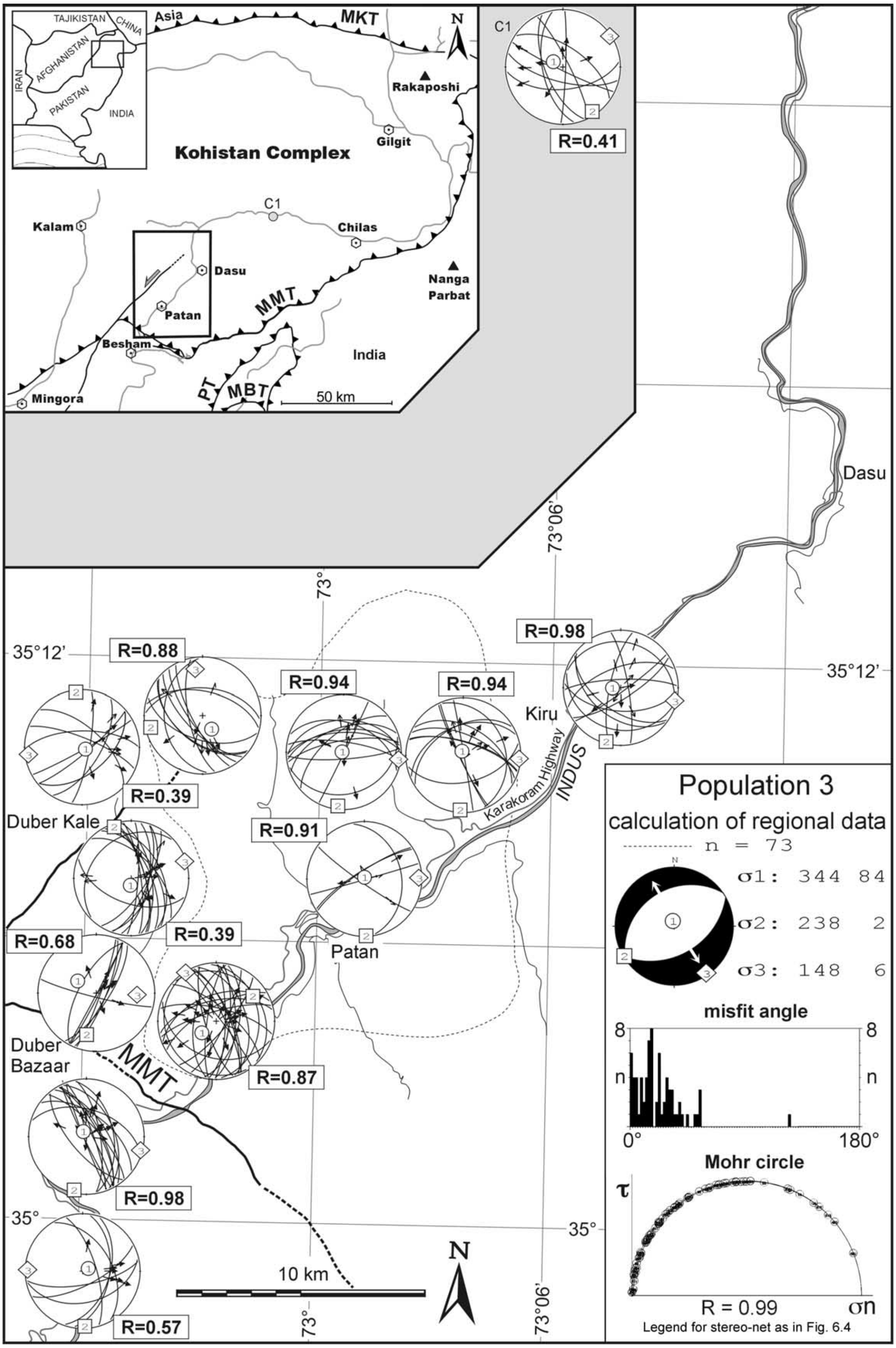

Fig. 6.7: Population 3, normal faulting. Legend as Fig. 6.5

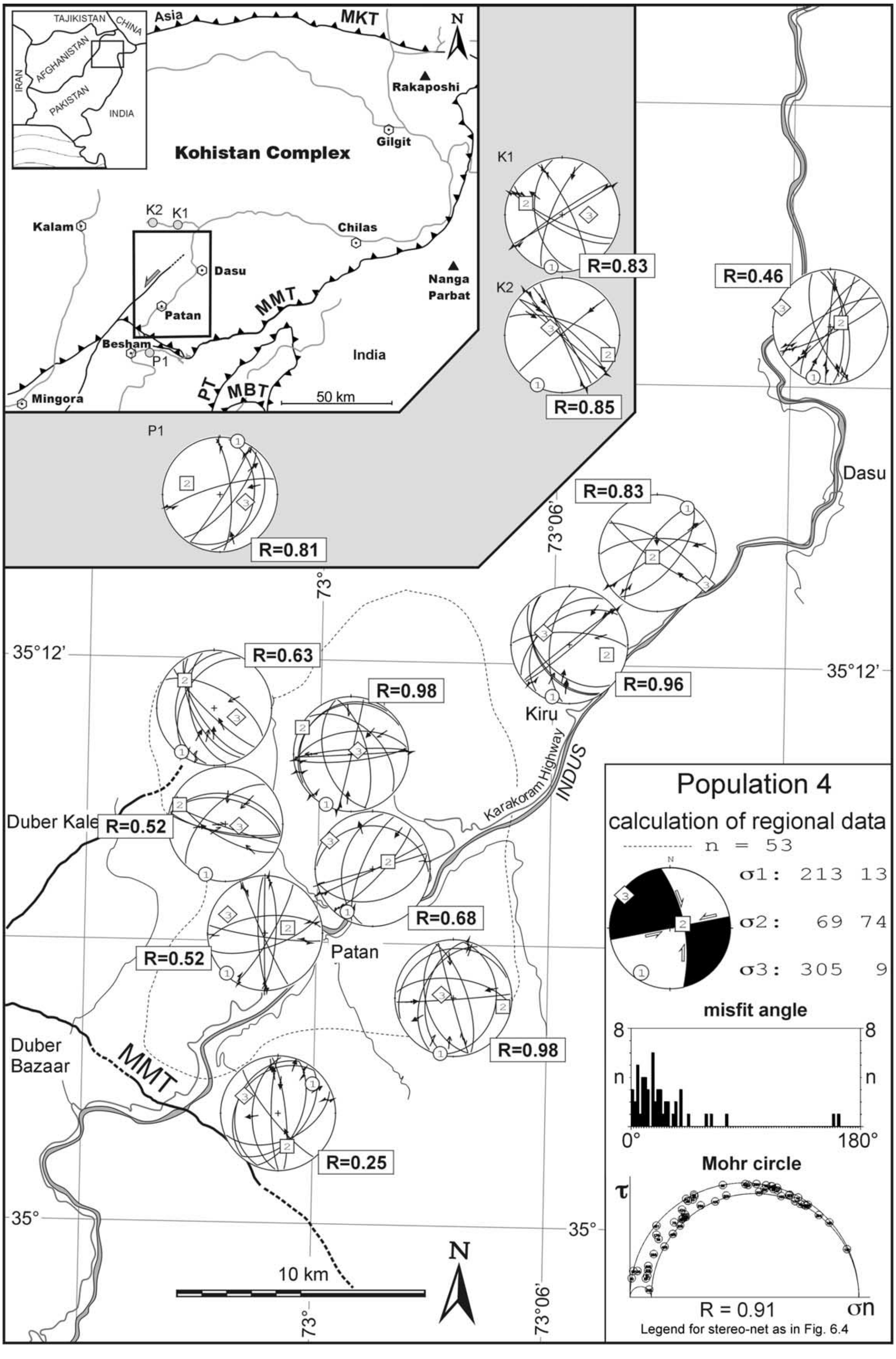

Fig. 6.8: Population 4, SSW–NNE directed σ1. Legend as Fig. 6.5

80% of the measurements from Kandiah valley (K1 and K2) and W of Chilas (C1) can be explained by the regional stress tensors. In these far distant sites, field observation and computer processing yielded a stress history similar to that obtained in the Patan region but with slightly different orientations. The orientation changes indicate that the regional stress fields have orientation variations not covered in this work.

6.4. Interpretation and Discussion

The analysis of the regional fault-framework provides evidence for four stress fields in the Patan region and probably over a large part of the Kohistan Complex. The idea of using a regional data set for separating subsets belonging to specific stress tensors is an appropriate way to depart from block rotations and noisy, background faulting. Block rotation in this area of complex faulting history was not large enough to seriously affect our separation procedure and is reflected in local, small plunges of the oldest stress axes. Supporting evidence is that, no significant, sudden change in attitude of ca. 90 Ma old shear zones and magmatic fabrics (Treloar *et al.*, 1990; Arbaret *et al.*, 2000) pointing to large block rotations has been observed.

The relative timing of the stress fields derived by crosscutting striations and fault planes that are unequivocally and separately attributable to one specific stress tensor yields the following sequence: population 1 is older than population 3, population 2 is older than population 3 and population 4 is younger than population 2. Relative age constraints for population 1 and 2 and population 3 and 4 were not found so that we were left with four possibilities: the adopted 1234 sequence or eventually 2134, 2143 and 1243 history. The proposed timing was inferred from the following observations:

-Fault planes containing chlorite fibres are the highest temperature faults and are thus likely to be the oldest. They essentially belong to population 1 which seems, therefore, older than population 2. The indicated SSE–NNW compression fits the convergence direction expected in this Himalayan region (e.g. Molnar & Tapponnier, 1975). Apatite fission track ages are 7.3±2 Ma 20 km N of Dasu and 5.6±2.3 Ma close to Besham (sample 79I-9 and 79I-12 in Zeitler, 1985). Assuming that chlorite, apatite and fibrous mineralisation found on population 1 fault planes were formed not much over 100-140°C, which is the range for the apatite fission track closure, a maximum age for these faults can be estimated at around 9 Ma (Fig. 6.9). This suggests, that the four brittle events recognised in this paper are younger than the normal faulting in ductile-brittle conditions along the Indus Suture (Burg *et al.,* 1996; Vince & Treloar, 1996) which has been dated as older than 18 Ma (Vince & Treloar, 1996).

We relate the E–W compression recorded in population 2 faults to the formation of N–S trending crustal antiforms such as the nearby Nanga Parbat and Indus syntaxes (Coward, 1985; DiPietro *et al*. 1999) (Fig. 6.1). They are crustal scale NS buckle folds that should reflect E–W compression sometime within the last 5 Ma (Zeitler, 1985). Indeed, reconnaissance work has revealed that the importance of E–W compression increases eastward towards the main syntaxes. The studied area is structurally the hangingwall of the syntaxes.

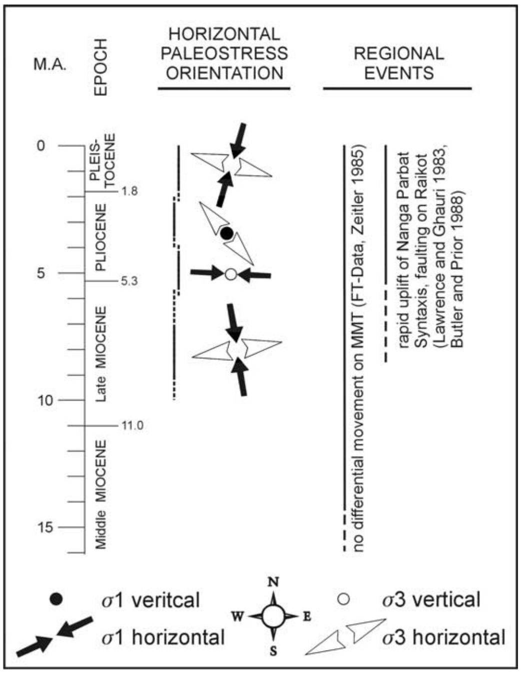

Fig. 6.9: Proposed time sequence and orientation of regional stress tensors.

Population 3 extension took place after the E-W compression. We tentatively relate this extension to lateral collapse of the hanging-wall of the crustal anticlines, in particular the Nanga Parbat structure.

-Fault characteristics of population 4 indicate cold, subsurface conditions, as expected for recent fracturing. The σ1 direction calculated from population 4 faults corresponds to the present-day compression (Fig. 6.10), which produced the Patan earthquake in December 1974 (Ambraseys *et al.*, 1975). Therefore, we deduce that population 4 documents the ongoing southward thrusting of the Kohistan Complex onto the Indian Plate (Pennington, 1979) and is younger than population 3.

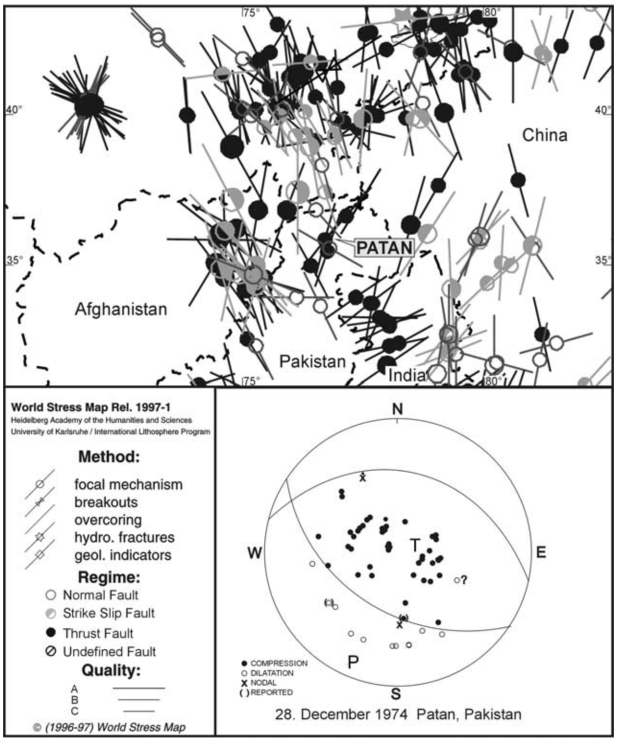

Fig. 6.10: Recent stress field in Northern Pakistan and adjacent countries (World stress map, release 1997/1). Additional: Focal mechanism solution for the Patan earthquake, lower hemisphere, indicating nearly pure thrusting in a NNE–SSW direction, along either of the two nodal planes (Pennington, 1979). Population 4 is in accordance with this record.

6.5. Conclusions

Faulting in and near the Indus Suture Zone results from the existence of four successive stress fields that point to a complex tectonic evolution. Early faults formed during southward thrusting of the Kohistan Complex, probably in Miocene times. Population 2 faults occurred during E–W compression related to the formation of N–S striking buckle folds such as the Nanga Parbat and Indus syntaxes. That compression disturbed the stress field related to N–S convergence between India and Eurasia. We speculate that population 3 developed as lateral collapse structures in the hanging-wall of the Nanga Parbat crustal anticline. Population 4 documents a present day return to the stress field controlled by the ongoing southward thrusting of the Kohistan Complex as documented by the focal mechanism solution of the Patan earthquake. Faults subjected to potential reactivation under these stress conditions can be identified with adequate computation.

ACKNOWLEDGEMENTS

Supported by the Swiss National Science Foundation (grant 20-49372.96). N. Chaudhry is supported by the Punjab University, Lahore. We thank Bernard Célérier for his software FSA (B. Célérier, 1999. FSA: Fault Slip Analysis software, http://www.isteem.univ-montp2.fr/PERSO/celerier/ftp.archive/fsa.html) and the description of the random tensor search procedure. The World Stress Map is available via Internet at: http://www-gpi.physik.uni-karlsruhe.de/pub/wsm/index.html. R. Spikings improved the English version. K. Burke and L. Ratschbacher are thanked for very useful reviews.

7. SUMMARY AND CONCLUSIONS

The KAC was installed on the oceanic crust somewhere in the Tethys around the equatorial zone and close to the southern marginal terrane (Karakoram block) of the Eurasian continent (e.g. Yoshida *et al*., 1996). The Indian plate was, during this time, in the southern hemisphere (Klootwijk *et al*., 1986a,b). The northward dipping subduction formed during Mid Cretaceous times produced a volcanic arc (Fig. 7.1, >100 Ma). The Sarangar gabbro emplaced 99 Ma ago at pressures of ca. 1.0 GPa. It shows a geochemical signature typical for island arcs. At this time the arc had already a thickened crust (Fig. 7.1, 100 – 90 Ma). Consequently, the initiation of subduction must have started before 100 Ma. Remnants of the oceanic crust on which the arc was built are most likely preserved as enclaves in the lower to mid crustal level of the arc (Jan, 1988; Khan *et. al*., 1993; Treloar *et. al*., 1996). PT conditions of emplacement, retrograde metamorphism and the continuous section with mantle rocks (Jijal Complex ultramafic sequence) at the base confirm that the Metaplutonic Complex is representing the lower – middle level of the arc. In the Indus area the Metaplutonic Complex is built up mainly by a) Sheared gabbro-diorites (Patan region) comprising retrograde metagabbros with locally preserved igneous layering; b) Kiru sequence consisting of more than hundred meters thick imbricate intrusions of gabbroic to dioritic composition; c) Kamila sequence, an amphibolitised sequence composed of gabbroic, dioritic, granitic and tonalitic rocks intruded in a crustal sequence, whose remnants are represented by fine layered amphibolites with epidote-rich lenses, enclaves of carbonates and quartzite bands.

The KAC evolved quickly from early arc buildup (Fig. 7.1, >100 Ma) to a mature stage with back-arc spreading and magmatism (starting at 85 and lasting to at least 80 Ma ago; Fig. 7.1, 90 – 80 Ma). As shown in Figure 7.1 (100 – 90 Ma) the buildup is represented by a suite of calc-alkaline to tholeiitic plutons intruded in the lower to mid crustal levels of the arc (the Metaplutonic Complex is symbolized in the lower central and southern part of the arc). Some of these plutons yield intrusion ages of 98.9±0.4, 97.1±0.2 and 91.8±1.4 Ma (Fig. 7.2, U/Pb ages) and represent parts of multiple, fast differentiation cycles from gabbros to granites.

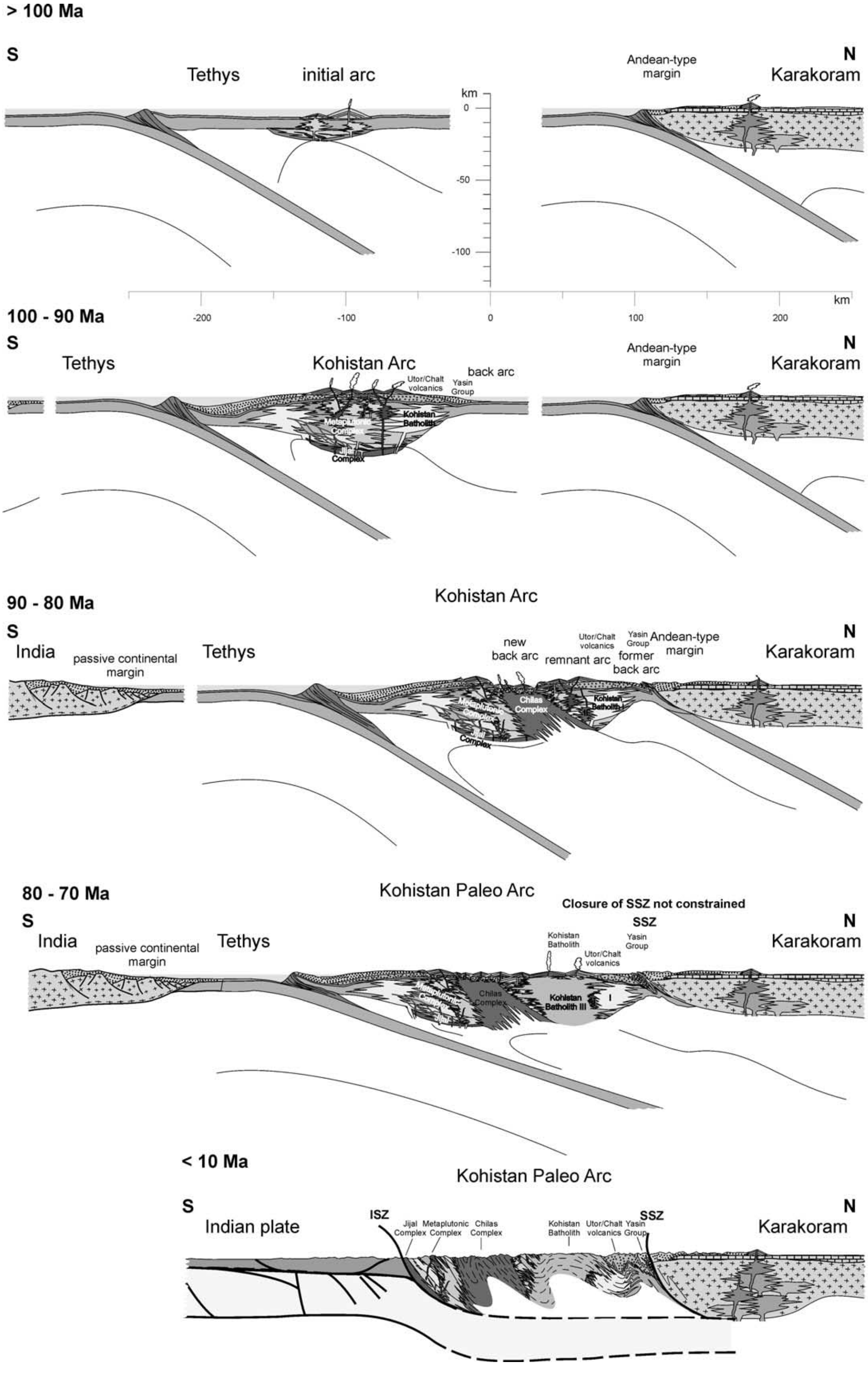

Fig. 7.1: Proposed model for the Kohistan Arc Complex build-up during northward-directed subduction of the Tethyan ocean and subsequent collision with Eurasia and India. The Chilas complex and Kohistan batholith III are drawn for simplicity as huge magma chambers, which are unlikely to have existed at this extend.

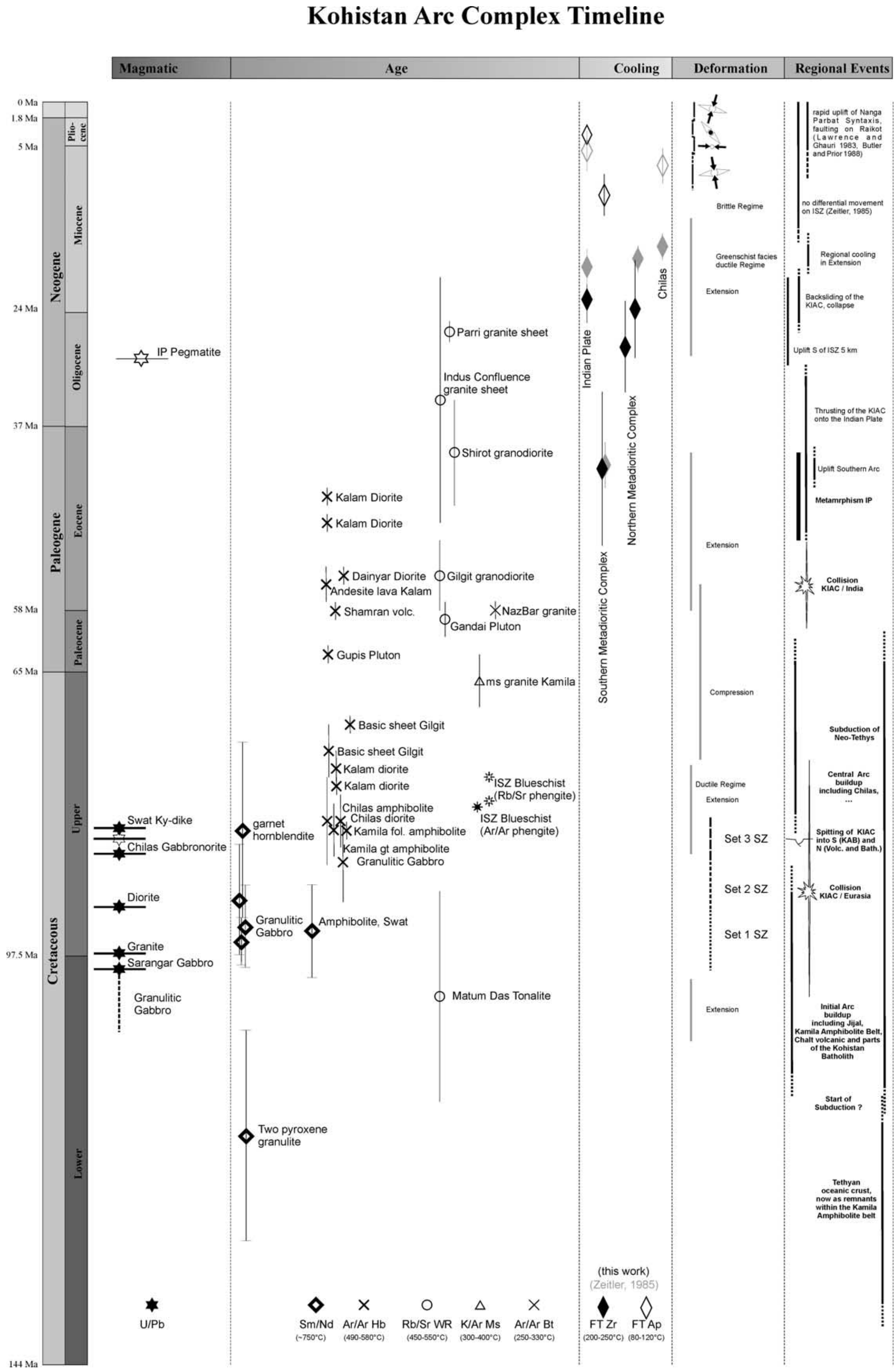

Fig. 7.2: Kohistan Arc Complex history showing dated and interpreted events covering the magmatic emplacement, metamorphic overprint, cooling, deformation events and the regional implication. Data from: Zeitler et al. (1981), Zeitler (1985), Peterson & Windley (1985), Treloar et al. (1989a), George et al. (1993), Yamamoto & Nakamura (1996, 2000), Anczkiewicz (1998), Anczkiewicz & Vance (2000) and this work. Extension and compression regime after Treloar et al. (1996).

The early gabbro-dioritic suite of the Kohistan batholith, drawn on a more northern position in the arc (Fig. 7.1, 100 – 90 Ma) was also formed within this island arc setting between 110 – 85 Ma (Petterson & Windley, 1991; Petterson *et al.*, 1991b). The Granulitic and Sarangar gabbros most likely intruded at the base of a thickened arcat pressures of ca. 1.0 – 1.2 GPa (equivalent to a depth of ~40 km) or higher as it is suggested by Ringuette *et al.* (1999). The mantle – crust transition is then supposed to have been at depths of 40 – 50 km around 100 – 90 Ma (Fig. 7.1). The Hf isotopes give further evidence that the Kohistan Arc Complex is an intraoceanic island arc with minimal continental influence. Subducted components derived by melting of the slab itself were negligible for the generation of the melts. In the highly dynamic setting above a subduction zone the intruding plutons recorded the deformation at the base of the island arc during their emplacement and subsequent solid state deformation. This is symbolized in Figure 7.1 (100 – 90 Ma) by the anastomosing pattern. The Metaplutonic Complex and the Granulitic gabbro (the unit just above the in dark grey drawn Ultramafic sequence at the base of the arc in Figure 7.1) preserved an intense, dominantly SW directed shear deformation.

To illustrate the early arc history a temperature, pressure and time relation (Fig. 7.3) is sketched where pressure is assumed to be overburden depth. The emplacement of gabbroic magmas occurred under high temperature > 1000 °C (Yoshino *et al.*, 1998) and pressures above or around 1.5 GPa at ca. 99 Ma (Sarangar gabbro) or earlier followed by a subsequent granulite facies metamorphism under intrusion conditions or with a prograde path of ΔP 0.3 GPa and ΔT 80 °C. The temperature, pressure and time relation suggests for both, the Granulitic and Sarangar gabbros cooling and decompression from 100 to 97 Ma and nearly "isothermal" decompression from 97 to 87 Ma, where the exhumation path follows the 600 °C isotherm (Fig. 7.3). Metamorphic conditions associated with set 2 shear zones (chapter 5.1) were estimated at 550 – 650 °C under pressures of 0.9 – 1.0 GPa (Bard, 1983; Treloar *et al.*, 1990).

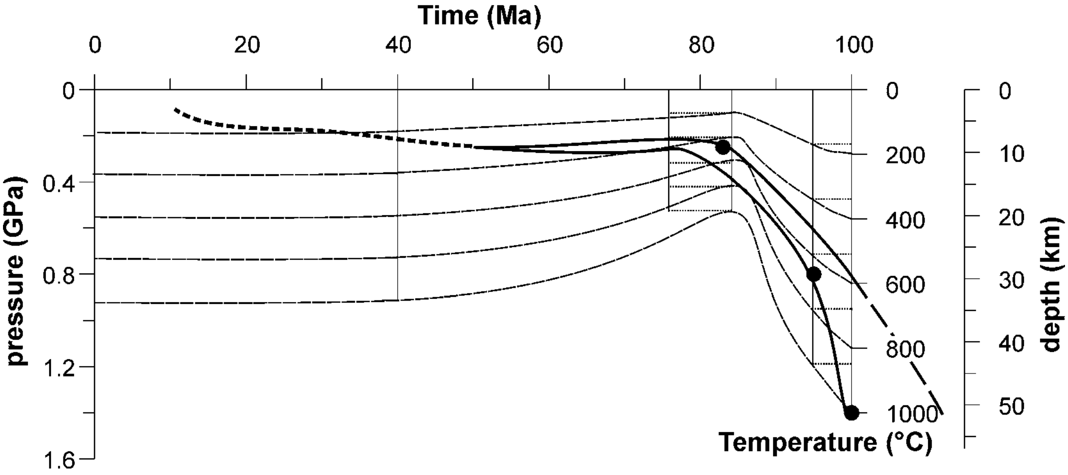

Fig. 7.3: Simplified geothermal and geobarometrical evolution of the lowest Kohistan Arc Complex (Jijal and Metaplutonic Complex). Pressure gradient is assumed constant with depth. PT values are estimates: at 100 Ma crystallisation of Sarangar gabbro, pressure of ca. 1.5 GPa in granulitic gabbro; at 95 Ma cooling below 700 °C (Sm-Nd age, Anczkiewicz & Vance, 2000); at 83 Ma cooling below 500 °C (Ar-Ar age of hornblende, Treloar et al., 1990); the stippled line represent the cooling path obtained by FT-dating (see Chapter 4.3). Pressures were taken from Fig. 3.11. Since 40 Ma a geothermal gradient of 30 °C/km was assumed. The strong "upwelling" of the isotherms coincides with the intrusion of the Chilas Complex at ca. 85 Ma.

Results presented earlier (chapter 3.1) imply that the onset of shearing happened under granulite facies conditions at ca. 800 °C and ~1.1 GPa and shearing was ongoing under amphibolite facies to conditions of 600 °C and 0.8 GPa. This range is in agreement with the conditions of the 97 – 87 Ma part of the history. Higher temperatures mentioned earlier are supported by the fact that partial melting in set 2 mylonites generated quartz-plagioclase-garnet bearing segregation veins and by the upper amphibolite facies crystal plasticity reported by Treloar *et al.* (1990). The minimum age for set 2 shear zones is inferred from the 86.7±4.6 Ma amphibole-epidote-paragonite assemblage that has partially overprinted the granulitic assemblage in the granulitic gabbro (Anczkiewicz, 1998, Ar-Ar, paragonite). Set 2 shear zones were then successively replaced by the later set 3 shear zones (chapter 5.1) which show lower amphibolite facies mylonitic assemblages. The set 2 mylonite analysed in the Sarangar gabbro recorded temperatures around 540 °C and pressures around 0.6 GPa (chapter 3.1). Therefore it cannot be excluded, that some of the set 2 shear zones were still active when most of the deformation was accommodated by flat lying and less anastomosed set 3 shear zones under lower amphibolite facies conditions.

At ca. 85 Ma a strong "upwelling" of isotherms occurred, coinciding with a drastic change in tectonic style. This was the onset of intra-arc rifting and the intrusion of the Chilas Complex 85.73±0.15 Ma ago (Fig. 7.1, 90 – 80 Ma; Fig. 7.2, U/Pb ages). The intrusive Chilas Complex is constituted of several intrusions of noritic to dioritic character with $^{87}Sr/^{86}Sr$ ratio typical for island arc magma (Miksohiba *et al.*, 1999). The relatively shallow isotherms at this time (Fig. 7.3) are most likely the result of the extensional emplacement of the Chilas Complex (Burg *et al.*, 1998). This stage is characterized by a shift in the Hf isotopic compositions of the magmatic liquids from MORB-type values (εHf = +14) to less radiogenic compositions (εHf = +10). The Chilas melts εHf value is significantly lower than the older magmatic rocks of the Metaplutonic Complex, but well within the range of oceanic basalts. This suggests that an old mantle component with a lower time-integrated Lu/Hf ratio than MORB, or even sedimentary or continental crustal contaminants, were involved in the generation of the Chilas parental melts.

The termination of shearing in the Set 3 shear zones is constrained to be under amphibolite facies conditions at ca. 550 °C and ~0.4 GPa, probably between 83 and 76 (Fig. 7.2, Ar-Ar ages) proposed for the end of the regional amphibolite facies metamorphism (Treloar *et al.*, 1989a; Wartho *et al.*, 1996). After ca. 83 Ma further cooling and decompression (exhumation) took place under apparently moderate gradients (Fig. 7.3) with a temperature decrease of 200 °C and only a slight pressure drop until 40 Ma.

What were the regional tectonic events for rapid decompression and cooling? An important hint for this question is provided by several N-side down epidote-amphibolite to amphibolite facies shear zones described by Treloar *et al.* (1990) and in Chapter 5.2 in the northern part of the Kiru sequence, which reflect extension. The metamorphic conditions recorded in the N-side down shear zones suggest, that they were not active later than the end of the regional amphibolite facies metamorphism (83 – 76 Ma, Ar-Ar age on hornblende, Treloar *et al.*, 1989a, Wartho *et al.*, 1996). The proposed intra arc-rifting at ca. 85 Ma (Khan *et al.*, 1989, 1993) could explain extension and resulting development of epidote-amphibolite to amphibolite facies normal sense shear zones. These shear zones may have supported a faster exhumation of the Metaplutonic

Complex. An essential question for the tectonic interpretation is the timing for collision of the Kohistan Arc with the Karakoram plate (Asia). This collision changed the system north of the Indian plate from an island arc to an active continental margin. The closure of the Northern Suture is bracketed between 102±12 and 85 – 75 Ma (Petterson & Windley, 1985; Treloar *et al.*, 1989a). Treloar *et al*. (1996) suggest an emplacement of the Chilas Complex "after suturing" of the Kohistan Arc to the Karakoram Plate due to the lower degree of deformation within the Chilas Complex compared to the Metaplutonic Complex. If this assertion is appropriate and the Rb-Sr, Ar-Ar and K-Ar dating is giving precise values, the closure of the Northern Suture was prior to the emplacement of the Chilas Complex or at the same time (Fig. 7.4a).

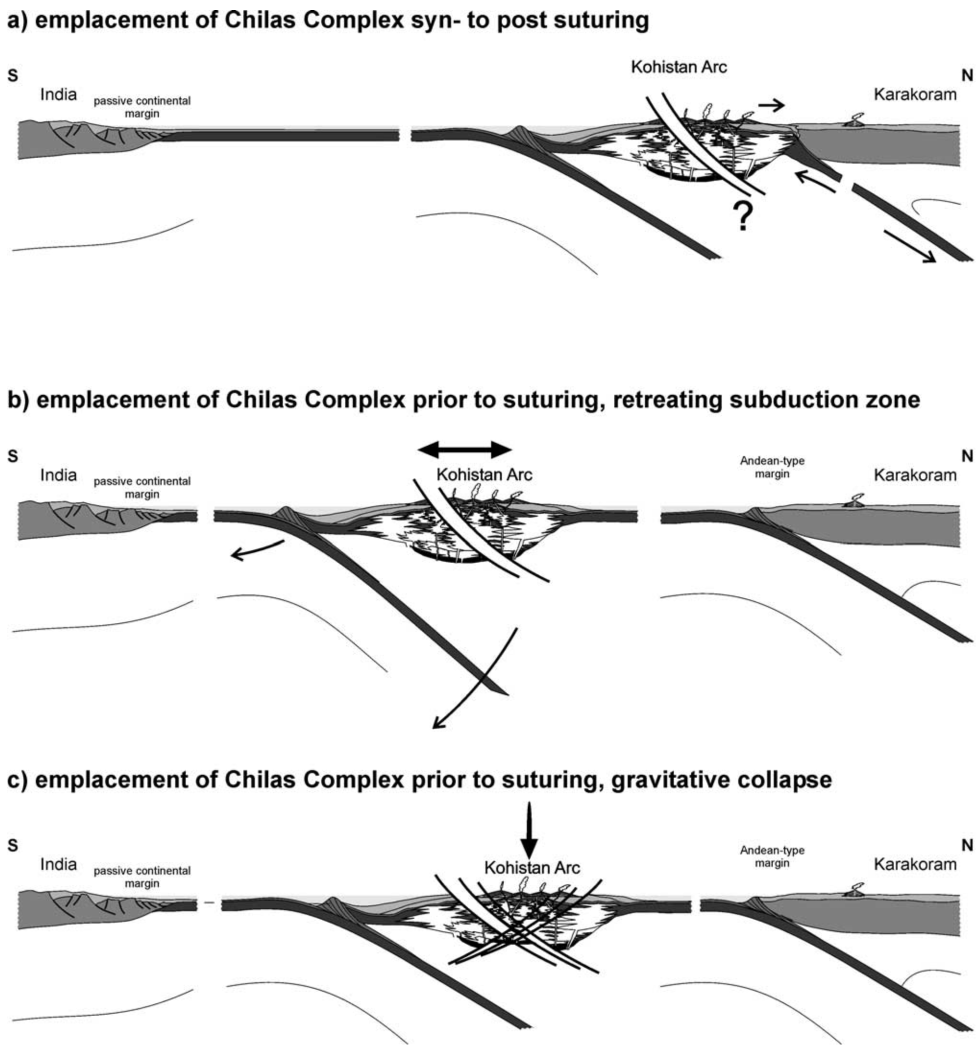

Fig. 7.4: Discussed settings during emplacement of the Chilas Complex at 85 Ma: a) post- to syn- collisional (Kohistan arc – Karakoram) emplacement; the reason of extension remains unclear; b) prior to the closure of the SSZ with extension induced in the upper plate by a retreating subduction zone; c) prior to closure of the SSZ with extension driven by gravity.

In this scenario, the extension would occur in a system, where general compression between the arc and the continental margin is expected. The emplacement of the Chilas Complex could have been also prior to closure of the Northern Suture. In this scenario following processes are possible: 1) Change in subduction angle/speed with retreating subduction zone as proposed by Treloar *et al*. (1996), based on a scenario described by Royden (1993) (Fig. 7.4b) and 2) gravity collapse of an abnormally thickened arc crust (Fig. 7.4c). Changes in plate tectonics movement pattern or combinations of the processes mentioned above cannot be excluded as potential reason for extension.

The mantle sources were different for the 99 – 92 Ma magmatism of the arc and the extensional magmatism at ca. 85 Ma. This reveals a change in tectonic setting. The early magmatism corresponds to a calc-alkaline to tholeiitic differentiation trend. Gabbros, diorites, tonalites and granites were emplaced in a island (volcanic-) arc setting. The related gabbros and diorites preserved a common geochemical signature from the melts and/or melt-source. The overall geochemical signature is similar to volcanics of the Tonga, New Hebrides and Mariana arc systems, clearly showing the arc-type character of the analysed gabbros and diorites. They are different to the high Ti- amphibolites (Khan *et al.*, 1993) and therefore do not represent a remnant ocean floor, which is suggested to be also present in the "Kamila Amphibolite Belt". Diorites intruded ca. 1865 Ma ago in the Indian Plate (at Duber Bazar) are within plate plutons with a clear discrepancy in the geochemical signature compared to the diorites and the arc rocks.

A dominantly basaltic juvenile arc crust is likely to evolve with time towards more acidic and HIE-enriched compositions similar to continental crust. The HIE depletion of the analysed gabbros and diorites tends to "balance" the enrichment of the continental crust. Different processes are likely involved in the arc differentiation and granite formation. Based on the preliminary dataset the cumulitic characters of the gabbros are relatively subtle and these gabbros cannot be considered as proper "cumulates", therefore fractional crystallisation seems to be a minor process. This also indicates that there was no common large magma chamber involved in the formation of the analysed gabbros and diorites. A dehydration of hornblendites possibly triggered incipient partial melting of the lower arc section along with pervasive upward migration of small melt fraction. The formation of granites is most likely the result of partial melting at the base of the arc. This process would efficiently remove granitic components from the base of the arc and transport them up to shallower levels.

The main bulk of the Kohistan batholith comprises a gabbro-diorite suite at 85 to 60 Ma (Fig. 7.1, 80 – 70 Ma) and a granitic suite, emplaced at 60 – 40 Ma (Petterson & Windley, 1991; Petterson *et al.*, 1991b). A postcollisional magmatism with leucogranitic sills and dikes occurred between 40 and 26 Ma (Petterson & Windley, 1985).

Extension took place after the collision between the Kohistan Complex and the passive margin of the Indian plate at ca. 55 Ma, and subsequent thrusting onto the Indian Plate. It is indicated by NE vergent folds, interpreted as collapse structures related to the backsliding of the Kohistan Arc (Burg *et al.*, 1996; Vince & Treloar, 1996; Anczkiewicz, 1998). The earliest onset of extension is estimated at 47 Ma (Burg *et al.*, 1996). Anczkiewicz *et al.* (2001) interpret the 29 Ma emplacement age of a pegmatite in the Swat valley, which is deformed by folds related to normal faulting, as expression of an already ongoing extension or as maximum age for reactivation of the ISZ as normal fault. The difference between the zircon FT ages representing footwall (~23 Ma) and hanging wall (~42 Ma) of today's ISZ geometry at the Indus valley (Fig. 7.1, < 10 Ma) is ca. 20 Ma. The onset of normal faulting occurred latest during this time span. Consequently normal faulting along the investigated part of the Indus Suture started at least ~23 Ma ago. Apatite FT ages are ~3.7 Ma for the footwall and ~10 Ma for the hanging wall. This suggests that normal faulting outlasted the termination of extension of other ISZ segments, where it is reported between ca. 20 Ma (Burg *et al.*, 1996; Vince & Treloar, 1996) and 15 Ma (Swat valley, Anczkiewicz *et al.*, 2001) based on FT ages from Zeitler (1985). The young differential movement across the ISZ in the Indus area is here a local phenomenon caused by the growth of the Besham antiform, a possible small-scale equivalent to the Nanga Parbat “Syntaxis” (Coward, 1986; Treloar *et al.*, 1989c).

Based on the paleostress analysis, four stress fields could be identified. They were chronologically ordered in SSE–NNW compression, E–W compression, radial extension and SSW–NNE compression (Fig. 7.2, deformation/regional events). The dynamic evolution during the brittle stage of the collision of India and Asia is interpreted by the four stress fields and their relative timing. The earlier stress fields were active during the Miocene, when convergence-related N–S directed stresses were dominant. That compression was disturbed by an E–W compression which is related to the formation of the nearby Nanga Parbat "Syntaxis" at ca. 10 – 5 Ma (e.g. Butler & Prior 1988). The radial extension is probably the expression of a lateral collapse in the hanging-wall of the Nanga Parbat crustal anticline. The last compression, related to N–S convergence between India and Eurasia fits the present-day stress field defined from seismic activity.

Appendix

APPENDIX CHAPTER 3

- Results of electron microprobe analysis.

Sample location:

Sarangar Gabbro GbS (16/01/01) E 73°01'23" N 35°07'16"

The sample was collected ca. 2 km ENE of Patan along the KKH. The mylonitic part covered by the sample belongs to a ca. 8 cm thick shear zone with a foliation dipping 20° towards N and a top to S shear sense.

Sarangar Gabbro GbS (90/02/01) E 73°01'37" N 35°07'01"

The sample was collected ca. 2 km E of Patan along the Jeep-road Patan – Chor Nala close to Shalkanabad. The gently NE dipping shear zone is ca. 50 cm thick and contains stretched plagioclase veins and numerous rotated plagioclase porphyroclasts. Sense of shear is towards SW.

Granulitic Gabbro GtGrlt (13/01/01) E 72°59'56" N 35°06'44"

The sample locality is ca. 200 m SW of the bridge crossing the Patan Banil Khwar at Patan at KKH. The shear zone is ca. 50° W dipping and yields a top to E sense of shear.

Granulitic Gabbro GtGrlt (94/04/01) E 72°59'57" N 35°06'43"

Ca. 40 m SSE of sample 13/01/01 in stronger retrogressed part of the granulitic Gabbro. Covered shear zone is ca. 20 cm thick. The shear zone is ca. 20° NE dipping and yields a top to SW shear sense.

Kiru Amphibolite AmKi (46/02/01) E 73°06'22" N 35°11'06"

The sample was collected ca. 150 m W of the metal bridge close to Kiru along the KKH within fine banded (cm scale) amphibolites. Foliation is steeply >70° N dipping and sense of shear is top to SSW. Protolith was a diorite.

Table Appendix 3.1: Representative chemical composition of plagioclase.

	Mineral: plagioclase							
	Granulitic Gabbro mylonitic 13/01/01							
Sample	p01s05pl1	p01s05pl2	p01s05pl3	p01s05pl4	p01s05pl5	p01s06pl1	p01s03in3	p01s03gt6
Site	s05	s05	s05	s05	s05	s06	s03	s03
nr.	24	25	26	27	28	29	38	43
note	in deformed part						incl. in gt	adj. to gt
SiO_2	58.22	57.98	57.80	57.85	57.98	58.35	60.12	63.48
TiO_2	0.00	0.00	0.09	0.00	0.00	0.00	0.00	0.00
Cr_2O_3	0.01	0.01	0.00	0.02	0.00	0.00	0.00	0.00
Al_2O_3	26.89	27.02	27.04	27.28	27.05	27.14	26.20	24.13
Fe_2O_3	0.00	0.00	0.03	0.00	0.04	0.00	0.00	0.32
FeO	0.06	0.04	0.00	0.02	0.00	0.00	0.16	0.10
MnO	0.00	0.02	0.00	0.05	0.00	0.03	0.05	0.03
MgO	0.00	0.00	0.00	0.00	0.00	0.00	0.00	0.00
NiO	0.00	0.00	0.00	0.00	0.00	0.00	0.00	0.00
CaO	8.35	8.74	8.68	8.57	8.46	8.31	7.37	4.86
Na_2O	6.79	6.66	6.72	6.70	6.87	6.92	7.44	9.02
K_2O	0.06	0.08	0.07	0.05	0.07	0.07	0.05	0.08
Total	100.37	100.55	100.43	100.53	100.46	100.82	101.41	102.01
Si	2.595	2.582	2.576	2.575	2.580	2.587	2.647	2.759
Ti	0.000	0.000	0.003	0.000	0.000	0.000	0.000	0.000
Cr	0.000	0.001	0.000	0.001	0.000	0.000	0.000	0.000
Al	1.413	1.418	1.420	1.431	1.419	1.418	1.360	1.236
Fe3	0.000	0.000	0.001	0.000	0.001	0.000	0.000	0.011
Fe2	0.002	0.002	0.000	0.001	0.000	0.000	0.006	0.004
Mn	0.000	0.001	0.000	0.002	0.000	0.001	0.002	0.001
Mg	0.000	0.000	0.000	0.000	0.000	0.000	0.000	0.000
Ni	0.000	0.000	0.000	0.000	0.000	0.000	0.000	0.000
Ca	0.399	0.417	0.414	0.409	0.403	0.395	0.348	0.226
Na	0.587	0.575	0.581	0.578	0.593	0.595	0.635	0.760
K	0.004	0.005	0.004	0.003	0.004	0.004	0.003	0.004
Σ Cations	5.000	5.000	5.000	5.000	5.000	5.000	5.000	5.000
Albite	0.593	0.577	0.581	0.584	0.593	0.599	0.644	0.767
Anorthite	0.403	0.419	0.415	0.413	0.403	0.397	0.353	0.228
Orthoclase	0.004	0.005	0.004	0.003	0.004	0.004	0.003	0.004

calculated with "Norm" program by P. Ulmer using: FELDSPAR Norm
Normalization CATIONS assuming stoichiometry and chargebalance

	Mineral: plagioclase							
	Granulitic Gabbro undeformed 13/01/01							
Sample	p02s03pl3	p02s03pl1	p02s03pl1	p02s03pl1	p02s03pl1	p02s03pl1	p02s03pl2	p02s03pl1
Site	s03	s03	s03	s03	s03	s03	s03	s03
note	in contact to amp							
SiO_2	58.44	61.35	59.05	58.81	57.26	61.54	57.78	58.45
TiO_2	0.00	0.01	0.00	0.00	0.02	0.04	0.00	0.00
Cr_2O_3	0.01	0.07	0.02	0.00	0.07	0.04	0.04	0.00
Al_2O_3	27.25	25.02	25.71	26.92	28.70	24.63	26.43	26.55
Fe_2O_3	0.00	0.05	0.03	0.02	0.00	0.04	0.00	0.00
FeO	0.04	0.00	0.00	0.00	0.00	0.00	0.10	0.06
MnO	0.00	0.05	0.02	0.02	0.00	0.04	0.00	0.02
MgO	0.00	0.00	0.03	0.00	0.00	0.00	0.00	0.01
CaO	8.57	5.56	6.13	8.33	6.57	4.80	8.28	6.74
Na_2O	6.75	8.17	7.42	6.99	6.05	8.34	6.55	6.89
K_2O	0.16	0.48	0.74	0.06	1.88	0.64	0.17	0.77
Total	101.22	100.76	99.17	101.16	100.55	100.09	99.33	99.49
Si	2.584	2.705	2.651	2.599	2.549	2.728	2.607	2.624
Ti	0.000	0.000	0.000	0.000	0.001	0.001	0.000	0.000
Cr	0.001	0.002	0.001	0.000	0.002	0.001	0.001	0.000
Al	1.420	1.300	1.361	1.402	1.506	1.286	1.405	1.405
Fe3	0.000	0.002	0.001	0.001	0.000	0.001	0.000	0.000
Fe2	0.002	0.000	0.000	0.000	0.000	0.000	0.004	0.002
Mn	0.000	0.002	0.001	0.001	0.000	0.001	0.000	0.001
Mg	0.000	0.000	0.002	0.000	0.000	0.000	0.000	0.000
Ca	0.406	0.263	0.295	0.395	0.313	0.228	0.400	0.324
Na	0.579	0.699	0.646	0.599	0.522	0.717	0.573	0.599
K	0.009	0.027	0.042	0.003	0.107	0.036	0.010	0.044
Σ Cations	5.000	5.000	5.000	5.000	5.000	5.000	5.000	5.000
Albite	0.582	0.707	0.657	0.601	0.554	0.731	0.583	0.619
Anorthite	0.408	0.266	0.300	0.396	0.333	0.232	0.407	0.335
Orthoclase	0.009	0.027	0.043	0.003	0.113	0.037	0.010	0.045

calculated with "Norm" program by P. Ulmer using: FELDSPAR Norm
Normalization CATIONS assuming stoichiometry and chargebalance

Mineral: plagioclase

Granulitic Gabbro mylonitic **94/04/01**

Sample	p04s01p01	p04s01p02	p04s01p03	p04s01p06	p04s01p14	p04s03p07	p04s03p09	p04s03p10	p04s03p20
Site	s01	s01	s01	s01	s01	s03	s03	s03	s03
nr.	1	2	3	6	14	32	34	35	45
note	plg porphyroclast				to gt	plg clasts (in contact to amp and gt)			
SiO_2	55.66	55.77	56.33	56.57	57.65	57.03	57.00	57.43	55.01
TiO_2	0.02	0.00	0.03	0.00	0.00	0.00	0.00	0.01	0.00
Cr_2O_3	0.04	0.00	0.04	0.00	0.03	0.00	0.00	0.01	0.00
Al_2O_3	28.49	28.79	28.45	28.04	27.34	28.07	27.11	27.99	28.88
Fe_2O_3	0.00	0.00	0.00	0.00	0.00	0.00	0.00	0.00	0.00
FeO	0.00	0.04	0.02	0.04	0.12	0.07	0.08	0.05	0.02
MnO	0.01	0.00	0.00	0.00	0.00	0.03	0.00	0.01	0.00
MgO	0.00	0.00	0.00	0.00	0.00	0.00	0.00	0.00	0.00
NiO	0.00	0.00	0.04	0.00	0.00	0.04	0.03	0.00	0.00
CaO	10.98	11.01	10.83	10.26	9.76	10.04	9.46	9.91	11.04
Na_2O	5.44	5.35	5.62	5.56	5.90	5.64	5.98	5.84	5.30
K_2O	0.12	0.14	0.13	0.10	0.08	0.08	0.08	0.05	0.07
Total	100.76	101.09	101.49	100.57	100.90	101.01	99.74	101.31	100.33
Si	2.490	2.488	2.501	2.536	2.573	2.546	2.571	2.552	2.472
Ti	0.001	0.000	0.001	0.000	0.000	0.000	0.000	0.000	0.000
Cr	0.002	0.000	0.001	0.000	0.001	0.000	0.000	0.001	0.000
Al	1.502	1.514	1.489	1.481	1.439	1.476	1.441	1.466	1.530
Fe3	0.000	0.000	0.000	0.000	0.000	0.000	0.000	0.000	0.000
Fe2	0.000	0.002	0.001	0.002	0.005	0.003	0.003	0.002	0.001
Mn	0.001	0.000	0.000	0.000	0.000	0.001	0.000	0.001	0.000
Mg	0.000	0.000	0.000	0.000	0.000	0.000	0.000	0.001	0.000
Ni	0.000	0.000	0.001	0.000	0.000	0.002	0.001	0.000	0.000
Ca	0.526	0.526	0.515	0.493	0.467	0.480	0.457	0.472	0.532
Na	0.472	0.463	0.484	0.483	0.511	0.488	0.523	0.503	0.462
K	0.007	0.008	0.007	0.006	0.005	0.005	0.005	0.003	0.004
Σ Cations	5.000	5.000	5.000	5.000	5.000	5.000	5.000	5.000	5.000
Albite	0.470	0.464	0.481	0.492	0.520	0.502	0.531	0.515	0.463
Anorthite	0.524	0.528	0.512	0.502	0.475	0.493	0.464	0.482	0.533
Orthoclase	0.007	0.008	0.007	0.006	0.005	0.005	0.005	0.003	0.004

calculated with "Norm" program by P. Ulmer using: FELDSPAR Norm

Normalization CATIONS assuming stoichiometry and chargebalance

Mineral: plagioclase

Granulitic Gabbro undeformed **94/04/01**

Sample	p06s01p04	p06s01p05	p06s01p10	p06s01p12	p06s01p14	p06s02p08	p06s02p09	p06s02p18	p06s02p26
Site	s01	s01	s01	s01	s01	s02	s02	s02	s02
nr.	4	5	10	12	14	33	34	8	17
note	in contact to cpx		to gt	in contact to gt		cpx and gt		in contact to gt	
SiO_2	58.60	57.68	58.99	55.80	57.11	56.98	56.14	54.55	58.66
TiO_2	0.01	0.02	0.00	0.02	0.04	0.00	0.00	0.00	0.00
Cr_2O_3	0.03	0.00	0.00	0.00	0.00	0.00	0.00	0.00	0.00
Al_2O_3	26.66	27.00	26.76	27.56	27.00	27.31	27.22	28.78	26.71
Fe_2O_3	0.00	0.00	0.00	0.00	0.08	0.00	0.07	0.07	0.00
FeO	0.07	0.03	0.05	0.05	0.07	0.19	0.00	0.00	0.06
MnO	0.00	0.00	0.01	0.01	0.01	0.00	0.03	0.00	0.02
MgO	0.00	0.03	0.00	0.00	0.00	0.00	0.01	0.00	0.00
NiO	0.05	0.00	0.00	0.03	0.04	0.00	0.00	0.00	0.00
CaO	9.10	9.55	8.74	10.45	9.34	9.64	9.83	11.14	9.06
Na_2O	6.35	6.19	6.39	5.56	6.27	6.14	6.03	5.44	6.24
K_2O	0.19	0.19	0.18	0.30	0.17	0.12	0.12	0.14	0.14
Total	101.08	100.69	101.13	99.77	100.13	100.38	99.45	100.13	100.91
Si	2.605	2.574	2.620	2.520	2.561	2.551	2.536	2.453	2.614
Ti	0.000	0.001	0.000	0.001	0.001	0.000	0.000	0.000	0.000
Cr	0.001	0.000	0.000	0.000	0.000	0.000	0.000	0.000	0.000
Al	1.397	1.420	1.401	1.467	1.427	1.441	1.449	1.525	1.403
Fe3	0.000	0.000	0.000	0.000	0.003	0.000	0.003	0.003	0.000
Fe2	0.003	0.001	0.002	0.002	0.003	0.007	0.000	0.000	0.002
Mn	0.000	0.000	0.001	0.001	0.001	0.000	0.001	0.000	0.001
Mg	0.000	0.002	0.000	0.000	0.000	0.000	0.001	0.000	0.000
Ni	0.002	0.000	0.000	0.001	0.001	0.000	0.000	0.000	0.000
Ca	0.434	0.456	0.416	0.506	0.449	0.462	0.476	0.537	0.433
Na	0.548	0.535	0.550	0.487	0.545	0.533	0.528	0.474	0.539
K	0.011	0.011	0.010	0.017	0.010	0.007	0.007	0.008	0.008
Σ Cations	5.000	5.000	5.000	5.000	5.000	5.000	5.000	5.000	5.000
Albite	0.552	0.534	0.563	0.482	0.543	0.532	0.522	0.465	0.550
Anorthite	0.437	0.455	0.426	0.501	0.447	0.462	0.471	0.527	0.442
Orthoclase	0.011	0.011	0.010	0.017	0.010	0.007	0.007	0.008	0.008

calculated with "Norm" program by P. Ulmer using: FELDSPAR Norm

Normalization CATIONS assuming stoichiometry and chargebalance

Mineral: plagioclase

Sarangar Gabbro mylonitic **90/02/01**

Sample	p07s05p17	p07s05p25	p07s05p29	p07s06p17	p07s06p18	p07s06p19	p07s06p20	p07s06p23	p07s06p25
Site	s05	s05	s05	s06	s06	s06	s06	s06	s06
nr.	87	95	99	117	118	119	120	123	125
note		at amp	at gt	at gt, amp, epi				at amp, epi	
SiO_2	59.43	60.41	59.10	59.37	60.16	59.46	59.88	60.02	59.89
TiO_2	0.00	0.00	0.00	0.02	0.03	0.02	0.00	0.04	0.00
Cr_2O_3	0.00	0.02	0.01	0.00	0.00	0.01	0.01	0.02	0.00
Al_2O_3	25.74	25.63	25.27	25.41	25.63	25.79	25.74	25.61	25.78
Fe_2O_3	0.17	0.00	0.12	0.39	0.11	0.07	0.10	0.13	0.10
FeO	0.00	0.16	0.00	0.00	0.00	0.00	0.00	0.00	0.00
MnO	0.05	0.00	0.00	0.02	0.04	0.05	0.02	0.03	0.00
MgO	0.00	0.02	0.00	0.00	0.00	0.00	0.03	0.00	0.00
NiO	0.08	0.00	0.03	0.06	0.00	0.00	0.00	0.08	0.01
CaO	7.42	6.78	7.19	7.01	7.19	7.48	7.25	7.60	7.72
Na_2O	7.78	7.65	7.70	7.88	7.80	7.66	7.59	7.76	7.57
K_2O	0.06	0.08	0.09	0.05	0.07	0.10	0.08	0.07	0.09
Total	100.75	100.75	99.52	100.20	101.03	100.65	100.72	101.36	101.16
Si	2.627	2.673	2.644	2.638	2.652	2.632	2.651	2.639	2.640
Ti	0.000	0.000	0.000	0.001	0.001	0.001	0.000	0.001	0.000
Cr	0.000	0.001	0.001	0.000	0.000	0.001	0.001	0.001	0.000
Al	1.341	1.337	1.333	1.331	1.332	1.345	1.343	1.327	1.339
Fe3	0.006	0.000	0.004	0.013	0.004	0.002	0.004	0.004	0.004
Fe2	0.000	0.006	0.000	0.000	0.000	0.000	0.000	0.000	0.000
Mn	0.002	0.000	0.000	0.001	0.002	0.002	0.001	0.001	0.000
Mg	0.001	0.001	0.000	0.000	0.000	0.000	0.002	0.000	0.000
Ni	0.003	0.000	0.001	0.002	0.000	0.000	0.000	0.003	0.000
Ca	0.351	0.321	0.345	0.334	0.340	0.355	0.344	0.358	0.365
Na	0.667	0.656	0.668	0.679	0.667	0.657	0.651	0.662	0.647
K	0.004	0.005	0.005	0.003	0.004	0.006	0.005	0.004	0.005
Σ Cations	5.000	5.000	5.000	5.000	5.000	5.000	5.000	5.000	5.000
Albite	0.653	0.668	0.656	0.669	0.660	0.646	0.651	0.647	0.636
Anorthite	0.344	0.327	0.339	0.329	0.336	0.348	0.344	0.350	0.359
Orthoclase	0.004	0.005	0.005	0.003	0.004	0.006	0.005	0.004	0.005

calculated with "Norm" program by P. Ulmer using: FELDSPAR Norm
Normalization CATIONS assuming stoichiometry and chargebalance

Mineral: plagioclase

Sarangar Gabbro undeformed **90/02/01**

Sample	p10s01p07	p10s01p08	p10s01p14	p10s01p16	p10s02p06	p10s03p14	p10s03p15	p10s03p24	p10s03p27	p10s03p28
Site	s01	s01	s01	s01	s02	s03	s03	s03	s03	s03
nr.	7	8	14	2	22	61	62	71	74	75
note	in contact to amp		in contact to amp		incl. in cpx	in contact to amp rim		in contact to amp rim		
SiO_2	53.82	54.18	54.45	54.27	54.65	52.24	52.24	53.31	53.35	54.15
TiO_2	0.02	0.01	0.00	0.01	0.02	0.03	0.00	0.00	0.03	0.01
Cr_2O_3	0.00	0.00	0.00	0.03	0.00	0.00	0.02	0.00	0.04	0.01
Al_2O_3	29.40	29.27	29.71	28.76	28.30	28.65	28.70	28.46	28.67	28.22
Fe_2O_3	0.00	0.00	0.00	0.00	0.00	0.13	0.08	0.10	0.13	0.09
FeO	0.18	0.07	0.17	0.18	0.22	0.00	0.00	0.00	0.00	0.00
MnO	0.00	0.03	0.00	0.01	0.01	0.01	0.00	0.04	0.00	0.00
MgO	0.00	0.00	0.00	0.11	0.00	0.00	0.00	0.00	0.00	0.00
NiO	0.04	0.00	0.00	0.02	0.00	0.00	0.05	0.00	0.02	0.04
CaO	12.19	12.09	12.00	11.92	11.36	12.57	12.47	12.12	11.90	11.78
Na_2O	4.09	4.12	4.18	4.73	5.05	4.43	4.60	4.78	4.86	5.09
K_2O	0.09	0.09	0.09	0.08	0.08	0.11	0.10	0.15	0.14	0.16
Total	99.83	99.87	100.61	100.12	99.70	98.19	98.27	98.97	99.14	99.56
Si	2.451	2.466	2.459	2.454	2.478	2.411	2.405	2.436	2.433	2.457
Ti	0.001	0.000	0.000	0.000	0.001	0.001	0.000	0.000	0.001	0.000
Cr	0.000	0.000	0.000	0.001	0.000	0.000	0.001	0.000	0.001	0.001
Al	1.578	1.570	1.582	1.533	1.512	1.558	1.557	1.533	1.541	1.509
Fe3	0.000	0.000	0.000	0.000	0.000	0.004	0.003	0.003	0.005	0.003
Fe2	0.007	0.003	0.006	0.007	0.009	0.000	0.000	0.000	0.000	0.000
Mn	0.000	0.001	0.000	0.001	0.001	0.001	0.000	0.001	0.000	0.000
Mg	0.000	0.000	0.000	0.007	0.000	0.001	0.000	0.001	0.000	0.000
Ni	0.001	0.000	0.000	0.001	0.000	0.000	0.002	0.000	0.001	0.002
Ca	0.595	0.590	0.581	0.578	0.552	0.621	0.615	0.593	0.582	0.572
Na	0.361	0.364	0.366	0.415	0.444	0.397	0.411	0.424	0.429	0.447
K	0.005	0.006	0.005	0.005	0.005	0.007	0.006	0.009	0.008	0.009
Σ Cations	5.000	5.000	5.000	5.000	5.000	5.000	5.000	5.000	5.000	5.000
Albite	0.375	0.379	0.385	0.416	0.444	0.387	0.398	0.413	0.421	0.435
Anorthite	0.619	0.615	0.610	0.579	0.551	0.606	0.596	0.578	0.571	0.556
Orthoclase	0.005	0.006	0.005	0.005	0.005	0.006	0.006	0.009	0.008	0.009

calculated with "Norm" program by P. Ulmer using: FELDSPAR Norm
Normalization CATIONS assuming stoichiometry and chargebalance

Mineral: plagioclase

Sarangar Gabbro mylonitic **16/01/01**

Sample	p11s08pl1	p11s08pl2	p11s08pl4	p11s08pl5	p11s07pl1	p11s04pl1	p11s04pl2	p11s04pl4	p11s04pl5	p11s04pl6	p11s09pl1	p11s09pl2	p11s09pl3
Site	s08	s08	s08	s08	s07	s04	s04	s04	s04	s04	s09	s09	s09
nr.													
note	around mica				at clast	in contact to epi (plg layer)					in contact to amp		
SiO_2	61.23	60.86	58.37	57.26	60.35	58.07	58.06	58.66	60.02	59.80	58.94	58.05	58.27
TiO_2	0.00	0.01	0.02	0.04	0.02	0.02	0.01	0.00	0.00	0.03	0.00	0.00	0.00
Cr_2O_3	0.00	0.00	0.01	0.01	0.03	0.02	0.00	0.00	0.00	0.00	0.02	0.00	0.00
Al_2O_3	25.33	25.86	27.09	27.53	25.64	26.31	26.26	25.86	26.47	26.31	27.39	27.01	27.71
Fe_2O_3	0.00	0.00	0.00	0.05	0.00	0.03	0.04	0.04	0.00	0.03	0.07	0.00	0.01
FeO	0.03	0.04	0.05	0.00	0.04	0.00	0.00	0.00	0.03	0.00	0.00	0.03	0.05
MnO	0.01	0.01	0.02	0.00	0.02	0.02	0.02	0.01	0.03	0.01	0.00	0.00	0.02
MgO	0.00	0.00	0.01	0.00	0.00	0.00	0.00	0.00	0.00	0.00	0.00	0.00	0.00
NiO													
CaO	6.00	6.70	8.73	9.39	7.06	6.99	7.14	6.64	7.32	7.33	8.17	8.34	8.75
Na_2O	8.09	7.82	6.58	6.39	7.61	7.73	7.62	7.94	7.43	7.54	7.14	6.77	6.68
K_2O	0.05	0.05	0.08	0.10	0.07	0.06	0.07	0.06	0.09	0.09	0.05	0.07	0.09
Total	100.72	101.36	100.96	100.77	100.83	99.26	99.22	99.22	101.39	101.15	101.77	100.27	101.59
Si	2.703	2.674	2.592	2.548	2.669	2.599	2.602	2.624	2.641	2.635	2.586	2.590	2.568
Ti	0.000	0.000	0.001	0.001	0.001	0.001	0.000	0.000	0.000	0.001	0.000	0.000	0.000
Cr	0.000	0.000	0.000	0.000	0.001	0.001	0.000	0.000	0.000	0.000	0.001	0.000	0.000
Al	1.318	1.339	1.418	1.444	1.336	1.388	1.387	1.364	1.373	1.367	1.417	1.421	1.440
Fe3	0.000	0.000	0.000	0.002	0.000	0.001	0.001	0.002	0.000	0.001	0.003	0.000	0.000
Fe2	0.001	0.001	0.002	0.000	0.002	0.000	0.000	0.000	0.001	0.000	0.000	0.001	0.002
Mn	0.000	0.001	0.001	0.000	0.001	0.001	0.001	0.000	0.001	0.000	0.000	0.000	0.001
Mg	0.000	0.000	0.001	0.000	0.000	0.000	0.000	0.000	0.000	0.000	0.000	0.000	0.000
Ni													
Ca	0.284	0.316	0.416	0.448	0.335	0.335	0.343	0.318	0.345	0.346	0.384	0.399	0.413
Na	0.692	0.667	0.566	0.552	0.652	0.671	0.662	0.689	0.634	0.645	0.607	0.586	0.571
K	0.003	0.003	0.004	0.006	0.004	0.004	0.004	0.003	0.005	0.005	0.003	0.004	0.005
Σ Cations	5.000	5.000	5.000	5.000	5.000	5.000	5.000	5.000	5.000	5.000	5.000	5.000	5.000
Albite	0.707	0.677	0.574	0.549	0.658	0.664	0.656	0.682	0.644	0.647	0.611	0.592	0.577
Anorthite	0.290	0.320	0.421	0.446	0.338	0.332	0.340	0.315	0.351	0.348	0.386	0.404	0.418
Orthoclase	0.003	0.003	0.004	0.005	0.004	0.003	0.004	0.003	0.005	0.005	0.003	0.004	0.005

calculated with "Norm" program by P. Ulmer using: FELDSPAR Norm
Normalization CATIONS assuming stoichiometry and chargebalance

Mineral: plagioclase

Sarangar Gabbro undeformed **16/01/01**

Sample	p13s1cpl3	p13s1cpl4	p13s3apl1	p13s3apl2	p13s3bpl2	p13s3bpl3
Site	s01	s01	s03	s03	s03	s03
nr.						
note	around amp		in contact to amp		in contact to amp	
SiO_2	54.80	54.81	52.39	52.56	53.68	54.03
TiO_2	0.02	0.00	0.00	0.03	0.02	0.01
Cr_2O_3	0.00	0.02	0.00	0.00	0.00	0.00
Al_2O_3	30.14	30.16	31.30	31.00	30.69	30.39
Fe_2O_3	0.00	0.00	0.00	0.00	0.10	0.00
FeO	0.08	0.06	0.07	0.11	0.00	0.02
MnO	0.06	0.00	0.03	0.00	0.00	0.00
MgO	0.00	0.00	0.00	0.02	0.00	0.00
NiO						
CaO	11.65	11.51	13.21	13.50	12.27	12.20
Na_2O	5.00	5.01	4.00	3.59	4.69	4.70
K_2O	0.08	0.07	0.13	0.20	0.09	0.08
Total	101.81	101.63	101.12	101.00	101.53	101.44
Si	2.431	2.435	2.351	2.370	2.390	2.408
Ti	0.001	0.000	0.000	0.001	0.001	0.000
Cr	0.000	0.001	0.000	0.000	0.000	0.000
Al	1.576	1.579	1.655	1.647	1.611	1.597
Fe3	0.000	0.000	0.000	0.000	0.003	0.000
Fe2	0.003	0.002	0.003	0.004	0.000	0.001
Mn	0.002	0.000	0.001	0.000	0.000	0.000
Mg	0.000	0.000	0.000	0.001	0.000	0.000
Ni						
Ca	0.554	0.548	0.635	0.652	0.586	0.583
Na	0.430	0.432	0.348	0.314	0.405	0.407
K	0.005	0.004	0.007	0.011	0.005	0.005
Σ Cations	5.000	5.000	5.000	5.000	5.000	5.000
Albite	0.435	0.439	0.351	0.321	0.407	0.409
Anorthite	0.560	0.557	0.642	0.667	0.588	0.586
Orthoclase	0.005	0.004	0.007	0.012	0.005	0.005

calculated with "Norm" program by P. Ulmer using: FELDSPAR Norm
Normalization CATIONS assuming stoichiometry and chargebalance

Mineral: plagioclase

Kiru Amphibolite **46/02/01**

Sample	p19s01p10	p19s01p11	p19s02p06	p19s02p07	p19s02p17	p19s02p18	p19s02p19	p19s03p22	p19s03p23	p19s03p29	p19s03p30	p19s04p06	p19s04p11	p19s04p12	p19s04p13	p19s04p14	p19s04p21	p19s05p03	p19s06p04
Site	s01	s01	s02	s02	s02	s02	s02	s03	s03	s03	s03	s04	s04	s04	s04	s04	s04	s05	s06
nr.	10	11	17	18	28	29	30	52	53	59	60	66	71	72	73	74	81	83	94
note	in contact to amp				in contact to amp											in contact to amp			
SiO_2	58.49	58.71	62.90	57.62	58.44	58.19	55.60	58.49	58.90	56.17	57.12	63.34	62.58	59.95	59.39	58.69	58.99	58.66	61.16
TiO_2	0.00	0.00	0.02	0.00	0.01	0.00	0.00	0.00	0.00	0.00	0.00	0.00	0.00	0.03	0.01	0.03	0.00	0.00	0.00
Cr_2O_3	0.01	0.00	0.00	0.02	0.01	0.02	0.00	0.00	0.00	0.00	0.00	0.00	0.00	0.00	0.00	0.02	0.00	0.01	0.00
Al_2O_3	25.86	25.80	22.77	25.08	25.83	26.02	25.94	26.67	26.74	25.52	24.73	22.19	23.53	25.25	25.53	25.64	26.03	25.86	23.38
Fe_2O_3	0.05	0.08	0.16	0.30	0.21	0.16	0.36	0.12	0.12	0.61	0.62	0.44	0.13	0.05	0.08	0.11	0.11	0.13	0.15
FeO	0.00	0.00	0.00	0.00	0.00	0.00	0.00	0.00	0.00	0.00	0.00	0.00	0.00	0.00	0.00	0.00	0.00	0.00	0.00
MnO	0.03	0.01	0.03	0.04	0.03	0.00	0.04	0.03	0.04	0.06	0.01	0.00	0.04	0.00	0.03	0.01	0.00	0.00	0.03
MgO	0.00	0.00	0.00	0.03	0.00	0.00	0.00	0.00	0.00	0.02	0.00	0.07	0.25	0.00	0.00	0.00	0.00	0.00	0.00
NiO	0.00	0.00	0.06	0.00	0.02	0.00	0.05	0.03	0.03	0.00	0.00	0.01	0.04	0.02	0.03	0.00	0.00	0.00	0.00
CaO	7.29	7.33	4.11	8.87	7.42	7.48	10.60	8.03	8.09	10.51	9.53	4.39	3.55	6.37	6.79	7.18	7.30	7.31	6.29
Na_2O	7.66	7.60	9.95	7.65	7.51	7.49	6.82	7.37	7.41	6.95	7.31	9.69	8.52	8.19	7.95	7.77	7.76	7.58	9.04
K_2O	0.11	0.14	0.05	0.05	0.13	0.07	0.03	0.10	0.09	0.03	0.04	0.07	1.13	0.15	0.13	0.13	0.05	0.08	0.04
Total	99.50	99.68	100.03	99.66	99.62	99.45	99.44	100.82	101.42	99.88	99.37	100.21	99.78	100.02	99.94	99.59	100.24	99.64	100.11
Si	2.615	2.622	2.766	2.574	2.614	2.606	2.501	2.587	2.590	2.517	2.569	2.790	2.778	2.660	2.641	2.621	2.618	2.622	2.702
Ti	0.000	0.000	0.001	0.000	0.000	0.000	0.000	0.000	0.000	0.000	0.000	0.000	0.000	0.001	0.000	0.001	0.000	0.000	0.000
Cr	0.000	0.000	0.000	0.001	0.000	0.001	0.000	0.000	0.000	0.000	0.000	0.000	0.000	0.000	0.000	0.001	0.000	0.001	0.000
Al	1.362	1.358	1.180	1.321	1.362	1.374	1.376	1.390	1.386	1.348	1.311	1.152	1.231	1.320	1.338	1.349	1.361	1.362	1.217
Fe3	0.002	0.003	0.005	0.010	0.007	0.006	0.012	0.004	0.004	0.021	0.021	0.015	0.005	0.002	0.003	0.004	0.004	0.005	0.005
Fe2	0.000	0.000	0.000	0.000	0.000	0.000	0.000	0.000	0.000	0.000	0.000	0.000	0.000	0.000	0.000	0.000	0.000	0.000	0.000
Mn	0.001	0.001	0.001	0.002	0.001	0.000	0.002	0.001	0.001	0.002	0.001	0.000	0.002	0.000	0.001	0.001	0.000	0.000	0.001
Mg	0.000	0.000	0.000	0.002	0.000	0.000	0.000	0.000	0.000	0.001	0.000	0.005	0.017	0.000	0.000	0.000	0.000	0.000	0.000
Ni	0.000	0.000	0.002	0.000	0.001	0.000	0.002	0.001	0.001	0.000	0.000	0.000	0.001	0.001	0.001	0.000	0.000	0.000	0.000
Ca	0.349	0.351	0.194	0.425	0.356	0.359	0.511	0.380	0.381	0.505	0.459	0.207	0.169	0.303	0.324	0.344	0.347	0.350	0.298
Na	0.664	0.658	0.848	0.663	0.651	0.651	0.595	0.632	0.632	0.604	0.637	0.827	0.734	0.704	0.685	0.673	0.667	0.657	0.775
K	0.006	0.008	0.003	0.003	0.007	0.004	0.002	0.005	0.005	0.001	0.002	0.004	0.064	0.009	0.007	0.007	0.003	0.005	0.002
Σ Cations	5.000	5.000	5.000	5.000	5.000	5.000	5.000	5.000	5.000	5.000	5.000	5.000	5.000	5.000	5.000	5.000	5.000	5.000	5.000
Albite	0.651	0.647	0.812	0.608	0.642	0.642	0.537	0.621	0.621	0.544	0.580	0.797	0.759	0.693	0.674	0.657	0.656	0.649	0.721
Anorthite	0.343	0.345	0.185	0.389	0.351	0.354	0.461	0.374	0.374	0.455	0.418	0.199	0.175	0.298	0.319	0.336	0.341	0.346	0.277
Orthoclase	0.006	0.008	0.003	0.002	0.007	0.004	0.002	0.005	0.005	0.001	0.002	0.004	0.066	0.009	0.007	0.007	0.003	0.005	0.002

calculated with "Norm" program by P. Ulmer using: FELDSPAR Norm

Normalization CATIONS assuming stoichiometry and chargebalance

Table Appendix 3.2: Representative chemical composition of garnet.

	Mineral: garnet																		
	Granulitic Gabbro mylonitic **13/01/01**																		
Sample	p01s01gt1	p01s01gt2	p01s01gt3	p01s01gt4	p01s01gt5	p01s01gt6	p01s01gt7	p01so2gt2	p01so2gt1	p01s03gt4	p01s03gt6	p01s03gt5	p01s03gt3	p01so4gt5	p01so4gt3	p01so4gt2	p01s04gt1	p01s09gt3	p01s09gt2
Site	s01	s01	s01	s01	s01	s01	s01	s02	s02	s03	s03	s03	s03	s04	s04	s04	s04	s09	s09
nr.																			
note	profile across porphyroclast							gt with inclusion S02		gt porpyroclast with inclusion				big gt porphyroclast in less def. part				gt in contact to amp	
SiO_2	39.78	39.88	39.71	39.86	39.80	39.81	40.00	39.81	39.66	39.98	39.64	39.97	40.00	39.66	39.59	39.76	39.81	39.40	39.19
TiO_2	0.10	0.10	0.11	0.09	0.12	0.09	0.12	0.15	0.14	0.11	0.10	0.09	0.10	0.06	0.05	0.05	0.05	0.15	0.26
Cr_2O_3	0.00	0.06	0.07	0.09	0.09	0.06	0.06	0.04	0.13	0.01	0.00	0.00	0.01	0.05	0.04	0.01	0.00	0.00	0.00
Al_2O_3	22.07	22.00	21.99	22.03	22.00	21.97	22.01	22.11	21.87	22.34	22.17	22.53	22.27	22.45	22.49	22.46	22.51	21.86	21.95
Fe_2O_3	1.10	0.91	0.76	1.35	1.64	1.17	0.10	0.77	1.24	0.14	0.48	0.64	0.66	0.57	1.12	0.01	0.69	1.13	0.93
FeO	20.71	20.75	20.79	20.61	20.49	20.28	21.06	20.74	20.31	21.79	22.76	21.31	21.38	20.20	19.50	20.57	20.28	21.39	21.37
MnO	0.57	0.61	0.60	0.62	0.63	0.60	0.57	0.53	0.50	0.47	0.71	0.54	0.54	0.51	0.52	0.56	0.56	0.48	0.44
MgO	9.55	9.58	9.56	9.60	9.80	9.73	9.36	9.76	9.65	9.69	8.27	9.58	9.62	10.02	9.69	9.85	9.60	9.17	9.20
NiO																			
CaO	7.17	7.10	7.02	7.17	6.93	7.25	7.36	6.94	7.31	6.39	7.14	6.92	6.79	6.81	7.62	6.78	7.43	7.03	6.84
Na_2O	0.02	0.03	0.04	0.03	0.04	0.01	0.03	0.04	0.03	0.03	0.03	0.01	0.03	0.03	0.05	0.05	0.02	0.01	0.02
K_2O	0.03	0.03	0.00	0.02	0.02	0.04	0.01	0.00	0.01	0.02	0.00	0.00	0.01	0.01	0.03	0.00	0.03	0.00	0.00
Total	101.10	101.06	100.64	101.46	101.55	101.01	100.68	100.88	100.84	100.98	101.30	101.58	101.42	100.37	100.70	100.09	100.98	100.60	100.20
Si	2.989	2.996	2.995	2.985	2.978	2.990	3.014	2.992	2.986	3.003	2.995	2.986	2.995	2.986	2.974	3.001	2.986	2.984	2.978
Ti	0.006	0.006	0.006	0.005	0.007	0.005	0.007	0.008	0.008	0.006	0.006	0.005	0.005	0.003	0.003	0.003	0.003	0.008	0.015
Cr	0.000	0.004	0.004	0.005	0.005	0.004	0.004	0.002	0.008	0.001	0.000	0.000	0.001	0.003	0.003	0.001	0.000	0.000	0.000
Al	1.954	1.948	1.955	1.945	1.940	1.945	1.955	1.959	1.940	1.978	1.975	1.984	1.966	1.992	1.991	1.998	1.989	1.951	1.966
Fe^3	0.062	0.052	0.043	0.076	0.092	0.066	0.006	0.043	0.070	0.008	0.027	0.036	0.038	0.032	0.063	0.000	0.039	0.064	0.053
Fe^2	1.301	1.304	1.312	1.291	1.282	1.274	1.327	1.304	1.279	1.369	1.438	1.332	1.339	1.272	1.225	1.298	1.272	1.355	1.358
Mn	0.036	0.039	0.038	0.039	0.040	0.038	0.037	0.034	0.032	0.030	0.046	0.034	0.034	0.033	0.033	0.036	0.036	0.031	0.028
Mg	1.069	1.073	1.075	1.071	1.093	1.089	1.052	1.093	1.083	1.085	0.931	1.067	1.073	1.125	1.085	1.108	1.073	1.035	1.042
Ni																			
Ca	0.577	0.572	0.567	0.576	0.555	0.584	0.594	0.559	0.590	0.515	0.578	0.554	0.545	0.550	0.614	0.548	0.597	0.571	0.557
Na	0.003	0.005	0.005	0.005	0.005	0.002	0.004	0.006	0.004	0.004	0.004	0.002	0.004	0.004	0.008	0.007	0.003	0.001	0.003
K	0.002	0.003	0.000	0.002	0.002	0.004	0.001	0.000	0.001	0.002	0.000	0.000	0.001	0.001	0.002	0.000	0.003	0.000	0.001
Σ Cations	8.000	8.000	8.000	8.000	8.000	8.000	8.000	8.000	8.000	8.000	8.000	8.000	8.000	8.000	8.000	8.000	8.000	8.000	8.000
Grossular	0.158	0.159	0.162	0.149	0.133	0.157	0.188	0.159	0.154	0.163	0.176	0.165	0.159	0.164	0.172	0.181	0.179	0.154	0.152
Almandine	0.435	0.436	0.438	0.433	0.431	0.426	0.440	0.435	0.428	0.456	0.480	0.445	0.447	0.427	0.414	0.434	0.427	0.453	0.454
Pyrope	0.358	0.358	0.359	0.359	0.367	0.364	0.349	0.365	0.362	0.361	0.311	0.357	0.358	0.377	0.367	0.370	0.360	0.346	0.349
Spessartite	0.012	0.013	0.013	0.013	0.013	0.013	0.012	0.011	0.011	0.010	0.015	0.012	0.011	0.011	0.011	0.012	0.012	0.010	0.009
Andradite	0.031	0.026	0.021	0.038	0.046	0.033	0.003	0.022	0.035	0.004	0.014	0.018	0.019	0.016	0.032	0.000	0.020	0.032	0.027

calculated with "Norm" program by P. Ulmer using: GARNET Norm

Normalization on the basis of 7 CATIONS and 24 CHARGES

Mineral: garnet

Granulitic Gabbro undeformed **13/01/01**

Sample	p02s01gt5	p02s01gt4	p02s01gt3	p02s01gt1	p02s02gt2	p02s02gt1	p02s04gt4	p02s04gt2	p02s04gt3	p02s04gt9	p02s04gt8	p02s04gt7	p02s04gt6	p02s04gt5	p02s05gt3	p02s05gt2	p02s06gt5	p02s06gt2	p02s06gt3
Site	s01	s01	s01	s01	s02	s02	s04	s04	s04	s04	s04	s04	s04	s04	s05	s05	s06	s06	s06
nr.																			
note	gt in contact to cpx				gt in contact to plg		gt profile								gt in contact to plg		gt in contact to plg		
SiO_2	40.25	40.43	40.34	40.57	39.83	39.82	39.87	40.34	40.29	40.19	40.25	38.97	40.25	40.17	40.34	40.46	40.12	38.83	40.22
TiO_2	0.07	0.04	0.05	0.06	0.09	0.08	0.04	0.08	0.01	0.07	0.05	0.07	0.04	0.04	0.12	0.08	0.07	0.08	0.12
Cr_2O_3	0.04	0.00	0.06	0.15	0.09	0.01	0.04	0.04	0.03	0.00	0.02	0.02	0.03	0.00	0.00	0.01	0.00	0.05	0.00
Al_2O_3	22.60	22.57	22.52	22.53	22.34	22.56	22.40	22.51	22.48	22.47	22.48	21.99	22.60	22.63	22.20	22.36	22.62	22.17	22.50
Fe_2O_3	0.00	0.00	0.00	0.00	0.98	0.17	0.04	0.39	0.27	0.26	0.60	1.75	0.51	0.55	0.00	0.00	0.78	1.79	0.23
FeO	20.80	20.69	20.78	20.81	20.17	20.69	21.60	20.41	20.14	20.34	20.18	18.96	20.40	20.12	21.30	21.21	20.09	18.21	20.39
MnO	0.54	0.56	0.58	0.55	0.65	0.49	0.67	0.60	0.55	0.61	0.57	0.61	0.64	0.65	0.53	0.63	0.52	0.58	0.50
MgO	9.61	9.48	9.44	9.55	9.99	9.78	8.39	9.82	9.39	9.95	9.77	10.00	9.66	9.58	9.51	9.45	10.18	9.76	9.94
NiO																			
CaO	7.43	7.68	7.66	7.42	6.97	6.96	8.18	7.53	8.28	7.19	7.62	6.99	7.60	7.88	7.17	7.26	7.00	7.79	7.25
Na_2O	0.02	0.02	0.03	0.01	0.03	0.03	0.00	0.02	0.03	0.04	0.03	0.05	0.02	0.02	0.04	0.05	0.05	0.06	0.05
K_2O	0.00	0.00	0.03	0.02	0.00	0.01	0.00	0.01	0.01	0.01	0.03	0.03	0.01	0.01	0.01	0.01	0.03	0.02	0.03
Total	101.36	101.48	101.50	101.66	101.13	100.59	101.22	101.74	101.48	101.13	101.60	99.44	101.77	101.66	101.22	101.53	101.45	99.35	101.23
Si	3.005	3.016	3.010	3.022	2.982	2.994	3.002	3.000	3.005	3.003	2.997	2.965	2.994	2.991	3.022	3.021	2.987	2.954	3.002
Ti	0.004	0.002	0.003	0.003	0.005	0.004	0.002	0.004	0.001	0.004	0.003	0.004	0.002	0.002	0.007	0.005	0.004	0.005	0.007
Cr	0.002	0.000	0.004	0.009	0.005	0.000	0.002	0.002	0.002	0.000	0.001	0.001	0.002	0.000	0.000	0.001	0.000	0.003	0.000
Al	1.989	1.985	1.980	1.978	1.971	1.999	1.988	1.973	1.976	1.979	1.973	1.971	1.982	1.986	1.960	1.967	1.984	1.988	1.979
Fe^3	0.000	0.000	0.000	0.000	0.055	0.010	0.003	0.022	0.015	0.015	0.034	0.100	0.029	0.031	0.000	0.000	0.044	0.103	0.013
Fe^2	1.299	1.291	1.297	1.297	1.263	1.301	1.360	1.269	1.256	1.271	1.257	1.206	1.269	1.253	1.334	1.325	1.251	1.159	1.273
Mn	0.034	0.036	0.037	0.035	0.041	0.031	0.043	0.038	0.035	0.039	0.036	0.039	0.040	0.041	0.033	0.040	0.033	0.037	0.032
Mg	1.070	1.054	1.050	1.061	1.115	1.095	0.941	1.088	1.044	1.109	1.085	1.134	1.072	1.063	1.062	1.052	1.130	1.106	1.105
Ni																			
Ca	0.595	0.614	0.612	0.592	0.559	0.561	0.660	0.600	0.662	0.576	0.608	0.570	0.606	0.629	0.575	0.581	0.559	0.635	0.579
Na	0.003	0.003	0.005	0.002	0.004	0.004	0.000	0.003	0.004	0.006	0.004	0.007	0.004	0.003	0.005	0.008	0.007	0.008	0.007
K	0.000	0.000	0.003	0.002	0.001	0.001	0.000	0.001	0.001	0.001	0.003	0.003	0.001	0.001	0.001	0.001	0.002	0.002	0.003
Σ Cations	8.000	8.000	8.000	8.000	8.000	8.000	8.000	8.000	8.000	8.000	8.000	8.000	8.000	8.000	8.000	8.000	8.000	8.000	8.000
Grossular	0.195	0.203	0.200	0.192	0.154	0.180	0.216	0.185	0.212	0.182	0.184	0.139	0.186	0.193	0.187	0.190	0.163	0.159	0.182
Almandine	0.433	0.431	0.432	0.434	0.423	0.435	0.453	0.423	0.419	0.424	0.421	0.408	0.425	0.419	0.443	0.441	0.420	0.394	0.425
Pyrope	0.357	0.352	0.350	0.355	0.374	0.366	0.313	0.363	0.348	0.370	0.363	0.384	0.359	0.356	0.353	0.350	0.380	0.376	0.369
Spessartite	0.011	0.012	0.012	0.012	0.014	0.010	0.014	0.013	0.012	0.013	0.012	0.013	0.013	0.014	0.011	0.013	0.011	0.013	0.011
Andradite	0.000	0.000	0.000	0.000	0.028	0.005	0.001	0.011	0.007	0.007	0.017	0.051	0.014	0.015	0.000	0.000	0.022	0.052	0.007

calculated with "Norm" program by P. Ulmer using: GARNET Norm

Normalization on the basis of 7 CATIONS and 24 CHARGES

Mineral: garnet

Granulitic Gabbro mylonitic **94/04/01**

Sample	p04s01p08	p04s01p09	p04s01p10	p04s01p11	p04s01p12	p04s01p16	p04s01p17	p04s02p01	p04s02p02	p04s02p03	p04s02p07	p04s02p08	p04s02p12	p04s02p13	p04s02p23	p04s02p24	p04s02p25	p04s03p01	p04s03p02
Site	s01	s01	s01	s01	s01	s01	s01	s02	s02	s02	s02	s02	s02	s02	s02	s02	s02	s03	s03
nr.	8	9	10	11	12	16	17	1	2	3	7	8	12	13	23	24	25	26	27
note	gt profile					gt in contact to plg		gt porphyroclast							gt porphyroclast			profile through gt clast	
SiO_2	39.46	38.81	39.58	39.59	39.78	39.58	39.31	38.97	39.38	39.27	38.94	39.47	39.36	39.18	38.85	39.36	39.06	39.64	39.42
TiO_2	0.07	0.09	0.10	0.09	0.08	0.09	0.08	0.08	0.10	0.08	0.09	0.05	0.08	0.05	0.08	0.06	0.06	0.07	0.06
Cr_2O_3	0.00	0.00	0.00	0.00	0.01	0.03	0.00	0.00	0.00	0.00	0.00	0.00	0.00	0.00	0.01	0.00	0.00	0.00	0.01
Al_2O_3	21.48	21.18	21.63	21.59	21.71	21.93	21.72	21.64	21.84	21.87	21.83	21.90	21.86	21.80	21.34	22.02	21.61	21.68	21.63
Fe_2O_3	0.76	0.00	0.08	0.67	0.00	0.59	0.34	1.90	1.79	1.32	1.48	1.43	1.22	1.31	1.41	1.73	1.57	0.71	0.00
FeO	21.42	21.60	22.10	22.07	22.26	21.67	21.77	21.75	20.41	20.26	21.47	20.64	20.53	20.56	21.15	19.98	19.98	20.70	20.45
MnO	0.42	0.43	0.46	0.50	0.41	0.45	0.45	0.70	0.55	0.55	0.74	0.58	0.55	0.55	0.62	0.49	0.50	0.47	0.45
MgO	7.52	7.24	7.83	7.95	7.88	7.59	7.27	7.32	8.57	8.65	7.59	8.71	8.73	9.36	8.15	9.01	8.53	8.37	8.33
NiO	0.00	0.00	0.00	0.00	0.00	0.00	0.00	0.03	0.00	0.00	0.00	0.05	0.00	0.02	0.00	0.02	0.00	0.03	0.00
CaO	9.30	8.67	8.46	8.19	8.33	9.02	9.29	8.55	8.51	8.30	8.36	8.12	8.18	7.08	7.95	8.23	8.52	8.80	8.78
Na_2O	0.01	0.06	0.00	0.03	0.04	0.04	0.00	0.04	0.00	0.03	0.03	0.01	0.00	0.00	0.00	0.00	0.03	0.00	0.00
K_2O	0.00	0.02	0.01	0.01	0.00	0.00	0.00	0.00	0.00	0.00	0.02	0.00	0.00	0.00	0.00	0.00	0.00	0.02	0.01
Total	100.46	98.12	100.27	100.70	100.51	101.00	100.22	100.99	101.16	100.33	100.54	100.96	100.50	99.93	99.58	100.91	99.87	100.49	99.16
Si	3.010	3.029	3.020	3.011	3.026	3.000	3.007	2.972	2.973	2.982	2.973	2.982	2.984	2.982	2.988	2.969	2.982	3.007	3.023
Ti	0.004	0.005	0.006	0.005	0.004	0.005	0.004	0.005	0.006	0.005	0.005	0.003	0.004	0.003	0.005	0.004	0.003	0.004	0.004
Cr	0.000	0.000	0.000	0.000	0.001	0.002	0.000	0.000	0.000	0.000	0.000	0.000	0.001	0.000	0.001	0.000	0.000	0.000	0.001
Al	1.931	1.948	1.945	1.936	1.946	1.960	1.958	1.945	1.943	1.957	1.965	1.950	1.953	1.956	1.934	1.958	1.945	1.939	1.955
Fe^3	0.044	0.000	0.005	0.038	0.000	0.034	0.020	0.109	0.102	0.076	0.085	0.082	0.070	0.075	0.081	0.098	0.090	0.040	0.000
Fe^2	1.367	1.410	1.410	1.404	1.416	1.374	1.392	1.387	1.288	1.287	1.371	1.304	1.302	1.309	1.360	1.260	1.276	1.313	1.312
Mn	0.027	0.029	0.030	0.032	0.027	0.029	0.029	0.046	0.035	0.035	0.048	0.037	0.035	0.036	0.040	0.031	0.032	0.030	0.029
Mg	0.855	0.843	0.891	0.901	0.893	0.858	0.829	0.831	0.964	0.979	0.864	0.981	0.986	1.062	0.934	1.013	0.970	0.947	0.952
Ni	0.000	0.000	0.001	0.000	0.000	0.000	0.000	0.002	0.000	0.000	0.000	0.003	0.000	0.001	0.000	0.002	0.000	0.002	0.001
Ca	0.760	0.725	0.692	0.668	0.679	0.732	0.762	0.698	0.688	0.676	0.684	0.657	0.665	0.577	0.655	0.665	0.697	0.715	0.721
Na	0.002	0.010	0.000	0.005	0.006	0.006	0.000	0.006	0.000	0.005	0.004	0.002	0.000	0.000	0.001	0.000	0.005	0.000	0.001
K	0.001	0.002	0.001	0.001	0.001	0.001	0.000	0.001	0.001	0.000	0.002	0.000	0.001	0.000	0.001	0.001	0.000	0.002	0.001
Σ Cations	8.000	8.000	8.000	8.000	8.000	8.000	8.000	8.000	8.000	8.000	8.000	8.000	8.000	8.000	8.000	8.000	8.000	8.000	8.000
Grossular	0.228	0.237	0.223	0.199	0.222	0.223	0.241	0.177	0.177	0.186	0.184	0.178	0.185	0.154	0.175	0.172	0.186	0.215	0.237
Almandine	0.454	0.468	0.466	0.466	0.469	0.458	0.462	0.467	0.433	0.432	0.461	0.438	0.436	0.439	0.455	0.424	0.428	0.437	0.435
Pyrope	0.284	0.280	0.295	0.299	0.296	0.286	0.275	0.280	0.324	0.328	0.291	0.329	0.330	0.356	0.312	0.341	0.326	0.315	0.316
Spessartite	0.009	0.010	0.010	0.011	0.009	0.010	0.010	0.015	0.012	0.012	0.016	0.012	0.012	0.012	0.014	0.011	0.011	0.010	0.010
Andradite	0.022	0.000	0.002	0.019	0.000	0.017	0.010	0.055	0.051	0.038	0.043	0.041	0.035	0.038	0.041	0.050	0.045	0.020	0.000

calculated with "Norm" program by P. Ulmer using: GARNET Norm
Normalization on the basis of 7 CATIONS and 24 CHARGES

Mineral: garnet

Granulitic Gabbro undeformed **94/04/01**

Sample	p06s01p06	p06s01p07	p06s01p08	p06s01p16	p06s01p17	p06s01p18	p06s01p25	p06s02p10	p06s02p11	p06s02p12	p06s02p13	p06s02p14	p06s02p15	p06s02p16	p06s02p17	p06s02p28	p06s02p29	p06s02p30	p06s02p31
Site	s01	s01	s01	s01	s01	s01	s01	s02	s02	s02	s02	s02	s02	s02	s02	s02	s02	s02	s02
nr.	6	7	8	16	17	18	25	35	1	2	3	4	5	6	7	19	20	21	22
note	gt in contact to plg			gt in contact to plg			gt to cpx	profile through gt								profile through gt			
SiO_2	39.63	39.38	39.59	39.30	39.52	39.32	38.98	38.58	38.17	37.61	38.16	38.54	39.47	39.53	38.73	39.60	39.44	39.65	39.63
TiO_2	0.07	0.05	0.06	0.06	0.07	0.07	0.08	0.06	0.07	0.07	0.04	0.04	0.05	0.09	0.05	0.05	0.08	0.09	0.06
Cr_2O_3	0.00	0.00	0.01	0.00	0.00	0.02	0.05	0.01	0.00	0.00	0.01	0.00	0.01	0.00	0.00	0.00	0.00	0.00	0.00
Al_2O_3	21.81	21.74	21.82	21.94	22.18	21.81	21.74	22.20	21.59	21.27	22.16	21.95	21.60	21.58	21.78	21.85	21.33	21.73	22.06
Fe_2O_3	0.00	0.62	0.95	0.56	1.16	0.19	1.20	0.94	2.18	2.70	2.66	2.15	0.23	1.18	1.52	0.36	0.00	0.47	0.75
FeO	22.14	21.95	21.63	23.04	20.83	21.30	20.48	20.20	19.70	21.09	19.03	19.51	20.73	20.97	20.69	21.63	22.40	21.43	20.81
MnO	0.43	0.47	0.40	0.62	0.39	0.36	0.38	0.47	0.46	0.59	0.50	0.50	0.46	0.49	0.52	0.47	0.45	0.50	0.46
MgO	7.95	7.92	7.86	5.97	7.66	7.70	8.15	7.75	7.81	5.65	7.70	7.70	7.14	7.72	7.85	8.10	6.11	8.05	7.75
NiO	0.00	0.00	0.00	0.06	0.00	0.00	0.00	0.03	0.03	0.03	0.00	0.00	0.00	0.08	0.00	0.00	0.00	0.05	0.00
CaO	8.10	8.27	8.77	9.87	9.59	9.10	8.71	8.99	9.01	10.32	9.64	9.68	10.37	9.15	8.48	8.42	9.70	8.70	9.63
Na_2O	0.05	0.00	0.02	0.00	0.02	0.00	0.02	0.02	0.01	0.00	0.00	0.00	0.00	0.06	0.05	0.02	0.04	0.00	0.00
K_2O	0.00		0.00	0.00	0.01	0.01	0.02	0.02	0.00	0.00	0.00	0.00	0.00	0.01	0.02	0.00	0.02	0.00	0.00
Total	100.17	100.40	101.12	101.44	101.44	99.89	99.79	99.28	99.04	99.33	99.92	100.06	100.07	100.85	99.70	100.51	99.56	100.68	101.17
Si	3.023	3.003	2.997	2.996	2.980	3.007	2.982	2.965	2.950	2.938	2.922	2.947	3.018	3.002	2.973	3.009	3.053	3.010	2.993
Ti	0.004	0.003	0.003	0.003	0.004	0.004	0.005	0.004	0.004	0.004	0.002	0.002	0.003	0.005	0.003	0.003	0.005	0.005	0.004
Cr	0.000	0.000	0.001	0.000	0.000	0.001	0.003	0.001	0.000	0.000	0.001	0.000	0.001	0.000	0.000	0.000	0.000	0.000	0.000
Al	1.961	1.954	1.947	1.971	1.971	1.966	1.960	2.011	1.967	1.958	2.000	1.978	1.947	1.931	1.970	1.957	1.946	1.944	1.964
Fe^3	0.000	0.035	0.054	0.032	0.066	0.011	0.069	0.055	0.127	0.159	0.153	0.124	0.013	0.067	0.088	0.020	0.000	0.027	0.043
Fe^2	1.412	1.400	1.370	1.469	1.313	1.363	1.310	1.299	1.273	1.378	1.219	1.247	1.325	1.331	1.328	1.375	1.450	1.361	1.315
Mn	0.028	0.030	0.026	0.040	0.025	0.024	0.024	0.031	0.030	0.039	0.032	0.032	0.030	0.032	0.034	0.030	0.030	0.032	0.029
Mg	0.904	0.900	0.887	0.679	0.861	0.878	0.929	0.888	0.899	0.658	0.878	0.877	0.814	0.873	0.898	0.917	0.704	0.910	0.873
Ni	0.000	0.000	0.000	0.004	0.000	0.000	0.000	0.002	0.002	0.002	0.000	0.000	0.000	0.005	0.001	0.000	0.000	0.003	0.000
Ca	0.662	0.675	0.712	0.806	0.775	0.746	0.714	0.741	0.746	0.864	0.791	0.793	0.849	0.744	0.697	0.685	0.804	0.708	0.779
Na	0.008	0.000	0.003	0.000	0.003	0.000	0.003	0.002	0.002	0.000	0.001	0.000	0.000	0.010	0.007	0.003	0.005	0.000	0.000
K	0.000	0.000	0.000	0.001	0.001	0.001	0.002	0.002	0.000	0.001	0.001	0.000	0.001	0.001	0.002	0.000	0.002	0.000	0.001
Σ Cations	8.000	8.000	8.000	8.000	8.000	8.000	8.000	8.000	8.000	8.000	8.000	8.000	8.000	8.000	8.000	8.000	8.000	8.000	8.000
Grossular	0.217	0.205	0.208	0.251	0.224	0.239	0.200	0.220	0.186	0.211	0.190	0.205	0.273	0.212	0.189	0.215	0.266	0.219	0.237
Almandine	0.469	0.466	0.457	0.491	0.441	0.453	0.439	0.438	0.432	0.469	0.417	0.423	0.439	0.446	0.449	0.457	0.484	0.452	0.439
Pyrope	0.300	0.299	0.296	0.227	0.289	0.292	0.312	0.300	0.305	0.224	0.301	0.297	0.270	0.293	0.303	0.305	0.235	0.302	0.291
Spessartite	0.009	0.010	0.009	0.013	0.008	0.008	0.008	0.010	0.010	0.013	0.011	0.011	0.010	0.011	0.011	0.010	0.010	0.011	0.010
Andradite	0.000	0.018	0.027	0.016	0.033	0.005	0.035	0.028	0.064	0.081	0.079	0.063	0.006	0.034	0.044	0.010	0.000	0.013	0.021

calculated with "Norm" program by P. Ulmer using: GARNET Norm
Normalization on the basis of 7 CATIONS and 24 CHARGES

Mineral: garnet

Sarangar Gabbro mylonitic **90/02/01**

Sample	p07s04p09	p07s04p10	p07s04p11	p07s05p04	p07s05p05	p07s05p06	p07s05p07	p07s05p09	p07s05p18	p07s05p19	p07s05p27	p07s06p01	p07s06p02	p07s06p03	p07s06p04	p07s06p06	p07s06p07
Site	s04	s04	s04	s05	s05	s05	s05	s05	s05	s05	s05	s06	s06	s06	s06	s06	s06
nr.	66	67	68	74	75	76	77	79	88	89	97	101	102	103	104	106	107
note	amp, qtz and plg			gt with plg incl, in contact to amp					gt at plg		at epi, plg	gt at amp, plg, cc					
SiO_2	37.84	37.95	37.88	37.72	37.54	37.48	38.13	37.45	37.76	37.72	37.84	37.50	37.72	37.47	38.00	37.83	37.73
TiO_2	0.09	0.00	0.04	0.04	0.08	0.03	0.03	0.07	0.00	0.04	0.05	0.05	0.11	0.15	0.06	0.06	0.05
Cr_2O_3	0.08	0.02	0.04	0.02	0.02	0.00	0.02	0.02	0.01	0.04	0.03	0.01	0.02	0.02	0.00	0.00	0.04
Al_2O_3	21.29	21.66	21.53	21.73	21.34	21.52	21.59	21.65	21.54	21.54	21.58	21.54	21.43	21.51	21.59	21.57	21.57
Fe_2O_3	0.41	0.03	0.00	1.10	1.16	1.27	0.88	2.10	1.04	1.26	1.92	2.05	0.32	0.88	0.15	0.73	0.35
FeO	25.68	25.94	26.08	25.36	25.18	24.67	25.85	24.84	25.29	25.07	25.04	25.03	25.63	25.34	25.84	25.72	26.02
MnO	2.30	2.42	2.08	2.28	1.77	1.86	1.76	2.35	2.26	2.40	2.38	2.31	2.25	2.10	2.20	2.23	2.15
MgO	4.16	4.09	3.89	4.19	3.68	3.93	4.17	4.06	4.19	4.20	4.24	3.99	4.03	4.22	3.99	4.12	3.96
NiO	0.00	0.07	0.03	0.00	0.03	0.00	0.01	0.05	0.00	0.00	0.00	0.00	0.00	0.00	0.05	0.00	0.04
CaO	7.54	7.40	7.60	7.79	8.63	8.55	8.01	8.02	7.69	7.89	7.88	8.01	7.69	7.58	7.77	7.77	7.61
Na_2O	0.05	0.03	0.00	0.00	0.07	0.06	0.06	0.01	0.05	0.00	0.04	0.02	0.04	0.05	0.07	0.00	0.03
K_2O	0.01	0.00	0.00	0.00	0.00	0.01	0.00	0.00	0.00	0.00	0.00	0.01	0.01	0.00	0.00	0.00	0.00
Total	99.44	99.63	99.19	100.24	99.52	99.39	100.52	100.63	99.86	100.17	101.00	100.52	99.28	99.33	99.71	100.02	99.55
Si	2.992	2.994	3.004	2.960	2.971	2.963	2.981	2.935	2.973	2.963	2.952	2.943	2.987	2.965	2.995	2.975	2.982
Ti	0.006	0.001	0.003	0.002	0.005	0.002	0.002	0.004	0.000	0.002	0.003	0.003	0.006	0.009	0.003	0.004	0.003
Cr	0.005	0.001	0.002	0.001	0.001	0.000	0.001	0.001	0.001	0.003	0.002	0.001	0.001	0.001	0.000	0.000	0.002
Al	1.984	2.014	2.012	2.010	1.990	2.006	1.989	1.999	1.999	1.994	1.983	1.992	2.001	2.006	2.005	1.999	2.010
Fe^3	0.025	0.002	0.000	0.065	0.069	0.076	0.052	0.124	0.062	0.075	0.113	0.121	0.019	0.052	0.009	0.043	0.021
Fe^2	1.699	1.711	1.730	1.664	1.666	1.631	1.690	1.628	1.665	1.647	1.633	1.643	1.698	1.677	1.703	1.692	1.720
Mn	0.154	0.162	0.139	0.152	0.119	0.125	0.117	0.156	0.150	0.160	0.158	0.153	0.151	0.141	0.147	0.148	0.144
Mg	0.490	0.481	0.460	0.490	0.435	0.463	0.486	0.475	0.492	0.492	0.492	0.466	0.476	0.497	0.469	0.483	0.466
Ni	0.000	0.004	0.002	0.000	0.002	0.000	0.001	0.003	0.000	0.000	0.000	0.000	0.001	0.000	0.003	0.000	0.003
Ca	0.639	0.625	0.646	0.655	0.732	0.724	0.671	0.673	0.649	0.664	0.659	0.674	0.653	0.643	0.656	0.655	0.645
Na	0.008	0.005	0.001	0.000	0.011	0.010	0.009	0.002	0.008	0.001	0.006	0.004	0.007	0.008	0.010	0.000	0.004
K	0.001	0.000	0.001	0.001	0.001	0.001	0.000	0.000	0.000	0.001	0.000	0.001	0.001	0.000	0.000	0.001	0.000
Σ Cations	8.000	8.000	8.000	8.000	8.000	8.000	8.000	8.000	8.000	8.000	8.000	8.000	8.000	8.000	8.000	8.000	8.000
Grossular	0.196	0.208	0.214	0.186	0.209	0.206	0.198	0.163	0.188	0.183	0.164	0.165	0.204	0.184	0.213	0.196	0.203
Almandine	0.569	0.574	0.581	0.562	0.564	0.554	0.570	0.555	0.563	0.556	0.555	0.559	0.569	0.565	0.572	0.568	0.578
Pyrope	0.164	0.161	0.155	0.165	0.147	0.157	0.164	0.162	0.166	0.166	0.167	0.159	0.159	0.168	0.157	0.162	0.157
Spessartite	0.051	0.054	0.047	0.051	0.040	0.042	0.039	0.053	0.051	0.054	0.054	0.052	0.051	0.047	0.049	0.050	0.048
Andradite	0.012	0.000	0.000	0.033	0.035	0.039	0.026	0.063	0.031	0.038	0.057	0.062	0.010	0.026	0.004	0.022	0.011

calculated with "Norm" program by P. Ulmer using: GARNET Norm
Normalization on the basis of 7 CATIONS and 24 CHARGES

Mineral: garnet

Sarangar Gabbro mylonitic **16/01/01**

Sample	p11s01gt1	p11s01gt2	p11s01gt3	p11s01gt4	p11s01gt6	p11s01in1	p11s01pr1	p11s01pr1	p11s01pr1	p11s01pr1	p11s01pr2	p11s01pr2	p11s01pr2	p11s01pr2	p11s01pr2	p11s01pr2	p11s01pr2	p11s03in3	p11s03in2
Site	s01	s01	s01	s01	s01	s01	s01	s01	s01	s01	s01	s01	s01	s01	s01	s01	s01	s03	s03
nr.																			
note			profile through half gt															inclusion	
SiO_2	37.25	38.58	38.63	38.75	38.79	38.34	38.73	38.67	38.04	38.80	39.10	39.21	38.68	38.80	38.72	38.68	38.73	38.95	38.83
TiO_2	0.04	0.04	0.12	0.12	0.04	0.08	0.04	0.08	0.05	0.09	0.07	0.07	0.03	0.04	0.08	0.00	0.08	0.09	0.02
Cr_2O_3	0.00	0.03	0.02	0.04	0.00	0.03	0.01	0.00	0.02	0.05	0.00	0.00	0.00	0.00	0.00	0.00	0.00	0.00	0.00
Al_2O_3	21.30	21.85	21.60	21.71	21.87	21.80	21.91	21.76	21.62	21.74	21.82	21.83	21.48	21.89	21.86	21.76	21.68	21.71	21.81
Fe_2O_3	2.78	0.22	0.00	0.00	0.00	0.00	0.00	0.00	0.85	0.00	0.00	0.00	0.00	0.40	0.01	0.00	0.00	0.00	0.00
FeO	24.96	25.63	25.02	25.66	25.67	25.47	26.46	25.61	24.95	25.34	25.93	25.91	25.57	25.83	25.84	26.04	25.45	25.35	25.99
MnO	3.54	3.55	3.08	3.19	3.32	3.63	3.69	3.56	3.49	3.35	3.32	3.26	3.27	3.52	3.75	3.99	3.28	3.31	3.84
MgO	4.39	4.50	4.68	4.82	4.89	4.45	4.48	4.32	4.25	4.58	4.84	4.98	4.83	4.82	4.28	4.30	4.77	4.70	4.49
NiO																			
CaO	6.20	6.83	7.32	6.78	6.65	6.78	6.07	6.89	7.27	7.20	6.63	6.59	6.68	6.43	7.02	6.35	6.75	6.73	6.56
Na_2O	0.06	0.03	0.01	0.02	0.02	0.01	0.02	0.01	0.03	0.03	0.02	0.00	0.03	0.03	0.01	0.00	0.02	0.04	0.02
K_2O	0.00	0.01	0.01	0.00	0.00	0.00	0.00	0.02	0.01	0.00	0.02	0.00	0.01	0.02	0.02	0.00	0.00	0.00	0.01
Total	100.52	101.27	100.50	101.11	101.25	100.61	101.42	100.91	100.60	101.19	101.75	101.86	100.58	101.78	101.59	101.13	100.76	100.89	101.57
Si	2.932	2.994	3.012	3.006	3.003	2.995	3.006	3.013	2.977	3.009	3.015	3.019	3.016	2.994	2.999	3.013	3.014	3.028	3.007
Ti	0.002	0.002	0.007	0.007	0.002	0.005	0.003	0.004	0.003	0.005	0.004	0.004	0.002	0.002	0.005	0.000	0.004	0.006	0.001
Cr	0.000	0.002	0.001	0.002	0.000	0.002	0.000	0.000	0.001	0.003	0.000	0.000	0.000	0.000	0.000	0.000	0.000	0.000	0.000
Al	1.976	1.998	1.985	1.985	1.996	2.007	2.004	1.998	1.994	1.987	1.983	1.981	1.974	1.991	1.996	1.997	1.989	1.989	1.991
Fe^3	0.165	0.013	0.000	0.000	0.000	0.000	0.000	0.000	0.050	0.000	0.000	0.000	0.000	0.023	0.001	0.000	0.000	0.000	0.000
Fe^2	1.643	1.663	1.632	1.665	1.662	1.664	1.718	1.669	1.632	1.643	1.672	1.668	1.667	1.667	1.674	1.696	1.657	1.648	1.683
Mn	0.236	0.233	0.204	0.210	0.218	0.241	0.243	0.235	0.232	0.220	0.217	0.213	0.216	0.230	0.246	0.264	0.216	0.218	0.252
Mg	0.515	0.521	0.545	0.557	0.564	0.519	0.519	0.502	0.496	0.530	0.556	0.572	0.562	0.554	0.494	0.500	0.553	0.545	0.518
Ni																			
Ca	0.522	0.568	0.612	0.564	0.552	0.567	0.505	0.576	0.610	0.599	0.548	0.544	0.558	0.531	0.583	0.530	0.563	0.560	0.544
Na	0.008	0.004	0.001	0.003	0.003	0.002	0.003	0.001	0.004	0.004	0.003	0.000	0.004	0.005	0.001	0.001	0.003	0.007	0.002
K	0.000	0.001	0.001	0.001	0.000	0.000	0.000	0.002	0.001	0.000	0.002	0.000	0.001	0.002	0.002	0.000	0.000	0.000	0.001
Σ Cations	8.000	8.000	8.000	8.000	8.000	8.000	8.000	8.000	8.000	8.000	8.000	8.000	8.000	8.000	8.000	8.000	8.000	8.000	8.000
Grossular	0.093	0.181	0.200	0.183	0.183	0.186	0.167	0.190	0.177	0.195	0.180	0.179	0.184	0.165	0.191	0.177	0.185	0.185	0.181
Almandine	0.563	0.557	0.545	0.555	0.554	0.556	0.575	0.559	0.549	0.549	0.558	0.557	0.555	0.558	0.558	0.568	0.554	0.554	0.561
Pyrope	0.176	0.174	0.182	0.186	0.188	0.173	0.174	0.168	0.167	0.177	0.186	0.191	0.187	0.186	0.165	0.167	0.185	0.183	0.173
Spessartite	0.081	0.078	0.068	0.070	0.073	0.080	0.081	0.079	0.078	0.073	0.072	0.071	0.072	0.077	0.082	0.088	0.072	0.073	0.084
Andradite	0.085	0.007	0.000	0.000	0.000	0.000	0.000	0.000	0.025	0.000	0.000	0.000	0.000	0.012	0.000	0.000	0.000	0.000	0.000

calculated with "Norm" program by P. Ulmer using: GARNET Norm

Normalization on the basis of 7 CATIONS and 24 CHARGES

Table Appendix 3.3: Representative chemical composition of pyroxene.

	Mineral: clinopyroxene							
	Granulitic Gabbro mylonitic **13/01/01**							
Sample	p01s11px9	p01s11px8	p01s11px6	p01s11px5	p01s11px4	p01s12am4	p01s12am3	p01s12am2
Site	s11	s11	s11	s11	s11	s12	s12	s12
nr.								
note	cpx relicts						cpx in contact to gt	
SiO_2	50.22	50.77	50.78	50.02	50.99	51.27	51.48	51.38
TiO_2	0.55	0.60	0.54	0.63	0.61	0.52	0.49	0.47
Cr_2O_3	0.05	0.13	0.07	0.12	0.08	0.04	0.07	0.04
Al_2O_3	6.08	6.20	6.40	6.52	6.37	5.55	5.87	5.45
Fe_2O_3	0.00	0.00	0.00	0.00	0.00	0.00	0.00	0.00
FeO	6.73	7.42	6.23	7.48	7.28	6.74	6.75	6.64
MnO	0.09	0.06	0.04	0.06	0.07	0.02	0.06	0.11
MgO	11.66	11.67	11.61	11.46	12.00	12.67	12.62	12.76
NiO								
CaO	21.18	20.80	20.76	20.59	21.20	21.44	21.29	21.81
Na_2O	1.32	1.37	1.50	1.30	1.23	1.18	1.25	1.07
K_2O	0.06	0.02	0.02	0.04	0.05	0.04	0.08	0.07
Total	97.94	99.04	97.94	98.23	99.89	99.47	99.95	99.80
Si	1.893	1.894	1.904	1.883	1.886	1.901	1.898	1.900
Ti	0.016	0.017	0.015	0.018	0.017	0.015	0.014	0.013
Cr	0.002	0.004	0.002	0.004	0.002	0.001	0.002	0.001
Al	0.270	0.273	0.283	0.289	0.278	0.243	0.255	0.238
Fe^3	0.000	0.000	0.000	0.000	0.000	0.000	0.000	0.000
Fe^2	0.212	0.232	0.195	0.235	0.225	0.209	0.208	0.205
Mn	0.003	0.002	0.001	0.002	0.002	0.001	0.002	0.003
Mg	0.655	0.649	0.649	0.643	0.662	0.700	0.694	0.703
Ni								
Ca	0.856	0.831	0.834	0.830	0.840	0.852	0.841	0.864
Na	0.096	0.099	0.109	0.095	0.088	0.085	0.089	0.077
K	0.003	0.001	0.001	0.002	0.002	0.002	0.004	0.004
Σ Cations	4.005	4.001	3.993	4.002	4.002	4.006	4.006	4.008
xMg Fe(tot)	0.755	0.737	0.769	0.732	0.746	0.770	0.769	0.774
Wollastonite	0.383	0.371	0.376	0.366	0.372	0.384	0.377	0.389
Enstatite	0.326	0.324	0.327	0.321	0.330	0.348	0.345	0.349
Ferrosilite	0.106	0.116	0.098	0.118	0.112	0.104	0.103	0.102

cpx calculated with "Norm" program by P. Ulmer using: CPX Norm (Cawthorn & Collerson)
cpx normalization on the basis of 12 CHARGES and Fe^{3+} = Acmite

	Mineral: clinopyroxene									
	Granulitic Gabbro undeformed **13/01/01**									
Sample	p02s01px5	p02s01px3	p02s01px2	p02s01px1	p02s01px6	p02s03pl1	p02s03pl1	p02s03uk1	p02s03uk2	p02s03pl1
Site	s01	s01	s01	s01	s01	s03	s03	s03	s03	s03
nr.										
note	cpx in contact to gt					cpx in contact to amp				
SiO_2	51.35	51.52	51.19	51.65	51.18	52.51	51.50	51.53	51.28	51.71
TiO_2	0.64	0.59	0.63	0.56	0.62	0.57	0.58	0.59	0.61	0.56
Cr_2O_3	0.06	0.03	0.14	0.10	0.08	0.07	0.08	0.14	0.10	0.03
Al_2O_3	5.90	5.65	5.87	5.77	5.91	5.60	5.97	6.03	5.91	5.86
Fe_2O_3	0.00	0.00	0.00	0.00	0.00	0.00	0.00	0.00	0.00	0.00
FeO	7.88	7.76	7.70	7.10	7.78	7.03	6.99	6.78	7.32	7.29
MnO	0.05	0.11	0.05	0.07	0.05	0.05	0.07	0.10	0.04	0.08
MgO	12.22	12.28	12.17	12.39	12.14	12.01	12.28	12.52	12.37	12.22
NiO										
CaO	21.13	21.07	21.18	21.32	21.03	20.56	21.19	21.32	21.20	21.39
Na_2O	1.29	1.35	1.29	1.33	1.38	1.24	1.32	1.23	1.21	1.26
K_2O	0.10	0.04	0.04	0.00	0.04	0.08	0.05	0.05	0.03	0.03
Total	100.60	100.40	100.25	100.29	100.22	99.73	100.01	100.29	100.05	100.44
Si	1.891	1.900	1.891	1.901	1.891	1.933	1.899	1.894	1.893	1.901
Ti	0.018	0.016	0.018	0.015	0.017	0.016	0.016	0.016	0.017	0.016
Cr	0.002	0.001	0.004	0.003	0.002	0.002	0.002	0.004	0.003	0.001
Al	0.256	0.245	0.256	0.250	0.258	0.243	0.259	0.261	0.257	0.254
Fe^3	0.000	0.000	0.000	0.000	0.000	0.000	0.000	0.000	0.000	0.000
Fe^2	0.243	0.239	0.238	0.219	0.240	0.216	0.216	0.208	0.226	0.224
Mn	0.002	0.004	0.002	0.002	0.002	0.002	0.002	0.003	0.001	0.003
Mg	0.671	0.675	0.670	0.679	0.669	0.659	0.675	0.686	0.681	0.669
Ni										
Ca	0.834	0.832	0.838	0.841	0.833	0.811	0.837	0.839	0.839	0.843
Na	0.092	0.097	0.092	0.095	0.099	0.089	0.094	0.088	0.086	0.090
K	0.005	0.002	0.002	0.000	0.002	0.004	0.002	0.002	0.001	0.001
Σ Cations	4.011	4.010	4.009	4.005	4.012	3.975	4.003	4.002	4.004	4.001
xMg Fe(tot)	0.734	0.738	0.738	0.757	0.736	0.753	0.758	0.767	0.751	0.749
Wollastonite	0.372	0.375	0.374	0.379	0.372	0.377	0.376	0.375	0.375	0.380
Enstatite	0.332	0.334	0.332	0.338	0.330	0.338	0.337	0.342	0.339	0.334
Ferrosilite	0.120	0.118	0.118	0.109	0.119	0.111	0.107	0.104	0.113	0.112

cpx calculated with "Norm" program by P. Ulmer using: CPX Norm (Cawthorn & Collerson)
cpx normalization on the basis of 12 CHARGES and Fe^{3+} = Acmite

Mineral: clinopyroxene

Granulitic Gabbro mylonitic **94/04/01**

Sample	p04s01p19	p04s01p20	p04s01p21	p04s01p22	p04s01p23	p04s05p01	p04s05p02	p04s05p16	p04s05p17
Site	s01	s01	s01	s01	s01	s05	s05	s05	s05
nr.	19	20	21	22	23	1	2	16	17
note	fractured cpx in contact to amp					big cpx clast in contact to gt			
SiO_2	50.82	49.36	50.45	50.38	50.56	50.23	50.82	52.31	52.65
TiO_2	0.54	1.03	0.53	0.47	0.58	0.55	0.44	0.35	0.37
Cr_2O_3	0.00	0.03	0.01	0.00	0.00	0.00	0.04	0.00	0.00
Al_2O_3	5.34	4.69	5.23	5.21	5.37	5.16	4.91	3.10	3.13
Fe_2O_3	0.00	0.00	0.00	0.00	0.00	0.00	0.00	0.00	0.00
FeO	8.15	9.75	8.37	8.62	8.48	8.76	9.31	7.80	7.42
MnO	0.06	0.07	0.07	0.07	0.06	0.07	0.09	0.08	0.09
MgO	11.75	11.76	11.57	11.75	11.57	11.64	12.36	12.95	13.11
NiO	0.03	0.05	0.00	0.03	0.00	0.00	0.00	0.00	0.02
CaO	22.36	21.55	21.81	21.48	22.11	21.28	20.26	22.73	22.65
Na_2O	1.23	1.00	1.30	1.25	1.31	1.27	1.21	1.04	1.09
K_2O	0.02	0.09	0.01	0.03	0.02	0.03	0.00	0.02	0.01
Total	100.30	99.38	99.37	99.30	100.06	98.98	99.44	100.39	100.54
Si	1.889	1.869	1.893	1.893	1.886	1.893	1.904	1.939	1.943
Ti	0.015	0.029	0.015	0.013	0.016	0.016	0.012	0.010	0.010
Cr	0.000	0.001	0.000	0.000	0.000	0.000	0.001	0.000	0.000
Al	0.234	0.209	0.231	0.231	0.236	0.229	0.217	0.135	0.136
Fe^3	0.000	0.000	0.000	0.000	0.000	0.000	0.000	0.000	0.000
Fe^2	0.253	0.309	0.263	0.271	0.265	0.276	0.292	0.242	0.229
Mn	0.002	0.002	0.002	0.002	0.002	0.002	0.003	0.002	0.003
Mg	0.651	0.663	0.647	0.658	0.643	0.654	0.690	0.715	0.721
Ni	0.001	0.001	0.000	0.001	0.000	0.000	0.000	0.000	0.001
Ca	0.890	0.874	0.877	0.864	0.884	0.859	0.813	0.903	0.896
Na	0.089	0.074	0.094	0.091	0.095	0.093	0.088	0.075	0.078
K	0.001	0.005	0.001	0.001	0.001	0.001	0.001	0.001	0.001
Σ Cations	4.024	4.036	4.024	4.025	4.027	4.024	4.019	4.021	4.018
xMg Fe(tot)	0.720	0.682	0.711	0.708	0.709	0.703	0.703	0.748	0.759
Wollastonite	0.399	0.390	0.395	0.388	0.396	0.387	0.367	0.427	0.426
Enstatite	0.318	0.321	0.316	0.321	0.313	0.320	0.338	0.350	0.355
Ferrosilite	0.124	0.149	0.128	0.132	0.129	0.135	0.143	0.118	0.113

cpx calculated with "Norm" program by P. Ulmer using: CPX Norm (Cawthorn & Collerson)
cpx normalization on the basis of 12 CHARGES and Fe^{3+} = Acmite

Mineral: clinopyroxene

Granulitic Gabbro undeformed **94/04/01**

Sample	p06s01p01	p06s01p03	p06s01p19	p06s01p21	p06s01p22	p06s02p21	p06s02p22	p06s02p23	p06s02p24	p06s02p25
Site	s01	s01	s01	s01	s01	s02	s02	s02	s02	s02
nr.	1	3	19	21	22	12	13	14	15	16
note	cpx in contact to plg		cpx in contact to amp			in contact to gt and plg				
SiO_2	49.30	49.83	50.37	49.70	50.30	50.06	50.52	50.89	50.25	49.62
TiO_2	0.60	0.58	0.63	0.46	0.45	0.64	0.62	0.53	0.61	0.69
Cr_2O_3	0.00	0.00	0.00	0.00	0.03	0.03	0.02	0.02	0.02	0.02
Al_2O_3	6.42	6.44	6.39	6.63	6.58	6.25	6.39	6.38	6.24	6.29
Fe_2O_3	0.00	0.00	0.00	0.00	0.00	0.00	0.00	0.00	0.00	0.00
FeO	8.51	8.68	7.83	8.95	8.77	7.56	7.49	8.79	7.47	7.92
MnO	0.03	0.04	0.06	0.03	0.07	0.05	0.06	0.00	0.00	0.03
MgO	11.18	10.92	11.37	11.19	11.11	11.57	11.63	11.13	11.61	11.51
NiO	0.00	0.00	0.06	0.03	0.02	0.00	0.00	0.06	0.06	0.03
CaO	21.83	21.70	21.98	21.49	21.36	21.75	22.04	21.36	22.12	22.07
Na_2O	1.21	1.14	1.27	1.17	1.25	1.24	1.19	1.23	1.24	1.10
K_2O	0.00	0.00	0.02	0.02	0.01	0.00	0.02	0.00	0.01	0.00
Total	99.09	99.34	99.99	99.69	99.95	99.14	99.99	100.40	99.63	99.26
Si	1.858	1.871	1.873	1.861	1.874	1.874	1.874	1.885	1.873	1.861
Ti	0.017	0.017	0.018	0.013	0.013	0.018	0.017	0.015	0.017	0.019
Cr	0.000	0.000	0.000	0.000	0.001	0.001	0.001	0.001	0.001	0.001
Al	0.285	0.285	0.280	0.293	0.289	0.276	0.279	0.278	0.274	0.278
Fe^3	0.000	0.000	0.000	0.000	0.000	0.000	0.000	0.000	0.000	0.000
Fe^2	0.268	0.273	0.243	0.280	0.273	0.237	0.233	0.272	0.233	0.248
Mn	0.001	0.001	0.002	0.001	0.002	0.001	0.002	0.000	0.000	0.001
Mg	0.628	0.611	0.630	0.625	0.617	0.646	0.643	0.615	0.645	0.644
Ni	0.000	0.000	0.002	0.001	0.001	0.000	0.000	0.002	0.002	0.001
Ca	0.881	0.873	0.876	0.862	0.853	0.873	0.876	0.848	0.883	0.887
Na	0.089	0.083	0.091	0.085	0.090	0.090	0.086	0.088	0.089	0.080
K	0.000	0.000	0.001	0.001	0.001	0.000	0.001	0.000	0.001	0.000
Σ Cations	4.027	4.012	4.016	4.022	4.013	4.015	4.012	4.005	4.017	4.020
xMg Fe(tot)	0.701	0.692	0.721	0.690	0.693	0.732	0.734	0.693	0.735	0.722
Wollastonite	0.381	0.381	0.385	0.371	0.372	0.384	0.385	0.375	0.389	0.386
Enstatite	0.306	0.302	0.311	0.306	0.305	0.318	0.318	0.307	0.318	0.316
Ferrosilite	0.130	0.135	0.120	0.137	0.135	0.117	0.115	0.136	0.114	0.122

cpx calculated with "Norm" program by P. Ulmer using: CPX Norm (Cawthorn & Collerson)
cpx normalization on the basis of 12 CHARGES and Fe^{3+} = Acmite

Mineral: clinopyroxene

Sarangar Gabbro undeformed **90/02/01**

Sample	p10s02p01	p10s02p02	p10s02p03	p10s02p04	p10s02p05	p10s02p07	p10s02p08
Site	s02	s02	s02	s02	s02	s02	s02
nr.	17	18	19	20	21	23	24
note	big cpx with ilm incl. and plg incl.					smaller cpx	
SiO_2	49.76	49.92	49.98	49.75	49.83	50.00	49.62
TiO_2	0.35	0.34	0.38	0.30	0.37	0.36	0.34
Cr_2O_3	0.16	0.16	0.18	0.14	0.15	0.09	0.06
Al_2O_3	3.78	3.73	3.79	3.54	3.37	3.98	3.82
Fe_2O_3	0.00	0.00	0.00	0.00	0.00	0.00	0.00
FeO	11.67	11.72	11.44	11.60	11.62	11.77	11.69
MnO	0.35	0.35	0.32	0.34	0.38	0.33	0.31
MgO	10.60	10.70	10.76	10.74	10.92	10.67	10.78
NiO	0.00	0.00	0.00	0.00	0.00	0.06	0.00
CaO	21.34	21.27	21.43	21.44	21.49	21.24	21.00
Na_2O	0.67	0.67	0.73	0.66	0.72	0.70	0.70
K_2O	0.02	0.00	0.00	0.02	0.00	0.02	0.00
Total	98.69	98.87	99.02	98.51	98.85	99.21	98.34
Si	1.910	1.912	1.910	1.914	1.912	1.908	1.910
Ti	0.010	0.010	0.011	0.009	0.011	0.010	0.010
Cr	0.005	0.005	0.005	0.004	0.005	0.003	0.002
Al	0.171	0.168	0.171	0.160	0.152	0.179	0.174
Fe^3	0.000	0.000	0.000	0.000	0.000	0.000	0.000
Fe^2	0.375	0.376	0.366	0.373	0.373	0.376	0.376
Mn	0.011	0.011	0.011	0.011	0.012	0.011	0.010
Mg	0.607	0.611	0.613	0.616	0.625	0.607	0.619
Ni	0.000	0.000	0.000	0.000	0.000	0.002	0.000
Ca	0.878	0.873	0.878	0.884	0.884	0.869	0.866
Na	0.050	0.050	0.054	0.049	0.053	0.052	0.052
K	0.001	0.000	0.000	0.001	0.000	0.001	0.000
Σ Cations	4.017	4.016	4.018	4.020	4.026	4.017	4.019
xMg Fe(tot)	0.618	0.619	0.627	0.623	0.626	0.618	0.622
Wollastonite	0.401	0.399	0.401	0.405	0.405	0.395	0.395
Enstatite	0.298	0.300	0.301	0.302	0.304	0.299	0.304
Ferrosilite	0.184	0.185	0.179	0.183	0.182	0.185	0.185

cpx calculated with "Norm" program by P. Ulmer using: CPX Norm (Cawthorn & Collerson)
cpx normalization on the basis of 12 CHARGES and Fe^{3+} = Acmite

Mineral: orthopyroxene

Sarangar Gabbro undeformed **90/02/01**

Sample	p10s02p09	p10s02p10	p10s02p11	p10s02p12	p10s03p03	p10s03p04	p10s03p05	p10s03p06	p10s03p07	p10s03p08	p10s03p09
Site	s02	s02	s02	s02	s03	s03	s03	s03	s03	s03	s03
nr.	25	26	27	28	50	51	52	53	54	55	56
note	in contact to opx				opx rimed by amp						
SiO_2	49.26	49.34	49.07	49.12	48.17	49.07	48.54	48.81	49.22	48.71	48.44
TiO_2	0.17	0.11	0.03	0.13	0.09	0.08	0.12	0.11	0.09	0.05	0.06
Cr_2O_3	0.03	0.05	0.04	0.02	0.02	0.04	0.02	0.04	0.04	0.01	0.00
Al_2O_3	2.77	2.59	2.54	2.54	2.57	2.54	2.66	2.63	2.75	2.54	2.91
Fe_2O_3	1.20	1.02	1.23	1.60	1.86	0.50	0.93	1.43	0.14	1.89	1.52
FeO	27.99	28.59	27.85	27.93	28.38	28.62	27.84	27.12	25.56	27.52	26.89
MnO	0.82	0.82	0.77	0.74	0.66	0.67	0.66	0.73	0.60	0.72	0.71
MgO	16.27	16.10	16.18	16.47	15.34	16.12	16.24	16.47	15.73	16.53	16.03
NiO	0.08	0.00	0.00	0.00	0.04	0.02	0.00	0.00	0.06	0.03	0.00
CaO	0.75	0.71	0.75	0.53	0.64	0.55	0.44	0.74	3.18	0.40	1.11
Na_2O	0.03	0.01	0.06	0.03	0.08	0.00	0.03	0.06	0.13	0.00	0.07
K_2O	0.00	0.00	0.00	0.00	0.01	0.00	0.00	0.01	0.00	0.00	0.02
Total	99.38	99.35	98.53	99.11	97.87	98.20	97.48	98.15	97.50	98.41	97.78
Si	1.915	1.922	1.924	1.915	1.913	1.931	1.921	1.917	1.936	1.912	1.911
Ti	0.005	0.003	0.001	0.004	0.003	0.003	0.004	0.003	0.003	0.001	0.002
Cr	0.001	0.002	0.001	0.001	0.001	0.001	0.001	0.001	0.001	0.001	0.000
Al	0.127	0.119	0.117	0.117	0.120	0.118	0.124	0.122	0.127	0.118	0.135
Fe^3	0.035	0.030	0.036	0.047	0.056	0.015	0.028	0.042	0.004	0.056	0.045
Fe^2	0.910	0.932	0.913	0.911	0.943	0.942	0.922	0.891	0.841	0.903	0.887
Mn	0.027	0.027	0.025	0.024	0.022	0.022	0.022	0.024	0.020	0.024	0.024
Mg	0.943	0.935	0.946	0.957	0.908	0.946	0.958	0.964	0.922	0.967	0.943
Ni	0.003	0.000	0.000	0.000	0.001	0.001	0.000	0.000	0.002	0.001	0.000
Ca	0.031	0.030	0.032	0.022	0.027	0.023	0.019	0.031	0.134	0.017	0.047
Na	0.003	0.001	0.004	0.002	0.007	0.000	0.002	0.004	0.010	0.000	0.005
K	0.001	0.001	0.000	0.000	0.001	0.000	0.000	0.001	0.000	0.000	0.001
Σ Cations	4.000	4.000	4.000	4.000	4.000	4.000	4.000	4.000	4.000	4.000	4.000
xMg Fe(tot)	0.499	0.493	0.499	0.500	0.476	0.497	0.502	0.508	0.522	0.502	0.503
Wollastonite	0.016	0.015	0.016	0.011	0.014	0.012	0.009	0.015	0.067	0.008	0.023
Enstatite	0.453	0.449	0.454	0.458	0.434	0.457	0.460	0.461	0.446	0.462	0.449
Ferrosilite	0.436	0.447	0.438	0.436	0.450	0.454	0.443	0.426	0.406	0.431	0.423

opx calculated with "Norm" program by P. Ulmer using: OPX Norm (Wood & Banno)
opx: CATIONS assuming stoichiometry and chargebalance

Mineral: orthopyroxene

Sarangar Gabbro undeformed **16/01/01**

Sample	ps04am9	ps04am13	ps04am14	ps04am15	ps04am16	ps05am6	ps05am8	ps05am9	ps05am10	ps05am11	ps05am12	ps05am13	ps05am14	ps05am15	ps05am16	ps05am16	ps05am16	ps05am16	ps05am16
Site	s04	s04	s04	s04	s04	s05	s05	s05	s05	s05	s05	s05	s05	s05	s05	s05	s05	s05	s05
nr.	21	25	26	27	28	59	60	61	62	63	64	65	66	67	83	84	85	86	87
note	opx in center of amp with small qtz at rim					opx in amp, section									opx in amp, profile				
SiO_2	53.66	55.01	54.42	54.86	54.36	54.37	53.37	54.00	54.01	55.14	53.41	53.10	53.84	51.58	54.19	53.59	50.70	52.68	52.89
TiO_2	0.08	0.01	0.05	0.02	0.05	0.05	0.06	0.07	0.09	0.09	0.10	0.07	0.02	0.12	0.08	0.04	0.16	0.08	0.09
Cr_2O_3	0.00	0.00	0.00	0.03	0.00	0.00	0.00	0.02	0.03	0.00	0.01	0.00	0.00	0.02	0.00	0.04	0.00	0.01	0.00
Al_2O_3	3.70	2.24	2.51	1.68	2.35	1.68	2.69	2.37	2.02	2.63	2.72	3.26	2.34	5.72	2.39	3.11	7.31	3.99	4.03
Fe_2O_3	0.00	0.00	0.00	0.00	0.00	0.00	0.00	0.00	0.00	0.00	0.00	0.00	0.00	0.00	0.00	0.00	0.00	0.00	0.00
FeO	19.47	19.81	20.18	20.75	19.82	21.82	21.85	21.68	22.01	21.60	21.24	21.50	21.69	19.49	21.13	20.66	18.49	20.36	20.34
MnO	0.76	0.93	0.88	0.89	0.83	0.81	0.79	0.79	0.80	0.78	0.83	0.82	0.84	0.69	0.81	0.77	0.59	0.79	0.77
MgO	17.38	17.76	17.76	18.33	18.10	17.49	16.95	17.25	17.41	18.01	16.90	16.82	17.37	15.57	17.87	16.98	14.70	16.61	16.56
NiO	0.00	0.00	0.00	0.00	0.00	0.00	0.00	0.00	0.00	0.00	0.00	0.00	0.00	0.00	0.00	0.00	0.00	0.00	0.00
CaO	3.65	2.53	2.89	1.94	2.54	1.58	2.19	2.02	1.71	2.21	2.34	2.56	2.04	4.81	1.97	2.69	6.13	3.41	3.37
Na_2O	0.32	0.26	0.29	0.19	0.30	0.29	0.31	0.26	0.31	0.35	0.34	0.42	0.28	0.61	0.29	0.40	0.71	0.40	0.43
K_2O	0.12	0.10	0.06	0.05	0.11	0.17	0.09	0.09	0.05	0.09	0.13	0.13	0.07	0.18	0.11	0.09	0.18	0.11	0.10
Total	99.13	98.66	99.04	98.73	98.46	98.26	98.31	98.55	98.43	100.90	98.03	98.69	98.48	98.79	98.83	98.37	98.98	98.45	98.57
Si	1.999	2.052	2.030	2.051	2.035	2.053	2.020	2.034	2.039	2.025	2.024	2.003	2.031	1.941	2.030	2.018	1.903	1.986	1.990
Ti	0.002	0.000	0.002	0.001	0.001	0.002	0.002	0.002	0.002	0.003	0.003	0.002	0.001	0.003	0.002	0.001	0.005	0.002	0.002
Cr	0.000	0.000	0.000	0.001	0.000	0.000	0.000	0.001	0.001	0.000	0.000	0.000	0.000	0.001	0.000	0.001	0.000	0.000	0.000
Al	0.162	0.098	0.110	0.074	0.104	0.075	0.120	0.105	0.090	0.114	0.121	0.145	0.104	0.254	0.105	0.138	0.323	0.178	0.179
Fe^3	0.000	0.000	0.000	0.000	0.000	0.000	0.000	0.000	0.000	0.000	0.000	0.000	0.000	0.000	0.000	0.000	0.000	0.000	0.000
Fe^2	0.607	0.618	0.629	0.649	0.621	0.689	0.692	0.683	0.695	0.663	0.673	0.678	0.684	0.613	0.662	0.651	0.581	0.642	0.640
Mn	0.024	0.030	0.028	0.028	0.026	0.026	0.025	0.025	0.026	0.024	0.027	0.026	0.027	0.022	0.026	0.025	0.019	0.025	0.025
Mg	0.965	0.988	0.988	1.022	1.010	0.984	0.956	0.968	0.979	0.986	0.954	0.946	0.976	0.874	0.998	0.953	0.823	0.934	0.929
Ni	0.000	0.000	0.000	0.000	0.000	0.000	0.000	0.000	0.000	0.000	0.000	0.000	0.000	0.000	0.000	0.000	0.000	0.000	0.000
Ca	0.146	0.101	0.115	0.078	0.102	0.064	0.089	0.081	0.069	0.087	0.095	0.104	0.082	0.194	0.079	0.109	0.247	0.138	0.136
Na	0.023	0.019	0.021	0.014	0.022	0.022	0.023	0.019	0.023	0.025	0.025	0.031	0.021	0.045	0.021	0.029	0.052	0.029	0.031
K	0.006	0.005	0.003	0.002	0.005	0.008	0.004	0.005	0.003	0.004	0.006	0.006	0.003	0.009	0.005	0.005	0.009	0.005	0.005
Σ Cations	3.933	3.910	3.925	3.919	3.925	3.922	3.931	3.923	3.926	3.931	3.929	3.941	3.929	3.955	3.928	3.928	3.961	3.939	3.936
xMg Fe(tot)	0.614	0.615	0.611	0.612	0.619	0.588	0.580	0.587	0.585	0.598	0.586	0.582	0.588	0.588	0.601	0.594	0.586	0.592	0.592
Wollastonite	0.073	0.050	0.058	0.039	0.051	0.032	0.044	0.041	0.035	0.043	0.047	0.052	0.041	0.097	0.040	0.054	0.123	0.069	0.068
Enstatite	0.482	0.494	0.494	0.511	0.505	0.492	0.478	0.484	0.490	0.493	0.477	0.473	0.488	0.421	0.499	0.476	0.385	0.463	0.462
Ferrosilite	0.303	0.309	0.315	0.324	0.310	0.345	0.346	0.341	0.347	0.332	0.336	0.339	0.342	0.295	0.331	0.325	0.271	0.319	0.319

opx calculated with "Norm" program by P. Ulmer using: OPX Norm (Lindsley)

opx: CATIONS assuming stoichiometry and chargebalance

Table Appendix 3.4: Representative chemical composition of amphiboles.

Mineral: amphibole

Granulitic Gabbro mylonitic **13/01/01**

Sample	p01s07mt4	p01s07mt6	p01s07mt8	p01s07mt9	p01s07mt1	p01s07mt1	p01s07mt2	p01s09hb3	p01s09hb1	p01s09hb4
Site	s07	s07	s07	s07	s07	s07	s07	s09	s09	s09
nr.	71	73	75	76	77	79	69	83	80	82
note	amphibole in matrix							amp in contact to gt		
SiO_2	43.59	44.17	49.83	45.17	48.49	44.23	44.22	44.02	43.02	42.53
TiO_2	0.50	0.48	0.46	0.43	0.44	0.44	0.50	0.34	0.38	0.39
Cr_2O_3	0.00	0.05	0.07	0.00	0.08	0.03	0.00	0.02	0.03	0.00
Al_2O_3	14.95	14.65	14.16	14.21	12.54	15.15	14.93	15.31	15.67	16.59
Fe_2O_3	3.38	4.32	0.00	4.68	0.83	4.31	4.43	5.87	4.41	5.59
FeO	8.94	8.23	11.20	7.87	10.22	8.41	8.03	7.89	8.85	8.79
MnO	0.16	0.13	0.12	0.16	0.18	0.17	0.09	0.13	0.20	0.12
MgO	11.50	11.81	10.07	12.36	11.99	11.69	11.85	11.33	10.90	10.44
NiO	0.00	0.00	0.00	0.00	0.00	0.00	0.00	0.00	0.00	0.00
CaO	11.45	11.26	10.19	11.46	10.76	11.37	11.33	10.93	11.27	10.96
Na_2O	1.82	1.85	1.80	1.79	1.61	1.90	1.77	2.04	1.87	2.16
K_2O	0.46	0.52	0.51	0.44	0.39	0.47	0.46	0.46	0.50	0.58
Cl	0.00	0.00	0.00	0.00	0.00	0.00	0.00	0.00	0.00	0.00
H_2O	2.05	2.07	2.11	2.10	2.10	2.08	2.08	2.08	2.05	2.07
Total	98.80	99.53	100.52	100.66	99.61	100.26	99.70	100.44	99.14	100.20
Si	6.375	6.402	7.088	6.460	6.938	6.368	6.388	6.333	6.289	6.172
Ti	0.054	0.052	0.049	0.046	0.047	0.048	0.054	0.037	0.042	0.042
Cr	0.001	0.006	0.007	0.000	0.009	0.003	0.001	0.003	0.003	0.000
Al	2.577	2.502	2.374	2.396	2.115	2.572	2.543	2.597	2.699	2.837
Fe^3	0.372	0.471	0.000	0.504	0.089	0.467	0.481	0.636	0.485	0.611
Fe^2	1.093	0.998	1.333	0.941	1.223	1.012	0.970	0.949	1.083	1.067
Mn	0.019	0.016	0.014	0.019	0.021	0.020	0.011	0.016	0.025	0.014
Mg	2.508	2.552	2.135	2.634	2.558	2.509	2.551	2.430	2.374	2.258
Ni	0.000	0.000	0.000	0.000	0.000	0.000	0.000	0.000	0.000	0.000
Ca	1.794	1.748	1.554	1.756	1.650	1.754	1.754	1.685	1.765	1.704
Na	0.516	0.521	0.497	0.497	0.446	0.532	0.496	0.570	0.529	0.608
K	0.086	0.095	0.093	0.080	0.071	0.086	0.085	0.084	0.093	0.107
OH	2.000	2.000	2.000	2.000	2.000	2.000	2.000	2.000	2.000	2.000
Σ Cations	15.397	15.364	15.143	15.333	15.167	15.372	15.335	15.340	15.387	15.420
xMg Fe(tot)	0.631	0.635	0.616	0.646	0.661	0.629	0.637	0.605	0.602	0.574
Tschermak	1.434	1.486	1.216	1.451	1.245	1.507	1.522	1.642	1.560	1.704
Edenite	0.397	0.364	0.143	0.333	0.167	0.372	0.335	0.340	0.387	0.420
Plagioclase	0.206	0.252	0.446	0.244	0.350	0.246	0.246	0.315	0.235	0.296

Sample	p01s09hb6	p01s09hb7	p01s09hb8	p01s09hb2	p01s13ri1	p01s13hb1	p01s13hb2	p01s13hb3	p01s13hb4
Site	s09	s09	s09	s09	s13	s13	s13	s13	s13
nr.	91	92	93	81	98	94	95	96	97
note									
SiO_2	41.44	43.08	42.82	43.65	49.70	42.19	42.51	42.73	42.93
TiO_2	0.39	0.43	0.41	0.31	0.31	0.20	0.21	0.21	0.21
Cr_2O_3	0.00	0.05	0.00	0.05	0.02	0.03	0.00	0.05	0.00
Al_2O_3	18.10	14.48	16.36	15.55	15.07	16.78	16.86	16.22	16.42
Fe_2O_3	4.91	3.24	5.15	5.39	0.00	6.31	5.48	6.10	5.00
FeO	8.97	9.34	8.45	8.17	11.35	7.73	8.34	7.41	7.91
MnO	0.13	0.15	0.13	0.18	0.10	0.15	0.11	0.13	0.11
MgO	10.11	11.24	10.79	11.19	8.86	10.73	10.78	11.27	11.38
NiO	0.00	0.00	0.00	0.00	0.00	0.00	0.00	0.00	0.00
CaO	11.23	11.23	11.11	10.98	9.92	11.06	11.23	11.14	11.35
Na_2O	2.11	1.94	1.98	2.10	1.74	2.07	2.09	2.05	2.05
K_2O	0.75	0.51	0.54	0.48	0.54	0.56	0.56	0.52	0.53
Cl	0.00	0.00	0.00	0.00	0.00	0.00	0.00	0.00	0.00
H_2O	2.06	2.02	2.07	2.08	2.09	2.06	2.07	2.07	2.07
Total	100.21	97.71	99.81	100.12	99.69	99.87	100.25	99.91	99.96
Si	6.023	6.391	6.217	6.308	7.140	6.130	6.154	6.190	6.210
Ti	0.043	0.048	0.045	0.034	0.034	0.022	0.023	0.023	0.023
Cr	0.000	0.006	0.000	0.005	0.003	0.003	0.000	0.006	0.000
Al	3.100	2.531	2.800	2.648	2.551	2.873	2.877	2.769	2.799
Fe^3	0.536	0.362	0.562	0.586	0.000	0.690	0.597	0.665	0.545
Fe^2	1.091	1.159	1.026	0.987	1.364	0.940	1.010	0.897	0.957
Mn	0.016	0.019	0.016	0.022	0.012	0.018	0.014	0.016	0.013
Mg	2.191	2.485	2.334	2.409	1.897	2.324	2.326	2.433	2.453
Ni	0.000	0.000	0.000	0.000	0.000	0.000	0.000	0.000	0.000
Ca	1.749	1.785	1.729	1.700	1.527	1.721	1.742	1.730	1.759
Na	0.595	0.557	0.557	0.588	0.484	0.583	0.585	0.577	0.575
K	0.139	0.097	0.100	0.089	0.098	0.105	0.104	0.097	0.098
OH	2.000	2.000	2.000	2.000	2.000	2.000	2.000	2.000	2.000
Σ Cations	15.483	15.439	15.385	15.377	15.108	15.408	15.431	15.404	15.432
xMg Fe(tot)	0.574	0.620	0.595	0.605	0.582	0.588	0.592	0.609	0.620
Tschermak	1.745	1.385	1.669	1.616	1.225	1.740	1.673	1.676	1.600
Edenite	0.483	0.439	0.385	0.377	0.108	0.408	0.431	0.404	0.432
Plagioclase	0.251	0.215	0.271	0.300	0.473	0.279	0.258	0.270	0.241

calculated with "Norm" program by P. Ulmer using: Amphibole Norm NAMP

CATIONS calculated on the bases of 23 oxygens and 13 cations + K + Na + Ca

Mineral: amphibole

Granulitic Gabbro undeformed

Sample	p02s03pl1	p02s03pl1	p02s03pl1	p02s03pl1	p02s03pl1	p02s03ri1	p02s03ri2	p02s03hb1	p02s03hb2	p02s07am1	p02s07am2	p02s07am3	p02s07am4	p02s07am6	p02s07am7	p02s07am8
Site	s03	s03	s03	s03	s03	s03	s03	s03	s03	s07	s07	s07	s07	s07	s07	s07
nr.	30	33	35	52	55	59	60	67	68	1	2	3	4	14	15	16
note	amp in contact to plg									amp in contact to cpx						
SiO_2	49.58	51.07	52.13	48.05	51.05	50.43	52.50	50.95	49.73	55.67	50.39	53.16	56.63	51.79	54.83	57.16
TiO_2	0.47	0.17	0.12	0.61	0.29	0.39	0.43	0.29	0.49	0.49	0.54	0.51	2.02	0.60	0.63	0.51
Cr_2O_3	0.08	0.05	0.10	0.08	0.09	0.07	0.14	0.04	0.01	0.05	0.07	0.09	0.07	0.08	0.07	0.05
Al_2O_3	6.43	7.17	6.26	11.03	6.26	7.92	6.43	7.07	7.53	6.29	7.26	6.19	6.07	6.46	6.36	6.18
Fe_2O_3	0.00	0.67	2.06	1.44	3.38	0.40	0.16	1.74	3.16	0.00	1.94	0.00	0.00	0.00	0.00	0.00
FeO	8.51	10.20	7.19	7.12	9.16	10.85	9.47	8.30	9.69	9.77	8.97	9.33	8.69	11.16	10.49	10.50
MnO	0.13	0.22	0.20	0.10	0.32	0.27	0.23	0.20	0.24	0.22	0.17	0.20	0.14	0.26	0.28	0.28
MgO	12.93	14.81	16.56	15.39	14.63	14.21	15.53	15.53	13.83	13.55	15.28	12.95	11.40	13.54	13.53	12.43
NiO	0.00	0.00	0.00	0.00	0.00	0.00	0.00	0.00	0.00	0.00	0.00	0.00	0.00	0.00	0.00	0.00
CaO	18.93	12.55	12.47	12.29	11.99	12.58	12.27	12.28	11.85	11.43	12.48	15.51	10.87	11.84	11.62	10.90
Na_2O	1.01	0.74	0.66	1.18	0.78	0.75	0.73	0.76	0.92	0.67	0.81	0.95	0.62	0.78	0.73	0.64
K_2O	0.13	0.19	0.18	0.93	0.21	0.21	0.17	0.27	0.19	0.14	0.37	0.12	0.21	0.19	0.18	0.13
Cl	0.00	0.00	0.00	0.00	0.00	0.00	0.00	0.00	0.00	0.00	0.00	0.00	0.00	0.00	0.00	0.00
H_2O	1.94	2.10	2.12	2.11	2.10	2.10	2.12	2.10	2.08	2.12	2.11	2.03	2.07	2.07	2.12	2.13
Total	100.13	99.94	100.06	100.32	100.26	100.18	100.19	99.54	99.73	100.40	100.39	101.04	98.79	98.75	100.84	100.90
Si	7.666	7.298	7.358	6.817	7.293	7.213	7.426	7.271	7.161	7.863	7.175	7.837	8.204	7.510	7.744	8.041
Ti	0.055	0.018	0.012	0.065	0.031	0.042	0.046	0.032	0.053	0.053	0.057	0.057	0.220	0.065	0.067	0.054
Cr	0.009	0.005	0.011	0.009	0.011	0.008	0.016	0.004	0.001	0.006	0.008	0.010	0.008	0.010	0.008	0.006
Al	1.172	1.208	1.042	1.845	1.054	1.335	1.072	1.190	1.277	1.047	1.218	1.076	1.036	1.103	1.059	1.024
Fe^3	0.000	0.072	0.219	0.154	0.363	0.043	0.018	0.187	0.342	0.000	0.208	0.000	0.000	0.000	0.000	0.000
Fe^2	1.100	1.219	0.848	0.844	1.094	1.297	1.120	0.990	1.167	1.154	1.068	1.150	1.053	1.353	1.239	1.236
Mn	0.017	0.027	0.024	0.012	0.039	0.032	0.028	0.025	0.029	0.027	0.021	0.025	0.017	0.031	0.033	0.034
Mg	2.980	3.154	3.485	3.254	3.116	3.029	3.275	3.302	2.969	2.852	3.244	2.845	2.461	2.927	2.848	2.606
Ni	0.000	0.000	0.000	0.000	0.000	0.000	0.000	0.000	0.000	0.000	0.000	0.000	0.000	0.000	0.000	0.000
Ca	3.137	1.922	1.887	1.868	1.835	1.928	1.860	1.878	1.829	1.729	1.904	2.449	1.687	1.839	1.758	1.644
Na	0.302	0.205	0.180	0.324	0.217	0.209	0.201	0.210	0.257	0.182	0.225	0.272	0.175	0.218	0.199	0.174
K	0.026	0.035	0.033	0.168	0.038	0.039	0.030	0.050	0.036	0.025	0.066	0.023	0.038	0.035	0.032	0.023
OH	2.000	2.000	2.000	2.000	2.000	2.000	2.000	2.000	2.000	2.000	2.000	2.000	2.000	2.000	2.000	2.000
Σ Cations	16.465	15.162	15.100	15.360	15.090	15.175	15.091	15.137	15.122	14.936	15.195	15.743	14.901	15.092	14.989	14.840
xMg Fe(tot)	0.730	0.710	0.766	0.765	0.681	0.693	0.742	0.737	0.663	0.712	0.718	0.712	0.700	0.684	0.697	0.678
Tschermak	0.006	0.619	0.655	0.955	0.783	0.684	0.623	0.715	0.888	0.345	0.725	0.000	0.010	0.558	0.487	0.155
Edenite	0.328	0.162	0.100	0.360	0.090	0.175	0.091	0.137	0.122	0.000	0.195	0.163	0.000	0.092	0.000	0.000
Plagioclase	0.000	0.078	0.114	0.132	0.165	0.072	0.140	0.122	0.171	0.207	0.096	0.000	0.214	0.161	0.231	0.196

calculated with "Norm" program by P. Ulmer using: Amphibole Norm NAMP

CATIONS calculated on the bases of 23 oxygens and 13 cations + K + Na + Ca

Mineral: amphibole

Granulitic Gabbro mylonitic

Sample	p04s02p04	p04s02p05	p04s02p09	p04s02p10	p04s02p14	p04s02p16	p04s02p17	p04s03p11	p04s03p12	p04s03p16	p04s04pro	p04s04pro	p04s04pro	p04s04pro	p04s04pro	p04s04p06	p04s05p08
Site	s02	s02	s02	s02	s02	s02	s02	s03	s03	s03	s04	s04	s04	s04	s04	s04	s05
nr.	4	5	9	10	14	16	17	36	37	41	4	14	15	16	17	51	8
note	amp matrix in contact with gt							amp in contact to gt and plg			amp matrix						to gt
SiO_2	42.57	41.63	40.20	39.68	44.02	50.44	50.97	41.07	43.63	47.94	49.60	44.77	43.11	42.12	49.24	42.93	41.11
TiO_2	0.06	0.12	0.14	0.10	0.23	0.22	0.21	0.11	0.08	0.06	0.37	0.34	0.29	0.73	0.44	0.33	0.12
Cr_2O_3	0.00	0.00	0.00	0.03	0.02	0.00	0.01	0.00	0.00	0.00	0.00	0.00	0.04	0.00	0.04	0.00	0.00
Al_2O_3	17.39	16.47	18.08	18.95	14.30	7.40	7.03	17.61	15.47	10.66	19.14	12.54	15.75	13.57	8.62	15.38	16.70
Fe_2O_3	6.45	6.84	8.86	8.79	3.29	5.37	5.91	6.55	7.43	5.60	0.00	6.39	4.33	6.46	7.07	3.36	6.46
FeO	6.57	6.22	6.03	7.42	9.31	5.43	4.94	6.94	5.54	5.80	8.04	7.36	9.86	8.03	5.76	8.73	7.46
MnO	0.05	0.05	0.09	0.07	0.09	0.05	0.06	0.02	0.02	0.05	0.05	0.08	0.10	0.06	0.08	0.00	0.05
MgO	11.92	11.71	11.00	10.08	11.79	16.06	16.23	11.36	12.64	14.42	7.92	12.41	10.65	11.56	14.63	11.41	11.07
NiO	0.00	0.00	0.00	0.00	0.02	0.00	0.01	0.00	0.02	0.04	0.00	0.00	0.03	0.00	0.01	0.00	0.01
CaO	11.21	11.14	11.05	11.08	11.04	11.44	11.29	11.29	11.10	11.18	8.39	10.77	10.86	11.03	10.92	10.84	11.06
Na_2O	2.54	2.27	2.53	2.72	2.52	1.36	1.29	2.25	2.24	1.61	3.87	2.15	2.58	2.10	1.46	2.40	2.38
K_2O	0.70	0.49	0.76	0.77	0.51	0.18	0.18	1.02	0.53	0.35	0.55	0.41	0.61	0.60	0.26	0.55	0.74
Cl	0.00	0.00	0.00	0.00	0.00	0.00	0.00	0.00	0.00	0.00	0.00	0.00	0.00	0.00	0.00	0.00	0.00
H_2O	2.11	2.05	2.07	2.08	2.05	2.12	2.13	2.07	2.10	2.10	2.10	2.06	2.06	2.02	2.12	2.03	2.04
Total	101.57	99.00	100.81	101.77	99.19	100.05	100.25	100.31	100.80	99.82	100.04	99.30	100.28	98.28	100.66	97.97	99.20
Si	6.063	6.083	5.820	5.730	6.430	7.137	7.184	5.958	6.232	6.835	7.084	6.516	6.268	6.256	6.974	6.332	6.037
Ti	0.007	0.013	0.015	0.011	0.026	0.023	0.022	0.012	0.008	0.007	0.040	0.037	0.032	0.081	0.047	0.037	0.014
Cr	0.000	0.000	0.000	0.003	0.003	0.000	0.001	0.000	0.000	0.000	0.000	0.001	0.004	0.000	0.004	0.000	0.000
Al	2.919	2.835	3.086	3.226	2.462	1.234	1.167	3.011	2.605	1.792	3.222	2.150	2.699	2.376	1.440	2.674	2.890
Fe^3	0.692	0.752	0.965	0.955	0.362	0.571	0.627	0.715	0.799	0.601	0.000	0.699	0.473	0.722	0.754	0.373	0.714
Fe^2	0.783	0.761	0.730	0.896	1.137	0.642	0.582	0.842	0.661	0.691	0.961	0.896	1.199	0.998	0.682	1.076	0.916
Mn	0.006	0.007	0.010	0.009	0.011	0.006	0.007	0.002	0.002	0.006	0.006	0.009	0.012	0.008	0.010	0.000	0.006
Mg	2.531	2.551	2.374	2.170	2.567	3.386	3.409	2.458	2.690	3.064	1.687	2.691	2.309	2.560	3.089	2.508	2.423
Ni	0.000	0.000	0.000	0.000	0.002	0.000	0.002	0.001	0.002	0.005	0.001	0.001	0.004	0.000	0.002	0.000	0.001
Ca	1.711	1.743	1.714	1.715	1.727	1.734	1.705	1.755	1.699	1.708	1.284	1.680	1.691	1.755	1.657	1.712	1.739
Na	0.701	0.644	0.711	0.761	0.712	0.373	0.351	0.634	0.620	0.445	1.071	0.608	0.728	0.605	0.401	0.688	0.679
K	0.127	0.091	0.141	0.143	0.095	0.033	0.032	0.189	0.097	0.064	0.101	0.077	0.114	0.114	0.047	0.104	0.138
OH	2.000	2.000	2.000	2.000	2.000	2.000	2.000	2.000	2.000	2.000	2.000	2.000	2.000	2.000	2.000	2.000	2.000
Σ Cations	15.539	15.478	15.566	15.619	15.535	15.140	15.088	15.577	15.416	15.216	15.455	15.364	15.532	15.474	15.105	15.504	15.556
xMg Fe(tot)	0.632	0.628	0.583	0.540	0.631	0.736	0.738	0.612	0.648	0.703	0.637	0.628	0.580	0.598	0.683	0.634	0.598
Tschermak	1.687	1.696	1.900	1.936	1.307	0.989	1.023	1.709	1.653	1.241	1.176	1.441	1.508	1.516	1.264	1.452	1.668
Edenite	0.539	0.478	0.566	0.619	0.535	0.140	0.088	0.577	0.416	0.216	0.455	0.364	0.532	0.474	0.105	0.504	0.556
Plagioclase	0.289	0.257	0.286	0.285	0.273	0.266	0.295	0.245	0.301	0.292	0.716	0.321	0.309	0.245	0.343	0.288	0.261

calculated with "Norm" program by P. Ulmer using: Amphibole Norm NAMP

CATIONS calculated on the bases of 23 oxygens and 13 cations + K + Na + Ca

Mineral: amphibole

Sarangar Gabbro mylonitic **90/02/01**

Sample	p07a01p05	p07a01p07	p07a01p11	p07a01p15	p07a01p16	p07a01p17	p07a03p10	p07a03p11	p07a04p02	p07a04p05	p07a04p07	p07a04p11	p07a04p12	p07a04p16	p07a04p20	p07a04p21	p07a05p13	p07a08p05	p07a08p07
Site	a01	a01	a01	a01	a01	a01	a03	a03	a04	a04	a04	a04	a04	a04	a04	a04	a05	a08	a08
nr.	5	7	11	15	16	17	36	37	53	56	58	62	63	67	71	72	89	105	107
note	amp at epi			amp at epi and plg			to epi and gt		porphyroclast in contact to epi			porphyroclast		amp in plg rich layer			amp at gt	in gt crack	
SiO_2	40.77	41.33	40.43	40.98	41.13	40.46	40.53	40.67	40.36	40.59	40.57	40.34	40.43	40.88	40.71	40.75	40.71	39.96	40.97
TiO_2	0.64	0.63	0.62	0.71	0.67	0.75	0.68	0.74	0.71	0.79	0.71	0.58	0.67	0.71	0.66	0.75	0.62	0.55	0.71
Cr_2O_3	0.00	0.02	0.05	0.02	0.04	0.01	0.00	0.03	0.04	0.03	0.00	0.03	0.04	0.03	0.03	0.04	0.03	0.02	0.04
Al_2O_3	16.91	16.60	16.52	16.36	17.35	16.30	16.01	15.89	16.12	15.47	15.15	15.44	16.23	16.14	15.83	15.72	16.44	16.31	16.38
Fe_2O_3	5.63	4.08	3.46	4.27	5.07	5.57	4.65	4.10	4.11	5.85	5.85	5.08	5.43	5.49	4.00	3.74	5.50	5.09	4.11
FeO	10.68	11.75	12.09	11.46	9.84	10.30	11.35	11.84	11.95	10.81	11.09	11.82	10.94	11.01	11.78	12.15	11.17	10.91	10.30
MnO	0.08	0.16	0.08	0.05	0.13	0.14	0.04	0.16	0.11	0.11	0.17	0.14	0.13	0.09	0.09	0.10	0.16	0.09	0.05
MgO	9.18	9.17	8.83	9.53	9.87	9.44	9.24	9.25	8.88	9.35	9.32	8.86	9.16	9.26	9.10	9.19	8.99	9.20	9.78
NiO	0.00	0.02	0.03	0.00	0.02	0.00	0.05	0.00	0.02	0.01	0.05	0.04	0.03	0.00	0.09	0.00	0.04	0.07	0.02
CaO	11.36	11.62	11.56	11.70	11.60	11.34	11.53	11.69	11.48	11.41	11.43	11.52	11.42	11.48	11.47	11.66	11.43	11.55	11.32
Na_2O	1.92	1.83	1.73	1.91	1.89	1.87	1.83	1.83	1.84	1.82	1.90	1.71	1.88	1.83	1.81	1.79	1.84	1.83	1.88
K_2O	0.64	0.65	0.67	0.66	0.65	0.66	0.59	0.62	0.62	0.57	0.58	0.63	0.64	0.58	0.66	0.64	0.66	0.64	0.62
Cl	0.00	0.00	0.00	0.00	0.00	0.00	0.00	0.00	0.00	0.00	0.00	0.00	0.00	0.00	0.00	0.00	0.00	0.00	0.00
H_2O	2.03	2.03	1.99	2.03	2.05	2.01	2.00	2.00	1.99	2.00	2.00	1.99	2.01	2.02	1.99	2.00	2.02	1.99	2.01
Total	99.86	99.88	98.06	99.67	100.32	98.88	98.50	98.82	98.23	98.82	98.81	98.18	99.03	99.52	98.22	98.53	99.61	98.19	98.19
Si	6.015	6.099	6.085	6.064	6.008	6.028	6.074	6.086	6.076	6.071	6.083	6.094	6.032	6.062	6.120	6.115	6.040	6.013	6.109
Ti	0.071	0.070	0.070	0.079	0.074	0.085	0.077	0.083	0.081	0.089	0.080	0.066	0.075	0.080	0.075	0.085	0.070	0.062	0.080
Cr	0.001	0.003	0.006	0.002	0.004	0.002	0.001	0.003	0.004	0.003	0.000	0.004	0.005	0.003	0.004	0.005	0.004	0.002	0.004
Al	2.941	2.887	2.931	2.854	2.988	2.863	2.828	2.802	2.860	2.726	2.678	2.749	2.854	2.820	2.806	2.781	2.874	2.892	2.878
Fe^3	0.625	0.453	0.392	0.475	0.557	0.624	0.524	0.462	0.465	0.658	0.660	0.577	0.610	0.612	0.453	0.422	0.614	0.576	0.462
Fe^2	1.318	1.450	1.522	1.418	1.202	1.284	1.423	1.481	1.505	1.353	1.390	1.493	1.366	1.365	1.481	1.525	1.386	1.372	1.285
Mn	0.010	0.020	0.011	0.006	0.016	0.018	0.006	0.020	0.014	0.014	0.021	0.018	0.017	0.012	0.012	0.012	0.021	0.011	0.007
Mg	2.019	2.017	1.980	2.101	2.149	2.097	2.063	2.063	1.993	2.085	2.082	1.995	2.038	2.046	2.040	2.055	1.988	2.064	2.173
Ni	0.001	0.002	0.003	0.000	0.002	0.000	0.006	0.000	0.003	0.002	0.006	0.005	0.004	0.000	0.011	0.001	0.005	0.008	0.002
Ca	1.796	1.838	1.864	1.854	1.815	1.810	1.851	1.874	1.851	1.828	1.836	1.864	1.826	1.824	1.847	1.875	1.817	1.862	1.808
Na	0.550	0.523	0.505	0.548	0.537	0.541	0.532	0.530	0.536	0.528	0.554	0.501	0.545	0.526	0.529	0.520	0.531	0.532	0.544
K	0.121	0.122	0.128	0.125	0.120	0.125	0.113	0.119	0.120	0.109	0.112	0.122	0.121	0.109	0.126	0.123	0.125	0.123	0.117
OH	2.000	2.000	2.000	2.000	2.000	2.000	2.000	2.000	2.000	2.000	2.000	2.000	2.000	2.000	2.000	2.000	2.000	2.000	2.000
Σ Cations	15.466	15.482	15.497	15.527	15.472	15.476	15.496	15.522	15.507	15.465	15.501	15.487	15.492	15.458	15.501	15.518	15.472	15.518	15.469
xMg Fe(tot)	0.510	0.514	0.509	0.526	0.550	0.524	0.515	0.515	0.503	0.509	0.504	0.491	0.508	0.508	0.513	0.513	0.499	0.514	0.555
Tschermak	1.724	1.581	1.554	1.554	1.704	1.686	1.580	1.519	1.566	1.636	1.580	1.555	1.651	1.657	1.531	1.492	1.671	1.607	1.613
Edenite	0.466	0.482	0.497	0.527	0.472	0.476	0.496	0.522	0.507	0.465	0.501	0.487	0.492	0.458	0.501	0.518	0.472	0.518	0.469
Plagioclase	0.204	0.162	0.136	0.146	0.185	0.191	0.149	0.127	0.149	0.172	0.164	0.136	0.174	0.177	0.153	0.125	0.183	0.138	0.192

calculated with "Norm" program by P. Ulmer using: Amphibole Norm NAMP

CATIONS calculated on the bases of 23 oxygens and 13 cations + K + Na + Ca

Mineral: amphibole

Sarangar Gabbro undeformed **90/02/01**

Sample	p10s01p17	p10s01p04	p10s01p05	p10s01p06	p10s01p10	p10s01p11	p10s01p12	p10s01p13	p10s02p18	p10s03p11	p10s03p12	p10s04p06	p10s04p07	p10s04p09	p10s04p14	p10s04p15	p10s04p16	p10s06p08	p10s06p18
Site	s01	s01	s01	s01	s01	s01	s01	s01	s02	s03	s03	s04	s04	s04	s04	s04	s04	s06	s06
nr.	3	4	5	6	10	11	12	13	34	58	59	82	83	85	91	92	93	7	17
note	to plg	amp in contact to plg			amp in contact to plg				to cpx	to opx and plg		around magn			around magn			rim around opx	
SiO_2	40.49	40.45	40.28	40.10	39.28	39.56	41.32	39.87	40.85	40.47	38.82	37.97	38.24	38.80	38.24	38.33	38.41	40.06	41.36
TiO_2	0.04	0.06	0.06	0.08	0.43	0.38	0.04	0.01	0.69	0.05	0.02	0.49	1.50	1.19	2.17	2.55	2.57	0.07	0.10
Cr_2O_3	0.03	0.00	0.00	0.00	0.03	0.05	0.01	0.00	0.08	0.02	0.03	0.02	0.08	0.03	0.03	0.06	0.03	0.00	0.03
Al_2O_3	16.85	18.78	18.90	17.81	19.42	19.12	17.50	19.98	14.92	15.32	17.54	18.92	15.80	15.21	14.10	13.97	14.40	15.85	13.83
Fe_2O_3	7.23	8.19	9.75	10.10	7.96	7.66	11.19	7.25	5.58	7.82	7.06	6.02	2.32	2.99	2.65	1.11	1.08	5.21	5.41
FeO	10.41	10.29	9.06	9.25	11.31	11.50	8.09	10.87	13.31	9.57	10.79	13.68	16.79	16.21	17.05	18.44	18.74	11.40	11.44
MnO	0.20	0.29	0.34	0.31	0.28	0.27	0.25	0.27	0.24	0.28	0.29	0.28	0.20	0.23	0.18	0.16	0.17	0.25	0.26
MgO	8.15	7.21	7.36	7.31	6.34	6.46	7.82	6.87	7.77	8.95	7.79	5.49	6.05	6.52	6.63	6.49	6.18	8.18	8.73
NiO	0.01	0.04	0.00	0.00	0.01	0.00	0.00	0.00	0.00	0.03	0.00	0.00	0.00	0.00	0.03	0.00	0.00	0.06	0.05
CaO	10.83	10.58	10.28	10.19	10.45	10.50	10.15	10.70	11.28	10.87	11.08	10.62	10.83	10.96	11.10	11.28	11.20	10.70	10.66
Na_2O	1.55	1.50	1.76	1.65	1.71	1.67	1.39	1.72	1.37	1.53	1.53	1.61	1.28	1.13	1.08	1.16	1.15	1.40	1.50
K_2O	0.84	0.91	0.68	0.70	0.83	0.84	0.62	0.81	0.86	0.92	1.16	1.14	2.28	2.34	2.50	2.48	2.55	1.43	0.97
Cl	0.00	0.00	0.00	0.00	0.00	0.00	0.00	0.00	0.00	0.00	0.00	0.00	0.00	0.00	0.00	0.00	0.00	0.00	0.00
H_2O	2.00	2.04	2.05	2.02	2.02	2.02	2.05	2.04	1.99	1.98	1.98	1.96	1.92	1.92	1.91	1.91	1.92	1.95	1.95
Total	98.65	100.34	100.50	99.53	100.09	100.04	100.44	100.40	98.94	97.81	98.09	98.20	97.28	97.53	97.67	97.92	98.40	96.56	96.29
Si	6.058	5.947	5.900	5.948	5.824	5.867	6.033	5.860	6.166	6.113	5.888	5.804	5.988	6.051	6.001	6.017	6.003	6.150	6.350
Ti	0.004	0.006	0.006	0.009	0.048	0.042	0.005	0.001	0.078	0.006	0.003	0.056	0.176	0.140	0.256	0.301	0.302	0.008	0.012
Cr	0.004	0.000	0.000	0.001	0.003	0.006	0.001	0.000	0.010	0.002	0.004	0.002	0.010	0.003	0.004	0.007	0.003	0.001	0.004
Al	2.972	3.255	3.262	3.114	3.394	3.342	3.011	3.461	2.653	2.728	3.134	3.409	2.915	2.795	2.608	2.585	2.652	2.866	2.503
Fe^3	0.815	0.906	1.074	1.127	0.889	0.855	1.229	0.802	0.634	0.889	0.806	0.693	0.273	0.351	0.313	0.131	0.127	0.601	0.625
Fe^2	1.303	1.266	1.110	1.148	1.402	1.427	0.988	1.337	1.680	1.209	1.368	1.749	2.199	2.114	2.238	2.421	2.449	1.464	1.469
Mn	0.026	0.037	0.042	0.039	0.035	0.034	0.030	0.033	0.030	0.037	0.038	0.037	0.026	0.030	0.024	0.021	0.023	0.033	0.033
Mg	1.818	1.580	1.607	1.615	1.402	1.427	1.702	1.506	1.749	2.015	1.760	1.251	1.413	1.516	1.551	1.518	1.441	1.871	1.998
Ni	0.001	0.004	0.000	0.000	0.002	0.000	0.001	0.000	0.000	0.003	0.000	0.000	0.000	0.000	0.003	0.000	0.000	0.007	0.006
Ca	1.737	1.667	1.613	1.619	1.660	1.669	1.587	1.685	1.824	1.760	1.801	1.739	1.816	1.831	1.866	1.897	1.876	1.760	1.754
Na	0.451	0.429	0.501	0.475	0.491	0.481	0.395	0.491	0.402	0.449	0.450	0.476	0.388	0.342	0.328	0.352	0.348	0.417	0.446
K	0.161	0.170	0.126	0.133	0.157	0.160	0.115	0.153	0.166	0.177	0.225	0.223	0.454	0.466	0.500	0.497	0.509	0.279	0.190
OH	2.000	2.000	2.000	2.000	2.000	2.000	2.000	2.000	2.000	2.000	2.000	2.000	2.000	2.000	2.000	2.000	2.000	2.000	2.000
Σ Cations	15.349	15.266	15.240	15.227	15.308	15.310	15.097	15.329	15.391	15.385	15.476	15.438	15.658	15.639	15.694	15.746	15.732	15.457	15.390
xMg Fe(tot)	0.462	0.421	0.424	0.415	0.380	0.385	0.434	0.413	0.430	0.490	0.447	0.339	0.364	0.381	0.378	0.373	0.359	0.475	0.488
Tschermak	1.856	2.120	2.248	2.207	2.208	2.154	2.284	2.125	1.619	1.742	1.836	2.019	1.538	1.479	1.439	1.341	1.390	1.633	1.506
Edenite	0.349	0.266	0.240	0.227	0.308	0.310	0.097	0.329	0.391	0.385	0.476	0.438	0.658	0.639	0.694	0.746	0.732	0.457	0.390
Plagioclase	0.263	0.333	0.387	0.381	0.340	0.331	0.413	0.315	0.176	0.240	0.199	0.261	0.184	0.169	0.134	0.103	0.124	0.240	0.246

calculated with "Norm" program by P. Ulmer using: Amphibole Norm NAMP

CATIONS calculated on the bases of 23 oxygens and 13 cations + K + Na + Ca

Mineral: amphibole

Sarangar Gabbro mylonitic **16/01/01**

Sample	p11s01pr1	p11s01pr2	p11s02px2	p11s02px2	p11s02px4	p11s02px5	p11s02px7	p11s02px8	p11s02px1	p11s02px1	p11s06hb2	p11s06hb3	p11s06hb7	p11s06hb8	p11s06hb9	p11s09hb1	p11s09hb2	p11s09hb3	p11s09hb4
Site	s01	s01	s02	s02	s02	s02	s02	s02	s02	s02	s06	s06	s06	s06	s06	s09	s09	s09	s09
nr.	80	100	55	56	57	58	60	61	63	64	71	72	76	77	78	51	52	53	54
note	in contact to gt		bigger amp								amp in contact to plg					amp in contact to plg			
SiO_2	41.88	42.22	42.17	42.13	42.32	42.48	42.25	42.56	42.87	42.70	42.34	42.45	42.67	42.66	42.26	42.27	41.92	42.41	42.44
TiO_2	0.68	0.17	0.70	0.73	0.74	0.67	0.58	0.54	0.61	0.64	0.50	0.59	0.61	0.61	0.76	0.55	0.52	0.56	0.83
Cr_2O_3	0.02	0.00	0.50	0.33	0.07	0.02	0.03	0.00	0.00	0.00	0.00	0.04	0.00	0.05	0.00	0.00	0.05	0.00	0.03
Al_2O_3	17.61	17.29	16.54	16.70	16.78	16.78	17.25	17.02	16.26	16.86	17.52	17.39	17.15	17.00	16.99	17.19	17.68	17.48	17.16
Fe_2O_3	5.10	5.10	5.24	5.77	5.74	5.85	6.68	4.41	5.49	5.45	5.07	5.30	4.74	6.09	5.23	5.53	5.43	5.11	5.56
FeO	9.22	10.93	9.86	9.38	9.61	9.11	8.55	10.05	9.33	9.27	9.65	9.37	10.05	9.03	9.62	9.17	9.43	9.51	9.38
MnO	0.25	0.30	0.27	0.32	0.26	0.29	0.26	0.27	0.25	0.29	0.28	0.25	0.25	0.24	0.33	0.25	0.24	0.23	0.20
MgO	9.81	8.51	9.56	9.72	9.71	9.78	9.67	9.65	9.90	9.84	9.57	9.73	9.64	9.72	9.70	9.79	9.51	9.62	9.76
NiO	0.00	0.00	0.00	0.00	0.00	0.00	0.00	0.00	0.00	0.00	0.00	0.00	0.00	0.00	0.00	0.00	0.00	0.00	0.00
CaO	11.12	10.91	11.03	11.05	11.11	10.89	10.80	11.13	10.88	10.96	11.10	11.03	11.13	10.86	11.06	11.02	11.06	11.10	10.98
Na_2O	1.98	1.83	1.91	1.92	1.88	1.87	1.88	1.84	1.83	1.88	1.90	1.92	1.89	1.88	1.91	1.87	1.92	1.80	1.89
K_2O	0.57	0.44	0.59	0.60	0.57	0.60	0.54	0.58	0.58	0.55	0.57	0.58	0.58	0.53	0.60	0.61	0.60	0.56	0.61
Cl	0.00	0.00	0.00	0.00	0.00	0.00	0.00	0.00	0.00	0.00	0.00	0.00	0.00	0.00	0.00	0.00	0.00	0.00	0.00
H_2O	2.07	2.04	2.06	2.07	2.07	2.07	2.07	2.06	2.06	2.07	2.07	2.07	2.07	2.08	2.07	2.07	2.07	2.07	2.08
Total	100.29	99.75	100.43	100.73	100.84	100.40	100.55	100.12	100.06	100.51	100.59	100.70	100.80	100.75	100.54	100.32	100.42	100.46	100.92
Si	6.080	6.191	6.142	6.115	6.130	6.162	6.113	6.192	6.234	6.181	6.132	6.135	6.170	6.161	6.133	6.135	6.086	6.142	6.127
Ti	0.074	0.019	0.076	0.080	0.080	0.073	0.063	0.059	0.066	0.069	0.054	0.064	0.066	0.066	0.083	0.060	0.056	0.061	0.090
Cr	0.002	0.000	0.058	0.038	0.008	0.002	0.004	0.001	0.000	0.000	0.000	0.004	0.001	0.006	0.001	0.001	0.005	0.000	0.003
Al	3.013	2.988	2.840	2.857	2.865	2.869	2.941	2.918	2.786	2.876	2.991	2.962	2.923	2.893	2.907	2.940	3.026	2.984	2.920
Fe^3	0.557	0.563	0.574	0.630	0.625	0.639	0.727	0.483	0.601	0.594	0.553	0.576	0.516	0.662	0.572	0.604	0.594	0.557	0.604
Fe^2	1.119	1.341	1.202	1.139	1.164	1.105	1.035	1.223	1.135	1.122	1.169	1.132	1.215	1.091	1.167	1.113	1.145	1.151	1.133
Mn	0.031	0.037	0.033	0.040	0.031	0.035	0.032	0.033	0.030	0.035	0.035	0.030	0.030	0.030	0.040	0.031	0.030	0.028	0.025
Mg	2.124	1.861	2.075	2.102	2.096	2.115	2.085	2.092	2.147	2.122	2.066	2.096	2.078	2.092	2.098	2.117	2.058	2.076	2.099
Ni	0.000	0.000	0.000	0.000	0.000	0.000	0.000	0.000	0.000	0.000	0.000	0.000	0.000	0.000	0.000	0.000	0.000	0.000	0.000
Ca	1.729	1.714	1.721	1.718	1.724	1.693	1.675	1.734	1.695	1.700	1.722	1.708	1.724	1.681	1.721	1.714	1.720	1.723	1.699
Na	0.556	0.519	0.541	0.539	0.527	0.526	0.526	0.520	0.515	0.529	0.533	0.538	0.531	0.525	0.538	0.526	0.540	0.505	0.530
K	0.106	0.083	0.109	0.110	0.106	0.110	0.100	0.108	0.107	0.102	0.106	0.107	0.108	0.098	0.110	0.113	0.111	0.103	0.111
OH	2.000	2.000	2.000	2.000	2.000	2.000	2.000	2.000	2.000	2.000	2.000	2.000	2.000	2.000	2.000	2.000	2.000	2.000	2.000
Σ Cations	15.391	15.315	15.371	15.368	15.357	15.329	15.301	15.363	15.317	15.331	15.362	15.352	15.363	15.304	15.369	15.352	15.371	15.330	15.340
xMg Fe(tot)	0.559	0.494	0.539	0.543	0.540	0.548	0.542	0.551	0.553	0.553	0.545	0.551	0.545	0.544	0.547	0.552	0.542	0.549	0.547
Tschermak	1.800	1.780	1.766	1.799	1.789	1.817	1.911	1.711	1.754	1.789	1.784	1.805	1.743	1.854	1.777	1.799	1.824	1.805	1.834
Edenite	0.391	0.315	0.371	0.368	0.357	0.329	0.301	0.363	0.317	0.331	0.362	0.352	0.363	0.304	0.369	0.352	0.371	0.330	0.340
Plagioclase	0.271	0.286	0.279	0.282	0.276	0.308	0.325	0.266	0.305	0.301	0.278	0.293	0.276	0.319	0.280	0.286	0.280	0.277	0.301

calculated with "Norm" program by P. Ulmer using: Amphibole Norm NAMP

CATIONS calculated on the bases of 23 oxygens and 13 cations + K + Na + Ca

Mineral: amphibole

Sarangar Gabbro undeformed **16/01/01**

Sample	p13s05am17	p13s05am18	p13s05am19	p13s05am20	p13s1auk1	p13s1auk5	p13s1chb1	p13s1chb3	p13s3ahb7	p13s3bam6	ps3csy4	ps3csy4	ps3ahb1	ps3ahb2	ps3ahb4	ps3bam1	ps3bam2	ps3bam5
Site	s05	s05	s05	s05	s1a	s1a	s1c	s1c	s3a	s3b	s3c	s3c	s3a	s3a	s3a	a3b	a3b	a3b
nr.	89	90	91	92	6	10	34	40	99	117	131	132	93	94	96	112	113	116
note	amp around opx, second site				amp around		amp around ilm		close to symplectite		amp at symplectite		amp at symplectite (epi)			amp at symplectite (epi)		
											*	*	*	*	*	*	*	*
SiO_2	42.44	42.81	42.80	40.42	40.40	41.52	40.15	39.90	44.01	43.87	51.77	51.45	51.42	53.63	51.12	52.49	51.26	51.60
TiO_2	0.26	0.24	0.32	0.08	0.52	0.60	0.52	0.55	0.41	0.42	0.25	0.24	0.35	0.25	0.28	0.27	0.26	0.27
Cr_2O_3	0.00	0.00	0.04	0.02	0.04	0.02	0.02	0.04	0.05	0.00	0.02	0.03	0.06	0.03	0.00	0.00	0.04	0.04
Al_2O_3	17.05	16.53	16.92	20.13	18.89	17.48	18.97	18.53	14.05	14.36	5.91	5.88	5.85	4.80	6.32	5.03	6.25	6.21
Fe_2O_3	5.86	5.89	5.53	5.96	7.67	5.27	4.74	5.35	5.51	5.55	1.88	1.83	1.86	0.96	2.12	1.81	2.36	1.78
FeO	10.21	10.20	10.45	10.91	10.45	11.69	14.52	14.55	9.29	10.66	11.97	11.55	10.82	10.71	10.83	11.20	10.96	10.74
MnO	0.20	0.28	0.29	0.32	0.30	0.22	0.31	0.26	0.28	0.27	0.30	0.24	0.27	0.27	0.28	0.21	0.28	0.26
MgO	8.96	8.98	8.98	7.39	7.34	8.01	5.57	5.62	10.57	9.91	14.65	14.61	14.85	16.30	14.99	15.23	14.61	15.04
NiO	0.00	0.00	0.00	0.00	0.00	0.00	0.00	0.00	0.00	0.00	0.00	0.00	0.00	0.00	0.00	0.00	0.00	0.00
CaO	10.94	10.88	11.01	10.80	10.45	10.85	10.84	10.69	11.08	11.23	11.03	11.10	11.60	11.55	11.06	11.55	11.35	11.32
Na_2O	1.69	1.64	1.61	1.79	1.73	1.75	1.49	1.62	1.45	1.57	0.66	0.69	0.65	0.45	0.68	0.67	0.81	0.70
K_2O	0.57	0.49	0.64	1.02	0.94	0.71	0.81	0.96	0.58	0.51	0.13	0.14	0.22	0.13	0.16	0.16	0.22	0.27
Cl	0.00	0.00	0.00	0.00	0.00	0.00	0.00	0.00	0.00	0.00	0.00	0.00	0.00	0.00	0.00	0.00	0.00	0.00
H_2O	2.06	2.05	2.07	2.06	2.05	2.04	2.01	2.01	2.05	2.06	2.10	2.09	2.09	2.13	2.09	2.11	2.10	2.10
Total	100.24	100.03	100.66	100.90	100.76	100.16	99.96	100.08	99.33	100.41	100.67	99.84	100.03	101.21	99.93	100.73	100.50	100.33
Si	6.185	6.248	6.214	5.896	5.916	6.102	5.985	5.965	6.440	6.394	7.389	7.394	7.370	7.540	7.327	7.466	7.326	7.361
Ti	0.028	0.026	0.035	0.009	0.057	0.066	0.058	0.062	0.045	0.046	0.027	0.026	0.037	0.026	0.030	0.029	0.028	0.029
Cr	0.001	0.001	0.005	0.002	0.005	0.002	0.003	0.004	0.005	0.000	0.002	0.003	0.007	0.003	0.000	0.000	0.005	0.005
Al	2.928	2.844	2.895	3.462	3.260	3.028	3.333	3.264	2.424	2.467	0.995	0.996	0.988	0.795	1.067	0.844	1.052	1.045
Fe^3	0.643	0.647	0.604	0.654	0.845	0.583	0.532	0.602	0.607	0.609	0.201	0.198	0.200	0.102	0.229	0.194	0.254	0.191
Fe^2	1.244	1.245	1.269	1.331	1.279	1.437	1.811	1.818	1.137	1.299	1.428	1.388	1.297	1.260	1.298	1.332	1.310	1.282
Mn	0.024	0.035	0.035	0.040	0.037	0.027	0.040	0.034	0.035	0.033	0.037	0.030	0.033	0.032	0.034	0.026	0.034	0.032
Mg	1.946	1.954	1.943	1.607	1.602	1.756	1.238	1.251	2.306	2.152	3.117	3.130	3.172	3.415	3.202	3.229	3.112	3.197
Ni	0.000	0.000	0.000	0.000	0.000	0.000	0.000	0.000	0.000	0.000	0.000	0.000	0.000	0.000	0.000	0.000	0.000	0.000
Ca	1.709	1.701	1.713	1.688	1.639	1.709	1.731	1.712	1.737	1.754	1.687	1.709	1.781	1.739	1.699	1.759	1.738	1.730
Na	0.477	0.465	0.454	0.507	0.491	0.499	0.429	0.469	0.411	0.443	0.184	0.191	0.181	0.122	0.190	0.184	0.225	0.193
K	0.106	0.092	0.119	0.189	0.176	0.134	0.154	0.184	0.109	0.095	0.023	0.025	0.040	0.024	0.030	0.029	0.041	0.050
OH	2.000	2.000	2.000	2.000	2.000	2.000	2.000	2.000	2.000	2.000	2.000	2.000	2.000	2.000	2.000	2.000	2.000	2.000
Σ Cations	15.292	15.259	15.286	15.384	15.306	15.342	15.314	15.365	15.256	15.291	15.089	15.089	15.105	15.057	15.104	15.092	15.123	15.112
xMg Fe(tot)	0.508	0.508	0.509	0.447	0.430	0.465	0.346	0.341	0.569	0.530	0.657	0.664	0.679	0.715	0.677	0.679	0.665	0.685
Tschermak	1.814	1.792	1.788	2.031	2.139	1.846	1.969	1.958	1.567	1.562	0.640	0.644	0.640	0.492	0.684	0.562	0.693	0.658
Edenite	0.292	0.259	0.286	0.384	0.306	0.342	0.314	0.365	0.256	0.291	0.089	0.089	0.105	0.057	0.104	0.092	0.123	0.112
Plagioclase	0.291	0.299	0.287	0.312	0.361	0.291	0.269	0.288	0.263	0.247	0.118	0.127	0.115	0.089	0.115	0.121	0.142	0.130

calculated with "Norm" program by P. Ulmer using: Amphibole Norm NAMP
CATIONS calculated on the bases of 23 oxygens and 13 cations + K + Na + Ca

***calculated with "Norm" program by P. Ulmer using: Amphibole Norm SK**
***CATIONS calculated on the bases of 23 oxygens and averaged Fe3+**

Mineral: amphibole

Kiru amphibolite **46/02/01**

Sample	p19s01p05	p19s01p06	p19s01p07	p19s02p11	p19s02p13	p19s03p01	p19s03p02	p19s03p04	p19s03p09	p19s03p12	p19s03p17	p19s03p18	p19s04p08	p19s04p10	p19s04p17	p19s04p18	p19s05p04	p19s05p05	p19s05p08
Site	s01	s01	s01	s02	s02	s03	s03	s03	s03	s03	s03	s03	s04	s04	s04	s04	s05	s05	s05
nr.	5	6	7	22	24	31	32	34	39	42	47	48	68	70	77	78	84	85	89
note	amp in contact to epi and plg			in contact to plg		amp in contact to chl			in contact to chl		in contact to plg		in contact to sph		in contact to plg		amp in contact to plg		
SiO_2	42.51	42.74	42.05	43.21	43.43	42.19	42.61	42.09	43.19	42.76	43.35	44.29	43.11	44.15	42.77	42.80	44.21	43.19	44.08
TiO_2	0.68	0.68	0.63	0.61	0.70	0.75	0.68	0.80	0.53	0.76	0.58	0.59	0.53	0.66	0.78	0.75	0.55	0.59	0.64
Cr_2O_3	0.02	0.04	0.00	0.03	0.02	0.04	0.01	0.03	0.00	0.03	0.05	0.05	0.03	0.04	0.04	0.03	0.02	0.03	0.00
Al_2O_3	14.13	14.21	13.68	13.88	13.21	13.50	13.69	13.88	13.81	14.02	13.60	12.78	13.76	13.06	13.58	13.62	12.98	13.61	12.38
Fe_2O_3	3.26	2.26	4.89	2.41	4.02	2.74	3.79	2.29	2.97	3.38	2.84	2.86	2.57	4.92	2.44	3.13	2.43	2.40	3.26
FeO	11.37	12.01	9.97	11.31	10.25	11.85	10.70	11.93	11.04	11.13	10.92	10.51	11.41	9.12	11.70	11.30	10.58	10.85	10.61
MnO	0.35	0.35	0.34	0.32	0.33	0.32	0.36	0.38	0.35	0.31	0.37	0.36	0.36	0.33	0.35	0.38	0.33	0.35	0.35
MgO	10.78	10.62	10.89	11.01	11.38	10.65	10.87	10.41	10.94	10.74	11.28	11.67	10.70	11.36	10.73	10.79	11.52	11.20	11.75
NiO	0.00	0.00	0.03	0.03	0.00	0.00	0.00	0.02	0.00	0.01	0.00	0.06	0.00	0.00	0.05	0.05	0.01	0.02	0.07
CaO	12.03	12.09	11.74	11.92	11.88	11.85	11.77	11.91	11.72	11.76	12.07	11.91	11.76	11.10	11.90	11.89	11.88	11.87	12.00
Na_2O	1.60	1.58	1.46	1.66	1.38	1.72	1.50	1.46	1.59	1.57	1.63	1.48	1.68	1.50	1.52	1.50	1.37	1.63	1.44
K_2O	1.05	1.01	1.05	0.89	1.03	1.01	1.07	1.13	1.10	1.10	0.77	0.84	0.73	0.96	1.05	1.06	0.80	0.81	0.96
Cl	0.00	0.00	0.00	0.00	0.00	0.00	0.00	0.00	0.00	0.00	0.00	0.00	0.00	0.00	0.00	0.00	0.00	0.00	0.00
H_2O	2.03	2.03	2.01	2.03	2.04	2.00	2.02	2.00	2.03	2.03	2.04	2.04	2.02	2.04	2.01	2.02	2.03	2.02	2.04
Total	99.80	99.63	98.74	99.31	99.67	98.64	99.08	98.32	99.27	99.59	99.51	99.43	98.65	99.24	98.92	99.32	98.71	98.56	99.57
Si	6.280	6.320	6.268	6.381	6.389	6.318	6.325	6.317	6.386	6.317	6.385	6.504	6.407	6.477	6.366	6.345	6.525	6.411	6.487
Ti	0.075	0.075	0.071	0.067	0.077	0.085	0.076	0.090	0.059	0.084	0.065	0.065	0.059	0.072	0.087	0.084	0.061	0.066	0.071
Cr	0.002	0.004	0.001	0.003	0.003	0.005	0.001	0.003	0.001	0.003	0.006	0.006	0.003	0.004	0.004	0.004	0.002	0.003	0.001
Al	2.460	2.477	2.403	2.416	2.290	2.382	2.395	2.454	2.406	2.441	2.361	2.213	2.410	2.259	2.383	2.381	2.259	2.381	2.147
Fe^3	0.363	0.252	0.548	0.268	0.445	0.309	0.423	0.258	0.330	0.376	0.315	0.316	0.288	0.543	0.273	0.349	0.270	0.268	0.361
Fe^2	1.404	1.486	1.242	1.397	1.260	1.484	1.329	1.497	1.365	1.375	1.345	1.290	1.418	1.119	1.457	1.401	1.306	1.347	1.306
Mn	0.044	0.044	0.043	0.040	0.042	0.041	0.045	0.049	0.044	0.039	0.046	0.045	0.045	0.042	0.045	0.047	0.042	0.044	0.043
Mg	2.373	2.341	2.420	2.424	2.495	2.377	2.405	2.329	2.410	2.365	2.477	2.554	2.370	2.485	2.380	2.384	2.535	2.478	2.577
Ni	0.000	0.000	0.004	0.003	0.000	0.000	0.000	0.003	0.000	0.001	0.000	0.007	0.000	0.000	0.005	0.006	0.002	0.002	0.008
Ca	1.905	1.916	1.874	1.886	1.872	1.902	1.872	1.916	1.856	1.861	1.904	1.875	1.872	1.744	1.897	1.889	1.878	1.887	1.892
Na	0.458	0.452	0.422	0.476	0.394	0.501	0.431	0.424	0.455	0.449	0.466	0.421	0.484	0.427	0.439	0.431	0.393	0.468	0.411
K	0.198	0.191	0.199	0.168	0.194	0.194	0.203	0.216	0.208	0.208	0.145	0.157	0.139	0.180	0.200	0.201	0.150	0.152	0.180
OH	2.000	2.000	2.000	2.000	2.000	2.000	2.000	2.000	2.000	2.000	2.000	2.000	2.000	2.000	2.000	2.000	2.000	2.000	2.000
Σ Cations	15.561	15.560	15.496	15.530	15.460	15.596	15.506	15.555	15.518	15.518	15.514	15.453	15.494	15.351	15.536	15.520	15.420	15.508	15.484
xMg Fe(tot)	0.573	0.574	0.575	0.593	0.594	0.570	0.579	0.570	0.587	0.575	0.599	0.614	0.582	0.599	0.579	0.577	0.617	0.605	0.607
Tschermak	1.254	1.204	1.362	1.203	1.280	1.184	1.298	1.213	1.240	1.304	1.197	1.168	1.226	1.428	1.200	1.246	1.177	1.194	1.137
Edenite	0.561	0.560	0.496	0.530	0.460	0.596	0.506	0.555	0.518	0.518	0.514	0.453	0.494	0.351	0.536	0.520	0.420	0.508	0.484
Plagioclase	0.095	0.084	0.126	0.114	0.128	0.098	0.128	0.084	0.144	0.139	0.096	0.125	0.128	0.256	0.103	0.111	0.122	0.113	0.108

calculated with "Norm" program by P. Ulmer using: Amphibole Norm NAMP

CATIONS calculated on the bases of 23 oxygens and 13 cations + K + Na + Ca

Table Appendix 3.5: Representative chemical composition of biotite, muscovite, chlorite.

	Mineral: biotite			*Mineral: biotite*						*Mineral: muscovite*				
	Granulitic Gabbro mylonitic **13/01/01**			Sarangar Gabbro undeformed **16/01/01**						Sarangar Gabbro mylonitic **16/01/01**				
Sample	p01s10bt2	p01s10bt1	p01s10bt3	p13s02bt1	p13s02bt6	p13s02bt2	p13s02bt3	p13s02bt5	p13s02bt4	p11s08wm1	p11s08ri1	p11s08wm4	p11s08wm2	p11s08wm3
Site	s10	s10	s10	s02	s02	s02	s02	s02	s02	s08	s08	s08	s08	s08
nr.														
note	bt in gt-fracture			bt in contact to amp						mica in contact to plg				
SiO_2	33.45	33.12	34.56	30.18	31.25	33.34	31.82	34.73	29.30	45.88	46.57	46.00	45.80	45.58
TiO_2	1.80	1.59	1.76	1.59	4.26	2.25	2.02	2.12	2.08	0.13	0.03	0.04	0.08	0.00
Cr_2O_3	0.58	0.70	0.60	0.12	0.17	0.18	0.14	0.23	0.20	0.00	0.04	0.00	0.00	0.00
Al_2O_3	17.22	16.37	17.44	18.15	16.68	17.87	18.51	18.56	18.59	37.25	37.37	36.37	36.66	35.90
Fe_2O_3	3.08	0.00	0.00	25.95	10.84	12.67	17.92	0.80	24.43	2.10	1.68	2.06	2.03	2.24
FeO	14.57	15.72	16.54	0.00	10.42	9.13	5.08	16.68	0.00	0.00	0.00	0.00	0.00	0.00
MnO	0.04	0.05	0.02	0.21	0.16	0.19	0.12	0.11	0.17	0.04	0.04	0.00	0.03	0.00
MgO	12.71	11.92	12.74	14.20	13.07	13.03	13.62	12.57	14.86	0.61	0.45	1.06	0.87	1.07
NiO														
CaO	0.14	0.25	0.09	0.54	2.91	0.50	0.34	0.09	0.96	0.03	0.05	0.01	0.01	0.02
Na_2O	0.18	0.21	0.25	0.08	0.08	0.11	0.08	0.27	0.11	1.16	1.49	1.13	1.09	1.05
K_2O	6.62	6.76	7.81	1.43	0.36	3.29	2.97	6.94	0.40	8.54	8.53	8.77	8.69	8.75
H_2O	3.81	3.65	3.84	4.02	3.89	3.98	4.00	3.93	4.01	4.62	4.63	4.60	4.59	4.56
Total	94.21	90.33	95.66	96.47	94.07	96.54	96.62	97.02	95.11	100.36	100.88	100.04	99.85	99.18
Si	2.629	2.724	2.695	2.254	2.411	2.510	2.385	2.649	2.191	2.979	3.016	2.999	2.990	3.000
Ti	0.107	0.098	0.103	0.090	0.247	0.127	0.114	0.122	0.117	0.006	0.002	0.002	0.004	0.000
Cr	0.036	0.045	0.037	0.007	0.010	0.011	0.009	0.014	0.012	0.000	0.002	0.000	0.000	0.000
Al	1.596	1.587	1.603	1.597	1.516	1.586	1.635	1.669	1.638	2.851	2.853	2.795	2.821	2.784
Fe^3	0.182	0.000	0.000	1.458	0.629	0.718	1.011	0.046	1.375	0.103	0.082	0.101	0.100	0.111
Fe^2	0.958	1.081	1.079	0.000	0.672	0.575	0.318	1.064	0.000	0.000	0.000	0.000	0.000	0.000
Mn	0.003	0.004	0.002	0.014	0.010	0.012	0.008	0.007	0.011	0.002	0.002	0.000	0.002	0.000
Mg	1.490	1.461	1.481	1.581	1.503	1.462	1.522	1.429	1.656	0.059	0.044	0.103	0.085	0.105
Ni														
Ca	0.012	0.022	0.008	0.043	0.241	0.040	0.027	0.007	0.077	0.002	0.003	0.001	0.001	0.001
Na	0.028	0.033	0.037	0.011	0.012	0.016	0.011	0.040	0.015	0.146	0.187	0.143	0.138	0.135
K	0.664	0.709	0.777	0.136	0.035	0.316	0.284	0.675	0.038	0.707	0.705	0.729	0.724	0.734
OH														
H	2.000	2.000	2.000	2.000	2.000	2.000	2.000	2.000	2.000	2.000	2.000	2.000	2.000	2.000
Σ Cations	7.703	7.764	7.822	7.190	7.287	7.372	7.322	7.722	7.130	6.855	6.895	6.872	6.863	6.870
xMg Fe(tot)	0.566	0.575	0.579	0.520	0.536	0.531	0.534	0.563	0.546	0.364	0.348	0.504	0.459	0.486

biotite calculated with "Norm" program by P. Ulmer using: Mica Norm BIO (Standard)
CATIONS calculated on the bases of 11 oxygens 7 cations + Na + K + Ca
muscovite calculated with "Norm" program by P. Ulmer using: Mica Norm MUS (Standard)
CATIONS calculated on the bases of 11 oxygens and 6 cations + Na + K + Ca
chlorite calculated with "Norm" program by P. Ulmer using: General OXIDE Norm all Fe(II+)
CATIONS calculated on the basis of 18. Oxygens

Mineral: chlorite

Sarangar Gabbro mylonitic **90/02/01**

Sample	p07a05p09	p07a05p11	p07a05p12	p07a05p15
Site	a05	a05	a05	a05
nr.	85	87	88	91
note	fracture fill in gt			
SiO_2	24.61	23.59	23.93	24.97
TiO_2	0.09	0.06	0.03	0.06
Cr_2O_3	0.00	0.05	0.00	0.02
Al_2O_3	20.88	20.10	21.03	21.33
Fe_2O_3	0.00	0.00	0.00	0.00
FeO	25.49	25.56	26.31	26.00
MnO	0.28	0.19	0.27	0.26
MgO	14.85	14.31	14.34	15.12
NiO	0.00	0.00	0.03	0.00
CaO	0.13	0.11	0.09	0.06
Na_2O	0.02	0.05	0.07	0.06
K_2O	0.03	0.03	0.04	0.00
H_2O	2.30	2.22	2.27	2.34
Total	88.68	86.26	88.41	90.23
Si	3.215	3.185	3.156	3.206
Ti	0.009	0.006	0.003	0.006
Cr	0.001	0.005	0.000	0.002
Al	3.215	3.198	3.269	3.228
Fe^3	0.000	0.000	0.000	0.000
Fe^2	2.785	2.886	2.902	2.792
Mn	0.031	0.022	0.030	0.028
Mg	2.890	2.880	2.819	2.894
Ni	0.000	0.000	0.003	0.000
Ca	0.018	0.015	0.012	0.009
Na	0.006	0.014	0.018	0.014
K	0.005	0.006	0.006	0.001
OH	2.000	2.000	2.000	2.000
H				
Σ Cations	14.174	14.217	14.218	14.180
xMg Fe(tot)	0.509	0.499	0.493	0.509

Mineral: chlorite

Sarangar Gb undef. **90/02/01**

Sample	p10s02p30	p10s03p10
Site	s02	s03
nr.	46	57
note	to cpx	at rim
SiO_2	29.88	29.73
TiO_2	0.02	0.17
Cr_2O_3	0.05	0.00
Al_2O_3	12.73	17.51
Fe_2O_3	0.00	0.00
FeO	28.96	23.43
MnO	0.14	0.23
MgO	13.16	15.45
NiO	0.00	0.04
CaO	0.31	0.31
Na_2O	0.03	0.02
K_2O	0.03	0.37
H_2O	2.23	2.37
Total	87.54	89.63
Si	4.010	3.768
Ti	0.002	0.016
Cr	0.005	0.000
Al	2.014	2.616
Fe^3	0.000	0.000
Fe^2	3.250	2.484
Mn	0.016	0.025
Mg	2.633	2.919
Ni	0.000	0.004
Ca	0.044	0.042
Na	0.008	0.005
K	0.005	0.060
OH	2.000	2.000
H		
Σ Cations	13.986	13.940
xMg Fe(tot)	0.448	0.540

Mineral: chlorite

Kiru amphibolite **46/02/01**

Sample	p19s03p06	p19s03p07	p19s03p08	p19s03p13	p19s03p14	p19s03p15	p19s06p05	p19s06p06	p19s06p07	p19s06p09	p19s06p10
Site	s03	s03	s03	s03	s03	s03	s06	s06	s06	s06	s06
nr.	36	37	38	43	44	45	95	96	97	99	100
note	chl in contact to amp			chl in contact to amp			in contact to qtz-rich layer				
SiO_2	29.34	33.83	36.45	36.30	36.19	31.30	28.47	35.05	30.17	34.89	37.03
TiO_2	4.69	2.12	1.76	1.87	1.73	0.79	1.72	1.52	1.78	2.01	2.19
Cr_2O_3	0.06	0.04	0.02	0.03	0.00	0.00	0.03	0.01	0.02	0.00	0.00
Al_2O_3	15.28	18.58	17.01	18.33	17.82	17.93	18.20	17.52	17.21	18.28	17.72
Fe_2O_3	0.00	0.00	0.00	0.00	0.00	0.00	0.00	0.00	0.00	0.00	0.00
FeO	13.68	14.73	14.18	14.15	13.98	17.36	15.47	16.08	16.24	13.82	13.66
MnO	0.19	0.16	0.15	0.15	0.19	0.22	0.26	0.20	0.21	0.13	0.17
MgO	14.37	14.10	13.73	14.07	13.79	17.93	14.66	15.66	16.35	14.07	14.20
NiO	0.03	0.05	0.05	0.00	0.03	0.00	0.02	0.00	0.00	0.05	0.05
CaO	3.90	0.40	0.57	0.08	0.03	0.25	1.25	0.64	1.06	0.39	0.00
Na_2O	0.06	0.10	0.09	0.14	0.14	0.06	0.08	0.05	0.06	0.28	0.22
K_2O	0.63	6.19	5.13	8.43	8.81	3.14	1.03	2.58	1.05	6.62	9.12
H_2O	2.30	2.50	2.51	2.58	2.55	2.46	2.27	2.52	2.35	2.52	2.60
Total	84.53	92.81	91.64	96.14	95.27	91.45	83.46	91.81	86.52	93.08	96.97
Si	3.822	4.058	4.361	4.216	4.252	3.821	3.756	4.176	3.843	4.156	4.268
Ti	0.460	0.191	0.158	0.163	0.152	0.073	0.171	0.136	0.171	0.180	0.190
Cr	0.006	0.004	0.002	0.002	0.001	0.001	0.003	0.001	0.002	0.001	0.001
Al	2.346	2.626	2.398	2.509	2.467	2.580	2.831	2.460	2.584	2.566	2.408
Fe^3	0.000	0.000	0.000	0.000	0.000	0.000	0.000	0.000	0.000	0.000	0.000
Fe^2	1.490	1.478	1.418	1.375	1.374	1.772	1.707	1.602	1.730	1.377	1.317
Mn	0.021	0.017	0.016	0.015	0.019	0.023	0.029	0.020	0.023	0.013	0.017
Mg	2.790	2.521	2.448	2.436	2.415	3.262	2.884	2.780	3.104	2.498	2.439
Ni	0.003	0.004	0.004	0.000	0.003	0.001	0.002	0.000	0.001	0.004	0.004
Ca	0.545	0.052	0.074	0.010	0.004	0.033	0.176	0.082	0.145	0.050	0.000
Na	0.015	0.024	0.020	0.032	0.032	0.014	0.020	0.011	0.014	0.064	0.049
K	0.105	0.947	0.784	1.249	1.320	0.489	0.173	0.392	0.170	1.006	1.341
OH	2.000	2.000	2.000	2.000	2.000	2.000	2.000	2.000	2.000	2.000	2.000
H											
Σ Cations	13.602	13.922	13.683	14.006	14.038	14.068	13.753	13.659	13.786	13.915	14.033
xMg Fe(tot)	0.652	0.630	0.633	0.639	0.637	0.648	0.628	0.634	0.642	0.645	0.649

biotite calculated with "Norm" program by P. Ulmer using: Mica Norm BIO (Standard)
CATIONS calculated on the bases of 11 oxygens 7 cations + Na + K + Ca
muscovite calculated with "Norm" program by P. Ulmer using: Mica Norm MUS (Standard)
CATIONS calculated on the bases of 11 oxygens and 6 cations + Na + K + Ca
chlorite calculated with "Norm" program by P. Ulmer using: General OXIDE Norm all Fe(II+)
CATIONS calculated on the basis of 18. Oxygens

Table Appendix 3.6: Representative chemical composition of epidote and sphene.

Mineral: epidote — Granulitic Gabbro mylonitic **94/04/01**

Sample	p04s01p07	p04s02p06	p04s03p18	p04s04pro	p04s04pro	p04s04pro	p04s05p12	p04s05p20
Site	s01	s02	s03	s04	s04	s04	s05	s05
nr.	7	6	43	1	2	12	12	22
note	to plg	to gt	epi at s03	profile through matrix			epi in contact to gt	
SiO_2	38.64	38.60	38.11	38.47	37.60	38.82	38.46	38.49
TiO_2	0.07	0.04	0.07	0.17	0.09	0.02	0.04	0.05
Cr_2O_3	0.00	0.00	0.00	0.03	0.03	0.00	0.00	0.00
Al_2O_3	26.35	26.61	26.83	29.00	28.11	28.42	27.07	26.01
Fe_2O_3	9.26	9.28	9.19	6.07	7.42	6.90	8.97	10.25
FeO	0.00	0.00	0.00	0.00	0.00	0.00	0.00	0.00
MnO								
Mn_2O_3	0.02	0.08	0.11	0.07	0.09	0.03	0.04	0.07
MgO	0.07	0.12	0.11	0.15	0.10	0.10	0.00	0.15
NiO	0.04	0.00	0.00	0.00	0.00	0.00	0.01	0.00
CaO	23.68	23.24	23.48	23.10	23.31	23.41	23.44	22.67
Na_2O	0.01	0.02	0.03	0.02	0.04	0.06	0.00	0.03
K_2O	0.04	0.02	0.00	0.02	0.01	0.01	0.01	0.00
H_2O	1.92	1.92	1.91	1.92	1.90	1.93	1.92	1.91
Total	100.10	99.93	99.83	99.02	98.69	99.71	99.97	99.64
Si	3.019	3.016	2.985	2.997	2.962	3.014	3.002	3.022
Ti	0.004	0.003	0.004	0.010	0.005	0.001	0.002	0.003
Cr	0.000	0.000	0.000	0.002	0.002	0.000	0.000	0.000
Al	2.426	2.450	2.476	2.663	2.609	2.600	2.490	2.406
Fe^3	0.545	0.545	0.542	0.356	0.440	0.403	0.527	0.606
Fe^2	0.000	0.000	0.000	0.000	0.000	0.000	0.000	0.000
Mn								
Mn^{3+}	0.001	0.005	0.006	0.004	0.006	0.002	0.003	0.005
Mg	0.008	0.014	0.013	0.018	0.012	0.011	0.000	0.018
Ni	0.003	0.000	0.000	0.000	0.000	0.000	0.001	0.000
Ca	1.982	1.945	1.970	1.928	1.967	1.947	1.960	1.906
Na	0.002	0.003	0.005	0.004	0.006	0.010	0.001	0.004
K	0.004	0.002	0.000	0.002	0.001	0.001	0.001	0.001
OH	1.000	1.000	1.000	1.000	1.000	1.000	1.000	1.000
Σ Cations	18.006	18.016	17.999	18.017	17.991	18.012	18.013	18.030
Zoisite	0.430	0.453	0.465	0.672	0.578	0.601	0.492	0.409
Epidote	0.545	0.545	0.535	0.328	0.422	0.399	0.508	0.591

Mineral: epidote — Sarangar Gb undef. **90/02/01**

Sample	p10s02p20	p10s02p22
Site	s02	s02
nr.	36	37
note	in contact to cpx	
SiO_2	38.40	38.29
TiO_2	0.02	0.00
Cr_2O_3	0.02	0.00
Al_2O_3	27.60	27.21
Fe_2O_3	8.20	8.88
FeO	0.00	0.00
MnO		
Mn_2O_3	0.18	0.12
MgO	0.06	0.08
NiO	0.00	0.00
CaO	23.26	23.24
Na_2O	0.04	0.00
K_2O	0.00	0.02
H_2O	1.92	1.92
Total	99.69	99.75
Si	2.997	2.994
Ti	0.001	0.000
Cr	0.001	0.000
Al	2.539	2.507
Fe^3	0.481	0.522
Fe^2	0.000	0.000
Mn		
Mn^{3+}	0.011	0.007
Mg	0.007	0.009
Ni	0.000	0.000
Ca	1.945	1.947
Na	0.007	0.000
K	0.001	0.002
OH	1.000	1.000
Σ Cations	18.010	18.011
Zoisite	0.538	0.501
Epidote	0.462	0.499

Mineral: epidote — Sarangar Gabbro mylonitic **16/01/01**

Sample	p11s01pr2	p11s01pr2	p11s01pr2	p11s01pr2	p11s04px2	p11s04px5	p11s07uk2
Site	s01	s01	s01	s01	s04	s04	s07
nr.	103	104	105	118	30	35	13
note	in contact to gt				in contact to plg		
SiO_2	38.74	38.67	39.28	38.41	37.44	38.93	38.77
TiO_2	0.03	0.07	0.04	0.04	0.06	0.07	0.10
Cr_2O_3	0.00	0.02	0.02	0.00	0.00	0.05	0.00
Al_2O_3	27.37	27.72	27.44	18.22	29.28	29.12	28.20
Fe_2O_3	8.88	9.01	9.31	27.75	6.38	6.77	7.51
FeO	0.00	0.00	0.00	0.00	0.00	0.00	0.00
MnO							
Mn_2O_3	0.21	0.24	0.27	4.86	0.13	0.28	0.17
MgO	0.09	0.09	0.09	3.49	0.06	0.08	0.08
NiO	0.00	0.00	0.00	0.00	0.00	0.00	0.00
CaO	22.91	22.98	22.97	6.12	23.03	23.33	23.24
Na_2O	0.00	0.03	0.01	0.09	0.02	0.01	0.04
K_2O	0.02	0.00	0.00	0.07	0.01	0.02	0.03
H_2O	1.93	1.94	1.95	1.89	1.91	1.95	1.93
Total	100.15	100.75	101.37	100.44	98.31	100.58	100.05
Si	3.010	2.989	3.017	3.042	2.946	2.993	3.005
Ti	0.002	0.004	0.002	0.003	0.003	0.004	0.006
Cr	0.000	0.001	0.001	0.000	0.000	0.003	0.000
Al	2.507	2.525	2.484	1.700	2.715	2.638	2.576
Fe^3	0.519	0.524	0.538	1.654	0.378	0.392	0.438
Fe^2	0.000	0.000	0.000	0.000	0.000	0.000	0.000
Mn							
Mn^{3+}	0.012	0.014	0.016	0.293	0.008	0.017	0.010
Mg	0.010	0.011	0.011	0.412	0.008	0.009	0.009
Ni	0.000	0.000	0.000	0.000	0.000	0.000	0.000
Ca	1.908	1.903	1.891	0.519	1.942	1.921	1.930
Na	0.000	0.004	0.002	0.014	0.003	0.002	0.006
K	0.002	0.001	0.001	0.007	0.001	0.002	0.003
OH	1.000	1.000	1.000	1.000	1.000	1.000	1.000
Σ Cations	18.030	18.023	18.038	18.358	17.997	18.020	18.018
Zoisite	0.509	0.520	0.488	0.003	0.664	0.638	0.582
Epidote	0.491	0.480	0.512	1.354	0.336	0.362	0.418

calculated with "Norm" program by P. Ulmer using: Epidote Norm

CATIONS calculated on the bases of 12 oxygens and 1 OH-group

Mineral: epidote

Sarangar Gabbro mylonitic **90/02/01**

Sample	p07a01p08	p07a01p09	p07a01p10	p07a02p15	p07a03p08	p07a03p23
Site	a01	a01	a01	a02	a03	a03
nr.	8	9	10	55	34	49
note	in contact to plg and amp			epi at amp	to amp	
SiO_2	37.61	37.51	37.99	36.27	36.99	37.61
TiO_2	0.17	0.16	0.22	0.15	0.13	0.16
Cr_2O_3	0.05	0.04	0.06	0.03	0.02	0.00
Al_2O_3	27.51	26.14	27.39	25.46	27.29	26.49
Fe_2O_3	8.78	8.38	8.09	8.24	8.50	8.73
FeO	0.00	0.00	0.00	0.00	0.00	0.00
MnO						
Mn_2O_3	0.09	0.21	0.17	0.17	0.15	0.14
MgO	0.10	0.10	0.12	0.09	0.09	0.11
NiO	0.00	0.00	0.00	0.01	0.00	0.04
CaO	24.32	24.18	24.72	23.19	23.82	24.18
Na_2O	0.02	0.00	0.03	0.00	0.00	0.00
K_2O	0.00	0.00	0.01	0.00	0.02	0.01
H_2O	1.92	1.89	1.93	1.83	1.89	1.90
Total	100.57	98.60	100.70	95.43	98.90	99.36
Si	2.931	2.981	2.953	2.976	2.929	2.968
Ti	0.010	0.010	0.013	0.009	0.008	0.010
Cr	0.003	0.002	0.004	0.002	0.001	0.000
Al	2.527	2.449	2.509	2.463	2.546	2.463
Fe^3	0.515	0.501	0.473	0.509	0.507	0.518
Fe^2	0.000	0.000	0.000	0.000	0.000	0.000
Mn						
Mn^{3+}	0.006	0.013	0.010	0.011	0.009	0.009
Mg	0.012	0.012	0.014	0.011	0.011	0.013
Ni	0.000	0.000	0.000	0.001	0.000	0.002
Ca	2.030	2.059	2.058	2.040	2.021	2.044
Na	0.004	0.000	0.005	0.001	0.001	0.000
K	0.000	0.001	0.001	0.000	0.002	0.001
OH	1.000	1.000	1.000	1.000	1.000	1.000
Σ Cations	17.964	17.973	17.961	17.978	17.967	17.972
Zoisite	0.471	0.442	0.478	0.451	0.484	0.441
Epidote	0.515	0.501	0.473	0.509	0.507	0.518

calculated with "Norm" program by P. Ulmer using: Epidote Norm
CATIONS calculated on the bases of 12 oxygens and 1 OH-group

Mineral: epidote

Sarangar Gabbro undeformed **16/01/01**

Sample	p13s3ahb8	p13s3asy1	p13s3asy3	p13s3asy6	p13s3asy7	p13s3asy9	p13s3cuk2	p13s3csy1	p13s3csy2
Site	s3a	s3a	s3a	s3a	s3a	s3a	s3c	s3c	s3c
nr.	100	101	103	106	107	109	127	128	129
note	epi between amp and plg (sympl) in contact to qtz.						epi between amp and plg (sympl)		
SiO_2	37.89	39.04	39.47	39.13	39.19	39.42	39.40	39.19	39.39
TiO_2	0.07	0.06	0.03	0.06	0.06	0.03	0.01	0.00	0.00
Cr_2O_3	0.00	0.05	0.00	0.01	0.02	0.04	0.02	0.00	0.02
Al_2O_3	27.42	27.67	28.32	28.35	28.44	28.70	29.41	28.44	28.02
Fe_2O_3	8.60	8.33	7.21	7.23	7.37	6.66	6.30	7.47	7.71
FeO	0.00	0.00	0.00	0.00	0.00	0.00	0.00	0.00	0.00
MnO									
Mn_2O_3	0.23	0.25	0.25	0.19	0.27	0.24	0.23	0.18	0.16
MgO	0.08	0.08	0.06	0.06	0.06	0.05	0.05	0.05	0.05
NiO	0.00	0.00	0.00	0.00	0.00	0.00	0.00	0.00	0.00
CaO	22.63	23.13	23.25	23.28	23.16	23.06	23.49	23.16	23.00
Na_2O	0.04	0.06	0.04	0.04	0.09	0.08	0.01	0.00	0.06
K_2O	0.03	0.02	0.04	0.04	0.07	0.04	0.01	0.00	0.04
H_2O	1.90	1.94	1.95	1.94	1.95	1.95	1.96	1.95	1.94
Total	98.86	100.61	100.59	100.31	100.65	100.23	100.89	100.42	100.39
Si	2.983	3.016	3.036	3.020	3.015	3.036	3.013	3.021	3.039
Ti	0.004	0.004	0.002	0.003	0.004	0.002	0.001	0.000	0.000
Cr	0.000	0.003	0.000	0.001	0.001	0.002	0.001	0.000	0.001
Al	2.545	2.520	2.567	2.579	2.580	2.605	2.650	2.584	2.548
Fe^3	0.509	0.484	0.417	0.420	0.427	0.386	0.363	0.433	0.448
Fe^2	0.000	0.000	0.000	0.000	0.000	0.000	0.000	0.000	0.000
Mn									
Mn^{3+}	0.014	0.015	0.015	0.011	0.016	0.014	0.014	0.010	0.010
Mg	0.009	0.009	0.007	0.006	0.007	0.006	0.006	0.005	0.006
Ni	0.000	0.000	0.000	0.000	0.000	0.000	0.000	0.000	0.000
Ca	1.909	1.914	1.916	1.925	1.909	1.903	1.924	1.912	1.901
Na	0.007	0.009	0.005	0.006	0.013	0.011	0.002	0.001	0.009
K	0.003	0.002	0.003	0.004	0.007	0.004	0.001	0.000	0.004
OH	1.000	1.000	1.000	1.000	1.000	1.000	1.000	1.000	1.000
Σ Cations	18.017	18.025	18.032	18.024	18.021	18.033	18.026	18.034	18.036
Zoisite	0.533	0.526	0.569	0.583	0.584	0.608	0.652	0.584	0.549
Epidote	0.467	0.474	0.417	0.417	0.416	0.386	0.348	0.416	0.448

calculated with "Norm" program by P. Ulmer using: Epidote Norm
CATIONS calculated on the bases of 12 oxygens and 1 OH-group

Mineral: epidote

Kiru amphibolite **46/02/01**

Sample	p19s01p01	p19s01p02	p19s01p03	p19s02p01	p19s02p02	p19s02p04	p19s02p05
Site	s01	s01	s01	s02	s02	s02	s02
nr.	1	2	3	12	13	15	16
note	epi in contact to amp			epi in contact to plg and qtz			
SiO_2	37.58	37.47	37.75	38.16	37.87	38.21	38.11
TiO_2	0.11	0.14	0.14	0.05	0.18	0.17	0.15
Cr_2O_3	0.02	0.01	0.03	0.02	0.00	0.02	0.02
Al_2O_3	27.57	27.64	27.60	27.75	27.24	27.76	27.59
Fe_2O_3	8.18	8.05	8.18	8.16	8.45	8.36	8.15
FeO	0.00	0.00	0.00	0.00	0.00	0.00	0.00
MnO							
Mn_2O_3	0.23	0.28	0.25	0.19	0.17	0.23	0.26
MgO	0.07	0.07	0.06	0.02	0.09	0.06	0.07
NiO	0.11	0.00	0.01	0.02	0.00	0.00	0.05
CaO	24.39	24.27	24.48	23.96	24.04	24.25	23.77
Na_2O	0.04	0.04	0.05	0.00	0.00	0.02	0.00
K_2O	0.02	0.05	0.03	0.00	0.00	0.00	0.00
H_2O	1.92	1.91	1.92	1.93	1.92	1.94	1.92
Total	100.22	99.90	100.48	100.25	99.95	100.99	100.08
Si	2.937	2.935	2.941	2.969	2.962	2.957	2.971
Ti	0.007	0.008	0.008	0.003	0.011	0.010	0.009
Cr	0.001	0.001	0.002	0.001	0.000	0.001	0.001
Al	2.539	2.551	2.534	2.545	2.511	2.532	2.534
Fe^3	0.481	0.474	0.479	0.478	0.497	0.486	0.478
Fe^2	0.000	0.000	0.000	0.000	0.000	0.000	0.000
Mn							
Mn^{3+}	0.014	0.017	0.015	0.011	0.010	0.014	0.016
Mg	0.009	0.009	0.007	0.003	0.011	0.007	0.008
Ni	0.007	0.000	0.001	0.001	0.000	0.000	0.003
Ca	2.042	2.036	2.044	1.998	2.015	2.010	1.985
Na	0.006	0.006	0.007	0.001	0.000	0.003	0.000
K	0.002	0.005	0.003	0.000	0.000	0.001	0.001
OH	1.000	1.000	1.000	1.000	1.000	1.000	1.000
Σ Cations	17.957	17.959	17.959	17.990	17.982	17.981	17.994
Zoisite	0.484	0.495	0.485	0.519	0.484	0.499	0.515
Epidote	0.481	0.474	0.479	0.478	0.497	0.486	0.478

calculated with "Norm" program by P. Ulmer using: Epidote Norm
CATIONS calculated on the bases of 12 oxygens and 1 OH-group

Mineral: sphene

Kiru amphibolite **46/02/01**

Sample	p19s02p08	p19s02p09	p19s02p10	p19s04p01	p19s04p02	p19s04p03	p19s04p04	p19s04p05
Site	s02	s02	s02	s04	s04	s04	s04	s04
nr.	19	20	21	61	62	63	64	65
note	new grown?			sph in contact to amp				
SiO_2	29.75	29.93	29.68	29.55	29.84	29.72	28.90	29.14
TiO_2	35.81	36.04	36.60	35.08	34.76	35.55	35.05	36.18
Cr_2O_3	0.03	0.03	0.02	0.07	0.05	0.02	0.01	0.02
Al_2O_3	1.04	1.17	1.22	0.66	0.83	0.93	0.69	0.66
Fe_2O_3	0.96	0.66	0.86	0.55	0.39	0.66	0.51	0.60
FeO	0.00	0.00	0.00	0.02	0.17	0.00	0.00	0.00
MnO	0.10	0.07	0.08	0.04	0.10	0.07	0.11	0.11
Mn_2O_3								
MgO	0.03	0.02	0.00	0.00	0.00	0.22	0.02	0.00
NiO	0.02	0.03	0.02	0.00	0.00	0.01	0.04	0.04
CaO	28.25	28.32	28.45	26.42	26.33	26.88	26.06	28.23
Na_2O	0.02	0.00	0.02	0.10	0.07	0.09	0.12	0.39
K_2O	0.00	0.02	0.00	0.03	0.06	0.03	0.05	0.07
H_2O	0.30	0.29	0.32	0.22	0.23	0.27	0.23	0.31
Total	96.31	96.59	97.28	92.73	92.83	94.47	91.81	95.77
Si	1.002	1.004	0.990	1.034	1.042	1.019	1.022	0.984
Ti	0.907	0.909	0.918	0.923	0.913	0.917	0.932	0.919
Cr	0.001	0.001	0.001	0.002	0.001	0.001	0.000	0.001
Al	0.041	0.047	0.048	0.027	0.034	0.038	0.029	0.026
Fe^3	0.024	0.017	0.022	0.015	0.010	0.017	0.014	0.015
Fe^2	0.000	0.000	0.000	0.001	0.005	0.000	0.000	0.000
Mn	0.003	0.002	0.002	0.001	0.003	0.002	0.003	0.003
Mn^{3+}								
Mg	0.002	0.001	0.000	0.000	0.000	0.012	0.001	0.000
Ni	0.001	0.001	0.001	0.000	0.000	0.000	0.001	0.001
Ca	1.019	1.018	1.017	0.990	0.985	0.988	0.987	1.022
Na	0.001	0.000	0.001	0.007	0.005	0.006	0.009	0.026
K	0.000	0.001	0.000	0.001	0.003	0.001	0.002	0.003
OH	0.068	0.065	0.072	0.052	0.053	0.063	0.053	0.071
Σ Cations	3.068	3.065	3.072	3.052	3.053	3.063	3.054	3.071

calculated with "Norm" program by P. Ulmer using: Sphene Norm
CATIONS calculated on the bases of 3 cations and 10 charges - Oh-group

- ICP-MS and XRF analysis.

Sample location:

Sarangar Gabbro, undeformed, GbS (16/01/01) E 73°01'23" N 35°07'16"

The sample was collected 1.95 km NE of Patan (road distance) along the KKH. The mylonitic part covered by the sample belongs to a ca. 8 cm thick shear zone with a foliation dipping 20° towards N and a top to S shear sense.

Sarangar Gabbro mylonite, GbS, (90/02/01) E 73°01'37" N 35°07'01"

The sample was collected 4.33 km E of Patan (road distance form Indus bridge) along the Jeep-road Patan – Chor Nala close to Shalkanabad. The gently NE dipping shear zone is ca. 50 cm thick and contains stretched plagioclase veins and numerous rotated plagioclase porphyroclasts. Sense of shear is towards SW.

Gabbro GbDrHbl (91/03/02) E 73°02'49" N 35°07'44"

Sample locality is 5.25 km NE of Patan (road distance). As shown in Fig. 3.16, this gabbro is intruded into hornblendites and was later intruded by the brighter gabbro (91/03/03). Successive magma injections produced the magmatic breccia.

Gabbro GbDrHbl (91/03/03) E 73°02'49" N 35°07'44"

See (91/03/02).

Meta–gabbro AmO (71/03/02) E 73°12'14" N 35°17'46"

This well foliated, fine graine amphibole rich gabbro was collected 4.8 km N of Dasu (road distance). The metamorphic foliation at the sample locality dips with 60° towards north.

Meta-diorite, shear zone, DrHbl (RK2) E 73°03'32" N 35°08'06"

The sample was collected 6.63 km NE of Patan (road distance). As shown in Fig. 3.16, the sample was taken from below a top to S amphibolite facies shear zone (Foliation: 249/16, Linear: 181/06). The steep foliation (335/84) outside the shear zone is bend by the mylonitic foliation.

Meta-diorite, undeformed, DrHbl (RK1) E 73°03'32" N 35°08'06"

See RK2 for locality. The sample was taken within the shear zone (Fig. 3.16).

Hornblende diorite HblDr (35/02/01) E 73°06'11" N 35°10'05"

Sample locality is 2.38 km S of metal bridge at Kiru (road distance). It is a coarse-grained hornblende diorite.

Hornblende diorite HblDr (91/07/01) E 73°06'25" N 35°10'40"

The sample was collected alongside the KKH 1.1 km S of metal bridge at Kiru (road distance). Detailed description in appendix 4.

Tonalite dike in Kiru Amphibolites AmKi (36/01/01) E 73°06'32" N 35°10'55"

The dike was sampled 550 m S of metal bridge at Kiru (road distance) (Fig. 3.16). It is a 5-10 cm thick undeformed tonalite dike (orientation: 292/42) cutting a meta-gabbro of the Kiru amphibolites.

Granite Gr (00/10/01) E 73°10'44,2" N 35°14'29,9"

The sample locality is ca. 200 m S of the bridge where the Karakoram Highway (KKH) and the Indus River bend sharply towards the E. Detailed description in appendix 4.

Granite Gr (91/08/01) E 73°08'56" N 35°13'01"

The sample was collected in a ca. 2 m thick granitic sheet 9.8 km S of Dasu (road distance).

Indian plate diorite (00/30/14) E 72°53'51,7" N 35°02'14,5"

The sample was collected 100 m S of Duber Bazar along the KKH. Detailed description in appendix 4.

Volcanoclastic Sediment CH-VcS (92/07/01) E 73°01'41" N 35°27'43"

Sample locality is in the Kandiah valley ca. 19.3 km (road distance) W of Kandiah river – Indus confluence.

APPENDIX CHAPTER 4

- U/Pb dating of zircons

Analytical techniques for high-precision U-Pb ages and initial Hf isotopic compositions of zircons:

Zircons were air-abraded and washed in distilled acetone and water in an ultrasonic bath. Dissolution in HF-HNO3, chemical separation on anion exchange resin and mass spectrometry using ion counting on a MAT262 mass spectrometer followed standard techniques. The ion counting system was calibrated by repeated analysis of the NBS 982 standard. The procedural Pb blank was estimated at 1.5 ± 0.75 pg; common lead in excess of this amount was corrected with depleted mantle isotopic compositions. The Hf fraction was isolated using Eichrom™ Ln-spec resin, and in static mode on a NuPlasma™ multi-collector ICP-MS using a MCN-6000 nebulizer for sample introduction. Zircons are commonly characterized by extremely low $^{176}Lu/^{177}Hf$ of less than 0.005; Hf isotopic values were therfore not corrected for in-situ radiogenic ingrowth from ^{176}Lu, because corrections for the 100 Ma old zircons are within the analytical uncertainty of the measured $^{176}Hf/^{177}Hf$ ratios. The Hf isotopic ratios were corrected for mass fractionation using a $^{179}Hf/^{177}Hf$ value of 0.7325 and normalized to $^{176}Hf/^{177}Hf$ = of 0.282160 of the JMC-475 standard (Blichert-Toft *et al.*, 1997). Mean ages and mean Hf isotopic values are given at the 95% confidence level.

Sample location and description:

Sarangar Gabbro (sample number 16/02/01) E 73°01'41,7" N 35°07'15,8"

The sample was taken ca. 2 km E of Patan next to the Karakoram Highway in an undeformed part of the Sarangar Gabbro. The gabbro shows spectacular shear zones anastomosing around undeformed and coarse grained, weakly deformed with well preserved magmatic fabric material (Arbaret *et al,*. 2000). The mineralogical composition within the main metamorphic fabric is dominantly pargasite and tschermakite, hypidioblastic clinopyroxene, plagioclase, rutile, garnet, epidote, quartz and zoisite. Some of the plagioclase shows anorthite richer cores as relicts of the magmatic origin. Albite twinning lamellae are gently bent. The amount of rutile is explained by the release of Ti during recrystallization of Ti-pargasite. Garnet is metamorphic intergrown with rutile along plagioclase rich domains. Large epidote grains are magmatic. Zoisite is growing as metamorphic phase within plagioclase cluster. Clinopyroxene shows breakdown in amphibole and quartz.

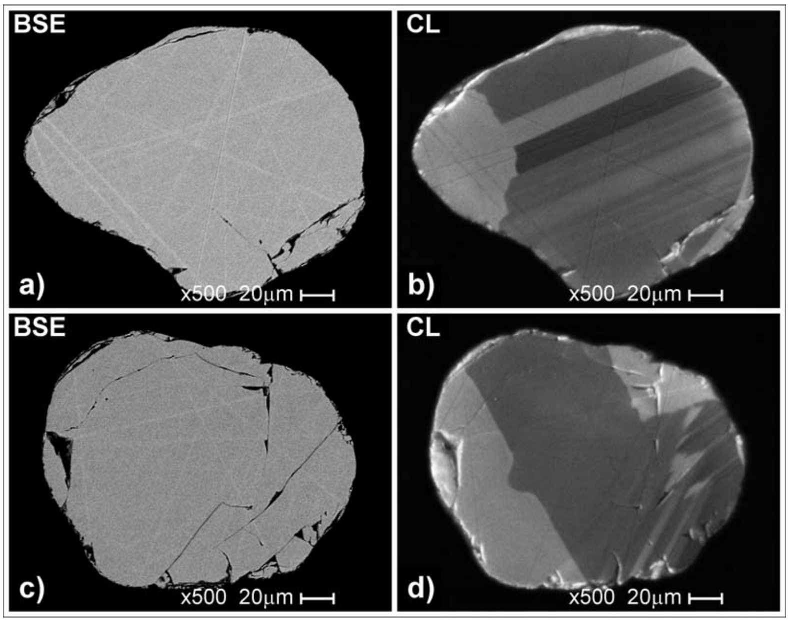

Fig. A4.1: Representative zircons used for U/Pb – dating of the Sarangar gabbro (16/02/01): a,c) backscattered electron image (BSE), b,d) cathodoluminescence image (CL).

Granite (00/10/01) E 73°10'44,2" N 35°14'29,9"

The sample locality is ca. 200 m S of the bridge where the Karakoram Highway (KKH) and the Indus River bend sharply towards the E. The coarse grained granite is composed of quartz, plagioclase, muscovite, garnet, idiomorph epidote, pyrite, chlorite, apatite and zircon. Deformation is concentrated in narrow zones and at the contacts. Quartz is dynamically recrystallized. Undeformed quartz occurs as inclusions in magmatic epidote. Albite rich plagioclase shows weak normal zoning. Twinning lamellae are deformed. Orthoclase is strongly seritisized and shows pertitic exsolution.

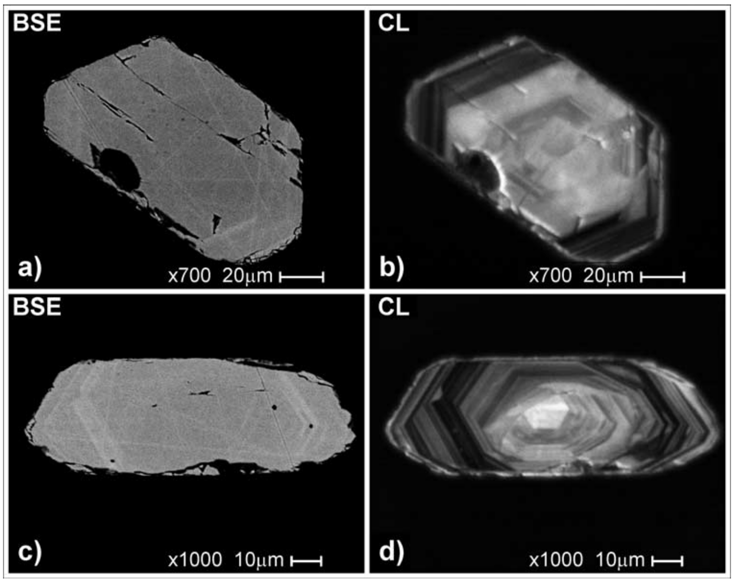

Fig. A4.2: Representative zircons used for U/Pb – dating of a granite (00/10/01): a,c) backscattered electron image (BSE), b,d) cathodoluminescence image (CL).

Diorite (91/07/01) E 73°06'25,5" N 35°10'40,3"

The sample was collected alongside the KKH ca. 1 km S of Kiru. It is a coarse-grained hornblende diorite composed of plagioclase, greenish hornblende, quartz and epidote, chlorite and titanite. The metamorphic fabric has overprinted the magmatic fabric. Subhedral plagioclase shows strong saussuritisation. Foliation is defined by the orientation of metamorphic hornblende. Cotectic fabric within the epidote is preserved as primary magmatic feature.

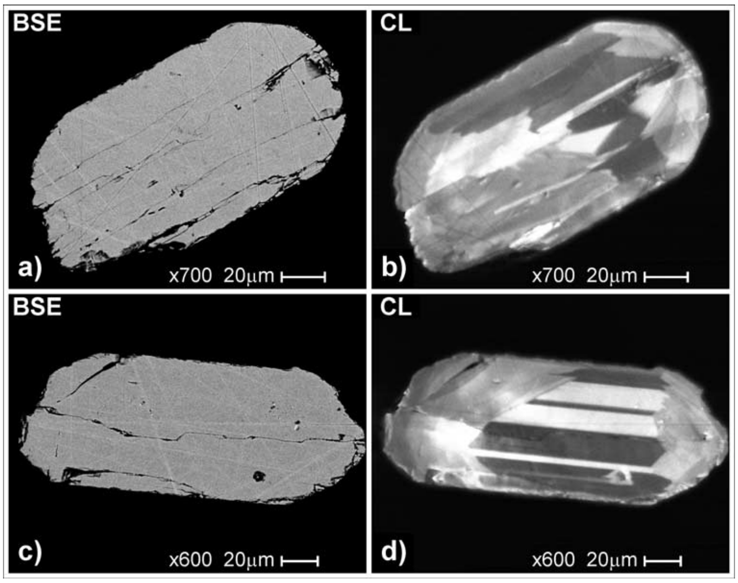

Fig. A4.3: Representative zircons used for U/Pb – dating of a diorite (91/07/01): a,c) backscattered electron image (BSE), b,d) cathodoluminescence image (CL).

Kyanite bearing dyke (38/02/01) E 72°27'08,8" N 34°55'02.2"

The sample from a 20cm thick vein cutting diorites and gabbros was collected 2 km S of Khwazakhela, in a small quarry next to the Road Mingora–Kalam. The dyke consists of quartz, plagioclase, zoisite, scapolite, prismatic to acicular kyanite and poikiloblastic garnet. Detailed mineralogy is described by Jan & Karim (1995).

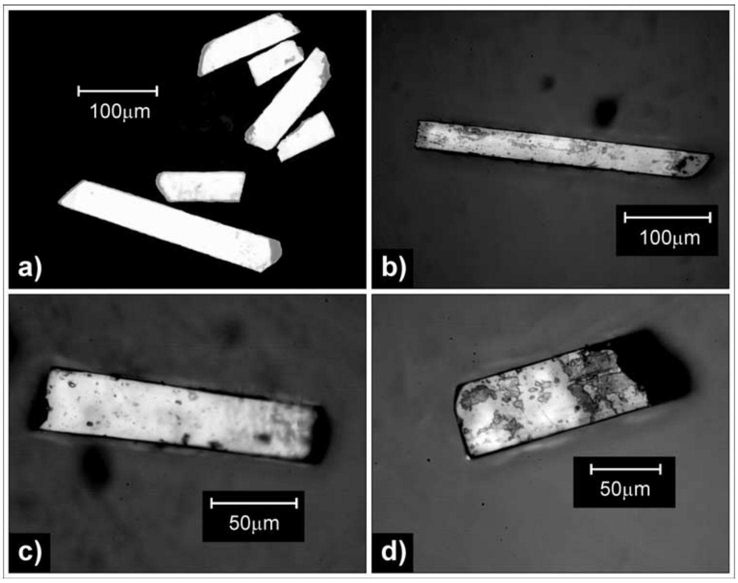

Fig. A4.4: Representative zircons used for U/Pb – dating of a kyanite bearing dyke (38/02/01).

Chilas gabbronorite (00/40/03) E 72°31'40,8" N 35°07'42,7"

The sample locality is 1.5 km S of Madyan (55 km NNE of Mingora, Swat valley) along the road Mingora – Kalam. The gabbronorite is composed of clinopyroxene, orthopyroxene, amphibole, plagioclase, quartz, biotite and minor oxides. The magmatic fabric is in parts preserved. The well-preserved orthopyroxenes show exsolution-lamellae with beginning amphibole growth and spinel during cooling. Clinopyroxenes are less well preserved. The amphiboles are of metamorphic origin. Plagioclase is strongly saussuritized and albite twins are bended. Few bigger grains preserved anorthite rich plagioclase (An 60) with pericline twinning. The dominant part of plagioclase is likely to have recrystallized at temperatures of around 800°C. Magnetite is an accessory mineral.

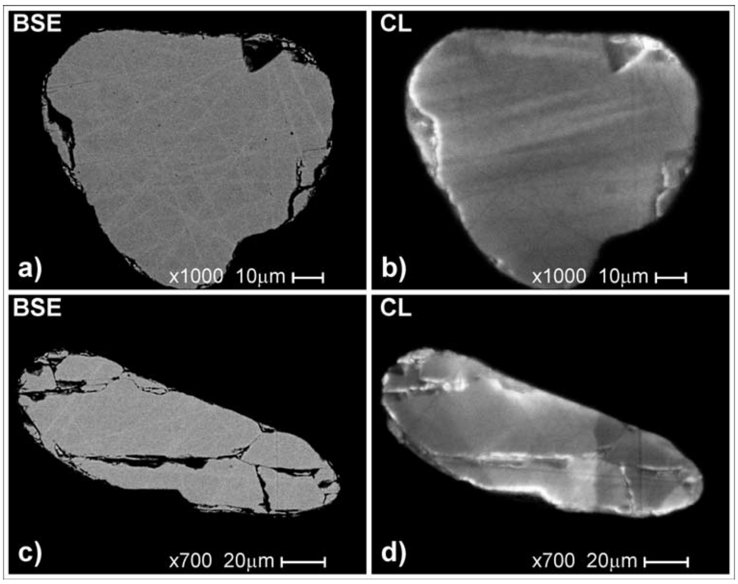

Fig. A4.5: Representative zircons used for U/Pb – dating of a Chilas gabbronorite (00/40/03): a,c) backscattered electron image (BSE), b,d) cathodoluminescence image (CL).

Indian plate diorite (00/30/14) E 72°53'51,7" N 35°02'14,5"

The sample was collected 100 m S of Duber Bazar along the KKH. The coarse grained diorite is composed of K-feldspar, hornblende, plagioclase, quartz ± opaque oxides and traces of zircon and epidote. The magmatic fabric is generally preserved; only in strong foliated parts the fabric shows a metamorphic overprint.

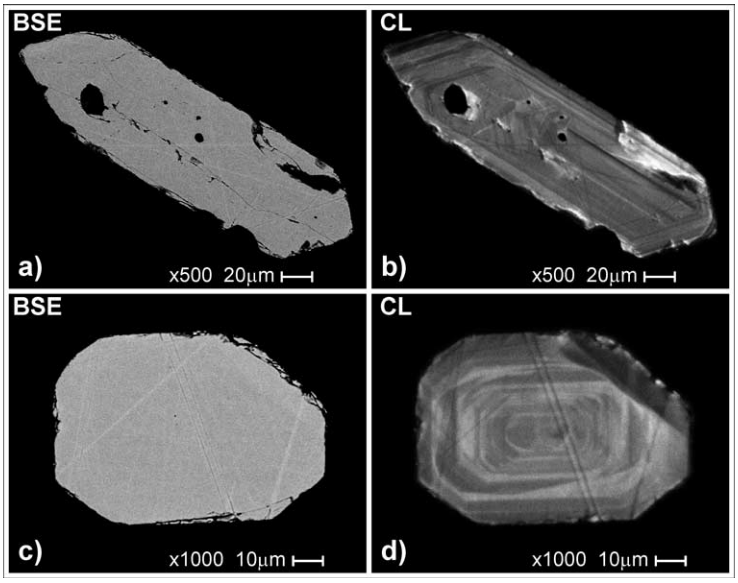

Fig. A4.6: Representative zircons used for U/Pb – dating of Indian plate diorite (00/30/14): a,c) backscattered electron image (BSE), b,d) cathodoluminescence image (CL).

Table Appendix 4.1: U-Pb isotopic data of zircons from all dated samples.

Nr.	Description	Weight	nr.	Concentrations				Atomic ratios							Apparent ages			Error
		[mg]	of	U	Pb	Pb	Th/U	206/204	206/238	Error	207/235	Error	207/206	Error	206/238	207/235	207/206	corr.
			grains		rad.	nonrad.				2σ [%]		2σ [%]		2σ [%]				
	a)				[ppm]	[pg]	b)	c)	d)		d)		d)					
Gabbro Sarangar																		
1	round	0.0756	15	149	2.44	4.1	0.53	2733	0.01553	0.37	0.1030	0.48	0.04808	0.31	99.3	99.5	103.1	0.76
2	round	0.0585	18	182	2.99	2.0	0.58	5191	0.01544	0.33	0.1022	0.41	0.04803	0.19	98.8	98.8	98.4	0.89
3	round	0.1494	17	129	2.10	3.1	0.55	6162	0.01545	0.33	0.1024	0.40	0.04806	0.17	98.9	99.0	102.3	0.91
4	round	0.0171	21	189	3.08	1.9	0.53	1661	0.01549	0.39	0.1026	0.65	0.04805	0.52	99.1	99.2	101.9	0.60
Granite																		
5	round	0.0066	3	358	5.82	1.7	0.60	1386	0.01517	0.41	0.1006	0.81	0.04807	0.68	97.1	97.3	102.9	0.54
6	prism incl	0.0061	8	507	8.98	8.5	0.55	369	0.01517	0.50	0.1005	1.68	0.04807	1.55	97.0	97.3	102.6	0.40
7	small prism	0.0017	13	1377	22.25	2.2	0.57	1056	0.01512	0.37	0.1006	0.90	0.04797	0.78	97.3	97.3	100.2	0.51
Diorite																		
8	prism	0.0049	8	16.26	0.25	2.8	0.68	44	0.01435	2.12	0.0869	31.00	0.04392	29.50	91.8	84.6	-	0.72
9	large oval	0.0118	5	38.20	0.59	5.8	0.68	88	0.01426	0.86	0.0895	7.94	0.04550	7.54	91.3	87.0	-	0.51
10	small oval	0.0067	10	33.23	0.53	1.0	0.67	226	0.01442	0.71	0.0964	4.19	0.04848	3.97	92.3	93.5	-	0.39
Swat dyke																		
11	acicular	0.0119	12	6.74	0.08	1.1	0.05	77	0.01304	2.40	0.0802	16.30	0.04459	15.70	83.5	78.3	-	0.32
12	prism	0.0172	14	2.75	0.03	1.5	0.01	45	0.01299	2.16	0.0730	36.50	0.04077	35.20	83.2	71.6	-	0.62
13	prism	0.0190	22	5.29	0.06	4.3	0.10	37	0.01272	2.44	0.0739	35.44	0.04214	33.80	81.5	72.4	-	0.69
Chilas gabbronorite																		
14	large round	0.1618	9	113	1.75	5.0	0.91	3097	0.01337	0.36	0.0882	0.45	0.04783	0.24	85.6	85.8	90.7	0.85
15	round	0.0850	15	107	1.74	4.5	1.09	1721	0.01337	0.35	0.0882	0.52	0.04778	0.36	85.7	85.8	88.6	0.72
16	round incl	0.1026	15	99	1.62	8.8	1.12	993	0.01337	0.37	0.0884	0.61	0.04792	0.45	85.7	86.0	95.2	0.68
17	prism	0.0328	3	103	1.67	1.7	1.08	1686	0.01340	0.36	0.0883	0.64	0.04776	0.51	85.8	85.9	87.6	0.61
Diorite Indian plate, Swat Valley																		
18	prism tips	0.0316	4	376	131.45	2.4	0.43	104052	0.32727	0.33	5.1298	0.38	0.11368	0.10	1825.1	1841.1	1859.1	0.97
19	small spr	0.0156	6	232	78.47	2.9	0.45	24992	0.31502	0.34	4.9295	0.38	0.11349	0.11	1765.4	1807.3	1856.1	0.96
20	frags	0.0209	5	273	91.62	3.9	0.42	28915	0.31528	0.33	4.9383	0.38	0.11360	0.11	1766.6	1808.8	1857.8	0.96
21	spr	0.0329	5	210	67.80	15.2	0.41	8739	0.30394	0.33	4.7610	0.38	0.11361	0.11	1710.8	1778.0	1857.9	0.96

a) all zircon fractions abraded; incl = inclusions; prism = prismatic; spr = short-prismatic

b) Calculated on the basis of radiogenic Pb208/Pb206 ratios, assuming concordance; c) Corrected for fractionation and spike

d) Corrected for fractionation, spike, blank and common lead (Stacey & Kramers, 1975)

- Fission track dating

Sample location:

Sarangar Gabbro GbS (16/02/01) E 73°01'31" N 35°07'16"

The sample was taken ca. 2 km E of Patan next to the Karakoram Highway in an undeformed part of the Sarangar Gabbro. Detailed description in appendix 4 U/Pb dating samples.

Indian Plate Diorite Dr (00/30/12) E 72°54'38" N 35°02'31"

The sample was collected ca. 1550 m E of Duber Bazar bridge (road distance) along KKH. The sample is similar to the diorite used for U/Pb – dating (00/30/14).

Pegmatite in Diorites/Hornblendites DrHbl (56/02/01) E 73°02'54" N 35°07'48"

The sample locality is ca. 5000 m NE of Patan (road distance at KKH). The coarse grained, undeformed pegmatite cuts the dioritic host rock.

Granite (00/10/01) E 73°10'44" N 35°14'30"

The sample locality is ca. 200 m S of the bridge where the Karakoram Highway (KKH) and the Indus River bend sharply towards the E. Detailed description in appendix 4 U/Pb dating samples.

Diorite (91/07/01) E 73°06'26" N 35°10'41"

The sample was collected alongside the KKH 1.1 km S of metal bridge at Kiru (road distance). Detailed description in appendix 4 U/Pb dating samples.

Swat Granite Gneiss (95-196) E 72°24'14" N 34°47'46" and (95-196) E 72°29'15" N 34°49'20"

Samples collected and described by Anczkiewicz (1998). FT dating carried out by R. Anczkiewicz and D. Seward (unpublished).

Appendix Table 4.2

Sample number	Alt. (m)	Mineral	Irradiation number	Number of grains	Standard track density x 10^4 cm^{-2} (counted)	ρ_s x 10^4 cm^{-2} (counted)	ρ_i x 10^4 cm^{-2} (counted)	U conc. ppm	$P(\chi^2)$ Variation (%)	Mean track length (μm)	std dev (μm)	Central Age ± 2σ (Ma)
95-196	800	A	eth-86-14	16	110 (2439)	12.9 (111)	225 (1929)	26	97 (0)	-----------	-----------	11.2 ± 2.2
95-198	1000	A	eth-86-11	20	122 (2439)	10.8 (82)	156 (1185)	16	83 (0.3)	-----------	-----------	15.0 ± 3.4
16/02/01 (GZ1)	900	A	eth-191-3	20	121 (2808)	0.73 (126)	14.5 (2509)	2	12 (25)	13.67 ± 0.30	1.99 (43)	10.6 ± 2.4
00/30/12 (GZ11)	825	A	eth-192-3	20	130 (2978)	3.64 (60)	24.3 (4007)	23	8 (25)	-----------	-----------	3.7 ± 1.0
95-196	800	Z	eth-88-15	12	49.1 (2376)	287 (378)	414 (546)	338	8 (18)	-----------	-----------	20.5 ± 3.6
95-198	1000	Z	eth-88-2	8	56.2 (2376)	473 (885)	563 (1054)	400	11 (9)	-----------	-----------	28.2 ± 3.4
56/02/01 (GZ3)	1000	Z	eth-193-4	20	73.3 (2543)	14.6 (180)	15.3 (189)	8	100 (0)	-----------	-----------	41.8 ± 8.8
00/10/01 (GZ4)	1000	Z	eth-193-11	4	64.8 (2543)	223 (151)	372 (252)	230	22 (9)	-----------	-----------	23.6 ± 5.6
91/07/01 (GZ8)	960	Z	eth-193-5	20	71.6 (2543)	39.2 (217)	60.7 (336)	33.9	66 (10)	-----------	-----------	27.9 ± 5.2
00/30/12 (GZ11)	825	Z	eth-193-7	20	69.3 (2543)	532 (1726)	1002 (3253)	578	0 (19)	-----------	-----------	22.6 ± 2.6

A = apatite, Z = zircon. ρ_S and ρ_i represent sample spontaneous and induced track densities; $P(\chi^2)$ is the probability of X^2 for v degrees of freedom where v = no. of crystals – 1. $\lambda_D = 1.55125 \times 10^{-10}$. Zeta = 355 ± 5 for apatite and CN5, 120 ± 5 for zircon and CN1. Samples were irradiated at the ANSTO facility, Australia. Ages are reported as central ages (Galbraith, 1981).

Appendix Chapter 5

Table A5.1: Shear zone orientations data used for analysis presented in chapter 5.2.

Station 1: N. Kamila sequence

	coordinates (decimal degree)		shear plane		lineation		
Outcrop	x (East)	y (North)	azimuth	dip	azimuth	dip	sense
7101	73.22339	35.29057	331	80	20	77	reverse
7101	73.22339	35.29057	336	84	66	28	reverse
7101	73.22339	35.29057	20	74	105	20	sinistral
7102	73.21670	35.29417	5	77	92	40	reverse (?)
7102	73.21670	35.29417	358	66	66	38	reverse (?)
7201	73.19398	35.30646	356	66	70	52	reverse
7201	73.19398	35.30646	310	80	294	71	reverse
7201	73.19398	35.30646	322	52	28	30	normal
7202	73.19112	35.30952	300	21	38	66	sinistral
7301	73.19219	35.31631	245	71	237	70	normal
7301	73.19219	35.31631	258	65	232	64	reverse (?)
7301	73.19219	35.31631	172	35	150	34	normal
7301	73.19219	35.31631	290	50	353	44	normal
7301	73.19219	35.31631	310	11	278	6	reverse
7301	73.19219	35.31631	238	72	189	65	normal
7301	73.19219	35.31631	232	34	209	26	normal
7302	73.19749	35.32006	12	88	98	39	dextral
7303	73.20033	35.32461	6	80	102	56	normal
7303	73.20033	35.32461	60	54	358	25	dextral
7902	73.17639	35.30878	342	32	315	30	reverse
7301	73.19219	35.31631	30	42	94	16	normal

Station 2: Kamila sequence

	coordinates (decimal degree)		shear plane		lineation		
Outcrop	x (East)	y (North)	azimuth	dip	azimuth	dip	sense
6503	73.14231	35.21221	19	50	44	48	reverse
6503	73.14231	35.21221	24	56	78	36	reverse
6504	73.14652	35.21541	94	53	90	46	reverse (?)
6504	73.14652	35.21541	290	61	240	50	reverse
6504	73.14652	35.21541	115	68	80	60	reverse (?)
6601	73.15185	35.21984	144	89	53	42	reverse (?)
6601	73.15185	35.21984	347	76	67	57	reverse (?)
6602	73.15594	35.22446	46	36	60	30	reverse
6602	73.15594	35.22446	120	48	110	47	reverse
6602	73.15594	35.22446	135	36	72	25	reverse (?)
6602	73.15594	35.22446	60	35	98	30	reverse (?)
6602	73.15594	35.22446	96	36	82	36	normal
6602	73.15594	35.22446	350	71	52	72	reverse (?)
6603	73.16220	35.22647	66	34	10	80	reverse (?)
6603	73.16220	35.22647	359	70	80	27	sinistral
6603	73.16220	35.22647	42	29	95	21	reverse (?)
6603	73.16220	35.22647	52	44	76	40	reverse
6603	73.16220	35.22647	50	52	72	50	reverse
6604	73.17318	35.23262	34	52	80	44	reverse
6604	73.17318	35.23262	15	72	72	60	reverse
6604	73.17318	35.23262	10	60	72	42	reverse (?)
6701	73.17588	35.23602	34	61	68	60	reverse
6701	73.17588	35.23602	52	45	60	45	reverse
6701	73.17588	35.23602	24	46	47	45	reverse
6701	73.17588	35.23602	28	56	68	52	reverse
6701	73.17588	35.23602	35	60	75	54	reverse
6701	73.17588	35.23602	40	57	76	50	reverse
6702	73.17647	35.23701	35	56	110	15	normal
6702	73.17647	35.23701	32	45	80	35	reverse
6703	73.17762	35.23888	4	31	70	16	reverse
6704	73.17887	35.24147	38	27	58	24	reverse
6705	73.18211	35.24460	10	54	71	24	reverse
6801	73.18343	35.24489	18	35	38	35	normal
6801	73.18343	35.24489	238	28	280	17	reverse (?)
6801	73.18343	35.24489	290	54	202	14	dextral
6801	73.18343	35.24489	33	36	56	26	reverse
6802	73.19036	35.24594	289	44	244	30	normal
6802	73.19036	35.24594	44	41	81	36	reverse
6802	73.19036	35.24594	62	60	108	42	reverse (?)
6803	73.19559	35.24671	14	53	310	20	reverse (?)
6803	73.19559	35.24671	338	85	28	70	sinistral
6803	73.19559	35.24671	18	60	72	50	reverse (?)
6901	73.20092	35.24607	60	38	76	35	reverse (?)
6901	73.20092	35.24607	70	24	80	22	reverse
6901	73.20092	35.24607	50	56	52	50	reverse (?)
6901	73.20092	35.24607	338	59	46	29	reverse
6901	73.20092	35.24607	41	76	107	56	reverse
6901	73.20092	35.24607	48	75	315	10	sinistral
6901	73.20092	35.24607	279	62	230	51	reverse
6902	73.20580	35.24525	23	73	114	1	sinistral
6902	73.20580	35.24525	20	39	4	15	reverse
6903	73.20876	35.24682	294	68	202	5	sinistral
6903	73.20876	35.24682	65	30	56	25	reverse (?)
6903	73.20876	35.24682	339	79	264	38	sinistral
7402	73.21815	35.27131	351	79	80	71	normal
7402	73.21815	35.27131	358	62	32	54	normal
7704	73.22846	35.21897	64	34	122	10	normal
8001	73.20614	35.22858	151	26	67	7	reverse
8001	73.20614	35.22858	132	30	70	19	reverse (?)
8002	73.20378	35.23462	90	44	100	46	normal
8202	73.20116	35.24146	70	46	130	33	reverse
8203	73.20471	35.24167	75	42	128	10	reverse
8203	73.20471	35.24167	69	86	340	9	sinistral
8302	73.20301	35.21055	186	86	88	13	dextral
8302	73.20301	35.21055	156	22	98	5	reverse (?)
8306	73.19836	35.19889	12	46	90	20	reverse (?)
8307	73.19525	35.19719	355	60	67	16	reverse
8401	73.15395	35.22531	140	24	68	8	reverse (?)
8401	73.15395	35.22531	290	24	248	16	reverse (?)
8403	73.15163	35.22490	130	27	65	10	reverse
8406	73.14608	35.22831	27	25	10	23	normal
8406	73.14608	35.22831	8	37	56	32	normal
4204	73.17867	35.24190	345	43	49	27	normal
4204	73.17867	35.24190	350	49	40	34	normal
6504	73.14652	35.21541	168	55	125	36	reverse (?)
6504	73.14652	35.21541	100	51	72	35	sinistral
6601	73.15185	35.21984	324	72	52	36	sinistral
6603	73.16220	35.22647	35	46	94	36	reverse
6701	73.17588	35.23602	27	52	57	50	reverse
6703	73.17762	35.23888	40	29	68	25	reverse
6603	73.16220	35.22647	28	57	75	45	reverse

Station 3: Kiru Amphibolites

	coordinates (decimal degree)		shear plane		lineation		
Outcrop	x (East)	y (North)	azimuth	dip	azimuth	dip	sense
6201	73.11351	35.18569	32	66	81	49	normal
6201	73.11351	35.18569	73	35	75	34	reverse
6201	73.11351	35.18569	330	70	63	11	sinistral
6201	73.11351	35.18569	36	37	42	36	reverse
6201	73.11351	35.18569	198	70	142	54	reverse (?)
6201	73.11351	35.18569	359	41	58	30	sinistral
6301	73.11567	35.18713	350	47	50	26	sinistral
6301	73.11567	35.18713	336	30	40	20	sinistral
6301	73.11567	35.18713	355	47	36	40	reverse
6301	73.11567	35.18713	334	24	40	9	reverse
6301	73.11567	35.18713	356	56	44	45	normal
6302	73.11785	35.18972	2	80	82	50	dextral
6302	73.11785	35.18972	18	46	40	45	reverse

	coordinates (decimal degree)		shear plane		lineation		
Outcrop	x (East)	y (North)	azimuth	dip	azimuth	dip	sense
6302	73.11785	35.18972	359	74	80	40	reverse (?)
6302	73.11785	35.18972	2	32	66	21	normal
6302	73.11785	35.18972	345	44	44	28	reverse (?)
6303	73.11877	35.19119	132	12	200	8	normal
6303	73.11877	35.19119	16	55	49	48	normal
6303	73.11877	35.19119	356	42	50	27	reverse (?)
6303	73.11877	35.19119	4	60	62	50	reverse (?)
6303	73.11877	35.19119	50	22	40	21	reverse
6303	73.11877	35.19119	3	25	38	25	reverse
6303	73.11877	35.19119	25	47	60	36	reverse
6303	73.11877	35.19119	358	57	44	47	sinistral
6401	73.12173	35.19361	8	30	70	26	reverse
6401	73.12173	35.19361	27	30	52	28	reverse
6401	73.12173	35.19361	58	42	67	38	reverse
6401	73.12173	35.19361	20	31	34	30	reverse
6401	73.12173	35.19361	40	40	58	38	reverse
6401	73.12173	35.19361	35	32	72	30	reverse (?)
6401	73.12173	35.19361	330	42	60	35	reverse

	coordinates (decimal degree)		shear plane		lineation		
Outcrop	x (East)	y (North)	azimuth	dip	azimuth	dip	sense
6401	73.12173	35.19361	339	51	42	29	reverse
6401	73.12173	35.19361	315	25	45	1	reverse
6402	73.12371	35.19805	343	34	4	31	reverse
6402	73.12371	35.19805	13	36	37	35	reverse (?)
6402	73.12371	35.19805	352	67	20	64	normal
6402	73.12371	35.19805	3	58	45	52	reverse
6403	73.12644	35.20133	205	88	94	74	reverse
6403	73.12644	35.20133	346	34	18	30	reverse
6403	73.12644	35.20133	36	67	60	64	reverse
6403	73.12644	35.20133	2	32	60	20	reverse
6403	73.12644	35.20133	48	55	50	55	reverse (?)
6403	73.12644	35.20133	35	72	70	69	normal
6404	73.12898	35.20352	11	51	345	45	reverse
6404	73.12898	35.20352	24	74	312	50	reverse (?)
6404	73.12898	35.20352	49	56	56	54	reverse (?)
6404	73.12898	35.20352	357	72	80	20	sinistral
6405	73.13300	35.20703	20	30	358	81	reverse
6405	73.13300	35.20703	16	85	294	60	normal
6405	73.13300	35.20703	11	82	69	74	normal
6501	73.13421	35.20741	262	25	268	24	normal
6501	73.13421	35.20741	359	76	88	2	sinistral
6501	73.13421	35.20741	345	74	35	68	reverse (?)
6501	73.13421	35.20741	2	74	42	66	reverse (?)
6502	73.13705	35.20920	3	74	6	73	normal
6502	73.13705	35.20920	8	82	321	65	normal
6502	73.13705	35.20920	2	63	275	8	sinistral
6502	73.13705	35.20920	5	55	70	20	reverse
6502	73.13705	35.20920	20	67	2	42	reverse (?)
6502	73.13705	35.20920	148	5	110	5	reverse
6502	73.13705	35.20920	128	6	55	1	reverse
6502	73.13705	35.20920	92	60	92	60	reverse
6502	73.13705	35.20920	248	28	72	26	normal
3403	73.09883	35.15655	305	45	30	10	sinistral
3403	73.09883	35.15655	350	56	51	39	sinistral
3403	73.09883	35.15655	337	52	5	50	normal
3403	73.09883	35.15655	325	70	30	64	reverse
3403	73.09883	35.15655	4	79	53	71	normal
3403	73.09883	35.15655	177	82	138	80	reverse
3403	73.09883	35.15655	176	80	103	69	reverse (?)
3403	73.09883	35.15655	254	15	188	6	normal
3404	73.10073	35.16039	18	30	342	20	reverse
3501	73.10168	35.16273	13	32	43	31	reverse
3501	73.10168	35.16273	322	71	10	62	reverse
3501	73.10168	35.16273	40	50	26	46	reverse
3501	73.10168	35.16273	322	58	20	40	reverse
3502	73.10305	35.16671	18	6	40	5	reverse
3502	73.10305	35.16671	330	20	20	16	reverse
3502	73.10305	35.16671	350	15	12	14	reverse

	coordinates (decimal degree)		shear plane		lineation		
Outcrop	x (East)	y (North)	azimuth	dip	azimuth	dip	sense
3504	73.10770	35.17750	12	68	53	51	reverse
3504	73.10770	35.17750	10	44	48	36	reverse
3504	73.10770	35.17750	2	70	53	51	reverse (?)
3505	73.10935	35.18161	18	82	70	75	reverse
3602	73.11104	35.18378	350	84	74	36	sinistral
3602	73.11104	35.18378	335	28	55	5	reverse
3602	73.11104	35.18378	15	56	60	51	reverse
3602	73.11104	35.18378	357	57	58	40	reverse
3602	73.11104	35.18378	25	43	58	40	reverse
2801	73.02574	35.18148	34	50	80	40	reverse (?)
2802	73.02639	35.18186	36	45	65	38	reverse (?)
2806	73.01304	35.18719	41	31	67	39	reverse
2905	73.02626	35.17333	35	25	40	25	reverse
2906	73.02602	35.17381	60	48	95	44	reverse (?)
4605	73.10063	35.15969	340	85	270	66	reverse (?)
6302	73.11785	35.18972	348	40	48	34	reverse

Station 4: Northern sheared Gabbros and Diorites							
	coordinates (decimal degree)		shear plane		lineation		
Outcrop	x (East)	y (North)	azimuth	dip	azimuth	dip	sense
1802	73.05584	35.13943	249	16	181	6	normal
6108	72.97931	35.17571	16	80	303	20	dextral
8904	72.98060	35.15927	30	22	32	20	normal
1703	73.04697	35.12888	340	70	54	40	reverse
1703	73.04697	35.12888	358	56	359	52	reverse (?)
1704	73.04795	35.12961	330	36	16	36	reverse
1704	73.04795	35.12961	358	42	20	40	reverse
1705	73.04989	35.13081	6	60	45	47	reverse
1706	73.05073	35.13108	59	61	61	59	normal
1706	73.05073	35.13108	346	40	29	26	normal
1706	73.05073	35.13108	54	25	62	22	reverse
1801	73.05722	35.13702	328	24	28	9	reverse
1801	73.05722	35.13702	345	35	7	34	reverse
1801	73.05722	35.13702	5	37	14	36	reverse
1802	73.05584	35.13943	344	76	50	64	reverse
1802	73.05584	35.13943	271	26	201	10	normal
1802	73.05584	35.13943	348	70	34	53	reverse
1802	73.05584	35.13943	345	60	51	40	reverse
1802	73.05584	35.13943	48	86	140	71	reverse
1803	73.05022	35.14135	48	29	24	36	reverse
1805	73.05745	35.14461	10	33	20	10	reverse
1805	73.05745	35.14461	16	24	35	22	reverse
1806	73.05994	35.14504	159	70	52	30	reverse
1806	73.05994	35.14504	30	46	64	16	reverse
1902	73.06980	35.14188	20	12	70	4	reverse
1902	73.06980	35.14188	40	74	104	25	reverse
1902	73.06980	35.14188	88	40	47	34	normal
1902	73.06980	35.14188	64	56	34	46	normal
1902	73.06980	35.14188	96	40	49	34	normal
1902	73.06980	35.14188	27	50	60	40	normal
1902	73.06980	35.14188	61	44	63	46	normal
1903	73.07417	35.14350	22	33	34	31	normal
1903	73.07417	35.14350	23	40	62	34	normal
1903	73.07417	35.14350	352	30	50	15	normal
1904	73.07792	35.14503	50	50	65	45	normal
1904	73.07792	35.14503	41	49	60	43	normal
1904	73.07792	35.14503	45	41	40	41	reverse
1904	73.07792	35.14503	22	32	30	26	reverse
1904	73.07792	35.14503	160	26	242	10	normal
1904	73.07792	35.14503	30	80	82	46	normal
1904	73.07792	35.14503	68	39	58	36	normal
1905	73.07929	35.14556	84	6	54	5	reverse
1905	73.07929	35.14556	18	73	348	69	normal
3205	73.06216	35.12827	0	46	50	34	reverse (?)
3207	73.06747	35.13175	2	48	16	50	reverse
3301	73.08405	35.13558	39	29	80	26	reverse
3302	73.08613	35.13051	332	49	24	42	normal

	coordinates (decimal degree)		shear plane		lineation		
Outcrop	x (East)	y (North)	azimuth	dip	azimuth	dip	sense
3302	73.08613	35.13051	326	50	35	30	sinistral
3302	73.08613	35.13051	335	56	34	41	dextral
3303	73.08728	35.13018	307	14	354	12	reverse
3303	73.08728	35.13018	304	62	30	13	sinistral
3303	73.08728	35.13018	250	13	230	11	normal
3303	73.08728	35.13018	266	25	200	9	normal
3305	73.08431	35.12575	224	26	214	25	normal
3306	73.08446	35.12149	275	54	208	15	sinistral
3306	73.08446	35.12149	328	66	45	26	sinistral
3306	73.08446	35.12149	358	27	40	21	reverse
3306	73.08446	35.12149	317	53	36	19	sinistral
3401	73.08600	35.14840	50	78	42	76	normal
3401	73.08600	35.14840	302	59	15	22	reverse
3401	73.08600	35.14840	38	56	2	55	normal
3401	73.08600	35.14840	10	42	26	37	normal
3401	73.08600	35.14840	57	28	29	24	normal
3402	73.08881	35.14965	26	28	42	26	reverse
3402	73.08881	35.14965	248	45	182	26	normal
3402	73.08881	35.14965	38	36	15	36	normal
3402	73.08881	35.14965	352	46	26	44	reverse (?)
2205	72.97700	35.14364	50	28	18	26	reverse
2505	72.98064	35.15889	220	76	297	28	reverse (?)
2509	72.97833	35.18225	34	28	52	29	reverse (?)
2510	72.97892	35.17989	50	52	77	64	reverse (?)
2510	72.97892	35.17989	48	77	50	75	reverse (?)
2511	72.97955	35.17514	322	35	316	36	reverse (?)
2901	73.04511	35.14342	20	44	5	43	reverse
2903	73.03230	35.15205	20	40	58	34	reverse (?)
4403	73.05253	35.13176	55	80	88	66	normal
4701	73.08569	35.14875	40	59	83	43	normal
8905	72.97778	35.14741	64	34	60	21	reverse

Station 5: Patan Area (Sarangar Gabbro and Granulitic Gabbro)							
	coordinates (decimal degree)		shear plane		lineation		
Outcrop	x (East)	y (North)	azimuth	dip	azimuth	dip	sense
1603	73.02804	35.11989	80	65	141	45	normal
5502	72.99897	35.08805	28	56	40	58	reverse
5502	72.99897	35.08805	50	32	15	28	reverse
5502	72.99897	35.08805	186	20	200	18	normal
5502	72.99897	35.08805	60	70	31	58	reverse
5901	73.08578	35.11160	282	34	224	24	normal
5902	73.08621	35.10807	170	70	200	62	reverse
5902	73.08621	35.10807	150	65	70	20	dextral
5903	73.09002	35.09814	290	29	9	1	reverse
5903	73.09002	35.09814	310	36	12	16	reverse
5903	73.09002	35.09814	344	64	36	43	reverse
5903	73.09002	35.09814	323	50	7	45	reverse
5903	73.09002	35.09814	324	70	359	69	reverse
5903	73.09002	35.09814	315	65	15	36	reverse
5903	73.09002	35.09814	336	69	312	67	reverse
5903	73.09002	35.09814	310	60	32	27	reverse
5904	73.09244	35.09359	332	85	40	80	reverse
5904	73.09244	35.09359	348	30	25	28	reverse
5904	73.09244	35.09359	300	79	30	15	dextral
5904	73.09244	35.09359	308	32	345	20	reverse
5904	73.09244	35.09359	316	72	36	34	reverse
5904	73.09244	35.09359	314	71	41	30	reverse
5904	73.09244	35.09359	280	40	220	36	sinistral
5904	73.09244	35.09359	346	80	49	66	reverse
8502	73.09766	35.07547	286	34	354	8	reverse (?)
8707	72.93088	35.10778	54	41	108	43	normal
8708	72.93099	35.11146	350	50	345	45	reverse (?)
8902	72.98505	35.12959	286	75	216	56	reverse
1210	73.00177	35.11261	170	35	252	6	normal
1210	73.00177	35.11261	299	25	354	10	reverse
1210	73.00177	35.11261	181	24	154	19	normal
1304	72.99934	35.11603	318	40	270	29	normal

	coordinates (decimal degree)		shear plane		lineation		
Outcrop	x (East)	y (North)	azimuth	dip	azimuth	dip	sense
1312	72.98158	35.08435	160	20	74	6	reverse
1404	73.00643	35.10259	125	52	85	21	reverse
1405	73.00842	35.10170	35	40	331	16	reverse
1405	73.00842	35.10170	236	44	236	44	normal
1406	73.01227	35.10378	198	89	135	70	reverse (?)
1407	73.01486	35.10708	72	35	350	5	reverse
1408	73.00008	35.11547	172	70	85	15	sinistral
1408	73.00008	35.11547	325	65	44	28	sinistral
1408	73.00008	35.11547	10	24	340	21	reverse
1501	73.01009	35.11599	305	38	302	35	reverse
1501	73.01009	35.11599	276	45	273	28	reverse
1501	73.01009	35.11599	206	32	205	31	normal
1501	73.01009	35.11599	234	48	306	16	normal
1501	73.01009	35.11599	21	38	10	40	reverse
1502	73.01299	35.11770	30	32	30	26	reverse
1502	73.01299	35.11770	76	15	20	5	reverse
1503	73.01402	35.11849	68	60	102	55	normal
1503	73.01402	35.11849	54	52	68	55	reverse
1505	73.01596	35.11935	16	27	1	20	reverse
1505	73.01596	35.11935	274	16	204	10	normal
1506	73.01862	35.12019	165	4	208	3	normal
1506	73.01862	35.12019	53	32	50	33	reverse
1506	73.01862	35.12019	53	44	30	36	normal
1506	73.01862	35.12019	90	26	70	21	normal
1506	73.01862	35.12019	0	66	58	49	reverse
1506	73.01862	35.12019	60	52	60	52	normal
1506	73.01862	35.12019	33	59	60	55	normal
1507	73.02193	35.12072	359	10	350	12	reverse
1507	73.02193	35.12072	28	54	92	36	reverse
1507	73.02193	35.12072	25	56	38	50	reverse
1507	73.02193	35.12072	0	33	45	24	reverse
1507	73.02193	35.12072	73	48	68	42	reverse
1507	73.02193	35.12072	40	34	87	30	reverse
1601	73.02239	35.12071	29	26	60	26	normal
1601	73.02239	35.12071	32	36	32	36	normal
1601	73.02239	35.12071	0	19	21	21	reverse
1601	73.02239	35.12071	54	36	30	30	reverse
1602	73.02483	35.12050	66	30	78	44	reverse
1602	73.02483	35.12050	54	16	70	15	normal
1602	73.02483	35.12050	338	36	70	1	normal
1602	73.02483	35.12050	296	46	235	26	reverse (?)
1602	73.02483	35.12050	92	41	88	45	normal
1602	73.02483	35.12050	85	66	77	65	normal
1603	73.02804	35.11989	24	26	310	10	reverse
1603	73.02804	35.11989	59	31	100	23	reverse (?)
1603	73.02804	35.11989	99	14	75	10	reverse
1603	73.02804	35.11989	98	22	80	32	reverse
1604	73.03278	35.11897	131	69	110	58	reverse
1605	73.03497	35.11853	50	22	90	18	normal
1605	73.03497	35.11853	279	49	212	30	normal
1607	73.03703	35.11789	22	40	68	36	reverse
1607	73.03703	35.11789	277	13	256	11	reverse
1607	73.03703	35.11789	293	56	215	2	normal
1607	73.03703	35.11789	91	36	113	37	reverse
1607	73.03703	35.11789	50	43	107	23	reverse (?)
1701	73.04574	35.12041	282	50	238	32	normal
1701	73.04574	35.12041	273	72	207	46	normal
1701	73.04574	35.12041	328	21	38	14	reverse
1701	73.04574	35.12041	64	55	48	49	reverse
1701	73.04574	35.12041	44	15	38	10	reverse
1701	73.04574	35.12041	276	40	275	25	normal
1701	73.04574	35.12041	356	18	34	15	reverse
1702	73.04777	35.12253	250	76	26	62	reverse
1702	73.04777	35.12253	37	40	34	30	reverse
1702	73.04777	35.12253	222	30	177	16	normal
1702	73.04777	35.12253	348	19	10	36	reverse
3002	73.01554	35.11005	78	42	42	45	normal
3002	73.01554	35.11005	66	70	82	68	reverse
3002	73.01554	35.11005	0	34	0	34	reverse

	coordinates (decimal degree)		shear plane		lineation		
Outcrop	x (East)	y (North)	azimuth	dip	azimuth	dip	sense
3002	73.01554	35.11005	210	15	194	12	normal
3002	73.01554	35.11005	348	58	288	30	dextral
3003	73.02413	35.11712	34	26	62	24	reverse
3004	73.02580	35.11728	52	42	62	42	reverse
3004	73.02580	35.11728	357	66	82	15	sinistral
3004	73.02580	35.11728	26	39	88	17	reverse
3005	73.02990	35.11622	40	26	60	23	reverse (?)
3005	73.02990	35.11622	54	20	130	6	reverse
3005	73.02990	35.11622	52	16	116	10	normal
3005	73.02990	35.11622	32	52	70	43	reverse (?)
3005	73.02990	35.11622	25	74	90	55	reverse
3005	73.02990	35.11622	60	61	65	61	reverse (?)
3005	73.02990	35.11622	42	41	62	39	reverse
3101	73.03110	35.11603	350	40	50	25	reverse
3101	73.03110	35.11603	258	5	240	4	reverse
3101	73.03110	35.11603	271	33	30	20	sinistral
3102	73.03192	35.11565	294	25	250	18	normal
3102	73.03192	35.11565	117	89	30	45	sinistral
3102	73.03192	35.11565	228	16	208	14	normal
3102	73.03192	35.11565	90	56	74	52	normal
3102	73.03192	35.11565	204	29	220	25	normal
3103	73.03382	35.11505	140	80	85	65	normal
3103	73.03382	35.11505	90	46	55	43	reverse
3103	73.03382	35.11505	278	32	243	30	reverse (?)
3103	73.03382	35.11505	306	11	35	5	reverse
3103	73.03382	35.11505	318	25	18	10	reverse
3104	73.03850	35.11380	116	40	78	34	normal
3104	73.03850	35.11380	162	66	241	26	reverse (?)
3104	73.03850	35.11380	315	40	227	5	sinistral
3104	73.03850	35.11380	176	57	100	22	reverse (?)
3105	73.04431	35.11298	284	70	249	58	sinistral
3105	73.04431	35.11298	270	40	204	25	sinistral
3105	73.04431	35.11298	305	22	242	10	normal
3105	73.04431	35.11298	280	71	8	22	sinistral

	coordinates (decimal degree)		shear plane		lineation		
Outcrop	x (East)	y (North)	azimuth	dip	azimuth	dip	sense
3106	73.04769	35.11456	27	46	14	45	normal
3106	73.04769	35.11456	23	24	10	23	reverse
3106	73.04769	35.11456	96	46	42	36	normal
3106	73.04769	35.11456	100	72	50	60	reverse (?)
3201	73.05086	35.11575	172	74	258	56	sinistral
3201	73.05086	35.11575	75	61	300	10	reverse
3202	73.05343	35.11895	322	10	45	4	reverse
3202	73.05343	35.11895	348	18	28	13	reverse
3203	73.05553	35.12295	330	16	26	7	reverse
3203	73.05553	35.12295	34	30	70	36	reverse
3203	73.05553	35.12295	330	45	49	16	reverse
3203	73.05553	35.12295	332	50	300	46	reverse (?)
2203	72.98422	35.13153	34	70	0	65	normal
2207	73.01397	35.07918	126	4	254	2	reverse (?)
2501	72.98090	35.13529	30	29	50	25	reverse
2501	72.98090	35.13529	54	60	20	39	reverse
2501	72.98090	35.13529	125	28	234	5	reverse (?)
2703	73.02275	35.06683	96	46	179	11	reverse (?)
4301	73.00968	35.11561	25	55	89	35	normal
4301	73.00968	35.11561	40	15	30	10	reverse
4304	73.01982	35.12058	52	46	60	43	normal
4305	73.02028	35.12066	58	34	54	31	normal

Station 6: Indian Plate							
	coordinates (decimal degree)		shear plane		lineation		
Outcrop	x (East)	y (North)	azimuth	dip	azimuth	dip	sense
1101	72.89736	35.03788	47	67	19	45	reverse
1101	72.89736	35.03788	330	65	50	31	reverse
1102	72.90066	35.03944	350	65	7	65	reverse
1103	72.91613	35.04110	104	59	36	12	reverse
1103	72.91613	35.04110	113	44	15	10	reverse
1104	72.91835	35.03995	74	41	7	15	reverse

Given coordinates represent the closest GPS point

APPENDIX CHAPTER 6

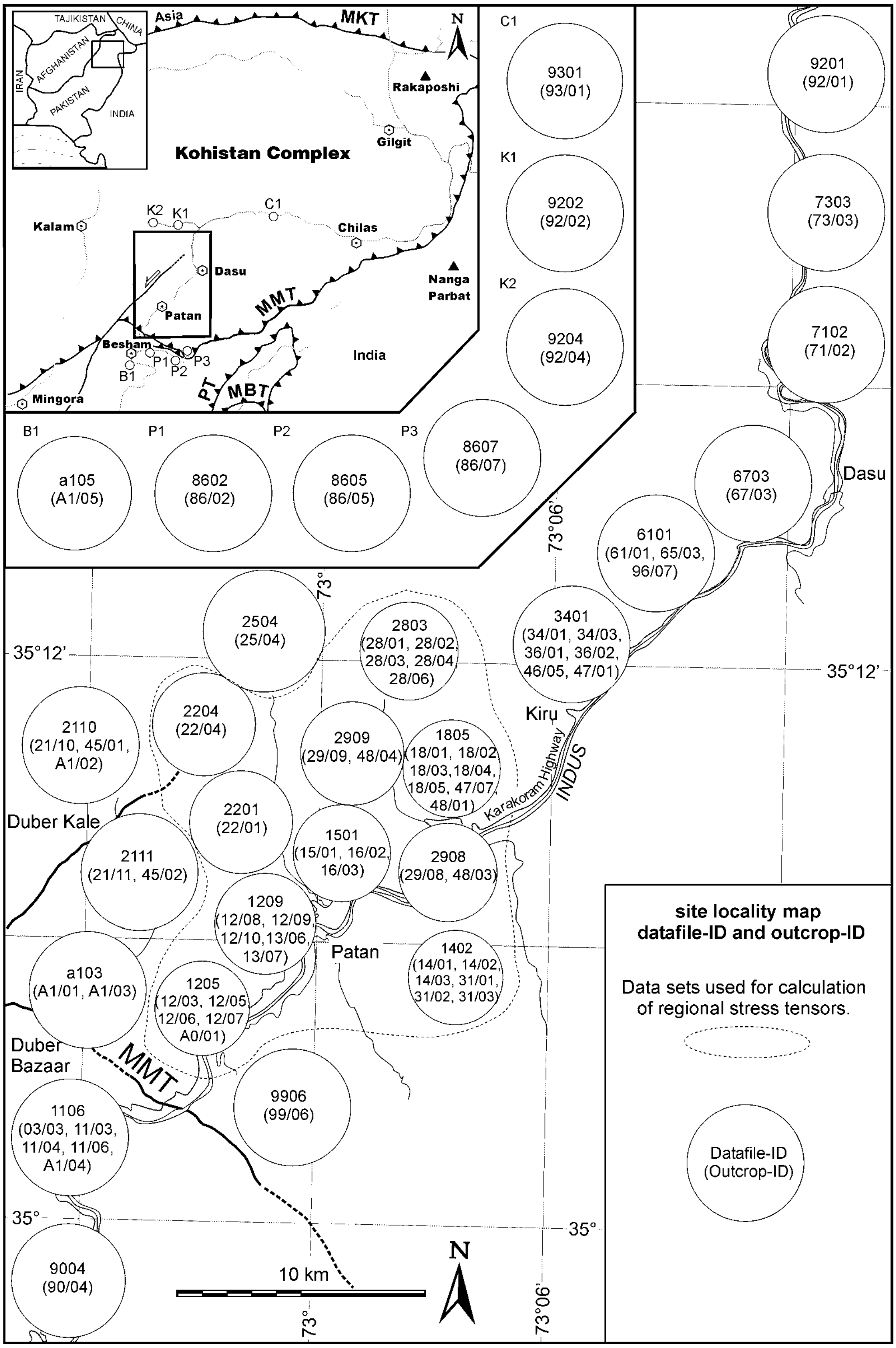

Fig. A6.1: Site locality map showing the data file-ID and outcrop-ID used for paleo-stress analysis presented in chapter 6.

Table A6.1: Fault data used for paleo-stress analysis presented in chapter 6

Continuous number	slip-plane		striation		Sense (relative movement of hanging block)	Quality-index	location	Generation	Regional-index
	Azimuth	Dip	Azimuth	Dip			Outcrop (see map)		
Data-file 1106, n = 27									
1	102	70	29	39	-	1	03/03	1	
2	97	76	12	20	-	1	A1/04	1	
3	96	70	17	28	-	1	A1/04	1	
4	105	66	26	23	-	1	A1/04	1	
5	107	65	22	11	-	1	A1/04	1	
6	102	74	13	5	-	1	A1/04	1	
7	236	71	320	16	+	1	11/03	2	
8	191	32	280	1	-	1	A1/04	2	
9	123	89	33	17	+	1	A1/04	2	
10	52	52	325	5	-	1	A1/04	2	
11	262	77	341	38	+	1	A1/04	2	
12	62	82	347	63	-	1	11/03	3	
13	230	67	291	49	-	1	11/03	3	
14	48	73	62	73	-	1	11/06	3	
15	249	86	186	81	-	1	11/06	3	
16	37	57	13	55	-	1	11/06	3	
17	80	70	96	69	-	1	11/06	3	
18	70	80	358	61	-	1	11/06	3	
19	17	50	17	50	-	1	11/06	3	
20	244	86	314	79	-	1	03/03	3	
21	62	69	54	69	-	1	03/03	3	
22	66	49	66	49	-	1	03/03	3	
23	56	61	71	60	-	1	03/03	3	
24	61	72	63	72	-	1	03/03	3	
25	79	50	17	29	-	1	A1/04	3	
26	228	85	143	45	-	3	11/04	6	
27	131	81	204	61	-	1	03/03	6	
Data-file 1205, n = 33									
28	320	68	42	18	+	1	12/05	1	reg
29	274	71	358	18	+	1	12/06	1	reg
30	72	84	159	32	+	1	12/07	1	reg
31	261	46	190	20	-	1	A0/01	1	reg
32	330	89	244	73	-	1	A0/01	1	reg
33	303	84	225	62	+	1	12/05	2	reg
34	231	59	312	15	+	1	12/07	2	reg
35	301	80	213	13	+	4	12/07	2	reg
36	200	36	236	30	-	1	12/03	3	reg
37	102	57	77	55	-	1	12/03	3	reg
38	91	77	56	74	-	1	12/03	3	reg
39	91	62	67	60	-	1	12/03	3	reg
40	40	70	349	60	-	1	12/05	3	reg
41	280	58	271	58	-	1	12/06	3	reg
42	97	71	157	56	-	1	12/07	3	reg
43	130	75	77	67	-	1	12/07	3	reg
44	253	74	203	66	-	1	12/07	3	reg
45	348	60	298	48	-	1	A0/01	3	reg
46	330	70	294	66	-	1	A0/01	3	reg
47	45	19	62	18	-	1	A0/01	3	reg
48	65	69	112	61	-	1	A0/01	3	reg
49	67	71	90	70	-	1	A0/01	3	reg
50	64	78	25	74	-	1	A0/01	3	reg
51	85	26	58	23	-	1	A0/01	3	reg
52	71	46	36	41	-	1	A0/01	3	reg
53	52	84	339	71	-	1	A0/01	3	reg
54	278	77	314	74	-	1	A0/01	3	reg
55	13	71	315	57	-	1	A0/01	3	reg
56	238	11	247	11	-	1	A0/01	3	reg
57	223	73	171	63	+	1	12/07	4	reg
58	116	77	192	46	-	1	12/05	6	reg
59	339	52	281	34	-	1	12/05	6	reg
60	344	76	273	53	-	1	12/06	6	reg
61	4	56	295	28	-	1	A0/01	6	reg
Data-file 1209, n = 20									
62	130	26	163	22	+	1	12/08	1	reg
63	128	80	39	7	-	1	12/08	1	reg
64	106	82	17	6	-	1	12/08	1	reg

Continuous number	Azimuth slip-plane	Dip slip-plane	Azimuth striation	Dip striation	Sense	Quality-index	Outcrop (see map)	Generation	Regional-index
65	150	89	239	35	+	2	13/06	1	reg
66	290	35	333	27	+	1	13/07	1	reg
67	219	60	135	9	+	1	13/07	1	reg
68	228	60	300	28	+	1	13/07	2	reg
69	180	63	251	33	-	4	12/08	3	reg
70	190	46	162	42	-	2	13/06	3	reg
71	330	76	21	69	-	4	13/07	3	reg
72	301	46	328	42	-	1	13/07	3	reg
73	93	74	5	6	+	1	12/08	4	reg
74	120	81	209	6	-	1	12/08	4	reg
75	268	80	179	4	+	1	12/08	4	reg
76	188	84	101	21	-	1	12/09	4	reg
77	270	89	360	20	+	4	12/10	4	reg
78	162	69	77	12	-	1	12/10	4	reg
79	246	86	335	15	-	1	12/10	4	reg
80	354	65	268	9	-	4	13/07	4	reg
81	78	48	152	17	+	1	12/10	6	reg
Data-file 1402, n = 16									
82	102	84	14	16	-	1	14/03	1	reg
83	272	40	182	1	-	3	31/01	1	reg
84	100	40	81	39	+	1	14/01	2	reg
85	255	50	236	48	+	3	31/02	2	reg
86	78	63	32	53	+	2	31/02	2	reg
87	235	47	285	34	-	1	14/01	3	reg
88	260	45	235	42	-	1	14/02	3	reg
89	295	44	241	30	-	1	14/02	4	reg
90	176	88	265	36	+	1	14/02	4	reg
91	100	26	16	3	+	1	14/03	4	reg
92	72	70	354	29	+	2	31/01	4	reg
93	255	50	185	21	+	2	31/02	4	reg
94	6	62	78	30	+	1	31/03	4	reg
95	255	88	166	25	+	3	31/03	4	reg
96	280	50	206	17	+	3	31/03	4	reg
97	339	15	19	11	+	4	31/03	4	reg
Data-file 1501, n = 29									
98	79	34	143	16	-	1	16/02	1	reg
99	323	49	21	31	+	1	16/02	1	reg
100	272	73	342	48	+	3	15/01	2	reg
101	350	73	5	72	+	2	15/01	2	reg
102	306	66	331	64	+	1	15/01	2	reg
103	268	86	355	28	+	2	15/01	2	reg
104	62	60	144	14	+	2	15/01	2	reg
105	9	67	96	7	+	2	15/01	2	reg
106	192	75	105	11	-	4	15/01	2	reg
107	194	88	284	11	+	3	15/01	2	reg
108	114	59	50	36	+	1	16/02	2	reg
109	328	78	55	12	-	1	16/02	2	reg
110	59	31	70	31	+	1	16/03	2	reg
111	326	79	346	78	-	3	15/01	3	reg
112	164	89	77	69	-	3	15/01	3	reg
113	215	84	130	35	-	3	15/01	3	reg
114	79	34	59	32	-	1	16/02	3	reg
115	328	78	259	59	-	1	16/02	3	reg
116	281	45	343	26	-	1	15/01	4	reg
117	164	89	254	8	-	4	15/01	4	reg
118	165	43	81	6	-	4	15/01	4	reg
119	154	88	244	4	+	1	15/01	4	reg
120	133	77	221	7	+	2	15/01	4	reg
121	292	74	207	18	-	1	16/02	4	reg
122	3	24	36	20	+	1	16/03	4	reg
123	334	75	359	73	+	2	15/01	6	reg
124	40	89	128	69	+	3	15/01	6	reg
125	333	88	61	45	+	1	15/01	6	reg
126	74	72	141	50	-	1	15/05	6	reg
Data-file 1805, n = 29									
127	320	80	231	7	-	1	18/02	1	reg
128	33	77	102	58	-	1	18/03	1	reg
129	47	72	124	33	-	1	18/05	1	reg
130	190	40	124	18	+	4	47/07	1	reg
131	29	80	109	42	-	2	47/07	1	reg
132	245	40	189	25	-	2	47/07	1	reg
133	280	70	10	1	+	3	47/07	1	reg
134	268	63	194	28	-	1	48/01	1	reg
135	97	65	180	14	+	1	48/01	1	reg
136	230	89	316	76	+	1	18/01	2	reg
137	230	89	320	5	-	1	18/01	2	reg
138	195	79	284	4	+	2	47/07	2	reg
139	30	48	104	17	+	1	48/01	2	reg

Continuous number	Azimuth slip-plane	Dip slip-plane	Azimuth striation	Dip striation	Sense	Quality-index	Outcrop (see map)	Generation	Regional-index
140	16	70	69	59	-	1	18/01	3	reg
141	246	85	329	52	-	1	18/02	3	reg
142	244	84	317	72	-	1	18/04	3	reg
143	68	26	68	26	-	1	18/05	3	reg
144	168	50	155	49	-	1	18/05	3	reg
145	80	89	80	89	-	2	47/07	3	reg
146	17	71	54	66	-	2	47/07	3	reg
147	338	46	341	46	-	2	47/07	3	reg
148	24	60	24	60	-	1	47/07	3	reg
149	329	47	354	44	-	1	47/07	3	reg
150	30	48	30	48	-	1	48/01	3	reg
151	168	50	238	22	-	1	18/05	6	reg
152	80	89	169	39	-	4	47/07	6	reg
153	30	67	94	46	+	3	47/07	6	reg
154	286	55	219	30	-	1	48/01	6	reg
155	74	84	352	50	+	1	48/01	6	reg
Data-file 2110, n = 26									
156	176	87	88	42	+	2	21/10	1	
157	149	76	65	24	+	1	45/01	2	
158	46	31	69	29	+	1	A1/02	2	
159	24	26	102	5	+	1	A1/02	2	
160	65	46	107	38	+	1	A1/02	2	
161	105	24	88	23	+	1	A1/02	2	
162	10	44	69	26	+	1	A1/02	2	
163	40	34	90	24	+	1	A1/02	2	
164	22	30	69	22	+	1	A1/02	2	
165	20	26	72	16	+	1	A1/02	2	
166	140	81	57	39	-	1	21/10	3	
167	42	61	118	22	-	1	21/10	3	
168	100	79	15	26	-	1	21/10	3	
169	151	86	69	62	-	2	21/10	3	
170	121	63	46	27	-	2	21/10	3	
171	22	76	100	40	-	2	21/10	3	
172	359	66	77	24	-	1	45/01	3	
173	140	52	95	42	-	1	45/01	3	
174	140	52	160	50	-	1	45/01	3	
175	217	84	134	47	+	1	21/10	4	
176	127	77	207	37	-	2	21/10	6	
177	80	60	143	38	-	1	21/10	6	
178	64	89	153	41	+	2	21/10	6	
179	140	52	190	40	-	1	45/01	6	
180	60	38	144	4	+	1	A1/02	6	
181	342	28	277	13	+	1	A1/02	6	
Data-file 2111, n = 25									
182	293	80	293	80	+	2	21/11	2	
183	70	87	346	62	-	2	21/11	2	
184	58	54	68	54	-	2	21/11	3	
185	122	68	42	24	-	3	21/11	3	
186	82	76	82	76	-	2	21/11	3	
187	62	45	68	45	-	1	21/11	3	
188	110	58	68	49	-	1	21/11	3	
189	316	28	275	22	-	2	21/11	3	
190	65	62	10	48	-	3	21/11	3	
191	200	53	266	28	-	2	21/11	3	
192	75	70	135	54	-	1	45/02	3	
193	94	80	20	55	-	1	45/02	3	
194	100	64	142	56	-	1	45/02	3	
195	80	60	84	60	-	1	45/02	3	
196	73	70	75	70	-	1	45/02	3	
197	45	56	114	27	-	1	45/02	3	
198	109	65	159	54	-	1	45/02	3	
199	320	80	234	20	-	1	45/02	4	
200	308	80	220	13	-	1	45/02	4	
201	40	62	339	42	-	2	21/11	6	
202	240	14	255	14	+	3	21/11	6	
203	292	60	4	28	-	2	21/11	6	
204	200	53	144	37	-	3	21/11	6	
205	70	87	156	56	+	2	21/11	6	
206	292	84	19	28	+	1	45/02	6	
Data-file 2201, n = 20									
207	252	54	186	29	-	3	22/01	1	reg
208	209	86	120	11	+	3	22/01	1	reg
209	100	89	190	9	-	1	22/01	1	reg
210	156	28	216	15	-	2	22/01	2	reg
211	196	69	110	9	-	2	22/01	2	reg
212	306	81	26	48	-	2	22/01	2	reg
213	345	56	38	42	-	2	22/01	2	reg
214	331	67	43	36	-	1	22/01	2	reg
215	198	80	266	65	-	3	22/01	3	reg
216	238	72	292	61	-	4	22/01	3	reg

Continuous number	Azimuth slip-plane	Dip slip-plane	Azimuth striation	Dip striation	Sense	Quality-index	Outcrop (see map)	Generation	Regional-index
217	238	72	180	59	-	2	22/01	3	reg
218	210	70	135	34	+	2	22/01	4	reg
219	315	61	4	50	+	2	22/01	4	reg
220	190	78	237	73	+	3	22/01	4	reg
221	200	86	267	80	+	3	22/01	4	reg
222	9	45	44	40	+	3	22/01	4	reg
223	12	53	45	48	+	2	22/01	4	reg
224	192	76	263	51	+	1	22/01	4	reg
225	12	30	326	22	-	3	22/01	6	reg
226	184	48	238	33	-	2	22/01	6	reg
Data-file 2204, n = 20									
227	226	46	244	45	+	2	22/04	2	reg
228	48	80	322	20	-	1	22/04	2	reg
229	257	75	195	60	+	2	22/04	2	reg
230	198	55	153	45	-	1	22/04	3	reg
231	220	51	182	45	-	2	22/04	3	reg
232	234	72	159	40	-	2	22/04	3	reg
233	226	66	163	45	-	2	22/04	3	reg
234	3	50	21	49	-	3	22/04	3	reg
235	218	52	170	41	-	1	22/04	3	reg
236	242	75	204	71	-	1	22/04	3	reg
237	12	55	303	26	-	2	22/04	3	reg
238	266	33	234	29	-	1	22/04	3	reg
239	258	70	197	53	-	4	22/04	3	reg
240	30	63	64	59	+	2	22/04	4	reg
241	258	55	209	43	+	1	22/04	4	reg
242	237	67	182	53	+	1	22/04	4	reg
243	224	80	156	65	+	1	22/04	4	reg
244	278	32	200	7	+	2	22/04	4	reg
245	298	42	213	4	-	1	22/04	4	reg
246	242	59	193	48	+	2	22/04	4	reg
Data-file 2504, n = 19									
247	81	76	156	45	+	3	25/04	1	
248	346	70	257	3	+	1	25/04	1	
249	235	44	165	18	-	1	25/04	1	
250	212	46	249	39	+	3	25/04	2	
251	92	41	46	31	+	2	25/04	2	
252	70	65	95	63	+	4	25/04	2	
253	164	68	238	32	-	1	25/04	2	
254	232	78	297	63	+	2	25/04	2	
255	220	10	216	10	-	1	25/04	2	
256	42	59	100	42	+	4	25/04	2	
257	80	27	82	27	+	4	25/04	2	
258	248	63	306	45	-	2	25/04	3	
259	235	44	274	37	-	4	25/04	3	
260	78	56	78	56	-	2	25/04	3	
261	238	72	220	71	+	4	25/04	6	
262	75	56	154	16	+	2	25/04	6	
263	52	46	331	8	-	2	25/04	6	
264	156	48	226	21	-	1	25/04	6	
265	66	20	139	6	+	1	25/04	6	
Data-file 2803, n = 11									
266	70	55	143	23	-	3	28/01	1	reg
267	18	56	74	40	-	3	28/01	1	reg
268	60	49	332	2	+	1	28/01	1	reg
269	50	64	121	33	-	3	28/01	1	reg
270	264	56	307	47	+	1	28/01	1	reg
271	112	39	72	31	+	2	28/01	1	reg
272	246	41	171	13	-	2	28/04	1	reg
273	36	45	111	15	+	1	28/02	2	reg
274	85	52	150	28	+	2	28/03	2	reg
275	50	56	123	24	+	3	28/03	2	reg
276	78	55	64	54	-	1	28/06	3	reg
Data-file 2908, n = 42									
277	68	72	143	39	-	3	29/08	1	reg
278	70	61	136	36	-	1	29/08	1	reg
279	85	89	174	42	+	3	29/08	1	reg
280	81	86	352	10	-	4	29/08	1	reg
281	288	85	17	6	+	1	48/03	1	reg
282	269	68	186	18	-	1	48/03	1	reg
283	260	75	177	24	-	1	48/03	1	reg
284	268	57	199	30	-	1	48/03	1	reg
285	322	10	330	10	+	1	48/03	1	reg
286	139	54	62	17	+	3	29/08	2	reg
287	163	57	77	7	+	1	48/03	2	reg
288	324	55	262	33	+	1	48/03	2	reg
289	116	89	28	56	-	4	29/08	3	reg
290	176	80	180	80	-	1	29/08	3	reg
291	358	42	17	41	-	1	29/08	3	reg
292	358	61	11	60	-	2	29/08	3	reg

Continuous number	Azimuth slip-plane	Dip slip-plane	Azimuth striation	Dip striation	Sense	Quality-index	Outcrop (see map)	Generation	Regional-index
293	19	46	352	43	-	2	29/08	3	reg
294	8	75	15	75	-	2	29/08	3	reg
295	350	73	294	61	-	3	29/08	3	reg
296	320	62	293	59	-	2	29/08	3	reg
297	340	54	24	45	-	1	29/08	3	reg
298	353	57	7	56	-	3	29/08	3	reg
299	164	26	164	26	-	1	48/03	3	reg
300	76	66	356	22	+	3	29/08	4	reg
301	356	83	270	27	-	2	29/08	4	reg
302	353	57	57	35	+	3	29/08	4	reg
303	103	89	193	5	+	1	48/03	4	reg
304	329	13	252	3	-	1	48/03	4	reg
305	310	12	222	1	-	1	48/03	4	reg
306	174	80	263	5	+	1	48/03	4	reg
307	254	50	184	23	+	1	48/03	4	reg
308	177	89	87	19	-	1	48/03	4	reg
309	42	47	42	47	+	1	48/03	4	reg
310	176	80	99	53	-	2	29/08	6	reg
311	7	85	6	85	+	2	29/08	6	reg
312	117	84	179	78	+	1	29/08	6	reg
313	76	66	140	45	-	4	29/08	6	reg
314	345	44	308	37	-	1	29/08	6	reg
315	291	20	223	8	+	1	48/03	6	reg
316	316	10	20	4	-	1	48/03	6	reg
317	335	58	259	20	-	1	48/03	6	reg
318	335	58	31	42	-	1	48/03	6	reg
Data-file 2909, n = 21									
319	212	89	301	36	-	2	29/09	1	reg
320	172	86	259	34	-	3	29/09	1	reg
321	244	23	200	17	+	3	29/09	1	reg
322	230	43	206	40	-	3	29/09	1	reg
323	265	46	194	18	-	1	48/04	1	reg
324	282	65	205	26	-	1	48/04	1	reg
325	324	72	234	1	-	1	48/04	1	reg
326	340	80	66	21	-	1	48/04	2	reg
327	166	76	166	76	-	2	29/09	3	reg
328	332	85	59	26	-	1	48/04	3	reg
329	252	65	199	53	-	1	48/04	3	reg
330	172	50	204	45	-	1	48/04	3	reg
331	252	64	183	37	-	1	48/04	3	reg
332	274	49	188	5	+	1	29/09	4	reg
333	250	55	205	46	+	4	29/09	4	reg
334	250	48	216	43	+	2	29/09	4	reg
335	268	70	178	1	+	1	48/04	4	reg
336	216	21	127	1	-	1	29/09	6	reg
337	6	79	284	35	+	1	29/09	6	reg
338	187	80	102	26	-	1	48/04	6	reg
339	300	80	210	1	+	1	48/04	6	reg
Data-file 3401, n = 40									
340	255	53	177	16	-	4	34/01	1	
341	289	73	210	33	-	1	34/03	1	
342	85	72	152	50	+	2	34/03	1	
343	80	79	166	22	+	2	34/03	1	
344	215	56	133	10	+	2	36/02	1	
345	64	75	150	14	-	3	46/05	1	
346	250	75	160	1	-	1	46/05	1	
347	270	78	180	1	-	3	46/05	1	
348	305	78	222	30	-	1	47/01	1	
349	325	2	1	2	+	1	47/01	1	
350	268	53	205	31	-	1	47/01	1	
351	205	51	160	41	+	1	47/01	1	
352	218	46	159	29	+	1	47/01	1	
353	300	75	216	20	+	2	34/01	2	
354	88	38	22	18	+	2	46/05	2	
355	184	56	152	52	-	2	34/01	3	
356	80	79	80	79	-	1	34/03	3	
357	282	74	346	57	-	4	36/01	3	
358	148	74	178	71	-	1	36/02	3	
359	215	56	256	48	-	4	36/02	3	
360	358	78	46	72	-	2	36/02	3	
361	340	60	26	51	-	3	36/02	3	
362	18	20	18	20	-	3	46/05	3	
363	144	84	208	76	-	2	46/05	3	
364	195	26	184	26	-	1	46/05	3	
365	218	46	232	45	-	1	47/01	3	
366	277	62	208	34	+	2	34/01	4	
367	322	88	52	11	+	1	34/03	4	
368	2	72	74	43	+	3	36/01	4	
369	140	85	51	15	-	1	46/05	4	
370	306	42	225	8	-	1	47/01	4	
371	328	51	36	24	+	1	47/01	4	
372	225	48	193	43	+	1	47/01	4	
373	238	42	186	29	+	1	47/01	4	
374	240	40	185	25	+	1	47/01	4	
375	315	56	8	42	-	3	34/01	6	
376	110	74	23	10	-	1	46/05	6	
377	77	74	156	33	-	4	46/05	6	
378	350	18	24	15	-	1	46/05	6	
379	334	55	48	21	-	1	47/01	6	
Data-file 6101, n = 27									
380	349	47	298	34	+	1	65/03	1	
381	353	65	274	21	+	1	65/03	1	
382	286	64	210	27	-	1	65/03	1	
383	20	56	304	19	+	1	65/03	1	
384	3	68	279	14	+	1	65/03	1	
385	6	64	94	4	-	1	65/03	1	
386	59	46	135	14	+	1	65/03	2	
387	10	62	88	20	+	1	65/03	2	
388	238	68	303	46	+	1	65/03	2	
389	97	75	8	3	+	1	65/03	2	
390	19	89	290	59	-	1	96/07	2	
391	223	75	283	63	+	1	96/07	2	
392	24	83	297	21	-	1	96/07	2	
393	179	78	105	53	+	1	96/07	2	
394	333	74	251	28	+	1	96/07	2	
395	242	52	223	51	+	1	61/01	2	
396	160	61	129	57	-	1	61/01	3	
397	186	60	194	60	-	1	61/01	3	
398	32	72	359	69	+	1	96/07	4	
399	359	69	79	24	+	1	61/01	4	
400	145	89	55	4	-	1	61/01	4	
401	305	72	221	19	-	1	61/01	4	
402	130	62	54	24	-	1	61/01	4	
403	215	80	133	41	+	1	61/01	4	
404	1	46	74	18	-	1	96/07	6	
405	330	47	247	7	+	1	61/01	6	
406	230	45	142	2	+	1	61/01	6	
Data-file 6703, n = 20									
407	126	24	189	11	+	1	67/03	1	
408	358	64	294	42	+	1	67/03	1	
409	192	68	280	6	-	1	67/03	1	
410	190	56	116	22	+	1	67/03	1	
411	239	51	159	11	-	1	67/03	1	
412	201	64	116	10	+	1	67/03	1	
413	187	61	113	27	+	1	67/03	1	
414	194	76	109	20	+	1	67/03	1	
415	192	74	113	32	+	1	67/03	1	
416	184	77	104	35	+	1	67/03	1	
417	180	81	92	15	+	1	67/03	1	
418	184	76	103	31	+	1	67/03	1	
419	182	74	105	40	+	1	67/03	1	
420	254	46	174	9	-	1	67/03	1	
421	251	51	169	9	-	1	67/03	1	
422	99	21	70	19	+	1	67/03	2	
423	60	37	41	35	+	1	67/03	6	
424	237	76	151	15	-	1	67/03	6	
425	201	74	122	35	-	1	67/03	6	
426	246	66	333	5	+	1	67/03	6	
Data-file 7102, n = 20									
427	80	67	352	5	-	1	71/02	1	
428	49	30	113	14	+	1	71/02	2	
429	98	56	66	51	+	1	71/02	2	
430	90	70	90	70	+	1	71/02	2	
431	17	47	85	22	+	1	71/02	2	
432	92	45	123	41	+	1	71/02	2	
433	244	88	333	21	+	1	71/02	2	
434	85	70	133	61	+	1	71/02	2	
435	294	55	294	55	+	1	71/02	2	
436	154	81	241	19	+	1	71/02	4	
437	135	86	223	24	+	1	71/02	4	
438	87	71	6	25	+	1	71/02	4	
439	80	64	163	15	-	1	71/02	4	
440	116	86	204	26	+	1	71/02	4	
441	251	68	171	24	+	1	71/02	4	
442	302	74	226	40	-	1	71/02	4	
443	329	71	246	19	-	1	71/02	4	
444	275	88	186	23	+	1	71/02	4	
445	128	86	41	35	+	1	71/02	6	
446	2	50	273	1	+	1	71/02	6	

Continuous number	Azimuth slip-plane	Dip slip-plane	Azimuth striation	Dip striation	Sense	Quality-index	Outcrop (see map)	Generation	Regional-index
Data-file 7303, n = 19									
447	112	52	170	35	+	1	73/03	1	
448	91	55	147	38	+	1	73/03	1	
449	83	56	158	21	+	1	73/03	1	
450	68	72	149	27	-	1	73/03	1	
451	122	71	195	40	+	1	73/03	1	
452	63	71	147	18	-	1	73/03	1	
453	76	62	154	20	-	1	73/03	1	
454	289	72	217	44	-	1	73/03	1	
455	69	78	154	23	-	1	73/03	1	
456	292	56	228	33	+	1	73/03	2	
457	280	60	225	45	+	1	73/03	2	
458	272	36	253	34	+	1	73/03	2	
459	250	41	263	40	-	1	73/03	3	
460	180	82	180	82	-	1	73/03	3	
461	54	64	5	53	+	1	73/03	4	
462	88	75	166	37	-	1	73/03	4	
463	78	84	167	8	-	1	73/03	4	
464	269	70	255	69	+	1	73/03	6	
465	15	86	101	44	+	1	73/03	6	
Data-file 8602, n = 12									
466	193	71	109	18	+	1	86/02	1	
467	5	73	73	50	-	1	86/02	1	
468	292	75	253	71	+	1	86/02	2	
469	130	69	50	24	-	1	86/02	4	
470	99	39	77	37	+	1	86/02	4	
471	122	85	33	10	-	1	86/02	4	
472	344	78	256	8	-	1	86/02	4	
473	86	74	359	9	+	1	86/02	4	
474	122	26	165	19	+	1	86/02	4	
475	123	73	157	69	+	1	86/02	6	
476	220	85	308	24	+	1	86/02	6	
477	125	51	196	22	-	1	86/02	6	
Data-file 8605, n = 14									
478	302	70	25	19	+	1	86/05	1	
479	141	69	87	57	+	1	86/05	1	
480	85	73	173	7	+	1	86/05	1	
481	78	49	57	47	+	1	86/05	1	
482	121	66	171	55	+	1	86/05	1	
483	324	86	240	55	-	1	86/05	1	
484	258	82	336	55	+	1	86/05	1	
485	243	84	313	72	+	1	86/05	1	
486	140	45	61	11	+	1	86/05	2	
487	267	70	281	69	+	1	86/05	2	
488	270	80	338	65	-	1	86/05	3	
489	117	50	145	46	-	1	86/05	4	
490	92	46	142	34	+	1	86/05	6	
491	250	66	179	36	-	1	86/05	6	
Data-file 8607, n = 16									
492	60	82	137	57	-	1	86/07	1	
493	220	61	149	30	+	1	86/07	1	
494	110	62	110	62	+	1	86/07	1	
495	210	70	129	24	+	1	86/07	1	
496	282	61	352	32	+	1	86/07	1	
497	270	70	350	26	+	1	86/07	1	
498	285	52	359	20	+	1	86/07	1	
499	282	68	211	39	-	1	86/07	1	
500	310	66	223	6	-	1	86/07	1	
501	22	88	295	62	-	1	86/07	2	
502	128	64	65	43	+	1	86/07	2	
503	208	61	293	10	+	1	86/07	2	
504	72	49	27	39	+	1	86/07	4	
505	294	86	23	13	-	1	86/07	6	
506	290	55	12	12	-	1	86/07	6	
507	122	36	176	23	-	1	86/07	6	
Data-file 9004, n = 20									
508	15	84	100	38	-	1	90/04	1	
509	159	34	115	26	+	1	90/04	1	
510	161	56	109	43	+	1	90/04	1	
511	72	76	121	69	-	1	90/04	1	
512	190	88	103	55	+	1	90/04	1	
513	86	56	38	45	+	1	90/04	2	
514	144	33	108	28	+	1	90/04	2	
515	214	84	300	36	+	1	90/04	2	
516	73	70	12	54	-	1	90/04	3	
517	168	43	107	25	-	1	90/04	3	
518	60	47	105	37	-	1	90/04	3	
519	170	70	105	50	-	1	90/04	3	
520	108	50	90	49	-	1	90/04	3	
521	153	69	80	36	-	1	90/04	3	
522	98	50	85	49	-	1	90/04	3	
523	114	79	106	79	-	1	90/04	4	
524	200	82	151	77	+	1	90/04	4	
525	248	80	334	20	+	1	90/04	6	
526	124	64	92	60	+	1	90/04	6	
527	108	63	129	62	+	1	90/04	6	
Data-file 9201, n = 20									
528	290	82	213	57	-	1	92/01	1	
529	39	45	95	29	-	1	92/01	1	
530	60	88	148	37	+	1	92/01	1	
531	284	24	280	24	+	1	92/01	1	
532	1	59	87	6	-	1	92/01	1	
533	269	86	181	22	-	1	92/01	1	
534	280	86	191	19	-	1	92/01	1	
535	74	86	160	42	+	1	92/01	1	
536	39	78	122	31	-	1	92/01	1	
537	272	88	185	62	-	1	92/01	1	
538	57	89	327	15	+	1	92/01	1	
539	242	70	268	68	-	1	92/01	3	
540	117	58	128	58	-	1	92/01	3	
541	115	66	115	66	-	1	92/01	3	
542	226	70	257	67	-	1	92/01	3	
543	238	31	254	30	+	1	92/01	6	
544	192	85	276	51	+	1	92/01	6	
545	97	50	89	50	+	1	92/01	6	
546	97	89	7	2	+	1	92/01	6	
547	74	86	345	10	+	1	92/01	6	
Data-file 9202, n = 10									
548	260	50	306	40	-	1	92/02	4	
549	211	70	296	13	-	1	92/02	4	
550	292	74	15	23	+	1	92/02	4	
551	326	85	56	4	+	1	92/02	4	
552	64	77	338	17	+	1	92/02	4	
553	149	89	59	6	-	1	92/02	4	
554	205	78	294	4	-	1	92/02	4	
555	276	66	0	13	+	1	92/02	6	
556	195	74	279	21	+	1	92/02	6	
557	52	72	332	27	+	1	92/02	6	
Data-file 9204, n = 23									
558	11	59	310	39	-	1	92/04	2	
559	215	56	148	30	-	1	92/04	2	
560	71	89	341	20	+	1	92/04	2	
561	324	40	324	40	+	1	92/04	2	
562	34	72	316	33	-	1	92/04	2	
563	215	63	286	32	+	1	92/04	2	
564	324	88	234	10	+	1	92/04	2	
565	80	48	69	48	+	1	92/04	2	
566	86	42	44	34	+	1	92/04	2	
567	95	46	70	43	+	1	92/04	2	
568	58	77	339	40	-	1	92/04	3	
569	231	88	321	11	-	1	92/04	4	
570	247	89	157	2	+	1	92/04	4	
571	220	89	310	26	+	1	92/04	4	
572	59	86	331	30	+	1	92/04	4	
573	19	69	303	32	+	1	92/04	4	
574	40	78	318	32	+	1	92/04	4	
575	320	88	49	33	+	1	92/04	4	
576	58	58	131	24	-	1	92/04	6	
577	339	72	296	65	-	1	92/04	6	
578	332	44	304	41	-	1	92/04	6	
579	123	62	198	25	-	1	92/04	6	
580	345	35	294	24	-	1	92/04	6	
Data-file 9301, n = 26									
581	296	76	24	7	+	1	93/01	1	
582	292	81	18	24	+	1	93/01	1	
583	250	51	310	32	-	1	93/01	1	
584	58	74	19	70	+	1	93/01	1	
585	284	84	12	18	+	1	93/01	1	
586	262	60	199	38	+	1	93/01	1	
587	207	88	296	27	-	1	93/01	1	
588	224	84	309	41	-	1	93/01	1	
589	286	80	335	75	+	1	93/01	1	
590	64	88	153	31	-	1	93/01	1	
591	65	80	348	53	-	1	93/01	1	
592	303	62	2	44	+	1	93/01	1	
593	322	35	254	15	+	1	93/01	2	
594	34	60	119	9	+	1	93/01	2	
595	203	87	292	12	+	1	93/01	2	
596	190	60	273	13	+	1	93/01	2	
597	259	60	211	49	-	1	93/01	3	

Continuous number	Azimuth slip-plane	Dip slip-plane	Azimuth striation	Dip striation	Sense	Quality-index	Outcrop (see map)	Generation	Regional-index
598	63	81	357	68	-	1	93/01	3	
599	248	64	278	61	-	1	93/01	3	
600	175	57	248	25	-	1	93/01	3	
601	194	68	268	35	-	1	93/01	3	
602	34	60	70	54	-	1	93/01	3	
603	206	85	294	27	-	1	93/01	3	
604	92	86	8	56	-	1	93/01	3	
605	340	89	340	89	-	1	93/01	6	
606	303	75	221	29	-	1	93/01	6	
Data-file 9906, n = 15									
607	228	66	266	61	+	1	99/06	2	
608	305	52	276	48	+	1	99/06	2	
609	290	18	274	17	+	1	99/06	2	
610	157	49	74	9	-	1	99/06	4	
611	273	52	262	51	-	1	99/06	4	
612	84	79	5	43	+	1	99/06	4	
613	270	80	354	35	-	1	99/06	4	
614	112	56	32	14	+	1	99/06	4	
615	130	49	58	20	-	1	99/06	4	
616	310	28	18	12	-	1	99/06	4	
617	231	79	158	56	+	1	99/06	4	
618	292	26	353	14	+	1	99/06	4	
619	35	74	316	35	-	1	99/06	6	
620	290	18	11	3	+	1	99/06	6	
621	270	26	190	5	-	1	99/06	6	
Data-file a103, n = 32									
622	290	64	207	15	-	1	A1/01	1	
623	16	79	104	12	-	1	A1/01	1	
624	22	85	109	29	-	1	A1/01	1	
625	9	83	97	21	-	1	A1/01	1	
626	3	75	88	19	-	1	A1/01	1	
627	9	74	95	14	-	1	A1/01	1	
628	292	42	349	26	+	1	A1/03	1	
629	81	88	171	11	+	1	A1/03	1	
630	92	86	166	76	-	1	A1/01	2	
631	142	82	53	9	+	1	A1/01	2	
632	277	74	277	74	+	1	A1/01	2	
633	300	65	225	30	+	1	A1/03	2	
634	353	85	290	80	-	1	A1/03	2	
635	313	80	38	24	-	1	A1/03	2	
636	302	78	30	8	-	1	A1/03	2	
637	248	41	296	30	+	1	A1/03	2	
638	299	68	254	61	+	1	A1/03	2	
639	194	84	113	55	-	1	A1/01	3	
640	112	76	65	70	-	1	A1/01	3	
641	118	89	30	59	-	1	A1/01	3	
642	123	72	160	68	-	1	A1/01	3	
643	117	86	48	80	-	1	A1/01	3	
644	298	65	340	57	-	1	A1/01	3	
645	117	76	58	64	-	1	A1/01	3	
646	110	84	40	72	-	1	A1/01	3	
647	249	85	161	30	+	1	A1/03	4	
648	53	36	110	22	-	1	A1/01	6	
649	263	81	183	47	+	1	A1/01	6	
650	195	79	111	27	-	1	A1/01	6	
651	129	88	42	58	-	1	A1/01	6	
652	129	88	39	21	-	1	A1/01	6	
653	310	51	25	17	-	1	A1/03	6	
Data-file a105, n = 11									
654	108	65	20	4	-	1	A1/05	1	
655	108	73	24	19	-	1	A1/05	1	
656	113	34	113	34	+	1	A1/05	1	
657	185	46	139	35	+	1	A1/05	1	
658	72	89	342	16	+	1	A1/05	1	
659	55	82	131	60	-	1	A1/05	3	
660	114	75	84	73	-	1	A1/05	3	
661	95	66	95	66	-	1	A1/05	3	
662	199	75	281	27	-	1	A1/05	3	
663	116	85	41	70	-	1	A1/05	3	
664	165	84	254	10	+	1	A1/05	6	
Additional fault data (not included in calculations for chapter 6)									
1	200	65	113	6	+	1	11/01	1	
2	58	67	347	36	-	1	11/01	6	
3	248	37	329	7	-	1	11/02	6	
4	208	62	127	17	+	1	12/01	1	
5	242	80	298	72	+	1	12/01	2	
6	203	88	284	77	+	1	12/01	4	
7	208	59	289	13	-	1	12/01	6	
8	232	85	321	11	-	1	12/11	1	
9	245	65	166	23	-	1	13/01	1	

Continuous number	Azimuth slip-plane	Dip slip-plane	Azimuth striation	Dip striation	Sense	Quality-index	Outcrop (see map)	Generation	Regional-index
10	292	86	203	12	+	1	13/01	2	
11	289	50	334	40	-	1	13/01	6	
12	260	80	344	29	-	4	13/01	6	
13	278	86	197	64	+	1	13/02	2	
14	235	83	319	43	-	2	13/03	3	
15	310	66	232	24	-	2	13/03	4	
16	285	45	333	33	-	1	14/07	4	
17	93	41	93	41	-	1	14/08	3	
18	76	25	25	16	-	2	14/08	3	
19	187	40	164	38	-	1	14/09	3	
20	73	51	143	22	+	1	15/07	2	
21	330	47	53	8	+	2	16/04	4	
22	100	69	29	39	+	1	16/07	2	
23	100	69	71	67	-	1	16/07	3	
24	150	79	62	9	+	1	17/01	2	
25	170	70	80	1	+	1	17/01	2	
26	99	40	158	24	-	1	17/01	4	
27	288	78	201	16	+	1	17/02	4	
28	299	86	299	86	+	1	17/03	6	
29	65	73	106	67	+	4	17/06	6	
30	259	45	195	24	-	1	19/02	1	
31	270	36	270	36	-	1	19/02	3	
32	22	89	110	64	-	3	19/02	4	
33	298	59	19	14	+	3	19/04	1	
34	50	89	321	18	-	1	19/05	2	
35	18	42	58	34	+	1	21/01	2	
36	156	76	236	36	+	1	21/01	4	
37	156	86	69	41	-	1	21/01	6	
38	177	85	90	26	+	1	21/03	1	
39	24	73	104	30	-	1	21/03	1	
40	187	75	106	31	+	1	21/03	1	
41	50	26	87	21	+	1	21/03	2	
42	165	51	100	27	+	1	21/03	2	
43	222	45	247	42	-	1	21/03	3	
44	114	80	59	73	-	1	21/03	3	
45	23	30	90	12	+	1	21/04	2	
46	85	71	4	26	+	1	21/05	4	
47	92	86	179	41	+	1	21/07	1	
48	11	52	290	12	+	2	25/09	1	
49	169	56	137	51	+	3	25/09	1	
50	252	60	325	27	+	1	25/09	2	
51	247	56	310	33	+	1	25/09	2	
52	206	88	292	67	+	2	25/10	2	
53	124	81	50	59	-	3	25/10	3	
54	35	85	111	69	+	2	25/10	6	
55	350	58	77	6	-	1	25/10	6	
56	326	80	54	9	-	4	26/03	2	
57	234	40	299	19	-	1	26/03	6	
58	61	81	338	37	-	1	27/01	2	
59	351	86	261	6	+	2	27/01	2	
60	210	82	293	41	+	4	27/01	2	
61	64	86	338	40	+	3	27/01	6	
62	300	87	23	65	-	2	27/01	6	
63	210	40	169	32	+	1	27/03	4	
64	116	28	159	21	+	2	29/01	1	
65	116	28	50	12	-	3	29/01	6	
66	50	52	122	22	-	1	29/03	1	
67	70	42	141	16	-	2	29/06	1	
68	50	25	1	17	+	1	30/02	4	
69	100	86	12	35	+	3	30/02	4	
70	335	55	3	52	+	2	30/03	1	
71	304	34	15	13	-	4	30/03	6	
72	6	88	277	15	-	2	30/04	2	
73	30	89	301	54	+	1	30/04	6	
74	50	76	333	40	-	3	30/05	2	
75	143	84	54	10	+	1	30/05	2	
76	118	80	204	24	-	2	32/01	2	
77	302	69	222	24	-	2	32/01	4	
78	275	70	3	6	-	3	32/02	4	
79	258	78	184	52	-	1	32/03	1	
80	342	55	16	50	-	2	32/03	3	
81	328	70	43	35	+	2	33/02	1	
82	208	65	126	16	+	1	33/02	1	
83	61	86	332	26	-	2	33/02	2	
84	254	81	166	13	+	1	33/02	4	
85	117	80	31	20	+	2	33/03	2	
86	346	51	52	27	+	2	33/03	4	
87	250	73	164	13	+	1	33/03	4	
88	336	63	60	10	+	2	33/03	4	
89	330	62	258	29	+	1	34/02	2	
90	87	68	4	17	+	1	34/02	4	

Continuous number	Azimuth slip-plane	Dip slip-plane	Azimuth striation	Dip striation	Sense	Quality-index	Outcrop (see map)	Generation	Regional-index
91	300	64	14	29	-	3	34/02	6	
92	335	39	288	29	+	3	34/02	6	
93	19	39	36	38	+	1	34/04	4	
94	22	75	103	30	-	2	35/01	1	
95	66	70	146	26	+	3	35/01	2	
96	60	48	72	47	-	1	35/01	3	
97	320	39	6	29	+	3	35/02	1	
98	328	46	254	15	-	2	35/02	4	
99	338	68	51	35	-	4	35/02	6	
100	175	78	252	46	-	1	35/05	6	
101	282	65	357	30	+	2	39/01	1	
102	275	55	234	47	+	3	39/02	2	
103	280	55	320	48	-	2	41/04	3	
104	58	24	20	19	+	1	41/04	4	
105	64	70	10	58	+	3	42/01	6	
106	85	86	356	11	-	3	42/02	1	
107	278	80	191	16	-	3	42/02	1	
108	76	70	354	21	-	2	42/02	1	
109	115	66	62	54	-	3	42/02	3	
110	116	48	189	19	-	1	42/02	4	
111	115	66	195	22	-	1	42/02	6	
112	280	80	197	32	+	3	42/03	2	
113	253	78	190	66	+	1	42/03	2	
114	190	75	106	22	-	3	42/04	6	
115	212	70	133	29	-	2	42/04	6	
116	291	51	237	36	+	3	43/03	2	
117	291	51	217	18	-	2	43/03	4	
118	60	60	134	25	-	1	43/04	1	
119	328	66	41	33	+	1	44/01	1	
120	268	46	356	2	-	1	44/01	4	
121	46	60	338	33	-	1	50/01	6	
122	35	55	35	55	-	1	50/05	3	
123	348	70	298	60	-	1	50/05	3	
124	85	80	166	39	+	1	51/03	1	
125	348	35	57	14	+	1	51/03	4	
126	345	56	55	27	+	1	51/03	4	
127	328	35	30	19	-	1	51/03	6	
128	334	62	37	41	-	1	51/03	6	
129	60	80	343	52	-	1	51/04	2	
130	105	76	193	9	+	1	51/05	1	
131	332	72	245	10	-	1	51/05	1	

Continuous number	Azimuth slip-plane	Dip slip-plane	Azimuth striation	Dip striation	Sense	Quality-index	Outcrop (see map)	Generation	Regional-index
132	174	82	101	65	-	1	95/01	3	
133	160	62	151	62	-	1	95/01	3	
134	179	73	194	73	-	1	95/01	3	
135	110	47	140	43	-	1	95/01	3	
136	153	56	172	55	-	1	95/01	3	
137	227	34	197	30	-	1	95/01	3	
138	186	86	145	85	-	1	95/01	3	
139	139	58	154	57	-	1	95/01	3	
140	164	50	139	47	-	1	95/01	3	
141	170	33	143	30	-	1	95/01	3	
142	130	44	130	44	-	1	95/01	3	
143	181	31	187	31	-	1	95/01	3	
144	184	42	186	42	-	1	95/01	3	
145	221	56	229	56	-	1	95/01	3	
146	130	44	216	4	+	1	95/01	4	
147	127	40	215	2	+	1	95/01	4	
148	130	33	214	4	+	1	95/01	4	
149	240	66	157	17	-	1	95/01	6	
150	211	38	167	29	-	1	95/01	6	
151	232	55	320	2	+	1	95/01	6	

Explanation:
sense of movement:
\+ reverse
\- normal
Population:
1: SSE – NNW directed $\sigma 1$ + ENE – WSW $\sigma 3$
2: E – W directed $\sigma 1$ + subvertical $\sigma 3$
3: WNW – ESE extension (subvertical $\sigma 1$)
4: SSW – NNE directed $\sigma 1$ + WNW – ESE $\sigma 3$
6: not assigned

References

Ambraseys, N., Lensen, G., and Moinfar, A., 1975, The Pattan earthquake of 28 December, 1974: Paris, UNESCO.

Anczkiewicz, R., 1998, *Structural and geochronological study of the India-Kohistan arc collision, lower swat region of Pakistan, NW Himalaya* [PhD thesis]: Zurich, ETH Zurich.

Anczkiewicz, R., Burg, J.P., Hussain, S.S., Dawood, H., Ghazanfar, M., and Chaudhry, M.N., 1998, Stratigraphy and structure of the Indus Suture in the lower Swat, Pakistan, NW Himalaya: *Journal of Asian Earth Sciences*, v. **16**, p. 225-238.

Anczkiewicz, R., and Vance, D., 2000, Isotopic constraints on the evolution of metamorphic conditions in the Jijal-Patan Complex and Kamila Belt of the Kohistan Arc, Pakistan Himalaya, *in* Khan, M.A., Treloar, P.J., Searle, M.P., and Jan, M.Q., eds., *Tectonics of the Nanga Parbat syntaxis and the western Himalaya*, Volume **170**: London, United Kingdom, Geological Society of London, p. 321-331.

Anczkiewicz, R., Oberli, F., Burg, J.P., Villa, I.M., Gunther, D., and Meier, M., 2001, Timing of normal faulting along the Indus Suture in Pakistan Himalaya and a case of major 231Pa/235U initial disequilibrium in zircon: *Earth and Planetary Science Letters*, v. **191**, p. 101-114.

Arbaret, L., Burg, J.P., Zeilinger, G., Chaudhry, N., Hussain, S., and Dawood, H., 2000, Pre-collisional anastomosing shear zones in the Kohistan Arc, NW Pakistan, *in* Khan, M.A., Treloar, P.J., Searle, M.P., and Jan, M.Q., eds., *Tectonics of the Nanga Parbat syntaxis and the western Himalaya*, Volume **170**: London, United Kingdom, Geological Society of London, p. 295-311.

Arculus, R.J., 1994, Aspects of magma genesis in arcs: *Lithos*, v. **33**, p. 189-208.

Baig, M.S., Snee, L.W., LaFortune, R.J., and Lawrence, R.D., 1989, Timing of pre-Himalayan orogenic events in the north-west Himalaya: $^{40}Ar/^{39}Ar$ constraints: *Kashmir Journal of Geology*, v. **8 & 9**, p. 19-23.

Baig, M.S., 1991, Geochronology of Pre-Himalayan and Himalayan tectonic events, northwest Himalaya, Pakistan: *Kashmir Journal of Geology*, v. **8 & 9**, p. 197.

Bally, A.W., 1983, Tectonics of extensional provinces; introduction, *Seismic expression of structural styles; a picture and work atlas; Volume 2*, Volume **15**: Tulsa, OK, United States, American Association of Petroleum Geologists, p. 211-212.

Bard, J.P., Maluski, H., Matte, P., and Proust, F., 1980, The Kohistan sequence; crust and mantle of an obducted island arc, *in* Tahirkheli, R.A.K., Jan, M.Q., and Majid, M., eds., *Proceedings of the International Committee on Geodynamics Group 6 meeting.*, Volume **13**: Geological Bulletin, University of Peshawar: Peshawar, Pakistan, University of Peshawar, Department of Geology, p. 87-94.

Bard, J.P., 1983, Metamorphic evolution of an obducted island arc: Example of the Kohistan Sequence (Pakistan) in the Himalayan collided range: *Geol. Bull. Univ. Peshawar*, v. **16**, p. 105-184.

Barker, F., and Arth, J.G., 1976, Generation of trondhjemitic-tonalitic liquids and Archean bimodal trondhjemite-basalt suites: *Geology (Boulder)*, v. **4**, p. 596-600.

Beck, R.A., Burbank, D.W., Sercombe, W.J., Khan, A.S., and Lawrence, R.D., 1996, Late Cretaceous ophiolite obduction and Paleocene India-Asia collision in the westernmost Himalaya: *Geodinamica Acta*, v. **9**, p. 114-144.

Blichert-Toft, J., and Albarede, F., 1997, The Lu-Hf isotope geochemistry of chondrites and the evolution of the mantle-crust system: *Earth and Planetary Science Letters*, v. **148**, p. 243-258.

Blichert-Toft, J., Chauvel, C., and Albarede, F., 1997, Separation of Hf and Lu for high-precision isotope analysis of rock samples by magnetic sector-multiple collector ICP-MS: *Contributions to Mineralogy and Petrology*, v. **127**, p. 248-260.

Bott, M.H.P., 1959, The mechanics of oblique slip faulting: *Geological Magazine*, v. **96**, p. 109-117.

Burg, J.P., Chaudhry, M.N., Ghanzanfar, M., Anczkiewicz, R., and Spencer, D., 1996, Structural evidence for back sliding of the Kohistan arc in the collisional system of northwest Pakistan: *Geology*, v. **24**, p. 739-742.

Burg, J.P., Bodinier, J.L., Chaudhry, S., Hussain, S., and Dawood, H., 1998, Infra-arc mantle-crust transition and infra-arc mantle diapirs in the Kohistan Complex (Pakistani Himalaya): petro-structural evidence: *Terra Nova*, v. **10**, p. 74-80.

Burg, J.P., and Podladchikov, Y., 2000, From buckling to asymmetric folding of the continental lithosphere; numerical modelling and application to the Himalayan syntaxes, *in* Khan, M.A., Treloar, P.J., Searle, M.P., and Jan, M.Q., eds., *Tectonics of the Nanga Parbat syntaxis and the western Himalaya*, Volume **170**: London, United Kingdom, Geological Society of London, p. 219-236.

Burnham, C.W., 1979, Magmas and hydrothermal fluids, *Geochemistry of hydrothermal ore deposits*: New York, NY, United States, John Wiley & Sons.

Burton, K.W., and O'Nions, R.K., 1988, Isotope systematics and chronology of granulite genesis in Sri Lanka, *International congress of geochemistry and cosmochemistry*, Volume **70**: Amsterdam, Netherlands, Elsevier, p. 5.

Butler, R.W.H., 1986, Thrust tectonics, deep structure and crustal subduction in the Alps and Himalayas: *Journal of the Geological Society of London*, v. **143**, p. 857-873.

Butler, R.W.H., and Prior, D.J., 1988, Tectonic control on the uplift of the Nanga Parbat Massif, Pakistan Himalayas: *Nature*, v. **333**, p. 247-250.

Calkins, J.A., Offield, T.W., Abdullah, S.K.M., and Ali, S.T., 1975, Geology of the southern Himalaya in Hazara, Pakistan and adjacent areas: *U.S. Geol. Survey, Prof. Paper*, v. **716-C**, p. 1-29.

Célérier, B., 1988, How much does slip on a reactivated fault plane constrain the stress tensor?: *Tectonics*, v. **7**, p. 1257-1278.

Célérier, B., 1995, Tectonic regime and slip orientation of reactivated faults: *Geophysical Journal*, v. **121**, p. 143-161.

Chen, Y., Courtillot, V., Cogne, J.P., Basse, J., Yang, Z., and Enkin, R., 1993, The configuration of Asia prior to the collision of India; Cretaceous paleomagnetic constraints, *Special section on Physical processes in geodynamics*, Volume **98**: Washington, DC, United States, American Geophysical Union, p. 21,927-21,941.

Compton, R.R., 1966, Analyses of Pliocene-Pleistocene deformation and stresses in northern Santa Lucia Range, California: *Geological Society of America Bulletin*, v. **77**, p. 1361-1379.

Coward, M.P., 1985, A section through the Nanga Parbat syntaxis, Indus Valley, Kohistan: *Geol. Bull. Univ. Peshawar*, v. **18**, p. 147-152.

Coward, M.P., and Butler, R.W.H., 1985, Thrust tectonics and the deep structure of the Pakistan Himalaya: *Geology*, v. **13**, p. 417-420.

Coward, M.P., Windley, B.F., Broughton, R.D., Luff, I.W., Patterson, M.G., Pudsey, C.J., Rex, D.C., and Khan, M.A., 1986, Collision tectonics in the NW Himalayas: *Collision Tectonics, Geological Society Special Publications*, v. **19**, p. 203-219.

Coward, M.P., Butler, R.W.H., Khan, M.A., and Knipe, R.J., 1987, The tectonic history of Kohistan and its implications for Himalayan structure: *J. Geol. Soc. London*, v. **144**, p. 377-391.

Coward, M.P., Butler, R.W.H., Chambers, A.F., Graham, R.H., Izatt, C.N., Khan, M.A., Knipe, R.J., Prior, D.J., Treloar, P.J., and Williams, M.P., 1988, Folding and imbrication of the Indian crust during Himalayan collision, *Tectonic evolution of the Himalayas and Tibet*, Volume **326**: London, United Kingdom, Royal Society of London, p. 89-116.

Cox, K.G., Bell, J.D., and Pankhurst, R.J., 1979, The Interpretation of igneous rocks: London, Allen and Unwin, XIII, 450 p.

Davidson, J.P., 1996, Deciphering mantle and crustal signatures in subduction zone magmatism: *Geophysical Monograph, American Geophysical Union*, v. **96**, p. 251-262.

Debon, F., Le-Fort, P., Dautel, D., Sonet, J., and Zimmermann, J.L., 1987, Granites of western Karakorum and northern Kohistan (Pakistan): a composite Mid- Creteceous to Upper Cenozoic magmatism: *Lithos*, v. **20**, p. 19-40.

DiPietro, J.A., Pogue, K.R., Hussain, A., and Ahmad, I., 1999, Geologic map of the Indus syntaxis and surrounding area, Northwest Himalaya, Pakistan, *Himalaya and Tibet; mountain roots to mountain tops*, Volume **328**: Boulder, CO, United States, Geological Society of America (GSA), p. 159-178.

DiPietro, J.A., Hussain, A., Ahmad, I., and Khan, M.A., 2000, The Main Mantle Thrust in Pakistan; its character and extent, *Tectonics of the Nanga Parbat syntaxis and the western Himalaya*, Volume **170**: London, United Kingdom, Geological Society of London, p. 375-393.

DiPietro, J.A., and Isachsen, C.E., 2001, U-Pb zircon ages from the Indian plate in northwest Pakistan and their significance to Himalayan and pre-Himalayan geologic history: *Tectonics*, v. **20**, p. 510-525.

Dumitru, T.A., 1993, A new computer-automated microscope stage system for fission-track analysis: *Nuclear Tracks and Radiation Measurements*, v. **21**, p. 575-580.

Elliott, T., Plank, T., Zindler, A., White, W., and Bourdon, B., 1997, Element transport from slab to volcanic front at the Mariana Arc: *Journal of Geophysical Research, B, Solid Earth and Planets*, v. **102**, p. 14,991-15,019.

Etchecopar, A., Vasseur, G., and Daignieres, M., 1981, An inverse problem in microtectonics for the determination of stress tensor from fault straition analysis: *Journal of Structural Geology*, v. **3**.

Etchecopar, A., 1984, *Etude des etats de contrainte en tectonique cassante et simulations de deformations plastiques (approche mathematique)* [These d'Etat thesis], Universite des Sciences et Techniques du Languedoc.

Fletcher, C.J.N., Leake, R.C., and Haslam, H.W., 1986, Tectonic setting, mineralogy and chemistry of a metamorphosed stratiform base metal deposit within the Himalayas of Pakistan: *Journal of the Geological Society of London*, v. **143**, p. 521-536.

Fraser, J., Searle, M.P., Parrish, R., and Noble, S., 1999, U-Pb geochronology on the timing of metamorphism and magmatism in the Hunza Karakoram: *TERRA NOSTRA*, v. **99**, p. 45-46.

Gaetani, M., and et al., 1995, Permian stratigraphy in the northern Karakorum, Pakistan: *Rivista Italiana di Paleontologia e Stratigrafia*, v. **101**, p. 107-152.

Gaetani, M., 1997, The Karakorum Block in Central Asia, from Ordovician to Cretaceous: *Sedimentary Geology*, v. **109**, p. 339-359.

Galbraith, R.F., 1981, On statistical models for fission track counts: *Journal of the International Association for Mathematical Geology*, v. **13**, p. 471-478.

Galbraith, R.F., and Laslett, G.M., 1993, Statistical-models for mixed fission-track ages: *Nuclear Tracks and Radiation Measurements*, v. **21**, p. 459-470.

Gansser, A., 1964, Geology of the Himalayas, *Interscience*: London, p. 289 pp.

Gapais, D., Bale, P., Choukroune, P., Cobbold, P.R., Mahjoub, Y., and Marquer, D., 1987, Bulk kinematics from shear zone patterns; some field examples: *Journal of Structural Geology*, v. **9**, p. 635-646.

George, M.T., Harris, N.B.W., and Butler, R.W.H., 1993, The tectonic implications of contrasting granite magmatism between the Kohistan island arc and the Nanga Parbat-Haramosh Massif, Pakistan Himalaya, *Himalayan tectonics*, Volume **74**: London, United Kingdom, Geological Society of London, p. 173-191.

Gibbs, A.D., 1983, Balanced cross-section construction from seismic sections in areas of extensional tectonics, *Balanced cross-sections and their geological significance; a memorial to David Elliott*, Volume **5**: Oxford-New York, International, Pergamon, p. 153-160.

Godard, M., Jousselin, D., and Bodinier, J.-L., 2000, Relationships between geochemistry and structure beneath a palaeo-spreading centre: a study of the mantle section in the Oman ophiolite: *EPSL*, v. **180**, p. 133-148.

Graham, C.M., and Powell, R., 1984, A garnet-hornblende geothermometer; calibration, testing, and application to the Pelona Schist, Southern California: *Journal of Metamorphic Geology*, v. **2**, p. 13-31.

Groshong, R.H., Jr., 1990, Unique determination of normal fault shape from hanging-wall bed geometry in detached half grabens, *The Hans Laubscher volume*, Volume **83**: Basel, Switzerland, Birkhaeuser Verlag, p. 455-471.

Hamblin, W.K., 1965, Origin of 'reverse drag' on the downthrown side of normal faults: *Geological Society of America Bulletin*, v. **76**, p. 1145-1164.

Hammarstrom, J.M., and Zen, E.a., 1986, Aluminum in hornblende; an empirical igneous geobarometer: *American Mineralogist*, v. **71**, p. 1297-1313.

Harris, L.B., and Cobbold, P.R., 1984, Development of conjugate shear bands during bulk simple shearing: *Journal of Structural Geology*, v. **7**, p. 37-44.

Holland, T., and Blundy, J., 1994, Non-ideal interactions in calcic amphiboles and their bearing on amphibole-plagioclase thermometry: *Contributions to Mineralogy and Petrology*, v. **116**, p. 433-447.

Hollister, L.S., Grissom, G.C., Peters, E.K., Stowell, H.H., and Sisson, V.B., 1987, Confirmation of the empirical correlation of Al in hornblende with pressure of solidification of calc-alkaline plutons: *American Mineralogist*, v. **72**, p. 231-239.

Hurford, A.J., and Green, P.F., 1983, The zeta age calibration of fission-track dating: *Chemical Geology*, v. **41**, p. 285-317.

Ionov, D.A., Savoyant, L., and Dupuy, C., 1992, Application of the ICP-MS technique to trace-element analysis of peridotites: *Geostandard Newslett.*, v. **16**, p. 311-315.

Jan, M.Q., 1980, Petrology of the obducted mafic metamorphites from the southern part of the Kohistan island arc sequence: *Geol. Bull. Univ. Peshawar*, v. **13**, p. 95-107.

Jan, M.Q., and Howie, R.A., 1980, Ortho- and clinopyroxene granulites of Swat Kohistan, northern Pakistan: *Mineral. Mag.*, v. **43**, p. 715-726.

Jan, M.Q., and Howie, R.A., 1981, The mineralogy and geochemistry of the metamorphosed basic and ultrabasic rocks of the Jijal Complex, Kohistan, NW Pakistan: *Journal of Petrology*, v. **22**, p. 85-126.

Jan, M.Q., Khattak, M.U.K., Parvez, M.K., and Windley, B.F., 1984, The Chilas stratiform complex: field and mineralogical aspects: *Geol. Bull. Univ. Peshawar*, v. **17**, p. 153-169.

Jan, M.Q., 1988, Geochemistry of amphibolites from the southern part of the Kohistan arc, N Pakistan: *Mineral. Mag.*, v. **52**, p. 147-159.

Jan, M.Q., and Windley, B.F., 1990, Chromian spinel-silicate chemistry in ultramafic rocks of the Jijal complex, northwest Pakistan: *Journal of Petrology*, v. **31**, p. 667-715.

Jan, M.Q., and Karim, A., 1995, Coronas and high-P veins in metagabbros of the Kohistan island arc, northern Pakistan; evidence for crustal thickening during cooling: *Journal of Metamorphic Geology*, v. **13**, p. 357-366.

Jochum, K.P., and Hofmann, A.W., 1998, Nb/ Ta in MORB and continental crust; implications for a superchondritic Nb/ Ta reservoir in the mantle, *AGU 1998 spring meeting*, Volume **79**: Washington, DC, United States, American Geophysical Union, p. 354.

Kakar, S.K., Mian, S.B., and Khan, J., 1971, The geology of Jandal valley, western Dir: *Geol. Bull. Univ. Peshawar*, v. **6**, p. 54-73.

Kalfoun, 2001, [PhD thesis], Montpellier Univ.

Kay, R.W., 1978, Aleutian magnesian andesites; melts from subducted Pacific Ocean crust: *Journal of Volcanology and Geothermal Research*, v. **4**, p. 117-132.

Kazmi, A.H., Lawrence, R.D., Dawood, H., Snee, L.W., and Hussain, S.S., 1984, Geology of the Indus Suture Zonr in the Mingora - Shangla area of Swat, North Pakistan: *Geol. Bull. Univ. Peshawar*, v. **17**, p. 127-144.

Kazmi, A.H., and Jan, M.Q., 1997, Geology and tectonics of Pakistan: Karachi, Graphic Puplishers, 554 p.

Khan, J., 1979, Geology of the Baraul valley, Dir: *Geol. Bull. Univ. Peshawar*, v. **11**, p. 153-162.

Khan, M.A., Jan, M.Q., Windley, B.F., Tarney, J., and Thirlwall, M.F., 1989, The Chilas mafic-ultramafic igneous complex; the root of the Kohistan island arc in the Himalaya of northern Pakistan, *Tectonics of the western Himalayas*, Volume **232**: Boulder, CO, United States, Geological Society of America (GSA), p. 75-94.

Khan, M.A., Jan, M.Q., and Weaver, B.L., 1993, Evolution of the lower arc crust in Kohistan, N. Pakistan; temporal arc magmatism through early, mature and intra-arc rift stages, *Himalayan tectonics*, Volume **74**: London, United Kingdom, Geological Society of London, p. 123-138.

Khan, T., 1994, *Evolution of the 'upper and middle crust' in the Kohistan island arc, northwestern Pakistan.* [PhD thesis]: Peshawar, University of Peshawar.

Khan, T., Khan, M.A., Jan, M.Q., and Latif, M., 1995, Geology of a part of the Kohistan Terrane between Gilgit and Chilas, North Pakistan; regional tectonic implications, *First Nepal geological congress*, Volume **12**: Kathmandu, United States, Nepal Geological Society, p. 9.

Klootwijk, C.T., Nazirullah, R., and de Jong Kees, A., 1986a, Palaeomagnetic constraints on formation of the Mianwali Reentrant, Trans-Indus and western Salt Range, Pakistan: *Earth and Planetary Science Letters*, v. **80**, p. 394-414.

Klootwijk, C.T., Sharma, M.L., Gergan, J., Shah, S.K., and Gupta, B.K., 1986b, Rotational overthrust of the northwestern Himalaya; further palaeomagnetic evidence from the Riasi thrust sheet, Jammu Foothills, India: *Earth and Planetary Science Letters*, v. **80**, p. 375-393.

Kohn, M.J., and Spear, F.S., 1990, Two new barometers for garnet amphibolites with applications to eastern Vermont: *American Mineralogist*, v. **75**, p. 89-96.

LaFrance, B., John, B.E., and Frost, B.R., 1998, Ultra high-temperature and subsolidus shear zones; examples from the Poe Mountain anorthosite, Wyoming: *Journal of Structural Geology*, v. **20**, p. 945-955.

Lahmeyer International, 1998, Allai Khwar Feasability study, Lahmeyer International.

Launeau, P., Bouchez, J.L., and Benn, K., 1990, Shape preferred orientation of object populations; automatic analysis of digitized images: *Tectonophysics*, v. **180**, p. 201-211.

Launeau, P., and Robin, P.Y.F., 1996, Fabric analysis using the intercept method: *Tectonophysics*, v. **267**, p. 91-119.

Lawrence, R.D., and Ghauri, A.A.K., 1983, Evidence for active faulting in Chilas district, NW Pakistan: *Geol. Bull. Univ. Peshawar*, v. **16**, p. 1-10.

Leake, B.E., 1978, Nomenclature of amphiboles: *The Canadian Mineralogist*, v. **16**, p. 501-520.

Lee, H.Y., and Ganguly, J., 1988, Equilibrium compositions of co-existing garnet and orthopyroxene; experimental determinations in the system FeO-MgO-Al (sub 2) O (sub 3) -SiO (sub 2) , and applications: *Journal of Petrology*, v. **29**, p. 93-113.

LeFort, P., Michard, A., Sonet, J., and Zimmermann, J.L., 1983, Petrography, geochemistry and geochronology of some samples from the Karakorum axial batholith, northern Pakistan, *Granites of Himalayas, Karakorum and Hindu Kush*: Lahore, Pakistan, Inst Geol. Punjab Univ.

Lisle, R.J., and Vandycke, S., 1996, Separation of multiple stress events by fault striation analysis; an example from Variscan and younger structures at Ogmore, South Wales: *Journal of the Geological Society of London*, v. **153**, p. 945-953.

Majid, M., and Shah, M.T., 1985, Mineralogy of the blue-schist metagraywacke from the Shergarh Sar, Allai kohistan, N. Pakistan area: *Geol. Bull. Univ. Peshawar*, v. **18**, p. 44-52.

Malinconico, L.L., 1989, Crustal thickness estimates for the western Himalaya, *in* Malinconico, L.L., and Lillie, R.J., eds., *Tectonics of the Western Himalayas*, Volume **232**, Geol. Soc. Amer., Spec. Paper, p. 237-242.

March, A., 1932, Mathematische Theorie der Regelung nach der Korngestalt bei affiner Deformation: *Zeitschrift Kristallographie*, v. **81**, p. 285-297.

McDonough, W.F., Sun, S.S., Ringwood, A.E., Jagoutz, E., and Hofmann, A.W., 1992, Potassium, rubidium, and cesium in the Earth and Moon and the evolution of the mantle of the Earth, *The Taylor Colloquium; Origin and evolution of planetary crusts*, Volume **56**: Oxford, International, Pergamon, p. 1001-1012.

McDougall, I., and Harrison, T.M., 1988, Geochronology and thermochronology by the "SUP 40" Ar/ "SUP 39" Ar method.

Mezger, K., Essene, E.J., and Halliday, A.N., 1992, Closure temperatures of the Sm-Nd system in metamorphic garnets: *Earth and Planetary Science Letters*, v. **113**, p. 397-409.

Mikoshiba, M.U., Takahashi, Y., Takahashi, Y., Kausar, A.B., Khan, T., Kubo, K., and Shirahase, T., 1999, Rb-Sr isotopic study of the Chilas igneous complex, Kohistan, northern Pakistan, *in* Macfarlane, A., Sorkhabi, R.B., and Quade, J., eds., *Himalaya and Tibet; mountain roots to mountain tops*, Volume **328**: Boulder, CO, United States, Geological Society of America (GSA), p. 47-57.

Miller, D.J., Loucks, R.R., and Ashraf, M., 1991, Platinum group elements mineralisation in the Jijal layered mafic-ultramafic complex, Pakistani Himalayas: *Economic Geology*, v. **86**, p. 1093-1102.

Mitra, G., 1978, Ductile deformation zones and mylonites: The mechanical processes involved in the deformation of crystalline basement rocks: *American Journal of Science*, v. **278**, p. 1057-1084.

Miyashiro, A., 1975, Classification, characteristics, and origin of ophiolites: *Journal of Geology*, v. **83**, p. 249-281.

Molnar, P., and Tapponnier, P., 1975, Cenozoic Tectonics of Asia: Effects of a Continental Collision: *Science*, v. **189**, p. 419-426.

Molnar, P., and Chen, W.P., 1978, Evidence of large Cainozoic crustal shortening of Asia: *Nature*, v. **273**, p. 218-220.

Molnar, P., 1984, Structure and tectonics of the Himalaya; constraints and implications of geophysical data: *Annual Review of Earth and Planetary Sciences*.

Morimoto, N., 1988, Nomenclature of pyroxenes: *Mineralogical Magazine*, v. **52**, p. 535-550.

Nemcok, M., and Lisle, R.J., 1995, A stress inversion procedure for polyphase fault/ slip data sets: *Journal of Structural Geology*, v. **17**, p. 1445-1453.

Newton, R.C., and Perkins, D., III, 1982, Thermodynamic calibration of geobarometers based on the assemblages garnet-plagioclase-orthopyroxene (clinopyroxene)-quartz: *American Mineralogist*, v. **67**, p. 203-222.

Nowell, G.M., Kempton, P.D., Noble, S.R., Fitton, J.G., Saunders, A.D., Mahoney, J.J., and Taylor, R.N., 1998, High precision Hf isotope measurements of MORB and OIB by thermal ionisation mass spectrometry; insights into the depleted mantle: *Chemical Geology*, v. **149**, p. 211-233.

Nunns, A.G., 1991, Structural restoration of seismic and geologic sections in extensional regimes: *AAPG Bulletin*, v. **75**, p. 278-297.

Patchett, P.J., and Tatsumoto, M., 1980, Hafnium isotope variations in oceanic basalts: *Geophysical Research Letters*, v. **7**, p. 1077-1080.

Patriat, P., and Achache, J., 1984, India-Eurasia collision chronology has implications for crustal shortening and driving mechanism of plates: *Nature (London)*, v. **311**, p. 615-621.

Pattison, D.R.M., and Newton, R.C., 1989, Reversed experimental calibration of the garnet-clinopyroxene Fe-Mg exchange thermometer: *Contributions to Mineralogy and Petrology*, v. **101**, p. 87-103.

Pearce, J.A., 1976, Statistical analysis of major element patterns in basalts: *Journal of Petrology*, v. **17**, p. 15-43.

Pearce, J.A., Harris, N.B.W., and Tindle, A.G., 1984, Trace element discrimination diagrams for the tectonic interpretation of granitic rocks: *Journal of Petrology*, v. **25**, p. 956-983.

Pearce, J.A., Kempton, P.D., Nowell, G.M., and Noble, S.R., 1999, Hf-Nd element and isotope perspective on the nature and provenance of mantle and subduction components in Western Pacific arc-basin systems: *Journal of Petrology*, v. **40**, p. 1579-1611.

Pearce, T.H., Gorman, B.E., and Birkett, T.C., 1977, The relationship between major element chemistry and tectonic environment of basic and intermediate volcanic rocks: *Earth and Planetary Science Letters*, v. **36**, p. 121-132.

Peate, D.W., Pearce, J.A., Hawkesworth, C.J., Colley, H., Edwards, C.M.H., and Hirose, K., 1997, Geochemical variations in Vanuatu Arc lavas; the role of subducted material and a variable mantle wedge composition: *Journal of Petrology*, v. **38**, p. 1331-1358.

Peate, D.W., and Pearce, J.A., 1998, Causes of spatial compositional variations in Mariana arc lavas: Trace element evidence: *Island Arc*, v. **7**, p. 479-495.

Pennington, W.D., 1979, Summary of field and seismic observations of the Pattan Earthquake- 28 December, 1974, *in* Farah, A., and Dejong, K.A., eds., *Geodynamics of Pakistan*: Quetta, Geol. Surv. Pak.

Petterson, M.G., Crawford, M.B., and Windley, B.F., 1993, Petrogenetic implications of neodymium isotope data from the Kohistan Batholith, North Pakistan: *Journal of the Geological Society of London*, v. **150**, p. 125-129.

Petterson, M.G., and Windley, B.F., 1985, Rb-Sr dating of the Kohistan arc-batholith in the Trans-Himalaya of North Pakistan, and tectonic implications: *Earth and Planetary Science Letters*, v. **74**, p. 45-57.

Petterson, M.G., and Windley, B.F., 1991, Changing source regions of magmas and crustal growth in the Trans-Himalayas; evidence from the Chalt Volcanics and Kohistan Batholith, Kohistan, northern Pakistan: *Earth and Planetary Science Letters*, v. **102**, p. 326-341.

Petterson, M.G., Windley, B.F., and Luff, I.W., 1991a, The Chalt Volcanics, Kohistan, N Pakistan; high-Mg tholeiitic and low-Mg calc-alkaline volcanism in a Cretaceous island arc, *Geology and geodynamic evolution of the Himalayan collision zone; Part 1*, Volume **17**: Oxford-New York-Toronto, International, Pergamon, p. 19-30.

Petterson, M.G., Windley, B.F., and Sullivan, M., 1991b, A petrological, chronological, structural and geochemical review of Kohistan Batholith and its relationship to regional tectonics, *Geology and geodynamic evolution of the Himalayan collision zone; Part 1*, Volume **17**: Oxford-New York-Toronto, International, Pergamon, p. 47-70.

Powell, R., and Holland, T.J.B., 1988, An internally consistent dataset with uncertainties and correlations; 3, Applications to geobarometry, worked examples and a computer program: *Journal of Metamorphic Geology*, v. **6**, p. 173-204.

Pudsey, C.J., Coward, M.P., Luff, I.W., Shackleton, R.M., Windley, B.F., and Jan, M.Q., 1985, Collision zone between the Kohistan Arc and the Asian Plate in NW Pakistan: *Transactions of the Royal Society of Edinburgh: Earth Sciences*, v. **76**, p. 463-479.

Pudsey, C.J., 1986, The northern suture, Pakistan: Margin of a Cretaceous island arc: *Geol. Mag.*, v. **123**, p. 405-423.

Ramsay, J.G., 1980, Shear zone geometry; a review: *Journal of Structural Geology*, v. **2**, p. 83-99.

Riedel, W., 1929, Zur Mechanik geologischer Brucherscheinungen: *Centralblatt Mineralogie, Abteilung B*, p. 354-368.

Ringuette, L., Martignole, J., and Windley Brian, F., 1999, Magmatic crystallization, isobaric cooling, and decompression of the garnet-bearing assemblages of the Jijal Sequence (Kohistan Terrane, western Himalayas): *Geology*, v. **27**, p. 139-142.

Rink, M., 1976, A computerized quantitative image analysis procedure for investigating features and an adapted image process: *Journal of Microscopy*, v. **107**, p. 267-286.

Rowan, M.G., and Kligfield, R., 1989, Cross section restoration and balancing as aid to seismic interpretation in extensional terranes: *AAPG Bulletin*, v. **73**, p. 955-966.

Royden, L.H., 1993, Evolution of retreating subduction boundaries formed during continental collision: *Tectonics*, v. **12**, p. 629-638.

Rudnick, R.L., and Fountain, D.M., 1995, Nature and composition of the continental crust; a lower crustal perspective: *Reviews of Geophysics*, v. **33**, p. 267-309.

Ruzhentsev, S.V., and Shvolman, V.A., 1981, Tectonics and structure of the Pamir metamorphics, *Metamorphic tectonites of the Himalaya*: New Delhi, India, Today and Tomorrow's.

Saunders, A.D., and Tarney, J., 1984, Geochemical characteristics and tectonic significance of back-arc basins, *Marginal basin geology; volcanic and associated sedimentary and tectonic processes in modern and ancient marginal basins*, Volume **16**: London, United Kingdom, Geological Society of London, p. 59-76.

Schaltegger, U., Zeilinger, G., Frank, M., and Burg, J.P., 2001, Multiple mantle sources during island arc magmatism: U-Pb and Hf isotopic evidence from the Kohistan arc complex, Pakistan.: *Geology*, v. **submitted**.

Schmidt, M.W., 1992, Amphibole composition in tonalite as a function of pressure; an experimental calibration of the Al-in-hornblende barometer: *Contributions to Mineralogy and Petrology*, v. **110**, p. 304-310.

Searle, M.P., 1991, Geology and tectonics of the Karakoram Mountains: Chichester, United Kingdom, John Wiley & Sons, 358 p.

Searle, M.P., and Tirrul, R., 1991, Structural and thermal evolution of the Karakoram crust: *Journal of the Geological Society of London*, v. **148p1**, p. 65-82.

Searle, M.P., and Khan, M.A., 1993, Geological Map of North Pakistan.

Seeber, L., and Armbruster, J., 1979, Seismicity of the Hazara Arc in northern Pakistan; decollement vs. basement faulting, *in* Farah, A., and Dejong, K.A., eds., *Geodynamics of Pakistan*: Quetta, Geological Survey of Pakistan, p. 131-142.

Seeber, L., Armbruster, J.G., and Quittmeyer, R.C., 1981, Seismicity and continental subduction in the Himalayan arc, *Zagros, Hindu Kush, Himalaya; geodynamic evolution*, Volume **3**: Washington, DC, United States, American Geophysical Union, p. 215-242.

Seward, D., 1989, Cenozoic basin histories determined by fission-track dating of basement granites, South Island, New Zealand: *Chemical Geology; Isotope Geoscience Section*, v. **79**, p. 31-48.

Shah, M.T., and Majid, M., 1985, Major and trace element variations in the lavas of Sergarh Sar area and their significance with respect to the Kohistan tectonic anomaly: *Geol. Bull Univ. Peshawar*, v. **18**, p. 163-188.

Shah, M.T., Thorpe, R.I., and Siddique, S.A., 1992, Lead isotope signature of the Proterozoic sediment-hosted base metal deposits at the margin of the Indian Plate in Besham area, northern Pakistan: *Geological Bulletin, University of Peshawar*.

Shvolman, V.A., 1978, Relicts of the Mesotethys in the Pamirs: *Himalayan Geology*.

Sigmarsson, O., Martin, H., and Knowles, J., 1998, Melting of a subducting oceanic crust from U-Th disequilibria in austral Andean lavas: *Nature*, v. **394**, p. 566-569.

Smith, H.A., Chamberlain, C.P., and Zeitler, P.K., 1994, Timing and duration of Himalayan metamorphism within the Indian Plate, Northwest Himalaya, Pakistan: *Journal of Geology*, v. **102**, p. 493-508.

Spear, F.S., and Kohn, M.J., 1995, Program Thermobarometry: Troy, Department of Geology, Rensselaer Polytechnic Institute, Troy, New York 12180.

Stacey, J.S., and Kramers, J.D., 1975, Approximation of terrestrial lead isotope evolution by a two-stage model: *Earth and Planetary Science Letters*, v. **26**, p. 207-221.

Sullivan, M.A., Windley, B.F., Saunders, A.D., Haynes, J.R., and Rex, D.C., 1993, A palaeogeographic reconstruction of the Dir Group; evidence for magmatic arc migration within Kohistan, N. Pakistan, *in* Treloar, P.J., and Searle, M.P., eds., *Himalayan tectonics.*, Volume **74**: Geological Society Special Publications: London, United Kingdom, Geological Society of London, p. 139-160.

Sun, S.S., 1980, Lead isotopic study of young volcanic rocks from mid-ocean ridges, ocean islands and island arcs, *The evidence for chemical heterogeneity in the Earth's mantle*, Volume **297**: London, United Kingdom, Royal Society of London, p. 409-445.

Sun, S.S., and McDonough, W.F., 1989, Chemical and isotopic systematics of oceanic basalts; implications for mantle composition and processes, *Magmatism in the ocean basins*, Volume **42**: London, United Kingdom, Geological Society of London, p. 313-345.

Tahirkheli, R.A.K., 1979, Geotectonic evolution of Kohistan, *in* Tahirkheli, R.A.K., and Jan, M.Q., eds., *Geology of Kohistan, Karakoram Himalaya, northern Pakistan.*, Volume **11**: Geological Bulletin, University of Peshawar: Peshawar, Pakistan, University of Peshawar, Department of Geology, p. 113-130.

Tahirkheli, R.A.K., Mattauer, M., Proust, F., and Tapponnier, P., 1979, The India-Eurasia Suture Zone in Northern Pakistan: Synthesis and interpretation of recent data of plate scale., *in* Farah, A., and Jong, K.A.D., eds., *Geodynamics of Pakistan*: Quetta, Geological Survey of Pakistan, p. 125-130.

Tahirkheli, R.A.K., 1982, Geology of the Himalaya, Karakoram and Hindukush in Pakistan: *Geol. Bull. Univ. Peshawar*, v. **15**, p. 1-51.

Taylor, S.R., and McLennan, S.M., 1981, The composition and evolution of the continental crust; rare earth element evidence from sedimentary rocks, *The origin and evolution of the Earth's continental crust*, Volume **301**: London, United Kingdom, Royal Society of London, p. 381-399.

Taylor, S.R., and McLennan, S.M., 1985, The continental crust its composition and evolution an examination of the geochemical record preserved in sedimentary rocks: Cambridge, Blackwell, XV, 312 p.

Taylor, S.R., and McLennan, S.M., 1995, The geochemical evolution of the continental crust: *Reviews of Geophysics*, v. **33**, p. 241-265.

Tchalenko, J.S., 1968, The evolution of kink bands and the development of compression textures in sheared clays: *Tectonophysics*, v. **6**, p. 159-174.

Treloar, P.J., Rex, D.C., Guise, P.G., Coward, M.P., Searle, M.P., Windley, B.F., Petterson, M.G., Jan, M.Q., and Luff, I.W., 1989a, K-Ar and Ar-Ar geochronology of the Himalayan collision in NW Pakistan; constraints on the timing of suturing, deformation, metamorphism and uplift: *Tectonics*, v. **8**, p. 881-909.

Treloar, P.J., Broughton, R.D., Williams, M.P., Coward, M.P., and Windley, B.F., 1989b, Deformation, metamorphism and imbrication of the Indian plate, south of the Main Mantle Thrust, north Pakistan: *Journal of Metamorphic Geology*, v. **7**, p. 111-125.

Treloar, P.J., Williams, M.P., and Coward, M.P., 1989c, Metamorphism and crustal stacking in the North Indian Plate, North Pakistan: *Tectonophysics*, v. **165**, p. 167-184.

Treloar, P.J., Brodie, K.H., Coward, M.P., Jan, M.Q., Khan, M.A., Knipe, R.J., Rex, D.C., and Williams, M.P., 1990, The evolution of the Kamila shear zone, Kohistan, Pakistan, *in* Salisbury, M.H., and Fountain, D.M., eds., *Exposed cross-sections of the continental crust; proceedings.*, Volume **317**: NATO ASI Series. Series C: Mathematical and Physical Sciences: Dordrecht-Boston, International, D. Reidel Publishing Company, p. 175-214.

Treloar, P.J., Rex, D.C., and Williams, M.P., 1991, The role of erosion and extension in unroofing the Indian Plate thrust stack. Pakistan, Himalaya: *Geological Magazine*, v. **128**, p. 465-478.

Treloar, P.J., Petterson, M.G., Jan, M.Q., and Sullivan, M.A., 1996, A re-evaluation of the stratigraphy and evolution of the Kohistan arc sequence, Pakistan Himalaya: implications for magmatic and tectonic arc-building processes: *Journal of the Geological Society*, v. **153**, p. 681-693.

Vince, K.J., and Treloar, P.J., 1996, Miocene, north-vergent extensional displacements along the Main Mantle Thrust, NW Himalaya, Pakistan: *Journal of Geological Society*, v. **153**, p. 677-680.

Wade, J., and Wood, B.J., 2001, The Earth's "missing" niobium may be in the core: *Nature (London)*, v. **409**, p. 75-78.

Wartho, J.-A., Rex, D.C., and Guise, P.G., 1996, Excess argon in amphiboles linked to greenschist facies alterations in the Kamila Amphibolite Belt, Kohistan island arc system, northern Pakistan: insights from 40Ar/39Ar step-heating and acid leaching experiments: *Geol. Mag.*, v. **133**, p. 595-606.

Weaver, B.L., and Tarney, J., 1984, Major and trace element composition of the continental lithosphere, *Structure and evolution of the continental lithosphere*, Volume **15**: Oxford-New York-Toronto, International, Pergamon, p. 39-68.

White, N., and Yielding, G., 1991, Calculating normal fault geometries at depth; theory and examples, *The geometry of normal faults*, Volume **56**: London, United Kingdom, Geological Society of London, p. 251-260.

White, W.M., and Patchett, J., 1984, Hf-Nd-Sr isotopes and incompatible element abundances in island arcs; implications for magma origins and crust-mantle evolution: *Earth and Planetary Science Letters*, v. **67**, p. 167-185.

Wilson, M., 1989, Igneous petrogenesis:,, p. XVII, 466 S.

Yamamoto, H., 1993, Contrasing metamorphic P-T-time paths of the Kohistan granulites and tectonics of of the western Himalayas: *Journal of the Geological Society*, v. **150**, p. 843-856.

Yamamoto, H., and Nakamura, E., 1996, Sm-Nd dating of garnet granulites of Jijal complex of the Kohistan arc, northern Pakistan.: *J. Geol. Soc., London*, v. **153**, p. 965-969.

Yamamoto, H., and Yoshino, T., 1998, Superposition of replacements in the mafic granulites of the Jijal Complex of the Kohistan Arc, northern Pakistan; dehydration and rehydration within deep arc crust: *Lithos*, v. **43**, p. 219-234.

Yamamoto, H., and Nakamura, E., 2000, Timing of magmatic and metamorphic events in the Jijal Complex of the Kohistan Arc deduced from Sm-Nd dating of mafic granulites, *in* Khan, M.A., Treloar, P.J., Searle, M.P., and Jan, M.Q., eds., *Tectonics of the Nanga Parbat syntaxis and the western Himalaya*, Volume **170**: London, United Kingdom, Geological Society of London, p. 313-319.

Yoshida, M., Zaman, H., and Ahmad, M.N., 1996, Paleopositions of Kohistan Arc and surrounding Terranes Since Cretaceous Time: the Paleomagnetic Constraints: *Proceedings of Geoscience Colloquim, Geoscience Lab, GSP*, v. **15**, p. 83-101.

Yoshino, T., Yamamoto, H., Okudaire, T., and Toriumi, M., 1998, Crustal Thickening of the lower crust of the Kohistan arc (N. Pakistan) deduced from Al zoning in clinopyroxene and plagioclase: *J. metamorphic Geol.*, v. **16**, p. 729-748.

Zanchi, A., 1993, Structural evolution of the North Karakoram cover, North Pakistan, *Himalayan tectonics*, Volume **74**: London, United Kingdom, Geological Society of London, p. 21-38.

Zeilinger, G., Burg, J.P., Chaudhry, N., Dawood, H., and Hussain, S., 2000, Fault systems and paleo-stress tensors in the Indus Suture Zone (NW Pakistan): *Journal of Asian Earth Sciences*, v. **18**, p. 547-559.

Zeitler, P., Tahirkheli, R.A.K., Naeser, C., Johnson, N., and Lyons, J., 1981, Preliminary fission track ages from the Swat valley, Northern Pakistan: *Geol. Bull. Univ. Peshawar*, v. **13**, p. 63-65.

Zeitler, P.K., Tahirkheli, R.A.K., Naeser, C.W., and Johnson, N.M., 1982, Unroofing history of a suture zone in the Himalayaof Pakistan by means of fission-track annealing ages: *Earth and Planetary Science Letters*, v. **57**, p. 227-240.

Zeitler, P.K., Sutter, J.F., Williams, I.S., Zartman, R.E., and Tahirkheli, R.A.K., 1989, Geochronology and temperature history of the Nanga Parbat-Haramosh Massif, Pakistan, *Tectonics of the western Himalayas*, Volume **232**: Boulder, CO, United States, Geological Society of America (GSA), p. 1-22.

Zeitler, P.K., 1985, Cooling history of the NW Himalaya, Pakistan: *Tectonics*, v. **4**, p. 127-151.

Zeitler, P.K., Chamberlain, C.P., and Smith, H.A., 1993, Synchronous anatexis, metamorphism, and rapid denudation at Nanga Parbat (Pakistan Himalaya): *Geology*, v. **21**, p. 347-350.

List of Figures and Tables

Curriculum Vitae

personal data

Surname:	Zeilinger
Given names:	Gerold Dieter
Date of birth:	21.11.1968
Place of birth:	Neuendettelsau (Germany)
Residence:	Scheuchzerstrasse 149, 8006 Zurich
Nationality:	German
Status:	not married

studies

1. July 1997 – 16. November 2001 Ph.D. studies at Swiss Federal Institute of Technology, Zurich, Switzerland

WS 1994/95 – SS 1997
Eberhard - Karls University Tübingen, Germany, Geology/Palaeontology
Diploma degree in Geology/Paleontology, June 1997

WS 1991/92 - SS 1994
Westf. Wilhelms-University Münster, Germany, Geology/Palaeontology
1. degree in Geology/Paleontology at October 1993

education, civil service, jobs

1990 – 1991	Haus der Volksbildung Ansbach e.G., stagemanager
1989 – 1990	civil service at Rangau - Hospital, Ansbach
1979 – 1989	August Graf v. Platen, secondary school, Ansbach

This research work aimed at elucidating two main questions: (1) Is there a fabric in the mid-crustal plutons that is related to the kinematics of the subduction system and (2) which deformation mechanisms were involved during the arc evolution.

The Kohistan Arc Complex (KAC), now located between the Eurasian and Indian Plates, and thus part of the NW Himalayan collisional system provides excellent outcrops to tackle the raised questions. Results of detailed mapping, structural traverses, petrological/geochemical analyses and geochronological measurements were linked with the structural analysis of shear zones to document the deformation history of the former lower part of the KAC.

The base of the arc is characterized by imbricate (meta-) gabbroic, dioritic, granitic and tonalitic rocks. Strain localisation took place continuously from magmatic emplacement to solid state deformation during cooling of the plutons and formed 3 successive sets of shear zones. The anastomosing pattern of shear zones described here represents arc-related deformation during subduction of the Tethys oceanic lithosphere below the KAC.